THE MINISTRY OF SCIENCE AND HIGHER EDUCATION OF THE RUSSIAN FEDERATION

ST. PETERSBURG STATE POLYTECHNICAL UNIVERSITY

JOURNAL

Physics and Mathematics

VOLUME 17, No. 3.2, 2024

Peter the Great St. Petersburg
Polytechnic University
2024

ST. PETERSBURG STATE POLYTECHNICAL UNIVERSITY JOURNAL.
PHYSICS AND MATHEMATICS

The journal is included in the List of leading peer-reviewed scientific journals and other editions to publish major findings of theses for the research degrees of Doctor of Sciences and Candidate of Sciences.

The publications are presented in the VINITI RAS Abstract Journal and Ulrich's Periodical Directory International Database.

The journal is published since 2008 as part of the periodical edition 'Nauchno-tekhnicheskie vedomosti SPb-GPU'.

The journal is registered with the Federal Service for Supervision in the Sphere of Telecom, Information Technologies and Mass Communications (ROSKOMNADZOR). Certificate ПИ № ФС77-52144 issued December 11, 2012.

The journal is distributed through the CIS countries catalogue, the «Press of Russia» joint catalogue and the «Press by subscription» Internet catalogue. The subscription index is **71823.**

The journal is in the **Web of Science** (Emerging Sources Citation Index), **Scopus**, the **Russian Science Citation Index** (RSCI) and the **Directory of Open Access Journals** (DOAJ) databases.

© Scientific Electronic Library (http://www.elibrary.ru).

Address: 195251 Politekhnicheskaya St. 29, St. Petersburg, Russia.

Phone: (812) 294-22-85.
http://ntv.spbstu.ru/physics

PREFACE

11th International School and Conference on Optoelectronics, Photonics, Engineering and Nanostructures (SPb OPEN – 2024) / 11-я Международная школа-конференция по оптоэлектронике, фотонике, инженерии и наноструктурам

The 11th International School and Conference on Optoelectronics, Photonics, Engineering and Nanostructures (Saint-Petersburg OPEN 2024) was held from May 14 to May 17, 2024. It continues the annual schools and seminars for young scientists on physics and technology of nanostructures, organized since 2009, spearheaded by Zhores Alferov, RAS Academician and winner of the 2000 Nobel Prize in Physics.

The School was organized by the St. Petersburg Higher School of Economics, Peter the Great St. Petersburg Polytechnic University, the World-Class Research Center for Advanced Digital Technologies and the Alferov University with the support of Photonics Russia, Special Systems Photonics LLC and OOO "Aktivnaia Fotonika".

The Program Committee of the School and Conference selected 281 papers by young scientists, graduate and undergraduate students from 25 cities in Russia. The same as last year, the average age of the attendees was under 27 years old, 78% of the reports were presented by attendees under 30.

Presentations were given in six panels:
- Synthesis and structural properties of semiconductor materials and nanostructures,
- Lasers, solar cells, other optoelectronic devices,
- Nanophotonics, spectroscopy, microresonators, optical properties, plasmonics,
- Biophysics, nanobiotechnology, biophotonics
- Electrical, magnetic and microwave characteristics and devices,
- Other aspects of nanotechnology.

The highest percentage of reports (26%) were given in the section "Nanophotonics...", closely followed by "Synthesis..." with 23% of reports.

In addition to poster presentations from young scientists, the programme included a series of keynote speeches by prominent researchers, outlining the main advances and challenges in various fields of physics and technology. In total, 89 leading scientists participated in the conference. The keynote speakers included:
- Victor Soyfer (Samara University, Samara)
- Anatoly Pushkarev (ITMO University, St. Petersburg)
- Vladimir Drachev (Skoltech, Skolkovo)
- Alexander Vul' (Ioffe Institute, St. Petersburg)
- Vitaly Shchukin (VI Systems, Germany)
- Anton Krivtsov (Peter the Great St. Petersburg Polytechnic University, St. Petersburg)
- Evgenii Lutsenko (B.I. Stepanov Institute of Physics, National Academy of Sciences of Belarus)
- Yuriy Dedkov (Shanghai University, China)
- Pavel Frantsuzov (Institute of Chemical Kinetics and Combustion, Novosibirsk)
- Evgeny Viktorov (ITMO University, St. Petersburg)

The same as last year, the peer-reviewed reports from the conference are published in St. Petersburg State Polytechnical University Journal: Physics and Mathematics. The Programme Committee of SPbOPEN-2024 hopes that the range of subjects presented at the conference will be of interest to the journal's audience. We would like to thank the journal for giving us the opportunity to publish the proceedings, and thank the reviewers for useful recommendations and constructive criticism. We of course express our gratitude to all participants of the conference.

We invite young scientists, graduate and undergraduate students to take part in the next Saint Petersburg OPEN School and Conference in 2025. Please visit https://spb.hse.ru/spbopen/ for more details.

Alexey Zhukov
Higher School of Economics, St. Petersburg
St. Petersburg School of Physics, Mathematics, and Computer Science
aezhukov@hse.ru

Contents

Condensed matter physics

Simulation of physical processes

Atom physics and physics of clusters and nanostructures

Experimental Technique and Devices

Physical electronics

Physical optics

Physical materials technology

Biophysics and medical physics

Radiophysics

CONDENSED MATTER PHYSICS

Conference materials
UDC 537.9
DOI: https://doi.org/10.18721/JPM.173.201

Hybrid state of Fabry–Perot and Tamm plasmon-polariton modes in structures with different plasmon layers

S.V. Osmanov✉, T.V. Mikhailova

V.I. Vernadsky Crimean Federal University, Simferopol, Russia

✉ osmanovfti1@mail.ru

Abstract. The paper presents the investigation of magnetophotonic crystals with different metal layers for the formation of a Tamm plasmon polariton. It was revealed that the structure with the Ag layer has the resonance with a higher optical quality factor. It is shown how a change in the symmetry of the structure affects the properties of the hybrid state of Fabry–Perot and Tamm plasmon polariton modes. The effect of oblique incidence and polarization of incident light on the localization of light in the layers of the structure is demonstrated.

Keywords: Tamm plasmon polariton, magnetophotonic crystals, magneto-optics

Funding: Project no. 19-72-20154, https://rscf.ru/project/19-72-20154

Citation: Osmanov S.V., Mikhailova T.V., Hybrid state of Fabry–Perot and Tamm plasmon-polariton modes in structures with different plasmon layers, St. Petersburg State Polytechnical University Journal. Physics and Mathematics. 17 (3.2) (2024) 10–13. DOI: https://doi.org/10.18721/JPM.173.201

Материалы конференции
УДК 537.9
DOI: https://doi.org/10.18721/JPM.173.201

Гибридное состояние мод Фабри – Перо и таммовского плазмон-поляритона в структурах с различными плазмонными слоями

С.В. Османов✉, Т.В. Михайлова

Крымский федеральный университет имени В.И. Вернадского, г. Симферополь, Россия

✉ osmanovfti1@mail.ru

Аннотация. В статье представлено исследование магнитофотонных кристаллов с различными металлическими слоями для формирования таммовского плазмон-поляритона. Было обнаружено, что структура со слоем Ag обладает наиболее добротным резонансом. Показано, как изменение симметрии структуры влияет на свойства гибридного состояния мод Фабри – Перо и таммовского плазмон-поляритона. Продемонстрировано влияние наклона и поляризации падающего излучения на локализацию света в слоях структуры.

Ключевые слова: Таммовский плазмон-поляритон, магнитофотонные кристаллы, магнитооптика

Финансирование: Проект № 19-72-20154, https://rscf.ru/project/19-72-20154.

Ссылка при цитировании: Османов С.В., Михайлова Т.В. Гибридное состояние мод Фабри-Перо и таммовского плазмон-поляритона в структурах с различными плазмонными слоями // Научно-технические ведомости СПбГПУ. Физико-математические науки. 2024. Т. 17. № 3.2. С. 10–13. DOI: https://doi.org/10.18721/JPM.173.201

Introduction

In magnetophotonic crystals (MPCs) based on iron garnet with a single Fabry–Perot mode, as well as in the structures with formation of optical Tamm plasmon-polariton mode (TPP), an increase in magneto-optical effects (MO) at resonant wavelengths arises [1, 2]. In previous works, the simulations of such structures were given and the amplification of MO effects by 20–50 times was shown. Then it was proposed to investigate not only structures with single modes, but also their hybrid state [3]. The presence of the hybrid state in such structures is due to the coincidence of the resonance conditions of the optical modes of Fabry–Perot and TPP: the selection of the thickness of the structure layers — the cavity layer of MPC and the layer adjacent to the metal plasmon layer. In this work, it is proposed to investigate how the hybrid state behaves if we change the symmetry of a microcavity MPC and the metal layer (Ag, Au, Cu) in cases of normal and oblique incidence.

Materials and Methods

The simulations were carried out using the 4×4 transfer matrix method, which uses the approach of Berreman et al. [3] to form transfer matrices of layers and the entire structure. MPCs with a next general formula are considered as the structures with hybrid state of Fabry–Perot and TPP modes:

$$GGG/[TiO_2/SiO_2]^{m1}/D1/[SiO_2/TiO_2]^{m2}/D2/Me, \quad (1)$$

where TiO_2 is the layer of TiO_2; SiO_2 is the layer of SiO_2; Me is the metal layer (Ag, Au or Cu); m_1 and m_2 are the numbers of layer pairs in Bragg mirrors; D1 and D2 are the layers on which the formation of Fabry–Perot and TPP modes depends, respectively. Double-layer film of composition $Gd_3Sc_2Ga_3O_{12}/Bi_{2.8}Y_{0.2}Fe_5O_{12}$ was selected as D1-layer. D2-layer was SiO_2. The thickness of D1-layer was selected to create the Fabry–Perot mode in the center of photonic band gap in the vicinity of 700 nm at normal incidence. To create hybrid state, the thickness of D2-layer sets the resonant wavelength of TPP at the vicinity of 700 nm also.

Assuming that it is possible to achieve a change in the hybrid state for asymmetric microcavity MPCs, we changed the number of layer pairs m1 and m2 in the calculations, actually transforming the localization of light inside D1- and D2-layers. Three configurations were considered for comparison: (2) $m_1 = 2$; $m_2 = 6$; (3) $m_1 = 4$; $m_2 = 4$; (4) $m_1 = 6$; $m_2 = 2$.

The interaction of light is described for each layer by a dielectric constant tensor of the form listed in publication [2]. Dielectric constants at a wavelength of 700 nm are as follows: for the iron-garnet layer: $\varepsilon_{xx} = 6.77 + 0.05 \cdot i$, $\varepsilon_{xy} = 0.03$; for Au-layer: $\varepsilon_{xx} = -15.00 + 2.16 \cdot i$; for Cu-layer: $\varepsilon_{xx} = -18.22 + 0.86 \cdot i$; for Ag-layer: $\varepsilon_{xx} = -19.8973 + 0.70 \cdot i$; for layer of TiO_2: $\varepsilon_{xx} = 5.42$; for layer of SiO_2: $\varepsilon_{xx} = 2.19$; for GGG: $\varepsilon_{xx} = 3.90$. The thickness of used layers was: $h(TiO_2) = 76$ nm, $h(SiO_2) = 120$ nm, $h(D1) = 286$ nm, $h(Me) = 30$ nm. To create a hybrid state at normal incidence, it is necessary that the thickness of D2-layer was, depending on the plasmon layer and configuration used, in the range 206–210 nm.

Results and Discussion

First of all, we will find out how the hybrid state of MPCs (2), (3) and (4) manifests itself at normal incidence. As can be seen from the simulated transmittance and Faraday rotation spectra of MPC (3) (Fig. 1), the hybrid state manifests itself in the form of two resonances located apart from each other at a certain spectral interval Δ (the splitting of hybrid mode), as it was shown earlier [4]. At the same time, the value of Δ it is weakly dependent on the metal used. Basically,

strong changes in the resonance values of the transmittance and Faraday rotation for two modes occur when Au is replaced by Ag. The resonances of modes become more pronounced, and the transmittance increases by 1.3–2 times. The angle of Faraday rotation also increases by 1.2–2 times. The characteristics of MPCs with Ag and Cu layers are very close to each other.

The splitting of hybrid mode Δ can be changed introducing the asymmetry of MPC (1). In the case of MPC (2), we observe the hybrid state in which a single resonance is observed, since the Fabry–Perot mode is weakly pronounced (Fig. 1, *c*). In this regard, we observe also a weak effect on Faraday rotation spectra (Fig. 1, *d*). When the parameters of the structure change, the competition and redistribution of intensity within MPC occurs. As a consequence, for MPC (4) Δ is the maximum, the TPP mode is dominant.

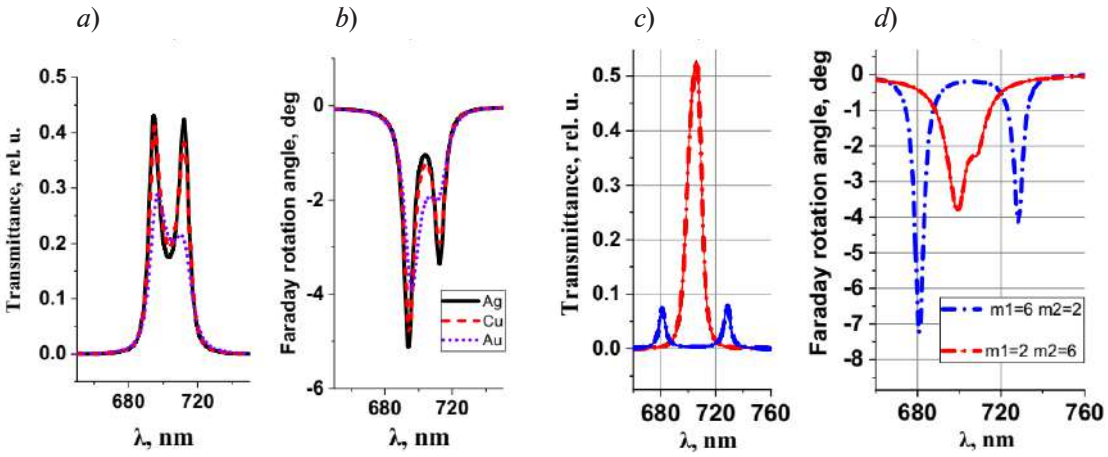

Fig. 1. Transmittance (*a*) and Faraday rotation angle (*b*) spectra of MPC (4) with a different metal layer. The thickness of D2-layer was 206, 209 and 208 nm for Au, Ag and Cu, respectively. Transmittance (*c*) and Faraday rotation angle (*d*) spectra of MPC (2) and (4). The thickness of D2-layer was 210 nm

After that, we simulated the properties of MPCs at oblique incidence of light. As shown earlier in the works [5–7] as the angle of incidence increases, the Fresnel reflection coefficients for *s*- and *p*-polarized waves become different. This results in an increase in *Q*-factors of the optical modes of MPC for s-polarized wave and a decrease for p-polarized wave, which arise with increasing the angle of incidence. As a result, the angle of Faraday rotation increases for s-polarized wave, and decreases for *p*-polarized wave. This is accompanied by the change in the localization of light within the structure when polarization changes (Fig. 2).

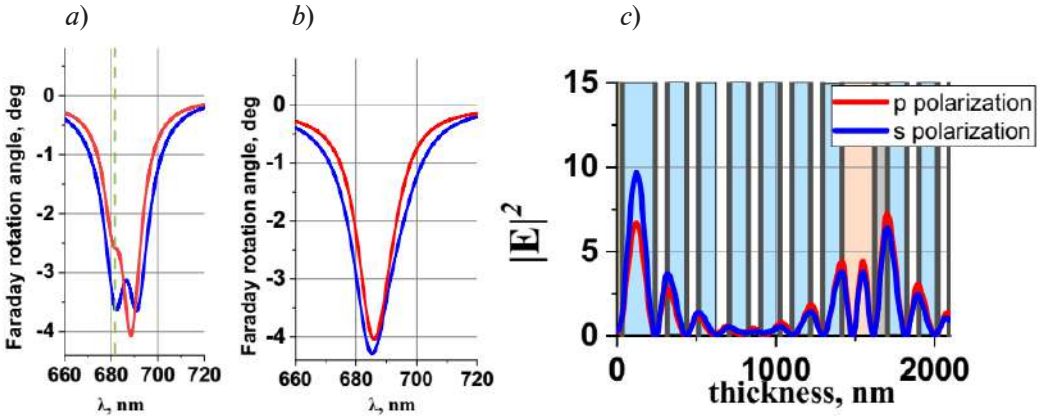

Fig. 2. Faraday rotation spectra of MPC (2) with Ag (*a*) and Au (*b*) layer with thickness of 30 nm at incidence angle of 25° for *s*- and *p*-polarization. Distribution of square of amplitude of electric field of light in MPC (2) with Ag-layer at wavelength of 681 nm (*c*)

For example, for MPC (2) at an angle of 25°, at which a hybrid state with equal amplitudes of Fabry–Perot and TPP resonances is observed for s-polarization in Faraday rotation spectrum, it is possible to achieve a change in the spectra by transition to p-polarization. TPP resonance located at 681 nm weakens, but Fabry–Perot resonance remains virtually unchanged (Fig. 2, *a*, *b*). By actually changing the polarization, we achieve a redistribution of light intensity exclusively in the vicinity of Ag-layer (Fig. 2, *c*). It is worth noting that for the other metal, Au, this effect will be absent.

Conclusion

The paper considers structures with a hybrid state of Fabry Perot and TPP modes. It is determined that the splitting of hybrid mode Δ can be controlled by changing the symmetry of MPC with cavity structure. It is determined that the use of different metals as a plasmon layer makes it possible to change the *Q*-factor of resonances of Fabry–Perot and TPP modes. It is indicated that the most pronounced resonance of TPP mode is possessed by MPC with Ag-layer. It has been revealed that in asymmetric structures at oblique incidence, we can controllably change the localization of light in the layers by polarization.

REFERENCES

1. **Inoue M., Baryshev A.V., Goto T., et. al.,** Magnetophotonic Crystals: Experimental Realization and Applications, Springer-Verlag Berlin Heidelberg. (163) (2013).

2. **Mikhailova T., Tomilin S., Lyashko S., Kozhaev M., Shaposhnikov A., Karavainikov A., Berzhansky V., Belotelov V.,** Tamm plasmon-polaritons and Fabry–Perot excitation in a magnetophotonic structure. Opt. Mater. Express. 12 (2) (2022) 685–696.

3. **Passler N.C., Paarmann A.,** Generalized 4 × 4 matrix formalism for light propagation in anisotropic stratified media: Study of surface phonon polaritons in polar dielectric heterostructures. J. Opt. Soc. Am. B. (34) (2017) 2128–2139.

4. **Grishin A.M., Khartsev S.,** Waveguiding in all-garnet heteroepitaxial magneto-optical photonic crystals, JETP Letters. (109) (2019) 83.

5. **Ignatyeva D.O., Belotelov V.I.,** Bound states in the continuum enable modulation of light intensity in the Faraday configuration, Opt. Lett. (45) (2020) 6422.

6. **Mikhailova T., Tomilin S., Lyashko S., Shaposhnikov A., Prokopov A., Karavainikov A., Bokova A., Berzhansky V.,** Tamm magnetophotonic structures with Bi-substituted iron garnet layers at oblique incidence, J. Phys.: Conf. Ser. (1124) (2018) 051062.

7. **Mikhailova T.V., Ignatyeva D.O., Lyashko S.D., Berzhansky V.N., Belotelov V.I.,** Odd Magneto-Optical Linear Dichroism in a Magnetophotonic Crystal, Photonics. 10 (11) (2023) 1237.

THE AUTHORS

OSMANOV Sebastyan V.
osmanovfti1@mail.ru
ORCID: 0000-0002-6919-5681

MIKHAILOVA Tatiana V.
taciamikh@gmail.com
ORCID: 0000-0002-1233-0109

Received 23.07.2024. Approved after reviewing 02.08.2024. Accepted 16.09.2024.

Conference materials
UDC 536.46
DOI: https://doi.org/10.18721/JPM.173.202

Chemical activity of dispersed particles of potassium compounds in a pyrotechnic flame

A.N. Lepaev[2]✉, S.I. Ksenofontov[1], O.V. Vasilyeva[3], K.Yu. Tashkova[1],

[1] Chuvash State Pedagogical University named after I. Y. Yakovlev, Cheboksary, Russia;

[2] Cheboksary Institute (branch) of the Moscow Polytechnic University, Cheboksary, Russia;

[3] Chuvash State University named after I. N. Ulyanov, Cheboksary, Russia

✉ it@polytech21.ru

Abstract. Modern developments of aerosol-generating compounds are associated with increased fire extinguishing efficiency and decreased temperature and chemical activity of two-phase combustion product flow. When burning these compounds in special generators, it is important to release particles as small as possible into the environment. The concentration of these particles must be commensurate with the concentration of active flame particles in the combustible material being extinguished. The structure of particles in pyrotechnic flames has been studied and the possibility of producing particles with reduced corrosion resistance has been demonstrated. A mechanism for the interaction between reacting particles and potassium iodide crystals has also been proposed.

Keywords: flame, dispersed particle, potassium oxide, potassium iodide

Citation: Lepaev A.N., Ksenofontov S.I., Vasilyeva O.V., Tashkova K.Yu., Chemical activity of dispersed particles of potassium compounds in a pyrotechnic flame, St. Petersburg State Polytechnical University Journal. Physics and Mathematics. 17 (3.2) (2024) 14–19. DOI: https://doi.org/10.18721/JPM.173.202

Материалы конференции
УДК 536.46
DOI: https://doi.org/10.18721/JPM.173.202

Химическая активность дисперсных частиц соединений калия в пламени пиротехнического состава

А.Н. Лепаев[2]✉, С.И. Ксенофонтов[1], О.В. Васильева[3], К.Ю. Ташкова[1],

[1] Чувашский государственный педагогический университет им. И.Я. Яковлева, г. Чебоксары, Россия;

[2] Чебоксарский институт (филиал) Московского политехнического университета, г. Чебоксары, Россия;

[3] Чувашский государственный университет им. И.Н. Ульянова, г. Чебоксары, Россия

✉ it@polytech21.ru

Аннотация. Современные разработки аэрозолеобразующих составов связаны с повышением эффективности пожаротушения, с понижением температуры и химической активности двухфазного потока продуктов сгорания. При горении аэрозолеобразующих составов в специальных генераторах в окружающую среду должны выбрасываться частицы как можно малых размеров. Концентрация дисперсных частиц тушащего состава должна быть соизмеримой с концентрацией активных частиц в пламени горючего вещества, подвергаемого тушению. Изучена структура дисперсных частиц в пламени пиротехнического состава. Показана возможность получения дисперсных

частиц целевого продукта с уменьшенной коррозионной способностью. Предложен механизм взаимодействия реагирующих дисперсных частиц с кристаллом йодида калия.

Ключевые слова: пламя, дисперсная частица, оксид калия, йодид калия

Ссылка при цитировании: Лепаев А.Н., Ксенофонтов С.И., Васильева О.В., Ташкова К.Ю. Химическая активность дисперсных частиц соединений калия в пламени пиротехнического состава // Научно-технические ведомости СПбГПУ. Физико-математические науки. 2024. Т. 17. № 3.2. С. 14–19. DOI: https://doi.org/10.18721/JPM.173.202

Introduction

Traditional fire extinguishing agents have several drawbacks that prevent them from being used in industrial facilities and chemical plants. Existing fire suppression systems, such as water, foam, powder, refrigeration, are characterized by high energy and material consumption. Therefore, the challenge of developing fire extinguishing devices based on aerosol-forming compounds for volume fire suppression in industrial, residential, and transportation facilities to replace current energy-intensive and costly fire suppression systems is urgent [1, 2].

During the study, pyrotechnic compositions based on nitrates, chlorates, and perchlorates of alkaline and alkaline earth metals, as well as various organic compounds, were found to have the highest fire extinguishing ability. These compounds, when burned, form an aerosol consisting of inert gases and ultradispersed and nanodispersed solid particles of chemically active compounds with a highly developed surface area. The fire extinguishing effect of these formulations is based on the inhibitory, phlegmatizing, cooling, and oxygen-binding mechanisms of action [3, 4]. For example, compositions such as C_3H_5O (20%) + $KClO_4$ (80%), C_3H_5O (20%) + $KClO_4$ (50%) + KNO_3 (30%) have been identified. The condensed phase of the aerosol consists mainly of oxide, hydroxide, and potassium salt particles ranging in size from 0.5 to 4 μm. These particles are chemically aggressive and cause corrosion of metal surfaces.

Satisfactory results were achieved with formulations containing potassium nitrate, sorbitol and ammonium iodide. The combustion products formed potassium iodide particles, which have minimal corrosive effects on protected objects. Currently, there is no literature available on the dispersed composition, morphology and elemental composition of these particles.

Materials and Methods

Two formulations based on sorbitol, potassium nitrate, ammonium iodide and iditol, potassium nitrate, dicyandiamide (DCDA) were studied in the work. The components were thoroughly mixed and pressed into a cardboard shell with a diameter of 20 mm at a specific pressure of 1000 kg/cm^2. Combustion of the composition was carried out at room conditions. Condensed dispersed particles were collected by passing glass plates through the flame.

Microphotographs of sampler areas were obtained, and the elemental composition of dispersed particles was studied using a Hitachi TM−4000Plus scanning electron microscope. In the flame, aerosol particles are formed, consisting of irregularly shaped hydrocarbon fuel residues (1), potassium carbonate (2) and potassium iodide (3). Potassium iodide is not present as an independent substance in the original pyrotechnic composition. The nucleation and growth of potassium iodide crystals to micron sizes is a new phenomenon.

Results and Discussion

The surface of the sampler is strewn with submicron-sized particles (Fig. 1, *a*). A large particle of potassium iodide (3) is presented in the form of a cube-shaped particle with an edge of 22 microns. On one of the ribs there is a particle of unburned hydrocarbon fuel (1). The sizes of the initial particles of the composition components are about 70 microns (sieve screening).

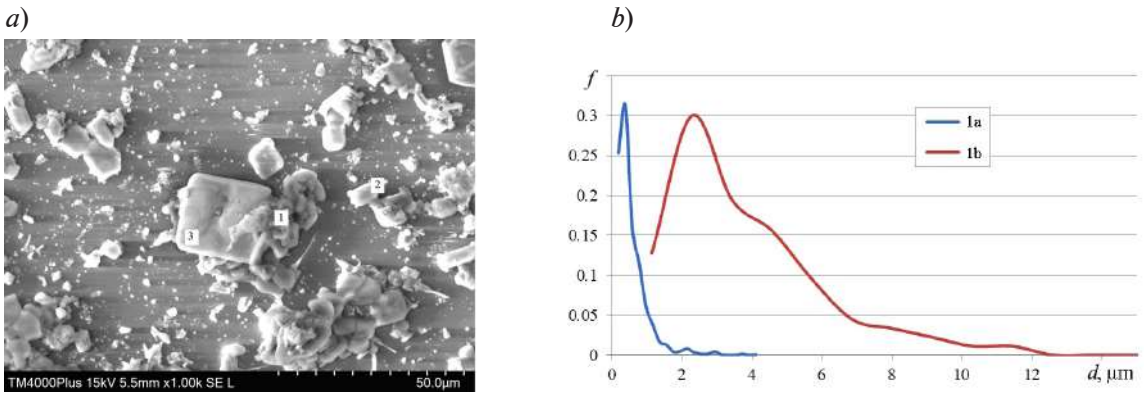

Fig. 1. Microphotograph of sampler section in SE mode of reflected electrons (*a*), particle size distribution (*b*)

The chemical composition of dispersed particles differs from each other. Separately selected areas (Fig. 1, *a*) of the sample were studied by X-ray spectral analysis, which makes it possible to judge the elemental structure of the substance under study (Fig. 2). The distribution of carbon, potassium and iodine is discrete and coincides with the contours of the particles. The coincidence of contours in the element distribution maps suggests that in the studied samples the substance can be presented in the form of K_2CO_3.

The particle size distribution function was determined using software [5]. Dispersed particles of submicron sizes (Fig. 1, *b*, curve *1a*) and large particles larger than one micron in size (Fig. 1, *b*, curve *1b*) are presented in the form of separate distribution curves. The value of the distribution function of curve 2 is increased by 7 times. The surface concentration of dispersed particles on the sampler is $109 \cdot 10^3$ particles/mm^2. Measuring the rate of passage of the sampler through the flame and the flow rate of combustion products makes it possible to determine the volumetric concentration of particles in the flame equal to $1.1 \cdot 10^6$ particles/cm^3.

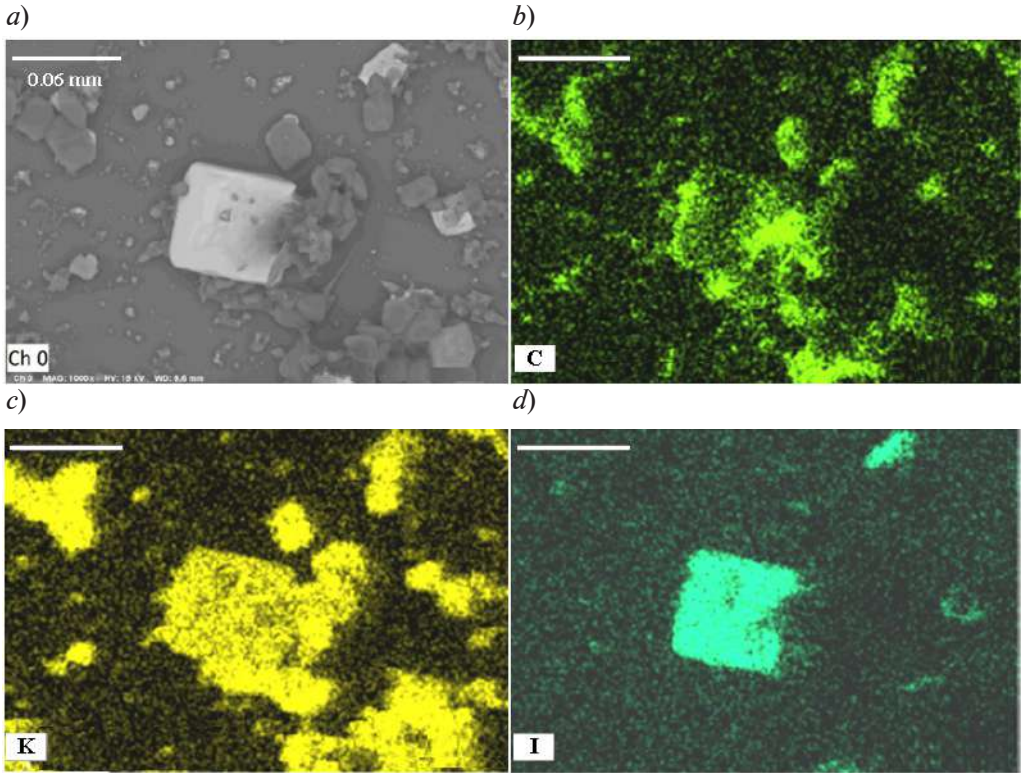

Fig. 2. Distribution maps of individual chemical elements from the analyzed area of the sample

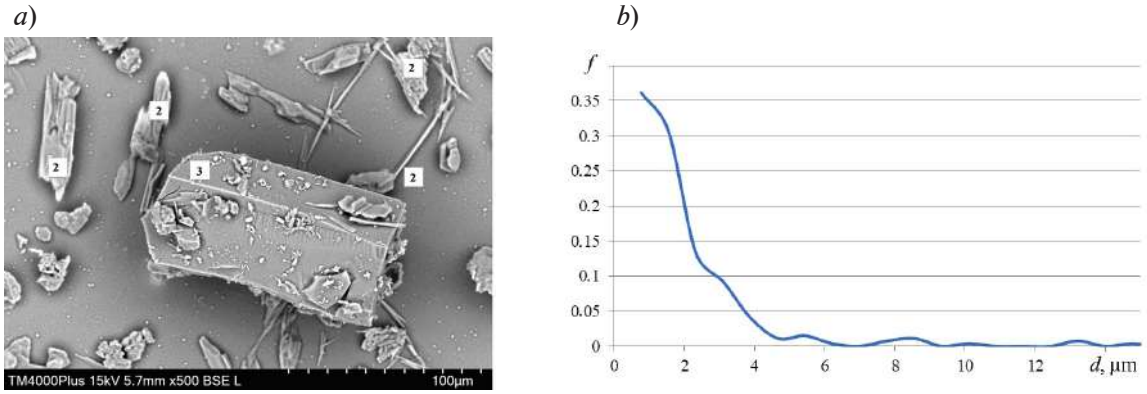

Fig. 3. Microphotograph of sampler section in SE mode of reflected electrons (*a*), particle size distribution (*b*)

Particles found in the peripheral zone of the flame are shown in Fig. 3, *a*. A large particle of potassium iodide (3) in the shape of an irregular prism is located in the center of the picture. A lot of particles, both submicron in size and particles in the form of thin plates and elongated rods, settled on the outer surface of the prism. The concentration of submicron particles on the surface of the sampler around the prism is almost zero. The particle size distribution is shown in Fig. 3, *b*. The maximum of the distribution function occurs on a particle with a size of 0.8 μm. The average surface density of particles on the prism is $6.3 \cdot 10^3$ particles/mm^2. Analysis of Fig. 3, *a* suggests that the surface of the potassium iodide particle serves as a "third particle" for the recombination of both active flame particles – ions and electrons, and dispersed reacting particles.

It is also characteristic that "foreign" settled particles do not create defects and do not penetrate into the crystal structure. The probability of introducing "foreign" particles is not small, since the melting point of potassium iodide is 954 K, and the flame temperature measured by the photopyrometric method is 1380 K [6].

The second composition is characterized by the fact that the majority of dispersed particles consist of potassium carbonate. The observed potassium carbonate particles (2) have an irregular shape. In all likelihood, the crystallization process occurs by the surface mechanism from the liquid phase [7]. In the central zones of the flame, part of the dispersed phase consists of melt drops. Only in a narrow zone of the flame does the transition of reacting particles from the liquid phase to the crystalline phase occur. From the literature it follows that at temperatures below 693 K, potassium carbonate has a monoclinic modification, and with increasing temperature the crystal exhibits a hexagonal modification [8].

Mechanical destruction of the crystalline shell of a particle as a result of a collision with the body of the sampler leads to the appearance of whisker crystals (Fig. 4). Whisker crystals are located not only near the surface of the sampler, but are also observed in the form of bulk structures. The time of collision of dispersed particles with the surface of the sampler and the growth of whiskers is small. It is less than one millisecond. The parameters of the whiskers shown in Fig. 4 were measured using Digimazer software. The capabilities of the software allow us to estimate the size of the measured micro-object up to one nanometer. The diameter at the base of the crystals is greater than at their top. Measurements to estimate the diameter were carried out at the middle of its length $l_i = 0.5l$. The average value of the diameter of whiskers is $d = (1.4 \pm 0.5)$ μm. The average length of the crystals is $l = (25.5 \pm 3.5)$ μm. The ratio of the length of a crystal to its diameter is $l/d = 18$. This makes it possible to classify these formations as whiskers. The specific surface area of whiskers is $s/(\rho V) = 1.15 \cdot 10^3$ m^2/kg [7].

The physicochemical properties of the filamentous structures of potassium carbonate are to be studied in the future. Dispersed particles with a developed surface are used in the form of catalysts and chemical adsorbents for gaseous media. Potassium carbonate powder is used in the production of fire extinguishing agents, where the specific surface area of the fire extinguishing powder is one of the important indicators of the efficiency of stopping combustion.

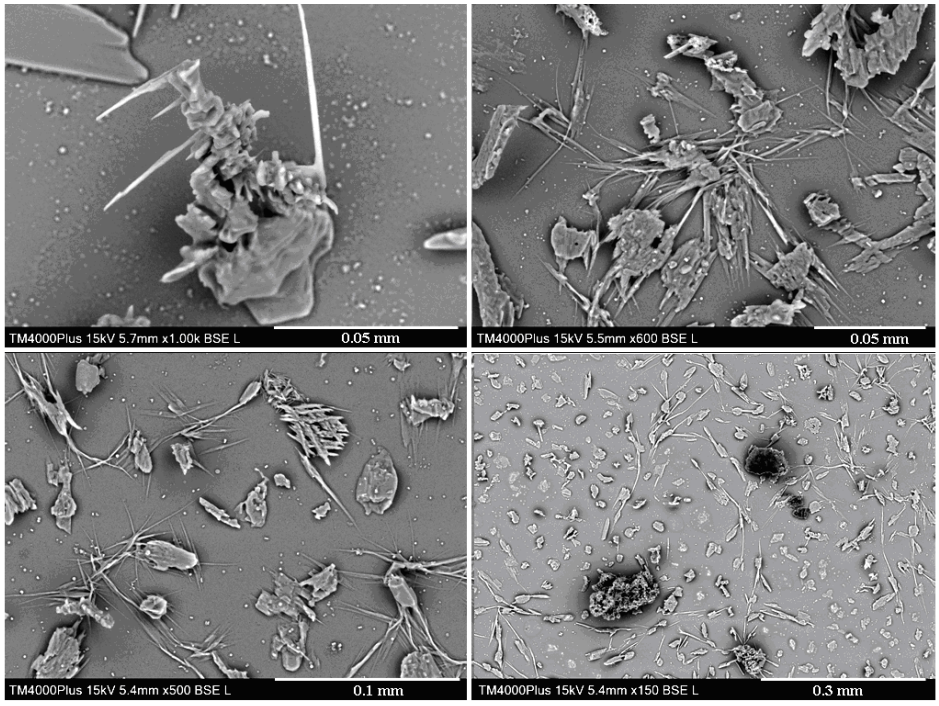

Fig. 4. Micrograph of sampler fragments

Conclusion

The substitution of potassium carbonate particles with potassium iodide particles through a chemical reaction reduces the corrosiveness of the final product.

A physical mechanism for the interaction between the reacting dispersed particles and potassium iodide crystals has been identified.

REFERENCES

1. **Bogateev G.G., Abdullin I.A., Reznikov M.S., Timofeev N.E., Moiseeva N.A.,** Pirotekhnicheskie aerozoleobrazuiushchie sostavy i generatory obemnogo pozharotusheniia: Vestnik Kazanskogo tekhnologicheskogo universiteta. 24 (15) (2012) 135–136.

2. **Ugolkova A.S., Timofeev N.E., Abdullin I.A., Reznikov M.S., Mingazov A.Sh.,** Ingibitory goreniia aerozoleobrazuiushchikh ognetushashchikh sostavov: Vestnik Kazanskogo tekhnologicheskogo universiteta. 14 (17) (2014) 219–220.

3. **Alikin V.N., Milekhin I.U.M., Pak Z.P., Lipanov A.M.,** Porokha, topliva, zariady. zariady. Zariady narodnokhoziaistvennogo naznacheniia, Himiia, Moscow, 2004.

4. **Korostylev V.G.,** Gashenie uglevodorodnykh plamen aerozol'generiruiushchimi pirotekhnicheskimi sostavami, Moscow, Materialy XXI Mezhd. Pirotekhnicheskogo seminara. (1995) 445–458.

5. **Porfiriev A.M., Ksenofontov S.I.,** Chastica, Nauka i obrazovanie. 6 (2010) URL: http://ofernio.ru/portal/newspaper/ofernio/2010/6.doc.

6. **Porfiriev A.M., Ksenofontov S.I.,** Programma opredeleniya polya temperatur plamen "Flame – temperature", Nauka i obrazovanie. 8 (2010) URL: http://ofernio.ru/portal/newspaper/ofernio/2010/8.doc.

7. **Ksenofontov S.I., Tashkova K.Yu., Lepaev A.N., Vasilyeva O.V.,** Morphology and elemental composition of whiskers of potassium carbonate in a pyrotechnic flame, St. Petersburg Polytechnical University Journal: Physics and Mathematics. 3 (16) (2023) 304–309.

8. **Grigoriev I.S., Meilikhov E.Z.,** Fizicheskie velichiny. Spravochnik, Energoatomizdat, Moscow, 1991.

THE AUTHORS

KSENOFONTOV Sergey I.
ksenofontovsi@mail.ru
ORCID: 0000-0002-9723-5652

TASHKOVA Ksenya Yu.
ksuha-92@inbox.ru

LEPAEV Alexander N.
it@polytech21.ru,
ORCID: 0000-0003-2498-1192

VASILYEVA Olga V.
dprostokvashino@mail.ru
ORCID: 0000-0001-8432-5635

Received 24.07.2024. Approved after reviewing 25.09.2024. Accepted 17.10.2024.

Conference materials
UDC 546.3-126:544.2
DOI: https://doi.org/10.18721/JPM.173.203

Deposition of tin and gold on porous silicon by vacuum thermal spraying

K.B. Kim[1]✉, S.S. Chernenko[1], S.I. Niftaliev[1], G.I. Kotov[1],
D.S. Zolotukhin[2], A.I. Chukavin[3], A.S. Lenshin[1,2]

[1] Voronezh State University of Engineering Technologies, Voronezh, Russia;

[2] Voronezh State University, Voronezh, Russia;

[3] Udmurt Federal Research Center of the Ural Branch of the RAS, Izhevsk, Russia

✉ kmkseniya@yandex.ru

Abstract. In this work, a tin-gold layer was deposited on porous silicon (KEF 100) substrates by vacuum-thermal process (VUP) to improve the performance of sensors. By the method of X-ray photoelectron spectroscopy (XPS) we analyzed the surface of the materials of the original porous silicon, as well as porous silicon with tin and gold, according to the method [1]). XPS overview spectra allow identifying elements present on the sample surface, as well as determining their oxidation state and concentration. Using this information, valuable data on the surface composition can be obtained and the chemical structure of the sample can be analyzed. The results obtained showed that using the vacuum-thermal method can be successfully applied to obtain nanocomposites of porous silicon with tin and gold. The obtained nanocomposites contain phases of tin dioxide, tin suboxide/monoxide and metallic tin. Compared to tin, the gold film is formed in a smoother, more uniform manner. XPS spectra show that the gold is metallic, free of impurities and oxides.

Keywords: porous silicon, composites, tin, gold, thin films

Funding: This work was supported by the Russian Science Foundation (no. 22-73-00154 of 28.07.2022).

Citation: Kim K.B., Chernenko S.S, Niftaliev S.I., Kotov G.I., Zolotukhin D.S., Chukavin A.I., Lenshin A.S., Deposition of tin and gold on porous silicon by vacuum thermal spraying, St. Petersburg State Polytechnical University Journal. Physics and Mathematics. 17 (3.2) (2024) 20–24. DOI: https://doi.org/10.18721/JPM.173.203

Материалы конференции
УДК 546.3-126:544.2
DOI: https://doi.org/10.18721/JPM.173.203

Осаждение олова и золота на пористом кремнии методом вакуумно-термического напыления

К.Б. Ким[1]✉, С.С. Черненко[1], С.И. Нифталиев[1], Г.И. Котов[1], Д.С. Золотухин[2], А.И. Чукавин[3], А.С. Леньшин[1,2]

[1] Воронежский государственный университет инженерных технологий, Воронеж, Россия;

[2] Воронежский государственный университет, Воронеж, Россия;

[3] Удмуртский федеральный исследовательский центр Уральского Отделения РАН, г. Ижевск, Россия

✉ kmkseniya@yandex.ru

Аннотация. Методами атомно-силовой микроскопии и рентгеновской фотоэлектронной спектроскопии получены данные о морфологии и составе образцов пористого кремния с вакуумно-термическим испарением оловом и золотом. Установлено, что химическое осаждение тонких металлических слоев на пористый кремний приводит к образованию композитной структуры, при этом наблюдается частичное окисление оловянной пленки, а пленка золота остается металлической.

Ключевые слова: пористый кремний, композиты, олово, золото, тонкие пленки

Финансирование: Работа выполнена при поддержке Российского научного фонда (№ 00154-73-22 от 28.07.2022 г).

Ссылка для цитирования: Ким К.Б., Черненко С.С., Нифталиев С.И., Котов Г.И., Золотухин Д.С., Чукавин А.И., Леньшин А.С. Осаждение олова и золота на пористом кремнии методом вакуумно-термического напыления // Научно-технические ведомости СПбГПУ. Физико-математические науки. 2024. Т. 17. № 3.2. С. 20–24. DOI: https://doi.org/10.18721/JPM.173.203

Introduction

Porous silicon (por-Si) is a very important material for the fabrication of various types of sensors. Its nanostructure with many micropores and a large internal surface area has a number of unique properties that make it attractive for a variety of applications. One application of porous silicon is the creation of sensing elements for gas and chemical sensors. Due to its large surface area, porous silicon can effectively sorb target substances and provide their detection at very low concentrations [1]. At the same time, the porous structure allows for a fast and sensitive sensor response. Functionalization of porous silicon surface with tin and gold is an important step in the process of creating sensors and other devices based on porous silicon. It allows to expand the capabilities and improve the properties of this material, making it even more attractive for a wide range of applications [2].

Materials and Methods

To obtain samples of porous silicon with deposited metals, the method of thermal vacuum sputtering through a mask on the VUP-4 unit was used. Porous silicon (KEF) with resistivity of 0.2 Ohm·cm^2, with orientation ⟨100⟩, obtained by electrochemical anodization in an electrolyte based on hydrofluoric acid and isopropyl alcohol [3] was used as a substrate.

The Sn (por-Si-Sn) and Au (por-Si-Au) layer with a thickness of about 200 nm was sputtered using VHF-000 grade tin and OSF gold wire on a "cold" porous silicon substrate. The sputtering rate was 3—5 nm/s, at a residual gas pressure in the chamber of about $5 \cdot 10^{-5}$ to 10^{-4} mmHg. The morphology of the obtained samples was examined on an atomic force microscope (SOLVER P47 PRO). Image processing using NOVA software allowed to analyze the morphological features of the surface. In addition to the morphology analysis, the surface of por-Si, por-Si-Sn and por-Si-Au samples was analyzed by XPS X-ray photoelectron spectroscopy at the SPECS facility, according to the method [4].

Results and Discussion

Fig. 1 shows AFM images of the surface. When tin and gold film is deposited on the porous silicon surface, the surface becomes smoother (Fig. 1, *b*, *c*). For the original porous silicon sample, the roughness is 70 nm, and when tin is deposited, the roughness decreases to 45 nm and gold decreases to 20 nm. The average particle size of tin on porous silicon is 50 nm and gold is about 60 nm, which is due to partial coagulation of the particles.

Survey spectra of XPS are required to investigate the chemical structure and composition of surface materials. The obtained results allow to understand the structure and composition of the material, as well as to optimize the manufacturing processes. The NIST database [5] was used to decipher the obtained XPS spectra.

Analysis of XPS-spectra of Si 2*p* porous silicon (Fig. 2) showed the presence of silicon dioxide (Si 2*p*, 103.5 eV), silicon suboxide (Si 2p, 100.5-103.0 eV) and unoxidized crystalline or amorphous silicon (Si 2*p*, 99.5 eV) in the sample [5—7].

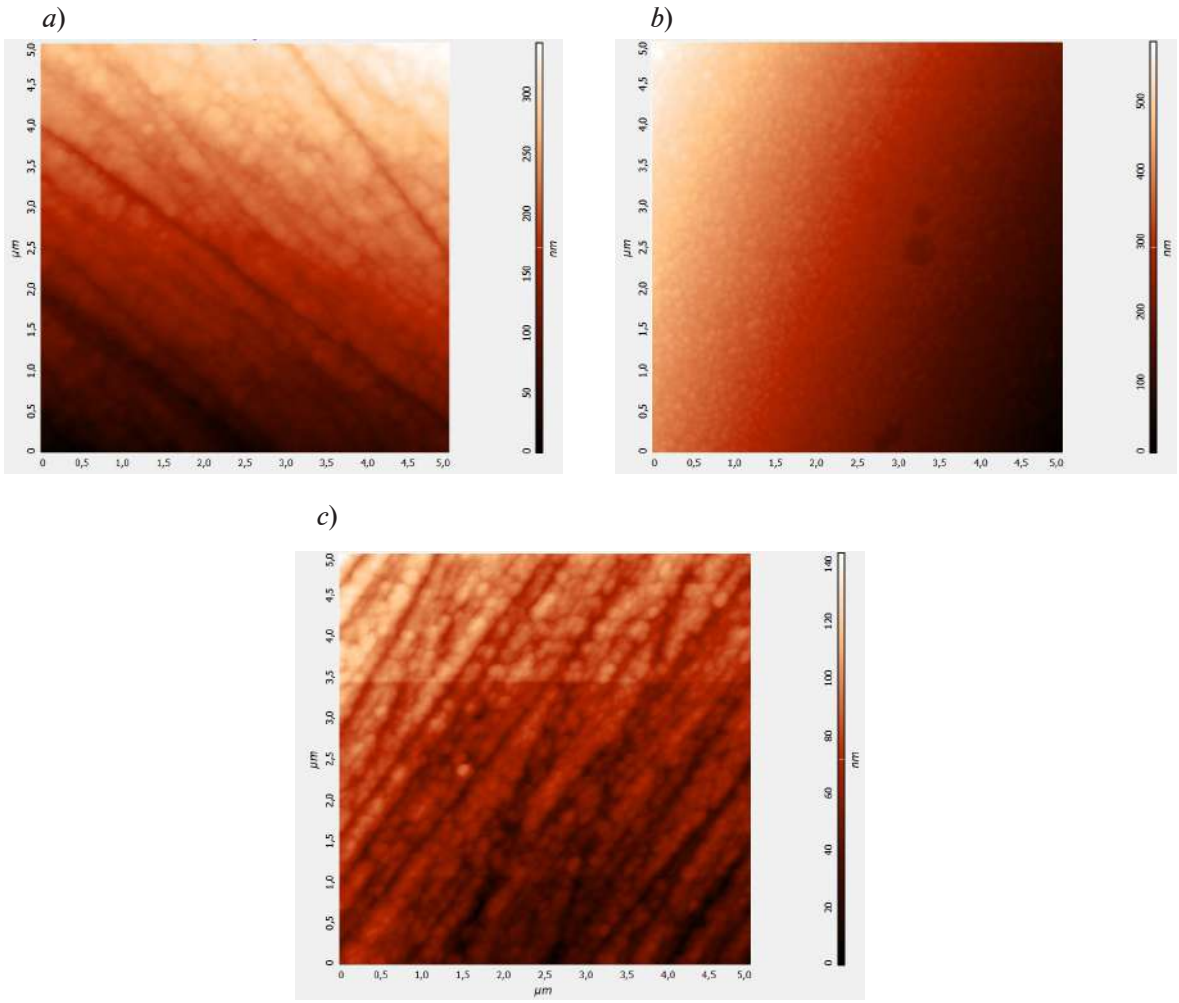

Fig. 1. Surface morphologies of samples obtained by AFM: por-Si (*a*), por-Si-Sn (*b*), por-Si-Au (*c*)

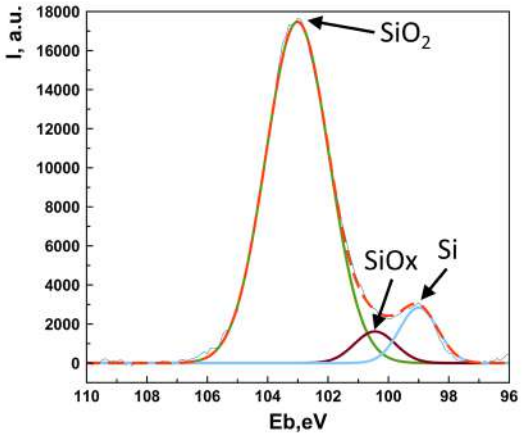

Fig. 2. XPS Si 2*p* spectra with decomposition into por-Si components
(each line corresponds to a spectrum component modeled using a Gaussian)

Fig. 3, *a* shows the XPS spectra of the Sn 3d level backbone. Analysis of the shape and position of XPS Sn 3*d*5/2 spectra and their decomposition into components shows that Sn in the surface layer is in the form of metallic tin (spectrum component with E_b = 485.0 eV) and natural oxide SnOx, where $x \approx 2$ (E_b = 486.5–487.0 eV).

Fig. 3, *b* shows the XPS spectra of the Au 4*f* gold film's Au 4*f* island levels. Analysis of the shape and position of the XPS Au 4f spectra and their decomposition into components shows the absence of visible oxidation of Au (spectrum component with E_b = 84.5 eV).

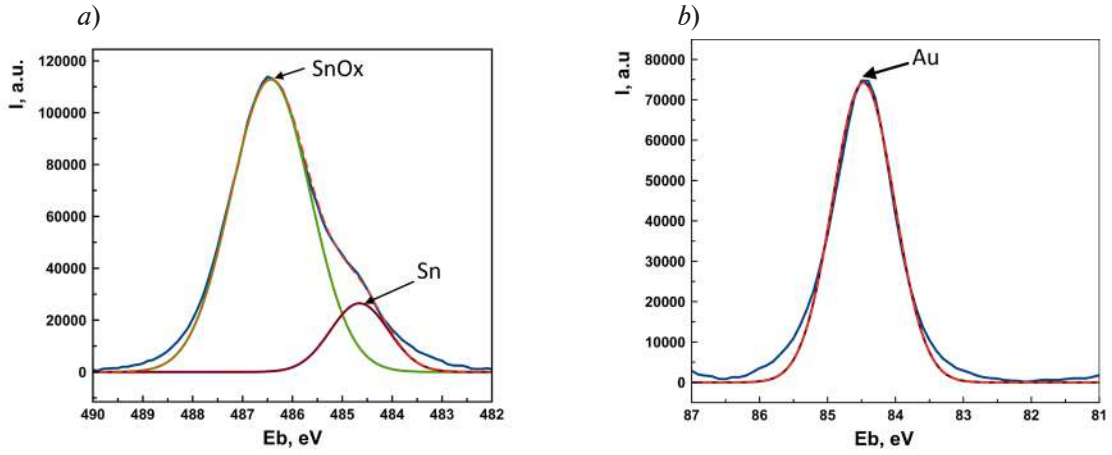

Fig. 3. XPS reference spectra of: Sn 3*d*5/2 tin film
with component decomposition (*a*); Au 4f gold film with component decomposition
(each line corresponds to a spectrum component modeled using a Gaussian) (*b*)

Conclusion

In this work, nanostructured composites of porous silicon with deposited layer of tin and gold were prepared by vacuum-thermal evaporation method. The results showed that the vacuum-thermal method can be successfully applied to obtain nanocomposites of porous silicon with tin and gold. The XPS data agree with the results of atomic force microscopy and confirm the formation of Sn and Au layers on the surface of porous silicon. The obtained nanocomposites with tin contain tin dioxide and metallic tin phases. Compared to tin, the gold film is formed smoother, more uniform, free of impurities and oxides. In general, the conducted studies provide a comprehensive view of the structure and chemical composition of por-Si-Sn and por-Si-Au film samples, which is important for understanding their physicochemical properties and potential applications in electronics and optoelectronics.

REFERENCES

1. **Alhmoud H., Brodoceanu D., Elnathan R., Kraus T., Voelcker N.H.,** A MACEing Silicon: Towards single-step etching of defined porous nanostructures for biomedicine, Progress in Materials Science. 116 (2019) 100636.

2. **Grevtsov N., Chubenko E., Bondarenko V., Gavrilin I., Dronov A., Gavrilov S.,** Electrochemical deposition of indium into oxidized and unoxidized porous silicon, Thin solid films. 734 (2021) 138860.

3. **Lenshin A.S., Seredin P.V., Kashkarov V.M., Minakov D.A.,** Materials science in semiconductor processing, Origins of photoluminescence degradation in porous silicon under irradiation and the way of its elimination. 64 (2017) 71–76.

4. **Lenshin A.S., Kashkarov V.M., Domashevskaya E.P., Bel'tyukov A.N., Gil'mutdinov F.Z.,** Investigations of the composition of macro-, micro- and nanoporous silicon surface by ultrasoft X-ray spectroscopy and X-ray photoelectron spectroscopy, Applied surface science. 359 (2015) 550.

5. NIST X-ray Photoelectron Spectroscopy Database. URL: http://srdata.nist.gov/xps

6. **Lenshin A.S., Kashkarov V.M., Turishchev S.Yu., Smirnov M.S., Domashevskaya E.P.,** Influence of natural aging on photoluminescence from porous silicon, Journal of technical physics. 82 (2) (2012) 150.

7. **Lu F., Ji X., Yang Y., Deng W., Craig B.,** Room temperature ionic liquid assisted well-dispersed core-shell tin nanoparticles through cathodic corrosion, RSC Advances. 3 (2013) 18791–18793.

THE AUTHORS

KIM Kseniya B.
kmkseniya@yandex.ru
ORCID: 0000-0001-5564-8267

ZOLOTUKHIN Dmitriy S.
zolotuhin@phys.vsu.ru
ORCID: 0000-0002-9645-9363

CHERNENKO Sergey S.
sergey.x173@mail.ru
ORCID: 0009-0005-4323-9163

CHUKAVIN Andrey I.
andrey_chukawin@mail.ru
ORCID: 0000-0002-9590-923

NIFTALIEV Sabukhi I.
sabukhi@gmail.com
ORCID: 0000-0001-7887-3061

LENSHIN Alexander S.
lenshinas@mail.ru
ORCID: 0000-0002-1939-253X

KOTOV Gennady I.
giktv@mail.ru
ORCID: 0000-0002-5690-5090

Received 25.07.2024. Approved after reviewing 27.08.2024. Accepted 27.08.2024.

Conference materials
UDC 539.23+535.39+537.32+537.622
DOI: https://doi.org/10.18721/JPM.173.204

CoSi ultrathin films on Si(111) substrate: comparison of the stage formation in ultra-high vacuum and during annealing in argon

D.L. Goroshko, K.N. Galkin, I.M. Chernev, A.M. Maslov, O.V. Kropachev, E.Yu. Subbotin, O.A. Goroshko, N.G. Galkin✉

Institute of Automation and Control Processes FEB RAS, Vladivostok, Russia

✉ galkin@iacp.dvo.ru

Abstract. As a result of the study, optimal conditions were identified for the formation of ultrathin films of cobalt monosilicide (CoSi) on a silicon substrate during a single annealing (T = 500–600 °C) of chromium layers (2–10 nm), both under ultra-high vacuum conditions and in an argon environment during isochronous annealing. The formation of the phase composition in ultrathin CoSi films is uniquely controlled in situ during growth in ultrahigh vacuum by the appearance of a bulk plasma frequency peak at 20.2–20.3 eV in the EELS spectrum, a Raman peak at 198 (204) cm^{-1} in ex situ Raman studies of the annealing in an argon environment (in vacuum) and characteristic of CoSi optical functions of refractive index and extinction and optical phonons at 223.7, 302.5 and 418.6 cm^{-1}. It has been established that cobalt films not subjected to thermal annealing in a vacuum begin to oxidize when annealed in an argon environment, which is convenient to monitor by the appearance of Raman peaks at 187 cm^{-1} and 670-677 cm^{-1}.

Keywords: cobalt layer, cobalt monosilicide, ultrathin films, isochronous annealing, ultra-high vacuum, argon environment, electronic structure, phonon structure, optical properties

Funding: This study was funded by the grant from the Russian Science Foundation (RSF) No. 22-12-00036, https://rscf.ru/project/22-12-00036.

Citation: Goroshko D.L., Galkin K.N., Chernev I.M., Maslov A.M., Kropachev O.V., Subbotin E.Yu., Goroshko O.A., Galkin N.G., CoSi ultrathin films on Si(111) substrate: comparison of the stage formation in ultra-high vacuum and during annealing in argon, St. Petersburg State Polytechnical University Journal. Physics and Mathematics. 17 (3.2) (2024) 25–30. DOI: https://doi.org/10.18721/JPM.173.204

Материалы конференции
УДК 539.23+535.39+537.32+537.622
DOI: https://doi.org/10.18721/JPM.173.204

Сверхтонкие пленки CoSi на подложке Si(111): сравнение стадий формирования в сверхвысоком вакууме и при отжиге в аргоне

Д.Л. Горошко, К.Н. Галкин, И.М. Чернев, А.М. Маслов, О.В. Кропачев, Е.Ю. Субботин, О.А. Горошко, Н.Г. Галкин✉

Институт автоматики и процессов управления ДВО РАН, г. Владивосток, Россия

✉ galkin@iacp.dvo.ru

Аннотация. Выявлены оптимальные условия формирования ультратонких пленок моносилицида кобальта (CoSi) на кремниевой подложке в процессе однократного отжига (T = 500–600 °C) слоев хрома (2–10 нм), как в условиях сверхвысокого вакуума, так и в аргоновой среде при изохронных отжигах. Формирование фазового состава в

ультратонких пленках CoSi однозначно контролируется *in situ* при росте в сверхвысоком вакууме по появлению пика объемной плазменной частоты при 20,2–20,3 эВ в спектре ХПЭЭ, КРС пика при 198 (204) $см^{-1}$ при *ex situ* КРС исследованиях отжига в аргоновой среде (в вакууме) и характерных для CoSi оптических функций коэффициентов преломления и экстинкции и оптических фононов при 223,7, 302,5 и 418,6 $см^{-1}$. Установлено, что окисление пленок кобальта удобно контролировать при отжиге в среде аргона по появлению КРС пиков при 187 $см^{-1}$ и 670–677 $см^{-1}$.

Ключевые слова: слой кобальта, моносилицид кобальта, ультратонкие пленки, изохронный отжиг, сверхвысокий вакуум, среда аргона, электронная структура, фононная структура, оптические свойства

Финансирование: Исследование выполнено за счет гранта Российского научного фонда (РНФ) № 00036-12-22, https://rscf.ru/project/00036-12-22.

Ссылка при цитировании: Горошко Д.Л., Галкин К.Н., Чернев И.М., Маслов А.М., Кропачев О.В., Субботин Е.Ю., Горошко О.А., Галкин Н.Г. Сверхтонкие пленки CoSi на подложке Si(111): сравнение стадий формирования в сверхвысоком вакууме и при отжиге в аргоне // Научно-технические ведомости СПбГПУ. Физико-математические науки. 2024. Т. 17. № 3.2. С. 25–30. DOI: https://doi.org/10.18721/JPM.173.204

Introduction

An urgent task is to study monosilicides of transition metals, such as Cr, Mn, Fe and Co, with a B20 cubic structure with space group P213 and breaking the symmetry of spatial inversion [1]. In addition, cobalt monosilicide (CoSi) is a topological Weyl semimetal [2] with interesting electrical and thermoelectric properties [3]. Research was mainly carried out on single crystals and bulk polycrystals of CoSi [3–6]. At the same time, the issue of the formation of thin (25–700 nm) CoSi films remains poorly studied at present [7, 8]. While ultrathin films (4–20 nm) and their formation by solid-phase epitaxy on silicon remain unstudied, both by *in situ* methods and by ex situ non-destructive phase- and structure-sensitive methods. Before proceeding to the study of the topological properties of ultrathin CoSi films, it is necessary to accurately establish the limits of temperature annealing of ultrathin cobalt films on silicon for the formation of CoSi, their phase homogeneity and temperature stability, which is the focus of this work. Also, CoSi, as shown in works [2, 3], despite their semi-metallic properties, are a promising material for thermoelectric converters in bulk form and in the form of thin epitaxial films on silicon.

Materials and Methods

Experiments on the deposition of ultra-thin Co layers were carried out on Varian ultra-high vacuum (UHV) units and UHV *A*-chambers with a base vacuum of 2×10^{-10} Torr, equipped, respectively, with an Auger electron spectroscopy (AES) and electron energy loss spectroscopy (EELS) analyzer and a diffractometer of low energy electrons (LEED), as well as sources of cobalt (Co) and silicon (Si). Before the growth of Co films, an atomically-clean surface of silicon substrate (Si(111)7×7) was formed. Silicon cleaning consisted of two stages: long-term (5–6 hours) degassing at $T = 650$°C and high-temperature short annealing at $T = 1150$ °C with a total duration of 5 minutes [9], followed by monitoring of the AES and EELS spectra or LEED patterns. In the first experiments, Co layers 2–10 nm thick were deposited at room temperature on the Si(111)7×7 surface. Initially, for a number of samples, solid-phase annealing was carried out in a UHV *A*-chamber at temperatures from 400 °C to 500 °C according to the data of CoSi formation temperature [7, 8]. In a Varian UHV chamber, in order to determine the CoSi formation temperature, isochronous annealing of a Co film with a thickness of 7.7 nm was carried out at temperatures from 275 °C to 700 °C with a step of 25 °C and step-by-step recording of the AES and EELS spectra. Individual Co films were unloaded without annealing, and then

annealed in a special attachment (Linkam THMS600) in the temperature range (30–550 °C, step 25 °C) with argon purging and simultaneous recording of Raman spectra (RS) on the NTEGRA SPECTRA II installation to control the onset of formation CoSi and its saturation. This setup was also used to record Raman spectra for a number of CoSi films formed by solid-phase annealing in UHV chambers. To control the optical properties and phonon structure of CoSi films, reflection and transmission spectra were recorded on spectrophotometers: U-3010 (Hitachi) and VERTEX v80 (BRUKER).

Results and Discussion

In order to determine the optimal formation temperature of a CoSi film, AES and EELS spectra were recorded and analyzed for a 7.7 nm thick Co layer at different annealing temperatures (Fig. 1, *a*, *b*). It has been established that the formation of CoSi begins at a temperature of 325 °C, which is confirmed by changes in the intensities of the AES spectra for Co and Si (Fig. 1, *a*) and shifts of the peaks from the initial positions (not shown), which corresponds to the entry of Co and Si into a chemical bond and a decrease in Co concentration and an increase in Si concentration (Fig. 1, *a*). The composition of the silicide, close to stoichiometric CoSi, is formed at temperatures of 400–600 °C (Fig. 1, *a*). More precisely, the phase composition is confirmed by the EELS spectra (Fig. 1, *b*), when surface (13.3 eV) and bulk (20.2–20.5 eV) plasmons corresponding to CoSi [10] are formed in the temperature range 400–600 °C. The transition from CoSi to $CoSi_2$ is observed at temperatures above 675 °C, which corresponds to a shift of the bulk plasmon to the position of 19.3 eV (Fig. 1, *b*), corresponding to $CoSi_2$ [10, 11]. The maximum bulk plasmon intensity of 20.2–20.2 eV is observed in the temperature range of 500–600 °C, which corresponds to the formation of the maximum amount of the CoSi phase and its best crystalline state, and also does not fully correlate in terms of the annealing temperature of Co layers with previously obtained data [7, 8].

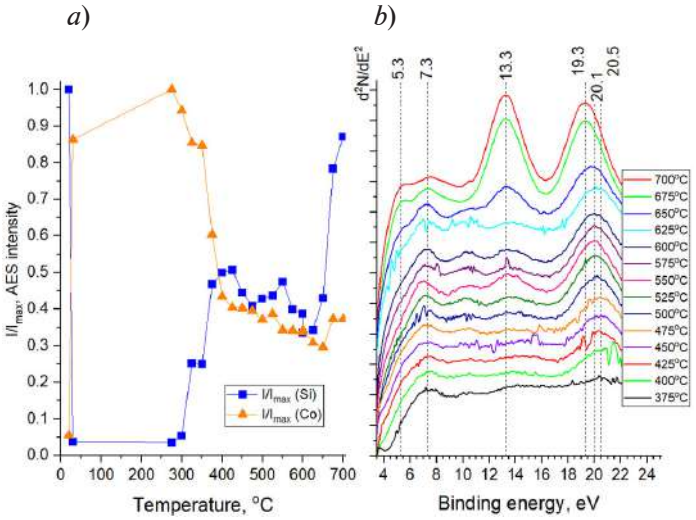

Fig. 1. Dependences of Co and Si concentrations by AES intensities data on annealing temperature (*a*); changes in the EELS spectra with increasing annealing temperature. Al data are presented for the Co film d_{Co} = 7.7 nm grown by SPE method at T = 275–700 °C (*b*)

Registration of Raman spectra during annealing of a Co film (4.8 nm) on Si substrate in an argon environment, unloaded from an UHV chamber without a protective layer (Fig. 2, *a*), confirmed the lower limit of the CoSi formation temperature (325 °C), when a Raman peak appears at 198 cm^{-1} that close to 204 cm^{-1} for CoSi films [12]. The maximum intensity of the Raman peak at 198 cm^{-1} is observed with increasing annealing temperature to 475–500 °C, which corresponds to the maximum amount of the formed CoSi phase (Fig. 2, *a*) and correlates with in situ control data: AES and EELS (Fig. 1, *a*, *b*, *c*, *d*). Simultaneously with the growth of the CoSi phase, the formation of peaks at 187 cm^{-1} and 677 cm^{-1} is observed, starting from a temperature of 375 °C, which correspond to the formation of Co oxide, which correlates with the data of [13], in which in the Raman spectra

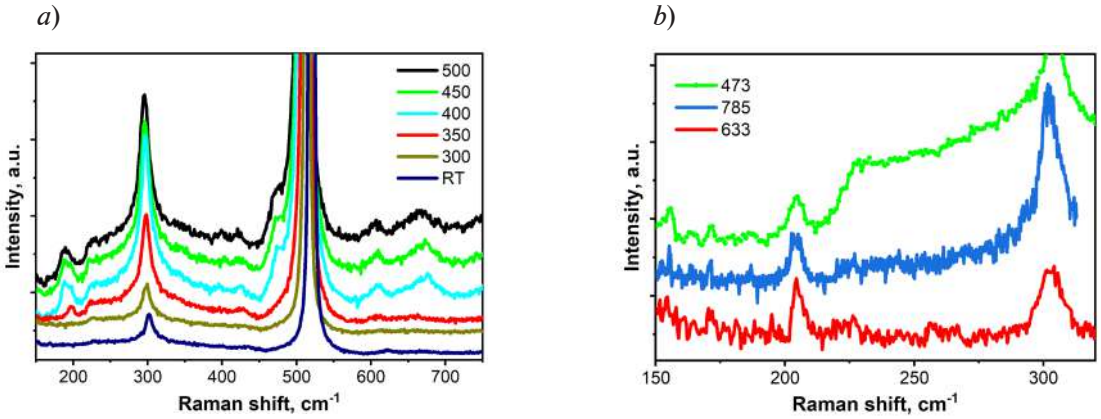

Fig. 2. Raman spectra at a laser wavelength of 785 nm at different annealing temperatures (300–500 °C) of the Co film (d_{Co} = 4.8 nm) (*a*). Raman spectra at laser wavelengths at 473, 633 and 785 nm for Co layer (4 nm) grown by SPE at 500 °C in UHV chamber (*b*)

during oxidation in argon or oxygen environment, peaks appeared at 195 cm^{-1} and 670–690 cm^{-1} during the annealing of the Co film. The intensity of the peaks at 187 cm^{-1} and 677 cm^{-1} (Fig. 2, *a*) increased with increasing annealing temperature in argon, which corresponds to an increase in the thickness of the cobalt oxide layer. Presumably, Co oxide is formed due to the decomposition of $Co(OH)_2$ formed on top of the Co layer after the sample with the Co film was unloaded into air without a protective layer, which correlates with the data of [14], which considered stepwise annealing processes of thick Co films in air. For a Co layer 4 nm thick, after annealing in vacuum at 500 °C, a peak at 204.1 cm^{-1} and additional weak peaks at 223.8 cm^{-1} and 242.1 cm^{-1} appear in the Raman spectra (Fig. 2, *b*), which corresponds to the data of work [12].

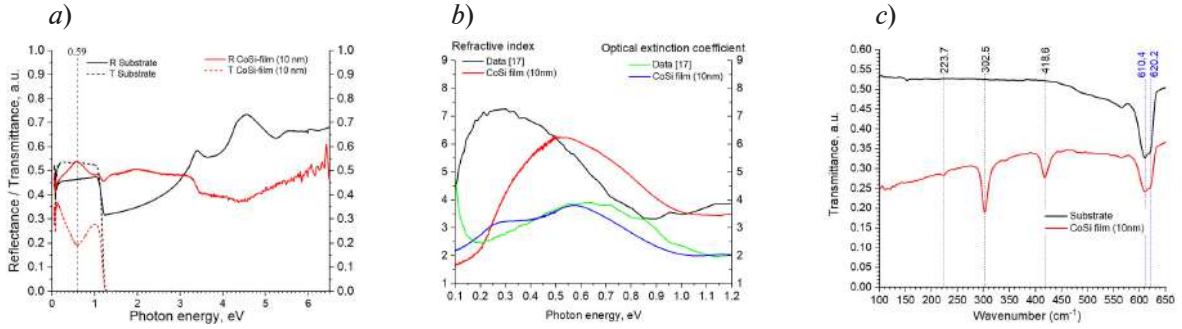

Fig. 3. Optical reflectance (*R*) and transmittance (*T*) spectra in UV-VIS-MIR range for grown CoSi films (10 nm of Co) and Si substrate (*a*), refractive index (*n*) and optical extinction coefficient (*k*) calculated for CoSi film and for CoSi bulk [17] (*b*) and *T*-spectra in the far infrared range (FIR) for CoSi film with Co thickness of 10 nm and Si substrate (*c*)

Registration of reflection spectra (*R*) and transmission spectra (*T*) (Fig. 3, *a*) showed that the CoSi film has a low reflectance in the mid- and near-IR ranges (0.2–1.1 eV), which is typical for materials usually, semiconductors [15] and semimetals such as CoSi [1, 2]. As the photon energy decreases (0.05–0.1 eV), a noticeable decrease in transmission is observed (Fig. 3, *a*), which is associated with an increase in the absorption coefficient for free carriers in “pockets” above and below the Fermi level [1–3]. Calculations of the refraction and extinction coefficient spectra within the framework of the two-layer model [16] showed (Fig. 3, *b*) not bad agreement with the data for bulk CoSi samples due, the optical properties of which were studied by spectral ellipsometry [17], which also proves the single-phase nature of the ultrathin CoSi films. FIR spectral data (Fig. 3,*c*) also confirmed the formation of CoSi with phonon peaks at 223.7, 302.5 cm^{-1} and 418.6 cm^{-1}, the amplitudes of which increase with the thickness of CoSi (not shown) and which belong to CoSi according to the literature [18].

Conclusion

Based on AES, EELS and Raman data, the temperature range (400–600 °C) for the formation of ultrathin CoSi films on a Si(111) substrate upon annealing of Co layers with a thickness of 2–10 nm was determined. It has been established that the maximum intensity of bulk plasmon peaks in the EELS spectra is observed at the temperatures of 500–600 °C. It was shown that UHV annealing and annealing in an argon environment lead to similar results, which is confirmed by both AES-EELS spectra, Raman spectroscopy and optical spectroscopy data. Raman data revealed the influence of a $Co(OH)_2$ layer adsorbed on Co in air on the formation of Co oxide. The dependences of the refractive index and extinction coefficient on the wavelength calculated from the optical spectra for ultrathin CoSi films are in not bad agreement with the data for bulk CoSi, which confirms their semi-metallic nature of the band energy structure. FIR spectroscopy data confirm the formation of ultrathin CoSi films, both after annealing Co layers in an ultra-high vacuum, and after annealing Co films in an argon environment after unloading from the UHV chamber.

REFERENCES

1. **Dutta P.**, **Pandey S.K.,** Investigating the electronic structure of MSi (M = Cr, Mn, Fe &Co) and calculating U_{eff} & J by using cDFT, Computational Condensed Matter. 16 (2018) e0035 (1–7).

2. **Pshenay-Severin D.A., Ivanov Y.V., Burkov A.A., Burkov A.T.**, Band structure and unconventional electronic topology of CoSi, Journal of Physics: Condensed Matter. 30 (2018) 135501.

3. **Pshenay-Severin D.A., Ivanov Yu. V., Burkov A.T., Novikov S.V., Zaitsev V.K.**, **Reith H.,** Electronic Structure and Thermoelectric Properties of Transition Metal Monosilicides, Journal of Electronic Materials. 47 (2018) 3277–3281.

4. **Ou-Yang T.Y., Shu G.J., Fuh H.R.,** Thermoelectric performance and electronic properties of transition metal monosilicides, EPL. 120 (2017) 17002.

5. **Schnatmann L., Lammel M., Damm C., Levin A.A., Pérez N., Novikov S., Burkov A., Reith H., Nielsch K., Schierning G.,** Crystal Structure Analysis and Magneto-Transport Investigation of $Co_{1-x}Fe_xSi$ (with x = 0% to x = 20%), Adv. Electron. Mater. 8 (2022) 2101081.

6. **Salamatin D.A., Bokov A.V., Kozin M.G., Romashkina I.L., Salamatin A.V., Mikhin M.V., Petrova A.E., Sidorov V.A., Nikolaev A.V., Fisk Z., Tsvyashchenko A.V.**, Anomalous Positron Lifetime in Single Crystal of Weyl Semimetal CoSi, Crystals. (13) (2023) 509.

7. **Normuradov M.T., Bekpulatov I.R., Imanova G.T., Igamov B.D.**, Structures for constructing devices from formed Mn_4Si_7 and CoSi films, Advanced Physical Research. 4 (2022) 142–154.

8. **Li Z., Yuan Y., Hübner R., Rebohle L., Zhou Y., Helm M., Nielsch K., Prucnal S., Zhou S.**, B20 Weyl Semimetal CoSi Film Fabricated by Flash-Lamp Annealing, ACS Applied Materials & Interfaces. 15 (2023) 30517–30523.

9. **Galkin N.G., Migas D.B., Medvedeva N.V., Filonov A.B., Dotsenko S.A., Maslov A.M., Chernev I.M, Subbotin E.Yu, Goroshko D.L., Samardak A.Yu., Gutakovskii A.K., Tkachenko I.A., Gerasimenko A.V.**, New monoclinic ground state of FeSi, Comp. Mater. Science. 233 (2024) 112762.

10. **Plusnin N.I., Milenin A.P., Prihod'ko D.P.**, Formation of the CoSi(111)7×7 interface: AES- and EELS-study. Applied Surface Science. (166) (2000) 125–129.

11. **De Crescenzi M., Derrien J., Chainet E., Orumchian K.**, Core-level electron-energy-loss spectroscopy as a local probe for the electronic structure of the Co/Si(111) interface, Physical Review B. 39 (8) (1989) 5520.

12. **Racu A.-M., Menzel D., Schoenes J., Doll K.**, Crystallographic disorder and electron-phonon coupling in $Fe_{1-x}Co_xSi$ single crystals: Raman spectroscopy study, Physical Review B. 76 (11) (2007) 115103.

13. **Liu F.M., Ye J.H., Ren B., Yang Z.L., Liao Y.Y., See A., Chan L., Tian Z.Q.,** Raman spectroscopic studies of the formation processes of cobalt silicide thin films, Thin Solid Films. 471(1–2) (2005) 257–263.

14. **Tompkins H.G., Augis J.A.,** The oxidation of cobalt in air from room temperature to 467 °C, Oxidation of Metals. 16 (5–6) (1981) 355–369.

15. **Seeger K.,** Semiconductor Physics, Springer Science & Business Media. 2013.

16. **Galkin N.G., Maslov A.M., Konchenko A.V.**, Optical and photospectral properties of $CrSi_2$ A-type epitaxial films on Si(111), Thin Solid Films. 311(1–2) (1997) 230–238.

17. **Van der Marel D., Damascelli A., Schulte K., Menovsky A.A.,** Spin, charge, and bonding in transition metal mono-silicides, Physica B: Condensed Matter. 244 (1) (1998) 138–147.

18. **Acun A.D., Soyalp F.,** Elastic and phonon properties of FeSi and CoSi in the B2 structure, Philosophical Magazine. 92 (5) (2012) 635–646.

THE AUTHORS

GOROSHKO Dmitrii L.
goroshko@iacp.dvo.ru
ORCID: 0000-0002-1250-3372

KROPACHEV Oleg V.
chernobez@gmail.com
ORCID: 0000-0003-4300-0070

GALKIN Konstantin N.
galkinkn@iacp.dvo.ru
ORCID: 0000-0001-5386-1013

SUBBOTIN Evgenii Yu.
jons712@mail.ru
ORCID: 0000-0001-9531-3867

CHERNEV Igor M.
igor_chernev7@mail.ru
ORCID: 0000-0002-8726-9832

GOROSHKO Olga A.
olgagoroshko@iacp.dvo.ru
ORCID: 0009-0008-2152-140x

MASLOV Andrei M.
maslov@iacp.dvo.ru
ORCID: 0000-0002-8656-3167

GALKIN Nikolay G.
galkin@iacp.dvo.ru
ORCID: 0000-0003-4127-2988

Received 26.07.2024. Approved after reviewing 14.08.2024. Accepted 15.08.2024.

Conference materials
UDC 539.23+539.25+537.32+537.9
DOI: https://doi.org/10.18721/JPM.173.205

Mg_2Si synthesis on silicon crystals with different aspect ratio

E.Yu. Subbotin[1]✉, A.G. Kozlov[2], D.L. Goroshko[1],
I.M. Chernev[1], D.A. Khoroshilov [1], O.E. Lisenkov [1],
A.Yu. Zhizhchenko[1], S.A. Kitan'[1], N.G.Galkin[1]

[1] Institute of Automation and Control Processes FEB RAS, Vladivostok, Russia;

[2] Far Eastern Federal University, Vladivostok, Russia

✉ jons712@mail.ru

Abstract. In the paper synthesis of magnesium silicide (Mg_2Si) features on silicon crystal with different aspect ratio were observed. These crystals were etched from monocrystalline borondoped silicon wafers with (100) orientation by metal-assisted chemical etching. The synthesis was occurred in ultra-high vacuum condition by a solid phase epitaxy and the modified reactive epitaxy with ultrafast Mg deposition. The substrate temperature range in both methods was 340–390 °C. As result co-axial core-shell Si/Mg_2Si heterostructures with magnesium silicide thickness 500–1200 nm were produced.

Keywords: silicon, magnesium silicide, Mg_2Si, epitaxy, metal-assisted chemical etching, MACE, Raman, SEM

Fundings: The work was supported by Russian Science Foundation, grant 23-72-01128.

Citation: Subbotin E.Yu., Kozlov A.G., Goroshko D.L., Chernev I.M., Khoroshilov D.A., Lisenkov O.E., Zhizhchenko A.Yu., Kitan' S. A., Galkin N.G., Mg_2Si synthesis on silicon crystals with different aspect ratio, St. Petersburg State Polytechnical University Journal. Physics and Mathematics. 17 (3.2) (2024) 31–35. DOI: https://doi.org/10.18721/JPM.173.205

Материалы конференции
УДК 539.23+539.25+537.32+537.9
DOI: https://doi.org/10.18721/JPM.173.205

Синтез Mg_2Si на кремниевых кристаллах с различным аспектным соотношением

Е.Ю. Субботин[1]✉, А.Г. Козлов[2], Д.Л. Горошко[1],
И.М. Чернев[1], Д.А. Хорошилов[1], О.Е. Лисенков[1],
А.Ю. Жижченко[1], С.А. Китань[1], Н.Г. Галкин[1]

[1] Институт автоматики и процессов управления ДВО РАН, г. Владивосток, Россия;

[2] Дальневосточный федеральный университет, г. Владивосток, Россия

✉ jons712@mail.ru

Аннотация. В данной работе были рассмотрены особенности синтеза силицида магния (Mg_2Si) на кремниевых кристаллах с различным аспектным соотношением. Получение кристаллов кремния с различным сечением осуществлялось методом металлстимулированного химического травления кремниевых монокристаллических подложек, легированных бором, с ориентацией (100). Синтез осуществлялся в условиях сверхвысокого вакуума методами модифицированной реактивной эпитаксией со сверхбыстрым осаждением магния и твердофазной эпитаксией. Температура формирования лежала в пределах 390–340 °C. В результате получились коаксиальные гетероструктуры типа «ядро-оболочка» Si/Mg_2Si с толщиной покрытия Mg_2Si 500–1200 нм в зависимости от метода формирования.

Ключевые слова: кремний, силицид магния, Mg_2Si, эпитаксия, металлстимулированное химическое травление, МСХТ, Raman, СЭМ, эпитаксия

Финансирование: Грант РНФ «Гетероструктуры типа «ядро-оболочка» на основе силицида магния и кремния в качестве основы для термоэлектрических преобразователей» № 23-72-01128.

Ссылка при цитировании: Субботин Е.Ю., Козлов А.Г., Горошко Д.Л., Чернев И.М., Хорошилов Д.А., Лисенков О.Е., Жижченко А.Ю., Китань С.А., Галкин Н.Г. Синтез Mg_2Si на кремниевых кристаллах с различным аспектным соотношением // Научно-технические ведомости СПбГПУ. Физико-математические науки. 2024. Т. 17. № 3.2. С. 31–35. DOI: https://doi.org/10.18721/JPM.173.205

Introduction

Recently research and development of micrometer-size thermoelectric devices (μ-TED) were in a focus of many science groups [1, 2]. The important feature of such devices is high surface density of thermocouples ($> 10^6$ cm^{-2}) [3] that allows to generate relatively high output voltage at low temperature gradient (less than 10 K) and to work with fast cooling response. Such devices can be used for power supplying wearable electronic, wireless sensors and Internet of Things.

Such high-density arrays of semiconductor crystals with controllable lateral size, length and surface density can be produced by metal-assisted chemical etching (MACE) combined with high-resolution lithography [4]. As a thermoelectrical material magnesium silicide (Mg_2Si) was chosen due to it perspective thermoelectric performance [5], Mg and Si are ecology-friendly and relatively cheap elements and Mg_2Si is well-developed and matured in thermoelectrical terms [6, 7]. The research of core-shell heterostructures based on silicon and magnesium silicide is interesting also for solar energy [8] and infra-red photodetectors [9].

Materials and methods

Applying the mask was occurred by a high-resolution electron lithography on scanning electron microscope (SEM) ThermoFisher Scios 2 DualBeam. Taking SEM images and energy dispersive X-ray spectroscopy (EDX) analysis were occurred by this microscope. The mask is stripes with 1 – 2 μm thickness separated for 1 – 5 μm to each other. A 30 nm gold film with 1.5 – 3 nm adhesive titanium film were used as a catalytic layer. The deposition of Ti/Au films was occurred by electron beam sputtering with pretreatment surface by Ar^+ ions. The metal-assisted chemical etching was used for etching silicon substrates and producing silicon crystals with different aspect ratio. The solution consists 4.6 M HF (40%) and 0.23 or 0.44 M H_2O_2 (31%). Substrates are boron-doped monocrystalline silicon with (100) orientation and resistivity 1–10 Ω×cm. SEM and atomic force microscope NT-MDT Solver P47 were used for control of etching process.

The growth of Mg_2Si on the etched silicon was occurred in ultrahigh vacuum (UHV) chamber with basic pressure 2×10^{-9} Torr. Before loading in the chamber samples were pre-cleaned in Piranha solution, rinsed is deionized water, ethyl alcohol and dried. Then samples were annealed at 650 °C for 10 hours for degassing and remove oxide at 950 C for 40 minutes (high aspect ratio structures) or at 1160 °C during 5 minutes (for low aspect ratio structures). As a magnesium source was used tantalum tube with Mg pillars 5N purity. Work features of Mg source for reactive epitaxy with ultrafast Mg deposition described in [10, 11]. Mg flow was calibrated by quartz microbalance. Mg_2Si was synthesized by solid phase epitaxy and reactive epitaxy with ultrafast Mg flow at substrate temperature of 340–390 °C. The temperature was controlled by infra-red pyrometer PhotriX with working range of 300–1400 °C.

By Raman (NT-MDT Ntegra Spectra II) was used for control the synthesize process. An estimation of silicide thickness was carried out with cross-section of samples by focused ion beam (Ga^+) in the SEM. EDX was used for mapping of chemical elements.

Result and discussion

Mg_2Si growth on silicon structure with low aspect ratio (height ~1.5 μm, width ~1 μm, Fig. 1, *a*) was conducted by reactive epitaxy with ultrafast Mg deposition at 340 °C [10]. The deposited portion was ~1200 nm. As a result, the magnesium silicide film with ~500 nm thickness was synthesized (Fig. 1, *b*). The peak at 267.1 cm^{-1} on Raman spectra (Fig. 1, *c*) indicates on Mg_2Si [12].

It can be seen that reaction with high-intense but short Mg deposition appropriately leak on the flat surface of crystals that normal to Mg flow. But there is no film on sidewalls such silicon crystals. Taking into account this fact and the growth of the thick film on a monocrystalline substrate case [11] it can be summarized that the growth method works for low aspect ratio structures: planar μ-TED [13], thin film thermoelectric converters.

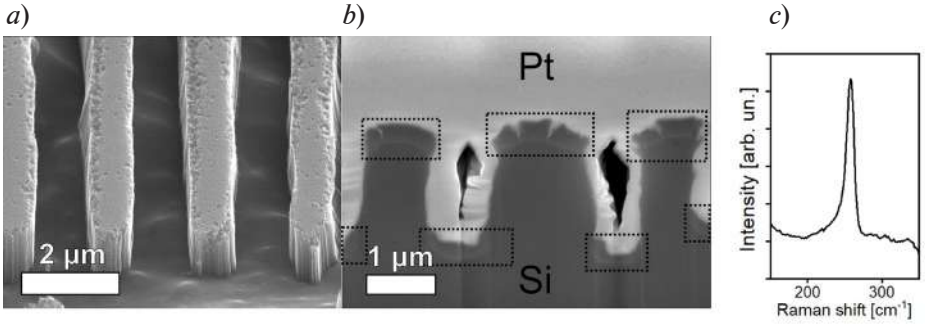

Fig. 1. SEM images of etched silicon crystals used as substrate for Mg_2Si layer growth (*a*) and cross-section of Mg_2Si/Si heterostructure (*b*) (silicide selected in dotted frames). Raman spectra with the peak at 267.1 cm^{-1} agree the silicide successful growth [12] (*c*)

Synthesis of the magnesium silicide on silicon patterns with high aspect ratio (width ≥ 290 nm, length > 20 μm, Fig. 2, *a*) was carried out by a solid phase epitaxy with step by step increasing recrystallization annealing temperature for 10 °C from 340 °C to 390 °C. The deposited portion was increased to ~5 μm.

By the method the Mg_2Si layer with maximum thickness ~1.2 μm was formed (Fig. 2, *b*, *c*). It is important to note that the method provide the silicide growths on sidewalls of crystals. Also, the silicide thickness was significantly increased. But the Mg_2Si growth on hidden (shaded) areas is not occurred. The difference in the deposited Mg portion and the film thickness is due to an intensive Mg desorption.

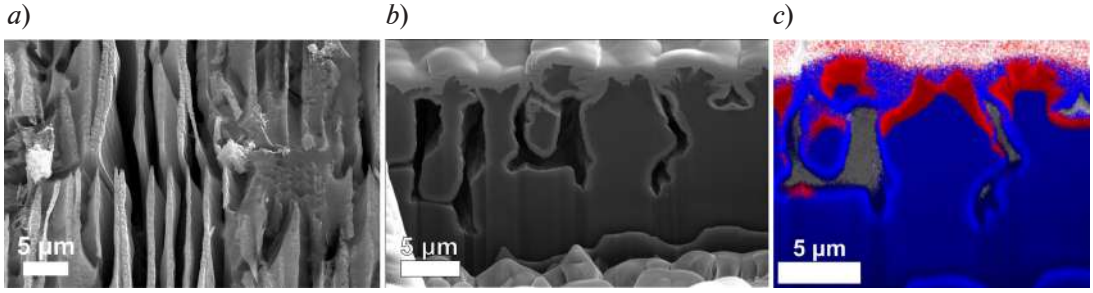

Fig. 2. SEM images of high aspect-ratio silicon crystals (*a*) and cross-section of Mg_2Si layers formed on the top of these crystals (*b*). EDX mapping of the chemical element's distribution (blue is silicon, red is Mg/Si mixture) (*c*)

For the next sample it was decided to modify the solid phase epitaxy method and to conduct the recrystallization annealing in the intensive magnesium flow (≥ 200 nm/min). The annealing was conduct for 40 minutes at fixed temperature 360 °C. The aspect ratio of silicon crystals of the sample is close to that shown on Fig. 1, *a*.

As can be seen, the method allows to growth the silicide shell both on sidewalls and shaded areas. The Mg_2Si layer thickness is ~1 μm.

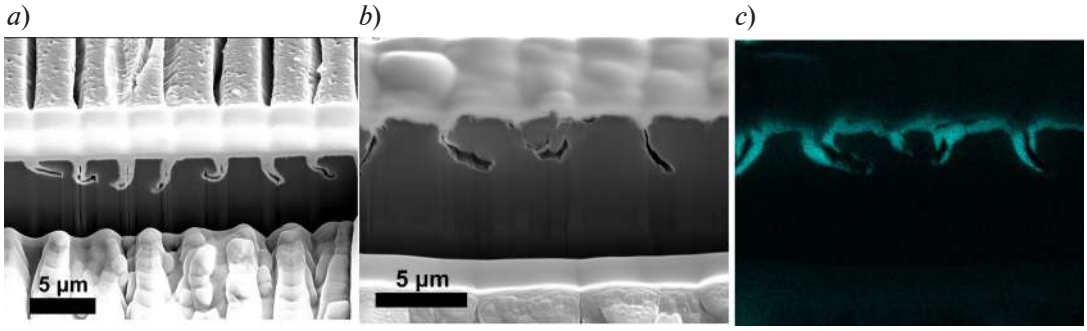

Fig. 3. SEM images of silicon crystals (*a*) and cross-section of Mg_2Si layers formed on the top of these crystals (*b*). EDX mapping of the chemical element's distribution (blue is a Mg/Si mixture) (*c*)

Conclusion

Using a solid phase epitaxy and reactive epitaxy with ultrafast magnesium deposition core-shell Mg_2Si/Si heterostructures were synthesized. It was showed that modified regime of reactive epitaxy is useful in cases of low aspect ratio structures, planar or thin film μ-TEDs. A solid phase epitaxy allows to increase the film thickness and to growth a shell around a silicon core.

REFERENCES

1. **Wang W., Zhao Z., Kuang N., et al.,** Experimental study and optimization of a combustion-based micro thermoelectric generator, Appl. Therm. Eng. 181 (2020) 115431.

2. **Zhang Q., Deng K., Wilkens L., et al.,** Micro-thermoelectric devices, Nat. El. 5 (2022) 333–347.

3. **Hu G., Edwards H., Lee M.,** Silicon integrated circuit thermoelectric generators with a high specific power generation capacity, Nat. El. 2 (2019) 300–306.

4. **Zhang X., Liu Y., Yao C., et al.,** Facile and stable fabrication of wafer-scale, ultra-black c-silicon with 3D nano/micro hybrid structures for solar cells, Nanoscale Advances. 5 (2023) 142–152.

5. **Ning H., Mastrorillo G.D., Grasso S., et al.,** Enhanced thermoelectric performance of porous magnesium tin silicide prepared using pressure-less spark plasma sintering, J. Mater. Chem. A. 3 (2015) 17426–17432.

6. **Singsoog K., Seetawan T.,** Effecting the thermoelectric properties of p-MnSi1. 75 and *n*-$Mg_{1.98}Ag_{0.02}Si$ module on power generation, Physica B Condens. Matter. 566 (2019) 1–5.

7. **Camut J., Ziolkowski P., Ponnusamy P., et al.,** Efficiency Measurement and Modeling of a High-Performance Mg_2 (Si, Sn)-Based Thermoelectric Generator, Advanced Engineering Materials. 25 (2023) 2200776.

8. **Shevlyagin A., Chernev I., Galkin N., et al.,** Probing the Mg_2Si/Si (111) heterojunction for photovoltaic applications, Sol. Energy. 211 (2020) 383–395.

9. **Zhu Q., Ye P., Tang Y., et al.,** High-performance broadband photoresponse of self-powered Mg_2Si/Si photodetectors, Nanotechnology. 33 (2021) 115202.

10. **Gouralnik A.S., Shevlyagin A.V., Chernev I.M., et al.,** Synthesis of crystalline Mg_2Si films by ultrafast deposition of Mg on Si (111) and Si (001) at high temperatures. Mg/Si intermixing and reaction mechanisms, Mater. Chem. Phys. 258 (2021) 123903.

11. **Chernev I.M., Subbotin E.Y., Kozlov A.G., et al.,** Thick p-type Mg_2Si film on Si: Growth, structure and transport properties, J. Alloys Compd. 964 (2023) 171301.

12. **Onari S., Cardona M.,** Resonant Raman scattering in the II-IV semiconductors Mg_2Si, Mg_2Ge, and Mg_2Sn, Phys. Rev. B. 14 (1976) 3520.

13. **Ohkubo I., Murata M., Lima M.S., et al.,** Miniaturized in-plane π-type thermoelectric device composed of a II–IV semiconductor thin film prepared by microfabrication. Materials Today Energy. 28 (2022) 101075.

THE AUTHORS

SUBBOTIN Evgenii Yu.
jons712@mail.ru
ORCID: 0000-0001-9531-3867

KOZLOV Alexey G.
kozlov.ag@dvfu.ru
ORCID: 0000-0001-8774-0631

GOROSHKO Dmitry L.
goroshko@iacp.dvo.ru
ORCID: 0000-0002-1250-3372

CHERNEV Igor M.
igor_chernev7@mail.ru
ORCID: 0000-0002-8726-9832

KHOROSHILOV Dmitry A.
khoroshilov.20092003@mail.ru
ORCID: 0009-0007-4827-2653

LISENKOV Oleg E.
oleglis2003@mail.ru
ORCID: 0009-0007-5206-5753

ZHIZHCHENKO Alexey Yu.
g89leksig@mail.ru
ORCID: 0000-0001-6878-679X

KITAN' Sergei A.
kitansa1981@gmail.com
ORCID: 0000-0003-3377-1912

GALKIN Nikolay G.
galkin@iacp.dvo.ru
ORCID: 0000-0003-4127-2988

Received 26.07.2024. Approved after reviewing 14.08.2024. Accepted 25.10.2024.

Conference materials
UDC 535.015
DOI: https://doi.org/10.18721/JPM.173.206

Random lasing in hydrothermal ZnO structures

S.A. Kadinskaya[1,2]✉, V.M. Kondratev[1,2], A.V. Nikolaeva[1,2], I.Kh. Akopyan[3], A.Yu. Serov[3], M.E. Labzovskaya[3], S.V. Mikushev[3], B.V. Novikov[3], I.V. Shtrom[3,4], A.D. Bolshakov[1,2,3,5]

[1] Alferov University, St. Petersburg, Russia;

[2] Moscow Center for Advanced Studies, Moscow, Russia;

[3] Saint Petersburg State University, St. Petersburg, Russia;

[4] Institute for Analytical Instrumentation RAS, St. Petersburg, Russia;

[5] Yerevan State University, Yerevan, Armenia

✉ skadinskaya@bk.ru

Abstract. In this manuscript, we present a study on the optical properties of ZnO nanowires synthesized via hydrothermal method. The nanowires were characterized by low temperature photoluminescence spectroscopy, revealing resonant modes indicative of random lasing behavior provided with scattering by misoriented nanowires. The spectral position of the resonant modes suggests lasing in the region of the P band of exciton-exciton interaction. Our results also indicate a correlation between the surface density of the nanostructures and peak intensity of the emission. Overall, our findings demonstrate the potential of hydrothermal synthesis for fabricating efficient light-emitting devices based on ZnO.

Keywords: zinc oxide, hydrothermal, photoluminescence

Funding: Ministry of Science and Higher Education of the Russian Federation: agreement 075-03-2023-106, project FSMG-2021-0005. Research project of St. Petersburg State University: no. 95440344. Russian science foundation (Grant 24-12-00225).

Citation: Kadinskaya S.A., Kondratev V.M., Nikolaeva A.V., Akopyan I.Kh., Serov A.Yu., Labzovskaya M.E., Mikushev S.V., Novikov B.V., Shtrom I.V., Bolshakov A.D., Random lasing in hydrothermal ZnO structures, St. Petersburg State Polytechnical University Journal. Physics and Mathematics. 17 (3.2) (2024) 36–41. DOI: https://doi.org/10.18721/JPM.173.206

Материалы конференции
УДК 535.015
DOI: https://doi.org/10.18721/JPM.173.206

Спонтанная генерация в гидротермальных структурах ZnO

С.А. Кадинская[1,2]✉, В.М. Кондратьев[1,2], А.В. Николаева[1,2], И.Х. Акопян[3], А.Ю. Серов[3], М.Е. Лабзовская[3], С.В. Микушев[3], Б.В. Новиков[3], И.В. Штром[3,4], А.Д. Большаков[1,2,3,5]

[1] Академический университет им. Ж.И. Алфёрова РАН, Санкт-Петербург, Россия;

[2] Московский физико-технический институт (национальный исследовательский университет), г. Долгопрудный, Россия;

[3] Санкт-Петербургский государственный университет, Санкт-Петербург, Россия;

[4] Институт аналитического приборостроения РАН, Санкт-Петербург, Россия;

[5] Ереванский Государственный Университет, Ереван, Армения

✉ skadinskaya@bk.ru

Аннотация. В данной работе мы представляем исследование оптических свойств нитевидных нанокристаллов (ННК) ZnO, синтезированных гидротермальным методом. ННК были охарактеризованы с помощью низкотемпературной спектроскопии фотолюминесценции, выявившей резонансные моды, указывающие на спонтанную генерацию, обусловленную рассеянием на неориентированных ННК. Спектральное положение резонансных мод предполагает генерацию в области P-полосы экситон-экситонного взаимодействия. Наши результаты также указывают на корреляцию между поверхностной плотностью наноструктур и пиковой интенсивностью излучения. В целом наши результаты демонстрируют потенциал гидротермального синтеза для изготовления эффективных светоизлучающих устройств на основе ZnO.

Ключевые слова: оксид цинка, гидротермальный, фотолюминесценция

Финансирование: Работа выполнена в рамках Государственного задания Министерства науки и высшего образования Российской Федерации (Соглашение 106-2023-03-075 от 13.01.2023, проект FSMG-2021-0005). Научный грант СПбГУ № 95440344. Грант Российского Научного Фонда (Грант 00225-12-24).

Ссылка при цитировании: Кадинская С.А., Кондратьев В.М., Николаева А.В., Акопян И.Х., Серов А.Ю., Лабзовская М.Э., Микушев С.В., Новиков Б.В., Штром И.В., Большаков А.Д. Спонтанная генерация в гидротермальных структурах ZnO // Научно-технические ведомости СПбГПУ. Физико-математические науки. 2024. Т. 17. № 3.2. С. 36–41. DOI: https://doi.org/10.18721/JPM.173.206

Introduction

Nano- and micro-sized structures find a wide range of applications in various fields from sensors [1] to UV [2,3] and visible range emitters [4]. In the era of information technology and digital multimedia, specific types of light sources based on wide-gap semiconductors, capable of generating violet and ultraviolet (UV) radiation, are becoming increasingly popular in modern optoelectronics and medicine. The high efficiency, rapid switching capabilities, low power consumption, and comparatively low heat dissipation of LEDs based on wide-gap semiconductors have led to their widespread use in both high-end and consumer technologies. For instance, high-efficiency LEDs have replaced traditional backlight units in LCDs.

Zinc oxide (ZnO), which band gap allows using it in UV devices, has attracted significant attention in recent years. Apart from its band gap of 3.37 eV at room temperature, a particularly noteworthy characteristic of ZnO is its large exciton binding energy (60 meV), which is significantly higher than the thermal energy at room temperature (about 26 meV) [5]. This fact indicates that the excitonic effect in ZnO can be maintained up to room temperature, allowing for efficient UV radiation. In addition, ZnO is cheap, relatively abundant, chemically stable, easy to synthesize, and nontoxic. Although there are currently a large number of light-emitting devices based on ZnO, fabrication of low-dimensional, high-performance, and technologically simple solutions remains challenging. This is an area where several unresolved issues exist.

In this study, we employ hydrothermal synthesis [6, 7] of ZnO nanostructures, a method that allows growth of various materials and compounds through physical and chemical processes in aqueous solutions. The advantages of hydrothermal synthesis include the broad ability to control growth conditions, the capability of low-temperature synthesis (below 100 °C), which significantly reduces cost, as well as decreasing the hazard class of the production. In addition, this method enables the synthesis of zinc oxide structures on various substrates, both lattice-matched and not, such as silicon, making this synthesis method suitable for integration with silicon technologies. We synthesized ZnO nanowires with different surface densities directly on a silicon substrate and investigated their low-temperature photoluminescence properties. Our results show that the luminescence properties of the nanowires change significantly with changes in the surface structure distribution. This study demonstrates the potential of this simple and low-cost synthesis method for advancing random laser sources.

Materials and Methods

In our study, we utilize silicon substrate Si (111) for the hydrothermal synthesis of ZnO nanostructures. An aqueous solution of zinc acetate was employed as the seed layer. These seed layers were applied using the spin-coating method. The solution consists of equimolar aqueous solutions of $Zn(NO_3)_2$ and hexamethylenetetramine (HMTA) at a concentration of 50 mmol·l^{-1}. The following reactions occur during the synthesis process:

$$C_6H_{12}N_4 + 6H_2O \rightarrow 6HCHO + 4NH_3, \quad (1)$$

$$NH_3 + H_2O \rightarrow NH^{4+} + OH^-, \quad (2)$$

$$Zn(NO_3)_2 \leftrightarrow Zn^{2+} + 2NO_3, \quad (3)$$

$$2OH^- + Zn^{2+} \leftrightarrow Zn(OH)_2, \quad (4)$$

$$Zn(OH)_2 \leftrightarrow ZnO + H_2O. \quad (5)$$

During the synthesis, a constant temperature of 85 °C was maintained. The synthesis duration for all samples was 3 hours.

The synthesized samples were placed in a closed-cycle helium cryostat (Janis Research Company, USA). The sample temperature was about 10 K. The PL was excited by a He-Cd laser (λ = 325 nm, excitation power W = 50 kW·cm^{-2}) and by an ultraviolet solid-state laser LCM-DTL-374QT (λ = 355 nm).

Results and Discussion

As a result of the synthesis, three characteristic samples with distinctive density were fabricated. SEM images obtained in the selected regions (see Fig. 1) were analyzed, showing the presence of disoriented ZnO NWs with hexagonal faceting and a high aspect ratio of about 10:1 across the entire surface of the sample.

The data on the surface distribution density and the average length of the NWs in different areas are presented in Table 1. It is noted that the distribution density of the NWs decreases towards the edges of the growth substrate, which is likely due to the design features of the sample holder that restrict access to the growth solution.

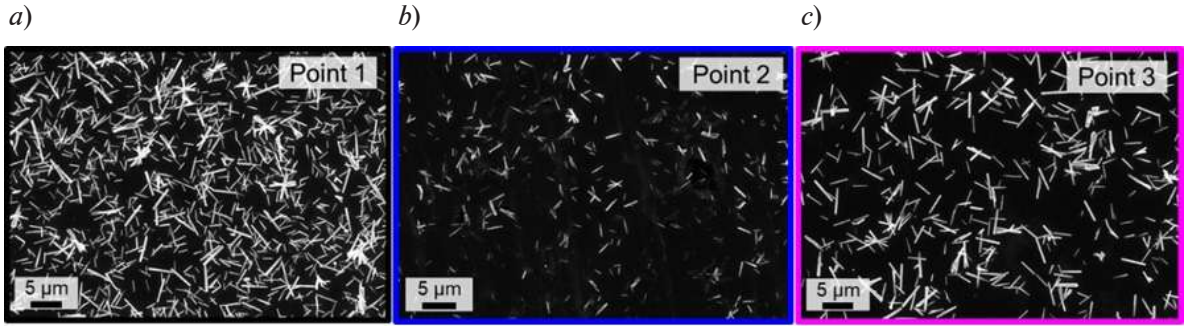

Fig. 1. SEM images showcasing three characteristic morphologies

Table 1

Data on distribution of NW density and their average length in different areas of the sample

Area	Distribution density, %	Average length, μm
Point 1	22.6	1.74
Point 2	4.3	1.24
Point 3	12	2.16

The optical properties of the synthesized ZnO were investigated using photoluminescence (PL) spectroscopy. The results of the PL measurements of the samples shown in Fig. 1 are depicted in Fig. 2, *a* and demonstrate UV emission centered near 372 nm for all of the samples. Remarkably, upon excitation narrow lines in the region $\lambda \simeq 373-376$ nm are observed in the PL spectra (Fig. 2, *a*). Such a behavior is a manifestation of the resonant action of the grown structures leading to the amplification of the resonant modes. Fig. 2, *b* shows the change in the luminescence intensity with increasing optical pumping. The obtained plot demonstrates a transition between two linear regimes which is typical for the occurrence of a stimulated emission. The threshold value is found at 140 kW·cm^{-2}. We believe that a cluster of disoriented ZnO crystals forms an optical structure that acts as a resonator providing peculiar scattering and stimulating occurrence of a closed optical circuit, which leads to selective amplification of the optical modes. The spectral position of the corresponding lines indicates that laser generation probably occurs in the P band region of the exciton–exciton interaction [8]. A correlation is observed between the density distribution and the intensity of peaks in the photoluminescence spectra. At Point

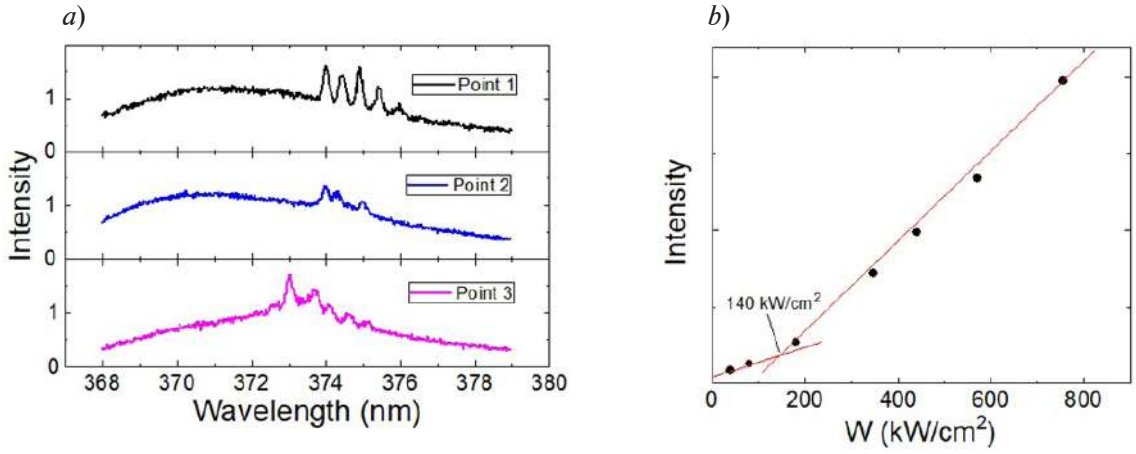

Fig. 2. Photoluminescence spectra taken at different points of synthesized sample (*a*); change in luminescence intensity with increasing excitation laser power *W* (*b*)

1, the NWs have the highest density, which leads to distinctly pronounced intense peaks in the spectra. Presumably, the high surface density leads to the formation of a greater number of closed circuits acting as resonators, resulting in an increased intensity of the PL. Based on the data obtained, it can be concluded that formation of lasing structures is feasible through the modification of structures density on the sample surface. Such a change in structures density can be implemented at the synthesis stage by adjusting seed layers' number and precursors concentration in the growth solution.

Conclusion

We synthesized via hydrothermal method and studied optical action of ZnO nanowires. Low temperature PL spectra revealed occurrence of the resonant modes observed at different points of the sample. Pump-power dependence of the intense modes demonstrate threshold behaviour typical for the stimulated emission. The spectral position of the resonant modes indicates that lasing most likely occurs in the region of the P band of the exciton–exciton interaction. We also observe correlation between the surface density of the nanostructures and peak intensity of the emission. The results show that a simple hydrothermal synthesis method is promising for fabricate efficient light-emitting devices based on ZnO.

Acknowledgments

S.A.K. and V.M.K acknowledge financial support of the microscopic studies by the Ministry of Science and Higher Education of the Russian Federation (agreement 075-03-2023-106, project FSMG-2021-0005). A.D.B. acknowledges Russian Science Foundation (Grant 24-12-00225) for financial support of the data analysis. I.V.Sh. acknowledges Saint Petersburg State University for a research project № 95440344.

REFERENCES

1. **Kondratev V.M., Morozov I.A., Vyacheslavova E.A., Kirilenko D.A., Kuznetsov A., Kadinskaya S.A., Nalimova S.S., Moshnikov V.A., Gudovskikh A.S., Bolshakov A.D.** Silicon Nanowire-Based Room-Temperature Multi-environment Ammonia Detection, ACS Applied Nano Materials. 5 (7) (2022) 9940–9949.

2. **Kadinskaya S.A., Kondratev V.M., Kindyushov I.K., Kuznetsov A., Punegova K.N.** Hydrothermal ZnO-based Nanostructures: Geometry Control and Narrow Band UV Emission, 2022 Conference of Russian Young Researchers in Electrical and Electronic Engineering (ElConRus). (2022) 958–961.

3. **Kadinskaya S.A., Kondratev V.M., Kindyushov I.K., Labzovskaya M.E., Novikov B.V., Shtrom I.V., Lihachev A.I., Nashchekin A.V. and Bolshakov A.D.** Hydrothermal zinc oxide nanostructures: geometry control and narrow band UV emission, J. Phys.: Conf. Ser. (2227) (2022) 012007.

4. **Kuznetsov A., Roy P., Kondratev V.M., Fedorov V.V., Kotlyar K.P., Reznik R.R., Vorobyev A.A., Mukhin I.S., Cirlin G.E., Bolshakov A.D.** Anisotropic Radiation in Heterostructured "Emitter in a Cavity" Nanowire, Nanomaterials. 12 (2) (2022) 241.

5. **Look D.C., Claflin B., Alivov Y.I., Park S.J.** The Future of ZnO Light Emitters. Phys. status solidi. 201 (2004) 2203–2212.

6. **Kadinskaya S.A., Kondratev V.M., Kindyushov I.K., Koval O.Yu., Yakubovsky D.I., Kusnetsov A., Lihachev A.I., Nashchekin A.V., Akopyan I.Kh., Serov A.Yu., Labzovskaya M.E., Mikushev S.V., Novikov B.V., Shtrom I.V., Bolshakov A.D.** Deep-Level Emission Tailoring in ZnO Nanostructures Grown via Hydrothermal Synthesis. Nanomaterials. 13 (1) (2022) 58.

7. **Gerbreders V., Krasovska M., Sledevskis E., Gerbreders A., Mihailova I., Tamanis E., Ogurcovs A.** Hydrothermal Synthesis of ZnO Nanostructures with Controllable Morphology Change. CrystEngComm. (2020) 22.

8. **Klingshirn C., Fallert J., Zhou H., Sartor J., Thiele C., Maier-Flaig F., Schneider D., Kalt H.,** 65 years of ZnO research – old and very recent results, Phys. Status Solidi B. 6 (2010) 1424.

THE AUTHORS

KADINSKAYA Svetlana A.
skadinskaya@bk.ru
ORCID: 0000-0003-2508-2244

KONDRATEV Valeriy M.
kvm_96@mail.ru
ORCID: 0000-0002-3469-5897

NIKOLAEVA Aleksandra V.
nikalex2000@bk.ru
ORCID: 0009-0008-4344-4863

AKOPYAN Irina Kh.
irina-akopyan@yandex.ru

SEROV Alexey Yu.
serovpobox@gmail.com

LABZOVSKAYA Mariana V.
xrul@mail.ru

MIKUSHEV Sergey V.
sergey.mikushev@gmail.com
ORCID: 0000-0002-3705-9706

NOVIKOV Boris V.
bono1933@mail.ru

SHTROM Igor V.
igorstrohm@mail.ru
ORCID: 0000-0001-8912-2570

BOLSHAKOV Alexey D.
acr1235@mail.ru
ORCID: 0000-0001-7223-7232

Received 29.07.2024. Approved after reviewing 19.08.2024. Accepted 26.08.2024.

Conference materials
UDC 538.975
DOI: https://doi.org/10.18721/JPM.173.207

Hierarchical self-assembly of SiO_2-SnO_2 nano- and microstructures in combined sol-gel systems

I.A. Filippov[1], N.D. Yakushova[1], A.A. Karmanov[1]✉,
I.A. Gubich[2], I.A.Pronin[1]

[1] Penza State University, Penza, Russia;

[2] Joint Stock Company "NIIFI", Penza, Russia

✉ starosta07km1@mail.ru

Abstract. Using the IR spectroscopy method, studies were carried out on the processes of hierarchical self-assembly of SiO_2-SnO_2 nano- and microstructures in combined sol-gel systems obtained by mixing film-forming sols with different maturation times, which meets the goals and objectives of nanostructural engineering. Characteristic absorption peaks were identified that correspond to the process of hydrolytic polycondensation and carry information about the process of self-assembly in the analyzed systems.

Keywords: nanostructure engineering, hierarchical self-assembly, sol-gel technology, spectroscopic investigation

Funding: The study was supported by a grant from the Russian Science Foundation no. 23-79-01280, https://rscf.ru/project/23-79-01280/.

Citation: Filippov I.A., Yakushova N.D., Karmanov A.A., Gubich I.A., Pronin I.A., Hierarchical self-assembly of SiO_2-SnO_2 nano- and microstructures in combined sol-gel systems, St. Petersburg State Polytechnical University Journal. Physics and Mathematics. 17 (3.2) (2024) 42–45. DOI: https://doi.org/10.18721/JPM.173.207

Материалы конференции
УДК 538.975
DOI: https://doi.org/10.18721/JPM.173.207

Иерархическая самосборка нано- и микроструктур SiO_2-SnO_2 в комбинированных золь-гель системах

И.А. Филиппов[1], Н.Д. Якушова[1], А.А. Карманов[1]✉,
И.А. Губич[2], И.А. Пронин[1]

[1] Пензенский государственный университет, г. Пенза, Россия

[2] АО «Научно-исследовательский институт физических измерений», г. Пенза, Россия

✉ starosta07km1@mail.ru

Аннотация. С использованием метода ИК-спектроскопии проведены исследования процессов иерархической самосборки нано- и микроструктур SiO_2-SnO_2 в комбинированных золь-гель системах, полученных путем смешения пленкообразующих золей с различным временем созревания, что отвечает целям и задачам наноструктурной инженерии. Установлены характеристические пики поглощения, соответствующие процессу гидролитической поликонденсации и несущие информацию о процессе самосборки в анализируемых системах.

Ключевые слова: наноструктурная инженерия, иерархическая самосборка, золь-гель технология, спектроскопические исследования

Финансирование: Исследование выполнено в рамках гранта Российского научного фонда № 23-79-01280, https://rscf.ru/project/23-79-01280/.

Ссылка при цитировании: Филиппов И.А., Якушова Н.Д., Карманов А.А., Губич И.А., Пронин И.А. Иерархическая самосборка нано- и микроструктур SiO_2-SnO_2 в комбинированных золь-гель системах // Научно-технические ведомости СПбГПУ. Физико-математические науки. 2024. Т. 17. № 3.2. С. 42–45. DOI: https://doi.org/10.18721/JPM.173.207

Introduction

In recent years, wide-bandgap semiconductor metal oxides such as ZnO, SnO_2, TiO_2, In_2O_3, etc. have attracted increasing interest. First of all, this is due to the wide scope of their practical application, including, among other things, solving gas sensory problems [1]. At the same time, it is becoming increasingly important to develop new methods and approaches to nanostructure engineering that make it possible to control the properties of these materials both through macro-level influences and by controlling the process of their synthesis at the earliest stages. For example, it is known that varying the maturation time of a film-forming sol leads to a new type of micro- and nanostructure of the metal oxide material [2].

Materials and Methods

Combined sol-gel SiO_2-SnO_2 systems were prepared within the framework of nanostructure engineering methods and approaches, which were first proposed to control the process of hierarchical self-assembly of zinc oxide nano- and microstructures [3]. The main idea is to mix film-forming sols with different maturation times in a given volume ratio (1:1, 2:1, 1:2). As part of this study, an analysis of a two-component SiO_2-SnO_2 system with a mass fraction of tin dioxide of 80 wt% was carried out. Thin films based on combined sol-gel systems were synthesized by applying film-forming sols to substrates made of oxidized monocrystalline silicon KEF (100) measuring 10×10 mm^2 by centrifugation (at a speed of 4000 rpm), followed by annealing in air atmosphere (for 30 min at temperature 550 °C).

The qualitative composition of film-forming sols, as well as the processes of hierarchical self-assembly, were studied by IR spectroscopy on an IR-Fourier spectrometer FSM 1201 (Infraspek LLC, Russia) within the method of multiple attenuation of total internal reflection using a MNPVO36 ZnSe cell. The surface morphology of the samples obtained on the basis of combined sol-gel systems was studied using the MIRA3 (Tescan) scanning electron microscope.

Results and Discussion

Fig. 1 shows the IR spectra of combined sol-gel systems SiO_2-SnO_2 with a maturation time of 1 hour (sample no. *1*) and 24 hours (sample no. *5*), respectively, as well as IR spectra of sols obtained by mixing samples no. *1* and no. *5* in a volume ratio of 2:1 (sample no. *2*), 1:1 (sample no. *3*) and 1:2 (sample no. *4*), respectively. Analysis of the presented IR spectra shows that mixing film-forming sols with different maturation times does not lead to the emergence of new characteristic vibrational modes. This allows concluding that new chemical bonds are not formed, and there is no noticeable change in the qualitative composition of combined sol-gel systems when mixing sols with different maturation times.

To analyze self-assembly processes occurring in the considered combined sol-gel systems, the most informative is the absorption peak with a maximum of 1010 cm^{-1} (inset in Fig. 1), which corresponds to the results of previous studies [4]. This vibrational mode corresponds to symmetrical stretching vibrations of Si-O-Si and a decrease in transmission with increasing maturation time of film-forming sols corresponds to the process of hydrolytic polycondensation, the consequence of which is the hierarchical self-assembly of nano- and microstructures of SiO_2-SnO_2, which have a fractal nature [5].

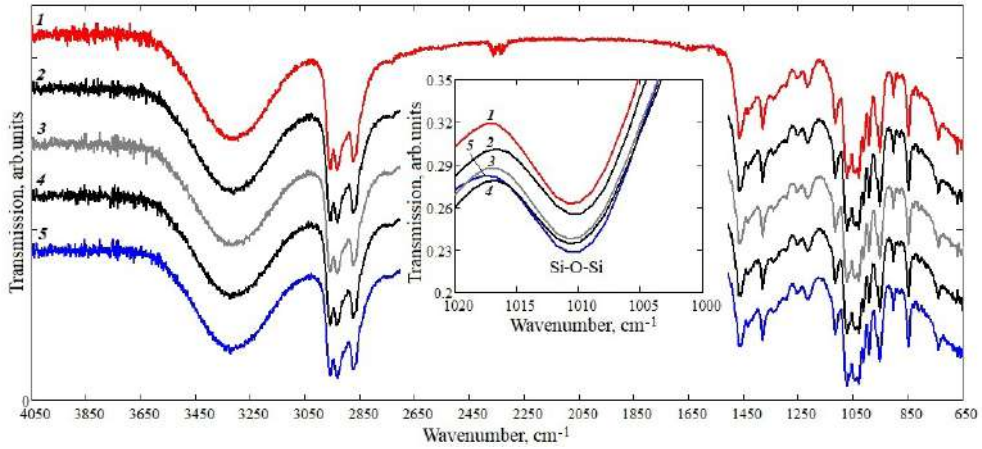

Fig. 1. IR transmission spectra of combined sol-gel systems with different maturation times: *1* corresponds to 1 hour, *2* to 1 hour + 24 hours in a volume ratio of 2:1, *3* to 1 hour + 24 hours in a volume ratio of 1:1, *4* to 1 hour + 24 hours in a volumetric ratio of 1:2, *5* to 24 hours

Fig. 2, *a* shows a diagram illustrating the relationship between the IR transmission rate of combined sol-gel systems and the maturation time, as well as the volume ratio of the mixed sols.

The analysis of the diagram indicates that for combined sol-gel systems under study, an increase in the maturation time leads to an apparent decrease in the transmission rate from 0.263 to 0.229 for 1 hour and 24 hours, respectively. Taking into account that the studied vibrational mode corresponds to the process of hydrolytic polycondensation, this can be attributed to the enlargement of fractal clusters during self-assembly [6]. Mixing film-forming sols in a given volume ratio results in the fact that in the illustrative diagram the minimum transmission rate of the analyzed vibrational mode is located closer to the film-forming sol, the ratio of which is larger. This leads to an assumption that mixing sols with different maturation times creates a new type of size distribution of fractal clusters and, ultimately, to a new type of structure of thin films synthesized from combined sol-gel systems. In particular, mixing film-forming sols with maturation times of 1 hour and 24 hours in the volumetric ratio of 2:1 results in forming SiO_2-SnO_2 nano- and microstructures (Fig. 2, *b*) with hierarchical spatial organization [7].

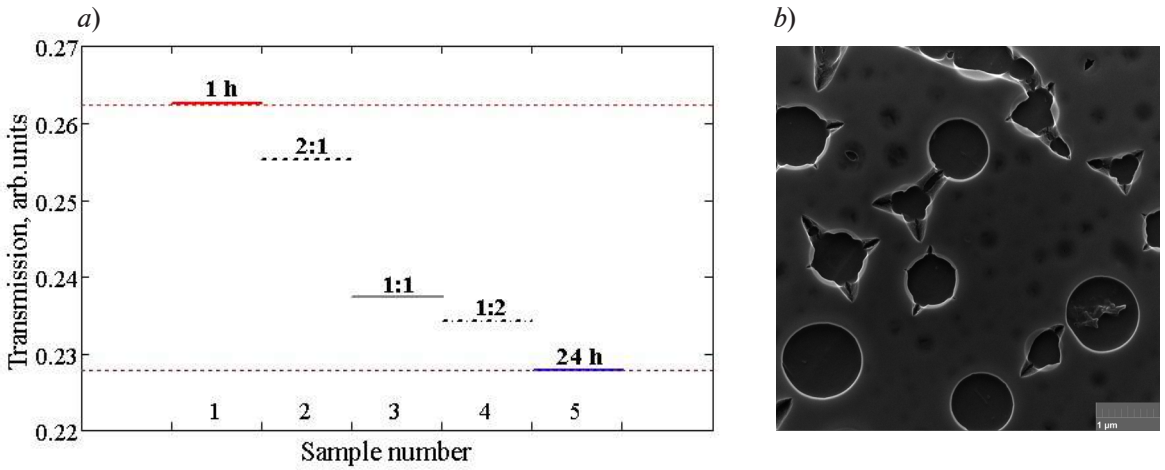

Fig. 2. Illustrative diagram (*a*) of IR transmission rate through combined sol-gel systems and SEM image (*b*) of thin film synthesized from combined sol-gel systems obtained by mixing sols with maturation time of 1 hour and 24 hours in volume ratio 2:1

Conclusion

Thus, this study shows that infrared spectroscopy is a promising method for studying the hierarchical self-assembly of SiO_2-SnO_2 nano- and microstructures in combined sol-gel systems. It has been established that the mixing of sols with different maturation times affects the intensity of the characteristic peaks and absorption bands corresponding to the process of hydrolytic polycondensation. The obtained spectroscopic patterns were verified by experimental data from scanning electron microscopy of thin films synthesized from combined sol-gel systems.

REFERENCES

1. **Ben Arbia M., Helal H., Comini E**. Recent Advances in Low-Dimensional Metal Oxides via Sol-Gel Method for Gas Detection, Nanomaterials. 4 (14) (2024) 359.

2. **Xiong L., Li J., Ye F., Wang H., Guo Y., Ming X., Chen Q., Zhang S., Xie R., Chen Z., Lv Y., Hu G., He Y., Fang G.** Bifunctional SnO_2 colloid offers no annealing time effect compact layer and mesoporous scaffold for efficient perovskite solar cells, Advanced Functional Materials. 36 (31) (2024) 2103949.

3. **Karmanov A.A., Sukhov I.V., Yakushova N.D., Igoshina S.E., Pronin I.A.** Hierarchical Self-Assembly of Nano- and Microstructures of Zinc Oxide in Combined Sol-Gel Systems, Nano- i mikrosistemnaya tekhnika. 2 (26) (2024) 96–103.

4. **Pronin I.A., Averin I.A., Yakushova N.D., Karmanov A.A., Moshnikov V.A., Ham M.-H., Cho B.K., Korotcenkov G.,** Structural features of silica coating obtained from sol cooled to the temperature of liquid nitrogen, Arabian Journal for Science and Engineering. 10 (42) (2017) 4299–4305.

5. **Hasmy A., Primera J., Woignier T.** Cluster–cluster aggregation with mobile impurities, Journal of Sol-Gel Science and Technology. 1 (90) (2019) 87–94.

6. **Kononova I., Kononov P., Moshnikov V.A.** Step by Step modeling and experimental study on the Sol-Gel porous structure of percolation nanoclusters, Coatings. 2 (13) (2023) 449.

7. **Vafaei S., Wolosz A., Ethridge C., Schnupf U., Hattori N., Sugiura T., Manseki K.** Elucidation of the Crystal Growth Characteristics of SnO_2 Nanoaggregates Formed by Sequential Low-Temperature Sol-Gel Reaction and Freeze Drying, Nanomaterials. 7 (11) (2021) 1738.

THE AUTHORS

FILIPPOV Ivan A.
iffilippoff@yandex.ru
ORCID: 0009-0008-7579-338X

YAKUSHOVA Nadezhda D.
yand93@mail.ru
ORCID: 0000-0002-0358-7818

KARMANOV Andrey A.
starosta07km1@mail.ru
ORCID: 0000-0001-8318-8149

GUBICH Ivan A.
gubich.niifi@gmail.com

PRONIN Igor A.
pronin_i90@mail.ru
ORCID: 0000-0003-3037-3601

Received 30.07.2024. Approved after reviewing 12.08.2024. Accepted 12.08.2024.

Conference materials
UDC 538.9
DOI: https://doi.org/10.18721/JPM.173.208

Johnson noise thermometry of CVD graphene bolometers

P.I. Bondareva[1,2]✉, K.V. Shein[1,2], A.N. Lyubchak[2], R.I. Izmaylov[1], E.M. Baeva[1], G.N. Goltsman[1], I.A. Gayduchenko[2]

[1] Moscow Pedagogical State University, Moscow, Russia;

[2] National Research University Higher School of Economics, Moscow, Russia

✉ p.bondareva2016@yandex.ru

Abstract. Graphene, due to its record low electron heat capacity and weak electron-phonon coupling at low temperatures, is considered as a promising material for creating terahertz hot electron bolometers. The main challenge to the development of such devices is the weak dependence of graphene resistance on temperature. Here we demonstrate measurement system based on Johnson noise thermometry to directly measure electron temperature in graphene. We measure thermal conductance due to electron-phonon coupling at bath temperature 4,2 K. Our graphene is synthesized by chemical vapor deposition (CVD) method and transferred to Si/SiO_2 substrate. The electron−phonon thermal conductance has a temperature power law of T^4 which is typical for highly disordered graphene. We estimate the sensitivity of CVD graphene based bolometer with Johnson noise readout. The internal noise equivalent power (NEP) is determined by thermodynamic fluctuations and is equal to 3 fW/$Hz^{0.5}$. The sensitivity of the detector is limited by the read out noise and is equal to 267 pW/$Hz^{0.5}$. The low internal NEP together with potential fast response time makes CVD graphene to be promising material in the area of bolometry.

Keywords: graphene, THz detectors, bolometers, noise thermometry

Funding: The study was supported by RNF (project no. 23-72-00014).

Citation: Bondareva P.I., Shein K.V., Lyubchak A.N., Izmaylov R.I., Baeva E.M., Goltsman G.N., Gayduchenko I.A., Johnson noise thermometry of CVD graphene bolometers, St. Petersburg State Polytechnical University Journal. Physics and Mathematics. 17 (3.2) (2024) 46−51. DOI: https://doi.org/10.18721/JPM.173.208

Материалы конференции
УДК 538.9
DOI: https://doi.org/10.18721/JPM.173.208

Шумовая термометрия болометров на основе графена, синтезированного методом химического осаждения из газовой фазы

П.И. Бондарева[1,2]✉, К.В. Шеин[1,2], А.Н. Любчак[2], Р.И. Измайлов[1], Э.М. Баева[1], Г.Н. Гольцман[1], И.А. Гайдученко[2]

[1] Московский педагогический государственный университет, Москва, Россия;

[2] Национальный исследовательский университет «Высшая школа экономики», Москва, Россия

✉ p.bondareva2016@yandex.ru

Аннотация. Графен, обладая рекордно низкой электронной теплоемкостью и слабой электрон-фононной связью при низких температурах, представляет собой многообещающий материал для разработки терагерцовых болометров на основе горячих электронов. Основной проблемой является слабая зависимость сопротивления графена от температуры. В данной работе мы демонстрируем использование метода шумовой термометрии Джонсона-Найквиста для прямого измерения температуры электронов в графене. Мы исследуем теплопроводность, обусловленную электрон-фононным взаимодействием, при температуре 4,2 K. Графеновая пленка была синтезирована методом химического осаждения из газовой фазы (CVD) и перенесена на подложку кремния, покрытую термическим оксидом SiO_2. Результаты исследования показали, что электрон-фононная теплопроводность имеет степенную зависимость от температуры T^4, что характерно для сильно разупорядоченного графена. Мы оценили внутреннюю эквивалентную мощность шума (ЭМШ) детектора, которая определяется термодинамическими флуктуациями и равна 3 фВт/Гц$^{0.5}$. Чувствительность детектора ограничена шумом схемы считывания сигнала и равна 267 пВт/Гц$^{0.5}$. Низкое значение внутренней ЭМШ вместе с потенциально быстрым временем отклика делает CVD-графен перспективным материалом в области болометрии.

Ключевые слова: графен, ТГц детекторы, болометры, шумовая термометрия

Финансирование: Исследование было проведено при поддержке РНФ (проект № 23-72-00014).

Ссылка при цитировании: Бондарева П.И., Шеин К.В., Любчак А.Н., Измайлов Р.И., Баева Э.М., Гольцман Г.Н., Гайдученко И.А. Шумовая термометрия болометров на основе графена, синтезированного методом химического осаждения из газовой фазы // Научно-технические ведомости СПбГПУ. Физико-математические науки. 2024. Т. 17. № 3.2. С. 46–51. DOI: https://doi.org/10.18721/JPM.173.208

Introduction

Currently, the terahertz (THz) range of the electromagnetic spectrum is of great interest due to a wide range of potential applications: medical diagnostics, non-destructive testing, security systems and data transmission [1]. These and many other applications require fast and sensitive THz detectors that can be easily combined into matrices. Graphene is a unique material for detection of THz radiation in the terahertz range due to its record-low electron heat capacity and weak electron-phonon coupling. This leads to a strong heating of the graphene electronic system under terahertz radiation. The main problem in the implementation of graphene terahertz detectors arises from the weak dependence of graphene resistance on temperature [2]. To measure the temperature of electron gas in graphene under electromagnetic radiation, various signal readout systems have been developed: noise thermometry method [3], Josephson junctions [4] and photo-thermoelectric

method [5]. In addition, sensitive infrared [6] and microwave [4] bolometers based on graphene have been demonstrated. However, most of the works presented in the literature to date investigate thermal transport in high-quality graphene encapsulated in boron nitride [7], as well as exfoliated graphene on a $Si0_2$ substrate [3], which are difficult to apply in practice.

In this paper, we present a study of the thermal transport of graphene synthesized chemical vapor deposition (CVD) method to develop THz bolometers. We measure thermal conductance due to electron-phonon coupling at bath temperature 4.2 K and estimate intrinsic performance limits of CVD graphene bolometers. The value of thermal conductance G is $G = 6.7$ nW/K which leads to internal noise equivalent power limited by thermodynamic fluctuations of 3 fW/Hz$^{0.5}$. The sensitivity of the detector is limited by the readout noise and is equal to 267 pW/Hz$^{0.5}$.

Results and Discussion

Our samples are field-effect transistors in which graphene acts as a conduction channel (Fig. 1, *a*). We have fabricated our devices based on graphene synthesized using chemical vapor deposition (CVD), which is the most industrially viable method for producing graphene. The detailed description of device fabrication is presented in [8].

The transport properties of the manufactured devices were characterized at 4.2 K (Fig 1, *b*). Following [9] we estimated field mobility, residual concentration of charge carriers, as well as concentration dependence on applied gate voltage of the CVD graphene-based device. The field mobility was 650 cm^{2}V^{-1}s^{-1} in our case. We note that the field mobility gives us a lower bound on the mobility estimation and strongly depends on the contact resistance.

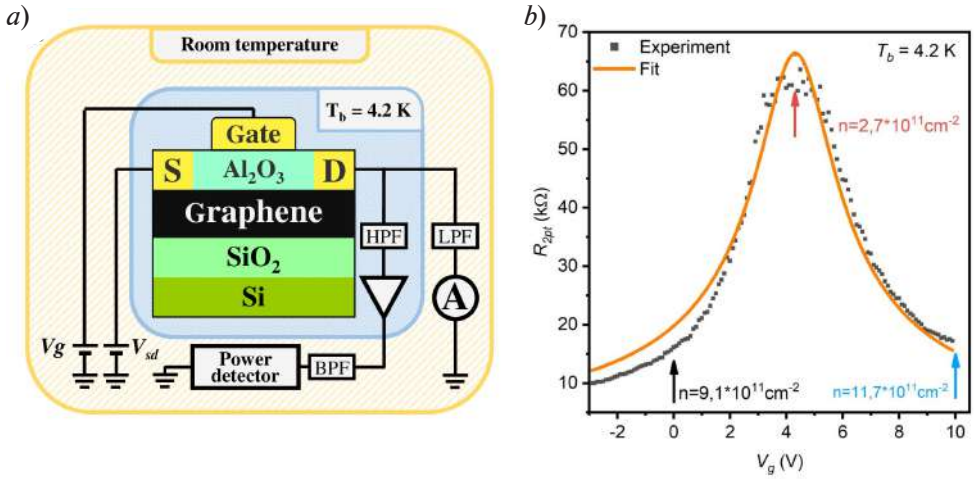

Fig. 1. Schematic of the device and Johnson noise thermometry scheme (*a*). Typical dependence of two-point resistance on gate voltage: the dots are the experimental data, the orange curve is a fitting curve according to [9]. Measured at $T = 4.2$ K. The arrows illustrate the values of charge carrier concentration at which the measurements were made using the noise thermometry method (*b*)

The temperature of the graphene electron system was measured as a function of applied DC current and concentration of charge carriers. The values of the charge carrier concentration at which the measurements were carried out are marked with arrows in Fig. 1, *b*. For noise thermometry we measure the current noise spectral density S_I in the current-biased regime and determine the noise temperature as $T_N = S_I\,(dV/dI)/4k_B$ (Fig. 2, *a*). A detailed description of the experimental technique is presented in [10]. The length of our samples ($L = 2$ μm) is chosen to be much longer than the electron-phonon length l_{e-ph} in CVD graphene, which allows us to ignore electron heat diffusion into contacts. The configuration also leads to practically uniformity of T_e along the length L and, as a consequence, $T_N = T_e$ [11].

Fig. 2, *a* demonstrates the dependence of electron temperature on applied DC current at different concentrations. We see strong heating of electron gas in graphene: the maximum temperature of the electron gas was about 30 K with a current of 30 μA.

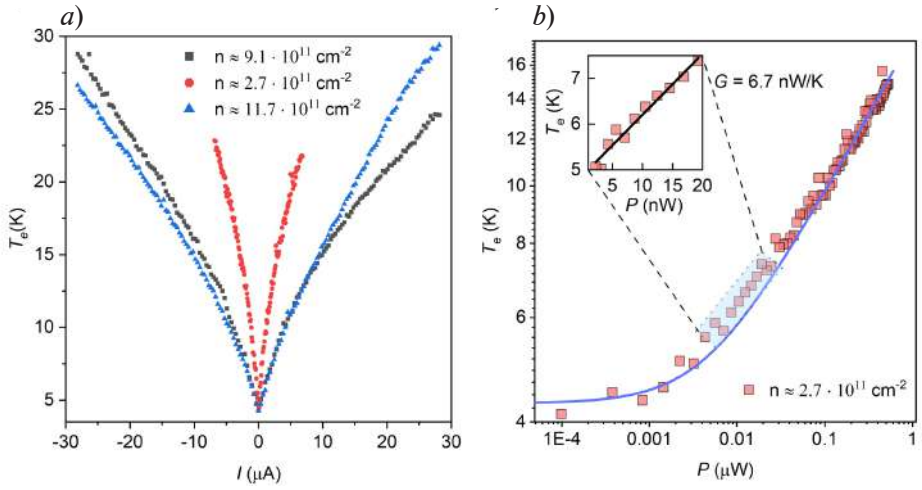

Fig. 2. Electron temperature T_e as a function of applied DC current at different carrier concentrations (*a*). Electron temperature T_e as a function of absorbed Joule heating power P. Solid blue line is the best fitting curve. Fitting parameters: $\delta = 4$ and $\Sigma = 0.5$ $Wm^{-2}K^{-\delta}$. Inset: The slope in the quasi-linear-response regime near zero P is the inverse of $G = P/(T_e - T_b)$ (black curve)

Next, we explore the dependence of the electron gas temperature T_e on the absorbed Joule heating power P (Fig. 2, *b*). $T_e(P)$ dependence transitions from a linear to a sublinear dependence with increased P. Following a standard analysis [3], we fitted the experimental data with the linear $P = G(T_e - T_b)$ dependence, where G is the thermal conductance describing the total heat escape from graphene to the bath, and obtained $G = 6.7$ nW/K (black line in inset to Fig. 2, *b*). This value agrees with previous experiments conducted using Johnson noise thermometry in the linear regime. Next, we fitted the nonlinear part of $T_e(P)$ dependence. There are two main mechanisms of heat dissipation in graphene devices: through electron diffusion and dissipation into the lattice via electron-phonon (e-ph) coupling [11]. We ignore the diffusion mechanism due to device geometry ($l_{e-ph} << L$). The dissipation into the lattice via e-ph coupling is described by power law $P = \Sigma A(T_e^{\delta} - T_b^{\delta})$, where A is the graphene area, Σ-electron photon coupling constant, T_b is the bath temperature, δ varies from 3 to 4 depending on temperature, concentration, device geometry and cleanliness. Theory predicts that $\delta = 4$ for electron coupling to phonons in pristine graphene at low temperatures. Weakly disordered graphene with $k_F l \gg 1$, where k_F is the Fermi wavevector and l is the electron mean free path, admits the possibility of $\delta = 3$ [11]. Blue line on Fig. 2, *b* shows the best fitting curve with fitting parameters $\delta = 4$ and $\Sigma = 0.5$ $Wm^{-2}K^{-n}$, which differ from the expected theoretical ones for weakly disordered graphene. Such power-law dependence with $\delta = 4$ was previously experimentally reported for highly disordered graphene in which $k_F l < 1$ [12]. These conditions are met in our sample. This indicates that there is a need to extend the theory of electron-phonon coupling in weakly disordered graphene to the strongly disordered limit. Finally, we calculate the noise equivalent power (NEP) of our detectors. There are two main sources of noise in the bolometers [13]. The first is due to intrinsic energy fluctuations in the device $NEP_{TF} = (4K_b T^2 G)^{0.5} = 3$ $fW/Hz^{0.5}$. The second source of noise is the accuracy limit with which one can measure the temperature of a device using Johnson-noise thermometry and can be calculated using the Dicke radiometer formula $NEP_{JN} = (T_e + T_{readout})G/(2B)^{0.5} = 267$ $pW/Hz^{0.5}$, where $T_{readout} = 50$ K is the readout noise temperature associated with amplifier noise, $B = 1$ MHz is the the readout bandwidth of measurement setup. The sensitivity of the detector is limited by the readout system which is determined by amplifier noise and bandwidth of measurement system.

Conclusion

We study thermal properties of CVD graphene on SiO_2 substrate using Johnson noise thermometry. We show that electron-phonon thermal conductance has a temperature power law of T^4 which is not typical for a disordered limit at low temperatures. This indicates that there is a need to extend the theory of electron-phonon coupling in weakly disordered graphene to the strongly

disordered limit. We estimate the sensitivity of CVD graphene based bolometer with Johnson noise read out. The internal noise equivalent power determined by thermodynamic fluctuations is equal to 3 fW/Hz$^{0.5}$. The sensitivity of the detector is limited by the readout noise and is equal to 267 pW/Hz$^{0.5}$. Further improvement of readout system by extending of broadband characteristics based on low-noise amplifiers can lead to NEP reduction by 2 orders of magnitude. The intere nal low NEP together with potential fast response time [6] and ease of fabrication makes CVD graphene to be promising material in the area of sensitive THz bolometry.

Acknowledgments

The research was supported by RSF project No. 23-72-00014 (device fabrication, experiment) and by Academic Fund Program at HSE University grant No 24-00-035 "Photodetectors for photonic integrated circuits based on new two-dimensional materials" (noise thermometry data analysis).

REFERENCES

1. **Leitenstorfer A., et al.,** The 2023 terahertz science and technology roadmap. J. Phys. D: Appl. Phys. (56) (2023) 223001.

2. **Du X., et al.,** Graphene-based bolometers. Graphene and 2D Materials. 2014 (1) 1.

3. **Fong Kin Chung, Schwab K.C.,** Ultrasensitive and Wide-Bandwidth Thermal Measurements of Graphene at Low Temperatures. Physical Review X. (2.3) (2012) 031006.

4. **Lee G.H., Efetov D.K., Jung W., et al.,** Graphene-based Josephson junction microwave bolometer. Nature. 586 (7827) (2020) 42–46.

5. **Castilla S., Terrés B., Autore M., et al.,** Fast and sensitive terahertz detection using an antenna-integrated graphene *pn* junction. Nano letters. 19 (5) (2019) 2765–2773.

6. **Efetov D.K., Shiue R.J., Gao Y., et al.,** Fast thermal relaxation in cavity-coupled graphene bolometers with a Johnson noise read-out. Nature nanotechnology. 13 (9) (2018) 797–801.

7. **Aamir M.A., Moore J.N., Lu X., et al.,** Ultrasensitive calorimetric measurements of the electronic heat capacity of graphene. Nano Letters. 21 (12) (2021) 5330–5337.

8. **Bondareva P.I., Shein K.V., Lyubchak A.N., et al.,** Sub-terahertz radiation detection using graphene noise thermometry method. St. Petersburg State Polytechnical University Journal. Physics and Mathematics. 16 (3.1) (2023) 128–132.

9. **Kim S., Nah J., Jo I., Shahrjerdi D., et al.,** Realization of a high mobility dual-gated graphene field-effect transistor with Al_2O_3 dielectric. Applied Physics Letters. 94 (6) (2009).

10. **Baeva E.M., Titova N.A., Veyrat L., et al.,** Thermal relaxation in metal films limited by diffuson lattice excitations of amorphous substrates. Physical Review Applied. 15 (5) (2021) 054014.

11. **Fried C., Russell B.J., Arnault E.G., et al.,** Performance limits to graphene single-photon bolometers by thermal transport. arXiv preprint arXiv:2311. (2023) 00228.

12. **Hemsworth N., Mahvash F., Lévesque P.L., et al.,** Measurement of electronic heat dissipation in highly disordered graphene. Physical Review B. 92(24) (2015) 241411.

13. **Karasik B.S., McKitterick C.B., Prober D.E.,** Prospective performance of graphene HEB for ultrasensitive detection of sub-mm radiation. Journal of Low Temperature Physics. (176) (2014) 249–254.

THE AUTHORS

BONDAREVA Polina I.
p.bondareva2016@yandex.ru
ORCID: 0009-0000-7820-2612

SHEIN Kirill V.
sheinkv97@gmail.com
ORCID: 0000-0001-6494-0147

LYUBCHAK Anastasia N.
anlyubchak@miem.hse.ru
ORCID: 0000-0002-4861-2466

IZMAYLOV Ramil I.
ramilizmaylov2001@gmail.com
ORCID: 0009-0008-4349-7332

BAEVA Elmira M.
ebaeva@hse.ru
ORCID: 0000-0002-6805-2670

GOLTSMAN Gregory N.
goltsman10@mail.ru
ORCID: 0000-0002-1960-9161

GAYDUCHENKO Igor A.
igaiduchenko@hse.ru
ORCID: 0000-0003-2560-6503

Received 29.07.2024. Approved after reviewing 13.08.2024. Accepted 14.08.2024.

Conference materials
UDC 621.3.035.221.14
DOI: https://doi.org/10.18721/JPM.173.209

Development of solid-state composite cathode material for solid-state lithium-ion batteries based on lithium ferrophosphate $LiFePO_4$

A.A. Lagutkina✉, V.A. Vizgalov

Moscow Institute of Physics and Technology (National Research University), Moscow, Russia

✉ lagutkina.aa@phystech.edu

Abstract. In the past few decades all-solid-state lithium-ion batteries have become a promising frontier due to their increased safety, higher energy density and unique mechanical properties. One of the main issues in this field is establishing steady transport of lithium ions across the electrode–electrolyte interface, which requires modifications of the electrode structure. In this research we investigated mechanical properties, capacity and cycling performance of a composite cathode based on solid polymer electrolyte as a binder, lithium ferrophosphate as active material and carbon black as electron conductor. Composite cathode was prepared with the help of ball-milling to reduce the particle size and increase the homogeneity of the material, which resulted in mechanically stable flexible crack-free electrodes after coating, drying and calendaring. Achieved specific capacity of the electrodes corresponds to theoretical values, electrodes show long-term sustainability in systems with liquid electrolyte and are applicable to solid-state systems.

Keywords: All-solid-state lithium-ion battery, composite electrodes, lithium ferrophosphate electrodes, solid electrolyte, polymer electrolyte

Citation: Lagutkina A.A., Vizgalov V.A., Development of solid-state composite cathode material for solid-state lithium-ion batteries based on lithium ferrophosphate $LiFePO_4$, St. Petersburg State Polytechnical University Journal. Physics and Mathematics. 17 (3.2) (2024) 52–56. DOI: https://doi.org/10.18721/JPM.173.209

Материалы конференции
УДК 621.3.035.221.14
DOI: https://doi.org/10.18721/JPM.173.209

Разработка твердотельного композитного катодного материала для твердотельных литий-ионных аккумуляторов на основе феррофосфата лития $LiFePO_4$

А.А. Лагуткина✉, В.А. Визгалов

Московский физико-технический институт (национальный исследовательский университет), Москва, Россия

✉ lagutkina.aa@phystech.edu

Аннотация. За последние несколько десятилетий твердотельные литий-ионные аккумуляторы стали перспективным направлением науки благодаря их повышенной безопасности, более высокой плотности энергии и уникальным механическим свойствам. Одной из основных проблем в этой области является обеспечение устойчивого переноса ионов лития через границу раздела электрод-электролит, требующего модификации структуры электрода. В данной работе были исследованы механические свойства, емкость и циклические характеристики композитного катода на основе твердого полимерного электролита в качестве связующего, феррофосфата лития в качестве

активного материала и сажи в качестве электронного проводника. Композитный катод был изготовлен с помощью планетарной мельницы для уменьшения размера частиц и повышения однородности материала, в результате чего после нанесения покрытия, сушки и каландрирования получились механически устойчивые гибкие электроды без трещин. Достигнутая удельная емкость электродов соответствует теоретическим значениям, электроды демонстрируют долговременную устойчивость в системах с жидким электролитом и могут быть использованы в твердотельных системах.

Ключевые слова: Твердотельные литий-ионные аккумуляторы, композитные электроды, электроды с феррофосфатом лития, твердый электролит, полимерный электролит

Ссылка при цитировании: Лагуткина А.А., Визгалов В.А. Разработка твердотельного композитного катодного материала для твердотельных литий-ионных аккумуляторов на основе феррофосфата лития $LiFePO_4$ // Научно-технические ведомости СПбГПУ. Физико-математические науки. 2024. Т. 17. № 3.2. С. 52–56. DOI: https://doi.org/10.18721/JPM.173.209

Introduction

Compared to the commonly used lithium-ion batteries with liquid electrolyte, all-solid-state lithium-ion batteries offer a number of significant advantages: increased safety due to the elimination of flammable organic liquid electrolyte materials, retarding dendritic growth, allowing to use metal lithium as anode, increased mechanical stability. Stable contact between the solid electrolyte and the electrodes can be achieved, for example, by using composite electrode materials that help blur the interphase boundary, reduce its resistance and increase the maximum battery current. Unlike traditional Li-ion batteries, where liquid electrolyte infiltrates the pores of an electrode during cell assembly, the pores of composite solid-state electrodes are filled with solid polymer electrolyte at the stage of manufacturing the electrodes themselves, before assembling the cell [1]. Polymer electrolyte used instead of traditional binder ensures both mechanical integrity and ionic conductivity throughout the volume of the electrode. Uniform distribution of the active material particles, carbon and electrolyte in the electrode material results in high and uniform ionic and electronic conductivity throughout the volume of the electrode, close contact of the particles with each other and with the current collector and decreasing resistance of the electrode–electrolyte interface. A schematic representation of a battery with a composite electrode is shown in Fig. 1.

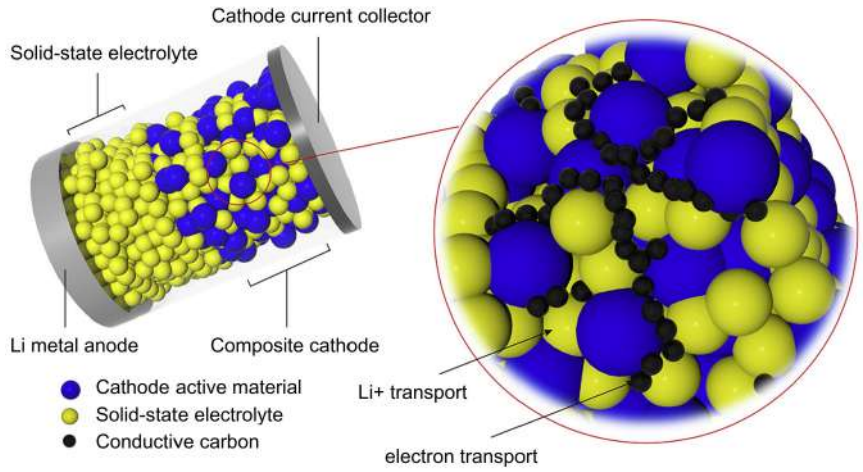

Fig. 1. Schematic of interfaces in all-solid-state Li-ion batteries [2]

Most solid polymer electrolytes for li-ion batteries are usually composed of polymer matrix and soluble lithium salt. The most common choice for polymer matrix is polyethylene oxide (PEO) since its ethylene oxide (EO) units have a higher donor number for Li^+ which determines relatively high ionic conductivity (10^{-4} Sm/cm). The most favorable candidates for lithium source in this system are salts with large complex anions that can easily dissociate in PEO matrix and release Li^+ ions like LiTFSI [3], LiFSI [4] or LiBETI [5]. Principles of ion transport in PEO via interchain or intrachain hopping across the chain while forming and breaking Li-O bonds are shown in Fig. 2.

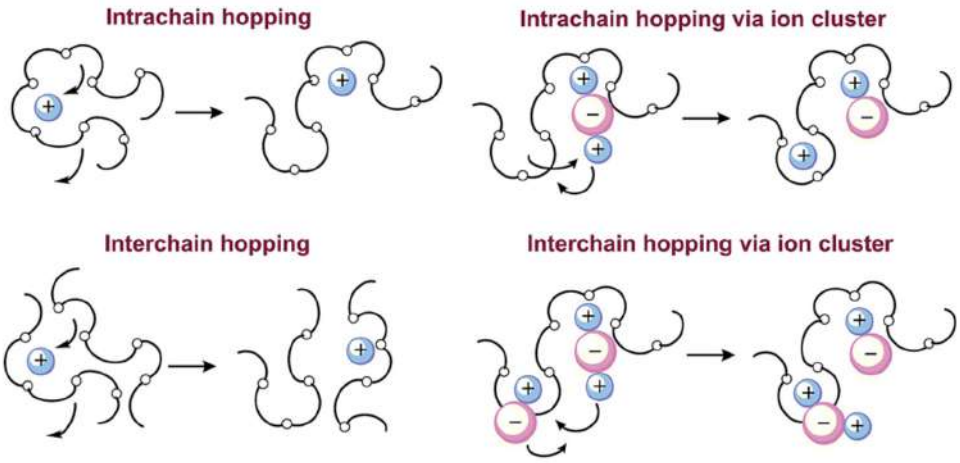

Fig. 2. Mechanism of ion transport in PEO [3]

Materials and Methods

Two modifications of composite positive electrodes based on lithium ferrophosphate were investigated: a mixture based purely on lithium bis(trifluoromethanesulfonyl)imide (LiTFSI) and polyethylene oxide (PEO) dissolved in acetonitrile (C_2H_3N), further referred to as electrode A, and similar mixture based on PEO and LiTFSI with the addition of polyvinylidene fluoride (PVDF) polymer binder for mechanical stability, further referred to as electrode B. The mass ratio for PEO and LiTFSI was calculated from the optimal molar ratio EO:Li = 8:1 (1 Li^+ ion per 8 ethylene oxide segments) that showed the highest ionic conductivity and transference number under standard operating conditions [6].

Polymer electrolyte was mixed with the help of TWCL-B Magnetic Stirrer in argon atmosphere. The optimal cathode slurry contained 35 mass% of electrolyte binder, 5 mass% of carbon black Super P, 60 mass% of active material $LiFePO_4$ and was ball-mixed in Retsch Planetary Ball Mill Pm 100 for 2 hours at 300 rpm at room temperature, then coated on aluminum foil with TMAX-TCC1 Compact Tape Casting Coater, dried at Vacuum Drying Chamber Binder VD-115 at 50 °C for 24 hours and subjected to pressing with the help of LabTools Laboratory Hydraulic Press. Laser cutting was utilized to define the electrode topology. Standard CR2032 coin-cell batteries with $LiPF_6$ liquid electrolyte were assembled to test capacity and efficiency of the electrode material.

Results and Discussion

By varying the composition and manufacturing conditions, high adhesion of the material to the aluminum current collector was achieved. The manufactured electrodes with mass loadings of 4.3 mg/cm^2 and 7.5 mg/cm^2 for electrode A and electrode B accordingly were examined in half-cells with lithium metal anode and liquid electrolyte. Capacity measurements were performed with the help of Neware Battery Testing System at 0.1C current rate. During the first five cycles the average specific capacity of mixture A reached and preserved a value of 149 mA·h/g with Coulomb efficiency of 97.8% whereas specific capacity of mixture B reached and preserved a value of 165 mA·h/g with Coulomb efficiency of 98.9%, which corresponded to theoretical

value of 165 mAh/g for LFP. Higher specific capacity and capacity retention of the latter during cycling proves the usage of additional polymer binder (in this case PVDF) to be beneficial for battery performance, despite possible increase in interphase resistance due to its poor conducting qualities. It is suggested that the presence of PVDF helped improve mechanical stability of the electrode and prevent microcracks formation during active material particles volume expansion within charge-discharge process.

Due to its promising specifications electrode B was also examined in coin-cell against similar anode based on PEO, PVDF, LiTFSI and S-360 graphite as active material. Specific capacity of resulting battery kept growing and reached 130 mA·h/g during the first five cycles; Coulomb efficiency increased from 95.5% to 98.5% as well. Charge-discharge curves for electrode A against metal Li, electrode B against metal Li and electrode B against graphite anode are present at Fig. 3.

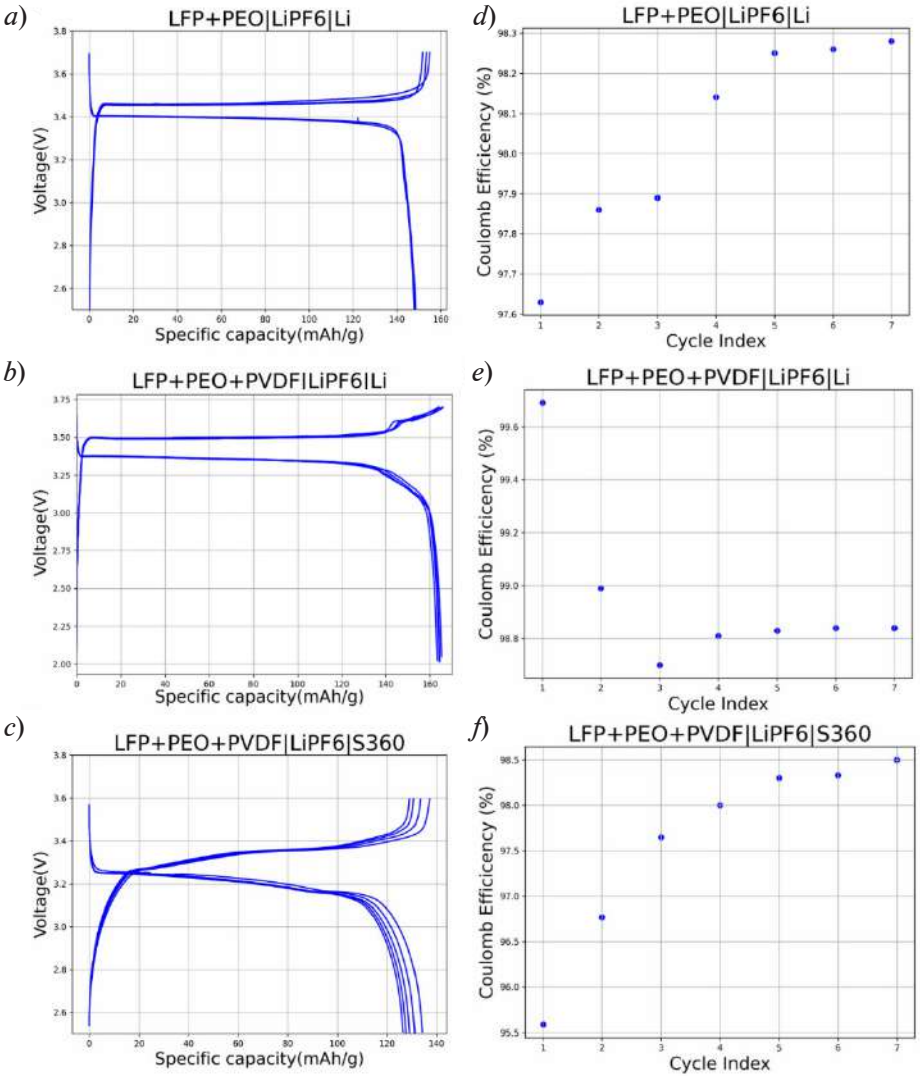

Fig. 3. Charge-discharge curves (*a*, *b*, *c*) and cycling performance (*d*, *e*, *f*) of electrode A and electrode B half-cells and electrode B full cell against graphite

Conclusion

Investigated polymer-based lithium ferrophosphate cathode material shows promising mechanical characteristics and specific capacity. It is applicable for batteries with PEO-based solid electrolytes, a popular subject of scientific research in the field of all-solid-state batteries. Electrochemical testing of LFP electrodes was carried out using coin-cells with lithium metal and

graphite negative electrodes. Electrodes with additional binder, PVDF, showed higher mechanical properties, increase in specific capacity (148.8 vs 165.4 mA·h/g) and Coulomb efficiency (97.8% vs 98.9% compared to those without due to higher mechanical stability and microcracks formation tolerance. Investigated material has the potential to be utilized in all-solid-state batteries Further research on composite electrode materials for all-solid-state Li-ion batteries is vital for development of safe, sustainable and mobile energy sources.

Acknowledgments

Authors would like to thank the Ministry of Science and Higher Education of the Russian Federation for financial support (State Assignment).

REFERENCES

1. **Al-Salih H., Houache M.S. E., Baranova E.A., Abu-Lebdeh Y.,** Composite Cathodes for Solid-State Lithium Batteries: "Catholytes" the Underrated Giants. Advanced Energy and Sustainability Research. 3 (8) (2022).

2. **Zhang J., Chen Z., Ai Q., et al.,** Microstructure engineering of solid-state composite cathode via solvent-assisted processing. Joule. 5 (7) (2021).

3. **Xue Z., He D., Xie X.,** Poly(ethylene oxide)-based electrolytes for lithium-ion batteries. J. Mater. Chem. A. Mater. 3 (38) (2015).

4. **Wang W., Fang Z., Zhao M., et al.,** Solid polymer electrolytes based on the composite of PEO–LiFSI and organic ionic plastic crystal. Chem Phys Lett.747 (2020).

5. **Appetecchi G.B., Henderson W., Villano P., et al.,** PEO-$LiN(SO_2CF_2CF_3)_2$ Polymer Electrolytes. J. Electrochem. Soc. 148(10) (2001).

6. **Ushakova E.E., Sergeev A.V., Morzhukhin A., et al.,** Free-standing Li^+-conductive films based on PEO–PVDF blends. RSC Adv. 10 (27) (2020).

THE AUTHORS

LAGUTKINA Aleksandra A.
lagutkina.aa@phystech.edu

VIZGALOV Victor A.
vizgalov.va@mipt.ru

Received 30.07.2024. Approved after reviewing 12.08.2024. Accepted 03.10.2024.

Conference materials
UDC 538.9
DOI: https://doi.org/10.18721/JPM.173.210

Peculiarities of the local electromagnetic field distribution in non-van-der-Waals $InGaS_3$ thin layers slot waveguides

E.S. Zavyalova[1]✉, A. Kuznetsov[1,2], A.D. Bolshakov[1,2]

[1] Moscow Center for Advanced Studies, Moscow, Russia;

[2] Alferov University, St. Petersburg, Russia

✉ ladieseniya@gmail.com

Abstract. $InGaS_3$ thin layers are promising nanostrures in the field of nanophotonics owing to the broad bandgap, sufficiently high refractive index and the simplicity of fabrication. Here we numerically investigate a system based on $InGaS_3$ waveguides, standing side by side. We demonstrate the localization of the electromagnetic field inside the gap between two waveguides and obtain the refractive indices and losses for the slot waveguide modes at a wavelength of 505 nm. Transmittance spectra of considered configurations of different geometrical parameters were obtained The waveguiding cut-off related to the absorption inside the material and the delocalization of the electromagnetic field was determined. The obtained results open the possibility for fabrication of novel photonic devices based on $InGaS_3$ thin layers.

Keywords: $InGaS_3$, slot waveguide, transmittance, thin layer, numerical simulations

Funding: This work is supported by the Russian Science Foundation (grant no. 24-22-20064).

Citation: Zavyalova E.S., Kuznetsov A., Bolshakov A.D., Peculiarities of the local electromagnetic field distribution in non-van-der-Waals $InGaS_3$ thin layers slot waveguides, St. Petersburg State Polytechnical University Journal. Physics and Mathematics. 17 (3.2) (2024) 57–61. DOI: https://doi.org/10.18721/JPM.173.210

Материалы конференции
УДК 538.9
DOI: https://doi.org/10.18721/JPM.173.210

Особенности распределения локального электромагнитного поля в щелевых волноводах на основе не-ван-дер-Ваальсовых тонких слоев $InGaS_3$

Е.С. Завьялова[1]✉, А. Кузнецов[1,2], А.Д. Большаков[1,2]

[1] Московский физико-технический институт (национальный исследовательский университет), г. Долгопрудный, Россия

[2] Академический университет им. Ж.И. Алфёрова РАН, Санкт-Петербург, Россия;

✉ ladieseniya@gmail.com

Аннотация. Тонкие слои $InGaS_3$ являются перспективными наноструктурами в области нанофотоники благодаря широкому диапазону прозрачности, высокому показателю преломления и простоте фабрикации. В данной работе численно исследовалась наноструктура на основе волноводов $InGaS_3$, расположенных рядом друг с другом. Была продемонстрирована высокая локализация электромагнитного поля внутри зазора между двумя волноводами и получены значения показателей преломления и оптических потерь для мод щелевого волновода на длине волны 505 нм. Получены спектры пропускания рассматриваемых конфигураций волнводов с различными геометрическими параметрами. Определена волноводная отсечка, связанная с поглощением внутри материала и делокализацией электромагнитного поля. Полученные результаты открывают возможность создания новых фотонных устройств на основе тонких слоев $InGaS_3$.

Ключевые слова: $InGaS_3$, щелевой волновод, пропускание, тонкие слои, численное моделирование

Финансирование: Работа выполнена при поддержке Российского научного фонда (грант № 24-22-20064).

Ссылка при цитировании: Завьялова Е.С., Кузнецов А., Большаков А.Д. Особенности распределения локального электромагнитного поля в щелевых волноводах на основе не-ван-дер-Ваальсовых тонких слоев $InGaS_3$ // Научно-технические ведомости СПбГПУ. Физико-математические науки. 2024. Т. 17. № 3.2. С. 57–61. DOI: https://doi.org/10.18721/JPM.173.210

Introduction

Nowadays, the research of new materials for the development of new element and component basis of integrated nanophotonics is important. One of the main task of integrated photonics is to increase the surface packing density of the functional elements, which can be achieved using an optically dense material, operating in the range of shorter wavelengths, for example in visible [1]. Also, the material should be technologically versatile in the context of circuits fabrication technology [2].

$InGaS_3$ is a semiconductor with a large bandgap (2.73 eV) and high refractive index (< 2.5) [3]. It is a novel layered material with hexagonal symmetry of the crystal lattice, however, it is not Van der Waals: the bonds between the layers are covalent, but in the plane of the layer they are distributed inhomogeneously and their density per unit area is rather small, which makes it quite easily to separate the layers from each other by various methods [3]. From the optics point of view, it is extremely promising in the context of developing passive elements of integrated optical circuits. By the example of other layered materials (MoS_2, $MoSe_2$, WS_2, WSe_2, etc.) the possibility

of separating thin layers of a given thickness and transferring them onto different substrates has been demonstrated [4]. The layered structure of the material allows the exfoliation method to separate the layers with monolayer accuracy, which will allow to integrate $InGaS_3$ into the processes of planar technology and control the geometry of elements precisely.

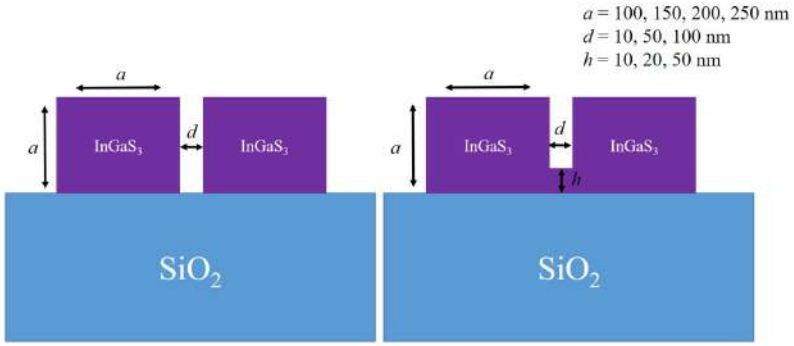

Fig. 1. Schematic of model geometry for numerical simulation

Materials and Methods

In this work, we study two different configurations of the $InGaS_3$ slot waveguides by numerical simulation methods, namely finite difference frequency domain (FDFD) and finite difference time domain (FDTD) in Ansys Lumerical software (see Fig. 1 for schematic). An inhomogeneous grid was modeled with a minimum grid step of 1.5 nm in the case of the FDFD solver and 7 nm of the FDTD solver. The absorbing boundary conditions were chosen in order to obtain a minimum reflection of the incident light [5]. The optical constants used were taken from the work [3]. The systems with the following geometry and parameters were investigated: two square waveguides with a 5 μm long, standing side by side, placed on SiO_2 substrate. The square side varied from 100 to 250 nm with step of 50 nm. The gap between two $InGaS_3$ waveguides varied from 10 to 100 nm by the same step. For the second configuration with an extra layer of the material between waveguides, the thickness of the unetched layer was 10, 20 and 50 nm. The waveguides properties of the considered system were studied at a wavelength of 505 nm. A model mode source was used to obtain the transmittance spectra in the range of 400 to 800 nm.

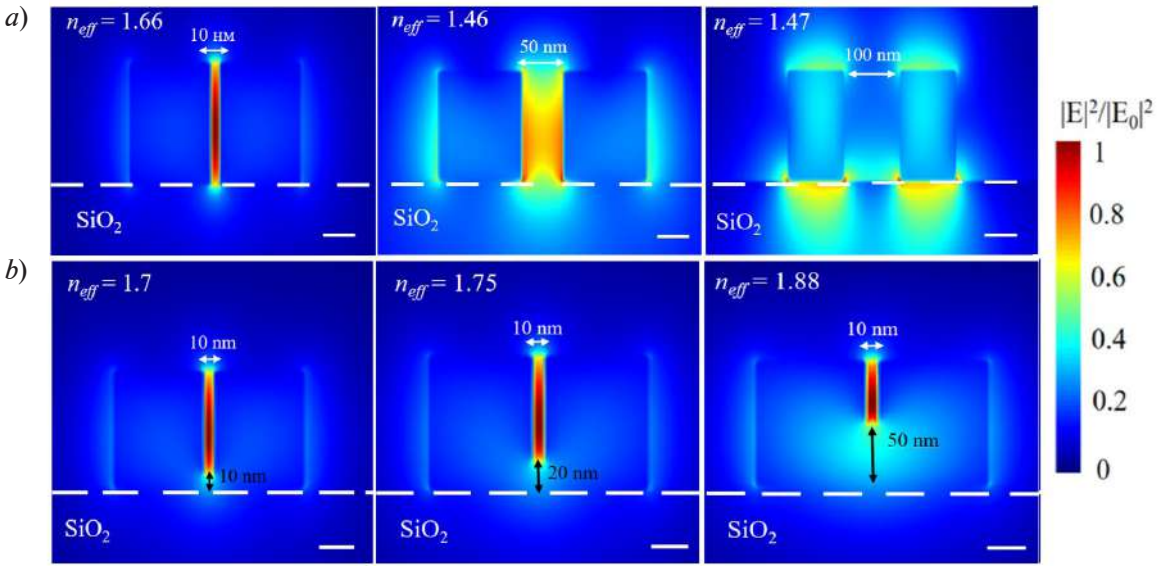

Fig. 2. Electric field distribution for slot waveguides with cross-sections of 100x100 nm^2 and gap width of 10, 50 and 100 nm (*a*) and for slot waveguides with extra layer (*b*)
The scale bar is 50 nm

Results and Discussion

Numerical simulation has demonstrated effective localization of the electromagnetic field inside the gap between two waveguides due to the high difference in refractive indices of $InGaS_3$ and air (see Fig. 2) and interaction of the both waveguides modes. The slot guided modes exist only in specific range of waveguides dimensions: for smaller waveguides it's easier for electric field to interact due to the waveguides eigenmodes worse localization. On the other hand, in case of very small cross-section field more actively penetrates the substrate and interaction between the waveguide modes fields become negligible so slot mode is no longer exist. For the thicker waveguides localization increases and slot mode is suppressed due to the shortening of the electric field evanescent tails. Adding extra layer of $InGaS_3$ to the slot region can shift the field maximum along the y-axis but it causes the mode leakage from the slot to the $InGaS_3$ (see Fig. 2, *b*). Furthermore, the bandwidth of the slot waveguide changes as the additional layer increases. These results indicate the possibility of creating an optical sensor based on $InGaS_3$ slot waveguides.

From the obtained transmission spectra, it was determined that with an increase in the gap between two waveguides, the mode inside the gap is delocalized due to less interaction of the electromagnetic field tails. Moreover, the transmission spectrum narrows in the long-wavelength region, as the gap between two waveguides increases, indicating that a tunable bandpass filter based on $InGaS_3$ slot waveguides can be fabricated.

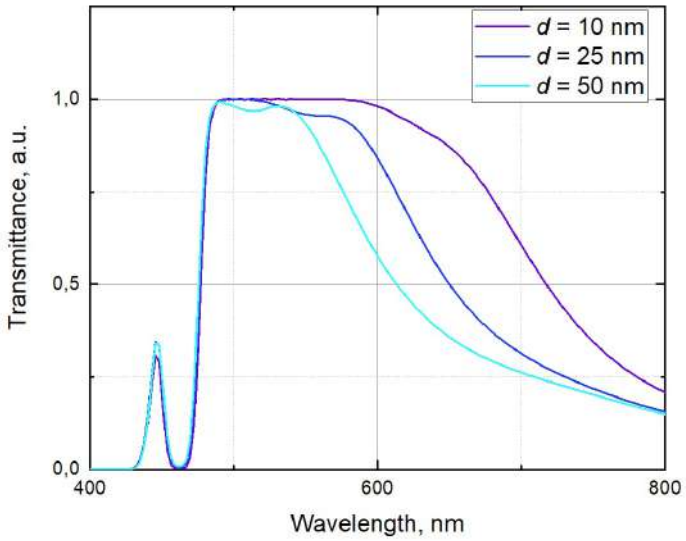

Fig. 3. Transmission spectra of 100×100 nm slot waveguides

Conclusion

We investigated the waveguide properties of the slot waveguides based on a novel layered not Van der Waals material. It was obtained, that 1) localization of the electromagnetic field between two waveguides increases due to waveguide dimension and gap decreasing; 2) the effective refractive index of the fundamental mode grows up with the increase of the waveguide dimension and the thickness of the unetched layer, and with the decrease of the gap between $InGaS_3$ waveguides; 3) with increasing gap between the two waveguides, the transmission spectrum narrows in the long-wavelength part of the spectrum. The results indicate that the slot waveguides based on $InGaS_3$ can be used as a passive element in integrated nanophotonics.

REFERENCES

1. **Thylén L., Wosinski L.,** Integrated photonics in the 21st century. Photonics Research. 2.2 (2014) 75–81.

2. **Okamoto K.,** Recent progress of integrated optics planar lightwave circuits. Optical and Quantum Electronics. 31.2 (1999)107–129.

3. **Toksumakov A.N., et al.,** High-refractive index and mechanically cleavable non-van der Waals $InGaS_3$, npj 2D Materials and Applications. 6.1 (2022) 85.

4. **Huo C., et al.,** 2D materials via liquid exfoliation: a review on fabrication and applications, Science bulletin. 60.23 (2015) 1994–2008.

5. **Zhou J., Hong W.,** Construction of the absorbing boundary conditions for the FDTD method with transfer functions. IEEE transactions on microwave theory and techniques. 46 (11) (1998) 1807–1809.

THE AUTHORS

ZAVYALOVA Eseniya S.
ladieseniya@gmail.com
ORCID: 0009-0003-5049-538X

BOLSHAKOV Alexey D.
bolshakov@live.com
ORCID: 0000-0001-7223-7232

KUZNETSOV Alexey
alkuznetsov1998@gmail.com
ORCID: 0000-0001-7143-6686

Received 30.07.2024. Approved after reviewing 12.08.2024. Accepted 14.08.2024.

Conference materials
UDC 537.9
DOI: https://doi.org/10.18721/JPM.173.211

Synthesis of aluminum nanoparticles using spark discharge for applications in ultraviolet plasmonics

M. Nouraldeen✉, N.S. Shestakov, O.V. Vershinina, V.V. Ivanov

Moscow Institute of Physics and Technology (National Research University), Dolgoprudny, Russia

✉ messannouraldeen@phystech.edu

Abstract. This work demonstrates synthesis Al metal nanoparticles with plasmon resonance in the ultraviolet region by the spark discharge method in an argon atmosphere. The resulting primary particles have an Al metal core and a natural oxide shell and size in range from 5 to 50 nm. Importantly, these nanoparticle ensembles show wide extinction peaks, with the highest point between 250 and 480 nm wavelength. The position of the peak can be varied by synthesis parameters. During our research, we employed laser radiation at a wavelength of 355 nm, with pulse energies reaching up to 350 μJ and pulse repetition rates of up to 2000 Hz. We observed that the sintering process of nanoparticles exhibited a dynamic change in size, which correlated with the energy of the laser pulses. This dependence was illustrated by an S-shaped shrinkage curve. By subjecting the initial agglomerates to a series of impacting laser pulses, we successfully achieved complete sintering, resulting in the transformation of the agglomerates into spherical nanoparticles.

Keywords: aluminum nanoparticles, nanoparticles sintering, laser sintering, plasmon resonance

Funding: The study was supported by the Ministry of Science and Higher Education of the Russian Federation (state assignment) no. 075-03-2024-117, project number FSMG-2024-0009.

Citation: Nouraldeen M., Shestakov N.S., Vershinina O.V., Ivanov V.V., Synthesis of aluminum nanoparticles using spark discharge for applications in ultraviolet plasmonics, St. Petersburg State Polytechnical University Journal. Physics and Mathematics. 17 (3.2) (2024) 62–65. DOI: https://doi.org/10.18721/JPM.173.211

Материалы конференции
УДК 537.9
DOI: https://doi.org/10.18721/JPM.173.211

Синтез наночастиц алюминия с использованием искрового разряда для применения в ультрафиолетовой плазмонике

М. Нуралдин✉, Н.С. Шестаков, О.В. Вершинина, В.В. Иванов

Московский физико-технический институт (национальный исследовательский университет), г. Долгопрудный, Россия

✉ messannouraldeen@phystech.edu

Аннотация. В данной работе продемонстрирован синтез металлических наночастиц Al с плазмонным резонансом в ультрафиолетовой области методом искрового разряда в атмосфере аргона. Полученные первичные частицы имеют металлическое ядро из алюминия и оболочку из натурального оксида, а их размер находится в диапазоне от 5 до 50 нм. Важно отметить, что эти ансамбли наночастиц демонстрируют широкие пики экстинкции с наивысшей точкой между длиной волны 250 и 480 нм. Положение пика можно варьировать параметрами синтеза. В ходе исследований мы использовали лазерное излучение с длиной волны 355 нм, с энергией импульсов до 350 мкДж и частотой следования

импульсов до 2000 Гц. Мы заметили, что процесс спекания наночастиц демонстрирует динамическое изменение размера, которое коррелирует с энергией лазерных импульсов. Эту зависимость проиллюстрировала S-образная кривая усадки. Подвергнув исходные агломераты серии воздействующих лазерных импульсов, мы успешно добились полного спекания, в результате чего агломераты превратились в сферические наночастицы.

Ключевые слова: наночастицы алюминия, спекание наночастиц, лазерное спекание, плазмонный резонанс

Финансирование: Исследование выполнено при поддержке Министерства науки и высшего образования Российской Федерации (госзадание) № 117-2024-03-075, номер проекта FSMG-2024-0009.

Ссылка при цитировании: Нуралдин М., Шестаков Н.С., Вершинина О.В., Иванов В.В. Синтез наночастиц алюминия с использованием искрового разряда для применения в ультрафиолетовой плазмонике // Научно-технические ведомости СПбГПУ. Физико-математические науки. 2024. Т. 17. № 3.2. С. 62–65. DOI: https://doi.org/10.18721/JPM.173.211

Introduction

Al nanoparticles are interesting due to their light absorption properties in the UV range, which has applications in light harvesting using solar cells, as well as enhancing light absorption in thin silicon solar cells [1, 2]. The reason behind this property is that Al nanoparticles are capable of absorbing light as a result of their interaction with conduction electrons and surface plasmon resonance, making them effective light absorbers. In addition, Al nanoparticles with different sizes have different optical properties [3]. Al nanoparticles that are small in size will act as excellent UV absorbers, while for bigger particles, this would be the role of an optical scatterer. There is active research in this area, and emerging applications of plasmonics are still being identified through ongoing research and development activities.

Materials and Methods

The spark discharge method was used to obtain Al nanoparticles [4]. Synthesis was carried out in argon of purity (99.9999%) at pressure of 1,2 atm and flow of 50 mL/min with the following conditions: capacitor of 107 nF, pulse repetition rate of 500 Hz and discharge voltage of 2 kV. The high purity of the starting material and gaseous medium, together with the vacuum tightness of the gas path and the synthesis chamber, ensured the highest possible purity of the nanoparticles under study during the experiment.

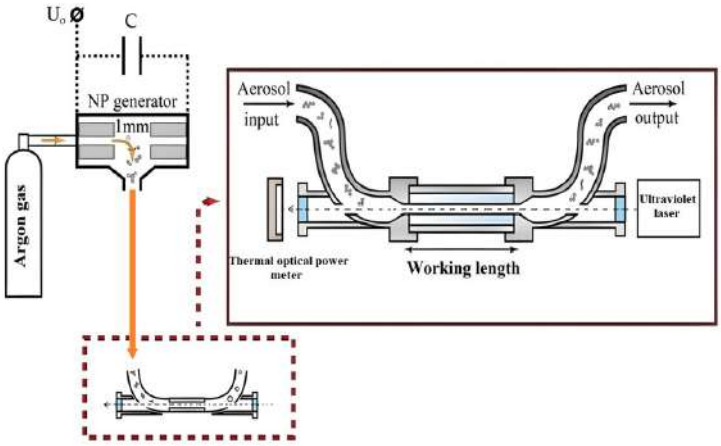

Fig. 1. Diagram of experimental setup: the inset shows a schematic representation of laser optimization cell combining aerosol flow and optical radiation

Schematically, the entire experimental setup is shown in Fig. 1, including the electrical part, the optical part for the spectroscopic tasks, and the necessary measurement options. Pairs of hollow aluminum cylinders with an outer diameter of 4 mm and an inner diameter of 2 mm were used as consumable electrodes in the setup. To conduct studies of the interaction of optical radiation with aerosol nanoparticles a specially designed laser modification cell was used, which made it possible to combine the aerosol flow with optical radiation along its length. The construction of laser modulation cell is described in [5]. The work used an aerosol flow Q = 50 ml/min, which defines the value for the speed of movement of nanoparticles in the aerosol in the working area inside a quartz capillary: υ = 117.9 mm/s.

The agglomerates size distribution in the flow was measured using a TSI SMPS 3936 Aerosol spectrometer. The impact on aerosol Al NPs was studied by nanosecond pulsed laser (CNI AO-355A) with wavelength of 355 nm, pulse repetition rate in the range of 0.2 to 10 kHz with a step of 100 Hz, pulse width of 15 ns and pulse energy in the range of up to 350 μJ. Aerosol HEPA filter were installed in the cell to collect NPs after the cell and deposited particles on it for 30 minutes, with laser frequencies 200, 1500 and 2000 Hz. Absorption spectra of nanoparticles in isopropanol solution were obtained using a JASCO V−770 spectrophotometer.

Results and Discussion

The change in mean diameter of the agglomerates with varying 355 nm laser energy due to sintering shows a size reduction from ~460 to ~290 nm (Fig. 2).

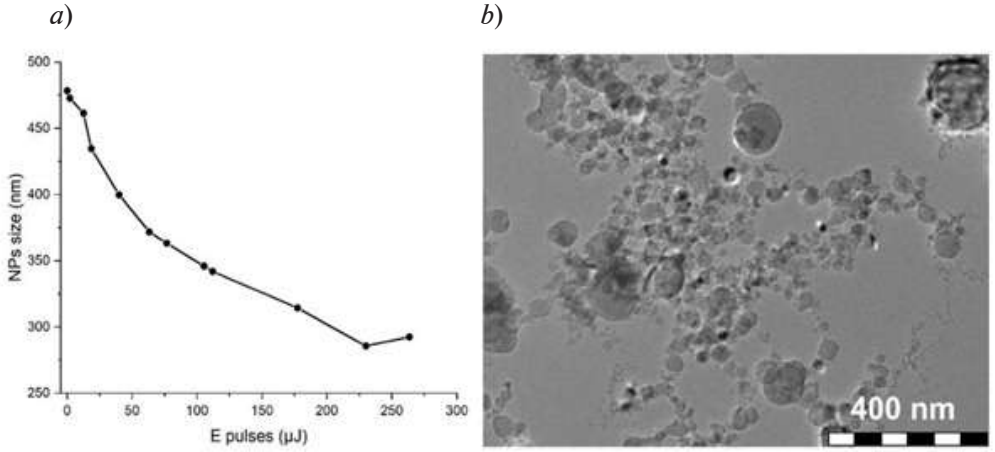

Fig. 2. Dependence of the average particle diameter of the agglomerates on the laser power (*a*), TEM image of typical particles (*b*) at laser pulse frequency of 1500 Hz and gas flow of 50 mL/min

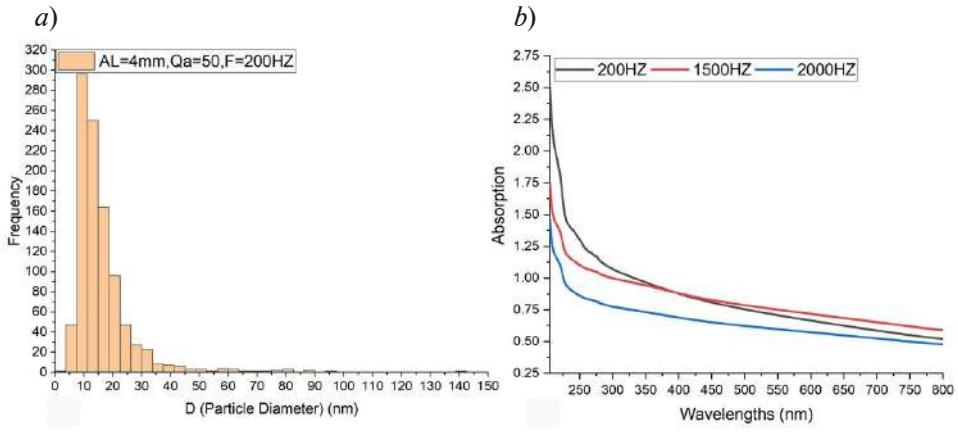

Fig. 3. Numerical distributions of nanoparticles by size at gas flow of 50 ml/min and laser frequency of 200 Hz (*a*), absorption of aluminum after laser sintering (*b*)

From the obtained TEM images, we collected statistics on the diameters of the modified spherical NPs, processing an average of 500 pieces, and rounding them as spheres. Most of the particles are characterized by sizes in the range from 5 to 50 nm. For samples interacting with the ultraviolet laser, the range increases from 5 to about 100 nm with some single particles with sizes of up to 140 nm.

According to spectrophotometry data, it has been proven that the absorption of aluminum after laser sintering is characterized by pronounced plasmonic absorption peaks in the ultraviolet region at position 218 nm.

Conclusion

We demonstrated that using the gas discharge method Al nanoparticles with plasmon resonance in the ultraviolet region can be produced. The results correspond with studies using thermal modification in which Al nanoparticles have weakly pronounced plasmonic peaks at 275 nm. The appearance of the second peak is caused by presence of large particles. Due to the spectral dependences of the absorption regions of NPs with an increase in the NP diameter, the maximum shifts to the long-wavelength region of the spectrum and expands.

REFERENCES

1. **Moulin E., Sukmanowski J., Luo P., Carius R., Royer F.X., Stiebig H.,** Improved light absorption in thin-film silicon solar cells by integration of silver nanoparticles, Journal of Non-Crystalline Solids. (354) (19–25) (2008) 2488–2491.

2. **Zhang Y., Cai B., Jia B.,** Ultraviolet Plasmonic Aluminium Nanoparticles for Highly Efficient Light Incoupling on Silicon Solar Cells, Nanomaterials.6 (6) (2016) 95.

3. Gold Nanoparticles: Optical Properties, nanoComposix. Accessed: May 27, 2024. [Online]. Available: https://nanocomposix.com/pages/gold-nanoparticles-optical-properties

4. **Efimov A. et. al.,** Synthesis of Nanoparticles by Spark Discharge as a Facile and Versatile Technique of Preparing Highly Conductive Pt Nano-Ink for Printed Electronics, Nanomaterials. 1 (11) (2021) 234.

5. **Khabarov K., Nouraldeen M., Tikhonov S., Lizunova A., Efimov A., Ivanov V.,** Modification of Aerosol Gold Nanoparticles by Nanosecond Pulsed-Periodic Laser Radiation, Nanomaterials. 10 (11) (2021) 2701.

THE AUTHORS

NOURALDEEN Messan
messannouraldeen@phystech.edu
ORCID: 0000-0001-5437-0021

VERSHININA Olesya V.
seraia.ov@phystech.edu
ORCID: 0000-0001-6945-4818

SHESTAKOV Nikita S.
shestakov.nr@phystech.edu
ORCID: 0009-0001-6926-5205

IVANOV Victor V.
ivanov.vv@mipt.ru

Received 31.07.2024. Approved after reviewing 02.08.2024. Accepted 02.08.2024.

Conference materials
UDC 537.9
DOI: https://doi.org/10.18721/JPM.173.212

Suppressed phase segregation in $CsPbIBr_2$ based PeLEC

R.Kenesbay[1]✉, A.S. Toikka[1,2], M.G. Baeva[1], I.S. Mukhin[3], D.M. Mitin[1]

[1] Alferov University, St. Petersburg, Russia;

[2] ITMO University, St. Petersburg, Russia;

[3] Peter the Great St. Petersburg Polytechnic University, St. Petersburg, Russia

✉ ramazan.kenesbay.1999@gmail.com

Abstract. In this work we describe some strategies to suppress phase segregation in perovskite light-emitting electrochemical cells based on mixed halide $CsPbIBr_2$ perovskite. Lead halide perovskites are widely used class materials used for creating optoelectronic devices. However, appearing phase segregation causes peak separation on photo- and electro luminance spectra, which limit efficiency and color rendering of devices based on lead halide perovskite materials. Improving crystallinity of perovskite film by annealing temperature controlling can affect halide separation. Mn^{2+} doping was used to enhance materials stability of lead halide perovskite. Another strategy is crystal grains passivation by polymers, i.e. polyethylene oxide and polyvinylidene fluoride, which reduce crystal defect density that cause phase segregation. All these strategies were applied in this work and demonstrate single peaks on photo- and electro luminance spectra. Suggested solution of phase segregation problem allows to create more stable and effective $CsPbIBr_2$ based perovskite light-emitting electrochemical cells that work in red range of visible spectrum (620-680 nm).

Keywords: $CsPbIBr_2$, perovskite, PeLEC, phase segregation, mixed anion

Funding: The research was supported by a grant from the Russian Science Foundation no. 22-79-10286.

Citation: Kenesbay R., Toikka A.S., Baeva M.G., Mukhin I.S., Mitin D.M., Suppressed phase segregation in $CsPbIBr_2$ based PeLEC, St. Petersburg State Polytechnical University Journal. Physics and Mathematics. 17 (3.2) (2024) 66–70. DOI: https://doi.org/10.18721/JPM.173.212

Материалы конференции
УДК 537.9
DOI: https://doi.org/10.18721/JPM.173.212

Подавленная фазовая сегрегация в $CsPbIBr_2$ PeLEC

Р.Кенесбай[1]✉, А.С. Тойкка[1,2], М.Г. Баева[1], И.С. Мухин[3], Д.М. Митин[1]

[1] Академический университет им. Ж.И. Алфёрова РАН, Санкт-Петербург, Россия;

[2] Университет ИТМО, Санкт-Петербург, Россия;

[3] Санкт-Петербургский политехнический университет Петра Великого, Санкт-Петербург, Россия

✉ ramazan.kenesbay.1999@gmail.com

Аннотация. В данной работе предложены способы подавления фазовой сегрегации в светоизлучающих ячейках на основе свинцово-галогенидных перовскитов со смешанным типом аниона. Оптимальный температурный режим отжига, легирование ионами марганца, а также пассивация кристаллических зерен полимерной матрицей позволяют улучшить стабильность перовскитного материала за счет улучшения кристаллической структуры перовскитных пленок.

Ключевые слова: $CsPbIBr_2$, перовскит, PeLEC, фазовая сегрегация, смешанный анион

Финансирование: Работа выполнена при поддержке Российского Научного Фонда, грант № 10286-79-22 (https://rscf.ru/project/22-79-10286/).

Ссылка при цитировании: Кенесбай Р., Тойкка А.С., Баева М.Г., Мухин И.С., Митин Д.М. Подавленная фазовая сегрегация в $CsPbIBr_2$ PeLEC // Научно-технические ведомости СПбГПУ. Физико-математические науки. 2024. Т. 17. № 3.2. С. 66–70. DOI: https://doi.org/10.18721/JPM.173.212

Introduction

Lead-halide perovskites (LHP) are semiconductor materials used as an active layer in light-emitting devices and solar cells. The advantages of LHP are the simplicity of synthesis and the high external quantum efficiency of the devices. Perovskite light-emitting electrochemical cell (PeLEC) is one of the possible device types based on LHP. PeLECs stand out due to their high luminance (~100 000 cd/m^2 for "green" PeLEC) and simple device design. [1].

Using of PeLECs is a relatively new approach to fabricating light-emitting devices. For the synthesis of all-inorganic lead-halide PeLECs operating in the red spectral range, it is necessary to use mixed anion (halide) ($CsPbI_xBr_{3-x}$) compositions to achieve luminance at the desired wavelength [2].

However, perovskites with a mixed halogen composition have a lower photoluminescence quantum yield and quantum efficiency compared to perovskites with single halogen, which is due to the occurrence of phase segregation, i.e., spatial separation of the different halide ions and formation of narrow and wide band gap areas. Phase segregation leads to trap states density increase and changes the band gap width, limiting the structure's external quantum efficiency and photoluminescence quantum yield. The domains with different bandgaps cause two or more peaks in the photo- (PL) and electroluminescence (EL) spectra [3].

There are several ways to suppress phase segregation:

1) improving crystallinity to reduce trap state density, which occurs on crystal surfaces and grain boundaries [4];

2) surface and grain boundary passivation (modification), for example, by polyethylene oxide (PEO) and polyvinylidene fluoride (PVDF) [1];

3) B-site doping, for example, by Mn^{2+}, Sn^{2+}, or Ba^{2+} [5].

In this work, we apply these techniques for reducing phase segregation in the all-inorganic $CsPbIBr_2$-based PeLECs, operating in a red spectral range. Improving the crystallinity of perovskite grains by temperature control, doping with Mn and passivation by the mixed polymer matrix PEO/PVDF allow to suppress phase segregation.

Materials and Methods

For studying the phase segregation phenomenon, two types of samples were fabricated. The first type is films, which consist of a perovskite-polymer layer on glass. The second type is devices, which consist of glass substrates with an indium tin oxide (ITO) layer (as a bottom electrode), a polystyrene sulfonate (PEDOT:PSS) layer (as a hole transport layer (HTL)), a perovskite-polymer layer, LiF (as a buffer layer), 2,2',2''-(1,3,5-Benzinetriyl)-tris(1-phenyl-1-H-benzimidazole) (as an electron transport layer (ETL)), and LiF/Al layers (as top contact). Fig. 1 shows the PeLEC device structure.

To create the perovskite light-emitting layer, a perovskite-polymer solution was made. It contains: 1) 0.4 molar concentration solution of $CsPb_xMn_{1-x}IBr_2$, 2) a solution of PEO with a molecular weight of 10^6 and a concentration of 20 mg/ml, 3) a solution of PVDF with a molecular weight of 534000 and a concentration of 40 mg/ml, and 4) a solution of lithium salts (10 mg/ml). Dimethyl sulfoxide (DMSO) was used as a solvent for all solutions. These four solutions were

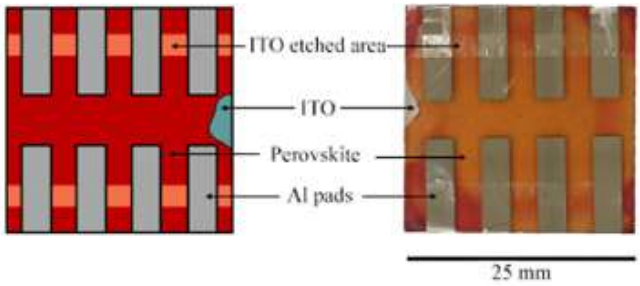

Fig. 1. Sample scheme (left panel) and photo (right panel) from the back (Al contact side)

stirred (300 rpm, 60 °C, 1 day). Then all the solutions had been mixed and stirred (300 rpm, 25 °C, 1 day). All solutions were made in a dry N_2 atmosphere in the glovebox system. The film was fabricated via composite solution drop-casting and spin-coating at 1000 rpm for 1 min. Then vacuum treatment was performed (10^{-3} bar ,1 min). In the final step, samples were annealed at (T_{ann})=70 or 80 °C for 5 min. To study the effects of improving crystallinity, polymer passivation and B-site doping films with different T_{ann} (70 and 80 °C), PEO:PVDF ratios (1:4 and 1:9) and Mn^{2+} amount (0 and 5%) were used. Sample notation and description are presented in Table 1.

Table 1

Sample notation and description

Notation	T_{ann}	Mn, %	PEO:PVDF ratio
S1	80	0	1:9
S2	80	5	1:9
S3	70	5	1:9
S4	70	5	1:4

For light-induced phase segregation analysis, PL spectra and PL optical images were obtained. Scanning electron microscopy (SEM) was performed to compare the film's morphology. To study electrical-field induced phase segregation, EL spectra measurements were obtained.

Results and Discussion

Fig. 2, *a* shows PL spectra of perovskite-polymer films. Among all the samples, only S4 demonstrated one PL peak, which shows that the proposed composition and treatments suppress phase segregation. Sample S4 presents the most homogenous surface morphology through all the obtained film, which is clearly seen on PL optical images (Fig. 2, *b*).

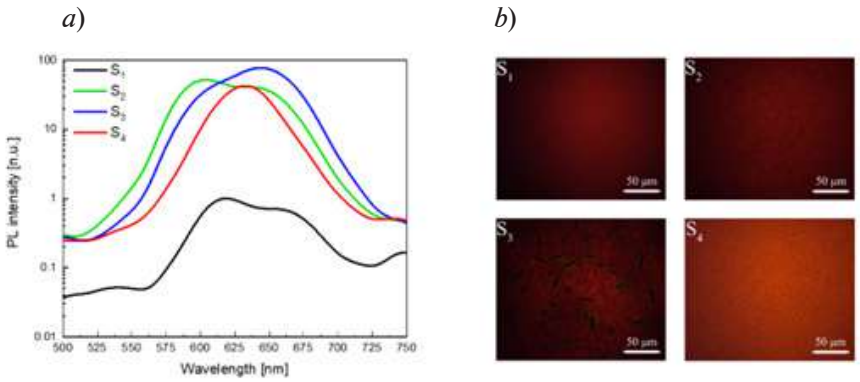

Fig. 2. PL spectra (*a*), PL optical images (*b*)

For a more detailed surface studying, SEM images were analyzed (Fig. 3, *a*). Sample S4 does not have long polymer-rich domains compared with other samples, which means better PEO:PVDF distribution and perovskite crystal passivation.

Sample S4 demonstrates outstanding properties due to its composition and technological treatment. A device was made based on the S4 film to study electrical-field induced phase segregation. Fig. 3, *b* shows dynamic EL spectra of developed device. As well as PL spectra, EL spectra demonstrate single peak, which indicates prevented phase segregation. It should be noted that EL peak position has a red shift compared with PL peak, which can be explained by increasing defect state density caused ion migration under applied voltage.

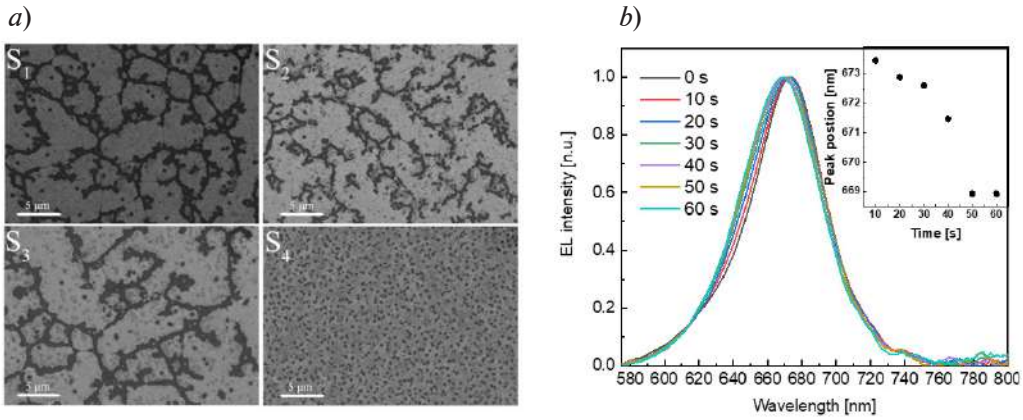

Fig. 3. SEM images (*a*), dynamic EL spectra (*b*)

Conclusion

We have described a method for suppressing phase segregation in inorganic mixed lead-halide PeLEC. B-site doping by Mn and PEO:PVDF passivation allows to obtain PeLEC stable to photo and electrical-field induced phase segregation.

Acknowledgments

The research was supported by the Russian Science Foundation grant № 22-79-10286 (https://rscf.ru/project/22-79-10286/).

REFERENCES

1. **Gets D., et al.**, Reconfigurable perovskite LEC: Effects of ionic additives and dual function devices, Advanced Optical Materials. 9 (3) (2021) 2001715.

2. **Ghosh P., Bruckbauer J., Trager-Cowan C., Jagadamma L.K.,** Crystalline grain engineered $CsPbIBr_2$ films for indoor photovoltaics, Applied Surface Science. 592 (2022) 152865.

3. **Chen Z., Brocks G., Tao S., Bobbert P.A.,** Unified theory for light-induced halide segregation in mixed halide perovskites, Nature communications, 12 (1) (2021) 2687.

4. **Hu M., Bi C., Yuan Y., Bai Y., Huang J.,** Stabilized wide bandgap $MAPbBr_xI_{3-x}$ perovskite by enhanced grain size and improved crystallinity, Advanced Science. 3 (6) (2016).

5. **Hurst T., Li Z.,** Perovskite solar cells, Georgia Journal of Science. 80 (2) (2022) 9.

THE AUTHORS

KENESBAY Ramazan
ramazan.kenesbay.1999@gmail.com
ORCID: 0000-0001-9002-3924

TOIKKA Andrei S.
astoikka.nano@gmail.com
ORCID: 0000-0002-8694-8497

BAEVA Maria
maria.baeva111@gmail.com
ORCID: 0000-0002-0331-5433

MUKHIN Ivan S.
imukhin@yandex.ru
ORCID: 0000-0001-9792-045X

MITIN Dmitry M.
mitindm@mail.ru
ORCID: 0000-0003-4517-0807

Received 31.07.2024. Approved after reviewing 21.08.2024. Accepted 10.09.2024.

Conference materials
UDC 538.9
DOI: https://doi.org/10.18721/JPM.173.213

Temperature performance of ring quantum-cascade laser with staircase-like distributed feedback grating

D.S. Papylev[1], E.S. Kolodeznyi[1]✉, A.V. Babichev[1], N.Yu. Kharin[1,2], G.V. Voznyuk[3], M.I. Mitrofanov[3,4], S.O. Slipchenko[3], A.V. Lyutetskii[3], V.P. Evtikhiev[3], L.Ya. Karachinsky[1], I.I. Novikov[1], V.Yu. Panevin[2], N.A. Pikhtin[3], A.Yu. Egorov[1]

[1] ITMO University, St. Petersburg, Russia;

[2] Peter the Great St. Petersburg Polytechnic University, St. Petersburg, Russia;

[3] Ioffe Institute, St. Petersburg, Russia;

[4] Submicron Heterostructures for Microelectronics, Research & Engineering Center RAS, St. Petersburg, Russia

✉ evgenii_kolodeznyi@itmo.ru

Abstract. Direct ion-beam lithography was used to realize the staircase-like second order distributed feedback grating formed in the top cladding layers of ring quantum-cascade laser. As a result, the depth of grating slits was varied from 0.6 to 2.6 μm along the ring cavity. The whispering gallery modes lasing with near 1 kA/cm^2 threshold current density at 77 K temperature was obtained with lasing wavelength close to 7.64 μm. Rise of the temperature up to 292 K yields the multi-mode lasing near to 7.94 μm with moderate threshold current density ~4 kA/cm^2. Time-resolved spectral characterization results are also discussed.

Keywords: molecular-beam epitaxy, quantum-cascade laser, indium phosphide, ion-beam etching, direct lithography, ring cavity

Funding: The authors from ITMO University acknowledge support in part by the grant of the Russian Science Foundation no. 20-79-10285-П, https://rscf.ru/project/20-79-10285/ for the laser fabrication and optical characterization.

Citation: Papylev D.S., Kolodeznyi E.S., Babichev A.V., Kharin N.Yu., Voznyuk G.V., Mitrofanov M.I., Slipchenko S.O., Lyutetskii A.V., Evtikhiev V.P., Karachinsky L.Ya., Novikov I.I., Panevin V.Yu., Pikhtin N.A., Egorov A.Yu., Temperature performance of ring quantum-cascade laser with staircase-like distributed feedback grating, St. Petersburg State Polytechnical University Journal. Physics and Mathematics. 17 (3.2) (2024) 71–77. DOI: https://doi.org/10.18721/JPM.173.213

Материалы конференции
УДК 538.9
DOI: https://doi.org/10.18721/JPM.173.213

Температурное поведение квантово-каскадного лазера с селективным кольцевым резонатором, сформированным за счет травления дифракционной решетки с переменной глубиной

Д.С. Папылев[1], Е.С. Колодезный[1]✉, А.В. Бабичев[1], Н.Ю. Харин[1,2], Г.В. Вознюк[3], М.И. Митрофанов[3,4], С.О. Слипченко[3], А.В. Лютецкий[3], В.П. Евтихиев[3], Л.Я. Карачинский[1], И.И. Новиков[1], В.Ю. Паневин[2], Н.А. Пихтин[3], А.Ю. Егоров[1]

[1] Университет ИТМО, Санкт-Петербург, Россия;

[2] Санкт-Петербургский политехнический университет Петра Великого, Санкт-Петербург, Россия;

[3] Физико-технический институт им. А.Ф. Иоффе РАН, Санкт-Петербург, Россия;

[4] Научно-технологический центр микроэлектроники и субмикронных гетероструктур РАН, Санкт-Петербург, Россия

✉ evgenii_kolodeznyi@itmo.ru

Аннотация. С помощью метода прямой ионно-лучевой литографии была реализована дифракционная решетка второго порядка, обеспечивающая распределенную обратную связь, вытравленная в верхних слоях обкладки волновода квантово-каскадного лазера с селективным колцевым резонатором. Глубина травления штрихов дифракционной решетки изменялась в диапазоне 0,6–2,6 мкм при движении вдоль поверхности кольцевого резонатора. Была получена многомодовая генерация на модах шепчущей галереи вблизи 7,64 мкм. Величина пороговой плотности тока составила около 1 кА/см^2 при температуре 77 K. Повышение температуры до 292 K приводит к появлению многомодовой генерации вблизи 7,94 мкм с величиной пороговой плотности тока ~ 4 кА/см^2. Также представлены результаты исследования время-разрешенных спектров лазерной генерации.

Ключевые слова: молекулярно-лучевая эпитаксия, квантово-каскадный лазер, фосфид индия, ионно-лучевое травление, прямая ионная литография, селективный кольцевой резонатор

Финансирование: Исследование авторов из Университета ИТМО выполнено при финансовой поддержке гранта Российского научного фонда № 10285-79-20–П, https://rscf.ru/project/20-79-10285/ в части формирования лазеров и исследования их характеристик.

Ссылка при цитировании: Папылев Д.С., Колодезный Е.С., Бабичев А.В., Харин Н.Ю., Вознюк Г.В., Митрофанов М.И., Слипченко С.О., Лютецкий А.В., Евтихиев В.П., Карачинский Л.Я., Новиков И.И., Паневин В.Ю., Пихтин Н.А., Егоров А.Ю. Температурное поведение квантово-каскадного лазера с селективным кольцевым резонатором, сформированным за счет травления дифракционной решетки с переменной глубиной // Научно-технические ведомости СПбГПУ. Физико-математические науки. 2024. Т. 3.2 № .17. С. 71–77. DOI: https://doi.org/10.18721/JPM.173.213

Introduction

Single-mode quantum-cascade lasers (QCLs) are attractive for optical spectroscopy since many gaseous species are absorbing in mid-infrared spectral range. QCL lasing wavelength could be tuned by drive current and temperature aimed to realize the 1–5 cm^{-1} tuning range for detection of the narrow gas absorption lines. As a result, quartz-enhanced photoacoustic spectroscopy (QEPAS) allows one to determine the methane (CH_4) trace in a gaseous species. In fact, usage of QEPAS sensor with 8 μm range QCLs as laser source allows one to evaluate the methane with concentrations from less than 0.5 ppm and up to 10000 ppm with accuracy about 10% [1]. Ring QCLs are very perspective to realize stable (mode-hop free) single mode surface emission lasing [2, 3], but emission from opposite sides of the ring results destructive interference along the axis of symmetry [4, 5]. Aimed to realize the center node of the beam profile one can apply two π-phase shifts at 90 and 270 degrees along the ring cavity or staircase-like second order distributed feedback (DFB) grating [4].

Herein, the first results on fabrication and optical study of surface-emitting ring QCL with staircase-like second order DFB grating are presented.

Materials and Methods

The QCLs heterostructure was grown by molecular-beam epitaxy on InP substrate with $(1–3)\cdot10^{17}$ cm^{-3} sulfur doping level. 500 nm thick bottom buffer layer was $In_{0.53}Ga_{0.47}As$ with $0.5\cdot10^{17}$ cm^{-3} silicon doping level. The active region included 50 stages and was based on two-phonon escape design. The top cladding was formed by 3.9 thick InP layer with $1\cdot10^{17}$ cm^{-3} silicon doping level. The doping level of $In_{0.53}Ga_{0.47}As$ top contact layers with total 120 nm thickness was in the range of $(0.5–1.0)\cdot10^{19}$ cm^{-3}. Ring double-channel mesa was fabricated by wet etching. The ring radius was fixed at 291 μm and the average mesa width was 25 μm. A 300 nm thick silicon dioxide (SiO_2) layer was used to isolate the ridge sidewalls. The top metallization was formed by Ti/Au. The bottom metallization was applied after substrate lapping down to 120 μm. The ring QCL was mounted on copper submount using indium solder. The DFB grating was formed by direct high-vacuum ion-beam lithography. The etched slits size was 0.71·16 $μm^2$ (see Fig. 1). The grating duty-cycle was fixed at 70%. As a result, the second order grating period was 2.37 μm. The depth of slits etching, d was variable along the ring cavity and described as $d = (0.605+1.95\cdot(k–1)/(772–1))$ μm, where k was the integer number in the range of 1–772. As a result, the maximal etching depth of slits was 2.55 μm.

The laser spectra were collected at 77–293 K temperature range by Bruker Vertex 80v Fourier-transform spectrometer operating in a step-scan mode. The spectral resolution was 0.5 cm^{-1}. The lasers were tested under pulsed pumping with a pulse width of 150 ns and a repetition rate of 15 kHz.

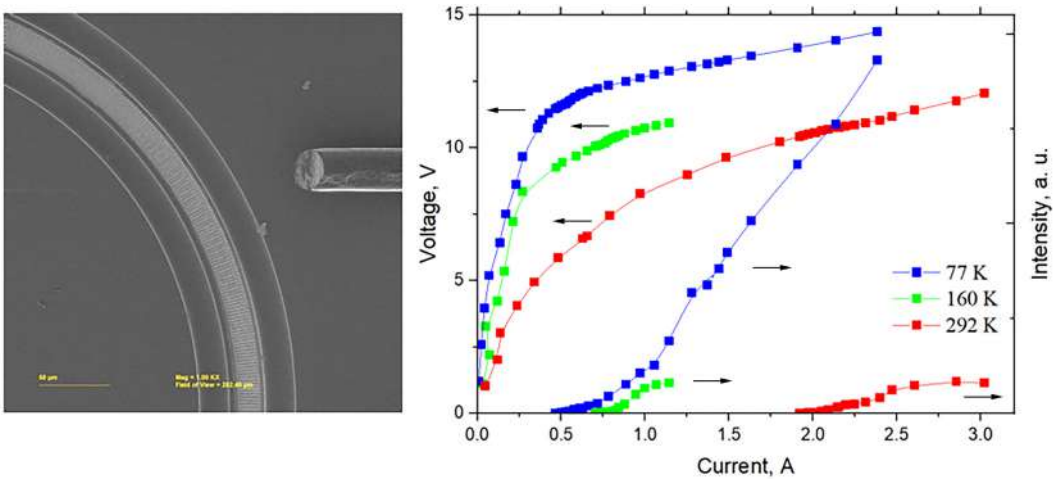

Fig. 1. SEM image of ring QCL (left panel). Light output characteristics of ring QCL measured at different temperatures

Results and Discussion

The threshold current determined at 77 K temperature was about 0.47 A (see Fig. 1) that coincided to about 1 kA/cm^2 threshold current density (j_{th}). The threshold voltage was around 12 V. Rise of the drive current to about five times above the threshold current reveals no reach to roll-over of light intensity versus current dependence due to high laser dynamic range. Near the threshold current the multi-mode lasing around 7.64 μm was measured with fringes distance coincided to whispering gallery modes (WGMs). The group of ten modes was evaluated in 7.59–7.68 μm spectral range (see Fig. 2). Above twofold threshold current (>1 A) the long wavelength modes group was demonstrated along with mode intensity redistribution. As a result, at 2.4 A drive current the modes sequence was observed in the 7.66–7.88 μm spectral range.

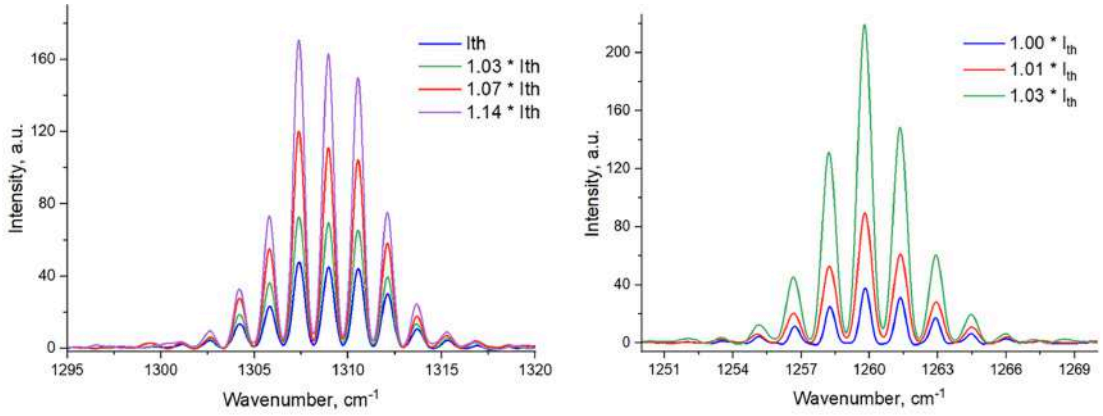

Fig. 2. Lasing spectra measured at 77 K (left panel) and at 292 K (right panel)

Increasing the temperature up to 160 K reveals the lasing with 0.7 A threshold current (j_{th}~1.5 kA/cm^2). The threshold voltage is around 18 V at 160 K. Near the threshold the multi-mode lasing spectrum has maximum close to 7.8 μm. Increase of the drive current up to 1.5 threshold value results no considerable chirp of the lasing wavelength.

At room temperature (292 K) the lasing was around 7.94 μm. The threshold current was about 1.9 A (j_{th}~4.2 kA/cm^2). Rise of the temperature results in falling of threshold voltage down to 10 V. Increase of the drive current up to 1.6 I_{th} yields to multi-mode lasing with four WGM modes with maximum intensity near 7.94 μm.

For a gas sensor based on a ring QCL, the spectroscopic characterization is important, especially its time-resolved tuning behavior [6]. Previously, for a ring QCL, the time-resolved spectra demonstrated a long-wavelength shift in the lasing wavelength during the pump pulse. The estimated time shift in the position of the lasing mode (the mean chirp rate) was $1.8 \cdot 10^{-2}$ cm^{-1}/ns [6]. As a result, the spectroscopic characterization of ring QCL under study was conducted.

Time-resolved spectra measured at a temperature of 77 K are presented in Fig. 3. Close to threshold, the spectrum is represented by several WGMs. Two characteristic peaks are observed, with a redistribution of their intensity during the pump pulse. The first peak corresponds to a time

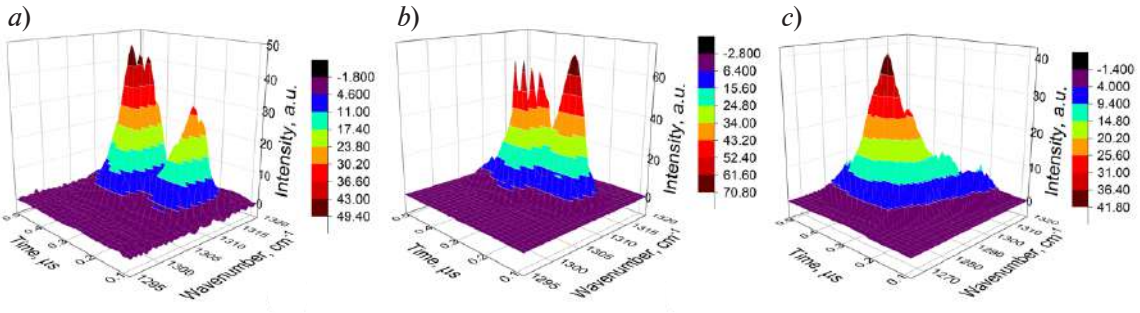

Fig. 3. Time-resolved lasing spectra measured at 77 K
Panels *a*, *b* and *c* are at I_{th}, $1.2I_{th}$ and $5.1I_{th}$

of 0.15 μs, the second peak – 0.3 μs. The intensity of the peak at a time of 0.15 μs is less the intense of the peak corresponding to a time of 0.3 μs. At a fixed time of 0.15 μs, the maximum intensity line corresponds to the wavenumber of 1310.5 cm^{-1}. On the contrary, at a fixed time of 0.3 μs, the maximum intensity line corresponds to the wavenumber of 1307 cm^{-1}.

At $1.2I_{th}$ (see Fig. 3,*b*), at the time of 0.3 μs the line at 1310 cm^{-1} is slightly less intense than the line at 1307 cm^{-1}, which differs from the case of evolution of the spectrum at the I_{th} and $1.1I_{th}$ pump level. It should also be noted that the intensity of the "minority" modes decreases in comparison with the spectra measured at lower current pump levels. Exceeding the I_{th} value to about 24% yields that the lasing line at 1310 cm^{-1} is maximum both at the time of 0.15 μs and at the time of 0.30 μs. The intensity of the "minor" modes noticeably decreased. An additional increase in the pumping level to $1.4I_{th}$ leads to the line at 1310 cm^{-1} is maximum at all times moment. The peaks at 0.15 and 0.30 μs begin to merge (there is no longer a gap between them). Exceeding the I_{th} value to about 90% yields that the in the intensity (time) graph, it is no longer possible to clearly distinguish two peaks. The line at 1310 cm^{-1} is also maximum at all times, but at the same time a noticeable suppression of the remaining WGMs lines also began.

At $2.2I_{th}$, the ring QCL begins to heat up and modes in the long-wavelength region are ignited, which were not there before (at all lower pumps there were no modes with a wavenumber less than 1302 cm^{-1}). A further increase in the pump level to $3.1I_{th}$ yields an expansion of the lasing spectrum due to an increase in the number of WGMs in the long-wavelength region. Increasing the current pump level to approximately five laser thresholds (see Fig. 3,*c*) results to an additional expansion of the lasing spectrum.

Based on the measured time-resolved spectra, a study was carried out of the shift in the position of the lasing mode during the action of a 150 ns pulse. At 160 K, the value of the initial position of the lasing mode was 1281.75 cm^{-1}, determined by the magnitude of the exponential decay of the wavenumber position (ν) from the pumping time [6]: $\nu = A \cdot \exp(-t/B(I)) - c$. The tuning time t was about 365 ns. At a temperature of 292 K and a pump current of $1.57 \times I_{th}$, the value of the initial position of the lasing mode was 1259.21 cm^{-1}. The tuning time was lower and amounted to 254 ns. The value of the initial position of the other WGM was 1263.62 cm^{-1}. The tuning time was about 177 ns. Similar t value (~189 ns) was obtained for the longer wavelength WGM (1258.9 cm^{-1}). Thus, due to the increase in the j_{th} value with temperature, a decrease in the tuning time is observed, which is due to an increase in thermal losses with temperature. As a result, thermal losses exceed the gain at the end of the pump pulse, resulting in shorter tuning times obtained at room temperature.

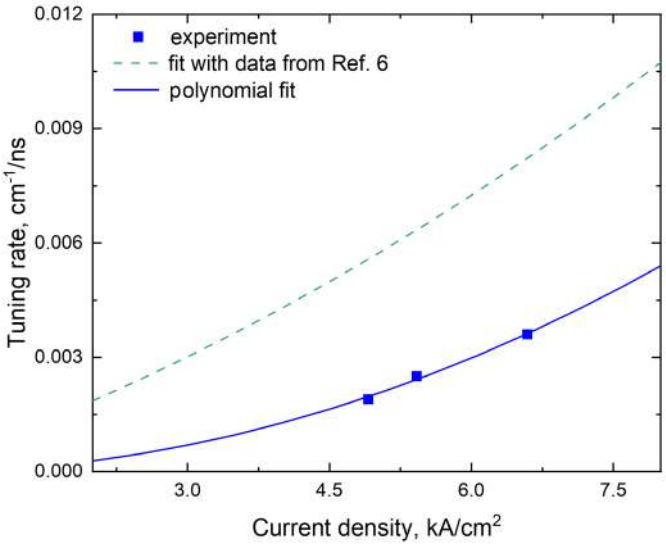

Fig. 4. Experimentally determined tuning rates of ring QCL under study depending on current densities (blue squares). The polynomial fit to the tuning rates is represented by the blue solid line. Polynomial approximation of tuning rates for ring QCL [6] is shown with a dashed line

During the duration of the pulse at $1.6I_{th}$, the tuning range was 0.67 cm^{-1}. Considering the estimated a temperature tuning rate under study is 0.092 cm^{-1}/K [7], which corresponds to previously presented data (0.085 cm^{-1}/K [6] – 0.1 cm^{-1}/K [8]) the observed shift corresponds to heating is on the order of 7.3 K during the pump pulse. This value correlates with the previously discussed heating value during the 200 ns pump pulse (7.2 K [6]). The average shift in the lasing mode during the pump pulse was estimated (~$3.6 \cdot 10^{-3}$ cm^{-1}/ns) and corresponds to a current density of 6.3 kA/cm^2.

During the duration of the pulse at $1.29I_{th}$, the tuning range was 0.33 cm^{-1}. Decreasing the pump current density to 5.2 kA/cm^2 leads to a smaller average shift in the lasing mode during the pump pulse, which amounted to $2.5 \cdot 10^{-3}$ cm^{-1}/ns. During the pulse action at $1.17I_{th}$, the tuning range was 0.23 cm^{-1}. A decrease in the pump current density to 4.7 kA/cm^2 leads to an average shift in the lasing mode during the pump pulse, which amounted to $1.9 \cdot 10^{-3}$ cm^{-1}/ns. During the duration of the pulse at a pump current level of $1.09I_{th}$, the tuning range was 0.01 cm^{-1}. Reducing the pump current density to 4.4 kA/cm^2 leads to the absence of a shift in the lasing mode during the pump pulse. The dependence of the average shift in the lasing mode during the pump pulse on the pump density is shown in Fig. 4. It was shown that the average shift in the lasing mode during the pump pulse was $3.2 \cdot 10^{-3}$ cm^{-1}/ns at a threshold current density of 3 kA/cm^2 and $1.8 \cdot 10^{-2}$ cm^{-1}/ns at a threshold current density of 12.37 kA/cm^2. Thus, a smaller shift in the lasing wavelength during the pump pulse was demonstrated compared to the previously presented results [5].

Conclusion

New type of surface emitting ring cavity quantum-cascade lasers was created and studied. The lasing of several whispering-gallery modes close to 8 μm was observed in 77–300 K temperature range with about 1–4 kA/cm^2 threshold current density. Time-resolved spectra were measured at different temperatures. The average shift of the lasing wavelength in a ring QCL with a radius increased to 291 μm has been assessed. It is shown that due to an increase in the threshold current density with temperature, a decrease in the tuning time during the pulse action is observed, which is due to an increase in thermal losses with temperature. As a result, thermal losses exceed the gain at the end of the pump pulse, resulting in lower tuning times at room temperature. It is shown that the average shift of the lasing wavelength during the pump pulse action is smaller (by a factor of two) in comparison with previously results for a ring QCL with 150 μm radius when comparing data for a similar current density. As a result, the thermal load decreases with increasing radius of the ring cavity.

REFERENCES

1. Quartz-enhanced photoacoustic sensor for methane. Available online: https://www.thorlabs.com/newgrouppage9.cfm?objectgroup_id=16188 (due to 01.04.2024).

2. **Slivken S., Shrestha N., Razeghi M.,** Development of high power, InP-based quantum cascade lasers on alternative epitaxial platforms. Proc. SPIE. 12895 (2024) 1289503.

3. **Babichev A., Kolodeznyi E., Gladyshev A., Kharin N., Panevin V., Shalygin V., Voznyuk G., Mitrofanov M., Slipchenko S., Lyutetskii A., Evtikhiev V., Karachinsky L., Novikov I., Pikhtin N., Egorov A.,** Single-mode lasing in ring-cavity surface-emitting lasers. J. Opt. Technol. 90 (8) (2023) 422–427.

4. **Figueiredo P.N., Muraviev A., Peale R.E.,** Ring cavity surface emitting quantum cascade laser with a near Gaussian beam profile. Proc. SPIE. 9466 (2015) 946602.

5. **Kacmoli, S., Gmachl, C. F.,** Quantum cascade disk and ring lasers. Appl. Phys. Lett. 124 (1) (2024) 010502.

6. **Brandstetter M., Genner A., Schwarzer C., Mujagic E., Strasser G., Lendl B.,** Time-resolved spectral characterization of ring cavity surface emitting and ridge-type distributed feedback quantum cascade lasers by step-scan FT-IR spectroscopy. Opt. Express. 22(3) (2014) 2656.

7. **Babichev A.V., Kolodeznyi E.S., Gladyshev A.G., Denisov D.V., Kharin N.Yu., Petruk A.D., Panevin V.Yu., Slipchenko S.O., Lyutetskii A.V., Karachinsky L.Ya., Novikov I.I., Pikhtin N.A., Egorov A.Yu.,** Features of single-mode emission in 7.5-8.0 μm range quantum-cascade lasers with a short cavity length. Tech. Phys. Lett. 48 (3) (2022) 6.

8. CW Quantum Cascade Laser L12007-1294H-C. Available online: https://www.hamamatsu.com/content/dam/hamamatsu-photonics/sites/documents/99_SALES_LIBRARY/ssd/L12007-1294H-C_E.pdf

THE AUTHORS

PAPYLEV Denis S.
dspapylev@itmo.ru
ORCID: 0009-0001-3683-5558

LYUTETSKII Andrey V.
lutetskiy@mail.ioffe.ru
ORCID: 0009-0007-6516-0936

KOLODEZNYI Evgenii S.
evgenii_kolodeznyi@itmo.ru
ORCID: 0000-0002-3056-8663

EVTIKHIEV Vadim P.
evtikhiev@mail.ioffe.ru
ORCID: 0000-0002-5608-2725

BABICHEV Andrey V.
a.babichev@itmo.ru
ORCID: 0000-0002-3463-4744

KARACHINSKY Leonid Ya.
karach@switch.ioffe.ru
ORCID: 0000-0002-5634-8183

KHARIN Nikita Yu.
kharin.nikita66@gmail.com
ORCID: 0000-0002-2220-881X

NOVIKOV Innokenty I.
novikov@switch.ioffe.ru
ORCID: 0000-0003-1983-0242

VOZNYUK Gleb V.
glebufa0@gmail.com
ORCID: 0009-0004-0718-1649

PANEVIN Vadim YU.
pvyu@rphf.spbstu.ru
ORCID: 0000-0003-4424-1722

MITROFANOV Maksim I.
maxi.mitrofanov@gmail.com
ORCID: 0000-0002-0351-8484

PIKHTIN Nikita A.
nike@hpld.ioffe.ru
ORCID: 0000-0002-0492-2227

SLIPCHENKO Sergey I.
serghpl@mail.ioffe.ru
ORCID: 0000-0003-4851-3641

EGOROV Anton Yu.
anton@beam.ioffe.ru
ORCID: 0000-0002-0789-4241

Received 31.07.2024. Approved after reviewing 16.08.2024. Accepted 20.08.2024.

Conference materials
UDC 538.9
DOI: https://doi.org/10.18721/JPM.173.214

Millifluidic polyol synthesis of Ag nanowires and microplotter printing of transparent conductive films

P.V. Arsenov✉, K.S. Pilyushenko, D.D. Kazarinova, I.S. Vlasov, I.A. Volkov

Moscow Institute of Physics and Technology (National Research University), Dolgoprudny, Russia

✉ arsenov.pv@mipt.ru

Abstract. Millifluidic polyol synthesis teflon tube (i.d. 1 mm) was studied and used to obtain silver nanowire dispersions. As a result of the experiments, the optimal concentrations of the reagents (silver nitrate $AgNO_3$, ethylene glycol and polyvinylpyrrolidone) were investigated and found to obtain homogeneous nanowires with high length-to-diameter ratios. As a result of the synthesis, Ag nanowires were obtained, which were used to form transparent conductive electrodes using microplotter printing. Transparent conductive electrodes with high transparency of more than 80% at a wavelength of 550 nm with a surface resistance of 52-229 Ohm/sq.

Keywords: Polyol synthesis, millifluidics, silver nanowires, microplotter printing, transparent electrode

Funding: This research was funded by the Russian Science Foundation grant no. 23-79-10081, https://rscf.ru/project/23-79-10081/.

Citation: Arsenov P.V., Pilyushenko K.S., Kazarinova D.D., Vlasov I.S., Volkov I.A., Millifluidic polyol synthesis of Ag nanowires and microplotter printing of transparent conductive films, St. Petersburg State Polytechnical University Journal. Physics and Mathematics. 17 (3.2) (2024) 78–83. DOI: https://doi.org/10.18721/JPM.173.214

Материалы конференции
УДК 538.9
DOI: https://doi.org/10.18721/JPM.173.214

Миллифлюидный полиольный синтез серебряных нанопроволок и микроплоттерная печать прозрачных электродов на их основе

П.В. Арсенов✉, К.С. Пилюшенко, Д.Д. Казаринова, И.С. Власов, И.А. Волков

Московский физико-технический институт (национальный исследовательский университет), г. Долгопрудный, Россия

✉ arsenov.pv@mipt.ru

Аннотация. Миллифлюидный полиольный синтез в тефлоновой трубке с внутренним диаметром 1 мм был изучен и использован для получения дисперсий серебряных нанопроволок. В результате экспериментов были исследованы и найдены оптимальные концентрации используемых реагентов (нитрат серебра $AgNO_3$, этиленгликоль и поливинилпирролидон) для получения однородных нанопроволок с высокими значениями отношения длины к диаметру). В результате синтеза были получены Ag нанопроволки, которые были использованы при формировании прозрачных проводящих электродов с помощью микроплоттерной печати. Были получены прозрачные проводящие электроды с высокой прозрачностью более 80% на длине волны 550 нм с поверхностным сопротивлением 229-52 Ом/кв.

Ключевые слова: Полиольный синтез, миллифлюидика, серебряные нанопроволки, микроплоттерная печать, прозрачный электрод

Финансирование: Исследование выполнено при финансовой поддержке гранта Российского научного фонда № 23-79-10081, https://rscf.ru/project/10081-79-23/.

Ссылка при цитировании: Арсенов П.В., Пилюшенко К.С., Казаринова Д.Д., Власов И.С., Волков И.А. Миллифлюидный полиольный синтез серебряных нанопроволок и микроплоттерная печать прозрачных электродов на их основе // Научно-технические ведомости СПбГПУ. Физико-математические науки. 2024. Т. 17. № 3.2. С. 78–83. DOI: https://doi.org/10.18721/JPM.173.214

Introduction

Transparent conductive electrodes (TCEs) are extensively utilized in electronic applications, including touch screens, solar panels, and optoelectronic devices. Currently, metal oxide films, particularly ITO, are the most commonly employed materials. However, these films are unsuitable for flexible or curved substrates due to their brittleness and limited mechanical flexibility [1–2]. Other drawbacks include their high refractive index and the expensive production processes associated with large-area metal oxide films. Consequently, TCEs made from carbon nanotubes, graphene, and metal nanowires are gaining popularity. A critical objective is to develop TCEs from elongated nano-objects that achieve a sheet resistance of less than 100 ohms per square while maintaining a transparency of at least 80% at a wavelength of 550 nm [3–6]. Among these materials, silver nanowires (AgNWs) are particularly advantageous due to their favorable optoelectronic properties [4, 5]. This study focuses on investigating TCEs based on AgNWs that are deposited using microplotter printing. Currently, several methods are employed to produce silver nanowires, including polyol synthesis, template methods, hydrothermal synthesis, wet chemical synthesis and ultraviolet irradiation methods. The polyol synthesis method is particularly noteworthy due to its advantages in both fundamental research and industrial applications. Benefits include a relatively straightforward reaction protocol that can be easily scaled, the elimination of templates, short synthesis times (often under an hour), and the high aspect ratios of the resulting elongated nanostructures. In this synthesis method, key components of the reaction system include polyols (such as ethylene glycol), which serve as reducing agents, polymers (specifically polyvinylpyrrolidone), which act as capping and growth-controlling agents for the formation of one-dimensional structures, and silver nitrate, which provides a source of metal cations. One of the known approaches to AgNW synthesis is synthesis in a thin capillary in a flow mode. The advantages of this approach are the possibility of implementing a continuous-action setup with subsequent scaling without changing the system parameters (increasing the number of channels), a lower synthesis temperature, and a reduction in synthesis time compared to the approaches to synthesis in a periodic mode presented in the literature [7, 8].

Materials and Methods

In this study, silver nanowires (AgNW) were synthesized using the polyol method. The schematic representation of the synthesis process is illustrated in Fig. 1. An electric syringe pump (SPLab02, UNIX Instruments) was used to inject the solutions into the millifluidic reactor, which pumped the solutions into the reactor at a given flow rate. As in the case of synthesis in a periodic mode, a polyol process was carried out in a millifluidic reactor, i.e., the reduction of silver by means of aldehydes obtained by thermal decomposition of polyhydric alcohols. The setup in Fig. 1 was a teflon tube with an internal diameter of 1 mm., the tube was immersed in an oil bath, the solution was supplied and the flow rate was controlled by a syringe pump, the temperature was controlled by a thermocouple, and a product receiver was placed at the outlet of the heating zone and cooled with cold water.

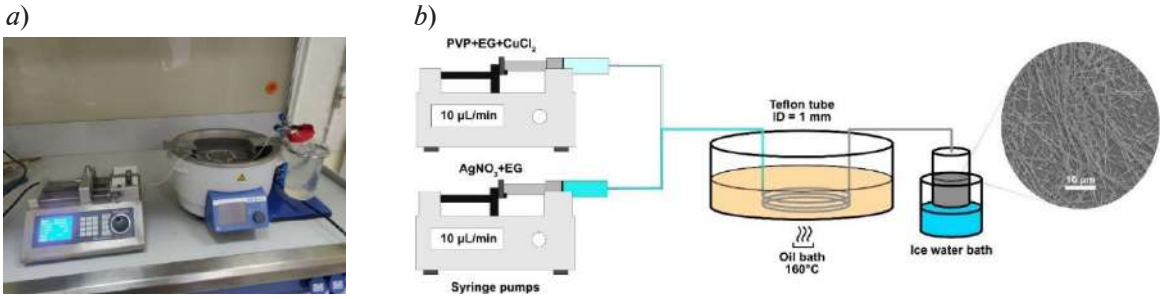

Fig. 1. Photo of experimental setup (*a*) and schematic illustration of AgNWs synthesis process (*b*)

It is known that the shape and size of Ag nanoparticles depend on such synthesis parameters as: temperature, reagent concentration and their molar ratios. Anisotropic growth of AgNWs is supported by a surfactant that covers certain faces of the growing crystal, leaving other faces free, thereby ensuring growth in one direction. In this regard, the influence of the molar ratio of surfactant to Ag becomes obvious. In the course of the work, polyvinylpyrrolidone (PVP) was used as such a surfactant. The literature reports on optimal PVP/Ag molar ratios. Some sources [9] claim that the optimal PVP/Ag molar ratio is 6/1, other sources [10] that it is 3/1, and the synthesis is also carried out at a molar ratio of 1.5 [11]. It follows that due to the complexity of the physicochemical processes occurring during the synthesis, the optimal values of the concentration parameters can vary depending on the system parameters. However, the PVP/Ag molar ratio is the most important factor influencing the morphology and size of the resulting Ag nanoparticles. Reagent solutions containing $CuCl_2$, polyvinylpyrrolidone (PVP), and $AgNO_3$ were prepared using ethylene glycol (EG) as the solvent. In the synthesis process, 40 µL of $CuCl_2$ was added to each solution of PVP and $AgNO_3$, which had concentrations of 20 mg/ml and 10 mg/ml in EG, respectively. Subsequently, 5 mL of the $AgNO_3$ solution and 5 mL of the PVP solution were injected into an oil bath through a syringe pump, utilizing a Teflon tube with a 1.0 mm inner diameter at a flow rate of 10 µL/min. The Teflon tube was coiled and immersed in an oil bath maintained at a temperature of 160°C. The duration of the reaction was controlled by adjusting the flow rate.

Ag nanowires based films were fabricated on quartz glass substrates with the use of SonoPlot GIX Microplotter II (SonoPlot, Middleton, USA). Ag NWs based inks were loaded into glass capillary with a tip inner diameter of about 340 µm, which was used for films deposition. Ag NWs based films with the size of 12×12 mm and various number of layers were printed by moving the dispenser at a speed of 10 mm/s. After printing, all the films were dried at a temperature of 100 °C for 1 hour in an air atmosphere.

Conductivity of transparent films based on a sparse grid of extended nanostructured objects with a transmission coefficient >50% (at 550 nm) can be described using a percolation theory [12]. The correlation between the transmission coefficient T and the sheet resistance R_s can be expressed as:

$$T = \left[1 + \frac{1}{\Pi}\left(\frac{Z_0}{R_s}\right)^{\frac{1}{n+1}}\right]^{-2}, \quad (1)$$

where Z_0 is the impedance of the free space (377 Ohm), n is the percolation exponent, and Π is the percolative figure of merit [12]:

$$\Pi = 2\left[\frac{\sigma_{dc,B}/\sigma_{op}}{\left(Z_0 t_{\min}\sigma_{op}\right)^n}\right]^{1/(n+1)}, \quad (2)$$

where $\sigma_{dc,B}$ is the bulk dc conductivity of the film, t_{min} is the thickness below which the dc conductivity becomes thickness dependent, σ_{op} is the optical conductivity related to the absorption coefficient α as $\sigma_{op} \approx \alpha/Z_0$.

Results and Discussion

The microstructural characteristics of the synthesized silver nanowires (AgNWs) were examined using electron microscopy. To perform the scanning electron microscopy (SEM) analysis, an AgNWs film was prepared by applying a suspension of the metallic structures in isopropyl alcohol onto a glass substrate using the drop casting method. After application, the film was dried at a temperature of 80 °C to ensure proper adhesion and removal of the solvent, allowing for detailed examination of the nanowire morphology and structure. In Fig. 2, images of the SEM of AgNWs obtained at different molar ratios are presented. As seen in Fig. 2, *a*, at a PVP/Ag molar ratio of 0.4, the product primarily consists of thick rods with a wide distribution in diameter and length, along with large spherical particles, indicating an insufficient amount of PVP. With an increase in the amount of PVP to a PVP/Ag molar ratio of 1.25, the main product consists of AgNWs (see Fig. 2, *b*). The obtained AgNWs have lengths ranging from 20 to 60 μm and diameters of 80–100 nm. Notably, as the molar ratio increases to 2.5, AgNWs are still predominantly formed; however, a slight increase in wire diameter (over 100 nm) is observed with the increasing PVP/Ag molar ratio, along with a larger amount of polymer in the resulting suspension, which needs to be removed to ensure good conductivity of the subsequently obtained films. An increase in the molar ratio to 3, as seen in Fig. 3, *c*, leads to the appearance of relatively large Ag nanoparticles. Further increasing the PVP/Ag molar ratio to 6 results in an even higher number of large Ag nanoparticles (see Fig. 2, *d*), indicating that a large amount of PVP relative to Ag results in complete coverage of all particle facets, leading to isotropic growth.

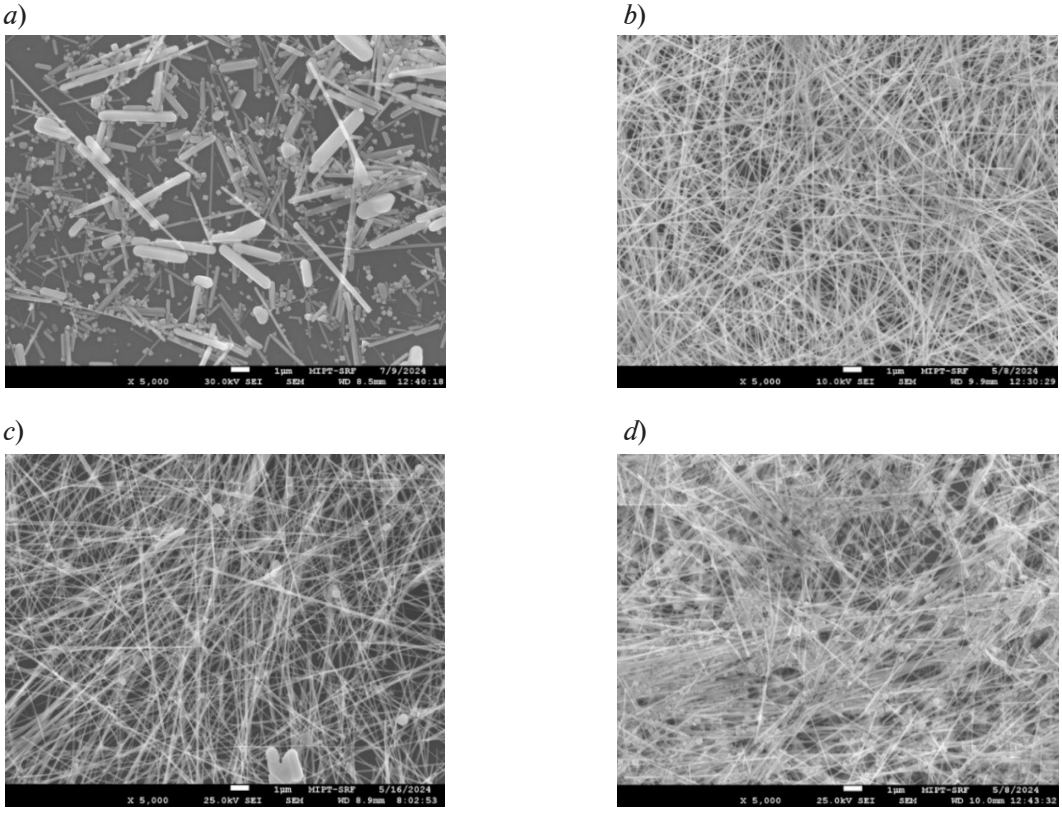

Fig. 2. SEM images of AgNWs obtained at PVP/Ag molar ratios of 0.4 (*a*), 1.24 (*b*), 3 (*c*) and 6 (*d*)

The sheet resistance of films was measured using digital multimeter APPA 505 (MGL APPA Corporation, Taipei). The transmission specrta in the range of 400–2500 nm was measured using spectrophotometer Jasco V-770 (Jasco, Easton). Fig. 3 demonstrates transmission spectra of the films (Fig. 3, *a*) and fitted dependence (according formula 1) of the film transmittance on the sheet resistance (Fig. 3, *b*), with fitting parameters on the insert.

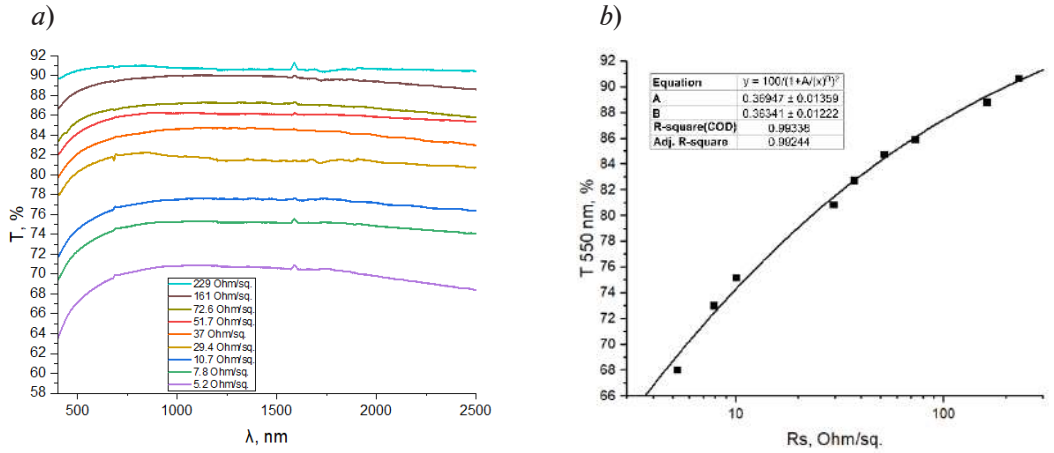

Fig. 3. Transmission spectra of dried printed films based on synthesized Ag nanowires (*a*); transmittance versus sheet resistance for printed films based on silver nanowires at a wavelength of 550 nm (*b*)

Conclusion

A study was carried out on the formation of silver nanostructures with different PVP/Ag molar ratios. It was found that PVP/Ag optimal molar ratio is 1.25, in that case the main product consists of AgNWs with lengths ranging from 20 to 60 μm and diameters of 80–100 nm. Obtained transmittance versus sheet resistance dependences of printed layers based on AgNWs are in good agreement with the theory known from the literature [7]. In addition, films with a high transparency of more than 80% were obtained at a wavelength of 550 nm with a sheet resistance of 52–229 ohms/sq. These microplotter printed films are suitable for creating transparent conductive electrodes in optoelectronic devices.

REFERENCES

1. **Kumar A., Kumar M., Goyat M.S., Avasthi D.K.,** A review of the latest developments in the production and applications of Ag-nanowires as transparent electrodes. Materials Today Communications. 33 (2022) 104433.

2. **Yu X., et al.,** Investigation of light transmission and scattering properties in silver nanowire mesh transparent electrodes. Materials Letters. 145 (2015) 219–223.

3. **Scardaci V., Coull R., Lyons P.E., et al.,** Spray deposition of highly transparent, low-resistance networks of silver nanowires over large areas, Small. 7 (18) (2011) 2621–2628.

4. **Lee J.Y., Connor S.T., Cui Y., Peumans P.,** Solution-processed metal nanowire mesh transparent electrodes. Nano letters. 8 (2) (2008) 689–692.

5. **Madaria A.R., Kumar A., Zhou C.,** Large scale, highly conductive and patterned transparent films of silver nanowires on arbitrary substrates and their application in touch screens. Nanotechnology. 22 (24) (2011) 245201.

6. **Wu H., Hu L., Rowell M.W., et al.,** Electrospun metal nanofiber webs as high-performance transparent electrode. Nano letters. 10 (10) (2010) 4242–4248.

7. **Gebeyehu M.B., Chala T.F., Chang S.Y., et al.,** Synthesis and highly effective purification of silver nanowires to enhance transmittance at low sheet resistance with simple polyol and scalable selective precipitation method. RSC advances. 7 (26) (2017) 16139–16148.

8. **Hemmati S., Harris M.T., Barkey D.P.,** Polyol silver nanowire synthesis and the outlook for a green process. J Nanomater. (2020) 1–25.

9. **Gebeyehu M.B., Chala T.F., Chang S.Y., et al.,** Synthesis and highly effective purification of silver nanowires to enhance transmittance at low sheet resistance with simple polyol and scalable selective precipitation method. RSC advances. 7 (26) (2017) 16139–16148.

10. **Yu J., Yang L., Jiang J., et al.,** Scalable Production of High-Quality Silver Nanowires via Continuous-Flow Droplet Synthesis. Nanomaterials. 12 (6) (2022) 1018.

11. **Xu F., Xu W., Mao B., et al.,** Preparation and cold welding of silver nanowire based transparent electrodes with optical transmittances > 90% and sheet resistances < 10 ohm/sq. Journal of colloid and interface science. 512 (2018) 208–218.

12. **De S., Coleman J.N.,** The effects of percolation in nanostructured transparent conductors. Mrs Bulletin. 36 (10) (2011) 774–781.

THE AUTHORS

ARSENOV Pavel V.
arsenov.pv@mipt.ru

PILYUSHENKO Konstantin S.
piliushenko.ks@mipt.ru

KAZARINOVA Daria D.
kazarinova.dd@mipt.ru

VLASOV Ivan S.
vlasov.is@mipt.ru

VOLKOV Ivan A.
volkov.ia@mipt.ru

Received 16.09.2024. Approved after reviewing 30.10.2024. Accepted 30.10.2024.

SIMULATION OF PHYSICAL PROCESSES

Conference materials
UDC 538.975, 538.958
DOI: https://doi.org/10.18721/JPM.173.215

Numerical investigation of influence GaP nanowire geometry to light extraction efficiency of red light-emitting diode

K.N. Novikova[1,2]✉, A. S.Funtikova[1,2], A. M.Mozharov[1,2], I. S.Mukhin[1,2]

[1] Alferov University, St. Petersburg, Russia;

[2] Peter the Great St. Petersburg Polytechnic University, St. Petersburg, Russia

✉ novikova_k@spbau.ru

Abstract. Currently, micro-LEDs are promising optoelectronic devices. Numerical investigation was carried out to study the influence of the GaP nanowires geometric parameters on the light extraction efficiency to improve micro-LEDs efficiency. The nanowires diameter has been shown to significantly alter the light extraction efficiency. The optimal nanowire diameter for a wavelength of 650 nm is close to 200 nm.

Keywords: Red LEDs, GaP, NWs, molecular beam epitaxy, light extraction efficiency

Funding: The study was funded by the St. Petersburg Science Foundation grant (23-RB-02-08).

Citation: Novikova K.N., Funtikova A.S., Mozharov A.M., Mukhin I.S., Numerical investigation of influence GaP nanowire geometry to light extraction efficiency of red light-emitting diode, St. Petersburg State Polytechnical University Journal. Physics and Mathematics. 17 (3.2) (2024) 84–87. DOI: https://doi.org/10.18721/JPM.173.215

Материалы конференции
УДК 538.975, 538.958
DOI: https://doi.org/10.18721/JPM.173.215

Численное исследование влияния геометрии нитевидных нанокристаллов GaP на эффективность экстракции света в красном светодиоде

К.Н.Новикова[1,2]✉, А.С.Фунтикова[1,2], А.М.Можаров[1,2], И.С.Мухин[1,2]

[1] Академический университет им. Ж.И. Алфёрова РАН, Санкт-Петербург, Россия;

[2] Санкт-Петербургский политехнический университет Петра Великого, Санкт-Петербург, Россия

✉ novikova_k@spbau.ru

Аннотация. В работе проведено численное исследование влияния геометрических параметров нитевидных нанокристаллов GaP на эффективность экстракции света. Было показано, что диаметр нитевидных нанокристаллов значительно изменяет эффективность экстракции света. Оптимальное значение диаметра ННК для длины волны 650 нм находится вблизи 200 нм.

Ключевые слова: красные светодиоды, фосфид галлия, нитевидные нанокристаллы, молекулярно-пучковая эпитаксия, эффективность экстракции света

Финансирование: Работа выполнена при финансовой поддержке гранта Санкт-Петербургского научного фонда 23-РБ-02-08.

Ссылка при цитировании: Новикова К.Н., Фунтикова А.С., Можаров А.М., Мухин И.С. Численное исследование влияния геометрии нитевидных нанокристаллов GaP на эффективность экстракции света в красном светодиоде // Научно-технические ведомости СПбГПУ. Физико-математические науки. 2024. Т. 3.2 № .17. С. 84–87. DOI: https://doi.org/10.18721/JPM.173.215

Introduction

Currently, micro-LEDs are promising optoelectronic devices [1, 2]. Gallium phosphide is advanced material for creating micro-LEDs due to its waveguide properties and the ability to form a direct-gap solid solution with the addition of As and N. In addition, the crystal lattice period proximity of GaP and silicon makes it possible to create optoelectronic devices based on established silicon technologies on cheap substrates. LED efficiency is a combination of internal quantum efficiency and light extraction efficiency (LEE). Unfortunately, when creating micro-LEDs using the standard «top-down» method, during microdevices etching, upon reaching a certain minimum size, the internal quantum efficiency decreases down to 1% [1]. The radiation generated in a planar micro-LED spreads in all directions and increases optical loss, so the light extraction efficiency in a planar micro-LED also needs to be optimized [3]. As an alternative to planar structures, nanowires (NWs) can be used to increase the micro-LEDs efficiency. NWs are synthesized using «bottom-up» technology without material etching stages. This approach ensures high crystalline perfection and when the active region is integrated inside the LED, for example, in the form of a quantum dot [4], the active region is completely isolated from the external environment and the internal quantum efficiency increases. In addition, the NWs geometric dimensions commensurability and the radiation wavelength makes it possible to control the LEE, which distinguishes the NWs from planar LEDs in which all radiation directions are equivalent even when micro-LED size is 10 μm in diameter.

Unfortunately, the extraction efficiency of NW-based LEDs in the GaP/GaPNAs material system has received insufficient attention to date, so this work aims to investigate LEE by optimizing the geometric parameters of NWs.

Materials and Methods

Full-wave optical modeling of light propagation was carried out using the COMSOL Multiphysics package to select the optimal geometric parameters of the LED. The system under study consisted of a GaP NW on a silicon substrate in an air environment. An optical point dipole was used as a radiation source, the orientation and position of which varied during the calculation. The system schematic cross-sectional representation is presented in Fig. 1, *a*.

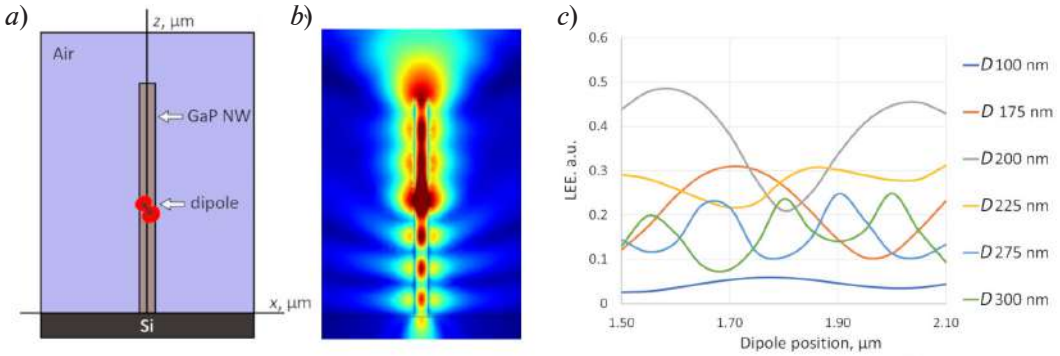

Fig. 1. System under study in cross section (*a*), typical distribution of normalized electric field in the system under study (*b*) and LEE depending graphs on dipole position on NW axis (*c*)

The length of the GaP NWs was fixed at a distance of 3 μm, and the diameter ranged from 50 to 500 nm. Material properties of Si and GaP are taken from [5, 6]. The calculation was carried out for a wavelength of 650 nm, which corresponds to the expected band gap for the GaPNAs solid solution [7].

Results and Discussion

As a result of full-wave optical light distribution modeling, the LEE dependences on the NW geometric parameters, as well as the normalized electric field distribution in the system under study, were obtained. As part of the calculation, for each geometric configuration, the dipole polarization angle was varied and the power fraction of the electromagnetic wave emitted by the dipole that went into the upper plane of the system under study was determined. A typical electric field distribution for a fixed dipole configuration is shown in Fig. 1, *b*. As a result of numerical modeling, the LEE in the vertical direction from the position of the emitting center along the NW axis was calculated for diameters from 50 to 500 nm. Fig. 1, *c* shows the LEE dependences for diameters from 100 to 300 nm. It has been established that the movement of the emission center on wavelength scales significantly affects the extraction efficiency. This is due to the fact that the NW is a resonator with a certain mode composition. Therefore, for effective radiation extraction, it is necessary to fulfill the condition of constructive interference for the output radiation, which will lead to modulation of the light extraction efficiency.

The LEE values were averaged over one LEE modulation period and a summary of the average light extraction efficiency as a function of NW diameter is presented in Fig. 2, *a*. A monotonous increase in the average LEE value is shown with an increase in the NW diameter to 200 nm and a further decrease. The maximum LEE value was almost 40% for random polarization and dipole position along the NW axis.

As part of the mode analysis, NWs with diameters equal to 100, 200 and 300 nm were studied (Fig. 2, *b*, *c*, *d*). At small NW diameters (Fig. 2, *b*), the electromagnetic wave goes upward, but diverges greatly. As the diameter increases, the NW begins to function as a resonator and the wave has greater directivity, as can be seen in Fig. 1, *b*. This is also noticeable from Fig. 2, *c* because the wave spreads throughout the NW. A further increase in the diameter (Fig. 2, *d*) leads to the dominance of higher-order modes, which are shifted from the NW axis and the point dipole does not emit in them.

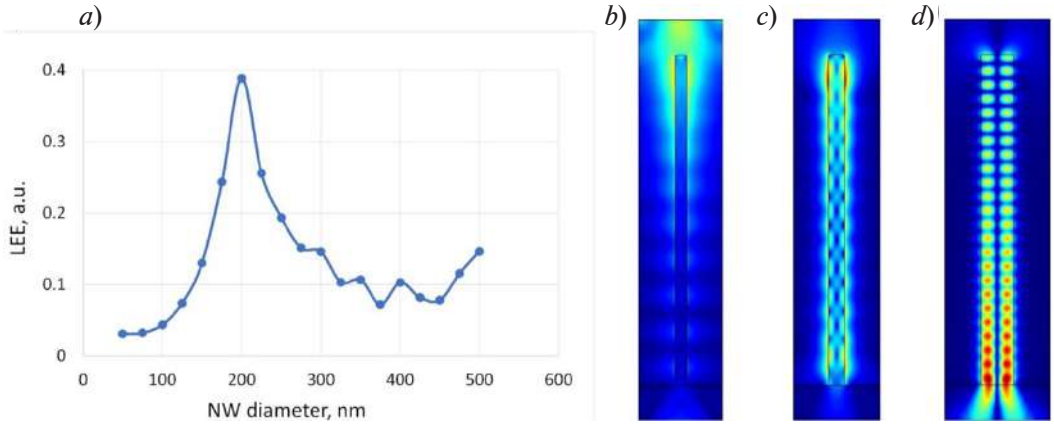

Fig. 2 Dependence of average LEE value on NW diameter (*a*) and eigenmodes for NW diameters equal to 100 nm (*b*), 200 nm (*c*) and 300 nm (*d*)

Conclusion

We demonstrated a numerical study of GaP NWs with a point-emitting center in various geometric configurations. The NWs diameter has been shown to significantly modify the light extraction efficiency. The optimal value of the NW diameter for a wavelength of 650 nm is close to 200 nm. The results of this simulation can be used to synthesize NWs with specified optimal geometric parameters and create highly efficient red micro-LEDs based on them.

Acknowledgments

The study was funded by the St. Petersburg Science Foundation grant (23-RB-02-08).

REFERENCES

1. **Pandey A., Malhotra Y., Wang P., et al.,** N-polar InGaN/GaN nanowires: overcoming the efficiency cliff of red-emitting micro-LEDs, Photonics Res. 4 (10) (2022) 1107.

2. **Belyaev V.,** Solid state and organic micro-LEDs – technology, market, prospects, ELECTRONICS: Science, Technology, Business. (8) (2018) 102–112.

3. **Hu R., Cao B., Zou Y., et al.,** Modeling the Light Extraction Efficiency of Bi-Layer Phosphors in White LEDs, IEEE Photonics Technology Letters. 12 (25) (2013) 1141–1144.

4. **Barettin D., Shtrom I.V., Reznik R.R., Cirlin G.E.,** Model of a GaAs Quantum Dot in a Direct Band Gap AlGaAs Wurtzite Nanowire, Nanomaterials. 11 (13) (2023) 1737.

5. **Green M.A.,** Self-consistent optical parameters of intrinsic silicon at 300K including temperature coefficients, Solar Energy Materials and Solar Cells. 11 (92) (2008) 1305–1310.

6. **Adachi S.,** Optical dispersion relations for GaP, GaAs, GaSb, InP, InAs, InSb, $Al_xGa_{1-x}As$, and $In_{1-x}Ga_xAs_yP_{1-y}$, J Appl Phys. 12 (66) (1989) 6030–6040.

7. **Mozharov A.M., Kudryashov D.A., Bolshakov A.D., et al.,** Numerical simulation of the properties of solar cells based on GaPNAs/Si heterostructures and GaN nanowires, Semiconductors. 11 (50) (2016) 1521–1525.

THE AUTHORS

NOVIKOVA Kristina N.
novikova_k@spbau.ru
ORCID: 0000-0001-8440-494X

MOZHAROV Alexey M.
mozharov@spbau.ru
ORCID: 0000-0002-8661-4083

FUNTIKOVA Anastasiia S.
n.fn@mail.ru
ORCID: 0009-0000-3147-6974

MUKHIN Ivan S.
imukhin@yandex.ru
ORCID: 0000-0001-9792-045X

Received 29.07.2024. Approved after reviewing 27.08.2024. Accepted 27.08.2024.

Conference materials
UDC 29.31.00
DOI: https://doi.org/10.18721/JPM.173.216

Polarization extinction ratio conversion due to pointing system impact in satellite quantum key distribution

A.V. Duplinsky[1,3]✉, A.V. Khmelev[1,4,5], R.M. Bakhshaliev[1,3], D.O. Sevryukov[1,3], K.A. Barbyshev[1,2], V.L. Kurochkin[1,2,5]

[1] QSpace Technologies, Moscow, Russia;

[2] National University of Science and Technology MISiS, Moscow, Russia;

[3] HSE University, Moscow, Russia;

[4] Moscow Institute of Physics and Technology, Dolgoprudny, Russia;

[5] Russian Quantum Center, Skolkovo, Russia

✉ al.duplinsky@goqrate.com

Abstract. Quantum key distribution via satellites enables the technology to be applied at transcontinental scale; nevertheless, in contrast to fiber systems, using a free-space optical communication channel presents certain extra technological obstacles. The contribution of the acquisition, pointing and tracking system's operation to the potential quantum bit error value is investigated in this research. The polarization extinction ratio measurements varying with the pointing mirror angular position are reported, based on these data, the upper limit of the quantum bit error is predicted for several types of satellite passages.

Keywords: quantum key distribution, polarimetry, polarization extinction ratio, free-space optics

Funding: This work was supported by the Ministry of Education and Science of the Russian Federation in the framework of the Program of Strategic Academic Leadership "Priority 2030" (Strategic Project "Quantum Internet").

Citation: Duplinsky A.V., Khmelev A.V., Bakhshaliev R.M., Sevryukov D.O., Barbyshev K.A., Kurochkin V.L., Polarization extinction ratio conversion due to pointing system impact in satellite quantum key distribution, St. Petersburg State Polytechnical University Journal. Physics and Mathematics. 17 (3.2) (2024) 88–92. DOI: https://doi.org/10.18721/JPM.173.216

Материалы конференции
УДК 29.31.00
DOI: https://doi.org/10.18721/JPM.173.216

Влияние системы наведения на изменение коэффициента поляризационной экстинкции в спутниковой квантовой криптографии

А.В. Дуплинский[1,3]✉, А.В. Хмелев[1,4,5], Р.М. Бахшалиев[1,3], Д.О. Севрюков[1,3], К.А. Барбышев[1,2], В.Л. Курочкин[1,2,5]

[1] КуСпэйс Технологии, Москва, Россия;

[2] Национальный университет науки и технологий НИТУ МИСиС, Москва, Россия;

[3] Национальный исследовательский университет «Высшая школа экономики», Москва, Россия;

[4] Московский физико-технический институт, г. Долгопрудный, Россия

[5] Российский квантовый центр, Сколково, Москва, Россия

✉ al.duplinsky@goqrate.com

Аннотация. Квантовое распределение ключей с использованием спутника позволяет применять эту технологию на трансконтинентальных масштабах; тем не менее, в отличие от оптоволоконных систем, использование оптического канала связи в свободном пространстве сопряжено с определенными дополнительными техническими препятствиями. Нами исследуется величина ошибок, вносимых в процессе работы системы сбора, наведения и слежения в величину потенциальной ошибки квантового бита. Приведены результаты измерений коэффициента поляризационной экстинкции, изменяющиеся в зависимости от углового положения наведения зеркала, и на основе этих данных прогнозируется верхний предел ошибки квантового бита для нескольких типов пролетов спутников.

Ключевые слова: квантовое распределение ключей, поляриметрия, коэффициент поляризационной экстинкции, оптика свободного пространства

Финансирование: Работа выполнена при поддержке Министерства образования и науки РФ в рамках Программы стратегического академического лидерства «Приоритет 2030» (Стратегический проект «Квантовый Интернет»).

Ссылка при цитировании: Дуплинский А.В., Хмелёв А.В., Бахшалиев Р.М., Севрюков Д.О., Барбышев К.А., Курочкин В.Л. Влияние системы наведения на изменение коэффициента поляризационной экстинкции в спутниковой квантовой криптографии // Научно-технические ведомости СПбГПУ. Физико-математические науки. 2024. Т. 17. № 3.2. С. 88–92. DOI: https://doi.org/10.18721/JPM.173.2.16

Introduction

Satellite quantum key distribution (QKD) requires acquisition, pointing and tracking system (APT) on both sides of the communication link, most often it is a closed feedback loop consisting of a controlled fast mirror and a camera [1, 2]. However, angular inclinations of the mirror cause polarization extinction ratio (PER) conversion during system operation, which negatively affects the quantum bit error (QBER).

In 2023, the Vector [2] payload was developed and successfully launched into orbit to demonstrate classical satellite laser communication. Moreover, it is also aimed at testing technical solutions and service systems for the future satellite payload to perform QKD, including APT. Vector's APT system uses a 671 nm laser beacon from a ground receiving station as a reference signal,

detecting it on the camera matrix. APT's purpose is to tilt the MEMS mirror so that the detected point on the matrix match with the target point, resulting in parallelism between both optical axis of the satellite's transmitting scheme and ground station receiving scheme. Simultaneously, a similar procedure occurs at the ground station, which operates using a 525 nm beacon laser mounted aboard the satellite. The payload optical scheme and satellite general view are shown in Fig. 1

To communicate with the satellite, we use customized Zvenigorod ground station, which was previously successfully utilized as receiver during satellite QKD experiments with Micius satellite [3].

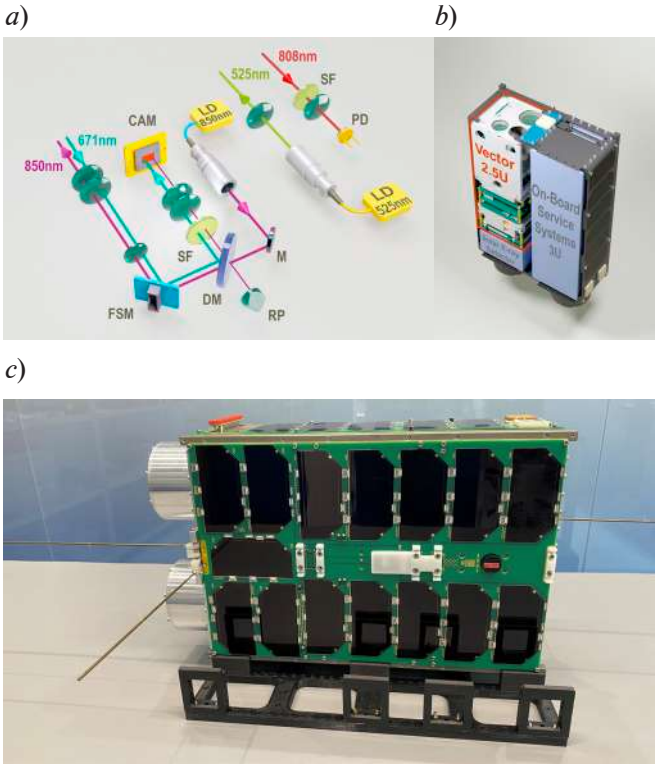

Fig. 1. Vector optical scheme. The payload has three apertures: two for downlink and uplink laser communications and one for downlink beacon laser operation. LD is the laser diode, M is the mirror, DM is the dichroic mirror, RP is the 180° reflective prism, SF is the spectral filters, CAM is the camera, FSM is the fast steering mirror, PD is the photodetector (*a*); 3D satellite model (*b*); general view of the satellite (*c*)

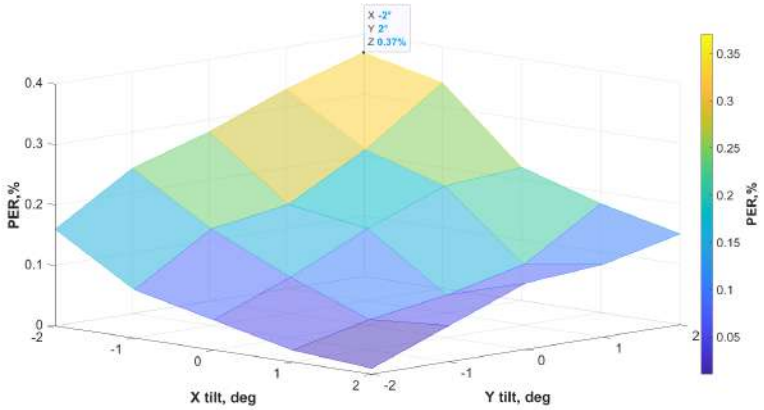

Fig. 2. Scanning results for different MEMS angles

Methods and Results

To assess the expected APT impact, Vector payload optical prototype was used. Its APT active element is performed by an aluminum-coated MEMS mirror with 5 mm aperture diameter. The optical signal of the prototype was measured using a polarimeter with ±2° deflection angles with a step of 1° for both axes. Thus, the entire working area of the MEMS mirror was scanned and PER for these points were measured. The scanning results are presented in Fig. 2.

The lowest PER point angular coordinates are (−2°; 2°), and its value is 0.37 %. Using this PER as the upper bound of the transmitter error, we estimate the potential maximum QBER.

$$e_{\text{det}}^{U} = e_{\text{det}}^{Rx} + e^{Tx,U}, \tag{1}$$

where e^{Rx}_{det} is the intrinsic error of the receiver when the input beam is perfectly polarized, $e^{Tx,U}$ is the upper bound of the transmitter error.

Utilizing the previously published model [4], we estimate the upper bound of the simulated QBER during a quantum key distribution session for a prospective satellite using a similar APT optical architecture.

$$\text{QBER}(t) = \frac{e_0 Y_0 + e_{\text{det}}^{U}\left(1 - e^{-\mu\eta(t)}\right)}{Y_0 + 1 - e^{-\mu\eta(t)}}, \tag{2}$$

where μ is the intensity of signal states, e_0 is the error rate of the background, Y_0 is the background signal, $\eta(t)$ is the link efficiency, e^{U}_{det} is the upper bound of an intrinsic error caused by measurement fidelity.

The predicted QBER function for two satellite passages with different maximum elevation angles $\theta_{El}^{max} = 32.5°$ and $\theta_{El}^{max} = 90°$, using $\mu = 0.8$, $e_0 = 0.5$, $Y_0 = 5 \cdot 10^{-6}$ clicks are presented in Fig. 3. The elevation angle reaches its maximum during the passage at 0 (s) - point, which also happens to be the instant with the lowest QBER value. The largest QBER occurs at the edges, when the angle between satellite and the ground station is at its minimum and the distance is at its maximum.

Fig. 3 shows that, during these QKD sessions, the QBER value remains under 3%; for any higher PER values, these lines will pass below.

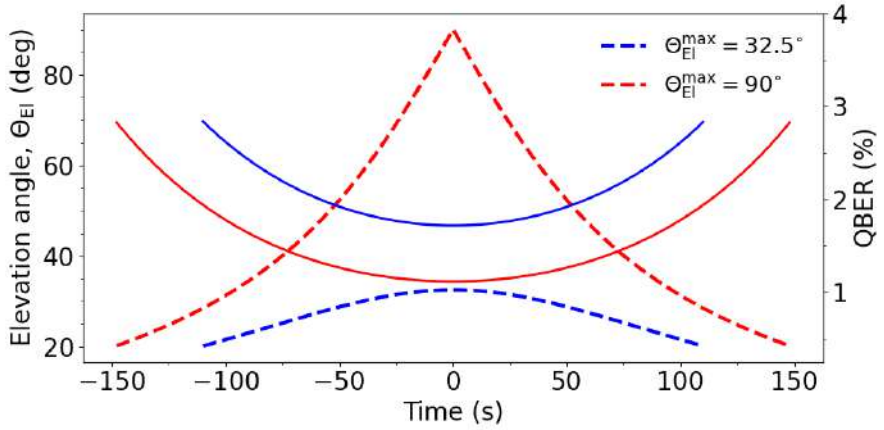

Fig. 3. QBER modeling results for two different passages

Conclusion

Polarization extinction ratio scanning and quantum bit error rate modeling show the possibility of using such an APT technical solution in the payload design for satellite quantum key distribution realization.

REFERENCES

1. **Liao S.K., Cai W.Q., Liu W.Y., et al.,** Satellite-to-ground quantum key distribution, Nature. 549 (7670) (2017) 43–47.

2. **Khmelev A.V., Duplinsky A.V., Mayboroda V.F., et al.,** Recording of a single-photon signal from low-flying satellites for satellite quantum key distribution. Technical Physics Letters. 47(12) (2021) 858–861.

3. **Miller A.V., et al.,** Vector – towards quantum key distribution with small satellites. EPJ Quantum Technology. 10 (1) (2023) 52.

4. **Khmelev A., Duplinsky A., Bakhshaliev R., et al.,** Eurasian-scale experimental satellite-based quantum key distribution with detector efficiency mismatch analysis. Optics Express. 32 (7) (2024) 11964–11978.

5. **Khmelev A.V., et al.,** Semi-Empirical Satellite-to-ground quantum key distribution model for realistic receivers. Entropy. 25 (4) (2023) 670.

THE AUTHORS

DUPLINSKY Alexey V.
al.duplinsky@goqrate.com
ORCID: 0000-0002-2964-1800

SEVRYUKOV Dmitriy O.
d.sevryukov@goqrate.com
ORCID: 0009-0000-8253-7263

KHMELEV Aleksandr V.
a.khmelev@goqrate.com
ORCID: 0000-0003-1511-1128

BARBYSHEV Konstantin A.
k.barbyshev@goqrate.com
ORCID: 0009-0002-2294-3731

BAKHSHALIEV Ruslan M.
r.bakhshaliev@goqrate.com
ORCID: 0009-0006-5851-6175

KUROCHKIN Vladimir L.
v.kurochkin@rqc.ru
ORCID: 0000-0002-1599-9801

Received 31.07.2024. Approved after reviewing 12.08.2024. Accepted 19.08.2024.

Conference materials
UDC 538.915, 519.688
DOI: https://doi.org/10.18721/JPM.173.217

Optimization of mid-infrared quantum cascade detectors

A.S. Dashkov[1,3]✉, N.A. Kostromin[1,2,3], D.A. Barykin[2,3], L.I. Goray[1,3,4,5]

[1] Alferov University, St. Petersburg, Russia;

[2] Peter the Great St. Petersburg Polytechnic University, St. Petersburg, Russia;

[3] St. Petersburg Electrotechnical University "LETI", St. Petersburg, Russia;

[4] Institute for Analytical Instrumentation of the RAS, St. Petersburg, Russia;

[5] University associated with IA EAEC, St. Petersburg, Russia

✉ dashkov.alexander.om@gmail.com

Abstract. In this work, the optimization of the design of quantum cascade detectors is considered. The initial design studied was a detector structure based on an AlGaAs/GaAs heteropair, consisting of four quantum wells. A genetic algorithm was utilized to optimize the responsivity and detectivity of the design under study by varying of the widths and chemical composition of the first five layers of the cascade. The responsivity and detectivity were simplified to the characteristics, that can be evaluated based on the solutions of the Schrödinger and Boltzmann equations. The results demonstrate a strong dependence on the optimization algorithm parameters and designate significant change from the initial design. We have shown that to achieve optimal output characteristics and improve the convergence rate, one must use larger populations and high mutation probability in the genetic algorithm. The analysis of the obtained designs also shows that additional regularization techniques are required to achieve better output characteristics of the device. Specifically, the appropriate weighting of the set of optimized characteristics must be determined before final optimization.

Keywords: quantum cascade detector, optimization, numerical simulations, Schrodinger equation

Funding: This study was funded by the Russian Science Foundation grant no. 23-29-00216.

Citation: Dashkov A.S., Kostromin N.A., Barykin D.A., Goray L.I., Optimization of mid-infrared quantum cascade detectors, St. Petersburg State Polytechnical University Journal. Physics and Mathematics. 17 (3.2) (2024) 93–97. DOI: https://doi.org/10.18721/JPM.173.217

Материалы конференции
УДК 538.915, 519.688
DOI: https://doi.org/10.18721/JPM.173.217

Оптимизация квантовых каскадных детекторов среднего инфракрасного диапазона

А.С. Дашков[1,3]✉, Н.А. Костромин[1,2,3], Д.А. Барыкин[2,3], Л.И. Горай[1,3,4,5]

[1] Академический университет им. Ж.И. Алфёрова РАН, Санкт-Петербург, Россия;

[2] Санкт-Петербургский политехнический университет Петра Великого, Санкт-Петербург, Россия;

[3] Санкт-Петербургский государственный электротехнический университет «ЛЭТИ» им. В.И. Ульянова (Ленина), Санкт-Петербург, Россия

[4] Институт аналитического приборостроения РАН, Санкт-Петербург, Россия

[5] АНО ВО «Университет при МПА ЕврАзЭС», Санкт-Петербург, Россия

✉dashkov.alexander.om@gmail.com

Аннотация. В данной работе рассматривается процесс оптимизации конструкций квантово-каскадных детекторов с помощью генетического алгоритма. Полученные результаты демонстрируют сильную зависимость выходных характеристик модифицированной конструкции от параметров алгоритма оптимизации и значительное изменение дизайна относительно исходного. Анализ полученных конструкций также показывает, что для достижения наилучших выходных характеристик устройства требуется применять дополнительные методы регуляризации целевой функции.

Ключевые слова: квантово-каскадный детектор, оптимизация, численное моделирование, уравнение Шредингера

Финансирование: Работа выполнена при финансовой поддержке гранта Российского научного фонда № 23-29-00216.

Ссылка при цитировании: Дашков А.С., Костромин Н.А., Барыкин Д.А., Горай Л.И. Оптимизация квантовых каскадных детекторов среднего инфракрасного диапазона // Научно-технические ведомости СПбГПУ. Физико-математические науки. 2024. Т. 17. № 3.2. С. *93*–97. DOI: https://doi.org/10.18721/JPM.173.217

Introduction

Quantum cascade detectors (QCD) are unipolar devices, which have a variety of applications in physics, chemistry, and medicine. Since the mid-infrared (MIR) region is characterized by the distinctive absorption lines of different molecules, the development and adaptation of existing designs of MIR QCDs provide even greater benefits for future studies [1]. However, the problem of the creation and adjustment of new QCD designs remains an important and relevant scientific task [2,3]. In this work, we present techniques for creating new, more robust QCD devices. These techniques include numerical optimization methods, including a genetic algorithm. Another challenge in creating high-efficiency QCDs is the design of efficient waveguides. Because in quantum wells only the polarization oriented parallel to the growth axis can be absorbed, such structures as transmission gratings [1], and metamaterials can be used as waveguides [4].

Materials and Methods

The research mainly focuses on the QCD designs based on AlGaAs/GaAs heterostructures. During the simulation process, the Schrödinger-Poisson system of equations is solved numerically using modified shooting and single band kp-methods and effective mass approximation and envelope

functions approximations with the constants from [5]. The optimization process is performed with a genetic algorithm, via the Python genetic algorithm package [6]. For the precise calculation of waveguide modes, it is essential to use accurate refractive index and extinction coefficient values. In the MIR, the Drude-Lorentz model is used to describe the complex dielectric permittivity. To calculate spectra, the refractive index and extinction coefficient (absorption index) are calculated by solving the Fresnel equation. To obtain the transmission and reflection spectra of the entire structure, the transfer matrix method through the entire QCD structure is used.

Results and Discussion

It was previously shown that a genetic algorithm can effectively solve similar tasks, such as quantum cascade laser optimization when the appropriate target function is chosen [7]. The result of the optimization process shows that the stated QCD problem can be also efficiently solved with several limitations and simplifications. The main limitation is that the loss function or the target function must be manually constructed. In this study, the target function was selected through empirical and iterative methods and is focused on maximizing the main output characteristics of the resulting QCD. In this work, we considered the combination (sum) of the weighted transition energy (first term, normalized to the target transition energy) and the weighted scattering time from the upper level multiplied by the inverse dipole matrix element of the corresponding optical transition (second term). The weighting coefficients were 0.4 and 0.6 for the first and second terms, respectively. The other important limitation is the necessity of using a rather extensive search strategy in the genetic algorithm approach: increasing the initial population size N and mutation probability p (Fig 1, *a*, *b*). One can also conclude that as a result of the optimization process, the optical transition scheme [8] is significantly altered, which without proper assessment may lead to the worsening of the sensitivity and operating speed of the detector (Fig 2, *a*, *b*). In this case, the initial design, which originally contained a single quantum well in the active region of the cascade (Fig 2, *a*), transformed into a structure with two quantum wells in the active region (Fig 2, *b*). Though each transition in the transformed quantum wells has a lower transition probability, the total estimated absorption exceeds the initial value.

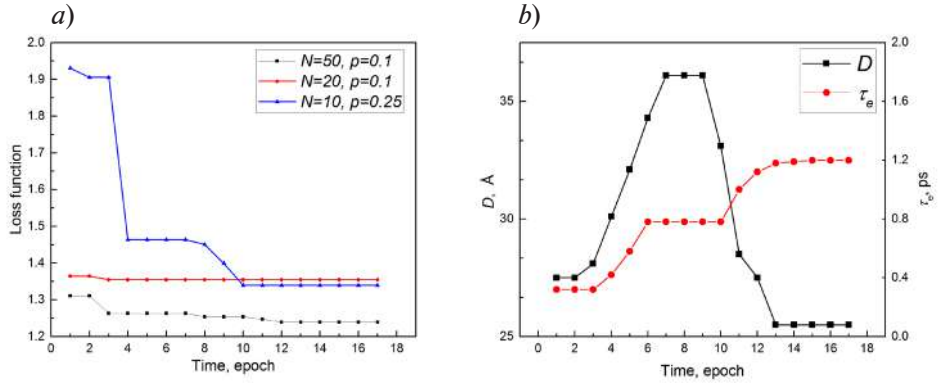

Fig. 1. Evolution curve obtained during optimization via genetic algorithm (*a*); dependence of figures of merits during the optimization process (*b*)

To evaluate the detectivity and responsivity improvement during and after the optimization process, the figures of merit were monitored. For responsivity R (1), we considered the dipole matrix element D, because this is the main influential factor in the linear approximation [9]:

$$R = \frac{\lambda q}{hc}\eta\frac{p_e}{p_c} \sim D^2, \quad (1)$$

where λ is the detected wavelength, η is the absorption efficiency, α is the absorption coefficient, p_e, p_c are the the upper escape and lower capture probability. The obtained transmission coefficient, estimated for the considered classical waveguide, was incorporated as a factor in the second term of the loss function, as it also significantly influences the responsivity.

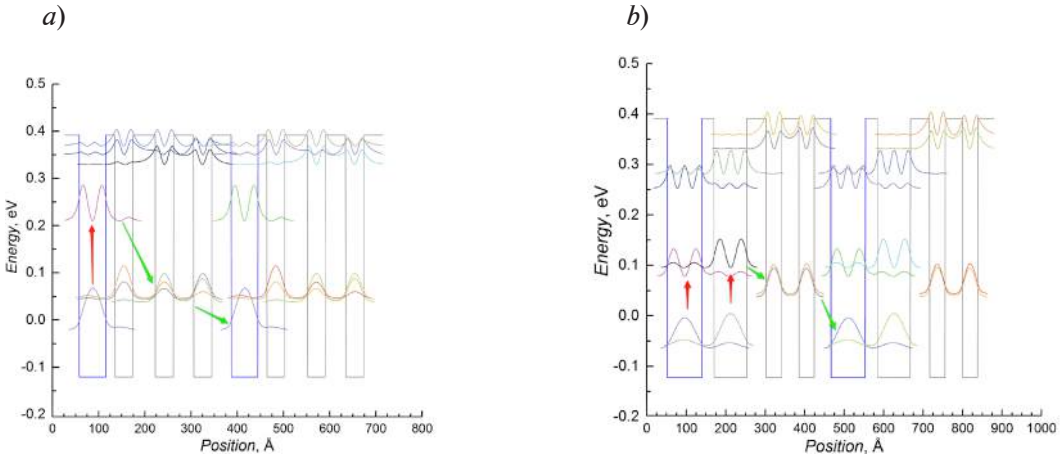

Fig. 2. Initial energy band diagram of QCD under study (*a*);
energy band diagram of optimized design (*b*)

As a figure of merit for the responsivity (2), we used the total escape time from the upper (excited) level, which determines the dominant part of the detector's cascade resistance (2):

$$D^* = R_p \sqrt{\frac{A_d R_d}{4k_B T}} \sim \tau_e, \tag{2}$$

where R_p is the peak responsivity, A_d is the detector area, R_d is the detector resistance, T is the temperature, and τ_e is the upper-level escape time.

The dependence of both of these characteristics on optimization time is shown in Fig. 1, *b*. The graphs indicate a non-monotonic growth of the escape time, while the dipole matrix element shows a plateau region with maximum values. Although we aimed to increase the escape time, the obtained low dipole matrix element values are undesirable. However, they are compensated by the emergence of the second optical transition in an adjacent quantum well, which has similar dipole matrix element values. As a result, the latter leads to higher responsivity.

Conclusion

The obtained results show the applicability of numerical evolutionary algorithms for the creation of new designs of quantum cascade detectors. However, these results also demonstrate the strong necessity of incorporating regularization techniques for better convergence and obtaining devices with advantageous output characteristics.

Acknowledgments

This study was funded by the Russian Science Foundation grant number 23-29-00216.

REFERENCES

1. **Delga A.,** Quantum cascade detectors: A review, Mid-infrared Optoelectronics. (2020) 337–377.
2. **Popp J., Haider M., Franckié M., et al.,** Bayesian optimization of quantum cascade detectors, Optical and Quantum Electronics. 6 (53) (2021) 287.
3. **Hillbrand J., Krüger L.M., Cin S.D., et al.,** High-speed quantum cascade detector characterized with a mid-infrared femtosecond oscillator, Optics Express. 29 (4) (2021) 5774.
4. **Benz A., Krall M., Schwarz S., et al.,** Resonant metamaterial detectors based on THz quantum-cascade structures, Scientific Reports. (2014) 4269.
5. **Vurgaftman I., Meyer J.Б.R., Ram-Mohan L.R.,** Band parameters for III–V compound semiconductors and their alloys, Journal of Applied Physics. 89 (11) (2001) 5815–5875.
6. Genetic Algorithm Package for Python. URL: https://github.com/rmsolgi/geneticalgorithm. Accessed Apr. 1, 2024.

7. **Bismuto A., Terazzi R., Hinkov B., et al.,** Fully automatized quantum cascade laser design by genetic optimization, Applied Physics Letters. 101 (2) (2012) 021103.

8. **Chen Y., Zhu Y., Guo K., et al.,** Broadband quantum cascade detectors with a cutoff wavelength of 20 μm. Infrared Physics & Technology. 105040 (2024) 136.

9. **Giorgetta F.R., Baumann E., Graf M., et al.,** Quantum Cascade Detectors, IEEE Journal of Quantum Electronics. 45(8) (2009) 1039–1052.

THE AUTHORS

DASHKOV Alexander S.
dashkov.alexander.om@gmail.com
ORCID: 0000-0002-8726-0416

BARYKIN Dmitrii A.
d.a.barykin02@mail.ru
ORCID: 0009-0003-3641-0511

KOSTROMIN Nikita A.
nik.kostromin.00@inbox.ru
ORCID: 0009-0006-9763-2830

GORAY Leonid I.
lig@pcgrate.com
ORCID: 0000-0002-0381-9607

Received 25.07.2024. Approved after reviewing 09.09.2024. Accepted 10.09.2024.

Conference materials
UDC 537.87, 519.688
DOI: https://doi.org/10.18721/JPM.173.218

Numerical optimization of semiconductor waveguide structure

N.A. Kostromin[1,2]✉, A.S. Dashkov[1,3], D.A. Barykin[1,2]

[1] Alferov University, St. Petersburg, Russia;

[2] Peter the Great St. Petersburg Polytechnic University, St. Petersburg, Russia;

[3] St. Petersburg Electrotechnical University "LETI", St. Petersburg, Russia

✉ nik.kostromin.00@inbox.ru

Abstract. Research on radiation sources in the IR and THz ranges operating at room temperature is still highly attractive to this day. Waveguides play a critical role in these structures and their improvement is also required. This paper studies the optimization of waveguides based on GaAs material with different doping levels of layers to reduce absorption losses and increase the optical confinement factor. The optimization is carried out in three steps: selection of optimization parameters, determination of initial values of parameters and Bayesian optimization. The thickness and doping level of heavily doped layers are chosen as optimization parameters. The results show the Bayesian algorithm converges to the desired values rather quickly. It was found that the dependence of the waveguide output characteristics on concentration is weaker than on layer thickness. An increase in layer thickness leads to an increase in losses. Weak asymmetry in the structure can lead to a slight improvement in the confinement factor value.

Keywords: quantum cascade laser, waveguide, gallium arsenide, optimization, Bayesian optimization

Funding: Russian Science Foundation grant no. 23-29-00216.

Citation: Kostromin N.A., Dashkov A.S., Barykin D.A., Numerical optimization of semiconductor waveguide structure, St. Petersburg State Polytechnical University Journal. Physics and Mathematics. 17 (3.2) (2024) 98–102. DOI: https://doi.org/10.18721/JPM.173.218

Материалы конференции
УДК 537.87, 519.688
DOI: https://doi.org/10.18721/JPM.173.218

Численная оптимизация полупроводниковой волноводной структуры

Н.А. Костромин[1,2]✉, А.С. Дашков[1,3], Д.А. Барыкин[1,2]

[1] Академический университет им. Ж.И. Алфёрова РАН, Санкт-Петербург, Россия;

[2] Санкт-Петербургский политехнический университет Петра Великого, Санкт-Петербург, Россия;

[3] Санкт-Петербургский государственный электротехнический университет «ЛЭТИ» им. В.И. Ульянова (Ленина), Санкт-Петербург, Россия

✉ nik.kostromin.00@inbox.ru

Аннотация. Исследования источников излучения в ИК- и ТГц-диапазонах, работающих при комнатной температуре, остаются крайне привлекательными вплоть до сегодняшнего дня. Волноводы играют важную роль в этих структурах, и их совершенствование также является необходимой задачей. В данной работе исследуется оптимизация волноводов на основе GaAs с различными уровнями легирования слоев для уменьшения потерь на поглощение и увеличения фактора оптического ограничения.

Оптимизация проводится в три этапа: выбор параметров оптимизации, определение начальных значений параметров и байесовская оптимизация. В качестве параметров оптимизации выбраны толщина и уровень легирования сильно легированных слоев. Результаты показывают, что байесовский алгоритм достаточно быстро сходится к желаемым значениям. Было обнаружено, что зависимость выходных характеристик волновода от концентрации слабее, чем от толщины слоя. Увеличение толщины слоя приводит к росту потерь. Слабая асимметрия структуры может привести к небольшому улучшению значения фактора оптического ограничения.

Ключевые слова: квантово-каскадный лазер, волновод, арсенид галлия, оптимизация, байесовская оптимизация

Финансирование: Грант Российского научного фонда № 23-29-00216.

Ссылка при цитировании: Костромин Н.А., Дашков А.С., Барыкин Д.А. Численная оптимизация полупроводниковой волноводной структуры // Научно-технические ведомости СПбГПУ. Физико-математические науки. 2024. Т. 17. № 3.2. С. 98–102. DOI: https://doi.org/10.18721/JPM.173.218

Introduction

Infrared (IR) and terahertz radiation sources at room temperature have recently attracted considerable interest. The study of such devices began in the early 1970s [1], but the first active quantum-cascade lasers emitting light from intersubband electronic transitions were created in the 1990s [2]. Waveguides play a critical role in these structures, coupling radiation in the active area and providing optical feedback with minimal absorption losses [3]. Optimizing such waveguides is an intensive task. Elaborate experimental research often requires regular fabrication of new structures, which is expensive. Another potential solution to this problem is to develop a model that can simulate the waveguide output from available experimental data and optimize designed structures [4]. Such an approach would eliminate the need for time-consuming modelling and high-cost experimental studies. In this paper we study the possibilities of optimizing waveguides based on the Bayesian algorithm.

Materials and Methods

In this paper, a GaAs-based waveguide with different doping levels of the layers is considered [5]. The structure of the waveguide is described in Table 1.

Table 1

Waveguide structure

Material	Parameters	
	Width, μm	Doping, cm^{-3}
GaAs	1.0	$6 \cdot 10^{18}$
(*a*) GaAs	3.5	$4 \cdot 10^{16}$
Active Region	1.63	
(*b*) GaAs	3.5	$4 \cdot 10^{16}$
GaAs	1.0	$6 \cdot 10^{18}$
GaAs substrate		$3 \cdot 10^{18}$

The main aim is to find a waveguide configuration in which the absorption loss is minimal and the optical wave confinement factor Γ in the structure is maximized. Optimization of the waveguide structure is carried out in three stages: selection of optimization parameters, which significantly influence on the values of output characteristics; their initialization and the optimization. We selected Bayesian optimization using the Python package BayesianOptimization [6, 7]. This method constructs a posterior distribution of functions using a Gaussian process to approximate the function to be optimized. At each iteration, this distribution is refined using the collected observations to guide the selection of the next point to investigate. The optimization focused on determining the thicknesses of layers (*a*) and (*b*) adjacent to the active region. We calculated values for the optical confinement factor and the loss factor over layer widths ranging from 0.01 μm to 10 μm [8]. The optimization process was initiated with 20 random points and then continued with 20 successive iterations. The algorithm parameters were the optimization function, and search area boundaries (from 0.01 to 10 μm for both widths). Additionally, a fixed random seed was used, while other package settings were left at their default values.

Results and Discussion

From the data, it appears that the mode confinement factor may decrease with increasing layer thickness. In the case of confinement factor optimization, the algorithm reached the best value after 10 iterations. When a weak asymmetry in the structure appears (the thickness of the GaAs layer located closer to the substrate is larger), there is a noticeable improvement in the values of Γ. One possible reason for this behavior may be features of the numerical calculations of the model used. As the thickness of the layers increases, it is reasonable to expect that losses will also increase. In the case of loss optimization, the best value was found after four iterations. In this case, the asymmetry of the structure did not play a significant role. In both cases, the algorithm reached the desired extremum quite quickly. The maximum confinement factor identified during the optimization process was 47%. The minimum loss was 36.1 cm^{-1}. Fig. 1 illustrates the progression of the maximum values of the confinement factor and minimum waveguide losses identified at each stage of the algorithm.

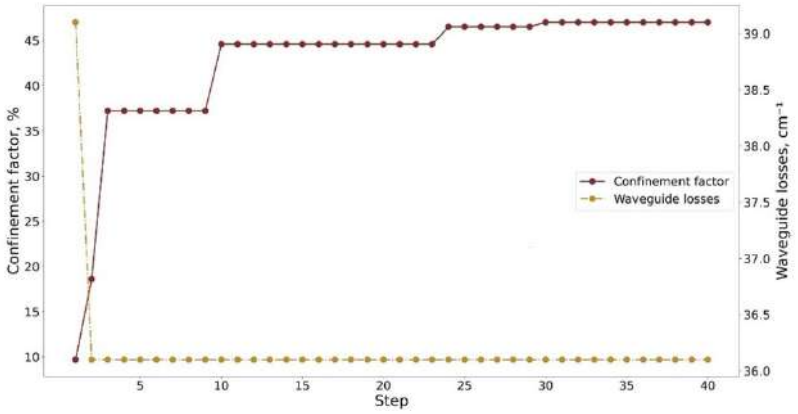

Fig. 1. Minimum value of waveguide losses and maximum value of confinement factor achieved at every step of optimization process

The most significant results were observed in the thickness range between 0.2 and 3.8 μm. In order to compare the optimization results with manually obtained data, the confinement factor and waveguide loss values were calculated for this range in steps of 0.2 μm. The results of the calculation are shown in Fig. 2.

The waveguide's output characteristics were determined using a one-dimensional approximation, incorporating complex dielectric constants to account for free carriers and losses [8]. These complex dielectric constants were described using the Drude model. The propagation constants for field calculations were derived from the multilayer equation. This equation is derived from the transmission matrix formalism. The confinement factor Γ was adjusted to consider the amplification of light polarized along the growth axis.

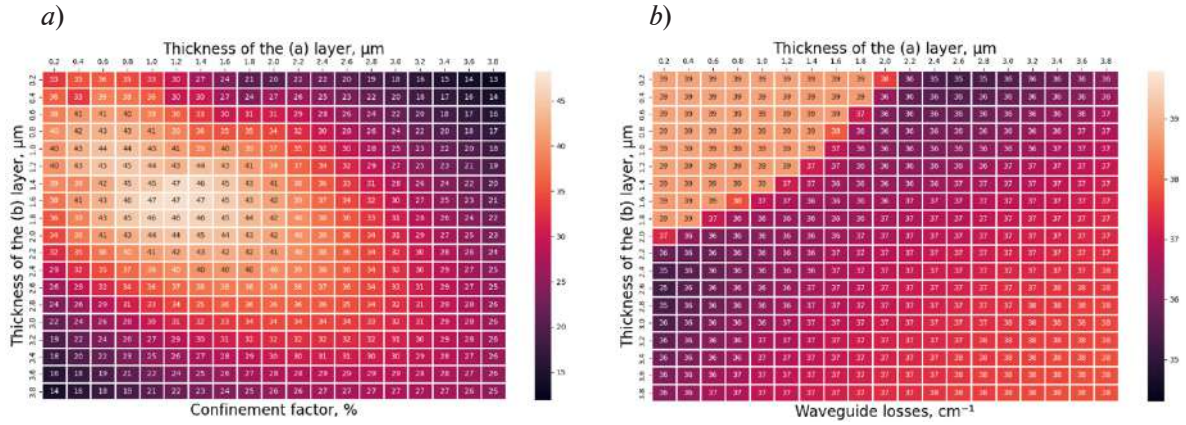

Fig. 2. Dependence of confinement factor (*a*) and waveguide losses (*b*) on layer thicknesses (*a*) and (*b*)

$$\Gamma = \frac{\int_{active} |E_x|^2 \, dx}{\int_{-\infty}^{\infty} |E|^2 \, dx}. \tag{1}$$

Conclusion

In this paper, ways to improve the structure of GaAs-based waveguide with different doping levels and thicknesses of layers using the Bayesian optimization are investigated. The dependences of the confinement factor and losses on the thickness of layers adjacent to the active region are obtained. It is shown that the algorithm used is able to obtain the best values for the minimum number of iterations.

Acknowledgments

This study was funded by the Russian Science Foundation grant number 23-29-00216.

REFERENCES

1. **Kazarinov R.F., Suris R.A.,** On the possibility of amplifying electromagnetic waves in a semiconductor with superlattices, Physics and Technology of Semiconductors. 5 (4) (1971) 797–801.

2. **Faist J., Capasso F., Sivco D.L., et al.,** Quantum Cascade Laser, Physical Review B. 50 (12) (1994) 8663–8667.

3. **Shahili M., Addamane S.J., Kim A.D., et al.,** Continuous-wave GaAs/AlGaAs quantum cascade laser at 5.7 THz, Nanophotonics. 13 (10) (2024) 1735–1743.

4. **Ushakov D.V., Afonenko A.A., Khabibullin R.A., et al.,** Influence of adhesion layers on optical losses in THz quantum cascade lasers, Journal of the Optical Society of America. B. 41 (5) (2024).

5. **Sirtori C., Kruck P., Barbieri S., et al.,** Low-loss Al-free waveguides for unipolar semiconductor lasers, Applied Physics Letters. 75 (25) (1999) 3911–3913.

6. **Franckié M., Faist J.,** Bayesian Optimization of Terahertz Quantum Cascade Lasers. Physical Review Applied. 13 (3) (2020).

7. **Williams B.S.,** Terahertz quantum-cascade lasers. Nat Photonics. 1 (9) (2007) 517.

THE AUTHORS

KOSTROMIN Nikita A.
nik.kostromin.00@inbox.ru
ORCID: 0009-0006-9763-2830

BARYKIN Dmitrii A.
d.a.barykin02@mail.ru
ORCID: 0009-0003-3641-0511

DASHKOV Alexander S.
dashkov.alexander.om@gmail.com
ORCID: 0000-0002-8726-0416

Received 25.07.2024. Approved after reviewing 16.08.2024. Accepted 19.08.2024.

Conference materials
UDC 535-15+539.21+539.25
DOI: https://doi.org/10.18721/JPM.173.219

The quest for direct band beta iron disilicide: collaboration of theoretical and experimental approaches

S.A. Balagan[1]✉, A.V. Shevlyagin[1]

[1] Institute of Automation and Control Processes FEB RAS, Vladivostok, Russia

✉ balagan@iacp.dvo.ru

Abstract. In the presented work, a theoretical study of the effect of β-$FeSi_2$ lattice deformation on the type and magnitude of the first transition in the electronic band structure was carried out. Images of nanocrystallites obtained using high-resolution transmission electron microscopy were used as a source of deformation data. All in all, 137 variants of β-$FeSi_2$ lattice deformation were considered in the work. Six types of first transitions different from the first transition in unstrained β-$FeSi_2$ were discovered. The values of the first transitions from 0.02 to 0.64 eV (direct) and from 0.01 to 1.12 eV (indirect) were obtained.

Keywords: silicon, beta Fe disilicide, *ab initio* calculation

Funding: The research was carried out within the state assignment of IACP FEB RAS (Theme FWFW-2022-0003).

Citation: Balagan S.A., Shevlyagin A.V., The quest for direct band beta iron disilicide: collaboration of theoretical and experimental approaches, St. Petersburg State Polytechnical University Journal. Physics and Mathematics. 17 (3.2) (2024) 103–106. DOI: https://doi.org/10.18721/JPM.173.219

Материалы конференции
УДК 535-15+539.21+539.25
DOI: https://doi.org/10.18721/JPM.173.219

Поиски прямозонного бета-дисилицида железа: взаимодействие теоретических и экспериментальных подходов

С.А. Балаган[1]✉, А.В. Шевлягин[1]

[1] Институт автоматики и процессов управления ДВО РАН, Владивосток, Россия;

✉ balagan@iacp.dvo.ru

Аннотация. В представленной работе было проведено теоретические исследование влияния деформации решетки β-$FeSi_2$ на тип и величину первого перехода в электронной зонной структуре. В качестве источника данных о деформации использовались изображения нанокристаллитов, полученных с помощью просвечивающей электронной микроскопии высокого разрешения. Всего в работе рассмотрено 137 вариантов деформации решетки β-$FeSi_2$. Обнаружено 6 типов первых переходов, отличающихся от первого перехода в недеформированном β-$FeSi_2$. Получены величины первых переходов от 0.02 до 0.64 эВ (прямые) и от 0.01 до 1.12 эВ (непрямые).

Ключевые слова: кремний, бета дисилицид Fe, первопринципные расчеты

Финансирование: Работа выполнена в рамках государственного задания ИАПУ ДВО РАН (тема № FWFW-2022-0003).

Ссылка при цитировании: Балаган С.А., Шевлягин А.В. Поиски прямозонного бета-дисилицида железа: взаимодействие теоретических и экспериментальных подходов // Научно-технические ведомости СПбГПУ. Физико-математические науки. 2024. Т. 17. № 3.2. С. 103–106. DOI: https://doi.org/10.18721/JPM.173.219

Introduction

In accordance with modern investigations β-$FeSi_2$ can be applied in light emitting, light absorbing and thermoelectric devices [1–5]. In all of these cases, it is significant to understand electron band structure nature of the material. Previous studies have shown that β-$FeSi_2$ light emitting ability depends on change of the fundamental transition as a consequence of lattice deformation. Lattice parameter variation is especially pronounced, when nanocrystallites (NCs) are embedded under different conditions. Within this investigation a wide range of high-resolution transmission electron microscopy (HRTEM) data was analyzed to extract information about β-$FeSi_2$ lattice deformation embedded into Si under different conditions. Based on the data obtained, *ab initio* calculations were carried out and the results will be discussed below.

Calculation details

The density-functional theory calculations were performed with the package VASP [6]. The plane-wave basis with the ultra-soft Vanderbilt pseudopotential [7] and the generalized gradient approximation (GGA) to the exchange-correlation functional were used. Non-spherical contributions from the gradient corrections were included. Monkhorst–Pack *k*-points grid [8] of 8×8×8 was used. The cut-off energy was of 350 eV. Relaxation was performed with respect to the atoms' positions, volume, and the shape of the cell. The obtained lattice constants were $a = 9.907$ Å, $b = 7.781$ Å, and $c = 7.833$ Å (experimental values are $a = 9.863$ Å, $b = 7.791$ Å, and $c = 7.833$ Å [9]). The indirect fundamental energy gap was found of 0.60 eV (the GGA theoretical value of Ref. [10] is 0.62 eV and the experimental value is 0.839 eV [11]).

Results and Discussion

HRTEM data of one sample was analyzed to obtain NCs sizes and lattice deformation value. Fig. 1, *a* shows broad NCs size distribution. For theoretical investigation bulk β-$FeSi_2$ cell was deformed in accordance with NCs deformation: 14 NCs in diameter range from 3.5 nm to 10 nm were considered. Calculation results are shown in (Fig 1, *b*, *c*). The first conclusion is even within one sample NCs with different first transition type can be observed. The second one is NC size is related to the first transition type, but this is not a determining factor, since there is a wide NC diameters range, where both direct and indirect first transition types coexist. The third one is general lattice strain expressed as a change in cell volume as well is not a determining factor for similar reason.

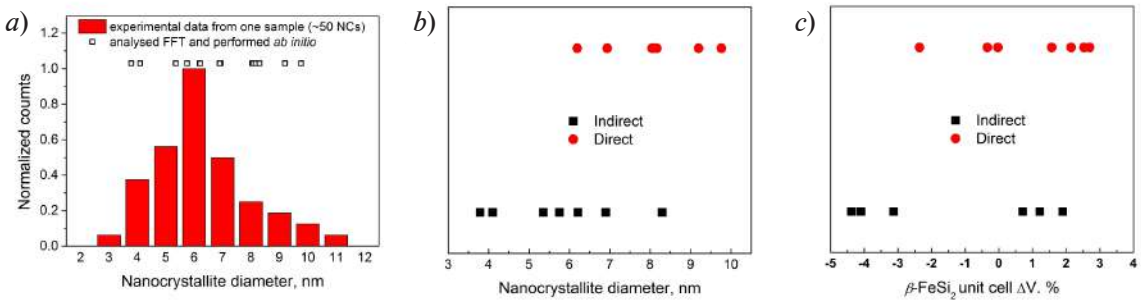

Fig. 1. Distribution of β-$FeSi_2$ nanocrystallite diameter within one sample (*a*) and calculated first transition type: depending on nanocrystallite diameter (*b*), depending on unit cell volume change (*c*)

The next step was to check how β-$FeSi_2$ band structure changes with a particular deformation with a significant data collection. HRTEM data were collected from literature and our previous experiments. All in all, 137 NCs were analyzed within this work to determine lattice deformation and then electron band structure was calculated for each strained cell. 113 of them had indirect type band gap and 24 ones had direct type band gap. Structures with direct band gap type are in deformations range of Δa from +0.6 to +7.3%, Δb from −8.1 to +6.2%, Δc from −4.1 to +1.8%. Structures with indirect band gap types are in deformations range of Δa from −9.7 to +10.4%, Δb from −6.0 to +7.3%, Δc from −7.7 to +5.3% as shown in Fig. 2. Positive Δ value corresponds to tension and negative one corresponds to compression. Thus β-$FeSi_2$ has narrow range of a and c lattice constants deformation, which allow existence of band structure with the first transition of direct type. On the other hand, β-$FeSi_2$ shows flexible band structure depending on deformation allowing to obtain band gap in range from 0.02 to 0.64 eV (direct type) and in range from 0.01 to 1.12 eV (indirect type), that is opportunity to create light emitting and receiving devices of different frequency ranges using different creation conditions, but same material.

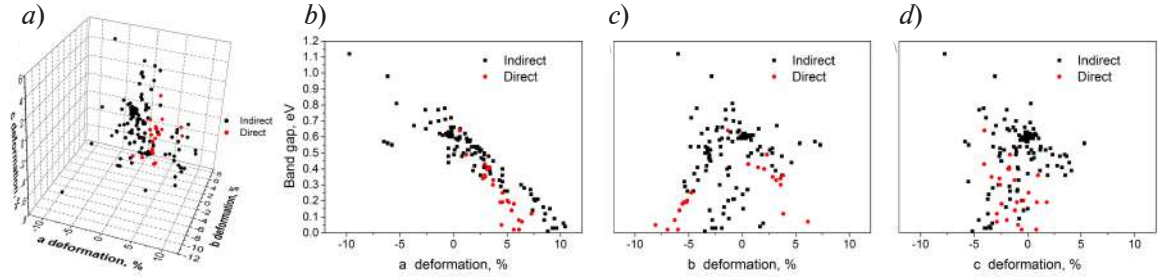

Fig. 2. First transition type in β-$FeSi_2$ depending on deformation: 3D plot of transition type (*a*) and band gap value depending on the deformation: lattice parameter *a* (*b*), lattice parameter *b* (*c*), lattice parameter *c* (*d*). Positive deformation corresponds to tension and negative one corresponds to compression. Points on *a* plot correspond to ones on *b*–*d*. Band gap axis on *b* plot is common for *b*–*d* ones

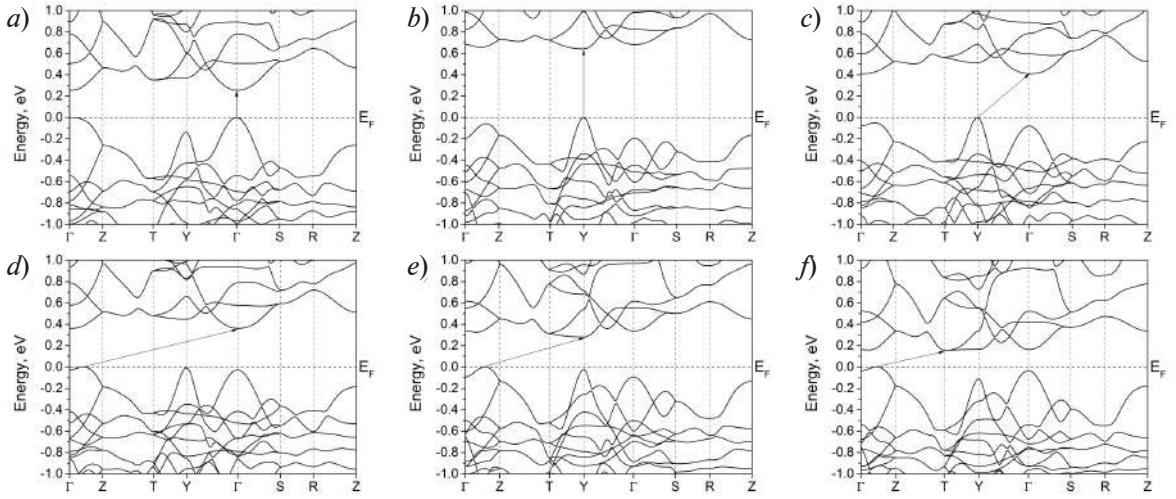

Fig. 3. Electron band structure in β-$FeSi_2$ depending on the deformation (Δa, Δb and Δc are specified for each plot): +4.6%, -4.8%, +0.1% (*a*), +0.6%, -1.3%, -4.0% (*b*), +2.9%, -1.2%, +3.2% (*c*), +4.5%, -1.3%, +1.9% (*d*), +6.6%, -0.5%, -3.2% (*e*), +8.4%, 1.7%, -2.0% (*f*)
The Fermi level is taken as the zero-energy point. Arrows show the first transition

The other side of β-$FeSi_2$ band structure flexibility is location of the first transitions in reciprocal space. Fig. 3 shows obtained band structures with examples of fundamentally different first transitions: 2 direct (Γ→Γ, Y→Y) and 4 indirect ones (Y→Γ, Λ*→Γ, Λ*→Y, Λ*→T). Unstrained bulk β-$FeSi_2$ has Y→Λ* first transition. On the one hand direct-indirect type change is a reason

why light radiation can be observed from some NCs, but not from others of similar size, on the other hand different direct transition positions in reciprocal space explain different experimentally observed luminescence spectra: band walleyes located in various points have various charge carrier effective mass, oscillator strength and energy with regard to Fermi level.

Conclusion

It was demonstrated that within one sample β-$FeSi_2$ NCs with both direct and indirect first transition type can coexist. Neither NC diameter nor cell volume change are not a factor determining the first transition types. There was shown that the first transition of direct type exists in narrow deformation range of 7.9%, 14.3% and 5.9% for a, b and c lattice constants, respectively. Whereas indirect one exists in wide range of 20.1%, 13.3% and 13.0% for a, b and c lattice constants, respectively. Six first transition types differed from fully relaxed bulk β-$FeSi_2$ were observed: 2 direct (Γ→Γ, Y→Y) and 4 indirect ones (Y→Γ, Λ*→Γ, Λ*→Y, Λ*→T).

Acknowledgments

All quantum mechanics calculations were distributed between computing facilities of IACP FEB RAS Shared Resource Center 'Far Easten Computing Resource' (https://cc.dvo.ru) and HPC cluster 'Academician V.M. Matrosov' (Irkutsk Supercomputer Center of SB RAS, https://hpc.icc.ru/).

REFERENCES

1. **Okuhara Y., et al.,** Thermal durability of solar selective absorbers consisting of β-$FeSi_2$ with low emissive Ag layers on stainless steel, Solar Energy Materials and Solar Cells. 206 (2020) 110304.

2. **Qiu P., et al.,** Exceptionally heavy doping boosts the performance of iron silicide for refractory thermoelectrics, Advanced Energy Materials. 12 (18) (2022) 2200247.

3. **Akiyama K., et al.,** MOCVD growth of β-$FeSi_2$ film on modified Si surface by silver and enhancement of luminescence. 506 (2019) 131–134.

4. **Shevlyagin A.V., et al.,** A room-temperature-operated Si LED with β-$FeSi_2$ nanocrystals in the active layer: μW emission power at 1.5 μm, Journal of Applied Physics. (121) (2017) 11.

5. **Balagan S.A., et al.,** Theoretical approach to embed nanocrystallites into a bulk crystalline matrix and the embedding influence on the electronic band structure and optical properties of the resulting heterostructures, Journal of Physics: Condensed Matter. 30 (24) (2018) 245301.

6. **Kresse G., Furthmüller J.,** Efficiency of ab-initio total energy calculations for metals and semiconductors using a plane-wave basis set, Comp. materials science 6 (1996) 15–50.

7. **Vanderbilt D.,** Soft self-consistent pseudopotentials in a generalized eigenvalue formalism, Physical review B. 41 (11) (1990) 7892.

8. **Monkhorst H.J., Pack J.D.,** Special points for Brillouin-zone integrations, Physical review B. 13 (12) (1976) 5188.

9. **Dusausoy Y., et al.,** Structure cristalline du disiliciure de fer, $FeSi_2$β, Acta Crystallographica Section B: Structural Crystallography and Crystal Chemistry. 27 (6) (1971) 1209–1218.

10. **Moroni E.G., et al.,** Cohesive, structural, and electronic properties of Fe-Si compounds, Physical Review B. 59 (20) (1999) 12860.

11. **Maeda Y.,** Luminescence properties of β-FeSi2 and its application to photonics, Applied surface science. 254 (19) (2008) 6242–6247.

THE AUTHORS

BALAGAN Semyon A.
balagan@iacp.dvo.ru
ORCID: 0000-0003-1634-7060

SHEVLYAGIN Alexander V.
shevlyagin@iacp.dvo.ru
ORCID: 0000-0003-2170-7972

Received 26.07.2024. Approved after reviewing 01.08.2024. Accepted 06.08.2024.

Conference materials
UDC 536.2+537.32+539.21
DOI: https://doi.org/10.18721/JPM.173.220

Effect of diameter on lattice thermal conductivity of α-$FeSi_2$ and ε-FeSi nanowires

S.A.Balagan[1]✉, N.G. Galkin[1]

[1] Institute of Automation and Control Processes, FEB RAS, Vladivostok, Russia

✉ balagan@iacp.dvo.ru

Abstract. In this study the effect of α-$FeSi_2$ and ε-FeSi nanowires diameter on the lattice thermal conductivity was considered. *Ab initio* modeling was performed in the temperature range of 100–700 ˚K and nanowires diameter range of 6–48 nm. Results showed that at minimal considered diameter nanowires have 1.4–4.5 times lower lattice thermal conductivity than bulk material depending on temperature and nanowire elongate direction.

Keywords: silicon, Fe silicides, nanowires, *ab initio* calculation, thermal conductivity

Funding: This study was supported by the Russian Science Foundation, grant no. 22-12-00036.

Citation: Balagan S.A., Galkin N.G., Effect of diameter on lattice thermal conductivity of α-$FeSi_2$ and ε-FeSi nanowires, St. Petersburg State Polytechnical University Journal. Physics and Mathematics. 17 (3.2) (2024) 107–111. DOI: https://doi.org/10.18721/JPM.173.220

Материалы конференции
УДК 536.2+537.32+539.21
DOI: https://doi.org/10.18721/JPM.173.220

Влияние диаметра на решеточную теплопроводность нанопроволок α-$FeSi_2$ и ε-FeSi

С.А. Балаган[1]✉, Н.Г. Галкин[1]

[1] Институт автоматики и процессов управления ДВО РАН, Владивосток, Россия

✉ balagan@iacp.dvo.ru

Аннотация. В данном исследовании рассмотрено влияние диаметра нанопроволок α-$FeSi_2$ и ε-FeSi на их решеточную теплопроводность. Моделирование из первых принципов производилось в диапазоне температур 100–700 ˚K и диапазоне диаметров нанопроволок 6–48 нм. Результаты показали, что у нанопроволок с минимальным из рассмотренных диаметров теплопроводность 1.4–4.5 раза ниже, чем у объемного материала в зависимости от температуры и направления, в котором вытянута нанопроволока.

Ключевые слова: кремний, силициды Fe, нанопроволоки, первопринципные расчеты, теплопроводность

Финансирование: Исследование поддержано Российским научным фондом, грант № 22-12-00036.

Ссылка при цитировании: Балаган С.А., Галкин Н.Г. Влияние диаметра на решеточную теплопроводность нанопроволок α-$FeSi_2$ и ε-FeSi // Научно-технические ведомости СПбГПУ. Физико-математические науки. 2024. Т. 3.2 № .17. С. 107–111. DOI: https://doi.org/10.18721/JPM.173.220

Introduction

The current technology evolution has resulted in high energy consumption. While it is necessary to increase energy efficiency, it is also important to look for new sources of energy [1]. Using heat released by burning fuel or electrical devices through the use of thermoelectric converters is one method of increasing energy efficiency. Another possible application of thermoelectrics is generating electricity for spacecraft [2]. The Seebeck coefficient, electrical conductivity, and thermal conductivity all affect a material's thermoelectric efficiency. In turn, thermal conductivity also encompasses phonon and electron thermal conductivity. The investigation of the lattice thermal conductivity of ε-FeSi and α-$FeSi_2$ is the main emphasis of this work.

Calculation details

The density-functional theory calculations were performed with the package VASP [3]. Generalized gradient approximation (GGA) to the exchange-correlation functional was used. Non-spherical contributions from the gradient corrections were included. The k-points and q-points grids were used with the center at the Γ-point and the cut-off energy was of 300 eV. Relaxation was performed with respect to the atoms' positions, volume, and the shape of the cell. For structure relaxation k-points grids were of 24×24×12 and 12×12×12 for α-$FeSi_2$ and ε-FeSi, respectively. The resulting lattice parameters was of a = 2.704 Å and c = 5.138 Å for α-$FeSi_2$ and a = 4.448 Å for ε-FeSi, which is in good agreement with the experimental data: a = 2.684 Å and c = 5.128 Å for α-$FeSi_2$ [4] and a = 4.467 Å for ε-FeSi [5]. Forces constants calculations were performed with the k-point grid of 3×3×3 for both materials and supercells were of 4×4×2 and 2×2×2 unit cells for α-$FeSi_2$ and ε-FeSi, respectively. The phonon properties were calculated within the harmonic approximation using Phonopy package [6]. The elements of dynamical matrix were determined by employing density-functional-perturbation theory. Lattice thermal conductivity was calculated by means of Boltzmann transport equation solving implemented in ShengBTE package [7]. Q-points grid was of 32×32×32 for both materials.

Results and Discussion

Phonon bands structures calculation results (Fig. 1) are in good agreement with that of in Refs. [8–9]. The results show that α-$FeSi_2$ has less acoustic phonon frequency value compared to ε-FeSi, which is one of the factors for lower lattice thermal conductivity, since usually the main contribution to lattice thermal conductivity comes from acoustic phonons.

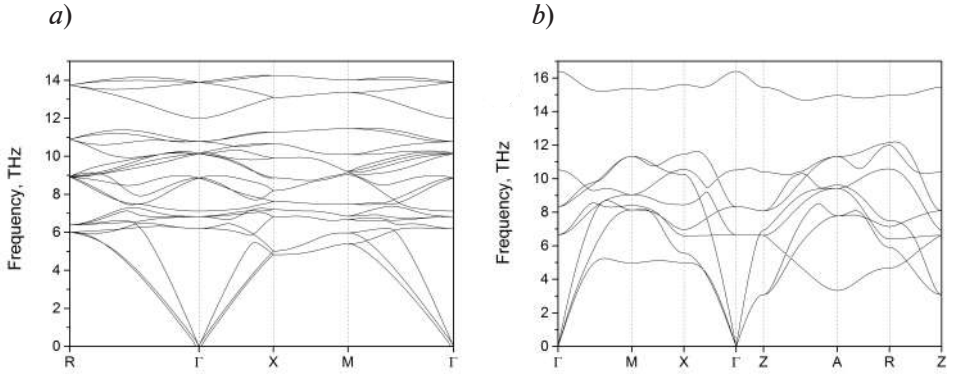

Fig. 1. Phonon band structure of bulk ε-FeSi (*a*) and bulk α-$FeSi_2$ (*b*) along high-symmetry *k*-points

Lattice thermal conductivity calculation show that approximately 80% of the contribution to lattice thermal conductivity comes from acoustic phonons in both materials, which as well means lower thermal conductivity value of α-$FeSi_2$ compared to ε-FeSi (Fig. 2, *a*). In the frequency range corresponding to the acoustic phonons on the one hand α-$FeSi_2$ and ε-FeSi have commensurable phonons group velocity (Fig 2, *b*) and on the other hand α-$FeSi_2$ has an order of magnitude higher scattering rate (Fig. 2, *c*), thereby one has an order of magnitude lower phonons mean free path (Fig. 2, *d*). This is the main reason why α-$FeSi_2$ has lower lattice thermal conductivity compared to ε-FeSi.

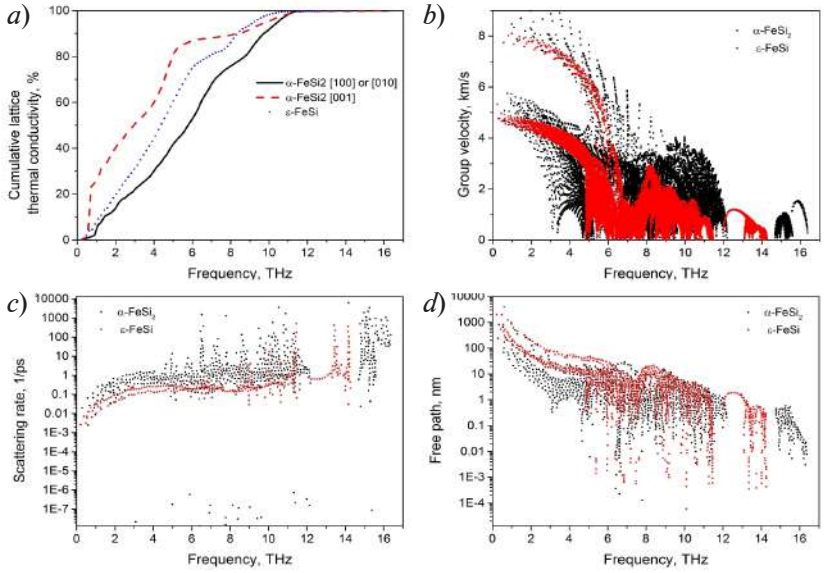

Fig. 2. Phonon transport properties of bulk α-$FeSi_2$ and bulk ε-FeSi: cumulative lattice thermal conductivity (*a*), group velocity (*b*), scattering rate (*c*) and free path (*d*)

Obtained lattice thermal conductivity values are shown in Fig. 3. The values of bulk materials are in agreement with results in Refs. [10–11]. Depending on temperature and heat spread direction bulk α-$FeSi_2$ has 2–4 times lower lattice thermal conductivity compared to that of ε-FeSi.

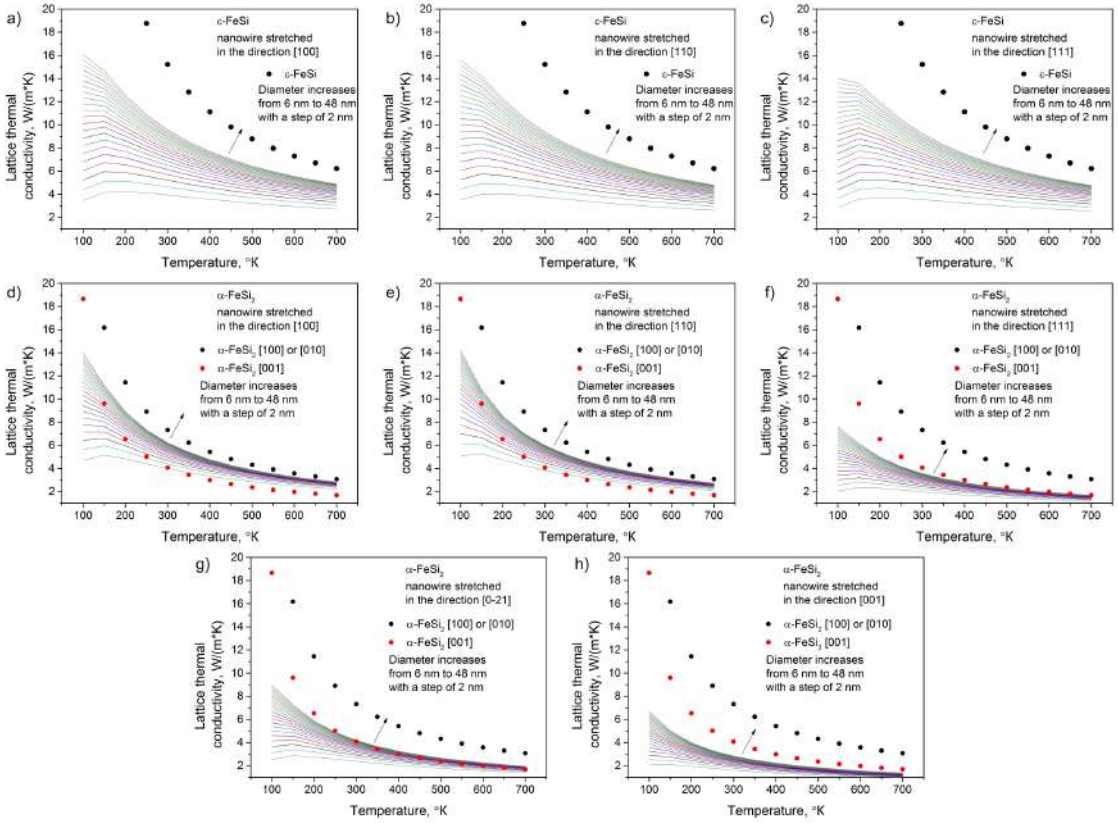

Fig. 3. Lattice thermal conductivity of ε-FeSi nanowires in directions: [100] (*a*), [110] (*b*), [111] (*c*) and that of α-$FeSi_2$: [100] (*d*), [110] (*e*), [111] (*f*), [0 $\bar{2}$ 1] (*g*) and [001] (*h*). Black and red dots are bulk crystal data

Lattice thermal conductivity calculation of α-$FeSi_2$ nanowires showed significant dependence on the direction in which the nanowire is elongated: 2–2.5 times. The same calculations performed for ε-FeSi showed weak dependence of 1.02–1.20 times. On the other hand ε-FeSi lattice thermal conductivity shows stronger dependence on nanowire diameter compared to the α-$FeSi_2$ one. Depending on temperature ε-FeSi [100] nanowires show 95–56% lower lattice thermal conductivity at 6 nm diameter and 79–22% lower one at 48 nm diameter compared to bulk [100] value. Wherein α-$FeSi_2$ [100] nanowires show 84–28% lower lattice thermal conductivity at 6 nm diameter and 51–8% lower one at 48 nm diameter compared to bulk [100] value. α-$FeSi_2$ [001] nanowires show similar behavior: 89–45% lower lattice thermal conductivity at 6 nm diameter and 64–18% lower one at 48 nm diameter compared to bulk [001] value. It is associated with signification difference in phonons mean free path: α-$FeSi_2$ has lower value and therefore smaller phonons number reach nanowire surface and are scattered on it before scattering occurs inside the wire, similar to scattering in the bulk material. Results of the calculation were applied in Ref. [12].

Conclusion

The effect of α-$FeSi_2$ and ε-FeSi nanowires diameter on the lattice thermal conductivity was considered. Calculations showed strong dependence of α-$FeSi_2$ nanowires lattice thermal conductivity on the direction in which nanowire is elongated and weak one for ε-FeSi nanowires.

Acknowledgments

Boltzmann transport equation solving and quantum mechanics calculations were performed with the use of the computing facilities of IACP FEB RAS Shared Resource Center 'Far Easten Computing Resource' (https://cc.dvo.ru) and HPC cluster 'Academician V.M. Matrosov' (Irkutsk Supercomputer Center of SB RAS, https://hpc.icc.ru/), respectively.

REFERENCES

1. **Hasan M.N., et al.,** Inorganic thermoelectric materials: A review, International Journal of Energy Research. 44 (8) (2020) 6170–6222.

2. **Candolfi C., et al.,** Thermoelectric materials for space applications, CEAS Space Journal. 13 (2021) 325–340.

3. **Kresse G., Furthmüller J.,** Efficiency of ab-initio total energy calculations for metals and semiconductors using a plane-wave basis set, Comp. materials science. 6 (1996) 15–50.

4. **Aronsson B., et al.,** A Note on the Compositions and Crystal Structures of MnB_2, Mn_3Si, Mn_5Si_3, and $FeSi_2$, Acta Chemica Scandinavica. 14 (1960) 1414–1418.

5. **Wever F., Mцller H.,** Über den Kristallbau des Eisensilizides FeSi, Z. Kristallogr. 75 (1930) 362–365.

6. **Togo A., Tanaka I.,** First principles phonon calculations in materials science, Scripta Materialia. 108 (2015) 1–5.

7. **Li W., et al.,** ShengBTE: A solver of the Boltzmann transport equation for phonons, Computer Physics Communications. 185 (2014) 1747–1758.

8. **Khan N., et al.,** Combined inelastic neutron scattering and ab initio lattice dynamics study of FeSi, Physical Review B. 105 (13) (2022) 134304.

9. **Kalt J., et al.,** Lattice dynamics and polarization-dependent phonon damping in αphase $FeSi_2$ nanostructures //Physical Review B. 101 (16) (2020) 165406.

10. **Waldecker G., Meinhold H., Birkholz U.,** Thermal conductivity of semiconducting and metallic $FeSi_2$, Physica Status Solidi (a). 15 (1) (1973) 143–149.

11. **Stern R., et al.,** Influence of point defects on the thermal conductivity in FeSi, Physical Review B. 97 (19) (2018) 195201.

12. **Galkin K.N., Chernev I.M., Subbotin E.Yu., et al.,** Ultrathin Cr and Fe monosilicides on Si(111) substrate: formation, optical and thermoelectrical properties, St. Petersburg State Polytechnical University Journal. Physics and Mathematics. 16 (3.1) (2023) 84–89.

THE AUTHORS

BALAGAN Semyon A.
balagan@iacp.dvo.ru
ORCID: 0000-0003-1634-7060

GALKIN Nikolay G.
galkin@iacp.dvo.ru
ORCID: 0000-0003-4127-2988

Received 26.07.2024. Approved after reviewing 06.08.2024. Accepted 08.08.2024.

Conference materials
UDC 53
DOI: https://doi.org/10.18721/JPM.173.221

Efficiency analysis of generative adversarial networks for single pixel imaging

D.V. Babukhin✉, D.V. Sych

P.N. Lebedev Physical Institute of the RAS, Moscow, Russia

✉ dv.babukhin@gmail.com

Abstract. The single-pixel camera provides a prospective tool for imaging beyond conventional pixel-matrix-based devices. In recent years, neural networks have become a part of single-pixel imaging as a method to restore an image from intensity measurements computationally. Generative adversarial networks (GANs) are particularly well suited for this task. In this paper, we investigate the performance of a generative adversarial least squares network in the task of image reconstruction from a single-pixel camera at low sampling rates. We demonstrate that stable successful image reconstruction is possible at sampling rates around 8%, and that the reconstructed images should match the structure of the images present in the training sample.

Keywords: Single pixel imaging, neural networks, image restoration

Funding: Grant no. 23-22-00381, https://rscf.ru/project/23-22-00381.

Citation: Babukhin D.V., Sych D.V., Efficiency analysis of generative adversarial networks for single pixel imaging, St. Petersburg State Polytechnical University Journal. Physics and Mathematics. 17 (3.2) (2024) 112–115. DOI: https://doi.org/10.18721/JPM.173.221

Материалы конференции
УДК 53
DOI: https://doi.org/10.18721/JPM.173.221

Анализ эффективности генеративных состязательных сетей в задаче однопиксельной визуализации

Д.В. Бабухин✉, Д.В. Сыч

Физический институт имени П. Н. Лебедева РАН, Москва, Россия

✉ dv.babukhin@gmail.com

Аннотация. Однопиксельная камера представляет собой перспективный инструмент для получения изображений, выходящий за рамки традиционных устройств на основе пиксельных матриц. В последние годы нейронные сети стали частью однопиксельной визуализации как численный метод восстановления изображения по измерениям интенсивности. Генеративные состязательные сети (GAN) особенно хорошо подходят для решения этой задачи. В данной работе мы исследуем производительность генеративной состязательной сети наименьших квадратов в задаче восстановления изображения с однопиксельной камеры при низкой частоте дискретизации. Мы демонстрируем, что стабильная успешная реконструкция изображений возможна при частоте дискретизации около 8%, и что реконструированные изображения должны соответствовать структуре изображений, присутствующих в обучающей выборке.

Ключевые слова: Однопиксельная визуализация, нейронные сети, восстановление изображения

Финансирование: Грант № 23-22-00381, https://rscf.ru/project/23-22-00381.

Ссылка при цитировании: Бабухин Д.В., Сыч Д.В. Анализ эффективности генеративных состязательных сетей в задаче однопиксельной визуализации // Научно-технические ведомости СПбГПУ. Физико-математические науки. 2024. Т. 17. № 3.2. С. 112–115. DOI: https://doi.org/10.18721/JPM.173.221

Introduction

Single-pixel imaging emerged as a mathematical development of approaches to image restoration [1]. The central problem of single-pixel imaging is the computational generation of an image from intensity measurements acquired via measuring a camera with a single light detector. These intensity data combined with specific light patterns, i.e., masks, responsible for spatial modulation of light, illuminating the object, allow the generation of an object image.

In the ideal circumstances (no noise in the device calibration and infinitely long exposition) we can simply obtain the image via inverse matrix multiplication. In practice, intensity measurements contain noise which makes a straightforward approach to image recovery inefficient and with bad quality of the produced image. One way to obtain an image with better quality is to use a compressed sensing approach [1] which uses an L_1-restricted optimization to produce the image.

In recent years, a conventional method for image generation was challenged via the use of neural networks [2] and in particular, generative adversarial networks [3]. Because neural networks can learn hard-to-find patterns from data and are highly flexible in terms of parameter choice (architecture and size), they provide a prospective tool in single pixel imaging. Here we analyze image restoration efficiency with low sampling rates for a least squares generative adversarial networks (GAN) – a neural network, consisting of two distinct networks that learn from each other outputs. We also demonstrate that a trained network can restore only images, matching image structure of the training set.

Materials and Methods

In this work we train a least squares GAN [4] on simulated intensity measurements of the MNIST dataset, processed with a single-pixel camera. A first part of the network, a generator, takes gathered intensity values as an input and produces a restored image of the target object (digits from 0 to 9 in our case). After initialization this network is untrained, and its restoration quality is unsatisfactory. The training procedure consists of producing the output of the generator and feeding it to the second part of the network, the discriminator, which evaluates the quality of the input image by labeling it with a number between 0 and 1, where 0 corresponds to false (generated image) and 1 corresponds to true (real image of a digit).

We use a set of digit images and simulated camera intensity values for every image to train a generator restoring digit images and a discriminator correct labeling of fake and real values via rounds of network training. Each round has two parts: generator training, when the parameters of the generator are optimized to produce a better image and the parameters of a discriminator are fixed, and discriminator training when the parameters of the generator are fixed and parameters of the discriminator are optimized to better labeling of images.

The difference between the two types of networks we use in this work is in the loss function we optimize. For least-squares GAN, the discriminator has a loss function

$$L_D^{LS}(D) = \frac{1}{2}E_x\left[\left(D(x)-1\right)^2\right] + \frac{1}{2}E_z\left[\left(D\left(G(x)\right)\right)^2\right], \quad (1)$$

and generator has a loss function

$$L_G^{LS}(G) = \frac{1}{2} E_z \left[\left(D\left(G(z)\right) - 1 \right)^2 \right]. \quad (2)$$

A set of images used for training, Z is a set of intensity vectors after camera process simulation, $E_{X(Z)}$ is averaging over set $X(Z)$ correspondingly. If only the above-mentioned loss functions are used for training a network, the generator may produce poor-quality images even after completion of training: images can be alike for different input vectors (mode collapse) or have spurious details, which look unrealistic to the human eye. To encourage the generator to produce plausible images, we use so-called content loss, an additional part of the generator loss function, which encourages the generator to produce images with realistic characteristics. The content loss is the following

$$L_G^{content}(G) = L_1(G) + L_{VGG}(G). \quad (3)$$

Here, the first component

$$L_1(G) = \frac{1}{WH} \sum\sum \left| x_{i,j} - G(z)_{i,j} \right|, \quad (4)$$

is a loss function, which encourages sparsity in a generated image. W and H denote width and height of the output image from a generator network, i and j are matrix indices. The second component

$$L_{VGG}(G) = \frac{1}{W_k H_k} \sum\sum \left(VGG_k\left(x_{i,j}\right) - VGG_k\left(G(z)_{i,j}\right) \right)^2, \quad (5)$$

is a loss function, which returns the squared difference between feature representations of a real image x and a generated image $G(z)$, calculated with a kth layer output of a pre-trained VGG network [6]. W_k and H_k denote width and height of the output image from the kth layer of VGG network. The latter loss function encourages the generator to produce images, that are similar to realistic images from another convolutional network point of view, which was trained for the classification task.

Results and Discussion

Here we provide result for image restoration via a trained least-square GAN. We trained several examples of this GAN for sampling rates 1%, 2%, 4% and 8%, where the sampling rate is defined as a ratio between the number of patterns, used to aquire intensity data, and the number of pixels in the target image. In Fig. 1 we provide several restored digits for every sampling rate along with ground truth images. We also provide restoration results for an image, which has different structure than images from the training data set (a pictorial smile).

From Fig. 1 one can see that for 8% single pixel camera sampling rate all restored images of digits have good quality. The situation changes as sampling rate decreases: images of digits with simple structure ("1") can be restored up to lowest sampling rates, and images of digits with more complicated structure ("2") cannot be restored with low sampling rate with our trained network. Nonetheless, for practical applications, 8% sampling rate is already a significant speed-up comparing to conventional methods (e.g., compressed sensing requires more than 30% sampling rate). It is a question of further research if we can find a neural network architecture, which requires lower sampling rate and does not require prohibitively large amount of training data and time.

Another point illustrated in Fig. 1 is that a least-squares GAN, trained to restore digits from intensity measurement via single pixel camera, cannot restore image of a pictorial smile, because there were no alike pictures in the training set. For practice, this result means that in order to successfully apply neural networks for single-pixel imaging we need to have a training data set, which includes images of target objects. As specific practical applications (for example, in medicine) can have only a limited amount of freely-available data, it is interesting to explore possibilities of overcoming the need of such data for training neural networks for imaging purposes.

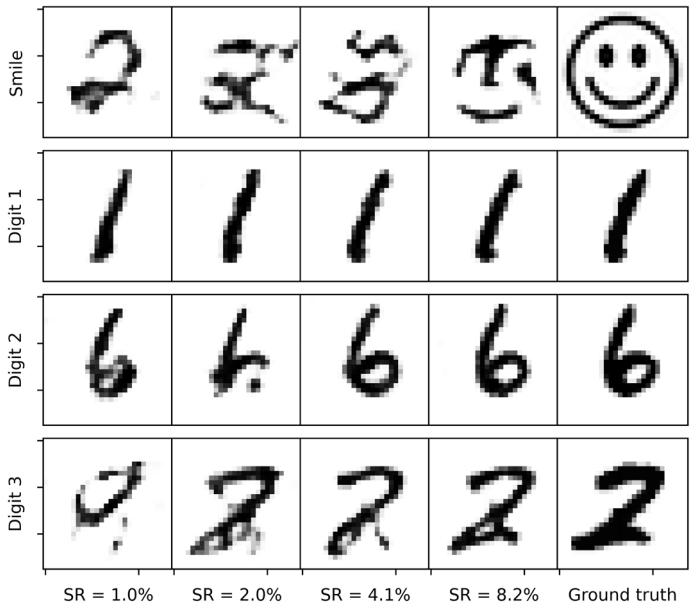

Fig. 1. Images from single-pixel camera simulation, restored via the least-squares GAN. Here we provide results for 1%, 2%, 4% and 8% sampling rates along with a ground truth image

Conclusion

In this work, we analyzed the efficiency of a least-squares generative adversarial network in the problem of image restoration in single-pixel imaging. We demonstrated how quality of the restored image depends on the sampling rate. We also demonstrated the importance of having target object images in the training set. Our work is aimed at advancing the development of computational tools for single-pixel imaging.

REFERENCES

1. **Duarte M.F., Davenport M.A., Takhar D., et al.,** Single-Pixel Imaging via Compressive Sampling, IEEE Signal Processing Magazine. 25 (83) (2008).

2. **Higham C.F., Murray-Smith R., Padgett M.J., Edgar M.P.,** Deep learning for real-time single-pixel video, Scientific Reports. 8 (2018).

3. **Zhao M., Li F., Huo F., Tian Z.,** Generative adversarial network-based single-pixel imaging, Soc for Inf Disp. 30 (8) (2022).

4. **Gui J., Sun Z., Wen Y., et al.,** A Review on Generative Adversarial Networks: Algorithms, Theory, and Applications, IEEE Transactions on Knowledge and Data Engineering 35 (4) (2023).

5. **Mao X., et al.,** Least Squares Generative Adversarial Networks, IEEE International Conference on Computer Vision (ICCV), Venice, Italy. (2017) 2813–2821.

6. **Simonyan K., Zisserman A.,** Very Deep Convolutional Networks for Large-Scale Image Recognition, arXiv:1409.1556 (2014).

THE AUTHORS

BABUKHIN Danila V.
dv.babukhin@gmail.com

SYCH Denis V.
denis.sych@gmail.com

Received 31.07.2024. Approved after reviewing 12.08.2024. Accepted 12.08.2024.

Conference materials
UDC 535.93
DOI: https://doi.org/10.18721/JPM.173.222

Waveguide-integrated graphene terahertz detector

A.N. Lyubchak[1,2,3]✉, K.V. Shein[1,2], G.N. Goltsman[1,2,3], I.A. Gayduchenko[1]

[1] National Research University Higher School of Economics, Moscow, Russia;

[2] Moscow Pedagogical State University, Moscow, Russia;

[3] LCC Scontel, Moscow, Russia;

✉ anlyubchak@miem.hse.ru

Abstract. Terahertz (THz) integrated circuits is a promising platform to create low cost and efficient components for high-speed sixth-generation (6G) communication networks. One of the key components for this application is detectors and mixers integrated on THz silicon waveguide. Graphene, due to its unique and tunable properties such as zero band gap, high charge mobility and low electronic heat capacity, has already demonstrated promise in free space THz detectors, mixers and modulators development. Moreover, graphene photodetectors integrated on the waveguide have already been demonstrated in visible and near infrared regions. In this work we present an electromagnetic model of graphene terahertz detector integrated on silicon waveguide. Graphene THz detector was designed for operation at 150 GHz and can be used in the next-generation wireless communications for an ultrafast on-chip THz signal processing.

Keywords: terahertz, dielectric waveguide, photonic-integrated circuit, dielectric effective-medium waveguide

Funding: This work is an output of a research project implemented as part of the Basic Research Program at the National Research University Higher School of Economics (HSE University).

Citation: Lyubchak A.N., Shein K.V., Goltsman G.N., Gayduchenko I.A., Waveguide-integrated graphene terahertz detector, St. Petersburg State Polytechnical University Journal. Physics and Mathematics. 17 (3.2) (2024) 116–120. DOI: https://doi.org/10.18721/JPM.173.222

Материалы конференции
УДК 535.93
DOI: https://doi.org/10.18721/JPM.173.222

Терагерцовый графеновый детектор, интегрированный на волновод

А.Н. Любчак [1,2,3]✉, К.В. Шеин[1, 2], Г.Н. Гольцман [1, 2,3], И.А. Гайдученко [1]

[1] Национальный исследовательский университет «Высшая школа экономики»,

Москва, Россия;

[2] Московский педагогический государственный университет, Москва, Россия;

[3] ООО Сконтел, Москва, Россия.

✉ anlyubchak@miem.hse.ru

Аннотация. В данной работе представлено электромагнитное моделирование терагерцового фотодетектора на основе графена, интегрированного на кремниевый волновод. Этот детектор, рассчитанный на работу на частоте 150 ГГц, может быть использован в сетях связи шестого поколения (6G) для высокоскоростной обработки терагерцовых сигналов на чипе. Графен, благодаря своим уникальным свойствам, таким

как нулевой зазор, высокая подвижность заряда и низкая электронная теплоемкость, является перспективным материалом для создания терагерцовых детекторов, смесителей и модуляторов.

Ключевые слова: терагерцы, диэлектрический волновод, фотонная интегральная схема, волновод с эффективной диэлектрической средой

Финансирование: Исследование осуществлено в рамках Программы фундаментальных исследований НИУ ВШЭ.

Ссылка при цитировании: Любчак А.Н., Шеин К., Гольцман Г.Н., Гайдученко И.А. Терагерцовый графеновый детектор, интегрированный на волновод // Научно-технические ведомости СПбГПУ. Физико-математические науки. 2024. Т. 3.2 № .17. С. 116–120. DOI: https://doi.org/10.18721/JPM.173.222

Introduction

The development of 6G mobile networks involves the use of the terahertz (THz) spectrum band, which plays a key role in enabling high-speed data transmission of up to one terabit per second over long distances via wireless networks [1]. At present, existing THz systems are quite bulky as they consist of separate components: transmitter, receiver, hollow metal waveguides. The creation of THz waveguides based on dielectrics opens up the possibility of creating a compact system for signal transmission and processing. To date, several attempts have been made to integrate various THz detectors on a silicon waveguide: Schottky diodes [2], resonant tunnel diodes [3] and hot electron bolometers (HEB) [4]. In the case of Schottky diodes and resonant tunnel diodes commercial detectors are welded on top of the silicon waveguide, which results in inefficient radiation coupling as well as difficulties in mass production. Hot electron bolometers require cryogenic temperatures, which limits the range of its potential applications.

In this paper we propose to use graphene to develop a THz detector integrated on silicon waveguide. Graphene is characterised by its broad light absorption spectrum [5], ease of fabrication and integration on various substrates, high light response rate [6] and tunable electrical and optical properties [7, 8], making it ideal for use in photonic and optoelectronic devices [8, 9]. Moreover, graphene has been already proved as a perspective material for the development of THz detectors in free space [10], as well as integrated photodetectors in the visible and near-IR range [11]. Here, we present an EM model of graphene THz detector integrated on silicon waveguide. Graphene THz detector was designed for operation at 150 GHz and can be used in the next-generation wireless communications for an ultrafast on-chip THz signal processing.

Results and Discussion

Currently, there are several implementations of dielectric waveguides: ribbon, photonic crystal and effective dielectric medium [12]. In this paper, we investigated the implementation of a waveguide based on an effective dielectric medium, as this approach enables the creation of waveguides with larger bandwidth [13]. To simulate an effective dielectric medium, it is necessary to create through-holes with a period smaller than the wavelength on the sides of the waveguide core. These holes form a triangular lattice with a constant a = 132 μm and a hole radius $r = d/2$= 38.5 μm (see Fig. 1, *a*). The fill factor for this lattice is $\zeta = 2\pi r^2/a^2\sqrt{3} = 0.327$. The dielectric permittivity around the waveguide can be calculated using the equations $\varepsilon_{TE} = \varepsilon(1 + \zeta + \varepsilon(1 - \zeta))/(1 - \zeta + \varepsilon(1 + \zeta))$ and $\varepsilon_{TM} = \zeta + \varepsilon(1 - \zeta)$. For our calculations, we used permittivity values of 11.9 for silicon and 1 for air. Consequently, the permittivity of the effective dielectric medium was determined to be $\varepsilon_{TE} = 6.8$ and $\varepsilon_{TM} = 8.4$ for the two polarizations. In this configuration, the waveguide operates on a principle akin to that of an optical fibre, where light propagates via total internal reflection. To couple radiation from a metal waveguide into a dielectric one, a silicon taper with an opening angle $\alpha = 10^\circ$ was employed.

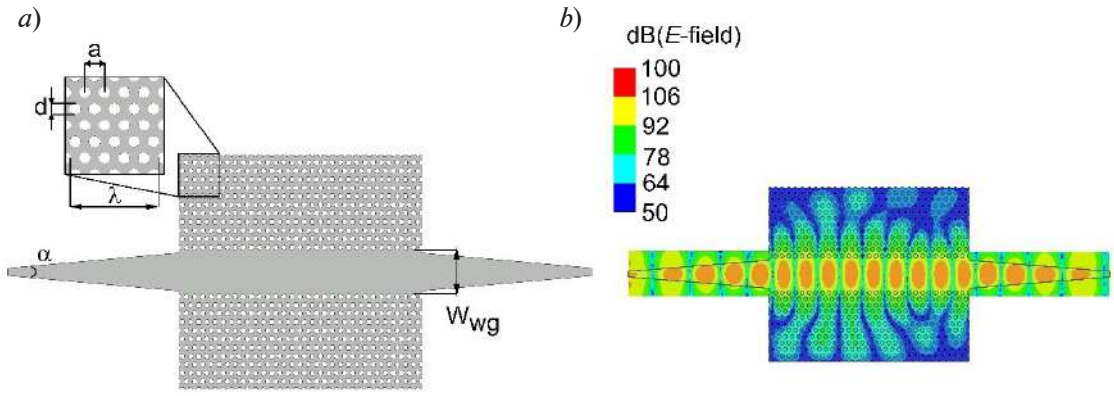

Fig. 1. Schematic illustration of a silicon waveguide with tapered (*a*) and electromagnetic model of a 150 GHz silicon waveguide (*b*)

Electromagnetic modelling was conducted using the Ansys Electronics program, employing the finite element method. The waveguide utilised was a silicon wafer with a thickness of H_{wg} = 400 μm and width W_{wg} = 585 μm. The dielectric constant of silicon was 11.9. Two waveguide ports (ports 1 and 2) were used to excite radiation in the structure at a frequency of 150 GHz (see Fig. 1, *b*). The waveguide was flanked by quarter-wave vacuum inserts with radiation boundary conditions.

Graphene was selected as the detecting material, showing promise for the development of THz radiation detectors [10]. The wavelength λ of electromagnetic radiation in silicon is 0.5 mm, necessitating detectors with larger working areas. This requirement increases the heat capacity of graphene, leading to a reduction in detector sensitivity. To enhance the absorption of electromagnetic radiation emitted from the waveguide by graphene, we are considering the implementation of a tapered slot line [4]. This approach reduces the graphene area to a 2×2 micron square, thereby improving detector sensitivity. The detector design incorporates asymmetric contacts, which have proven effective in graphene THz detector fabrication, leveraging both photovoltaic and thermoelectric effects [14].

The electromagnetic model of the detector was calculated on a dielectric waveguide of the ribbon type in order to facilitate the calculations (see Fig. 2, *a*). At the centre of the ribbon, a tapered slot line with a length of L_{tsl} = 1287 μm, made of gold plates, was positioned with a concentric port (port 3). Fig. 2, *b* shows the optimal aperture angle θ = 165°. Graphene with a resistance of 500 ohms was chosen as the detection material for the third port. For this configuration, reflection and transmission coefficients were observed with values of $S33 = -10$ dB and $S31 = S32 = -4.3$ dB.

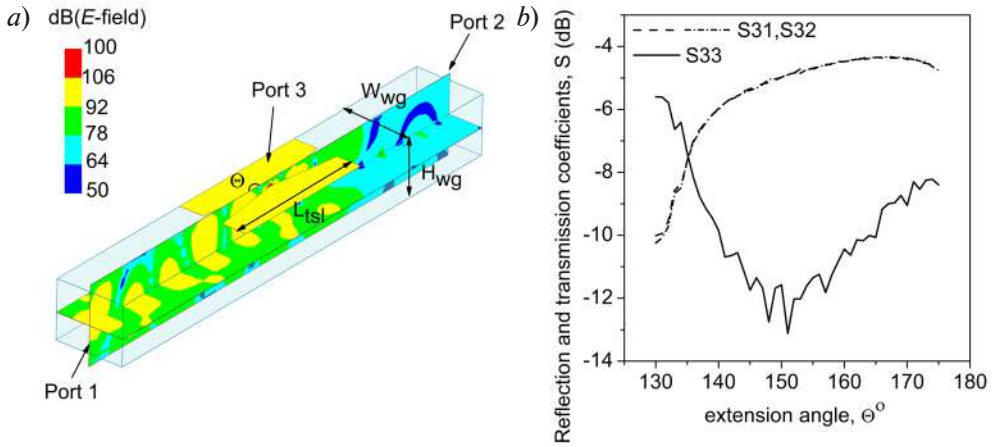

Fig. 2. Electromagnetic model of 150 GHz silicon ribbon waveguide with graphene detector (*a*) and dependence of reflection and transmission coefficients on opening angle θ (*b*)

Conclusion

A EM model of graphene-based photodetector integrated on silicon photonic crystal waveguide has been demonstrated. The design has been evaluated by electromagnetic modelling, resulting in an input loss of 0.18 dB. Reflection and transmission coefficients are observed for a graphene photodetector structure with values of $S33 = -10$ dB and $S31 = S32 = -4$ dB. The graphene THz detector was designed to operate at 150 GHz and can be used in next-generation wireless communications for ultrafast on-chip THz signal processing. The ease with which graphene CVD films and flakes can be transferred allows for the fabrication of detectors on waveguides based on two-dimensional materials.

Acknowledgments

This work is an output of a research project implemented as part of the Basic Research Program at the National Research University Higher School of Economics (HSE University).

REFERENCES

1.**Yang Y., Yamagami Y., Yu X., et al.,** Terahertz topological photonics for on-chip communication, Nature Photonics. 14 (7) (2020) 446–451.

2. **Torres-Garcна A.E., Pérez-Escudero J.M., Teniente J., et al.,**Silicon integrated subharmonic mixer on a photonic-crystal platform, IEEE Transactions on Terahertz Science and Technology. 11 (1) (2020) 79–89.

3. **Yu X., Hosoda Y., Miyamoto T., et al.,**Terahertz fibre transmission link using resonant tunnelling diodes integrated with photonic-crystal waveguides, Electronics Letters. 55 (7) (2019) 398–400.

4. **Shurakov A.S., Belikov I.I., Prikhodko A.N., et al.,** Superconducting Electronic–Photonic Platform for HEB-Based Terahertz Spectrometers. Applied Sciences. 13 (10) (2023) 5892.

5. **Xia F.N., Wang H., Xiao D., et al.,** Two-dimensional material nanophotonics, Nat. Photonics. 8 (2014) 899–907.

6. **Xia F.N., Mueller T., Lin Y.M., et al.,**Ultrafast graphene photodetector. Nat. Nanotechnol. 4 (2009) 839–843.

7. **Novoselov K.S., Geim A.K., Morozov S.V., et al.,** Electric field effect in atomically thin carbon films. Science. 306 (2004) 666–669.

8. **Mueller T., Xia F.N., Avouris P.**, Graphene photodetectors for high-speed optical communications. Nat. Photonics. 4 (2010) 297–301.

9. **Urich A., Unterrainer K., Mueller T.**, Intrinsic response time of graphene photodetectors. Nano Lett. 11 (2011) 2804–2808.

10. **Bandurin D.A., Svintsov D., Gayduchenko I., et al.,**Resonant terahertz detection using graphene plasmons. Nature communications. 9 (1) (2018) 5392.

11. **Guo J., Li J., Liu C., et al.,** High-performance silicon– graphene hybrid plasmonic waveguide photodetectors beyond 1.55 μm. Light, Science & Applications. 9 (1) (2020) 29.

12. **Koala R.A., Fujita M., Nagatsuma T.**, Nanophotonics-inspired all-silicon waveguide platforms for terahertz integrated systems. Nanophotonics. 11 (9) (2022) 1741–1759.

13. **Gao W., Yu X., Fujita M., et al.,**Effective-medium-cladded dielectric waveguides for terahertz waves. Optics express. 27 (26) (2019) 38721–38734.

14. **Gayduchenko I.A., Moskotin M.V., Matyushkin Y.E., et al.,** The detection of sub-terahertz radiation using graphene-layer and graphene-nanoribbon FETs with asymmetric contacts. Materials Today: Proceedings. 5(13) (2018) 27301–27306.

THE AUTHORS

LYUBCHAK Anastasia N.
anlyubchak@miem.hse.ru
ORCID: 0000-0002-4861-2466

GOLTSMAN Grigory N.
goltsman@rplab.ru
ORCID: 0000-0002-1960-9161

SHEIN Kirill V.
sheinkv97@gmail.com
ORCID: 0000-0001-6494-0147

GAYDUCHENKO Igor A.
igaiduchenko@hse.ru
ORCID: 0000-0003-2560-6503

Received 31.07.2024. Approved after reviewing 25.09.2024. Accepted 25.09.2024.

Conference materials
UDC 51-74
DOI: https://doi.org/10.18721/JPM.173.223

Effect of internal mechanical stresses in a multilayer structure on displacement for various designs of microelectromechanical membranes

S.V. Malokhatko[1]✉, E.Yu. Gusev[1], Jiang L.[2], O.A. Ageev[1]

[1] Institute of Nanotechnology, Electronics and Electronic Equipment Engineering, Taganrog, Russia;

[2] Laser Institute, Qilu University of Technology, Shandong Academy of Sciences, Jinan, China

✉ malohatko@sfedu.ru

Abstract. In the manufacture of microelectromechanical sensors based on multilayer membranes, internal mechanical stresses arise in the structure. A preliminary assessment of the effect of internal mechanical stresses on the initial displacement of structures of various shapes will allow to choose the most appropriate design solution for various applications. The paper presents the results of numerical modeling of the structures of multilayer membranes of three types: round, square and square with transverse and angular beams. The displacement values for each type of multilayer membranes are obtained in accordance with the influence of internal mechanical stresses in each layer. The results showed that the effect of internal mechanical stresses in films (SiO_2, Mo, ZnO) of a multilayer structure on square and round membranes is insignificant (values ranged from $2.43 \cdot 10^{-13}$ to $7.83 \cdot 10^{-13}$ nm). Internal mechanical stresses in membrane layers with transverse and angular beams make a significant contribution to the initial displacement of the structure (values ranged from 20 to 570 nm), however, the sensitivity of such structures is higher than that of rigid structures. The influence of technological conditions of film formation in multilayer membranes on their stress-strain state in ultrasonic sensors is investigated. The values of internal mechanical stresses in SiO_2 films are obtained.

Keywords: microelectromechanical sensors, multilayer membrane, internal mechanical stress

Citation: Malokhatko S.V., Gusev E.Yu., Jiang L., Ageev O.A., Effect of internal mechanical stresses in a multilayer structure on displacement for various designs of microelectromechanical membranes, St. Petersburg State Polytechnical University Journal. Physics and Mathematics. 17 (3.2) (2024) 121–124. DOI: https://doi.org/10.18721/JPM.173.223

Материалы конференции
УДК 51-74
DOI: https://doi.org/10.18721/JPM.173.223

Влияние внутренних механических напряжений в многослойной структуре на смещение для различных конструкций микроэлектромеханических мембран

С.В. Малохатко[1]✉, Е.Ю. Гусев[1], Цзян Л.[2], О.А. Агеев[1]

[1] Институт нанотехнологий, электроники и приборостроения (ЮФУ), г. Таганрог, Россия;

[2] Лазерный институт, Технологический университет Цилу, Шаньдунская академия наук, Цзинань, Китай

✉ malohatko@sfedu.ru

Аннотация. В работе представлены результаты моделирования конструкций многослойных мембран трех типов: круглой, квадратной и квадратной с поперечными и угловыми подвесами. Получены значения прогиба для каждого типа многослойных

мембран по действие внутренних механических напряжений в каждом слое. Исследовано влияния технологических условий формирования пленок в многослойных мембранах на их напряженно-деформированное состояние в ультразвуковых датчиках.

Ключевые слова: микроэлектромеханические датчики, многослойная мембрана, внутреннее механическое напряжение

Ссылка при цитировании: Малохатко С.В., Гусев Е.Ю., Цзян Л., Агеев О.А. Влияние внутренних механических напряжений в многослойной структуре на смещение для различных конструкций микроэлектромеханических мембран // Научно-технические ведомости СПбГПУ. Физико-математические науки. 2024. Т. 17. № 3.2. С. 121–124. DOI: https://doi.org/10.18721/JPM.173.223

Introduction

Microelectromechanical devices cover more and more fields of application [1]. Such devices include ultrasonic microelectromechanical sensors (includes piezoelectric micromachined ultrasonic transducers) that can be used for industrial and medical purposes [2]. The output characteristics of such devices depend on a sensing element consisting of a multilayer membrane-type structure. By changing the membrane design, certain functional parameters of the sensor can be improved [3]. However, at the stage of multilayer structure fabrication, under the influence of various factors, internal mechanical stresses arise in the layers, which lead to displacement of structures without external influence [4]. The displacement of the structure leads to a decrease in sensitivity. Thus, an actual task is to study the effect of internal mechanical stresses on the displacement of a multilayer membrane, depending on its design.

A previously conducted assessment on the influence of physical and mechanical parameters of the base materials on the resonant frequency for the typical (widely used [2,3]) structure Si/SiO_2/Metal/Piezoelectric/Metal showed the promise and technological feasibility of using zinc oxide and molybdenum which also have high resistance and strength.

Materials and Methods

Modeling in the Comsol Multiphysics was carried out for three types of membranes: round (diameter of 500 μm), square (side length of 500 μm) and square with transverse and angular beams (length of 50 μm, width of 25 μm). The multilayer structure included the following layers $Si/SiO_2/Mo/ZnO$ (50/2/0.1/0.1 μm). The internal mechanical stresses that were taken into account during the simulation ranged from -80 to -500 MPa [5], from -1.5 to +1.5 GPa [6] and from -0.7 to +0.7 GPa [7] for SiO_2, Mo and ZnO films, respectively. The fabrication of SiO_x films was carried out by plasma chemical deposition from the gas phase [8]. Further, the obtained films were subjected to rapid thermal annealing at a temperature of 600 °C for 3 minutes.

Results and Discussion

Fig. 1 shows the displacement of a square membrane and a square membrane with transverse and angular beams under the action of internal compressive stresses of -100 MPa in the SiO_2 layer.

Depending on the internal mechanical stresses in the multilayer structure, displacement values are obtained for each type of membrane, which are presented in Table 1.

As can be seen from the results obtained, the more rigid the fixation of the membrane, the less the effect of internal mechanical stresses on the initial displacement of the membrane. However, square membranes with angular and transverse beams have higher sensitivity. The mechanical sensitivity of square membranes and square membranes with angular and transverse beams under the influence of an external pressure of 5.19 kPa was 0.05 nm/kPa and 0.26 nm/kPa, respectively. This behavior is due to the direct dependence of the rigidity of the structures on the type of membrane attachment.

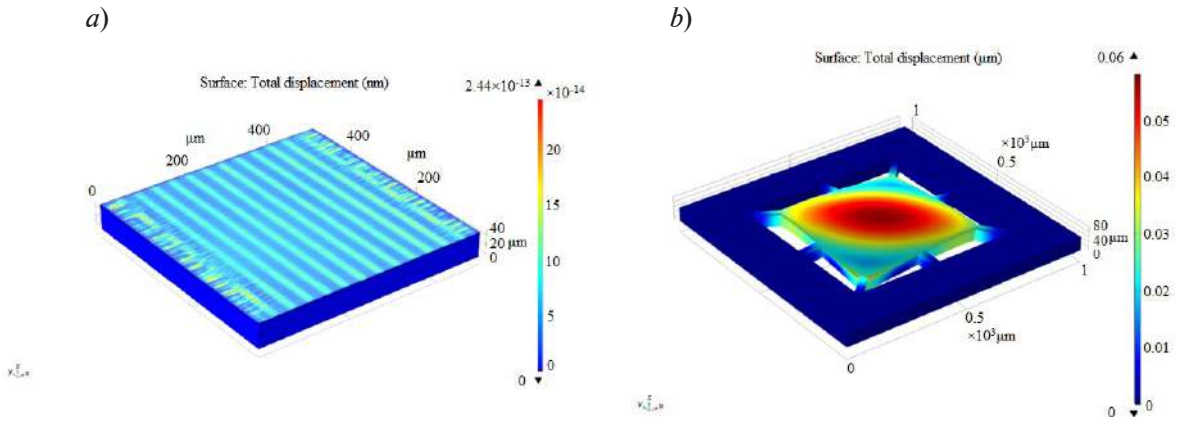

Fig. 1. Displacement of membranes: square (*a*) and square with transverse and angular beams (*b*) under the action of internal compressive stresses of −100 MPa in a SiO_2 film

Table 1

Displacement values of the multilayer membrane, nm

Membrane shape	Layer		
SiO_2		Mo	ZnO
	From –80 to –500 MPa	From -1.5 to +1.5 GPa	From -0.7 to +0.7 GPa
Round	From $2.95 \cdot 10^{-14}$ to $2.72 \cdot 10^{-13}$ (↑)	From $4.35 \cdot 10^{-13}$ (↑) to $5.23 \cdot 10^{-13}$ (↓)	From $2.64 \cdot 10^{-13}$ (↑) to $2.63 \cdot 10^{-13}$ (↓)
Square	From $7.83 \cdot 10^{-13}$ to $5.09 \cdot 10^{-13}$ (↑)	From $6.23 \cdot 10^{-13}$ (↑) to $6.23 \cdot 10^{-13}$ (↓)	From $2.44 \cdot 10^{-13}$ (↑) to $2.43 \cdot 10^{-13}$ (↓)
Square with transverse and angular beams	From 20 to 570 (↑)	From 90 (↑) to 90 (↓)	From 40 (↑) to 40 (↓)

The average value of mechanical stresses in the SiO_x films obtained was -168±5 MPa, which is consistent with theoretical data [5]. Thus, with the streamlined process of obtaining multilayer structures at the design stage, it becomes possible to consider the influence of internal mechanical stresses in each layer on the output characteristics of microelectromechanical membranes.

Conclusion

The analysis of the results showed that for the development of microelectromechanical sensors based on multilayer membranes with increased sensitivity, it is necessary to use structures partially released along the perimeter. However, due to the significant contribution of internal mechanical stresses to the initial displacement of such structures, their consideration is required at the design stage of the structure. The obtained results can be extended to multilayer Si/SiO_2/Metal/Piezoelectric/Metal structures with another material of the piezoelectric and metal layers. The presented results can be used to optimize the designs and fabrication processes of multilayer structures used in acoustic sensors, micromirrors and resonators.

Acknowledgments

The work was done on the infrastructure of the Research and Education Center "Nanotechnologies" of Southern Federal University and Laser Institute, Qilu University of Technology (Shandong Academy of Sciences).

REFERENCES

1. **Ageev O.A., Konoplev B.G.**, Nanotechnology in microelectronics, Nauka, Moscow. 2019.
2. **Jung J., Lee W., Kang W., et al.,** Review of piezoelectric micromachined ultrasonic transducers and their applications, Journal of Micromechanics and Microengineering. 27 (11) (2017) 1—24.
3. **Qiu Y., Gigliotti J.V., Wallace M., et al.,** Piezoelectric micromachined ultrasound transducer (PMUT) arrays for integrated sensing, actuation and imaging, Sensors. 15 (4) (2015) 8020—8041.
4. **Abadias G., Chason E., Keckes J., et al.,** Review Article: Stress in thin films and coatings: Current status, challenges, and prospects, Journal of Vacuum Science and Technology A: Vacuum, Surfaces, and Films. 36 (2) (2018) 020801.
5. **Dostanko A.P.,** The integrated technologies functional micro-and nanostructures, Bestprint, Minsk. 2013.
6. **Shen Y.G.,** Effect of deposition conditions on mechanical stresses and microstructure of sputter-deposited molybdenum and reactively sputter-deposited molybdenum nitride films, Materials Science and Engineering. 359 (1-2) (2003) 158—167.
7. **Conchon F., Renault P.O., Goudeau P., et al.,** Residual stresses in sputtered ZnO films on (100) Si substrates by XRD, Materials Research Society Symposium Proceedings. 1201 (2009) 1201-H05-03.
8. **Gusev E.Yu., Jityaeva J.Y., Ageev O.A.,** Effect of PECVD conditions on mechanical stress of silicon films, Materials Physics and Mechanics. 37 (1) (2018) 67—72.

THE AUTHORS

MALOKHATKO Sofya V.
malohatko@sfedu.ru
ORCID: 0000-0001-7989-6513

JIANG Liyuan
jiangliyuan@sdlaser.cn

GUSEV Evgeny Yu.
eyugusev@sfedu.ru
ORCID: 0000-0001-8635-2573

AGEEV Oleg A.
ageev@sfedu.ru
ORCID: 0000-0003-1755-5371

Received 31.07.2024. Approved after reviewing 25.09.2024. Accepted 26.09.2024.

Conference materials
UDC 535.14
DOI: https://doi.org/10.18721/JPM.173.224

Modeling the dynamics and properties of the squeezed state of light in a phase modulator

A.V. Tabieva✉, A.I. Trifanov, G.V. Tushavin, M.V. Matveeva

ITMO University, St. Petersburg, Russia

✉ tabieva.arina@itmo.ru

Abstract. In this work, we investigate the transformation of a squeezed by photon-number quantum state of a single-mode optical signal during phase modulation process. Within the framework of the semiclassical model of the phase modulator, we obtained estimations for the statistical properties of individual modes and mode sub-ensembles of the signal spectrum. We shown that for the case of modulation of squeezed vacuum, the entire spectrum of the modulated signal evaluates to the entangled state of a number of frequency modes. The results obtained in this work enable the use of squeezed modulated light states in quantum key distribution systems and various interferometric applications.

Keywords: phase modulator, multimode quantum optical signal, SU(1.1) algebra, squeezed state of light

Citation: Tabieva A.V., Trifanov A.I., Tushavin G.V., Matveeva M.V., Modeling the dynamics and properties of the compressed state of light in a phase modulator, St. Petersburg State Polytechnical University Journal. Physics and Mathematics. 17 (3.2) (2024) 125–129. DOI: https://doi.org/10.18721/JPM.173.224

Материалы конференции
УДК 535.14
DOI: https://doi.org/10.18721/JPM.173.224

Моделирование динамики и свойств сжатого состояния света в фазовом модуляторе

А.В. Табиева✉, А.И. Трифанов, Г.В. Тушавин, М.В. Матвеева

Университет ИТМО, Санкт-Петербург, Россия

✉ tabieva.arina@itmo.ru

Аннотация. В данной работе мы исследуем преобразование сжатого по числу фотонов квантового состояния оптического сигнала в процессе фазовой модуляции света. В рамках полуклассической модели фазового модулятора мы получили оценки статистических свойств отдельных частотных мод спектра сигнала и их подансамблей. Мы показали, что в случае модуляции сжатого вакуума весь спектр модулированного сигнала представляет собой запутанное состояние ансамбля частотных мод. Полученные в этой работе результаты позволяют использовать сжатые модулированные состояния света в системах квантового распределения ключей и различных интерферометрических приложениях.

Ключевые слова: фазовый модулятор, многомодовый квантовый оптический сигнал, алгебра SU(1,1), сжатое состояние света

Ссылка при цитировании: Табиева А.В., Трифанов А.И., Тушавин Г.В., Матвеева М.В. Моделирование динамики и свойств сжатого состояния света в фазовом модуляторе // Научно-технические ведомости СПбГПУ. Физико-математические науки. 2024. Т. 17. № 3.2. С. 125–129. DOI: https://doi.org/10.18721/JPM.173.224

Introduction

Transformation of the spectral and statistical properties of multimode quantum-optical signals is of great practical importance due to the use of such processes in quantum communication and cryptography systems [1, 2]. This transformation may be implemented in phase modulators [3], which semi-classical model was proposed and studied in the [4–6], where the process of modulating an optical signal in a fully quantum state was considered. The property of a modulator to transform the spectra of optical signals can be utilized to obtain collective states that possess a number of important characteristics necessary for quantum communication systems. In particular, this pertains to the generation of entangled ensembles [7, 8]. Although the modulator is a linear optical device and cannot generate entangled states from classical light on its own, it can be used for this purpose. In this work, we propose a model for transforming a single-mode signal in a squeezed vacuum state into an entangled ensemble of frequency modes. Using numerical simulations, we obtained dependencies of the entanglement characteristics we employed (such as the trace of the square of the reduced density matrix and Shannon entropy) on the degree of squeezing of the initial optical signal.

Materials and Methods

In this work the dynamics of squeezed photon states is considered. A single-tone signal arriving at the input of the electro-optical modulator. The statistical characteristics of the ensemble of modes at the output of the device are analyzed.

A monochromatic signal is fed into the modulator, where upon modulation, it decomposes into a superposition of different modes. At the input of the device, we consider the squeezed state of the central mode, which is expressed through the squeezing operator [9] in the standard manner:

$$\left|\psi_{in}\right\rangle = S\left(\xi\right)\left|\psi_0\right\rangle, \tag{1}$$

where S is the squeezing operator, ψ_0 is the vacuum state. After the modulator this state is transformed according to the evolution operator $U(t)$ and has the following form:

$$U\left(t\right)\left|\psi_{in}\right\rangle = \left|\psi_{out}\right\rangle = U\left(t\right)S\left(\xi\right)\left|\psi_0\right\rangle. \tag{2}$$

The action of the operator $U(t)$ on the mode operators a_μ can be written as follows [5, 10, 11]:

$$U\left(t\right)aU^{\dagger}\left(t\right) = a\left(t\right) = c\left(t\right) = \sum_{v=-s}^{s} D_{\mu v}^{(s)\dagger}\left(t\right)a_v. \tag{3}$$

Let us denote the value of the operator $a(t)$ at a fixed interaction time with the modulator $t = t_0$. Then, using the operator transformation [12]:

$$\begin{aligned}\left|\psi_{out}\right\rangle = U\left(t_0\right)\left|\psi_{in}\right\rangle = U\left(t_0\right)S\left(\xi\right)\left|\psi_0\right\rangle = \\ = U\left(t_0\right)S\left(\xi\right)U\left(t_0\right) + U\left(t\right)\left|\psi_0\right\rangle = S\left(\xi, t_0\right)\left|\psi_0\right\rangle,\end{aligned} \tag{4}$$

where the operator $S(\xi, t_0)$ has the form:

$$S(\xi, t_0) = \exp\left\{-i\left(\frac{\overline{\xi}}{2}c^2 - \frac{\xi}{2}c^{\dagger 2}\right)\right\}. \quad (5)$$

Results and Discussion

To investigate the statistical properties of the resulting state $|\psi_{out}\rangle$, let us consider the corresponding density matrix:

$$\rho_{out} = |\psi_{out}\rangle\langle\psi_{out}|. \quad (6)$$

An indicator of the presence of entanglement in a pure state can be represented by the mixed state of its subsystem. For this purpose, let us consider the partial trace over the subspace A, which consists of certain modes of the ensemble:

$$\rho' = Tr_A |\psi_{out}\rangle\langle\psi_{out}|. \quad (7)$$

The mixed state corresponds to such a matrix ρ′ for which

$$m = Tr(\rho'^2) < 1. \quad (8)$$

Fig. 1 presents a graph showing the dependence of the quantity *m* on the squeezing parameter ξ of the initial state. The following parameters were chosen for numerical modeling: there were the angle of the phase state ϕ = 0, 5 modes, from which the three middle ones were removed, and then the compression parameter r was changed from 0 to 1 in increments of 0.05.

Another important parameter reflecting the informational capacity of the state is the entropy,

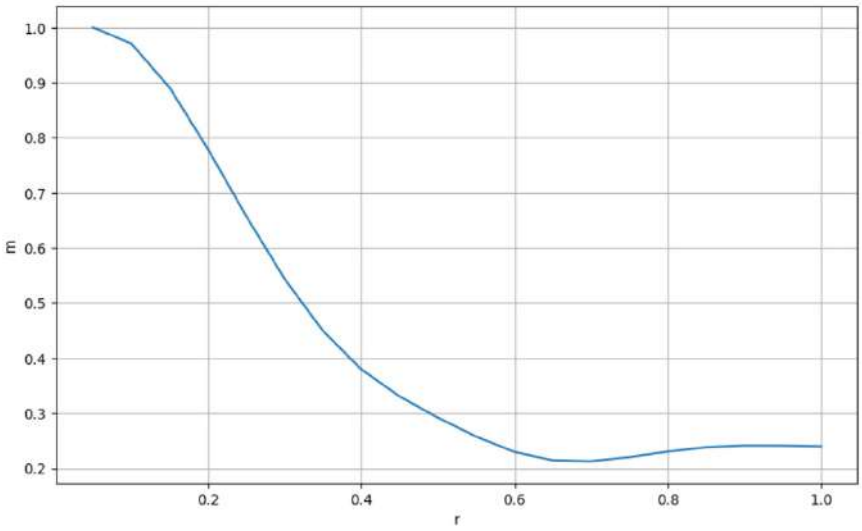

Fig. 1. Dependence of parameter *m* on the squeezing parameter (*r*)

which in the case of a quantum carrier in state ρ can be computed as follows:

$$I_{sh} = -Tr(\rho \log_2 \rho). \quad (9)$$

In the case of a pure state of the full ensemble, this quantity is equal to zero; however, for subsystem A with density matrix ρ′, this quantity should be non-zero if the original full ensemble was in an entangled state [13–14]:

$$I_{sh} = -Tr(\rho' \log_2 \rho) > 0. \quad (10)$$

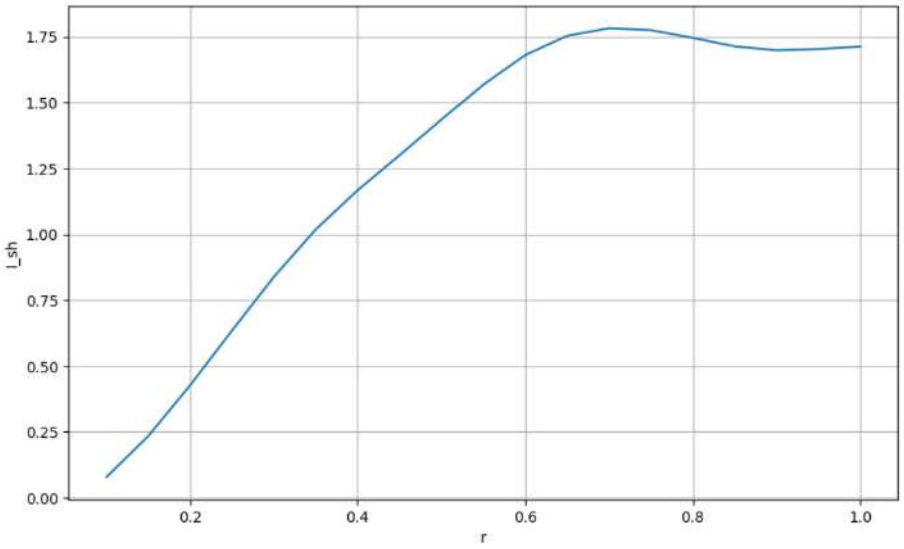

Fig. 2. Dependence of the quantum Shannon entropy as a function of the squeezing parameter ξ with the logarithm of purity $\log_2\rho$

Fig. 2 models the dependence of the quantum Shannon entropy as a function of the squeezing parameter ξ. The graph is constructed with the same parameters as for the first graph.

Conclusion

In this study, we have explored the transformation of a single-mode squeezed vacuum state into an entangled ensemble of frequency modes using an electro-optical modulator. Our model demonstrates that while the modulator itself is a linear optical device and does not generate entangled states from classical light, it can effectively facilitate the generation of entangled ensembles when applied to quantum states. Through numerical simulations, we analyzed the dependence of entanglement characteristics, such as the trace of the square of the reduced density matrix and Shannon entropy, on the degree of squeezing of the input optical signal.

The findings underscore the potential of phase modulators in enhancing the spectral and statistical properties of multimode quantum-optical signals, which are crucial for advancing quantum communication and cryptography systems. By successfully demonstrating the transformation process, this work lays the groundwork for further investigations into optimizing entanglement generation and exploring new applications in quantum technologies. Future research could focus on refining the modulation techniques and investigating their effects on different types of quantum states, ultimately contributing to the development of more robust and efficient quantum communication protocols.

REFERENCES

1. **Andersen U.L., Leuchs G., Silberhorn C.,** Continuous-variable quantum information processing. Laser Photon. Rev. (4) (2010) 337–354.

2. **Capmany J., Fernandez-Pousa C.R.,** Laser Photonics Rev. 5 (6) (2011) 750–772.

3. **Carson J.R.,** Notes on the theory of modulation, Proc. IRE. 10 (1) (1922) 57–64.

4. **Miroshnichenko G.P., et al.,** JOSA B. 34 (7) (2017) 061177–14.

5. **Miroshnichenko G.P., et al.,** Optics express. 26 (9) (2018) 11292–11308.

6. **Trifanov A.I., Miroshnichenko G.P.,** Reduced Conditional Dynamic of Quantum System Under Indirect Quantum Measurement. Nanosystems: Physics, Chemistry, Mathematics. 4 (5) (2013) 635–647.

7. The ATLAS Collaboration. Observation of quantum entanglement with top quarks at the ATLAS detector. Nature. (633) (2024) 542–547.

8. **Tushavin G.V., Zaitseva E.V., Trifanov A.I.,** Ladder operators approach to representation classification problem for Jordan–Schwinger image of SU(2) algebra. Nanosystems: Phys. Chem. Math. 13 (3) (2022) 299–307.

9. **Gordon J.P., Louisell W.H., Walker L.R.,** Quantum fluctuations and noise in parametric processes: II // Phys. Rev. 129 (1963) 481–485.

10. **Gelfand I.D., Shapiro Z., Minlos R.A.,** Representations of the Rotation and Lorentz Groups and Their Applications. Oxford:The Pergamon Press. 1963.

11. **Biedenharn L.C., Louck J.D.,** Angular Momentum in Quantum Physics. Massachusetts: Addison-Wesley Publishing Company Reading. (8) (1981) 302.

12. **Perelomov A.M.,** Generalized coherent states and some of their applications, Phys. Usp. (20) (9) (1977) 703–720.

13. **Campos R., Bahaa S., Malvin T.,** Quantum mechanical lossless beam splitter: SU(2) symmetry and photon statistics. Physical Review A. 40 (3) (1989) 1371.

14. **Fearn H., Loudon R.,** Quantum theory of the lossless beam splitter. Optics Communications. 64 (6) (1987) 485–490.

THE AUTHORS

TABIEVA Arina V.
tabieva.arina@itmo.ru
ORCID: 0009-0004-6560-7409

TUSHAVIN Gleb V.
tushavin@itmo.ru
ORCID: 0000-0002-6482-0951

TRIFANOV Alexander I.
alextrifanov@itmo.ru
ORCID: 0000-0002-5109-2086

MATVEEVA Milena V.
mvmatveeva@itmo.ru
ORCID: 0009-0006-8671-1752

Received 01.08.2024. Approved after reviewing 17.10.2024. Accepted 21.10.2024.

Conference materials
UDC 517.986.5
DOI: https://doi.org/10.18721/JPM.173.225

Investigation of entangled states of a three-mode electro-optical modulator

M.V. Matveeva✉, A.I. Trifanov, G.V. Tushavin, A.V. Tabieva

ITMO University, St. Petersburg, Russia

✉ mvmatveeva@itmo.ru

Abstract. We study the dynamic properties and algebraic invariants of the model of phase modulation of quantum light by microwave radiation. The quasi-energy levels of the system are described by the eigenvalues of the effective Hamiltonian, which generators obbey to su(2) algebra and have a nontrivial internal structure. The dynamics of states is studied in Fock space. Invariant Hamiltonian spaces are associated with irreducible representations of the su(2) algebra, within which the Hamiltonian matrix is partitioned into finite blocks. Within this model we investigate the generating process of two-mode entangled states using the single-tone Fock state at the input of phase modulator.

Keywords: Phase modulator, Hamiltonian, entangled states, ladder operators

Citation: Matveeva M.V., Trifanov A.I., Tushavin G.V., Tabieva A.V., Investigation of entangled states of a three-mode electro-optical modulator, St. Petersburg State Polytechnical University Journal. Physics and Mathematics. 17 (3.2) (2024) 130–134. DOI: https://doi.org/10.18721/JPM.173.225

Материалы конференции
УДК 517.986.5
DOI: https://doi.org/10.18721/JPM.173.225

Исследование запутанных состояний трехмодового электрооптического модулятора

М.В. Матвеева[1]✉, А.И. Трифанов[1], Г.В. Тушавин[1], А.В. Табиева[1]

[1] Университет ИТМО, Санкт-Петербург, Россия

✉ mvmatveeva@itmo.ru

Аннотация. Рассматриваются динамические свойства и алгебраические инварианты модели фазовой модуляции квантового света микроволновым излучением. Уровни квазиэнергии системы описываются собственными значениями эффективного гамильтониана, генераторы которого подчиняются алгебре su(2) и имеют нетривиальную внутреннюю структуру. Динамика состояний исследуется в пространстве Фока. Инвариантные гамильтоновы пространства связаны с неприводимыми представлениями алгебры su(2),где матрица гамильтониана разбивается на конечные блоки. В рамках этой модели исследуется процесс генерации двухмодовых запутанных состояний с использованием однотонального фоковского состояния на входе фазового модулятора.

Ключевые слова: Фазовый модулятор, Гамильтониан, запутанные состояния, лестничные операторы

Ссылка при цитировании: Матвеева М.В., Трифанов А.И., Тушавин Г.В., Табиева А.В. Исследование запутанных состояний трехмодового электрооптического модулятора // Научно-технические ведомости СПбГПУ. Физико-математические науки. 2024. Т. 17. № 3.2. С. 130–134. DOI: https://doi.org/10.18721/JPM.173.225

Introduction

The work [1] presented an explicitly solvable algebraic model of the process of electro-optic modulation of light by a microwave field based on the linear electro-optic effect. To describe the inter-mode interaction of light, the corresponding operators were obtained by applying the Jordan-Schwinger mapping [2] to generators of the matrix algebra su(2). It was shown that in the high-intensity approximation of the modulating microwave radiation, the model reduces to a semiclassical one, and the dynamic problem becomes exactly solvable. However, when the number of interacting optical modes exceeds three, the irreducible representations of the su(2) algebra related to invariant spaces turn out to be degenerate— the induced classification by the su(2) algebra is incomplete. To address this issue, a method of ladder operators for the Casimir operator image of the su(2) algebra was proposed in [3]. The obtained algebra of ladder operators generates the spectrum and eigenvectors of the Casimir operator, allowing for a description of all invariant spaces within the problem with three interacting frequency modes.

Materials and Methods

In this work, within the model described above, we investigate the generating process of two-mode entangled state using the single-tone optical signal in two-photon Fock state at the input of phase modulator. To the end we consider the image of the su(2) algebra represented by operators J_z, J_+, J_-. These operators through Jordan-Schwinger mapping are expressed by polynomials of bosonic operators a_μ, a_μ^+ of of frequency modes, associated with the eigenvalue s (non-negative integer or non-negative half-integer), $n = 2s + 1$.

$$J_z \sum_{\mu=-s}^{s} \mu a_\mu^+ a_\mu, \tag{1}$$

$$J_+ \sum_{\mu=-s}^{s-1} \sqrt{(s+\mu+1)(s-\mu)}\, a_{\mu+1}^+ a_\mu = (J_-)^+. \tag{2}$$

The operators J_z, J_+, J_- satisfy the the following commutation relations:

$$[J_z, J_+] = \pm J_+, [J_+, J_-] = 2J_z. \tag{3}$$

In order to obtain the basis of the invariant subspace associated with the irreducible representation of the su(2) algebra, we act on the vacuum vector with the ladder operator $\tau_1^+ = p_0^+ (j+1) + 2p_1^+$, resulting in the Fock state $\sqrt{\frac{2}{3}}|020\rangle + \frac{1}{\sqrt{3}}|101\rangle$, which is a coherent state of the su(2) algebra corresponding to state $|n = 2, j = 2, j_z = 0\rangle$ Acting on this obtained basis element with the operators J_+ and J_- yields the other Fock states $|200\rangle$, $|110\rangle$, $|011\rangle$, $|002\rangle$.These states form a basis for a five-dimensional invariant space (with "total moment" $j = 2$). The corresponding two-photon Fock space is six-dimensional thus, there exists an additional one-dimensional invariant space corresponding to $j = 0$, with its basis vector being the orthogonal vector $\frac{1}{\sqrt{3}}|020\rangle - \sqrt{\frac{2}{3}}|101\rangle$.

In the following we consider the Hamiltonian of the phase modulator:

$$H = \omega m_{opt} N + \omega J_z + \gamma \cdot \left(J_+ e^{-i\varphi} + J_- e^{i\varphi} \right), \tag{4}$$

the obtained basis of the five-dimensional invariant space, when we have $H = \gamma \cdot V$:

$$V = \begin{pmatrix} 0 & 2e^{i\varphi} & 0 & 0 & 0 \\ 2e^{-i\varphi} & 0 & \sqrt{6}e^{i\varphi} & 0 & 0 \\ 0 & \sqrt{6}e^{-i\varphi} & 0 & \sqrt{6}e^{i\varphi} & 0 \\ 0 & 0 & \sqrt{6}e^{-i\varphi} & 0 & 2e^{i\varphi} \\ 0 & 0 & 0 & 2e^{-i\varphi} & 0 \end{pmatrix}. \tag{5}$$

Then we can analyze the spectral properties of matrix V and find the eigenvectors corresponding to the stationary states of the system:

$$\sigma_V = \{-4\gamma_0, -2\gamma_0, 0, 2\gamma_0, 4\gamma_0\}, \tag{6}$$

$$v_{-4} = \frac{1}{4}\begin{pmatrix} e^{2i\varphi} \\ -2e^{i\varphi} \\ \sqrt{6} \\ -2e^{-i\varphi} \\ e^{-2i\varphi} \end{pmatrix}, \; v_{-2} = \frac{1}{2}\begin{pmatrix} e^{2i\varphi} \\ -e^{-i\varphi} \\ 0 \\ -e^{-i\varphi} \\ -e^{-2i\varphi} \end{pmatrix}, \; v_0 = \frac{1}{2}\begin{pmatrix} -\sqrt{\frac{3}{2}}e^{2i\varphi} \\ 0 \\ 1 \\ 0 \\ -\sqrt{\frac{3}{2}}e^{-2i\varphi} \end{pmatrix}, \tag{7}$$

$$v_2 = \frac{1}{2}\begin{pmatrix} e^{2i\varphi} \\ e^{i\varphi} \\ 0 \\ -e^{-i\varphi} \\ -e^{-2i\varphi} \end{pmatrix}, \; v_4 = \frac{1}{4}\begin{pmatrix} e^{2i\varphi} \\ 2e^{i\varphi} \\ \sqrt{6} \\ 2e^{-i\varphi} \\ e^{-2i\varphi} \end{pmatrix}.$$

Each eigenvector can be expressed in terms of a Fock basis $|200\rangle$, $|110\rangle$, $|011\rangle$, $|002\rangle$.

Results and Discussion

Here we use eigenstates of the Hamiltonian to model initial state evolution during the phase modulation process.

The figure illustrates the action of the evolution operator on the initial state $|020\rangle$. This allows us to determine the time dependence of the probability amplitudes of the Fock state components. The green curve corresponds to the dynamics of the components $|200\rangle$ and $|002\rangle$ of the Fock state vector $\sqrt{\frac{2}{3}}|020\rangle + \frac{1}{\sqrt{3}}|101\rangle$. It is evident from this that there is a specific moment in time when no other components are present in the expansion of this state vector.

To construct the dynamics of the state $|020\rangle$, we will act with the evolution operator on the initial state, as a result of which we obtain this expression with coefficients $\alpha = \frac{\sqrt{6}}{4}$, $\beta = \frac{1}{2}$.

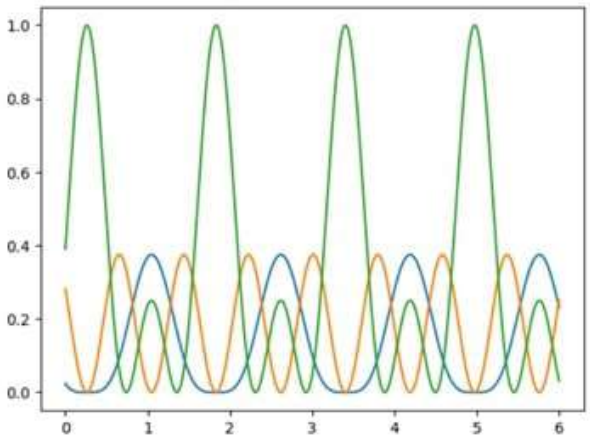

Figure. Probability amplitudes of state $|020\rangle$ in dynamics

$$\frac{\alpha}{4}\begin{pmatrix} e^{2i\varphi} \\ -2e^{i\varphi} \\ \sqrt{6} \\ -2e^{-i\varphi} \\ e^{-2i\varphi} \end{pmatrix} e^{-4it} + \frac{\beta}{2}\begin{pmatrix} -\sqrt{\frac{3}{2}}e^{2i\varphi} \\ 0 \\ 1 \\ 0 \\ -\sqrt{\frac{3}{2}}e^{-2i\varphi} \end{pmatrix} + \frac{\alpha}{4}\begin{pmatrix} e^{2i\varphi} \\ -2e^{i\varphi} \\ \sqrt{6} \\ -2e^{-i\varphi} \\ e^{-2i\varphi} \end{pmatrix} e^{4it} = 0. \tag{8}$$

Passing to the system of equations and expressing the components, we obtain

$$\begin{aligned} -\frac{\alpha}{2}e^{i\varphi}e^{-4it} + \frac{\alpha}{2}e^{i\varphi}e^{4it} &= 0, \\ -\frac{\alpha}{2}e^{-i\varphi}e^{-4it} + \frac{\alpha}{2}e^{-i\varphi}e^{4it} &= 0, \\ -\frac{\alpha}{4}\sqrt{6}e^{-4it} + \frac{\beta}{2} + \frac{\alpha}{4}\sqrt{6}e^{4it} &= 0. \end{aligned} \tag{9}$$

Hence, from here we can conclude that a required moment of time is approximately $t \approx \pi/5$ That is, in the process of evolution quantum multimode states of the following form can arise

$$\alpha|200\rangle + \beta|020\rangle + \alpha|002\rangle. \tag{10}$$

In which the states $|011\rangle$ and $|110\rangle$. At the same time, we have determined a point in time at which the component $|020\rangle$ is absent in expression (10).

Conclusion

In this work, we have shown that a phase modulator performs electromagnetic field quantum state transformations that transcend the boundaries of local operations in quantum communication (LOCC) systems, inducing an essentially quantum channel for state transformation.

REFERENCES

1. **Miroshnichenko G.P., Kiselev A.D., Trifanov A.I., Gleim A.V.,** Journal of the Optical Society of America B. 34 (6) (2017) 1177–1183.

2. **Biedenharn L.C., Louck J.D.,** Angular momentum in quantum physics, Cambridge univerisity press, London. 1984.

3. **Tushavin G.V., Trifanov A.I., Zaitseva E.V.,** Nanosystems: Physics, Chemistry, Mathematics.13 (3) (2022) 299–307.

4. **Trifanov A.I., Miroshnichenko G.P.,** Nanosystems: Physics, Chemistry, Mathematics. 4 (5) (2013) 635–647.

5. **Gelfand I.D., Shapiro Z.Ya., Minlos R.A.,** Representations of the Rotation and Lorentz Groups and Their Applications, The Pergamon Press. 1963.

6. **Perelomov A.M.,** Generalized Coherent States and Their Applications, Springer. 1986.

THE AUTHORS

MATVEEVA Milena V.
mvmatveeva@itmo.ru
ORCID: 0009-0006-8671-1752

TUSHAVIN Gleb V.
tushavin@itmo.ru
ORCID: 0000-0002-6482-0951

TRIFANOV Alexander I.
alextrifanov@itmo.ru
ORCID: 0000-0002-5109-2086

TABIEVA Arina V.
tabieva.arina@itmo.ru
ORCID: 0009-0004-6560-7409

Received 01.08.2024. Approved after reviewing 25.09.2024. Accepted 25.09.2024.

ATOM PHYSICS AND PHYSICS OF CLUSTERS AND NANOSTRUCTURES

Conference materials
UDC 539.232; 542.06; 546–1; 544.654.2
DOI: https://doi.org/10.18721/JPM.173.226

The method of obtaining Ni and Co nanowires in porous anodic alumina matrices

E.A. Grushevsky✉, N.G. Savinsky, O.S. Trushin

[1]Valiev Institute of Physics and Technology of RAS, Yaroslavl Branch, Yaroslavl, Russia

✉ yaregor@mail.ru

Abstract. This paper focuses on the investigation of producing Ni and Co nanowire arrays synthesized using Al_2O_3 porous template. Porous alumina samples were obtained by double electrochemical anodizing of the prepared foil in 0.5 M oxalic acid, at a voltage of 60 V and a temperature of 25 °C. The pore diameter distribution maximums are about 85 nm. Nanowires were electrodeposited in a 3-electrode electrochemical cell into prepared matrices in a potentiostatic and galvanostatic mode. Studies of the surface of porous membranes and the geometry of nanowires were carried out using scanning electron microscope.

Keywords: anodization, aluminum oxide matrices, nanowires, electrochemical deposition

Funding: The work was carried out within the framework of the State program no. FFNN-2022-0018 of the Ministry of Science and Higher Education of Russia on the equipment of the center for the collective use of scientific equipment "Diagnostics of micro- and nanostructures".

Citation: Grushevsky E.A., Savinsky N.G., Trushin O.S. The method of obtaining Ni and Co nanowires in porous anodic alumina matrices, St. Petersburg State Polytechnical University Journal. Physics and Mathematics. 17 (3.2) (2024) 135–138. DOI: https://doi.org/10.18721/JPM.173.226

Материалы конференции
УДК 539.232; 542.06; 546–1; 544.654.2
DOI: https://doi.org/10.18721/JPM.173.226

Метод получения Ni и Co нанопроволок в матрицах пористого анодного оксида алюминия

Е.А. Грушевский✉, Н.Г. Савинский, О.С. Трушин

Ярославский филиал Физико-Технологического института РАН им. К.А. Валиева, г. Ярославль, Россия

✉ yaregor@mail.ru

Аннотация. Данная статья посвящена исследованию создания массивов нанопроволок Ni и Co, синтезированных с использованием пористого шаблона Al_2O_3. Образцы пористого оксида алюминия были получены методом двойного электрохимического анодирования подготовленной фольги в 0.5 М щавелевой кислоте, при напряжении 60 В и температуре 25 °C. Максимумы распределения пор по диаметру составляют около 85 нм. Нанопроволоки электроосаждались в 3-электродной электрохимической ячейке на подготовленные матрицы в потенциостатическом и гальваностатическом режимах. Исследования поверхности пористых мембран и геометрии нанопроволок проводились с помощью сканирующего электронного микроскопа.

Ключевые слова: анодирование, матрицы оксида алюминия, нанопроволоки, электрохимическое осаждение

Финансирование: Государственное задание ФТИАН им. К.А. Валиева РАН Минобрнауки РФ по теме № FFNN-2022-0018.

Ссылка при цитировании: Грушевский Е.А., Савинский Н.Г., Трушин О.С. Метод получения Ni и Co нанопроволок в матрицах пористого анодного оксида алюминия // Научно-технические ведомости СПбГПУ. Физико-математические науки. 2024. Т. 17. № 3.2. С. 135–138. DOI: https://doi.org/10.18721/JPM.173.226

Introduction

One of the best and most extensive methods for ensuring repeatability and high quality of the resulting nanostructures is the use of porous anodic aluminium oxide (PAAO) templates [1–3], in particular arrays for the growth of controlled, self-organizing, as well as highly ordered structures, including nanorods, nanowires, nanotubes, nanocomposite materials with strict adherence to product dimensions at a packing density of 10^9–10^{11} units/cm^2. Much attention has been drawn to the study of magnetic nanomaterials and nanostructures with strong shape anisotropy, promising for use in nanosensors, spintronic devices and high-density magnetic recording. It is known that one of the most common method obtaining such nanowires (NW) is a template synthesis – filling required material in narrow channels in porous matrices. The unique properties of porous anodic aluminum oxide (PAAO) membranes make this material potentially the best template for electrochemical deposition of Ni nanowires [4–5].

Materials and Methods

To produce porous matrices of aluminum oxide, we used 2×2 cm Al (99, 9% purity) plates with a 1 mm thickness. To obtain a smooth surface, the samples were electropolished, resulting in a mirror-like surface. Anodizing was carried out using 0.5 M oxalic acid with the temperature about 25 °C in a potentiostatic mode at 60 V. The duration of the first anodization was τ = 60 minutes, after which the oxide layer was removed in CrO_3 (1.8%) + H_3PO_4 (6%) at T = 80 °C for 10 minutes. Second anodization for all samples was carried out for 1 hour. Then the voltage was lowered to 5 V at a speed of 60 mV/s to thin the barrier layer out. In this work, aluminum was not removed, and the barrier layer was destroyed when the polarity was reversed at the beginning of the deposition process. [3] Ni nanowires were electrodeposited in a 3-electrode electrochemical cell using $NiSO_4 \cdot 7H_2O + NiCl_2 \cdot 6H_2O + H_3BO_3 + H_2O$ solution into prepared matrices in a galvanostatic mode at a current density of 75 mA/cm^2 for 10 minutes. Co nanowires were electrodeposited in a 3-electrode electrochemical cell using $CoSO_4 \cdot 7H_2O + CoCl_2 \cdot 6H_2O + H_3BO_3 + H_2O$ solution into prepared matrices in a potentiostatic mode at a voltage of 850 mV for 10 minutes.

Results and Discussion

Fig. 1, *a* shows an SEM image of the PAAO template before deposition. The SEM image of PAAO was further analyzed using ImageJ software, and pore diameter (D_p) = 85 ± 2.2 nm, pore distance (D_c) = 116 ± 5 nm and pore length (L_p) = 50 ± 1.5 microns were determined.

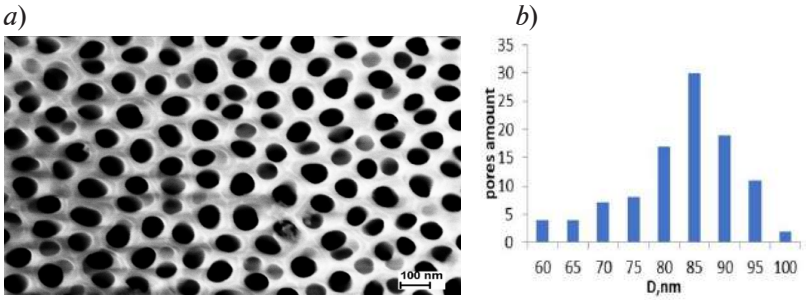

Fig. 1. SEM image of the PAAO template before deposition (*a*) with pores distribution (*b*)

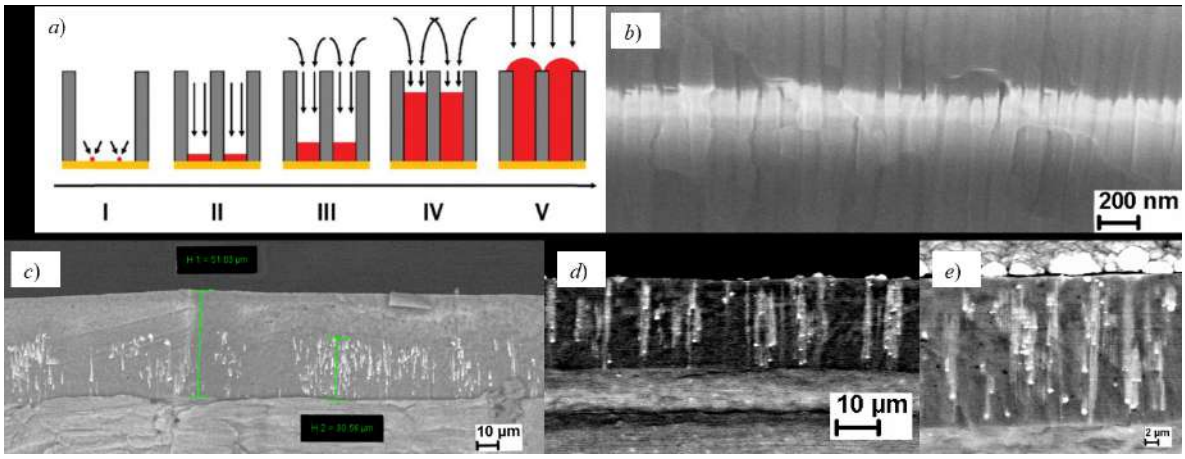

Fig. 2. Scheme of deposition process (*a*) [6], empty pores (*b*), SEM image of Ni nanowires on stage II-III (*c*), SEM image of Ni nanowires on stage IV (*d*), SEM image of Ni nanowires on stage V (*e*)

Fig. 2 shows a diagram of filling nanopores with metals during the electrodeposition process. This process can be divided into 5 conventional stages, the first of which is the formation of a seed at the bottom of the pore. Then metal begins to precipitate predominantly on this seed. The process continues until the pore is completely filled and ends with the release of metal to the surface in the form of a "cap". With further deposition, the metal is preferentially deposited on this cap, forming a continuous film and slowing down the deposition process in adjacent pores. This happens because the transport of the substance goes to the development of the emerging cap. The cap grows faster because planar diffusion towards the cap surface becomes greater than hemispherical diffusion in the pore. As a result, the diffusion current density decreases, while the total current increases due to the increase in surface area. The influence of the conditions of nanowire growth at the pore mouth and subsequent growth into a continuous horizontal layer has a very strong effect on the magnetic properties of nanowires. It is well known [7], that the magnetization vector of magnetic films lies in the plane of the magnetic film, but in nanowires shape anisotropy appears and the magnetization vector is directed perpendicular to the surface. Thus, in nickel agglomerations "caps" forming a film on the upper surface of PAAO, the magnetization vector is directed horizontally to the surface, which makes a significant contribution to the magnetization of the entire sample. Obviously, to direct the easy magnetization axis along the nickel nanowire, it is necessary to eliminate the growth of a horizontal nickel film on the surface of PAAO. There are two possible ways to form metal nanowires in a porous substrate: galvanic and potentiostatic. At the same time, the potentiostatic method is more applicable for growing multicomponent/segmented structures, and the galvanostatic method for monocomponent structures. Fig. 3 shows SEM images of nickel (Fig. 3, *a*) and cobalt (Fig. 3, *b*) nanowires obtained by galvanic and potentiostatic methods, respectively.

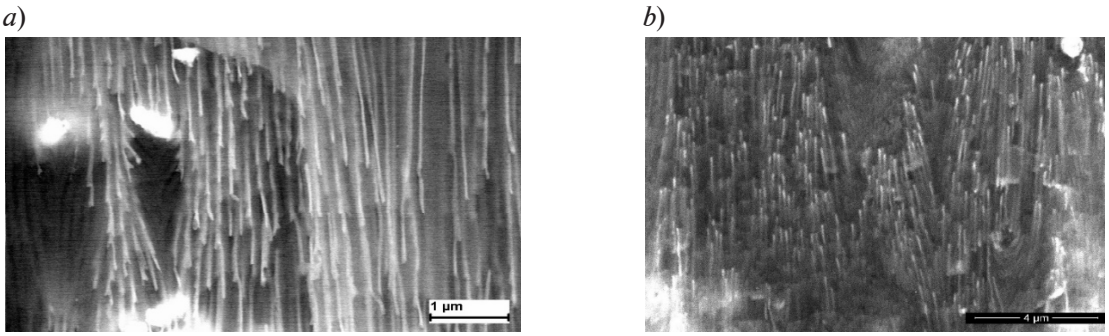

Fig. 3. SEM image of the PAAO template with nanowires of Ni (*a*) and Co (*b*)

The process of electrodeposition of nanowires must be carried out in such a way as to ensure uniform filling of all pores with metal. It is necessary to find the end point of the electrodeposition process, i.e., stop or sharply slow down the process of further metal deposition after the nanowire formed in the pore reaches the surface of the membrane.

Conclusions

Porous templates were obtained by double electrochemical anodizing in 0.5 M oxalic acid at a temperature of 25 °C in a potentiostatic mode at 60 V. A technological scheme for obtaining Ni and Co nanowires with 250 aspect ratio in porous anodic alumina matrices has been developed and were investigated by scanning electron microscopy.

Acknowledgments

The work was carried out within the framework of the State program № FFNN-2022-0018 of the Ministry of Science and Higher Education of Russia on the equipment of the center for the collective use of scientific equipment "Diagnostics of micro- and nanostructures".

REFERENCES

1. **Masuda H., Yamada H., Satoh M.,** Highly-ordered nanochannel-array architecture in anodic alumina, Appl. Phys. Lett. 71 (1997) 2770.

2. **Muratova E.N.,** Artificially and naturally ordered micro- and nanoscale capillary membranes based on anodic aluminum oxide: Ph.D. Thesis, St. Petersburg: ETU "LETI"/. (2014) 232.

3. **Vorobeva A.I., Utkina E.A., Komar O.M.,** Homogeneous deposition of nickel in the pore of ordered thin aluminum oxide, Russian Microelectronics. 42 (2013) 79–88.

4. **Safeer A., Ahmad N., Khan S., et al.,** Magnetization behavior of electrochemically synthesized Co2MnSn full Heusler alloy nanowire arrays, J. Appl. Phys. 125 (2019) 034302.

5. **Varvaro G., Casoli F.,** Ultrahigh–density magnetic recording storage materials and media designs, Stanford: Pan Stanford Publishing (2016) 509.

6. **Jaugstetter M., Blanc N., Kratz M., Tschulik K.,** Electrochemistry under confinement Chem. Soc. Rev. 51 (2022) 2491.

7. **Grushevski E.A., Savinski N.G., Trushin O.S., Shendrikova L.A.,** Magnetic Properties of Ni Nanowires in Porous Anodic Alumina Matrix Russian, Russian Microelectronics. 52 (2023) 67–70.

THE AUTHORS

GRUSHEVSKY Egor A.
yaregor@mail.ru

TRUSHIN Oleg S.
otrushin@gmail.com

SAVINSKY Nikolay G.
savinski1@yandex.ru
ORCID: 0000-0003-1913-0924

Received 30.07.2024. Approved after reviewing 12.08.2024. Accepted 13.08.2024.

Conference materials
UDC 539.27, 539.234
DOI: https://doi.org/10.18721/JPM.173.227

Study of the formation mechanisms of Ge terraces on Si(100) during MBE using the RHEED method

O.I. Kukenov✉, V.V. Dirko, K.A. Lozovoy,
A.P. Kokhanenko, A.V. Voitsekhovskii, X.A. Maier[1]

[1] National Research Tomsk State University, Tomsk, Russia

✉ okukenov@mail.ru

Abstract. In the work, a comparison of the widths of Ge and Si terraces on Si(100) at temperatures in the range from 200 °C to 800 °C was made using diffraction patterns in the [100] direction. The temperatures at which the growth mechanisms for the formation of monoatomic steps of Ge on Si(100) change have been established.

Keywords: molecular beam epitaxy, reflection high-energy electron diffraction, step-flow growth, heteroepitaxy

Funding: The study was carried out within the framework of the state assignment of the Ministry of Science and Higher Education of the Russian Federation, project no. FSWM-2020-0038.

Citation: Kukenov O.I., Dirko V.V., Lozovoy K.A., Kokhanenko A.P., Voitsekhovskii A.V., Maier X.A., Study of the formation mechanisms of Ge terraces on Si(100) during MBE using the RHEED method, St. Petersburg State Polytechnical University Journal. Physics and Mathematics. 17 (3.2) (2024) 139–142. DOI: https://doi.org/10.18721/JPM.173.227

Материалы конференции
УДК 539.27, 539.234
DOI: https://doi.org/10.18721/JPM.173.227

Изучение механизмов формирования террас германия на кремнии (100) при МПЭ методом ДБОЭ

О.И. Кукенов[1]✉, В.В. Дирко[1], К.А. Лозовой[1],
А.П. Коханенко[1], А.В. Войцеховский[1], К.А. Майер[1]

[1] Национальный исследовательский Томский государственный университет, г. Томск, Россия

✉ okukenov@mail.ru

Аннотация. В работе по картинам дифракции в направлении [100] проведено сравнение ширины террас Ge и Si на Si(100) при температурах в диапазоне от 200 °C до 800 °C. Установлены температуры, при которых происходит смена механизмов роста формирования моноатомных ступеней Ge на Si(100).

Ключевые слова: молекулярно-пучковая эпитаксия, дифракция быстрых отраженных электронов, рост по механизму сдвига ступеней, гетероэпитаксия

Финансирование: Исследование выполнено в рамках государственного задания Министерства науки и высшего образования Российской Федерации, проект № FSWM-2020-0038.

Ссылка при цитировании: Кукенов О.И., Дирко В.В., Лозовой К.А., Коханенко А.П., Войцеховский А.В., Майер К.А. Изучение механизмов формирования террас германия на кремнии (100) при МПЭ методом ДБОЭ // Научно-технические ведомости СПбГПУ. Физико-математические науки. 2024. Т. 17. № 3.2. С. 139–142. DOI: https://doi.org/10.18721/JPM.173.227

Introduction

Modern electronics require increasingly higher performance from components. Nanostructures, due to quantum effects, exhibit unique properties that enhance the capabilities of devices. Silicon, as an affordable semiconductor, is attracting attention in electronics, optoelectronics and solar energy. Germanium with a lattice that differs from silicon by 4.2% makes it possible to create Ge-Si nanostructures, such as quantum wells, wires and dots [1]. The parameters of these nanostructures depend on the synthesis conditions, including temperature, deposition rate, vacuum, and surface angle relative to the crystalline plane of the substrate. The growth of Ge on Si(100) obeys the Stranski–Krastanov mechanism, where the formation of nanoislands begins after the formation of a wetting layer [2]. This process is accompanied by surface changes associated with the movement of steps and the formation of $2\times N$ and $M\times N$ superstructures.

The mechanism of movement of steps during the deposition of Si on Si(100) has not been fully studied, but has theoretical and experimental foundations [3]. The article is devoted to the growth of germanium and silicon on a silicon substrate by the MBE method, specifically to the study of terrace formation at different growth temperatures by the RHEED method.

Materials and Methods

The experiments were carried out on a "Katun-100" molecular beam epitaxy (MBE) installation. The MBE method makes it possible to create pure nanostructures with a minimum number of defects, a sharp heterointerface and specified parameters [4]. After standard pre-epitaxial cleaning of the substrate and application of a 50 nm buffer layer, Ge was deposited on Si(100) at a rate of 0.02 ML/s. The surface morphology was studied by reflection high-energy electron diffraction (RHEED). RHEED is a universal method for obtaining in situ information about a surface and is used by scientists around the world [5]. The substrate was positioned so that the electron beam passed in the [100] direction to the Si(100) surface. Diffraction patterns on a luminescent screen were recorded with a video camera and analyzed using computer programs.

Pre-epitaxial cleaning of the substrate and application of a buffer layer make it possible to eliminate various defects associated with dislocations and impurities; however, atomic steps [6] associated with misorientation will inevitably be present on the surface. As is known, the homoepitaxial growth of Si on Si(100) occurs with the formation of alternating terraces of two types: T_A and T_B terraces with 1×2 and 2×1 superstructures with parallel and orthogonal orientation of dimer rows relative to the edge of the terrace [7]. The growth of Si on Si(100) leads to the fact that each subsequent layer on the terrace turns it into a terrace of the opposite type. At certain temperatures and growth rates, steps can double, and the width of terraces of one type significantly exceeds the width of terraces of another type [8].

When synthesizing Ge on Si(100), the width of the terraces has a great influence on the nucleation of quantum dots on them. Heteroepitaxial synthesis of Ge on Si(100) involves the formation of a wetting layer followed by a transition to 3D growth. In our study, we focused on the mechanisms of wetting layer formation taking into account the presence of monatomic steps on the Si(100) substrate. To do this, after the standard preparation of the plate described above, germanium was deposited onto the Si(100) surface with a misorientation angle of 0.1° at a rate of 0.02 ML/s at different temperatures.

Results and Discussion

In the course of studying the heteroepitaxial growth of Ge on Si(100) using the RHEED method in the [100] direction, the dependences of the ratio of the intensities of the 2×1 and 1×2 reflections ($I_{2\times1}$ and $I_{1\times2}$) on temperature were plotted (Fig. 1). These reflections were located in 1/2 of the

Laue zone. Each point in Fig. 1 corresponds to the maximum ratio of $I_{2\times1}$ to $I_{1\times2}$ during the growth process. The intensity ratio $I_{2\times1}/I_{1\times2}$ corresponds to the area ratio T_B/T_A [3, 9]. For ease of data perception, the "Gauss Fit" approximation method built into the Origin software package was used.

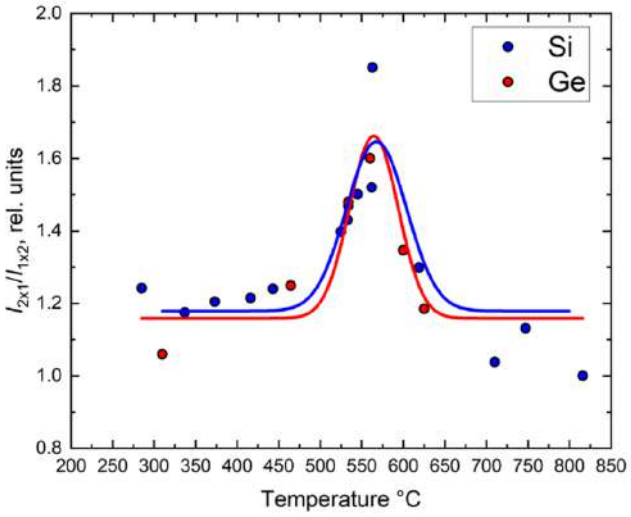

Fig. 1. Temperature dependences of the ratio of $I_{2\times1}$ to $I_{1\times2}$ during the synthesis of Si on Si(100) and Ge on Si(100)

Previously, the mechanism of formation of atomic steps by the RHEED method was studied during homoepitaxial growth of Si on Si(100). At growth temperatures from 200 to 500 °C, the atoms have an insufficient diffusion length to reach the step edges. The growth mechanism due to step displacement is practically not manifested, and the terrace overgrowth occurs due to the formation of two-dimensional islands. In the growth temperature range of 800–625 °C, each atom reaches the step edge and the growth is step-flow. And in the range from 500 to 625 °C, a transient process occurs [9].

As can be seen from Fig. 1, the temperature dependences of the intensity ratio during the growth of Ge and Si on Si(100) are similar. At temperatures of 200–500 °C, the atoms have a diffusion length that is insufficient to reach the terrace edges, since the terrace width ratio remains practically unchanged. In the temperature range of 500–550 °C, an increase in the terrace width ratio is observed, which indicates that one type of terrace (T_B) is overgrown faster than the other (T_A). This feature, as in the case of homoepitaxial growth of Si on Si(100), is caused, firstly, by the fact that the diffusion length of Ge atoms is sufficient to reach the terrace edges; secondly, atoms reaching the edge of the T_B terrace rich in kinks are easily embedded in it, and atoms at the smooth edge of the T_B terrace with a small number of kinks travel a longer path along the step before they find a kink; and, finally, in this temperature range, there is an effect of type A step permeability, when atoms can overcome the smooth A step and continue their path along the T_B terrace [9–10]. Therefore, near 550 °C, a critical point is observed at which one terrace significantly exceeds the other in area. After a temperature of 550 °C, the width of the terraces begins to equalize with increasing temperature. The steps move away because at the edge of the T_A step, Ge atoms with a large diffusion length can meet each other, thereby forming a new kink and accelerating the mechanism of incorporation of Ge atoms into a step of this type. As an alternative explanation, it can be assumed that after 550 °C, the atoms have enough energy to overcome the edge of the T_B terrace.

As shown by the similarity of the graphs in Fig. 1, the same growth mechanisms take place during epitaxial growth of two-dimensional Si and Ge layers on Si(100). In addition, the coincidence of the maxima of the two curves indicates that the diffusion length of Ge on Si(100) at a temperature of 550 °C is close to the diffusion length of Si on Si(100). Undoubtedly, at later stages of growth the processes become more complicated due to the presence of elastic stresses in the Ge/Si(100) system and the emergence of $2\times N$ type superstructures on the surface of the epitaxial layer during the deposition of several monolayers of germanium.

Conclusion

The formation mechanisms of Ge terraces on the Si(100) surface with a misorientation angle of 0.1° are complex. In general, during the growth of Ge/Si(100), the transition from the island mechanism of layer growth to the degree shift mechanism occurs at similar temperatures as during the growth of Si/Si(100) with a critical point of about 550 °C. The processes of terrace formation become more complicated with the emergence of elastic stresses in the system. The formation of the 2×*N* superstructure affects the intensity of the 2×1 and 1×2 reflections. This leads to difficulties in their interpretation. Despite the fact that the heteroepitaxial growth of Ge on Si(100) has been studied for a long time, some processes still remain unexplored. The results of this work are of a fundamental research nature. Studying the processes of formation of nanostructures based on Ge and Si will undoubtedly improve the quality of creating nanostructures with specified parameters for optoelectronic devices.

REFERENCES

1. **Arapkina L.V., Chizh K.V., Dubkov V.P., et al.,** Evolution of Ge wetting layers growing on smooth and rough Si (001) surfaces: Isolated {105} facets as a kinetic factor of stress relaxation, Applied Surface Science. 608 (2023) 155094.

2. **Douhan R., Lozovoy K., Kokhanenko A., et al.,** Recent Advances in Si-Compatible Nanostructured Photodetectors, Technologies. 11(1) (2023) 17.

3. **Yesin M.Y., Deryabin A.S., Kolesnikov A.V., Nikiforov A.I.,** Kinetics of Convergence the Si(100) Surface Steps. Phys. Solid State. 64 (2022) 609–615.

4. **Hajime A., Yoshiji H.,** Molecular Beam Epitaxy: Materials and Applications for Electronics and Optoelectronics, Wiley Series in Materials for Electronic & Optoelectronic Applications. 2019.

5. **Mohamed A.H., Mohamed K.Z., Hani E.E.-Ali,** Review: Geometric interpretation of reflection and transmission RHEED patterns, Micron. 159 (2022) 103286.

6. **Voigtländer B.,** Fundamental processes in Si/Si and Ge/Si epitaxy studied by scanning tunneling microscopy during growth, Surface Science Reports. 43 (5-8) (2001) 127–254.

7. **Mo Y.-W., Lagally M.G.,** Anisotropy in surface migration of Si and Ge on Si(001), Surface Science. 248 (3) (1991) 313–320.

8. **Sakamoto K., Sakamoto T., Miki K., Nagao S.,** Observation of Si (001) vicinal surfaces on RHEED, Journal of the Electrochemical Society. 136 (9) (1989) 2705.

9. **Kukenov O.I., Sokolov A.S., Dirko V.V., et al.,** Analysis of the temperature dependence of homoepitaxial growth of Si on Si by reflection high-energy electron diffraction, St. Petersburg State Polytechnical University Journal. Physics and Mathematics. 16 (3.1) (2023) 112–116.

10. **Hervieu Y.Y.,** Formation of Double Steps on Si (100): Effect of Permeability of the A-Steps, Russian Physics Journalthi. 63 (6) (2020) 901–906.

THE AUTHORS

KUKENOV Olzhas I.
okukenov@mail.ru
ORCID: 0000-0002-8189-3749

KOKHANENKO Andrey P.
kokh@mail.tsu.ru
ORCID: 0000-0002-7091-3011

DIRKO Vladimir V.
vovenmir@gmail.com
ORCID: 0009-0008-8052-3253

VOITSEKHOVSKII Alexander V.
vav43@mail.tsu.ru
ORCID: 0000-0002-1196-6199

LOZOVOY Kirill A.
lozovoymailbox@mail.ru
ORCID: 0000-0002-4029-8353

MAIER Xeniya A.
kseniamajer05@gmail.com
ORCID: 0009-0000-9839-894X

Received 26.07.2024. Approved after reviewing 16.08.2024. Accepted 17.08.2024.

Conference materials
UDC 538.975
DOI: https://doi.org/10.18721/JPM.173.228

Growth of long core-shell InGaN nanowires by plasma-assisted molecular beam epitaxy with gradually increasing substrate temperature

V.O. Gridchin[1,2,4]✉, T. Shugabaev[1,2,4], V.V. Lendyashova[1,2], K.P. Kotlyar[1,2,4], A.I. Khrebtov[2], A.S. Dragunova[3], N.V. Kryzhanovskaya[3], R.R. Reznik[2], G.E. Cirlin[1,2,4,5]

[1] Alferov University, St. Petersburg, Russia;

[2] St. Petersburg State University, St. Petersburg, Russia;

[3] National Research University Higher School of Economics, St. Petersburg branch, St. Petersburg, Russia;

[4] Institute for Analytical Instrumentation of the RAS, St. Petersburg, Russia;

[5] ITMO University, St. Petersburg, Russia

✉ gridchinvo@gmail.com

Abstract. This work presents the results of a study on the morphological and optical properties of InGaN nanowires grown using two different substrate temperature regimes. It is obtained that a gradual increase in the substrate temperature during the growth process makes it possible to obtain long morphologically homogeneous nanowires with a core-shell structure. The photoluminescence of nanowires is in the green range and is three times higher than that of similar structures grown in a stationary temperature regime.

Keywords: InGaN, nanowires, core-shell, MBE, photoluminescence, gradually increasing substrate temperature

Funding: The growth experiments and optical measurements were carried out under support of the Russian Science Foundation (project no. 23-79-00012). Optical measurements were performed, in part, in a large-scale research facility Complex Optoelectronic Stand operated by HSE University. For the morphological properties studies of grown samples the authors acknowledge Saint-Petersburg State University for a research project 95440344. Carrying out chemical etching procedures were supported by the Ministry of Science and Higher Education of the Russian Federation, research project no. 2019-1442 (project reference number FSER-2020-0013).

Citation: Gridchin V.O., Shugabaev T., Lendyashova V.V., Kotlyar K.P., Khrebtov A.I., Dragunova A.S., Kryzhanovskaya N.V., Reznik R.R., Cirlin G.E., Growth of long core-shell InGaN nanowires by plasma-assisted molecular beam epitaxy with gradually increasing substrate temperature, St. Petersburg State Polytechnical University Journal. Physics and Mathematics. 17 (3.2) (2024) 143–147. DOI: https://doi.org/10.18721/JPM.173.228

Материалы конференции
УДК 538.975
DOI: https://doi.org/10.18721/JPM.173.228

Выращивание длинных нитевидных нанокристаллов InGaN со структурой ядро-оболочка методом плазменно-активированной молекулярно-пучковой эпитаксии при постепенном повышении температуры подложки

В.О. Гридчин[1,2,4]✉, Т. Шугабаев[1,2,4], В.В. Лендяшова[1,2], К.П. Котляр[1,2,4], А.И. Хребтов[2], А.С. Драгунова[3], Н.В. Крыжановская[3], Р.Р. Резник[2], Г.Э. Цырлин[1,2,4,5]

[1] Академический университет им. Ж.И. Алфёрова РАН, Санкт-Петербург;

[2] Санкт-Петербургский государственный университет, Санкт-Петербург, Россия, Россия;

[3] Национальный исследовательский университет «Высшая школа экономики», Санкт-Петербургский филиал, Санкт-Петербург, Россия;

[4] Институт аналитического приборостроения РАН, Санкт-Петербург, Россия;

[5] Университет ИТМО, Санкт-Петербург, Россия

✉ gridchinvo@gmail.com

Аннотация. В данной работе представлены результаты исследования морфологических и оптических свойств нитевидных нанокристаллов InGaN, выращенных с использованием двух различных температурных режимов. Установлено, что постепенное повышение температуры подложки в процессе роста позволяет получать длинные морфологически однородные нитевидные нанокристаллы со структурой ядро-оболочка. Фотолюминесценция таких нитевидных нанокристаллов находится в зеленом диапазоне и в три раза выше, чем у аналогичных структур, выращенных в стационарном температурном режиме.

Ключевые слова: InGaN, нитевидные нанокристаллы, ядро-оболочка, МПЭ, фотолюминесценция, постепенное повышение температуры

Финансирование: Ростовые эксперименты и исследования оптических свойств выполнены при поддержке Российского Научного Фонда (РНФ) (проект номер 23-79-00012). Оптические измерения проводились на исследовательской установке «Комплексный оптоэлектронный стенд» НИУ ВШЭ. Исследования морфологических свойств выращенных образцов были выполнены при поддержке СПбГУ, шифр проекта 95440344. Процедуры химического травления были проведены при поддержке Министерства науки и высшего образования Российской Федерации, проект тематики научных исследований № 2019-1442 (код научной темы FSER-2020-0013).

Ссылка при цитировании: Гридчин В.О., Шугабаев Т., Лендяшова В.В., Котляр К.П., Хребтов А.И., Драгунова А.С., Крыжановская Н.В., Резник Р.Р., Цырлин Г.Э. Выращивание длинных нитевидных нанокристаллов InGaN со структурой ядро-оболочка методом плазменно-активированной молекулярно-пучковой эпитаксии при постепенном повышении температуры подложки // Научно-технические ведомости СПбГПУ. Физико-математические науки. 2024. Т. 3.2 № .17. С. 143–147. DOI: https://doi.org/10.18721/JPM.173.228

Introduction

InGaN binary and ternary compounds are important solids for new-generation optoelectronic devices due to their direct band gap and the possibility to tune a band gap energy from ~ 0.7 to 3.4 eV [1]. However, InGaN ternary compounds with a high In content (In > 30 %) tend to phase decomposition because of the notable difference in bond lengths between In-N and Ga-N (miscibility gap) [2]. This feature complicates the growth of InGaN thin films on the commercially available substrates (c-Al_2O_3, SiC, Si) and results in poor crystal quality of the InGaN thin films with high In content.

A promising method for the fabrication of InGaN ternary compounds with high In content and high crystal quality is the growth of nanowires (NWs) [3]. Recently, we have revealed a novel type of InGaN NWs with spontaneously formed core-shell structure directly grown on Si substrate by plasma-assisted molecular beam epitaxy (PA-MBE) [4, 5]. As it was shown, this type of structures is highly sensitive to the local III/N flux ratio and growth temperature which complicates the fabrication of homogeneous nanowires with needful properties [6]. In the present work, we study an approach to grow morphologically homogeneous long InGaN NWs with core-shell structure by gradually increasing substrate temperature during the growth.

Materials and Methods

The growth experiments were carried out on a Riber Compact 12 MBE system equipped with an Addon RF-N 600 plasma source and effusion cells of Ga and In. The (111)-oriented silicon substrates with n-type conductivity were used. Before the growth the substrates were etched in $HF:H_2O$ solution and thermally annealed at 850 °C for 20 min in the growth chamber for silicon oxide removing. The growth experiments were carried out under slightly nitrogen-rich growth conditions. The beam equivalent pressures of the In and Ga sources were equal to each other and corresponded to $1 \cdot 10^{-7}$ Torr. In the first case, we carried out growth with stationary substrate temperature which consisted of 650 °C. The growth time corresponds to 51h. In the second case, we gradually increased substrate temperature after 21h of the growth process. The rate of the increase of substrate temperature was 1 °C per hour.

A study of the morphology properties was conducted via a Carl Zeiss Supra 25 scanning electron microscopy (SEM) system. The optical properties of the samples are investigated using photoluminescence (PL) spectroscopy at room temperature with a He-Cd laser (325 nm) and pump power of 6.5 mW and silicon photodetector. The polarity of long InGaN NWs was determined by wet chemical etching of NWs in a $KOH:H_2O$ solution according to the method described in [7]. The etching time was 40 seconds.

Results and Discussion

Fig. 1, *a*, *b* demonstrates typical SEM images in cross-section and plan view of InGaN nanowires grown at a stationary substrate temperature (Fig. 1, *a*) and gradually increasing substrate temperature (Fig. 1, *b*). On the left side, the substrate temperature change graphs are presented. Three-dimensional nanostructures consisting of nanowires near the substrate surface and partly-coalesced nanostructures above are obtained in the stationary growth regime (Fig. 1, *a*). These nanostructures correspond to similar ones grown at lower substrate temperatures [6]. The formation mechanism of them can be explained by the decreasing effective temperature on the growth surface with increasing the height of nanostructures. To eliminate the influence of the effective growth temperature, the substrate temperature was gradually increased starting from 21 h of growth. In this growth regime, the formation of morphologically homogeneous NWs with height of about 7.5 μm was achieved (Fig. 1, *b*). From the plan-view SEM image "cracks" are visible that definitely indicate the spontaneously formed core-shell structure within the NWs [5].

To identify the polarity of long core-shell InGaN NWs they were treated in the KOH solution [7]. For the first time, it was obtained that the cores and shells of NWs exhibit a Me-polarity and N-polarity, respectively.

Fig. 1, *c* demonstrates room-temperature PL spectra of grown samples. The PL spectrum consisting of relatively low-intensive areas in the range from 350 to 750 nm was obtained for the sample grown at the stationary temperature regime (green line in Fig. 1, *c*) that explained by the formation of InGaN nanostructures with different indium content. The relatively homogeneous PL spectrum with a maximum at 540 nm and corresponding full-width at half-maximum

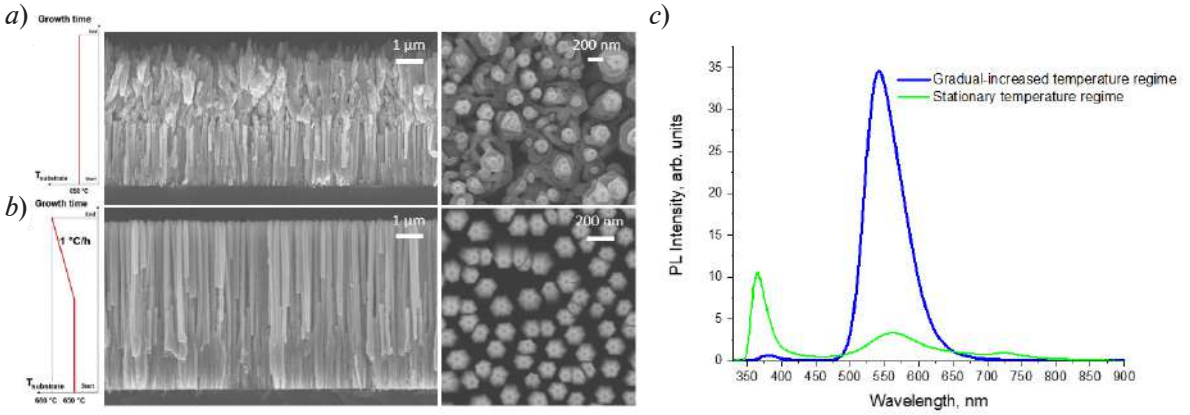

Fig. 1. Typical SEM images in cross-section view and plan-view of InGaN nanowires grown at stationary substrate temperature (*a*) and gradual-increased substrate temperature (*b*). Room-temperature PL spectra of grown samples (*c*). On the left side, the substrate temperature change graphs are presented

about 64 nm was obtained in the gradual-increased temperature regime (blue line in Fig. 1, *c*). Moreover, the integral PL intensity of these NWs is 3 times higher than that of nanostructures grown at stationary temperature regime. A relatively low-intensity PL area near 380 nm corresponds to the emission from the shell of NWs.

Conclusion

In this work, the results of studies on the morphological and optical properties of InGaN nanowires grown at two different substrate temperature modes were presented. It was obtained that using gradual-increased temperature growth allows one to fabricate morphological homogeneous long NWs with core-shell structure. The PL spectrum of these NWs corresponds to the green range and 3 times higher than similar ones for nanostructures grown at steady-state temperature growth mode. The results obtained could provide valuable data in the field of nanomaterials engineering.

REFERENCES

1. **Pandey A., Reddeppa M., Mi Z.,** Recent progress on micro-LEDs, Light: Advanced Manufacturing. 4 (2024) 519–542.

2. **Ho I., Stringfellow G.,** Solid phase immiscibility in GaInN, Applied Physics Letters. 69 (18) (1996) 2701–2703.

3. **Dubrovskii V., Cirlin G., Ustinov V.,** Semiconductor nanowhiskers: synthesis, properties, and applications, Semiconductors. 43 (2009) 1539–1584.

4. **Gridchin V.O., Kotlyar K.P., Reznik R.R., et al.,** Multi-colour light emission from InGaN nanowires monolithically grown on Si substrate by MBE, Nanotechnology. 32 (33) (2021) 335604.

5. **Soshnikov I.P., Kotlyar K.P., Reznik R.R., et al.,** Specific Features of Structural Stresses in InGaN/GaN Nanowires, Semiconductors. 55 (10) (2021) 795–798.

6. **Reznik R.R., Gridchin V.O., Kotlyar K.P., et al.,** Synthesis of morphologically developed InGaN nanostructures on silicon: influence of the substrate temperature on the morphological and optical properties, Semiconductors. 54 (2020) 1075–1077.

7. **Lendyashova V.V., Kotlyar K.P., Reznik R.R., et al.,** Wet chemical etching of GaN or InGaN nanowires on Si substrate for micro and nano-devises fabrication. 1695 (1) (2020) 012047.

THE AUTHORS

GRIDCHIN Vladislav O.
gridchinvo@gmail.com
ORCID: 0000-0002-6522-3673

SHUGABAEV Talgat
talgashugabaev@mail.ru
ORCID: 0000-0002-4110-1647

LENDYASHOVA Vera V.
erilerican@gmail.com
ORCID: 0000-0001-8192-7614

KOTLYAR Konstantin P.
konstantin21kt@gmail.com
ORCID: 0000-0002-0305-0156

KHREBTOV Artem I.
khrebtovart@mail.ru

DRAGUNOVA Anna S.
anndra@list.ru
ORCID: 0000-0002-0181-0262

KRYZHANOVSKAYA Natalia V.
nataliakryzh@gmail.com
ORCID: 0000-0002-4945-9803

REZNIK Rodion R.
moment92@mail.ru
ORCID: 0000-0003-1420-7515

CIRLIN George E.
george.cirlin@mail.ru
ORCID: 0000-0003-0476-3630

Received 23.07.2024. Approved after reviewing 12.08.2024. Accepted 12.08.2024.

Conference materials
UDC 504.064.3
DOI: https://doi.org/10.18721/JPM.173.229

Electrical properties of ZnO/Au and ZnO/SnO_2 nanorod arrays when exposed to UV irradiation with controlled intensity

A.P. Starnikova✉, V.V. Petrov

Institute of Nanotechnologies, Electronics, and Equipment Engineering, Southern Federal University, Taganrog, Russia;

✉a.starnikova@mail.ru

Abstract. Arrays of zinc oxide (ZnO) nanorods were synthesized on quartz substrates by the hydrothermal method. The nanorods were grown mainly in a vertical orientation, had a length of 500–800 nm and an average cross-sectional size of 40–80 nm. Gold nanoclusters with average sizes of 9 ± 1 nm and 4 ± 0.5 nm and tin with average sizes of 30 ± 5 nm and 15 ± 3 nm were formed on top of the ZnO nanorods. Annealing was carried out at 300 °C for 2 hours with the formation of arrays of ZnO/SnO_2 nanorods. For the manufacture of resistive sensor elements, V/Ni contact metallization was applied on top of the samples. The study of the electrophysical characteristics of the ZnO/Au and ZnO/SnO_2 nanorods arrays showed that exposure to UV radiation of different intensity leads to a change in the electrical resistance of the sensor structure, and also affects the time of establishing the readings of the obtained samples.

Keywords: ZnO, nanorods, electrophysical properties, ultraviolet irradiation

Funding: This study was supported by the Russian Science Foundation under grant no. 23-29-00742, (https://rscf.ru/en/project/23-29-00742/) at the Southern Federal University.

Citation: Starnikova A.P., Petrov V.V., Electrical properties of ZnO/Au and ZnO/SnO_2 nanorod arrays when exposed to UV irradiation with controlled intensity, St. Petersburg State Polytechnical University Journal. Physics and Mathematics. 17 (3.2) (2024) 148–151. DOI: https://doi.org/10.18721/JPM.173.229

Материалы конференции
УДК 504.064.3
DOI: https://doi.org/10.18721/JPM.173.229

Электрофизические свойства массивов ZnO/Au и ZnO/SnO_2 наностержней при воздействии УФ-излучения с регулируемой интенсивностью

А.П. Старникова✉, В.В. Петров

Институт нанотехнологий, электроники и приборостроения (ЮФУ), Таганрог, Россия

✉ a.starnikova@mail.ru

Аннотация. Массивы наностержней оксида цинка (ZnO) были синтезированы на кварцевых подложках гидротермальным методом. Наностержни были выращены преимущественно вертикальной ориентации, имели длину 800–500 нм и средний размер поперечного сечения 80–40 нм. Поверх наностержней ZnO формировались нанокластеры золота со средними размерами 9 ± 1 нм and 4 ± 0.5 нм и олова со средними размерами 30 ± 5 нм и 15 ± 3 нм. Отжиг проводился при 300 °C в течение 2 ч с образованием массивов ZnO/SnO_2 наностержней. Для изготовления резистивных сенсорных элементов поверх образцов была нанесена V/Ni контактная металлизация.

Исследование электрофизических характеристик массивов ZnO/Au и ZnO/SnO_2 наностержней показало, что воздействие УФ-излучения разной интенсивности приводит к изменению электрического сопротивления сенсорной структуры, а также влияет на время установления показаний полученных образцов.

Ключевые слова: ZnO, наностержни, электрофизические свойства, ультрафиолетовое облучение

Финансирование: Работа выполнена при поддержке Российского научного фонда в рамках гранта № 23-29-00742 (https://rscf.ru/ru/project/23-29-00742/) в Южном федеральном университете.

Ссылка при цитировании: Старникова А.П., Петров В.В. Электрофизические свойства массивов ZnO/Au и ZnO/SnO_2 наностержней при воздействии УФ-излучения с регулируемой интенсивностью // Научно-технические ведомости СПбГПУ. Физико-математические науки. 2024. Т. 17. № 3.2. С. 148–151. DOI: https://doi.org/10.18721/JPM.173.229

Introduction

Zinc oxide (ZnO) is a promising metal oxide that is widely used as a sensitive layer in chemoresistive sensors [1]. One of the ways to increase the selectivity of semiconductor oxides is to modify their surface with metal nanoparticles and metal oxides, for example Au and SnO_2. It is known that when UV radiation is applied to gas-sensitive materials, the higher the radiation intensity, the higher the response [2]. However, the impact of radiation with an intensity above 500 μW/cm^2 on gas molecules can lead to the destruction of molecules [3]. At the same time, when measuring the gas-sensitive properties of the materials under study with simultaneous exposure to gas and UV radiation, it is necessary to know the time of establishing equilibrium between and recombination of charge carriers (photo-response time). Studies of the electrophysical characteristics of ZnO/Au and ZnO/SnO_2 nanorods arrays under the influence of UV radiation with adjustable intensity in the range from 55 to 133 μW/cm^2 have not yet been conducted. These studies are the purpose of this work.

Materials and Methods

Arrays of ZnO nanorods were synthesized by the hydrothermal method on quartz substrates. The obtained samples had mainly nanorods with a length of 500-800 nm and an average cross-sectional size of 40-80 nm. Gold nanoclusters with average sizes of 9 ± 1 nm (ZnO/Au sample (1)) and 4 ± 0.5 nm (ZnO/Au sample (2)) were formed on top of ZnO nanorods by vacuum thermal evaporation. A similar number of samples were obtained by tin spraying. For tin, the calculated nanocluster sizes were 30 ± 5 nm (sample ZnO/SnO_2 (1)) and 15 ± 3 nm (sample ZnO/SnO_2 (2)). For the final formation and stabilization of the electrophysical characteristics of ZnO/Au and ZnO/SnO_2 nanostructures, annealing was performed at a temperature of 300 °C for 2 hours [4]. Further, for the manufacture of sensor elements on top of nanorods, V/Ni contact metallization with a metal layer thickness of 0.2 microns was formed by thermal vacuum evaporation.

Results and Discussion

Studies of the electrophysical properties of the obtained samples were carried out on a hardware and software measuring complex that allows measurements of the electrophysical characteristics of sensory structures, including when exposed to UV radiation [5]. Previously, we estimated the relaxation time constant of photoconductivity (τ) when exposed to UV radiation with a wavelength of 400 nm and a radiation intensity of 133 μW/cm^2 [4]. The time constant values were similar for the ZnO/SnO_2(1) and ZnO/SnO_2(2) samples and ranged from 8 to 12 s. For the samples

ZnO/Au(1) and ZnO/Au(2), the time constant values were close to 10 and 8 s. Large values of τ correspond to large values of E_a and φ_b. This indicates the influence of the activation energy of the conductivity and the potential barrier of the ZnO nanostructure on the current transfer mechanism. The data obtained also indicate that it is necessary to wait more than 3 minutes to stabilize the resistance of the gas sensor after turning on the UV radiation.

In this work, additional studies were carried out in which the samples were irradiated with UV radiation from an LED with a wavelength of 400 nm with an adjustable radiation intensity from 55 to 133 μW/cm^2. Fig. 1 shows the dependences of the resistance (R) of the studied samples on the time of exposure to UV radiation of different intensities. The photoconductivity was estimated as a change in the resistance of the sample of the Ri nanorods over time after 0 s. The resistance values were normalized by the resistance R_0. The measurements were carried out before the curves were flattened.

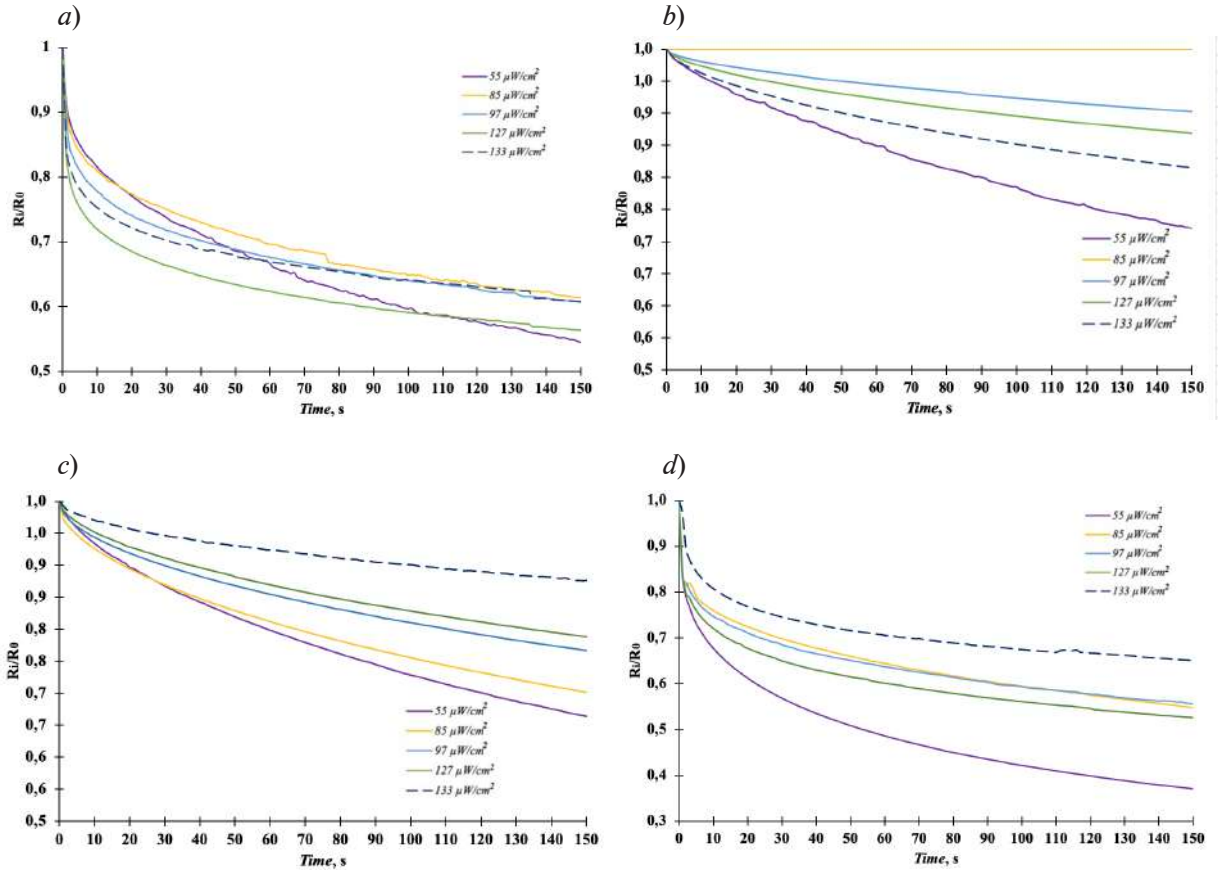

Fig. 1. Dependence of the resistance of samples ZnO/SnO_2(1) (*a*), ZnO/SnO_2(2) (*b*), ZnO/Au(1) (*c*), ZnO/Au(2) (*d*) on the time of exposure to UV radiation with an adjustable intensity of 55 μW/cm^2 (purple lines), 85 μW/cm^2 (yellow lines), 97 μW/cm^2 (blue lines), 127 μW/cm^2 (green lines), 133 μW/cm^2 (blue lines)

Studies have shown that when exposed to ZnO/Au and ZnO/SnO_2 samples of UV nanorods, their electrical conductivity increases due to the generation of photoexcited charge carriers. This leads to an activated state of the surface due to an increase in the concentration of free electrons. The estimation of the photo response time was carried out by the time 90% of the maximum change of signal value was reached. The photo-response times for the sample when exposed to UV radiation with an intensity of 55, 85, 97, 127 and 133 μW/cm^2 are calculated in Table 1.

It can be seen from the data in Table 1 that the onset of balance between the generation of charge carriers by UV radiation and their recombination occurs faster in samples with large tin nanoclusters and smaller gold nanoclusters.

Table 1

Sample	Photo response time (s) when exposed to UV radiation with adjustable intensity				
	55 μW/cm^2	85 μW/cm^2	97 μW/cm^2	127 μW/cm^2	133 μW/cm^2
ZnO/SnO_2(1)	123	96	92	77	87
ZnO/SnO_2(2)	125	141	126	124	124
ZnO/Au(1)	122	122	120	121	122
ZnO/Au(2)	91	102	92	86	84

Conclusion

The conducted studies have shown that an increase in the intensity of UV radiation from 55 to 133 μW/cm^2 causes an increase in the electrical conductivity of the studied samples. The onset of equilibrium between the generation of charge carriers by UV radiation and their recombination occurs faster in samples with large tin nanoclusters and smaller gold nanoclusters. The ZnO/SnO_2(1) sample with an average tin nanocluster size of 30 ± 5 nm has the shortest photo-response time.

Acknowledgments

Electrophysics measurements were conducted using equipment from the Centre for Collective Use, Microsystem Technics and Integral Sensors, Southern Federal University (SFedU).

REFERENCES

1. **Que M., Lin C., Sun J., et al.,** Progress in ZnO nanosensors. Sensors. 21 (16) (2021) 5502.

2. **Chinh N.D., Hien T.T., Do Van L., et al.,** Adsorption/desorption kinetics of nitric oxide on zinc oxide nano film sensor enhanced by light irradiation and gold-nanoparticles decoration. Sens. Actuators B Chem. 281 (2019) 262–272.

3. **Chizhov A.S., Rumyantseva M.N., Gaskov A.M.,** Light Activation of Nanocrystalline Metal Oxides for Gas Sensing: Principles, Achievements, Challenges. Nanomaterials. 11 (4) (2021) 892.

4. **Ivanisheva A.P., Sysoev V.V., Abdullin Kh. A., et al.,** The Application of Combined Visible and Ultraviolet Irradiation to Improve the Functional Characteristics of Gas Sensors Based on ZnO/SnO_2 and ZnO/Au Nanorods. Chemosensors 11 (3) (2023) 200.

5**. Gulyaeva I.A., Ivanisheva A.P., Volkova M.G., et al.,** Investigation of electrophysical, photo- and gas-sensitive properties of ZnO–SnO_2 sol–gel films J. Adv. Dielect. (14) (1) (2024) 2245002.

THE AUTHORS

STARNIKOVA Alexandra P.
a.starnikova@mail.ru
ORCID: 0000-0002-3779-8242

PETROV Viktor V.
vvpetrov@sfedu.ru
ORCID: 0000-0003-3725-6053

Received 23.07.2024. Approved after reviewing 26.08.2024. Accepted 28.08.2024.

Conference materials
UDC 621.315.592
DOI: https://doi.org/10.18721/JPM.173.230

Influence of in-situ plasma treatment during PE-ALD of GaN on growth rate and morphology

A.A. Maksimova[1]✉, A.V. Uvarov[2], E.A. Vyacheslavova[2], A.I. Baranov[2], E.Y. Yarchuk[1], A.S. Gudovskikh[2]

[1] St. Petersburg Electrotechnical University "LETI", St. Petersburg, Russia;

[2] Alferov University, St. Petersburg, Russia

✉ deer.blackgreen@yandex.ru

Abstract. In this work, the plasma-enhanced atomic layer deposition (PE-ALD) technique, including continuous hydrogen plasma, was studied for GaN growth. Also, the use of plasma at the nitrogen step only as well as argon plasma surface activation were explored. The structural properties of GaN layers grown on Si substrates at different conditions were studied by atomic force microscopy (AFM). It was shown that in-situ Ar plasma treatment during the PE-ALD process of GaN growth leads to improvement of the surface roughness as well as an increase in growth rate. On the contrary, the use of hydrogen plasma during the process leads to a drastic increase in surface roughness due to parasitic deposition.

Keywords: gallium nitride, plasma treatment, atomic layer deposition

Funding: The research was supported by the Russian Science Foundation Grant no. 24-29-00735, https://rscf.ru/project/24-19-00150/.

Citation: Maksimova A.A., Uvarov A.V., Vyacheslavova E.A., Baranov A.I., Yarchuk E.Y., Gudovskikh A.S., Influence of in-situ plasma treatment during PE-ALD of GaN on growth rate and morphology, St. Petersburg State Polytechnical University Journal. Physics and Mathematics. 17 (3.2) (2024) 152–156. DOI: https://doi.org/10.18721/JPM.173.230

Материалы конференции
УДК 621.315.592
DOI: https://doi.org/10.18721/JPM.173.230

Влияние плазменной обработки in situ при атомно-слоевом осаждении GaN на скорость роста и морфологию пленки

А.А. Максимова[1]✉, А.В. Уваров[2], Е.А. Вячеславова[2], А.И. Баранов[2], Э.Я. Ярчук[1], А.С. Гудовских[2]

[1] Санкт-Петербургский государственный электротехнический университет «ЛЭТИ» им. В.И. Ульянова (Ленина), Санкт-Петербург, Россия;

[2] Академический университет им. Ж.И. Алфёрова РАН, Санкт-Петербург, Россия

✉ deer.blackgreen@yandex.ru

Аннотация. В данной работе для выращивания GaN был использован метод плазменного атомно-слоевого осаждения (PE-ALD) с непрерывной водородной плазмой. Также было исследовано использование плазмы только на этапе осаждения монослоя азота, а также активация поверхности аргоновой плазмой. Методом атомно-силовой микроскопии (АСМ) исследованы структурные свойства слоев GaN, выращенных на подложках Si в различных условиях. Было показано, что плазменная обработка Ar in situ в процессе PE-ALD роста GaN приводит к улучшению шероховатости поверхности,

а также к увеличению скорости роста. Напротив, использование водородной плазмы в процессе приводит к резкому увеличению шероховатости поверхности за счет паразитных осаждений.

Ключевые слова: нитрид галлия, плазменная обработка, атомно-слоевое осаждение

Финансирование: Работа выполнена в рамках проекта РНФ № 24-29- 00735, https://rscf.ru/project/24-19-00150/.

Ссылка при цитировании: Максимова А.А., Уваров А.В., Вячеславова Е.А., Баранов А.И., Ярчук Э.Я., Гудовских А.С. Влияние плазменной обработки in situ при атомно-слоевом осаждении GaN на скорость роста и морфологию пленки // Научно-технические ведомости СПбГПУ. Физико-математические науки. 2024. Т. 3.2 № .17. С. 152–156. DOI: https://doi.org/10.18721/JPM.173.230

Introduction

The efficiency of solar cells based on monocrystalline Si has already approached the theoretical limit. Further development of photoelectric conversion of solar radiation requires increasing efficiency. The efficiency of solar energy conversion is limited by losses, some of which are of a fundamental nature. The strongest limitation on the maximum achievable efficiency of single-junction solar cells comes from carrier the thermalization losses, where excess photon energy transferred to the generated charge carriers is transferred to thermal vibrations of the lattice. The most effective approach to reducing losses due to thermalization of charge carriers consists of the formation of tandem (multijunction) solar cells.

GaP-based diluted nitride is a potential material for tandem III-V/Si solar cells [1]. However, a low-temperature mass production technology is more preferable for its successful photovoltaic application.

Among a wide variety of semiconductor growth methods, atomic layer deposition (ALD) has several advantages, such as high-quality uniform deposition on large areas, conformal layer growth on textured surfaces with a high aspect ratio. Due to these advantages, the layers obtained by this method are currently used in the fields of nanoelectronics, photonics, and photovoltaics [2, 3]. ALD can be used to create thin layers of material over large areas with high throughput, which is one of the main advantages for photovoltaic applications.

To avoid the problem of nitrogen incorporation control, a sub-monolayer digital alloy (SDA) approach to PE-ALD process was successfully applied to improve the control of nitrogen incorporation into GaPN [4]. Using a combination of a sequence of layers in the form of short-period superlattices (digital alloys), GaN/GaP allowed for precise control of the band gap with compensation of elastic stresses arising from the difference in the lattice constant. However, the growth rate and morphology of the GaN layers should be precisely controlled during the growth of the short-period superlattices.

Recently, the use of in-situ annealing in argon plasma was shown to improve the crystalline quality at the epitaxial level of AlN [5] and GaP [6] layers obtained by PE-ALD. Here we explore the influence on the growth rate and morphology of GaN layers using PE-ALD at temperatures below 400 °C using in-situ annealing in hydrogen and argon plasma.

Materials and Methods

To form the required structures, Oxford Instruments Plasmalab 100 PECVD with capacitive coupled RF (13.56 MHz) plasma equipment with the ability to control the precursor flow rate, heater table temperature, and capacitance-coupled plasma RF power was used. The system was evacuated with a BOC Edwards iH600 dry vacuum pump to a minimum pressure of <1 mTorr. Immediately before the beginning of the deposition process, the c-Si substrates were treated in a 10% HF/H_2O solution to remove the natural oxide and hydrogenate the surface.

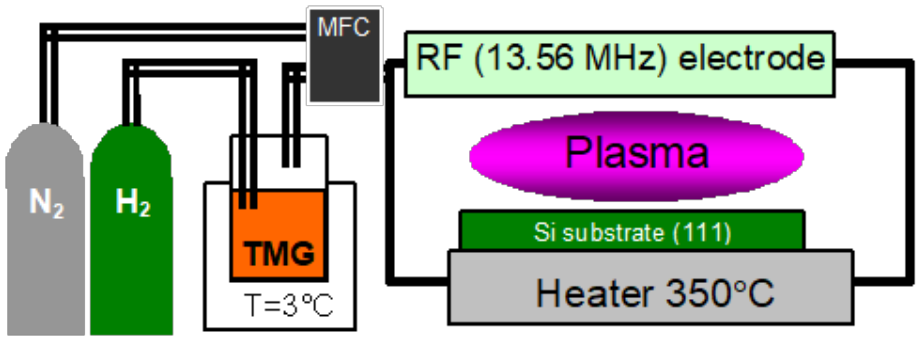

Fig. 1. Schematic representation of deposition chamber

Deposition of GaN layers was carried out at 350 °C on crystalline p-type Si substrates (111). A metalorganic precursor of gallium, trimethylgallium ($Ga(CH_3)_3$, TMG) 8% diluted in hydrogen (H_2) was entered into the chamber using a bubbling system; H_2 was used as a gas carrier with chamber pressure at 350 mTorr (see Fig. 1).

To realize the PE-ALD process, the Ga monolayer was followed by the N_2 plasma step, leading to the formation of the GaN sub-monolayer. The schematic presentation of the PE-ALD process without and with Ar in-situ plasma treatment (Fig. 2, *a*, *b*). After exposure to each precursor, the chamber was purged with argon to avoid mixing precursors and parasitic CVD growth. Continuous hydrogen plasma mode with RF power increase was also used to guarantee ignition and hold of discharge.

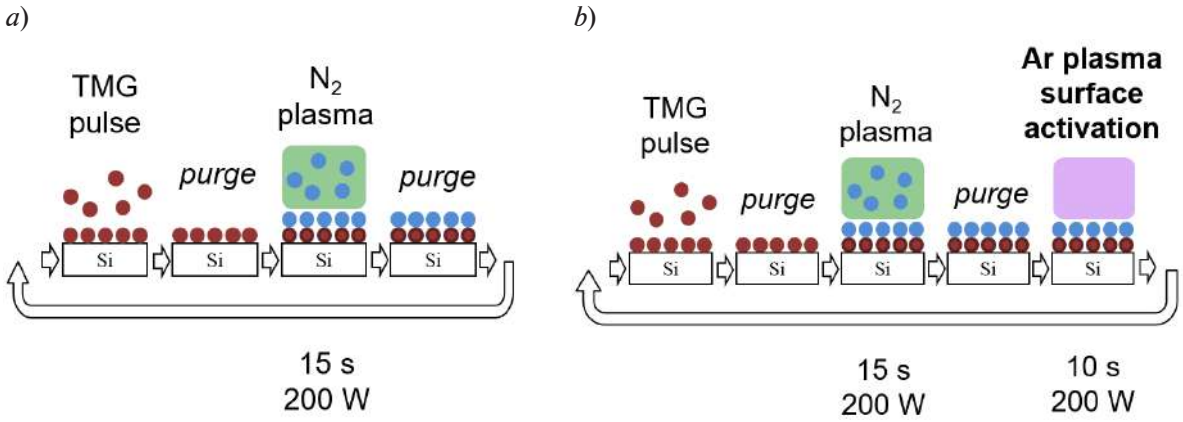

Fig. 2. PE-ALD realization of GaN growth (*a*) with Ar in-situ plasma treatment (*b*)

To study structural properties and surface morphology, an image of the GaN layer deposited on a silicon substrate was obtained using scanning electron microscopy (SEM) from a Zeiss Supra 25 set-up. Furthermore, film surface roughness was studied by atomic force microscopy (AFM) using the BioScope Catalyst Bruker setup.

Results and Discussion

An SEM image of GaN film grown by PE-ALD with continuous H_2 plasma is presented in Fig. 3. The GaN layer grown by PE-ALD with continuous hydrogen plasma has a rough surface and a film thickness of 40 nm.

The AFM 3D topology images of the 40 nm thick GaN samples are presented in Figure 4. The growth rate and surface roughness strongly depend on plasma treatment. Growth per cycle (GPC) and root mean square (RMS) roughness are equal to 0.095 nm/cycle and 0.49 nm, respectively, for PE-ALD without plasma, while Ar in-situ plasma treatment leads to GPC increasing to 0.185 nm/cycle and RMS decresing to 0.38 nm. Such behaviour is associated with local surface heating, which leads to the enhancment of gallium precursor mobility.

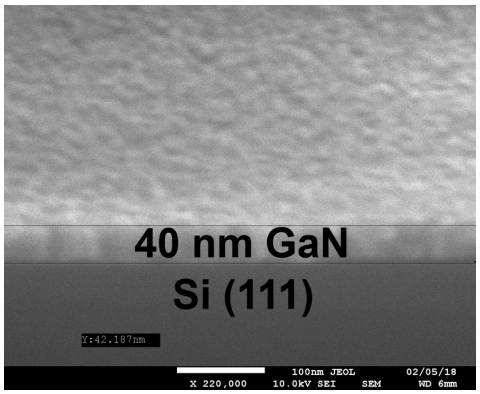

Fig. 3. SEM image of PE-ALD grown GaN film

Continuous hydrogen plasma treatment leads to GPC rising to about 0.2 nm/cycle while the surface roughness increases (Fig. 4, *c*) with an RMS of 1.19 nm. The parasitic deposition during hydrogen plasma treatment is supposed to occur in this case (all data are presented in Table 1).

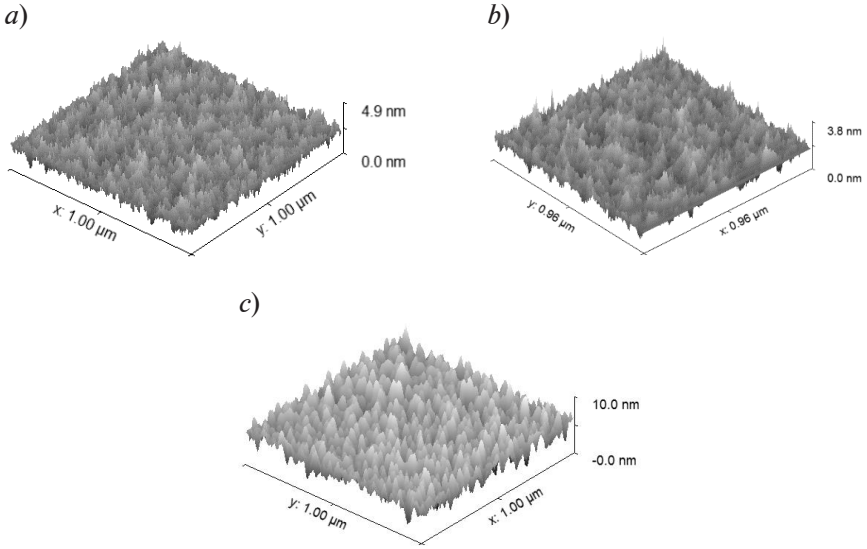

Fig. 4. AFM 3D images of 40 nm thick GaN on Si grown by PE-ALD without (*a*) and with Ar plasma treatment (b), with continuous hydrogen plasma mode (*c*)

Table 1

PE-ALD additional treatment influence on roughness and deposition rate

PE-ALD GaN 350°C	No Ar treatment	Ar plasma treatment	H_2 continuous plasma
RMS, nm	0.49	0.38	1.19
GPC, nm/cycle	0.095	0.185	0.2

Conclusion

In this study, the use of atomic layer deposition (ALD) for the growth of GaN layers on Si was investigated. The results showed that the ALD method, combined with in-situ annealing in argon and continuous hydrogen plasma mode, could affect the growth rate and morphology of GaN layers. The way to improve the surface roughness as well as increase the growth rate by using in-situ Ar plasma treatment during PE-ALD growth of GaN was demonstrated. On the contrary, usage of hydrogen plasma during the process leads to a drastic increase in surface roughness due to parasitic plasma deposition.

REFERENCES

1. **Geisz J.F., Olson J.M., Friedman D.J., et al.,** Lattice-Matched GaNPAs-on Silicon Tandem Solar Cells, in Proceedings of the 31th IEEE Photovoltaic Specialists Conference. (2005) (695).
2. **Johnson R.W., Hultqvist A., Bent S.F.**, Mater. Today. (17) (2014) (236).
3. **Niu W., Li X., Karuturi S.K., et al.,** Nanotechnology. (26) (2015) 064001.
4. **Gudovskikh A.S., Kudryashov D.A., Baranov A.I., et al.,** Low-Temperature Plasma Deposition of III-V Compounds on Silicon for Multijunction Solar Cells, ACS Applied Energy Materials. (5, 5) (2022) 5356–5366.
5. **Shih H.-Y., Lee W.-H., Kao W.-C., et al.,** Sci. Rep. (7) (2017) 39717.
6. **Uvarov A.V., Gudovskikh A.S., Nevedomskiy V.N., et al.,** Low temperature epitaxial growth of GaP on Si by atomic-layer deposition with plasma activation J. Phys. D: Appl. Phys. (53) (2020) 345105.

THE AUTHORS

MAKSIMOVA Alina A.
deer.blackgreen@yandex.ru
ORCID: 0000-0002-3503-7458

BARANOV Artem I.
itiomchik@yandex.ru
ORCID: 0000-0002-4894-6503

UVAROV Alexander V.
lumenlight@mail.ru
ORCID: 0000-0002-0061-6687

YARCHUK Ernst Y.
ernst_yarchuk@mail.ru
ORCID: 0009-0005-9558-4583

VYACHESLAVOVA Ekaterina A.
cate.viacheslavova@yandex.ru
ORCID: 0000-0001-6869-1213

GUDOVSKIKH Alexander S.
gudovskikh@spbau.ru
ORCID: 0000-0002-7632-3194

Received 29.07.2024. Approved after reviewing 27.08.2024. Accepted 27.08.2024.

EXPERIMENTAL TECHNIQUE AND DEVICES

Conference materials
UDC 544.478-03
DOI: https://doi.org/10.18721/JPM.173.231

Sensor of fast-variable and static pressure

D.V. Agafonov[1]✉, M.D. Novichkov[1], A.E. Shepeleva[1],
S.A. Gurin[1], A.A. Ryzhov[1], V.S. Volkov[2]

[1] Joint Stock Company "Research Institute of Electronic and Mechanical Devices", Penza, Russia;

[2] Penza State University, Penza, Russia

✉ dmitryagafonov@list.ru

Abstract. A new design and technological solution has been developed for the sensing element of a static and rapid-change pressure sensor based on the integration of strain-resistant and piezoelectric films of nanometer size, which made it possible to create a multifunctional sensor element with small pressure deviations from the actual values.

Keywords: sensing element, pressure sensor, strain gauge, piezoelectric thin films, static pressure, dynamic pressure

Citation: Agafonov D.V., Novichkov M.D., Shepeleva A.E., Gurin S.A., Ryzhov A.A., Volkov V.S., Sensor of fast-variable and static pressure, St. Petersburg State Polytechnical University Journal. Physics and Mathematics. 17 (3.2) (2024) 157–160. DOI: https://doi.org/10.18721/JPM.173.231

Материалы конференции
УДК 544.478-03
DOI: https://doi.org/10.18721/JPM.173.231

Датчик быстропеременного и статического давления

Д.В. Агафонов[1]✉, М.Д. Новичков[1], А.Э. Шепелева[1],
С.А. Гурин[1], А.А. Рыжов[1], В.С. Волков[2]

[1] АО «Научно-исследовательский институт электронно-механических приборов», г. Пенза, Россия;

[2] Пензенский государственный университет, г. Пенза, Россия

✉ dmitryagafonov@list.ru

Аннотация. Разработано новое конструктивно-технологическое решение для чувствительного элемента датчика статического и быстропеременного давления на основе интеграции тензорезистивных и пьезоэлектрических пленок нанометрового размера, что позволило создать многофункциональный чувствительный элемент с малыми отклонениями давления от действительных значений.

Ключевые слова: чувствительный элемент, датчик давления, тензорезистор, пьезоэлектрические тонкие пленки, статическое давление, динамическое давление

Ссылка при цитировании: Агафонов Д.В., Новичков М.Д., Шепелева А.Э., Гурин С.А., Рыжов А.А., Волков В.С. Датчик быстропеременного и статического давления // Научно-технические ведомости СПбГПУ. Физико-математические науки. 2024. Т. 17. № 3.2. С. 157–160. DOI: https://doi.org/10.18721/JPM.173.231

Introduction

The current stage of development for the management of new generation special equipment is characterized by increased accuracy, stability and performance in such areas as automotive, aircraft, mining and nuclear energy, where static and dynamic pressure is the most important parameter for measurement and control, with the help of which it is possible to prevent the possibility of emergency situations, thereby avoiding spending on expensive equipment repairs and at the same time saving human lives, that is why the number of pressure sensors is inevitably increasing every day [1]. Currently, pressure sensors are based on different physical principles: strain-resistive and piezoelectric sensors are used to measure static and pulse pressures, respectively. Sensor designs capable of measuring both pressures simultaneously and with a given technique do not currently exist. This is why users have to use two different sensors, which can burden the system, take up a lot of space and be expensive [2]. The goal of the work was to develop and study a new design of the sensor, which will significantly expand its functionality, in particular, to use the sensor to measure pressure in various frequency ranges.

Materials and Methods

The sensing element of the rapid-change and static pressure sensor (Fig. 1), which converts the energy of mechanical deformation into an electric charge and a change in resistance, is built on the basis of a round silicon membrane with a rigid center. The substrate surface is oxidized to form a dielectric layer with a thickness that provides reliable electrical insulation. Piezoelectric capacitive structures of a bending type made of ZnO, as well as four strain gages made of alloy nichrome, are applied to it.

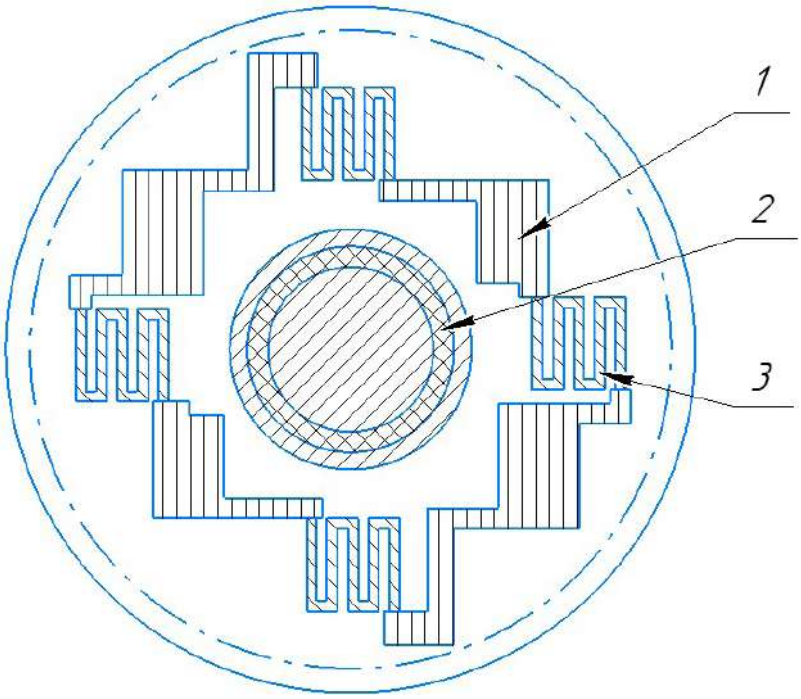

Fig. 1. Topology of the sensing element:
contact pads *1*, piezoelectric thin films *2*, strain gages *3*

Piezoelectric structures are formed in the center of the silicon wafer using the free mask method. The technology for producing ZnO thin films with piezoelectric properties is implemented at the Caroline D12A vacuum plasma spraying installation using the magnetron sputtering method. The essence of this method is the bombardment of the target surface, made of zinc oxide ZnO, with ions of the working gas.

To obtain piezoelectric structures on a sensitive element, the technological mode presented in Table 1 is proposed.

Table 1

Mode of production of piezoelectric films from ZnO

Spray parameters of mixers	Working gas	Working gas pressure, Pa	Power, kW	Membrane temperature, °C
ZnO	Argon	5	0.8	350

Compression and tension strain gauges are located at the places of the greatest inflection of the membrane. The formation of resistive films is carried out by thermal spraying of the alloy nichrome from a tungsten evaporator [3]. The current through the evaporator with a nichrome resistive material attachment smoothly increases to 260–270 A until the attachment melts. Then, simultaneously with the opening of the flap, the current is instantly increased by about 15%. Spraying is carried out until the required resistance value of the control witness sample is reached within 60 seconds, while the substrate temperature reaches 350 °C.

To obtain strain-resistant structures on a sensitive element, the technological mode presented in Table 2 is proposed.

Table 2

Spraying mode of nichrome layer

Vaporizer	Evaporator current, A	Initial residual pressure in chamber, mmHg	Final residual pressure in chamber, mmHg	Substrate temperature, °C	Control sample resistance, kOm/□	Spraying time, s
Nichrome	280–350	$2 \cdot 10^{-5}$	$3.5 \cdot 10^{-5}$	350	1,050–1,080	60

Gold with an adhesive sublayer of vanadium is used as a conductive material in the formation of interconnections and contact pads of strain gages and piezoelectric transducer plates [4]. The deposition of V-Au layers is carried out by the resistive method at a substrate temperature of 250 °C, followed by exposure for 30 minutes.

Results and Discussion

A technology has been developed for the manufacture of sensors sensitive elements for rapidly alternating and static pressures based on the integration of nanoscale piezoelectric and strain gauge films, which provide the following parameters for thin-film strain gages, presented in Table 3.

Table 3

Parameters of thin-film resistors

Parameter	Value
Thickness *d* of strain-resistant film, nm	80–100
Temperature coefficient of resistance TCS, 1/°C	2.0–3.6
TCS spread of strain gauges in strain gauge, 1/°C	$5 \cdot 10^{-6}$
Strain sensitivity coefficient	$2 \cdot 10^{-7}$

The parameters for piezoelectric films are presented in Table 4.

Table 4

Parameters of piezoelectric thin films

Parameter	Value
Layer thickness, nm	60–100
Frequency range, Hz	10^{-2}–10^{6}
Operating temperature range, °C	-100–+250
Voltage sensitivity d_{33}, pC/N	500
Sensitivity to relative influences with minimum output signal of 5 mV	10^{-9}

Conclusion

The topology of the pressure sensor sensing element, as well as the technology for manufacturing highly sensitive and thermally stable strain gages made of alloy nichrome and piezoelectric thin films made of ZnO deposited on an elastic silicon membrane by magnetron sputtering has been developed [5]. All this made it possible to obtain the desired properties of thin films and enhanced heat dissipation at increased electrical loads. This type of sensor is capable of analyzing the results and transmitting pressure information over a wider frequency range than sensors currently manufactured.

REFERENCES

1. **Belozubov E.M., Vasil'ev V.A., Gromkov N.V.,** Problems and Basic Research Directions in the Field of Thin-film Nano- and Microelectromechanical Systems of Pressure Sensors // Automation and Remote Control – USA, Pleiades Publishing, Ltd. 11 (72) (2011) 345–352.

2. **Ryabov D.V., Pecherskaya E.A., Shepeleva J.V., Pecherskaya R.M.,** Automated method of measuring the temperature dependences of the dielectric parameters of ferroelectrics with second kind phase transition J. Phys. Conf. Ser., 2014.

3. **Khor C.W., Leung C., Le Neel O.,** Reliability analysis of CrSi Thin Film Resistors Proc. 19th IEEE International Symposium on the Physical and Failure Analysis of Integrated Circuits. (2012) 1–4.

4. **Zelentsov Y.A., Zelentsov V.Y.,** An investigation of the relation between the temperature dependences of the initial unbalance and the output signal of resistance strain sensor bridge circuits Measurement Techniques. 50 (1) (2007) 66–8.

5. **Fimin A.V., Gurin S.A., Pecherskaya E.A., et al.,** Sensitive elements of microelectronic sensors of fast variable and static pressure Journal of Physics: Conference Series. 1410 (1) (2019) 156697.

THE AUTHORS

AGAFONOV Dmitriy V.
dmitryagafonov@list.ru
ORCID: 0009-0009-4548-3724

GURIN Sergey A.
teslananoel@rambler.ru
ORCID: 0000-0001-9602-7221

NOVICHKOV Maksim D.
novichkov1998maks@gmail.com
ORCID: 0000-0001-9319-2475

RYZHOV Alexandr A.
pgufr@mail.ru
ORCID: 0009-0006-3140-5897

SHEPELEVA Anastasiya E.
anastasiya.shepeleva.01@mail.ru

VOLKOV Vadim S.
vadimv_1978@mail.ru
ORCID: 0009-0009-7458-5324

Received 25.07.2024. Approved after reviewing 12.08.2024. Accepted 28.08.2024.

Conference materials
UDC 621.382.088
DOI: https://doi.org/10.18721/JPM.173.232

Threshold current of separate spectral components of the emission spectrum of InGaN LEDs

I.V. Frolov[1,2]✉, O.A. Radaev[1], V.A. Sergeev[1]

[1] Ulyanovsk Branch of Kotel'nikov Institute of Radio-Engineering and Electronics of RAS, Ulyanovsk, Russia;

[2] Ulyanovsk State Technical University, Ulyanovsk, Russia

✉ info@ulireran.ru

Abstract. The results of measurements of the threshold current of ultraviolet, blue and green InGaN LEDs on different spectral components of the full emission spectrum are presented. It is shown that the threshold current of long-wave components of the spectrum is greater than the threshold current of short-wave components. The relative difference in the values of the threshold current of the spectral components of the short-wave and long-wave wings of the emission spectrum at the level of half the radiation power is associated with the inhomogeneous distribution of indium concentration in the quantum well of the InGaN/GaN heterostructure and for the studied ultraviolet LEDs is 2.8%, 4.4% for blue, 25.7% for green.

Keywords: LED, InGaN/GaN heterostructure, emission spectrum, threshold current, measurement

Funding: The work was carried out within the framework of the state task of the Kotelnikov Institute of Radioengineering and Electronics of Russian Academy of Sciences.

Citation: Frolov I.V., Radaev O.A., Sergeev V.A., Threshold current of separate spectral components of the emission spectrum of InGaN LEDs, St. Petersburg State Polytechnical University Journal. Physics and Mathematics. 17 (3.2) (2024) 161–165. DOI: https://doi.org/10.18721/JPM.173.232

Материалы конференции
УДК 621.382.088
DOI: https://doi.org/10.18721/JPM.173.232

Пороговый ток отдельных спектральных составляющих спектра излучения светодиодов на основе InGaN

И.В. Фролов[1,2]✉, О.А. Радаев[1], В.А. Сергеев[1]

[1] Ульяновский филиал Института радиотехники и электроники им. В.А. Котельникова РАН, г. Ульяновск, Россия;

[2] Ульяновский государственный технический университет, г. Ульяновск, Россия

✉ info@ulireran.ru

Аннотация. Представлены результаты измерений порогового тока ультрафиолетовых, голубых и зеленых InGaN светодиодов на разных спектральных составляющих полного спектра излучения. Показано, что пороговый ток длинноволновых составляющих спектра больше, чем пороговый ток коротковолновых составляющих. Относительная разница в значениях порогового тока спектральных компонентов коротковолнового и длинноволнового крыльев спектра излучения на уровне половины мощности излучения связана с неоднородным распределением концентрации индия в квантовой яме гетероструктуры InGaN/GaN и для исследованных ультрафиолетовых светодиодов составляет 2,8%, для синего – 4,4%, для зеленого – 25,7%.

Ключевые слова: светодиод, спектр излучения, пороговый ток, измерение

Финансирование: Работа выполнена в рамках государственного задания ИРЭ им. В.А. Котельникова РАН.

Ссылка при цитировании: Фролов И.В., Радаев О.А., Сергеев В.А. Пороговый ток отдельных спектральных составляющих спектра излучения светодиодов на основе InGaN // Научно-технические ведомости СПбГПУ. Физико-математические науки. 2024. Т. 17. № 3.2. С. 161–165. DOI: https://doi.org/10.18721/JPM.173.232

Introduction

Light-emitting InGaN/GaN heterostructures with multiple quantum wells are characterized by a nonuniform distribution of indium in the InGaN quantum well [1] and a significantly nonuniform distribution of defects over the volume of the active region of the heterostructure [2]. The development of methods and means for assessing the inhomogeneity of indium distribution for the purpose of diagnostic quality control of InGaN/GaN heterostructures is an urgent task. In [3] it is shown that the P–I characteristics measured in the range of extreme currents are sensitive to defects in the heterostructure. The threshold current of a light-emitting heterostructure, i.e., the minimum current at which radiation occurs, is an informative parameter characterizing its quality [4]. The paper presents the results of measurements of the threshold current on different spectral components of the emission spectrum.

Objects of research and methods

Commercial LEDs based on $In_xGa_{1-x}N$/GaN heterostructure ultraviolet (UV) (λ_{max} = 363 nm, x = 0.02), blue (λ_{max} = 465 nm, x = 0.19) and green (λ_{max} = 525 nm, x = 0.38) luminescence have been investigated.

Emission spectra of LEDs at several values of low currents (100–1000 nA for blue and green LEDs and 25–70 μA for UV LEDs) were measured with an Ocean Optics USB 2000 spectrometer having a resolution of 1.5 nm and saved into text files. The exposure time of the optical signal during measurements was set in the range of 100 ms–5 s. From the complete emission spectra, components in different parts of the spectrum were programmatically separated with a step of 5 nm and the *P–I* characteristic was constructed. To determine the threshold current I_{th}, the measured *P–I* characteristic was approximated by a function obtained in work [5] based on the ABC model of charge carrier recombination in a heterostructure in the range of low currents, at which the effect of Auger recombination can be neglected, and the parameters m and q of which are related to the recombination parameters of the light-emitting structure.

$$P(I) = \frac{m}{2}\left(\sqrt{1+2q(I-I_{th})}-1\right)^2, \quad (1)$$

where $m = \eta_{extr} V \frac{hc}{\lambda}\frac{A^2}{2B}$ is the scale factor; $q = \frac{\eta_{inj}}{eV}\frac{2B}{A^2}$ is the form factor, that determines the curvature of the characteristic; I_{th} is the threshold current; η_{extr} is light extraction efficiency; h is Planck's constant; c is speed of light; λ is emission wavelength; e is elementary charge; V is heterostructure active region volume; η_{inj} is coefficient of charge carrier injection into the active region; A and B are coefficients of nonradiative Shockley-Reed-Hall recombination and radiative recombination, respectively.

Results and Discussion

The results of measuring of the threshold currents of separate spectral components of the investigated LEDs are shown in Fig. 1. For all LEDs, the threshold current of long-wavelength components of the spectrum is greater than the threshold current of short-wavelength components. The relative difference in the threshold current values of the spectral components of the short-wave and long-wave wings of the emission spectrum at the level of half the emission power is 2.8% for ultraviolet, 4.4% for blue, and 25.7% for green.

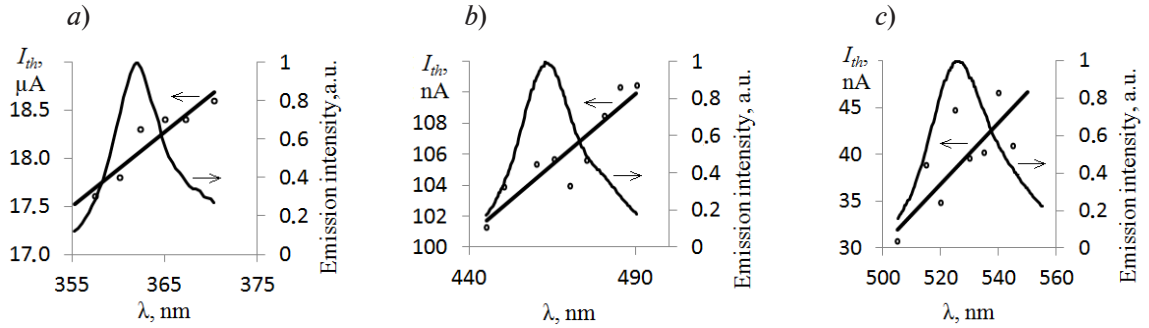

Fig. 1. Results of measurements of threshold current of violet (*a*), blue (*b*) and green (*c*) LEDs in different parts of emission spectrum

To explain the obtained results, let us consider the model of the formation of the emission spectrum of an InGaN/GaN heterostructure with a nonuniform distribution of indium, presented in [6]. According to the model, an LED can be represented by a set of parallel-connected microdiodes that have the same parameters of wide-gap *n*-GaN and *p*-GaN emitters, but differ from each other in the indium concentration *x* in quantum wells (Fig. 2).

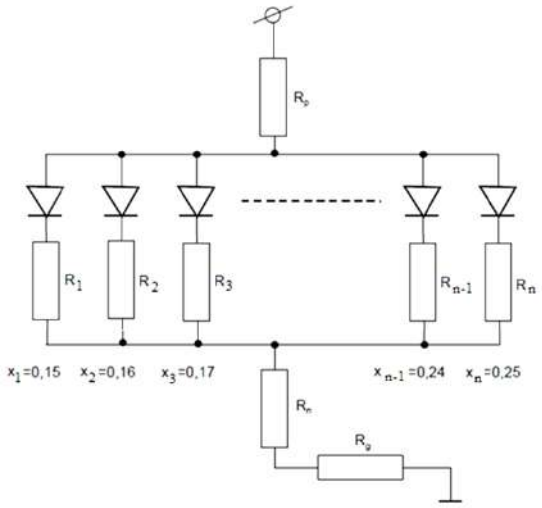

Fig. 2. Electrical model of LED with inhomogeneous distribution of indium in InGaN/GaN heterostructure quantum well [6]

The total contact resistance is connected in series with this set of microdiodes. The areas of microdiodes (sectors, areas) $S(x)$ with different indium content x in quantum wells can, to a first approximation, be described by a Gaussian distribution relative to the average values $x = 0.4$ for green LEDs and $x = 0.2$ for blue ones. At values $x = 0.15–0.17$, the current density is significantly higher than at values $x = 0.18–0.25$. Each microdiode has a threshold voltage U_{th_i} ($I = 1,...,n$), which is directly proportional to the band gap width and inversely proportional to the indium concentration x in the quantum wells. Since the difference between U_{th_1} and U_{th_n} is a few percent, the difference in the threshold current values I_{th_1} and I_{th_n} is due to the difference in the series (differential) resistances of the microdiodes R_i: $R_1 < R_n$, which is consistent with the results of modeling the current-voltage characteristics of blue LEDs based on the principle of distributing areas with different In_x contents, presented in [6].

An increase in the indium concentration x in a quantum well leads not only to the formation of clusters, but also to an increase in the degree of inhomogeneity of its distribution [7]. The experimental results presented in [8] show that at indium concentrations exceeding $x = 0.1$, there is a significant increase in the inhomogeneity of its distribution, which is confirmed by the broadening of the optical absorption edge.

Consequently, the experimental results can be interpreted as follows: when current passes through the heterostructure, radiative recombination first occurs in regions with lower indium concentrations, forming the short-wavelength wing of the emission spectrum. As the current increases, emission occurs in areas with higher concentrations of indium. The greater the inhomogeneity of the indium concentration in the quantum well, the greater the relative difference in the I_{th} values in the long- and short-wavelength components of the spectrum. The relative difference in the values of the threshold current of the spectral components of the short-wave and long-wave wings of the emission spectrum at the level of half the emission power can be used to indirectly estimate the degree of inhomogeneity of the indium concentration distribution in the InGaN/GaN quantum well.

Conclusion

The paper presents the results of measurements of the threshold current of ultraviolet, blue and green InGaN LEDs on different spectral components of the full spectrum of emission. It is shown that the threshold current of long-wave components of the spectrum is greater than the threshold current of short-wave components. The relative difference in the values of the threshold current of the spectral components of the short-wave and long-wave wings of the emission spectrum at the level of half the emission power is associated with the inhomogeneous distribution of indium concentration in the quantum well of the InGaN/GaN heterostructure and for the investigated ultraviolet LEDs is 2.8%, 4.4% for blue, for 25.7% green. The results obtained can be used to develop a technique for indirectly assessing the degree of uniformity of indium distribution in InGaN/GaN light-emitting heterostructures.

REFERENCES

1. **Baek S.-H., Lee H.-J., Lee S.-N.,** High-performance flat-type InGaN-based light-emitting diodes with local breakdown conductive channel, Scientific Reports. 9 (2019) 13654.

2. **Peng Z., Lu Y., Gao Y., et al.,** Effect of Carrier Localization and Shockley-Read-Hall Recombination on the Spatial Distribution of Electroluminescence in InGaN LEDs, IEEE Photonics Journal. 10 (2018) 8201908.

3. **De Santi C., Buffolo M., Renso N., et al.,** Evidence for defect-assisted tunneling and recombination at extremely low current in InGaN/GaN-based LEDs, Applied Physics Express. 12 (5) (2019) 052007.

4. **Sergeev V.A., Frolov I.V., Radaev O.A.,** The Relationship between the Defectness of Emitting Nanoheterostructures of Green InGaN/GaN LEDs and Their Threshold Current Values, Technical Physics Letters. 43 (2) (2017) 224–226.

5. **Sergeev V.A., Radaev O.A., Frolov I.V.,** LED Internal Quantum Efficiency Meter, Instruments and Experimental Techniques. 66 (6) (2023) 987–994.

6. **Nikiforov S.G.,** Development of measuring instruments and methods for monitoring the parameters of semiconductor emitters based on III-V compounds used in highly reliable devices: dis. ...Dr. Tech. Sciences: 05.11.13. – Accredited center for certification testing of lighting devices and radiation sources, ARHILIGHT LLC. – M., 2015. – 386 p. (In Russian).

7. **Di Vito A., Pecchia A., Di Carlo A., et al.,** Characterization of non-uniform InGaN alloys: spatial localization of carriers and optical properties, Japanese Journal of Applied Physics. 58 (2019) SCCC03.

8. **Buttė R., Lahourcade L., Uždavinys T.K., et al.,** Optical absorption edge broadening in thick InGaN layers: Random alloy atomic disorder and growth mode induced fluctuations, Applied Physics Letters. 112 (3) (2018) 032106.

THE AUTHORS

FROLOV Ilya V.
ilya-frolov88@mail.ru
ORCID: 0000-0003-0608-4754

SERGEEV Viacheslav A.
sva@ulstu.ru
ORCID: 0000-0003-4854-2813

RADAEV Oleg A.
oleg.radaev.91@mail.ru
ORCID: 0000-0002-8156-9412

Received 31.07.2024. Approved after reviewing 15.08.2024. Accepted 15.08.2024.

Conference materials
UDC 535,015
DOI: https://doi.org/10.18721/JPM.173.233

A new method of managing the discretization of the scale in a mobile differential refractometer

D.S. Provodin[1]✉, M.A. Yakusheva[1], V.V. Davydov[1,2]

[1] Peter the Great St. Petersburg Polytechnic University, St. Petersburg, Russia;

[2] Bonch-Bruevich Saint Petersburg State University of Telecommunications, St. Petersburg, Russia

✉ provodindanya@gmail.com

Abstract. The necessity of developing a new method for managing the discretization of the scale in a mobile differential refractometer has been justified. The implementation of this method is necessary to expand the functional capabilities of the developed mobile differential refractometer (providing a measurement mode of the refractive index of a liquid medium ranging from 1.23 to 2.63 with an error of 0.0001). All existing liquid media and their mixtures worldwide fall within this measurement range. When using other models of compact and mobile refractometers for express control, such a measurement range of n cannot be provided. Within the range of change of *n* from 1.23 to 2.63, a new management method has been implemented, which ensured a measurement error of 0.0001. Studies of various media have been conducted, confirming the adequacy of our development.

Keywords: refraction, liquid, refractive index, Anderson cuvette, laser radiation, photodiode array, measurement error

Funding: This research was funded by Russian Science Foundation (RSF), grant 21-72-20029.

Citation: Provodin D.S., Yakusheva M.A., Davydov V.V., A new method of managing the discretization of the scale in a mobile differential refractometer, St. Petersburg State Polytechnical University Journal. Physics and Mathematics. 17 (3.2) (2024) 166–172. DOI: https://doi.org/10.18721/JPM.173.233

Материалы конференции
УДК 535,015
DOI: https://doi.org/10.18721/JPM.173.233

Новая методика управления дискретностью шкалы в мобильном дифференциальном рефрактометре

Д.С. Проводин[1]✉, М.А. Якушева [1], В.В. Давыдов[1,2]

[1] Санкт-Петербургский политехнический университет Петра Великого, Санкт-Петербург, Россия;

[2] Санкт-Петербургский государственный университет телекоммуникаций им. проф. М.А. Бонч-Бруевича, Санкт-Петербург, Россия

✉ provodindanya@gmail.com

Abstract. Обоснована необходимость разработки новой методики управления дискретностью шкалы в дифференциальной кювете Андерсона. Для расширения функциональных возможностей использования разработанного мобильного дифференциального рефрактометра в его конструкции обеспечен режим измерения показателя преломления жидкой среды от 1,23 до 2,63 с погрешностью 0,0001. В этот диапазон измерения n попадают все существующие в мире жидкие среды и их смеси. Другим моделям малогабаритных и мобильных рефрактометров для экспресс-контроля данный диапазон измерения *n* не доступен. Для реализации контроля значения *n* в

диапазоне изменения от 1,23 до 2,63 был разработан новый метод измерения. Проведены исследования различных сред, которые подтвердили адекватность нашей разработки.

Keywords: рефракция, показатель преломления жидкости, кювета Андерсона, лазерное излучения, фотодиодная линейка, погрешность измерения

Финансирование: Работа выполнена при финансовой поддержке Российского научного фонда в рамках программы «Суперкомпьютерное моделирование и технология биомолекулярных пленочных структур» (грант № 20029-72-21).

Ссылка при цитировании: Проводин Д.С., Якушева М.А., Давыдов В.В. Новая методика управления дискретностью шкалы в мобильном дифференциальном рефрактометре // Научно-технические ведомости СПбГПУ. Физико-математические науки. 2024. Т. 17. № 3.2. С. 166–172. DOI: https://doi.org/10.18721/JPM.173.233

Introduction

The development of scientific and technological progress has led to an increase in the number of liquid media and their mixtures used in various research, industrial, and pharmaceutical production, among other fields [1–4]. To obtain reliable results, both in research and in ensuring the technological cycle in production, it is necessary to monitor the state of the liquid medium [1, 2, 5–8]. The greatest difficulties arise in the express monitoring of liquid media. These difficulties are related to the fact that the device for express monitoring must, on the one hand, be mobile, and on the other hand, provide measurements for monitoring the state of a large number of liquid media and their mixtures [8–11]. Currently, only two devices meet these requirements: nuclear magnetic resonance (NMR) meters and refractometers [9–15].

Refractometers are the most preferred among these two devices due to their ease of use, lightweight design, and cost. To date, a large number of different mobile refractometers have been developed for the express monitoring of liquid media. All of these devices have limitations regarding the type of liquid being measured and the measurement accuracy of liquid medium parameters, which restricts their application in various fields. One of the most promising solutions to these problems is the use of our developed differential refractometer [8, 15], which allows measuring the refractive index n_m of a liquid medium in the range from 1.23 to 2.63 (covering all existing liquid media and their mixtures).

When solving the problem of measuring n_m in this range (from 1.23 to 2.63), measurements using a mobile differential refractometer must ensure a measurement error of 0.0001 (in relative units) or less, as this is a requirement for the rapid control of liquid media and their mixtures [7, 8, 10, 11]. The problem of conducting n_m measurements with such accuracy lies in the following. Direct measurement of refractive index in differential refractometer designs is extremely difficult, as the photodiode array contains 4096 pixels, which, with a measurement step of refractive index at 0.0001, will not allow for measurements across the entire range. Therefore, the goal of our work is to develop a new measurement methodology that will allow managing the discretization of the refractive index measurement scale to ensure a measurement error of 0.0001 in the range from 1.23 to 2.63.

Differential Anderson cuvette and new method for managing the optical axis of laser radiation

The main measuring elements in the design of the differential refractometer are the Anderson cuvette and the photodiode array, on which the position of the optical axis of the laser radiation is registered. Fig. 1 shows the design of the Anderson cuvette and the change in the trajectory of the optical axis of the laser radiation for calculating its displacement on the photodiode array. To register the position of the laser radiation axis in the developed refractometer design [8, 15], a photodiode array with 2048 sensors (pixels) is used. This allows, at the first measurement step, to

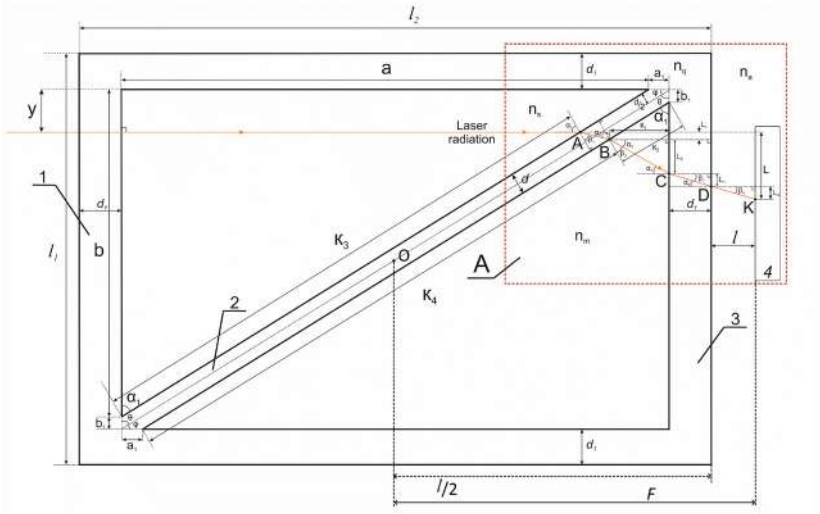

Fig. 1. Structural diagram of optical part of laboratory model of differential refractometer for measuring refractive index: Anderson cuvette wall *1* through which laser radiation is introduced; partition *2* in differential Anderson cuvette; cuvette face *3* for laser radiation output; photodiode array *4*

control the change in the refractive index n_m in the range from 1.230 to 2.630 with a step of 0.001 (with a margin of 600 sensors on each end of the array).

This construction ensures the necessary measurement range of n_m with a 20% margin, which meets modern requirements for measuring instruments. This construction of the laser radiation axis registration scheme allows measurements of n_m to start from the 310th sensor, significantly reducing edge effects that previously occurred when using 1024 sensors in the photodiode array. To determine the value of n_m (of the studied liquid) in the two compartments of the Anderson cuvette, reference and test liquids are used (Fig. 1). Then, laser radiation is introduced into the cuvette at a right angle (Fig. 1), and its axis, after several refractions, is registered by the photodiode array 4. Relative to the initial position of the laser radiation axis on the photodiode array (without the Anderson cuvette), the displacement L is determined considering the parameters of the cuvette, the distance l, and the values of n_m and n_s (reference liquid). The works [8, 15] thoroughly examine the processes of laser radiation axis refraction and the various conditions for its reception by the photodiode array sensors, deriving a relation for determining L:

$$L = L_1 + L_2 + L_3 + L_4 = \sin\alpha_1 \left(d\left(1 - \frac{n_2 \cos\alpha_1}{\sqrt{n_q^2 - n_s^2 \sin^2\alpha_1}}\right) + \left(\sqrt{n_m^2 - n_s^2 \sin^2\alpha_1} - n_s \cos\alpha_1\right) \cdot \right.$$

$$\cdot \left(\frac{l}{\sqrt{n_a^2 - \sin^2\alpha_1 \left(n_m^2 - n_s^2 \sin^2\alpha_1 + n_s^2 \cos^2\alpha_1 - 2n_s \cos\alpha_1 \sqrt{n_m^2 - n_s^2 \sin^2\alpha_1}\right)}} + \right. \quad (1)$$

$$+ \frac{d_1}{\sqrt{n_q^2 - \sin^2\alpha_1 \left(n_m^2 + n_s^2 \cos^2\alpha_1 - n_s^2 \sin^2\alpha_1 - 2n_s \cos\alpha_1 \sqrt{n_m^2 - n_s^2 \sin^2\alpha_1}\right)}} +$$

$$\left. \left. + \frac{K_1}{\cos\alpha_1 \sqrt{n_m^2 - n_s^2 \sin^2\alpha_1} + n_s \sin^2\alpha_1} \right) \right),$$

where α_1–α_4, β_1–β_4 are the angles of laser beam refraction at the boundaries of the cuvette; L_1–L_4 are the distances between the points (A, B, C, D, K) of laser beam refraction on the photodiode array, which are summed into the desired value L; n_s is the refractive index of the standard liquid;

n_m is the refractive index of the measurement liquid; n_a is the refractive index of the air; n_q is the refractive index of the cuvette material (quartz); l_1, l_2 are the external dimensions of the Anderson cuvette; l is the distance between the wall of the Anderson cuvette and the photodiode array; d, d_1 are the thicknesses of the partition and the cuvette wall; K_1 is the distance from point B to the inner right wall of the Anderson cuvette; a, b, a_1, b_2 are the internal dimensions of the Anderson cuvette.

For obtaining reliable values, in accordance with express control requirements, the refractive index n_m of the liquid medium must be measured with an error of 0.0001 or less in range from 1.23 to 2.63. In the refractometer design we developed for measuring n_m, a 2048-pixel array is used. For the measurements, we can use 1600 pixels (with 220 pixels reserved to ensure the safety limit at the boundary of the measurement range). This allows us to determine the position of the laser beam peak at the edges of the n_m measurement range. The smallest step with which we can cover the range from 1.23 to 2.63 using this number of pixels for measurement is 0.001. The refractometer design also has a reserve of 200–300 pixels in case new liquid media are introduced and the n_m values increase. The measurement step in this case defines the measurement error. Other factors (tolerances in the manufacturing of optical materials, pixel size of the photodiode array and distance between pixels, error in determining distance), which influence the n_m measurement error, according to data from industrial refractometers using photodiode arrays for measuring the angle of total internal reflection or the position of the light-shadow boundary, begin to affect the refractive index measurement error starting from a value of 0.00005 or less.

To ensure a refractive index measurement error of n_m in the differential refractometer at 0.0001, we developed a new method for modifying the scale resolution without changing the position of the optical elements, photodiode array, or laser, as well as without altering the laser radiation registration principle. For the n_m value measured in the first stage, it is necessary to select a new design for the Anderson cuvette and a new reference liquid (new ns value) so that a change in n_m by 0.0001 corresponds to the shift of the laser beam peak of one sensor on the photodiode matrix (Fig. 2).

Previously, the value of n_m was determined to the third decimal place (e.g., n_m = 1.753). After such replacement, the measurement range of n_m will be from 1.6730 to 1.8330 with a step of 0.0001 (measurement error of 0.0001). The remaining factors, as noted earlier, do not have a

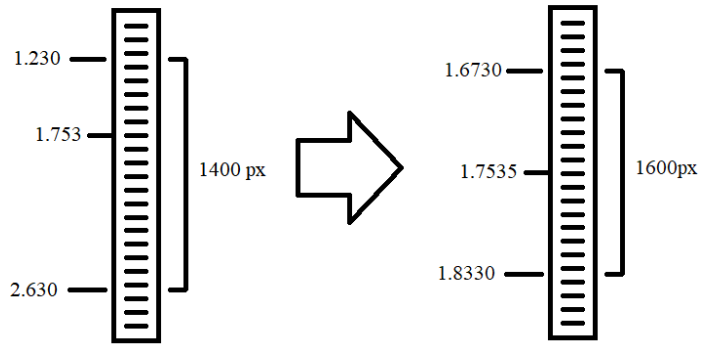

Fig. 2. Method for changing the measurement scale discreteness of refractive index n_m on the photodiode array

significant impact on the measurement error of n_m. This pixel reserve, when changing the scale resolution of the measurement range, is necessary for sharp temperature changes, which will lead to a change in the refractive index value of n_m. The optical axis of the laser beam will not go beyond the measurement range, and rapid control will be maintained. This fundamentally distinguishes this work from what was presented earlier in [16–18] based on the developments for the mobile differential refractometer. This work is a continuation of the research and developments in [8, 16–18] for the mobile differential refractometer.

Results and discussion

The developed methodology for changing the scale discreteness of the refractive index was tested on the previously developed design of the differential refractometer during the study of hydrocarbon media and their mixtures. Fig. 3, as an example, shows the results of the study of the refractive index changes of various gasoline brands with changes in temperature T.

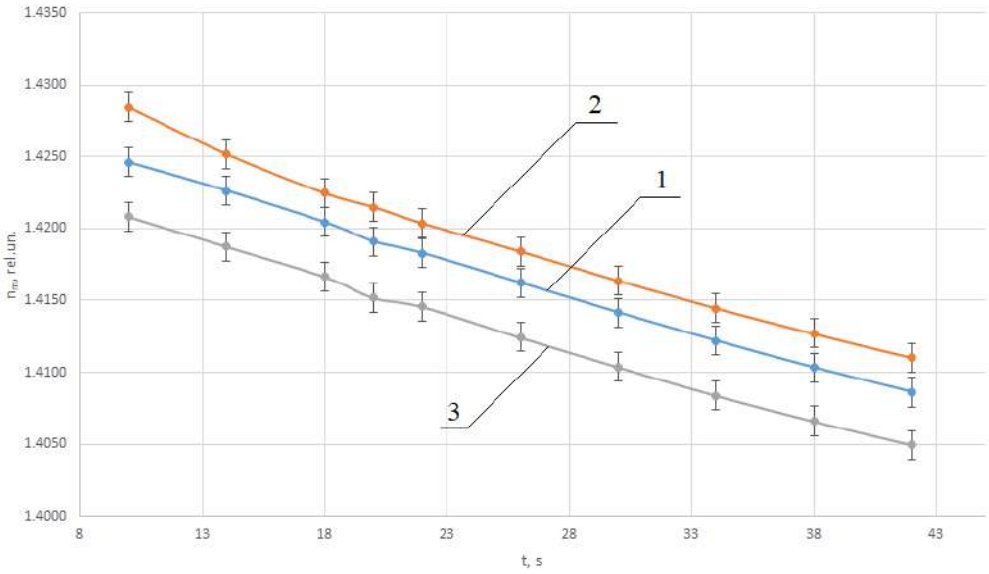

Fig. 3. Change in refractive index n_m with temperature T for various gasoline brands. Graphs *1*, *2*, and *3* correspond to gasoline brands: AI-95+, AI-98, and AI-100

Analysis of the obtained dependencies shows that the nature of the change in n_m corresponds to the previously obtained results on stationary refractometers and reflects the physical processes occurring in gasoline during heating.

To verify the reliability of the developed methodology for changing the scale discreteness of the refractive index n_m, studies of gasoline mixtures at various temperatures were conducted and compared with the results of measurements on the industrial refractometer SNEL-105 (measurement error of 0.00005). Tables 1 and 2 present the research results using both devices.

Analysis of the data in Tables 1 and 2 shows that the measurement results of n_m match within the measurement error, confirming the reliability of our developed measurement methodology using scale discreteness changes. This allows for a measurement error of 0.0001 or less.

Table 1

Change in refractive index n_m of mixture of AI-95 and AI-95+ gasolines in 50% to 50% ratio with temperature T

T, °C	Laboratory layout of differential refractometer	Industrial refractometer SNEL-105
10.0 ± 0.1	1.4239 ± 0.0001	1.42384 ± 0.00005
14.0 ± 0.1	1.4217 ± 0.0001	1.42165 ± 0.00005
18.0 ± 0.1	1.4194 ± 0.0001	1.41936 ± 0.00005
20.0 ± 0.1	1.4185 ± 0.0001	1.41844 ± 0.00005
22.0 ± 0.1	1.4173 ± 0.0001	1.41723 ± 0.00005
26.0 ± 0.1	1.4151 ± 0.0001	1.41493 ± 0.00005
30.0 ± 0.1	1.4131 ± 0.0001	1.41305 ± 0.00005
34.0 ± 0.1	1.4110 ± 0.0001	1.41093 ± 0.00005
38.0 ± 0.1	1.4092 ± 0.0001	1.40914 ± 0.00005
42.0 ± 0.1	1.4074 ± 0.0001	1.40733 ± 0.00005

Table 2

Change in refractive index n_m of mixture of three gasolines in following ratio: 60% AI-100, 20% AI-98, 20% AI-95 with temperature T

T, °C	Laboratory layout of differential refractometer	Industrial refractometer SNEL-105
10.0 ± 0.1	1.4262 ± 0.0001	1.42613 ± 0.00005
14.0 ± 0.1	1.4244 ± 0.0001	1.42434 ± 0.00005
18.0 ± 0.1	1.4222 ± 0.0001	1.42214 ± 0.00005
20.0 ± 0.1	1.4205 ± 0.0001	1.42043 ± 0.00005
22.0 ± 0.1	1.4202 ± 0.0001	1.42014 ± 0.00005
26.0 ± 0.1	1.4182 ± 0.0001	1.41815 ± 0.00005
30.0 ± 0.1	1.4162 ± 0.0001	1.41613 ± 0.00005
34.0 ± 0.1	1.4144 ± 0.0001	1.41434 ± 0.00005
38.0 ± 0.1	1.4125 ± 0.0001	1.41244 ± 0.00005
42.0 ± 0.1	1.4110 ± 0.0001	1.41093 ± 0.00005

Conclusion

The results of the study showed that changing the parameters of the differential Anderson cuvette and the refractive index n_s of the reference liquid allows for managing the scale discreteness of the measurement n_m within various ranges. This ensures a measurement error of 0.0001 in the range of the refractive index of the tested medium from 1.23 to 2.63, fully meeting the requirements for express control.

In the future, there is a possibility to achieve a measurement error of about 0.00005 or less by selecting the parameters of the Anderson cuvette and the refractive index n_s. For this, it is necessary to determine the tolerances for the fabrication of the faces and partitions in the Anderson cuvette and to ensure the value of n_s of the reference liquid with an accuracy of no worse than 0.00001. In such a case, the developed model of the differential refractometer can be used for scientific research and other applications.

REFERENCES

1. **Davydov V.V.,** Determination of the Composition and Concentrations of the Components of Mixtures of Hydrocarbon Media in the Course of its Express Analysis, Measurement Techniques. 62 (2) (2020) 1090–1098.

2. **Kuzmin M.S., Rogov S.A.,** On the use of a multi-raster input of one-dimensional signals in two-dimensional optical correlators," Computer Optics. 43 (3) (2019) 391–396.

3. **Myazin N.S., Smirnov K.J., Logunov S.J.,** Spectral characteristics of InP photocathode with a surface grid electrode, Journal of Physics: Conference Series. 929 (1) (2017) 012080.

4. **Grevtseva A.S., Smirnov K.J., Greshnevikov K.V., et al.,** Method of assessment the degree of reliability of the pulse wave image in the rapid diagnosis of the human condition, Journal of Physics: Conference Series. 1368 (2) (2018) 022072.

5. **Marusina M.Y., Fedorov A.V., Prokhorovich V.E., et al.,** Development of Acoustic Methods of Control of the Stress-Strain State of Threaded Connections, Measurement Techniques. 61 (3) (2018) 297–302.

6. **Davydov V.V., Dudkin V.I.**, On the Possibility of Express Recording of Nuclear Magnetic Resonance Spectra of Liquid Media in Weak Fields, Technical Physics. 63 (12) (2018) 1845–1850.

7. **Grebenikova N.M., Davydov R.V., Rud V.Yu.,** Features of the signal registration and processing in the study of liquid flow medium by the refraction method, Journal of Physics: Conference Series. 1326 (1) (2019) 012012.

8. **Provodin D.S., Borodaenko V.I.,** Optical method for express control of the state of liquids, Proceeding of VIII International Conference on Information Technology and Nanotechnology (ITNT). Samara, Russian Federation. 21992029 (2022) 217–222.

9. **Davydov V.V., Dudkin V.I.,** On the Possibility of Express Recording of Nuclear Magnetic Resonance Spectra of Liquid Media in Weak Fields, Technical Physics. 63(12) (2018) 1845–1850.

10. **Karabegov M.A.,** Metrological and technical characteristics of total internal reflection refractometers, Measurement Techniques. 47 (11) (2004) 1106–1112.

11. **Davydov V.V., Smirnov K.J.,** An Optical Method of Monitoring the State of Flowing Media with Low Transparency That Contain Large Inclusions, Measurement Techniques. 62 (6) (2019) 519–526.

12. **Contreras-Tello H., García-Valenzuela A.,** Refractive index measurement of turbid media by transmission of backscattered light near the critical angle, Applied Optics. 53 (21) (2014) 4768–4778.

13. **Chen J., Guo W., Xia M., et al.,** In situ measurement of seawater salinity with an optical refractometer based on total internal reflection method, Optics Express. 26 (20) (2018) 25510–25523.

14. **Kazanskiy N.L., Butt M.A., Degtyarev S.A., Khonina S.N.,** Achievements in the development of plasmonic waveguide sensors for measuring the refractive index. Computer Optics. 44 (3) (2020) 295–318.

15. **Davydov V.V., Provodin D.S., Gol'dberg A.A., Kochetkov I.D.,** A new method for describing the change of the laser beam axis trajectory in the Anderson differential cuvette to measure the refractive index of liquids. Computer Optics. 48 (2) (2024) 217–224.

16. **Provodin D.S., Davydov V.V.,** New technique for control of liquid media state by optical method in express mode. St. Petersburg State Polytechnical University Journal: Physics and Mathematics. 15 (3.2) (2022) 124–129.

17. **Goldberg A.A., Kochetkov I.D., Davydov V.V.,** Research on the character of laser radiation propagation in a differential Anderson cuvette, St. Petersburg State Polytechnical University Journal: Physics and Mathematics. 15 (3.2) (2022) 118–123.

18. **Goldberg A.A., Provodin D.S., Kochetkov I.D., Davydov V.V.** Features of investigation of liquid media by optical differential method in express-control. St. Petersburg State Polytechnical University Journal. Physics and Mathematics. 16 (3.1) (2023) 170–175.

THE AUTHORS

PROVODIN Daniil S.
provodindanya@gmail.com
0000-0002-7007-9215

DAVYDOV Vadim V.
davydov.vv@spbstu.ru
0000-0001-9530-4805

YAKUSHEVA Maria A.
yakusheva.ma@edu.spbstu.ru
0000-0002-0198-6209

Received 15.09.2024. Approved after reviewing 14.10.2024. Accepted 14.10.2024.

PHYSICAL ELECTRONICS

Conference materials
UDC 53.06
DOI: https://doi.org/10.18721/JPM.173.234

Investigation of microfluidic topology formation with the use of IR pulse laser

V.V. Lavrinenko✉, A.V. Vasilieva, V.A. Parfenov, I.A. Novikov

[1] St. Petersburg Electrotechnical University "LETI", St. Petersburg, Russia

✉lavrinenko_valerav@inbox.ru

Abstract. The work considers the possibility of creating microfluidic topology elements on a stainless-steel plate using laser processing. The results of multi-stage exposure of near IR laser radiation to a metal surface in order to create microchannel parts (grooves) with a semicircular profile, as well as through holes that form part of typical microfluidic topologies, are presented. This paper describes the main technological features of the effect of laser radiation on a metal plate, which affect the effectiveness of creating microtopology elements.

Keywords: microfluidics, microfluidic topology, laser processing, laser perforation

Citation: Lavrinenko V.V., Vasilieva A.V., Parfenov V.A., Novikov I.A., Investigation of microfluidic topology formation with the use of IR pulse laser, St. Petersburg State Polytechnical University Journal. Physics and Mathematics. 17 (3.2) (2024) 173–176. DOI: https://doi.org/10.18721/JPM.173.234

Материалы конференции
УДК 53.06
DOI: https://doi.org/10.18721/JPM.173.234

Исследование формирования микрофлюидной топологии с использованием инфракрасного импульсного лазера

В.В. Лавриненко✉, А.В. Васильева, В.А. Парфёнов, И.А. Новиков

[1] Санкт-Петербургский государственный электротехнический университет «ЛЭТИ» им. В.И. Ульянова (Ленина), Санкт-Петербург, Россия

✉ lavrinenko_valerav@inbox.ru

Аннотация. В работе рассматривается возможность создания элементов микрофлюидной топологии на пластине из нержавеющей стали с помощью лазерной обработки. Представлены результаты многоступенчатого воздействия инфракрасного лазерного излучения ближнего диапазона на металлическую поверхность с целью создания элементов, имитирующих микроканалы (канавки) полукруглого профиля, а также сквозных отверстий, которые являются частью типичных микрофлюидных топологий. В данной работе описаны основные технологические особенности воздействия лазерного излучения на металлическую пластину, влияющие на эффективность создания элементов микротопологии.

Ключевые слова: микрофлюидика, микрофлюидная топология, лазерная обработка, лазерная перфорация

Ссылка при цитировании: Лавриненко В.В., Васильева А.В., Парфенов В.А., Новиков И.А. Исследование формирования микрофлюидной топологии с использованием инфракрасного импульсного лазера // Научно-технические ведомости СПбГПУ. Физико-математические науки. 2024. Т. 17. № 3.2. С. 173–176. DOI: https://doi.org/10.18721/JPM.173.234

Introduction

Lab-on-a-chip systems are currently one of the fastest growing fields in applied photonics and, in particular, biophotonics. Technologies based on microfluidic systems are very diverse. For instance, they are used by biochemists and medical scientists to analyze biological and chemical liquids, to create new drugs, to manipulate different groups of cells, and even to simulate the work of human and animal organs [1–3]. The main requirements for such systems are high energy and economic efficiency, low weight, compactness, high sensitivity and high operating speed [4].

In a separate group of chips, one can select microfluidic devices for monitoring and analyzing fluids. They can be made from a wide range of materials such as transparent silicone elastomer, photoresist, glass, silicon and various metals. Depending on the material used microfluidic topology can be created using soft lithography, casting, hot stamping, mechanical milling, 3D printing and laser micro-processing [5].

The creation of a microfluidic pattern using laser microprocessing has a number of features and advantages compared to other methods, for example, environmental friendliness, lack of mechanical contact with materials and adaptability to production needs, and the use of metal as a material for the workpiece reduces the cost of manufacturing these products, which makes them more accessible to a wide range of research and applications. However, the process of interaction of laser radiation with metals is very complex and represents a set of physical phenomena such as heating, formation of a liquid phase, evaporation of metal and the effect of shielding the area of exposure with vapor-plasma formation [6]. It requires solving complex technological problems of laser processing of metals, which makes this research relevant and in demand.

The main task of this work is to study the modes of laser surface treatment of steel to obtain geometrically accurate microchannels with low roughness and taper, as well as surface morphology without microcracks.

Materials and Methods

The research was carried out on a 2 mm thick stainless steel metal plate, which was exposed to a precision laser system MiniMarker2 (Laser Center LLC, Russia), based on a fiber ytterbium laser (wavelength of 1064 nm, the beam diameter in the focal plane is 50 μm, the average laser power is up to 30 W, pulse duration from tens to hundreds of nanoseconds, pulse repetition rate up to 100 kHz). The topology elements were designed using specialized software MaxiGraf (Laser Centre LLC) supplied with a laser marker. The laser treatment was performed in several stages, during which processing parameters such as pulse duration, pulse repetition rate, scanning speed of the laser beam and the plane of focus changed.

The transverse dimensions of grooves were measured using an optical microscope NVMicro (NORGAU LLC, Russia). The width of the grooves was measured in three places: in the center and additionally one dimension at the edges of the structure. If an element of the topology had a "threshold", then it was measured in a similar way. This allowed us to find an error in measuring the width of microchannels, which turned out to be about 1%.

The depth of the grooves was measured using a high-precision manual 3D measuring machine Sinowon iTouch (MSP METROLOGY, Malaysia). To obtain an accurate depth value, the surface focusing method was used. The change in focal length when the scan line hit the topology was the value of the groove depth. Five measurements were made on each groove, after which the average depth value was calculated along the entire length of the groove. The measurement error was about 1%.

The roughness of the structures was assessed using an Industrial NSRT-100 profilometer (NORGAU LLC, Russia) with a standard probe installed. The measurement error of Ra parameter was about 5%.

3-D dimensional images of the surface of microchannels were obtained using the NTEGRA II atomic force microscope (NT-MDT LLC, Russia).

Results and Discussion

During multi-stage exposure to a steel plate with a fiber ytterbium laser, it was possible to identify the processing modes of the workpiece to create experimental grooves representing elements of a microfluidic system (Fig. 1, *a*, *b*). Generally one can identify two main parts of processing: hard regimes, which allow penetrating into material, and smoothing final processing regimes for polishing the surface.

During the work, it was found an oxide film formation at the bottom of the structures (Fig. 1, *a*), which is observed due to the fact that heated ambient gases react with the heated plate material, forming iron oxides and other impurities on its surface.

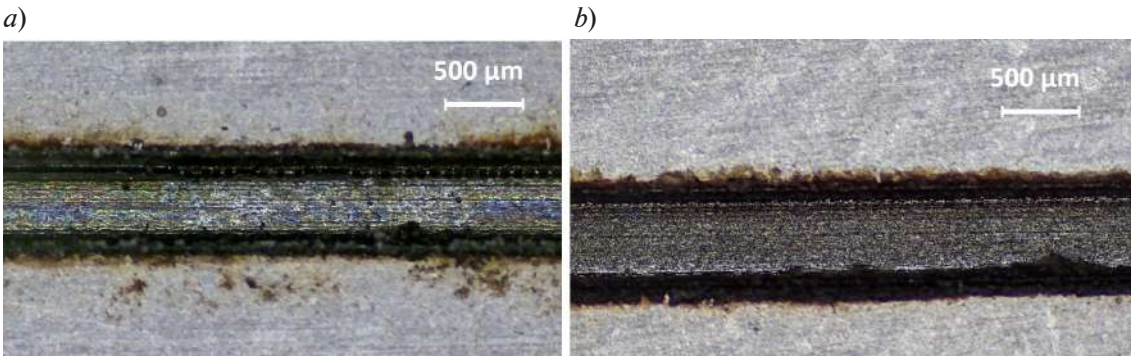

Fig. 1. Photos of grooves with an oxide film (*a*) and with roughness at the bottom (*b*)

To assess the effect of oxide film formation, 12 grooves with different processing modes, which imitated the final polishing step of laser processing, were obtained: 9 of them led to the formation of oxide, each of which was obtained at different power densities, and 3 were purely cellular. The roughness of the obtained structures was measured with profilometer (Table 1).

Table 1

Roughness of structures

Groove	Oxide presence	R_a, μm	Groove	Oxide presence	R_a, μm
1	–	0.382	7	+	0.838
2	–	0.400	8	+	0.744
3	+	0.892	9	+	0.903
4	–	0.409	10	+	0.553
5	+	0.831	11	+	0.544
6	+	0.795	12	+	0.648

From the data obtained, it can be seen that the oxide film leads to increasing the roughness of the structure, and the presence of a metallic luster indicates a lower value of R_a. Thus, the formation of oxide is undesirable for microfluidic purposes.

Also, these processing modes were investigated using AFM, some typical images are shown below (Fig. 2). Nanoscale particles remained in some microchannels (Fig. 2, *a*) after laser treatment, due to the fact that not all the material was able to fall out of the processing area. But in some cases, microcracks appeared during the processing (Fig. 2, *b*), which is a negative effect, since cracks of this size will create additional resistance when liquid flows.

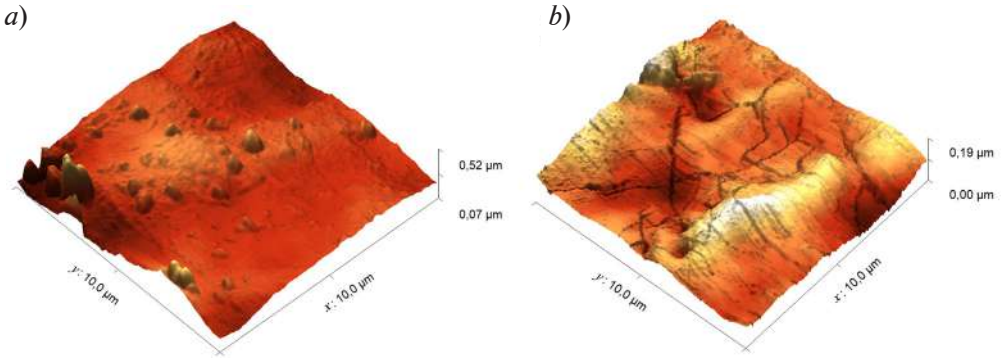

Fig. 2. AFM images of microchannels with the presence of nanopoils (*a*) and microcracks (*b*)

Conclusion

Using laser treatment with IR radiation, it was possible to obtain grooves on the surface of stainless steel with a profile close to a semicircular one, up to 500 microns thick. The experimental data allowed us to identify significant factors affecting the result of microprocessing.

The presence of oxide films, the appearance of which occurred when the power density decreased to 10^6 W/cm^2, increases the surface roughness. On the contrary, when the power density increased to 10^8 W/cm^2, microcracks appeared on the surface of the channels, which can lead to additional resistance when liquid flows. Thus, this study determines that laser power densities from 10^6 W/cm^2 to 10^8 W/cm^2 are most suitable for the final stages of processing and eliminate the main undesirable effects that interfere with obtaining a smooth surface after processing.

REFERENCES

1. **Halimova A.A., Kovalenko A.V., Paramonov G.V.**, Organs-on-a-chip: assessment of prospects for use in the pharmaceutical industry, Medical & pharmaceutical journal "Pulse". 24 (5) (2022) 81–87.

2. **Bovard D., Iskandar A., Luettich K., et. al.,** Organs-on-a-chip: A new paradigm for toxicological assessment and preclinical drug development, Toxicology Research and Application. **1** (2017) 1–16.

3. Cap**lin J.D., Granados N.G., James M.R., et. al.,** Microfluidic Organ-on-a-Chip Technology for Advancement of Drug Development and Toxicology, Advanced Healthcare Materials. 4 (10) (2015) 1426–1450.

4. **Zakoyan A.G., Voronkov G.S., Aleksakina Ya.V., et. al.,** Multichannel sensor system for simultaneous polling of several refractometric sensors based on a photonic integrated circuit, Special issue of "Foton-Ekspress-Nauka". 6 (2023) 135–136 (in Russian).

5. **Wlodarczyk K.L., Hand D.P., Maroto-Valer M.M.**, Maskless, rapid manufacturing of glass microfuidic devices using a picosecond pulsed laser, Scientific Reports. 9 (2019) 1–13.

6. **Glotov A.N., Golubenko Yu.V., Desyatskov V.A., Stepanov A.V.**, Some features of the interaction of laser radiation with metals, Vestnik MGTU im. N.E. Baumana. Ser. Priborostroenie. 1 (2020) 15–32 (in Russian).

THE AUTHORS

LAVRINENKO Valeriy V.
Lavrinenko_valerav@inbox.ru
ORCID: 0009-0001-8930-5438

VASILIEVA Anastasia V.
anastasiastru@mail.ru
ORCID: 0000-0002-5317-3322

PARFENOV Vadim A.
vadim_parfenov@mail.ru
ORCID: 0000-0002-2048-4677

NOVIKOV Ivan A.
ianovikov@stud.etu.ru
ORCID: 0009-0003-0155-4208

Received 25.07.2024. Approved after reviewing 16.08.2024. Accepted 26.08.2024.

Conference materials
UDC 628.9.038
DOI: https://doi.org/10.18721/JPM.173.235

Competing processes in nitride alloys in MQWs of LEDs

A.E. Ivanov[1,2]✉, A.E. Chernyakov[1], N.A. Talnishnikh[1],
E.I. Shabunina[3], N.M. Shmidt[3]

[1] Submicron Heterostructures for Microelectronics Research and Engineering Center RAS, St. Petersburg, Russia;

[2] St. Petersburg State Electrotechnical University "LETI", St. Petersburg, Russia;

[3] Ioffe Institute, St. Petersburg, Russia

✉ a-e-ivano-v@yandex.ru

Abstract The nature of competing processes leading to narrowing and broadening of the electroluminescence spectra width at half maximum under the injection current in nitride LEDs emitting at wavelengths of 270–280 nm and 530–540 nm has been studied. It was found out that there may be local regions with disturbed stoichiometry of random alloy fluctuations, enriched in excited defects ("deep center + local vibrations") in nitride MQWs with random alloy fluctuations. The capture of injected charge carriers by such defects in MQWs located in the space charge region of the pn junction was shown to lead to their coordination rearrangement in the lattice. This also results in a more equilibrium state of random alloy fluctuations and is accompanied by a narrowing of the full width at half maximum electroluminescence spectrum. However, this mechanism is a source of carrier loss that reduces the external quantum efficiency of LEDs at the maximum. It was shown experimentally that the higher the level of disorder in random alloy fluctuations, the lower the external quantum efficiency values. The non-equilibrium filling of the lateral random allow fluctuation by charge carriers in MQWs located outside the space charge region causes the broadening of the full width at half maximum electroluminescence spectrum in LEDs. This mechanism leads to a drop in external quantum efficiency at current densities $j > 30$ A/cm^2.

Keywords: MQW LEDs, alloy level disorder, FWHM, random alloy fluctuation

Citation: Ivanov A.E., Chernyakov A.E., Talnishnikh N.A., Shabunina E.I., Shmidt N.M., Competing processes in nitride alloys in MQWs of LEDs, St. Petersburg State Polytechnical University Journal. Physics and Mathematics. 17 (3.2) (2024) 177–181. DOI: https://doi.org/10.18721/JPM.173.235

Материалы конференции
УДК 628.9.038
DOI: https://doi.org/10.18721/JPM.173.235

Конкурирующие процессы в нитридных твёрдых растворах светодиодов с множественными квантовыми ямами

А.Е. Иванов[1,2]✉, А.Е. Черняков[1], Н.А. Тальнишних[1], Е.И. Шабунина[3], Н.М. Шмидт[3]

[1] Научно-технологический центр микроэлектроники и субмикронных гетероструктур РАН, Санкт-Петербург, Россия;

[2] Санкт-Петербургский государственный электротехнический университет «ЛЭТИ» им. В.И. Ульянова (Ленина), Санкт-Петербург, Россия;

[3] Физико-технический институт им. А.Ф. Иоффе РАН, Санкт-Петербург, Россия

✉ a-e-ivano-v@yandex.ru

Аннотация. Исследована природа конкурирующих процессов, приводящих к сужению и уширению ширины спектров электролюминесценции на полувысоте под действием тока в нитридных светодиодах, излучающих на длинах волн 270–280 нм и 530–540 нм. Выяснено, что в нитридных с множественных квантовых ямах (МКЯ), наряду со случайными флуктуациями состава, могут присутствовать локальные области с нарушенной стехиометрией состава твердого раствора, обогащенные возбужденными дефектами. Показано, что захват инжектируемых носителей заряда такими дефектами в МКЯ, находящихся в области объемного заряда p–n перехода, приводит к их координационной перестройке в решетке, а также к более равновесному состоянию твердого раствора и сопровождается сужением ширины спектра на половине высоты. Однако этот процесс является источником потерь носителей заряда, снижающим внешнюю квантовую эффективность светодиодов в максимуме. Экспериментально показано, что чем выше уровень разупорядоченности твердого раствора, тем ниже значения внешней квантовой эффективности. Увеличение ширины спектра светодиодов на половине высоты вызвано неравновесным заполнением латеральных неоднородностей состава твердого раствора носителями заряда в МКЯ, находящихся вне области объемного заряда. Этот процесс вызывает падение внешней квантовой эффективности при плотностях тока $j > 30$ А/см^2.

Ключевые слова: светодиоды с квантово-размерной активной областью, разупорядоченность твердого раствора, ширина спектра на полувысоте, случайные флуктуации состава

Ссылка при цитировании: Иванов А.Е., Черняков А.Е., Тальнишних Н.А., Шабунина Е.И., Шмидт Н.М. Конкурирующие процессы в нитридных твердых растворах светодиодов с множественными квантовыми ямами // Научно-технические ведомости СПбГПУ. Физико-математические науки. 2024. Т. 17. № 3.2. С. 177–181. DOI: https://doi.org/10.18721/JPM.173.235

Introduction

It is mentioned in the latest review [1] that insufficiently studied features of nitride-based alloy disorder prevent the realization of potential in the creation of emitting devices with high external quantum efficiency (EQE) in ultraviolet and green spectral range. The disorder can lead to the existence of local areas with impaired stoichiometry. According to [2], such phenomena as a narrowing spectra full width at half maximum (FWHM), as well as a FWHM broadening in electroluminescence (EL) spectra in QWs of LEDs under the injection current can also decrease EQE values [2]. However, the mechanisms causing these phenomena in MQWs and alloy disorder are understood relatively poorly [1, 3]. Our study is aimed at revealing reasons for these phenomena.

Materials and Methods

In this work, we study commercial green and UV LEDs. We also investigated blue LEDs as a reference. These LEDs have 1 mmI active area and flip-chip design. The external quantum efficiency (EQE) of green LEDs is EQE ranging from 13% to 30% at wavelengths 530 nm. The lowest EQE values (3–7%) are observed in UV LEDs at 270–280 nm. Referent blue LEDs emitting at 450 nm exhibit EQE ranging from 50% to 70%. Current-voltage (*I–V*) characteristics of LEDs were obtained using a KEITHLEY 6487 power source. EL spectra and EQE measurements were conducted on LEDs at 300K, employing an Optronic Laboratories OL770-LED system with an OL ISA-670 integrating sphere. We carried out a joint analysis of changes in FWHM values and the dependence of EQE versus the injection current of these LEDs, with additional near-field distribution of EL parameters. Near-field was monitored by Mitutoyo optical microscope with Avantes AvaSpec-2048. The field of view of the optical system was 536×357 μm^2 with the best spatial resolution of 25 μm.

To assess the level of disorder in nitride alloy of LEDs (alloy LD), we used the value Δ_V which evaluates the difference between the values of the threshold voltage (u_{th}) determined from the direct branch of the *I–V* characteristics and the voltage corresponding to the peak wavelength of the study LEDs at the maximum (u_0), $\Delta_V = u_{th}\text{-}u_0$ [3, 4]. Previous studies have shown a good correspondence of this value with other techniques to estimate the alloy LD in LEDs [3]. Moreover, they found a correlation between a decrease in the values of Δ_V and the improvement in ordering. All the LEDs under the study were classified according to the parameter Δ_V.

Results and discussion

A study of the spectrum of green (λ_{peak} = 530 nm) LEDs with 30% EQE in the near field at 0.2 mA and 50 mA showed that at a low injection level, local areas intensively emit with a different peak wavelength with exceed the maximum on 4 nm of LED radiation. As the injection current increases, the radiation intensity of these regions does not increase, which suggests that there is some disturbed of the stoichiometry of nitride allow in these areas. At the same time, the value of Δ_V in these LEDs significantly exceeds the value of Δ_V in blue LEDs, with a relatively low EQE of 50%. Fig. 1 shows the experimental dependencies of FWHM and EQE versus the injection current in green LEDs with different alloy LD and referent blue LEDs.

There is a correlation between decreasing EQE at maximum in MQWs located in the space charge region (SCR) around *p–n* junction (curves 1 on all dependencies with decreasing values of Δ_V). It should be noted that in blue LEDs with 70% EQE, Δ_V does not exceed 0.1 V, while in green LEDs with 13% EQE, Δ_V is 1 V. At the same time, there is a narrowing of the FWHM EL spectra under the injection current in MQWs, located in the SCR of the *p–n* junction, of all LEDs (Fig. 1, curves *2*). This effect is most pronounced for LEDs with a maximum value of Δ_V and a minimum EQE (Fig. 1, *a*). It is clearly visible in Fig. 1, *a* that this process is accompanied by an increase in EQE under injection current curve *2*, which indicates a transition to a more equilibrium composition in the solid solution. Narrowing of the FWHM EL spectra under the injection current reveals complex mechanisms of capture and recombination of charge carriers in MQWs based on nitrides [5, 6]. Such complex processes have been studied in gallium arsenide-based solid solutions by representations of excited defects, such as “deep center + local vibrations” [5].

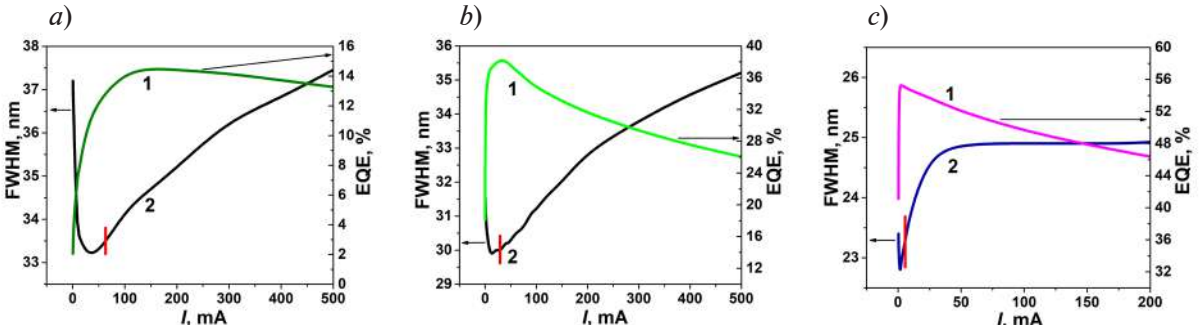

Fig. 1. Dependences of EQE (*1*) and FWHM (*2*) versus injection current in LEDs with different alloy LD and EQE: green 0.72V, 14% (*a*); green 0.46V, 30% (*b*); 0.13 V, 50% (*c*)
Red lines mark the FWHM corresponding the current when the *p–n* junction is full open

The possibility of the existence of such defects is due to fundamental properties of A3B5 such as the excess elastic energy of deformed bonds of main components in the lattice, which are characterized by the Huang-Rhys factor. It should be noted that the value of the Huang-Rhys factor is higher in nitrides than in arsenides [6]. According to theoretical concepts [6], the capture of injected charge carriers by such defects in MQWs located in the SCR region around pn junction leads to their coordination rearrangement in the lattice and multiphonon defect recombination. It seems that local areas with impaired stoichiometry are enriched by such defects. The observed narrowing of the FWHM EL spectra under the injection current in MQWs reflects the mechanism of transition of a nitride alloy in such areas to a more equilibrium state. However, this process is a source of carrier loss, reducing the EQE of LEDs to the maximum. The results presented in Fig. 1 show that the higher the alloy LD, the lower the EQE values. Thus, the presence of local areas with impaired stoichiometry is one of the reasons behind the low EQE in green LEDs. It seems that this conclusion is confirmed by the study of the optical properties of UV LEDs. Indeed, the estimated Δ_V in UV LEDs shows values of 1.5 V, i.e., the highest among all the studied LEDs, and the lowest EQE ~ 4–7%.

Fig. 2 shows EQE (*1*) and FWHM (*2*) dependencies versus injection current (Fig. 2, *a*) and EL spectra (Fig. 2, *b*) in UV LEDs. A more complex FWHM dependence (curve *2*) versus injection current than the LEDs shown in Fig. 1 is observed. It consists of two regions: Δ_V = 0.13 V and Δ_V = 1.5 V. Analysis of the EL spectra in UV LEDs in Fig. 2, *b* allows us to understand the reasons behind this complexity. The typical EL spectrum in UV LEDs in Fig. 2, *b* (curve *1*) at 1 mA demonstrates the phase separation of the alloy in the region 240–350 nm. At the same time, a narrow peak with a maximum intensity in the region of 270–280 nm (Fig. 2, *b*, curve *2*) does not change the magnitude of FWHM over a current increase, while the appearance of the spectrum in areas with lower intensity around this peak changes with increasing current. This kind of change in the type of spectrum with the injection level suggests that a narrow peak in the spectrum is caused by radiative recombination in MQW regions with an equilibrium composition, and in the 200–270 nm and 280–350 nm ranges there are local regions with impaired stoichiometry. Moreover, the number of such regions may significantly exceed the number of regions with an equilibrium composition. The FWHM broadening (Fig. 1, curves *2*) in MQWs located outside of SCR is caused by the process of none-equilibrium filling of spatial random alloy fluctuations by injected charge carriers. This process leads to a drop in EQE at $j > 30$ A/cm^2.

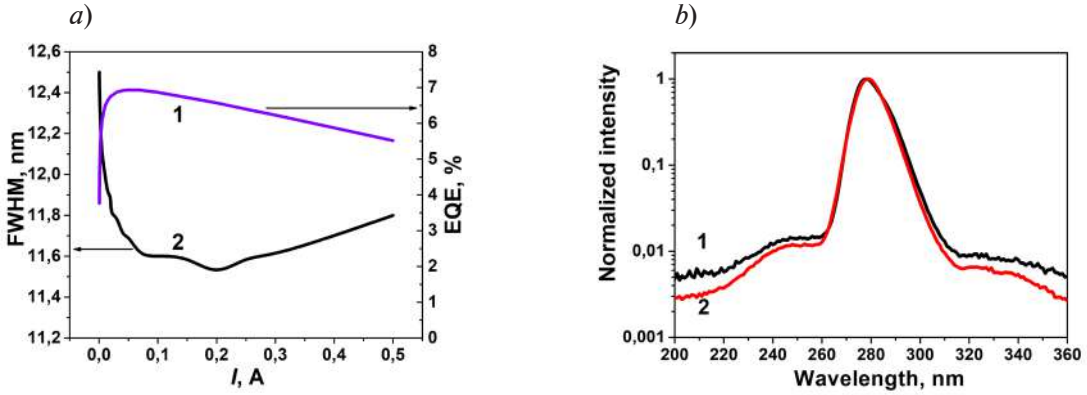

Fig. 2. Dependences of EQE (1) and FWHM (2) versus injection current of UV LEDs (λ_{peak} = 280 nm) (*a*) and EL spectra at 0.2 mA (*1*), 50 mA (*2*) (*b*)

Conclusion

The presence of local areas with impaired stoichiometry was revealed when studying the near-field distribution of self EL at small current of green LEDs with allow disorder. The processes occurring in such areas under the influence of injection current have been clarified. A study of competing processes leading to narrowing and broadening of FWHM in the EL spectra of green LEDs with different allow LD showed that both processes lead to loss of injected charge carriers

and a decrease in EQE values. At the same time, the decrease in EQE values at the maximum is due to the presence in MQWs of the local regions with disturbed stoichiometry allow, enriched by excited defects. The source of charge carrier losses is the process of the capture of injected charge carriers by such defects in MQWs located in SCR of the $p-n$ junction. UV LEDs, which have the lowest EQE values among all the studied LEDs, have the highest values of solid solution disorder. The results obtained suggest that one of the ways to increase the efficiency of LEDs is to reduce the level of disordered solids. A quantitative assessment of the level of disorder in terms of magnitude Δ_V can be used in the development of a technology for the growth of ordered solid solutions. The broadening of the FWHM EL spectrum of LEDs is caused by the nonequilibrium filling of the lateral random allow fluctuation by charge carriers in MQWs located outside the SCR. This process causes the beginning a drop in the EQE with the opening of $p-n$ junction.

REFERENCES

1. **Weisbuch C., Nakamura S., Wu Y.-R., Speck J. S., Disorder effects in nitride semiconductors: impact on fundamental and device properties.** Nanophotonics. 10 (1) (2021) 3–21.

2. **Pant N., Li X., DeJong E., et al.,** Origin of the injection-dependent emission blueshift and linewidth broadening of III-nitride light-emitting diodes. AIP Advances. 12(12) (2022) 125020.

3. **Shabunina E., Chernyakov A., Ivanov A., et. al.,** Contribution of Zone Fluctuation Potential and Disordering of Heteroboundaries to the Decreased Efficiency of Nitride-Based Leds. J Appl Spectrosc. (90) (2023) 24–28.

4. **Robin Y., Pristovsek M., Amano H., et al.,** What is red? On the chromaticity of orange-red InGaN/GaN based LEDs. J. Appl. Phys. (124) (2018) 183102.

5. **Yassievich I.N.**, Recombination-induced defect heating and related phenomena. Semicond Sci Technol 9,1433 (1994).

6. **Mandurrino M., Goano M., Vallone M., at al.,** Semiclassical simulation of trap-assisted tunneling in GaN-based light-emitting diodes. J. Comput. Electron. 14 (444) (2015).

THE AUTHORS

CHERNYAKOV Anton E.
chernyakov.anton@yandex.ru
ORCID: 0000-0002-8153-9512

SHMIDT Natalia M.
natalia.shmidt@mail.ioffe.ru
ORCID: 0000-0003-3585-5116

IVANOV Anton E.
a-e-ivanov@yandex.ru
ORCID: 0000-0003-2819-1534

TALNISHNIKH Nadezhda A.
nadya.fel@mail.ru
ORCID: 0000-0003-1127-0973

SHABUNINA Evgeniia I.
jenni-85@mail.ru
ORCID: 0000-0003-4457-8149

Received 26.07.2024. Approved after reviewing 05.08.2024. Accepted 06.09.2024.

Conference materials
UDC 621.383.525
DOI: https://doi.org/10.18721/JPM.173.236

Influence of the doping level in the absorption layer of InGaAs/InP 2.5 μm photodetectors on their electrical properties

O.V. Barantsev[1]✉, E.I. Vasilkova[1,2], E.V. Pirogov[1], K.Yu. Shubina[1], A.I. Baranov[1], K.O. Voropaev[3], A.A. Vasil'ev[3], L.Ya. Karachinsky[1], I.I. Novikov[1], M.S. Sobolev[1,2]

[1] Alferov University, St. Petersburg, Russia;

[2] St. Petersburg Electrotechnical University "LETI", St. Petersburg, Russia;

[3] JSC "OKB-Planeta", Velikiy Novgorod, Russia

✉ ovbarantsev@gmail.com

Abstract. $In_{0.83}Ga_{0.17}As$/InP PIN-photodiode heterostructures with different doping levels have been grown by molecular beam epitaxy. Metamorphic buffer layers were applied to prevent misfit dislocations nucleation in active layers. Capacitance-voltage and current-voltage curves of fabricated photodiodes have been measured and analysed. The impact of various dark current mechanisms has been estimated after the measurements of current-voltage curves at different temperatures.

Keywords: metamorphic buffer layers, infrared photodetectors, molecular beam epitaxy

Funding: The study was funded by the Ministry of Science and Higher Education of the Russian Federation (grant no. FSRM-2023-0006 and no. FSRM-2022-0002).

Citation: Barantsev O.V., Vasilkova E.I., Pirogov E.V., Shubina K.Yu., Baranov A.I., Voropaev K.O., Vasil'ev A.A., Karachinsky L.Ya., Novikov I.I., Sobolev M.S., Influence of the doping level in the absorption layer of InGaAs/InP 2.5 μm photodetectors on their electrical properties, St. Petersburg State Polytechnical University Journal. Physics and Mathematics. 17 (3.2) (2024) 182–186. DOI: https://doi.org/10.18721/JPM.173.236

Материалы конференции
УДК 621.383.525
DOI: https://doi.org/10.18721/JPM.173.236

Влияние степени легирования активной области InGaAs/InP 2.5 мкм фотодетекторов на их электрофизические характеристики

О.В. Баранцев[1]✉, Е.И. Василькова[1,2], Е.В. Пирогов[1], К.Ю. Шубина[1], А.И. Баранов[1], К.О. Воропаев[3], А.А. Васильев[3], Л.Я. Карачинский[1], И.И. Новиков[1], М.С. Соболев[1,2]

[1] Академический университет им. Ж.И. Алфёрова РАН, Санкт-Петербург, Россия;

[2] Санкт-Петербургский государственный электротехнический университет «ЛЭТИ» им. В.И. Ульянова (Ленина), Санкт-Петербург, Россия;

[3] АО «ОКБ Планета», г. Великий Новгород, Россия

✉ ovbarantsev@gmail.com

Аннотация. $In_{0,83}Ga_{0,17}As/InP$ PIN-фотодиодные гетероструктуры с различными концентрациями легирующей примеси в поглощающем слое были выращены методом молекулярно-пучковой эпитаксии. Метаморфные буферные слои использованы для уменьшения плотности дислокаций несоответствия в активной области гетероструктур. Были изучены вольт-фарадные и вольт-амперные характеристики полученных кристаллов фотодиодов. На основе вольт-амперных характеристик, полученных при разных температурах, был исследован вклад различных механизмов образования темновых токов.

Ключевые слова: метаморфные буферные слои, инфракрасные фотодетекторы, молекулярно-пучковая эпитаксия

Финансирование: Государственные задания № FSRM-2023-0006 и № FSRM-2022-0002 при поддержке Министерства Науки и Высшего Образования Российской Федерации.

Ссылка при цитировании: Баранцев О.В., Василькова Е.И., Пирогов Е.В., Шубина К.Ю., Баранов А.И., Воропаев К.О., Васильев А.А., Карачинский Л.Я., Новиков И.И., Соболев М.С. Влияние степени легирования активной области InGaAs/InP 2.5 мкм фотодетекторов на их электрофизические характеристики // Научно-технические ведомости СПбГПУ. Физико-математические науки. 2024. Т. 17. № 3.2. С. 182–186. DOI: https://doi.org/10.18721/JPM.173.236

Introduction

InGaAs/InAlAs/InP photodetectors operating in the spectral range of 2.2–2.6 um have a wide range of applications. They can be used in infrared spectroscopy devices, gas and night vision sensors [1]. However, to achieve a high performance in this spectral range, $In_{0.83}Ga_{0.17}As$ absorption layer should be used. Since the absorption layer and InP substrate have a mismatch of 2.1% in the lattice constant, metamorphic buffer layers (MBLs) need to be implemented.

The properties of optoelectronic devices are closely connected with the density of misfit dislocations. In photodiodes, such defects can lead to a high value of dark current. Dark current is a noise, which decreases sensitivity of photodiodes at low luminous intensities [2].

MBLs could effectively suppress generation of misfit dislocations in the absorption layer, but it is necessary to find optimal design and growth parameters to achieve the best device characteristics. In the present work, influence of the doping level of the absorption layer on dark current has been investigated.

Materials and Methods

PIN-photodiode heterostructures were grown by molecular beam epitaxy using a semi-industrial Riber MBE49 setup. We used n^+-type "epi-ready" InP (100) wafers to grow two structures with different doping levels of the absorption layer, called S-1 and S-2.

At the beginning of growth, substrates were annealed. After that, a thin 100 nm lattice-matched $In_{0.52}Ga_{0.48}As$ layer was grown. Next, n^+-$In_xAl_{(1-x)}As$ metamorphic buffer layers were formed by gradually increasing indium (In) mole fraction at growth temperatures of 500–510 °C (thermocouple). MBLs contained three InAlAs/InAs superlattice inserts. Structure S-1 was made with an inverse step in MBLs: indium mole fraction was increased up to 86%. S-2 was manufactured without an inverse step, but $In_{0.83}Ga_{0.17}As/In_{0.83}Al_{0.17}As$ digital superlattice inserts before and after the absorption layer were formed. MBLs growth was followed by thermocycling process of peak temperature rising up to 630 °C and slow cooling down to 50 °C. The growth process of MBLs is described in more detail in [3]. After MBLs, 1.5 um $In_{0.83}Ga_{0.17}As$ active layer was grown. The absorption layer was slightly n-doped using silicon (Si). The doping concentration of the active layer was on the order of 10^{16} cm^{-3} in both samples, but its estimated value in S-2 was specially made 4 times higher than in S-1. At the end, 0.6 um p^+-type contact layers doped with beryllium (Be) were formed on the top of the heterostructure.

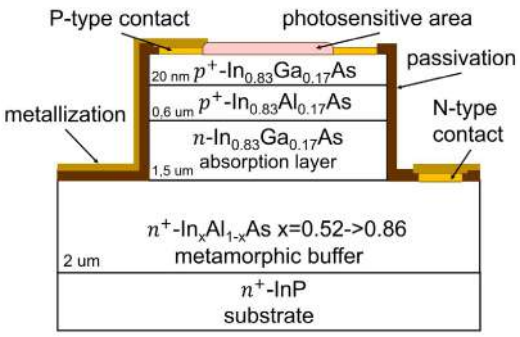

Fig. 1. Schematic structure of PIN-photodiode

Photosensitive areas with the diameter of 140 μm and contact areas were fabricated using a standard photolithography procedure. The overall photodiode mesa size was 325×325 μm². A schematic structure of produced PIN-photodiodes is presented in Fig. 1.

ECV profiles were measured by Electrochemical capacitance voltage profiler ECV Pro (Nanometrics, USA). The $C-V$ curves were gained using LCR Agilent E4980A setup. The $I-V$ curves at different temperatures were obtained using The Keithley 2400 measuring setup. The samples were cooled using Janis VPF-100 cryostat.

Results and Discussion

ECV measurements helped to calculate carrier concentrations in the active layer of two samples. In S-1 its value was $10 \cdot 2^{16}$ cm^{-3}, and in S-2 it was $8 \cdot 10^{16}$ cm^{-3}, which is 4 times higher, as expected. In p^+-type and n^+-type contact layers, respective main carrier concentrations were $2 \cdot 10^{18}$ cm^{-3}, showing that PIN structures were successfully manufactured.

$I-V$ curves of both samples at room temperature of 300K are shown in Fig. 2. They are highly asymmetrical, showing a diode-like behavior. At reverse bias voltages less than 0.2 V, dark currents values of samples are different: in S-2 the dark current is higher by almost an order of magnitude. However, at higher bias voltages, the dark currents of structures are nearly identical, reaching the value of ~ $1.2 \cdot 10^{-5}$ A (which corresponds to dark current density of $7.8 \cdot 10^{-2}$ $A \cdot cm^{-2}$) at a bias voltage of −1.0 V. This probably could indicate that high doping of active layers leads to an increase in diffusion dark current. But, as it was shown in [4], it is still necessary to slightly dope absorption layers. Therefore, for lowering dark current at small bias voltages doping concentration should probably be ~ $(1-2) \cdot 10^{16}$ cm^{-3}.

The suggested doping concentration value is close to the one recommended by some works [4]. However, it is much lower than in other studies, where the optimal doping concentration is claimed to be ~$(1-5) \cdot 10^{17}$ cm^{-3} for the lower leakage current [5].

It should be mentioned that the doping concentration is connected with the device capacitance. Consequently, it defines the response time and the thermal noise. Therefore, the impact of higher doping levels of the absorption layer on photodiode capacitance should also be researched. For this reason, capacitance-voltage curves were acquired to study manufactured PIN-structures S-1 and S-2.

The plot in Fig. 2 shows that $1/C^2-V$ characteristics are highly linear, which may indicate an abrupt $p-n$ junction [6]. As expected, higher doping concentration led to higher capacitance

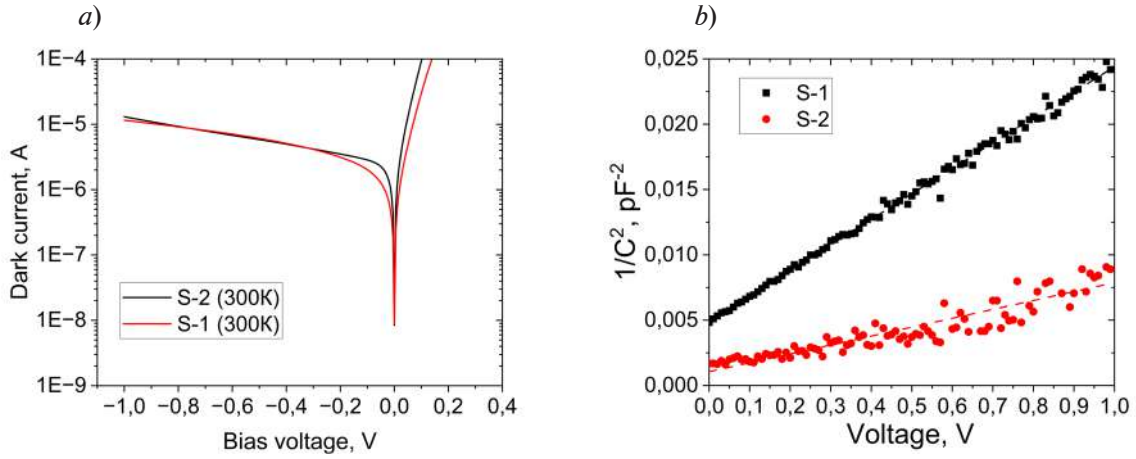

Fig. 2. $I-V$ (*a*) and $C-V$ (*b*) curves of samples

(lower $1/C^2$). Nevertheless, capacitance values for both samples were of the same order of magnitude: at a zero bias voltage it was 14 pF in S-1 and 24 pF in S-2. This might indicate that the doping level does not significantly affect the operating speed of manufactured pin-photodiode chips, which should be relatively high in both PIN-structures. Although, further measurements of response time are required.

Since sample S-1 had lower dark current, it was chosen for the investigation of current–voltage curves, obtained at different temperatures. Dark current decreases with temperature decline, showing the largest drop by more than two orders of magnitude at reverse bias voltages less than 0.4 V. It presumably indicates the high influence of diffusion dark current mechanism at lower reverse biases, which supports the idea of higher diffusion dark current in sample S-2 at room temperature. $I-V$ curves obtained at different temperatures are presented in Fig. 3.

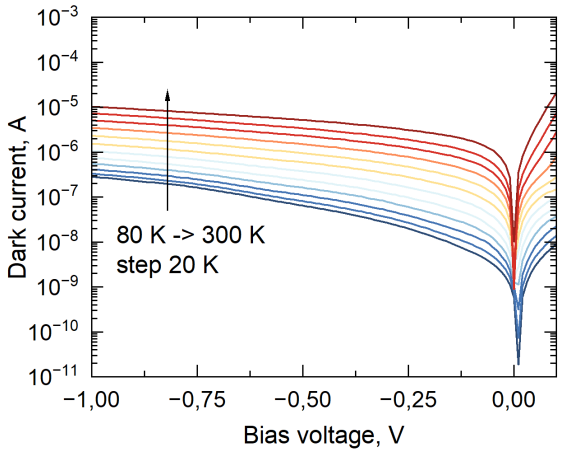

Fig. 3. Temperature dependence of $I-V$ curves

Conclusion

$In_{0.83}Ga_{0.17}As$/InP PIN-photodiode heterostructures with different doping levels of the absorption layer and superlattice inserts have been studied. It was discovered, that doping concentrations of active layers should be ~ $(1 - 2)\cdot10^{16}$ cm^{-3} for achieving better performance. The value of the dark current was determined to be ~ $1.2\cdot10^{-5}$ A at a bias voltage of −1.0 V at room temperature. Capacitance-voltage measurements have shown that an increase of the doping concentration led to an increase of the capacitance from 14 pF to 24 pF. The influence of different dark current mechanisms was determined based on dark current temperature dependence.

REFERENCES

1. **Burlakov I.D., Grinchenko L.Y., et al.,** Short wavelength infrared InGaAs detectors, Advances in Applied Physics (Uspekhi Prikladnoi Fiziki). 2 (2) 2014.

2. **Li P., Li T., Deng S., et al.,** Dark current analysis of mesa type In0.83Ga0.17As *p-i-n* photodiodes with different annealing treatment, Infrared and Laser Engineering. 45 (5) 2016.

3. **Vasilkova Ye.I., Pirogov Ye.V., Sobolev M.S., et al.,** Molecular beam epitaxy of metamorphic buffer for InGaAs/InP photodetectors with high photosensitivity in the range of 2.2–2.6 um, Condensed Matter and Interphases. 25 (1) (2023) 20–26.

4. **Chen X.Y., Gu Y., Zhang Y.G., et al.,** $In_{0.83}Ga_{0.17}As$ photodetectors with different doping concentrations in the absorption layers, Infrared Physics & Technology. 89 (2018) 381–386.

5. **Joshi A.M., Olsen G.H., Mason S.M., et al.,** Near-infrared (1-3 micron) InGaAs detectors and arrays - Crystal growth leakage current and reliability, Proc. SPIE 1715, Optical Methods in Atmospheric Chemistry. 1993.

6. **Sze S.M., Li Y., Ng K.K.,** Physics of semiconductor devices. – John wiley & sons. 2021.

7. **Ji X., Liu B., Tang H., et al.,** 2.6 μm MBE grown InGaAs detectors with dark current of SRH and TAT, AIP Advances. 4 (8) (2014) 087135.

THE AUTHORS

BARANTSEV Oleg V.
ovbarantsev@gmail.com
ORCID: 0000-0002-4894-6503

VOROPAEV Kirill O.
kirill.voropaev@novsu.ru
ORCID: 0000-0002-6159-8902

VASILKOVA Elena I.
elenvasilkov@gmail.com
ORCID: 0000-0002-0349-7134

VASIL'EV Andrey A.
Wasiliew.andre@yandex.ru
ORCID: 0009-0009-2615-6795

PIROGOV Evgeny V.
zzzavr@gmail.com

KARACHINSKY Leonid Ya.
karach@switch.ioffe.ru
ORCID: 0000-0002-5634-8183

SHUBINA Ksenya Yu.
rein.raus.2010@gmail.com
ORCID: 0000-0003-1835-1629

NOVIKOV Innokenty I.
novikov@switch.ioffe.ru
ORCID: 0000-0003-1983-0242

BARANOV Artem I.
itiomchik@yandex.ru

SOBOLEV Maxim S.
sobolevsms@gmail.com
ORCID: 0000-0001-8629-2064

Received 31.07.2024. Approved after reviewing 12.08.2024. Accepted 20.08.2024.

Conference materials
UDC 539.23
DOI: https://doi.org/10.18721/JPM.173.237

Electrical characteristics of semiconductor film structures obtained on a flexible substrate

A.V. Kozlowski✉, L.D. Volkovoynova, A.A. Serdobintsev

Saratov State University, Saratov, Russia

✉ kozlowsky@bk.ru

Abstract. In the frame of this work the current-voltage characteristics of thin films of polycrystalline silicon on a flexible polymer substrate were studied, measured when the film was bent in both tension and compression modes. The samples were fabricated by laser-stimulated metal-induced crystallization of amorphous Si films, deposited by magnetron sputtering on a flexible polyimide film both in constant power and pulsed mode. It has been established that the resistance of a polycrystalline Si film depends on the degree and type of deformation. The change in electrical resistance can be associated with an increase and decrease in the intergranular distance when the film is stretched and compressed, respectively. The resulting films are promising for the fabrication of semiconductor strain sensors and active elements of flexible electronics

Keywords: crystallization of amorphous silicon, metal-induced crystallization, laserstimulated crystallization, infrared laser radiation, flexible electronics

Funding: This study was funded by the Russian Science Foundation (project no. 23-22-00047, https://rscf.ru/project/23-22-00047/).

Citation: Kozlowski A.V., Volkovoynova L.D., Serdobintsev A.A., Electrical characteristics of semiconductor film structures obtained on a flexible substrate, St. Petersburg State Polytechnical University Journal. Physics and Mathematics. 17 (3.2) (2024) 187–191. DOI: https://doi.org/10.18721/JPM.173.237

Материалы конференции
УДК 539.23
DOI: https://doi.org/10.18721/JPM.173.237

Электрические характеристики полупроводниковых пленочных структур, полученных на гибкой подложке

А.В. Козловский✉, Л.Д. Волковойнова, А.А. Сердобинцев

Саратовский государственный университет имени Н.Г. Чернышевского, г. Саратов, Россия

✉ kozlowsky@bk.ru

Аннотация. В рамках данной работы были исследованы вольт-амперные характеристики тонких пленок поликристаллического кремния на гибкой полимерной подложке, измеренные при изгибе пленки как в режиме растяжения, так и в режиме сжатия. Образцы были изготовлены методом лазерно-стимулированной металл-индуцированной кристаллизации аморфных пленок Si, нанесенных методом магнетронного распыления на гибкую полиимидную пленку. Установлено, что сопротивление пленки поликристаллического кремния зависит от степени и вида деформации. Изменение электрического сопротивления может быть связано с увеличением и уменьшением межзеренного расстояния при растяжении и сжатии пленки, соответственно. Полученные пленки перспективны для изготовления полупроводниковых тензодатчиков и активных элементов гибкой электроники.

Ключевые слова: кристаллизация аморфного кремния, металл-индуцированная кристаллизация, лазер-стимулированная кристаллизация, инфракрасное лазерное излучение, гибкая электроника

Финансирование: Инновационный подход к формированию кристаллических кремниевых структур на гибких подложках с помощью лазер-стимулированной металл-индуцированной кристаллизации (Проект РНФ № 00047-22-23).

Ссылка при цитировании: Козловский А.В., Волковойнова Л.Д., Сердобинцев А.А. Электрические характеристики полупроводниковых пленочных структур, полученных на гибкой подложке // Научно-технические ведомости СПбГПУ. Физико-математические науки. 2024. Т. 17. № 3.2. С. 187–191. DOI: https://doi.org/10.18721/JPM.173.237

Introduction

Over the past decades, flexible electronics have undergone significant development due to its wide range of applications in various fields, including telecommunication systems, medicine, sensors, wearable devices, etc. [1–4]. An important problem in flexible electronics is the deposition of polycrystalline semiconductor thin films on flexible polymer substrates, which have a melting temperature lower than the crystallization temperature of semiconductor materials. In [5] reports a new method for the crystallization of thin silicon films, combining the advantages of laser and metal-induced crystallization technologies, which makes it possible to fabricate a polycrystalline silicon film on a flexible polyimide substrate. However, the stability of the electrical characteristics of polycrystalline films synthesized by this method on a polyimide film during its deformation has not previously been studied.

Therefore, the purpose of this work is to study the current-voltage characteristics (I–V curves) of thin films of polycrystalline silicon obtained by laser-stimulated metal-induced crystallization, measured when the film is bent in both tension and compression modes.

Materials and Methods

The samples were fabricated by magnetron sputtering of an amorphous silicon (a-Si) layer with 1 μm tick onto a 0.5-mm-thick polyimide substrate, followed by a layer of tin. Sputtering was carried out in a Nexdep installation (Angstrom Engineering, Canada), equipped with two magnetron sources with disk targets with a diameter of 76 mm. The residual pressure in the chamber was $2 \cdot 10^{-5}$ Torr. Argon was filled into the chamber until the operating pressure was $3.4 \cdot 10^{-3}$ Torr. Two samples were formed, differing in the silicon deposition mode. In the first case, silicon deposition occurred in direct current mode (constant mode, CM), in the second in pulsed mode with a frequency of 25 kHz and duty cycle of 75% (pulse mode, PM). Thus, two variants of a thin-film structure were obtained on a flexible polymer substrate, consisting of a 1-μm-thick silicon layer deposited directly on the polyimide substrate and a 40-nm-thick tin layer on top of the silicon. The power of the silicon magnetron source during the deposition process stabilized at the level of 500 W, the metal one at the level of 300 W. The thickness of the sprayed layers was controlled using piezoquartz sensors installed in a vacuum chamber and a digital spraying rate control system (Sycon, USA).

The resulting structures were processed on a MiniMarker-2 machine (Laser Center, Russia), equipped with a pulsed fiber laser with a wavelength of 1064 nm. Laser processing was carried out at the pulse energy was $1 \cdot 10^{-5}$ J, a pulse repetition rate of 200 kHz and a laser beam speed of 1200 mm/s. The duration of the pulse was 14 ns. Thus, the metal film served simultaneously as a laser radiation absorption layer and a crystallization inductor. A laser spot diameter is 20 μm. Since the distance between pulses is less than the diameter of the laser spot, these scanning parameters make it possible to obtain evenly crystallization of silicon over the entire treatment area. The presence of the crystalline phase was confirmed by the method of Raman's spectroscopy

using the InVia (Renishaw, Great Britain). The spectrometer has a laser with a wavelength of 532 nm, a laser power up to 0.01 mW, a lens with a 50-fold increase. The obtained samples were studied by atomic force microscopy (AFM) by NTEGRA Spectra (NT-MDT Spectrum Instruments, Russia).

To realize the bending of the resulting films at a given angle, both in the stretching and compression modes, 3D printed equipment was manufactured that made it possible to secure two clamps. In this case, one clamp was stationary, and the second could be moved around the circle (Fig. 1).

Current-voltage characteristics (I–V curves) were measured using a probe station and an

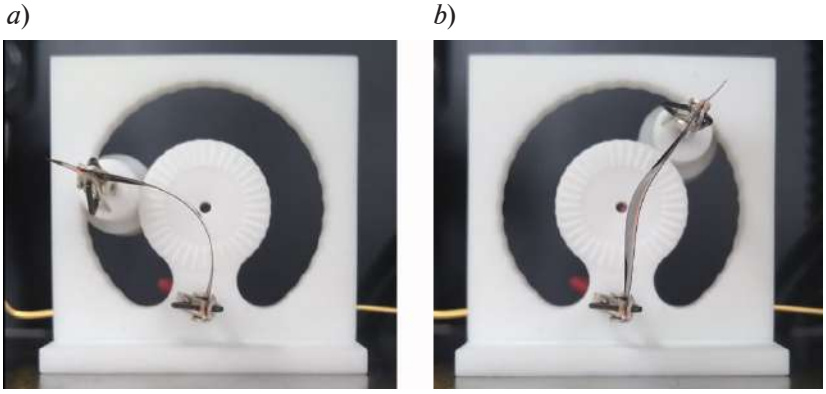

Fig. 1. Implementation of tension (*a*) and compression (*b*) modes of a polycrystalline silicon film on a flexible substrate when it is bent at a given angle

Agilent B1500a semiconductor device analyzer.

Results and Discussion

Fig. 2 shows AFM-images for the surface of an amorphous silicon film obtained both in constant and pulsed mode. From each AFM image, the surface roughness and average grain size were determined. Amorphous silicon films obtained in constant mode have an average surface roughness of 1.440.79± nm. For films fabricated in a pulsed mode, the average surface roughness is lower: 0.95±0.64 nm. Moreover, these films have a larger average grain size (52.98 nm) than that of films obtained in constant mode (32.73 nm). Laser processing of films with Sn layer leads to a hundredfold increase in surface roughness, regardless of the mode of obtaining the amorphous silicon film.

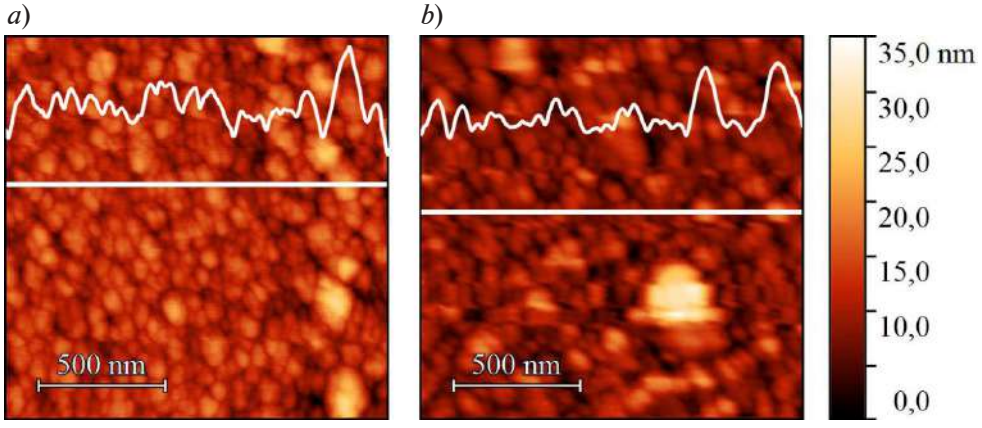

Fig. 2. AFM-images of studied amorphous silicon films on flexible polyimide substrate, obtained in constant power mode (*a*) and in pulsed mode (*b*)

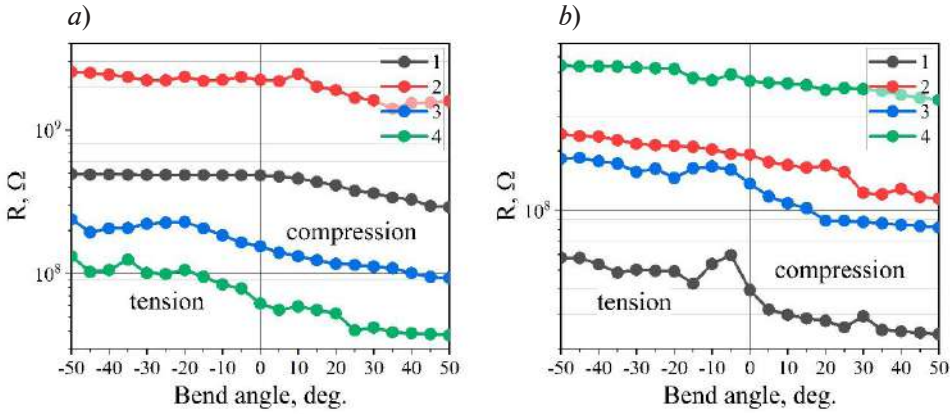

Fig. 3. Influence of bending on resistance of thin Si films: silicon films deposited at constant mode (*a*); silicon film was deposited at pulsed mode (*b*); bare silicon film *1*; Si film after laser treatment *2*; Si film with Sn layer *3*; Si film with Sn layer after laser processing *4*

The $I-V$ curves of amorphous silicon films are linear, while curves of polycrystalline silicon films are nonlinear. When the film is bent in tension mode, its conductivity decreases, and when it is bent in compression mode, it increases. Moreover, the resistance of amorphous silicon films changes nonmonotonic with increasing bending angle. Fig. 3 shows the effect of Si film bending on its resistance after laser-stimulated metal-induced crystallization.

When the film is stretched, its resistance is on average $1.57 \cdot 10^9$ Ω, and when compressed it is $5.26 \cdot 10^7$ Ω. Such changes may be associated with an increase and decrease in the intergranular distance when the film is stretched and compressed, respectively.

The resistance of pure amorphous silicon films is poorly dependent on the bending angle. After laser processing, the resistance increases by an order of magnitude. This change can be associated with a predominance of ablation, which leads to thinner film and therefore to greater resistance. Also, this change can occur due to an increase in the density of defects caused by laser radiation. Adding a metal layer over a layer of amorphous silicon predictably leads to an increase in conductivity, and laser processing increases the conductivity even more. This change is associated with significant crystallization of the silicon film, which is confirmed by the data of AFM and Raman spectroscopy. Analysis of changes in the resistance of Si films obtained in pulsed mode requires additional comprehensive studies of the chemical and phase composition, for example, by methods of secondary ion masses of spectrometry and X-ray analysis.

Conclusion

Thus, thin films of polycrystalline silicon were obtained on a flexible substrate. It was found that the film resistance depends on the degree and type of deformation, therefore these films are promising for the fabrication of semiconductor strain sensors and active elements of flexible electronics.

Acknowledgments

This study was funded by the Russian Science Foundation (project No. 23-22-00047, https://rscf.ru/project/23-22-00047/).

REFERENCES

1. **Gao W., Ota H., Kiriya D., et al.,** Flexible electronics toward wearable sensing, Accounts of Chemical Research. 52 (3) (2019) 523–533.

2. **Dong X., Chen L., Su X., et al.,** Flexible aqueous lithium-ion battery with high safety and large volumetric energy density, Angewandte Chemie International Edition. 55 (26) (2016) 7474–7477.

3. **Cao Y., Zhang G., Zhang Y., et al.,** Direct fabrication of stretchable electronics on a polymer substrate with process-integrated programmable rigidity, Advanced Functional Materials. (2018) 1804604.

4. **Chortos A., Liu J., Bao Z**., Pursuing prosthetic electronic skin, Nature Materials. 15 (9) (2016) 937–950.

5. **Serdobintsev A.A., Luzanov V.A., Kozhevnikov I.O., et al.,** Thin amorphous silicon films crystallization upon flexible substrates, J. Phys. Conf. Ser. 1400 (2019) 055034.

THE AUTHORS

KOZLOWSKI Alexander V.
kozlowsky@bk.ru
ORCID: 0000-0002-3612-9776

SERDOBINTSEV Alexey A.
alexas80@bk.ru
ORCID: 0000-0003-3281-8352

VOLKOVOYNOVA Larisa D.
loris.volkoff@gmail.com
ORCID: 0000-0001-6780-9865

Received 27.07.2024. Approved after reviewing 08.08.2024. Accepted 10.08.2024.

Conference materials
UDC 621.373.826
DOI: https://doi.org/10.18721/JPM.173.238

The use of Raman and laser-induced breakdown spectroscopy for the study of iron-containing inks

O.S. Gribovskaya[1]✉, N.A. Sharkova[1], A.V. Vasilieva[1], V.A. Parfenov[1]

[1] St. Petersburg Electrotechnical University "LETI", St. Petersburg, Russia

✉ fen.tefal2@gmail.com

Abstract. The paper presents experimental results of combined use of Raman and laser-induced breakdown spectroscopy (LIBS) for determining elemental composition of iron-containing inks. It was shown that proposed approach allows to solve the problem of iron-containing components identification for paper artifacts.

Keywords: iron gall ink, Raman spectroscopy, laser-induced breakdown spectroscopy, LIBS, chemical composition analysis

Citation: Gribovskaya O.S., Sharkova N.A., Vasilieva A.V., Parfenov V.A., The use of Raman and laser-induced breakdown spectroscopy for the study of iron-containing inks, St. Petersburg State Polytechnical University Journal. Physics and Mathematics. 17 (3.2) (2024) 192–195. DOI: https://doi.org/10.18721/JPM.173.238

Материалы конференции
УДК 621.373.826
DOI: https://doi.org/10.18721/JPM.173.238

Использование Рамановской и лазерно-искровой эмиссионной спектроскопии для исследования железосодержащих чернил

О.С. Грибовская[1]✉, Н.А. Шаркова[1], А.В. Васильева[1], В.А. Парфенов[1]

[1] Санкт-Петербургский государственный электротехнический университет «ЛЭТИ» им. В.И. Ульянова (Ленина), Санкт-Петербург, Россия

✉ fen.tefal2@gmail.com

Аннотация. В статье представлены экспериментальные результаты совместного использования методов Рамановской и спектроскопии лазерно-индуцированной плазмы (LIBS) для определения элементного состава железосодержащих чернил. Показано, что предложенный подход позволяет решить проблему идентификации железосодержащих компонентов для бумажных артефактов.

Ключевые слова: железосодержащие чернила, Рамановская спектроскопия, спектроскопия лазерно-индуцированного пробоя, лазерно-искровая эмиссионная спектроскопия, LIBS, исследование химического состава

Ссылка при цитировании: Грибовская О.С., Шаркова Н.А., Васильева А.В., Парфенов В.А. Использование Рамановской и лазерно-искровой эмиссионной спектроскопии для исследования железосодержащих чернил // Научно-технические ведомости СПбГПУ. Физико-математические науки. 2024. Т. 17. № 3.2. С. 192–195. DOI: https://doi.org/10.18721/JPM.173.238

Introduction

Iron gall ink is one of the earliest materials used by humans for writing, which is made from iron salts (most commonly from vitriol) and a mixture of organic colorants and tannins. Comparing with inks, containing copper salts as a base, iron gall inks can eventually cause damage to paper [1], which is a significant obstacle to preserving paper manuscripts and ancient books. In order to address the issue of detecting iron and other chemical elements within ink, it becomes necessary to develop techniques for its detection in various ways.

One of the modern methods for study chemical composition of different materials is Raman spectroscopy. Despite the fact that Raman spectroscopy is a highly effective, non-invasive technique, working with inks can be challenging [2]. This may be due to the complex nature of inks and the presence of fluorescent additives that can hinder the detection of weaker band intensities [3, 4]. That is why it is necessary to create an investigation technique for inks, which includes some alternative methods of identification.

Laser-induced breakdown spectroscopy (LIBS) technique, unlike many others, can detect the presence of specific elements in a material's composition. The method is not completely nondestructive, but it does allow for measurements with minimal damage to the surface of the sample [5]. Thus, in this work chemical composition of model ink sample is studied with Raman spectroscopy and LIBS to create a technique for paper artifacts investigation.

Materials and Methods

In experiments we used model sample imitation the sheet of manuscript. The model sample was created in a cellulose paper, where the inks, made by hot infusion of gall nuts, iron vitriol, cherry resin and drinking water were put with the brush.

For this work a Raman Confocal microscope Confotec MR350 (SOL instruments Ltd., Germany) with 785 and 850 nm working wavelength and 1 micron laser spot was used. The detector had special cooling system to increase temperature up to −30 °C. In order to avoid the thermal heating of the paper by laser and the destruction of the sample, the ND filter (absorber) was installed either. The sample was placed on the working surface, then it was pressed with a weight to avoid fluctuations. Spectral range for Raman spectra detection was from 99 cm^{-1} to 1734 cm^{-1} with spectral resolution of at least 0.145 cm^{-1}.

For the study, LIBS setup (Onteko, USA) was employed. A pulsed Nd:YAG nanosecond laser with focal spot size up to 30 microns operated at a wavelength of 1064 nm with a maximum pulse energy of 28 mJ. USB4000 spectrometer (Ocean Insight, USA) operated in the spectral range of 200−1100 nm with spectral resolution ranging from 0.1−10 nm and an integration time ranging from 3.8 milliseconds to 10 seconds. Additionally, part of the setup included the following software programs: OceanView (a specialized spectrometer software), and LIBS Identification Software for processing the acquired spectra. The sample was placed at 7 cm from the laser outlet. A two-pulse laser mode with pulse energy of 5 mJ was used for measurements.

In both cases, for Raman and LIBS, measurements of paper uncoated with ink and paper covered with ink were carried out, when subtracting the first measurement from the second, a spectra of pure ink were obtained.

Results and Discussion

Analysis of Raman spectrum (Fig. 1) showed no peaks of iron-containing components, however clear peaks corresponding to glucose and fructose, as well as peaks corresponding to tannin, were detected in the spectrum, making possible the identification of cherry resin (1400 cm^{-1}) and gall nuts (550 cm^{-1}).

It is worth noting that to interpret the Raman spectra of ink, a personal library of Raman spectra of some substances typical for ink composition was created. More details about this study are shown in the previous work [6].

The obtained LIBS spectrum (Fig. 2) was compared with the National Institute of Standards and Technology (NIST) database [7]. Peaks corresponding to iron at wavelengths of 274.7, 357.8, 374.1, 382.4, 385.6 and 393 nm, as well as sodium at 589 nm, were detected in the spectrum.

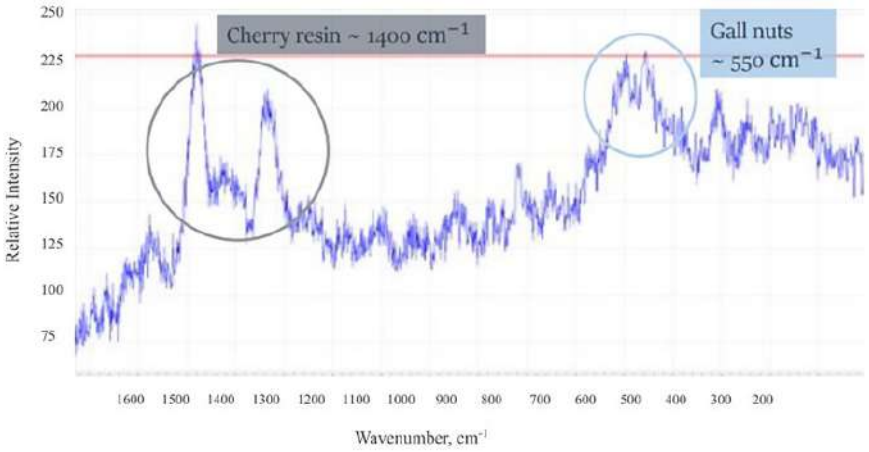

Fig. 1. Raman spectra of iron gall ink

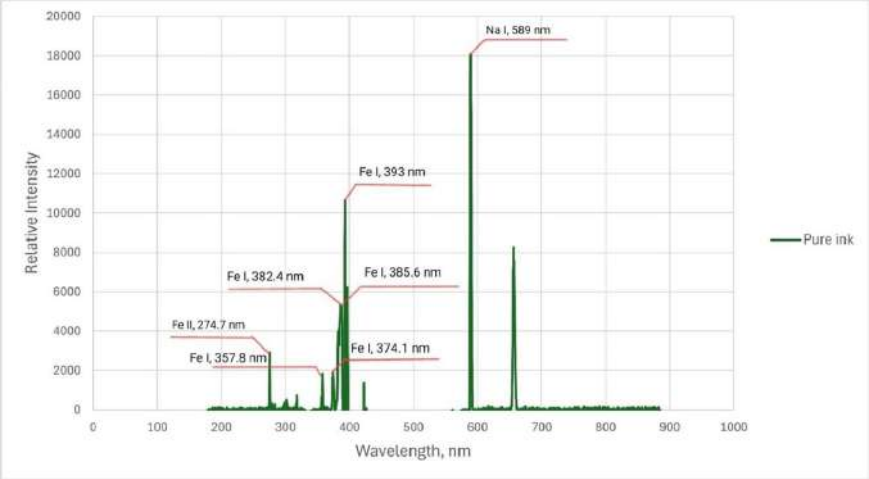

Fig. 2. LIBS spectra of iron gall ink

After reviewing relevant literature [8, 9, 10], it was determined that the spectral data obtained from LIBS method agrees with reference data, indicating that the method can detect iron and sodium in various compounds.

Conclusion

The problem of iron-containing components identification in Raman spectroscopy could be explained by alternative prohibition rule: in a molecule with an inversion center, all infrared bands will be prohibited in the raman spectrum and all Raman bands will be prohibited in the infrared ranges. This study showed that combined use of LIBS and Raman spectroscopy techniques for the ink investigation allows neglecting this problem. The Raman spectroscopy is suitable for identifying organic components of inks such as gall nuts and cherry resin, while LIBS peaks indicated the presence of iron and sodium. Sodium could be referring to contaminations or hand marks. In both spectral measurements no paper destroy was observed. Therefore, the combination of Raman and LIBS methods is a very effective analytical technique which can be recommended for paper artifacts studies.

REFERENCES

1. **Hidalgo D., Cyrdoba R., Nabais P., et al.,** New insights into iron-gall inks through the use of historically accurate reconstructions. Heritage Science. 6 (2018) 1–15.

2. **Cicconi F., Lazic V., Palucci A., et al.,** Forensic analysis of commercial inks by Laser-Induced Breakdown Spectroscopy (LIBS). Sensors. 20 (2020) 1–20.

3. **Edwards H.G.M.,** Raman Spectroscopy in Archaeology and Art History. The Royal Society of Chemistry, Cambridge. (2) 2018.

4. **Lee A.S., Mahon P.J., Creagh D.C.,** Raman analysis of iron gall inks on parchment. Vibrational Spectroscopy. 41 (2) (2006) 170–175.

5. **Goltz D.M.,** A Review of Instrumental Approaches for Studying Historical Inks. Analytical Letters. 45 (4) (2012) 314–329.

6. **Sharkova N.A., Vasilieva A.V., Parfenov V.A.,** Application of Raman and LIBS Spectroscopy for Qualitative Analysis of Historical Ink. Conference of Young Researchers in Electrical and Electronic Engineering (ElCon). (2024) 761 – 764.

7. NIST LIBS Database. URL: https://physics.nist.gov/PhysRefData/ASD/LIBS/libs-form.html. Accessed Mar. 25, 2024.

8. LIBS Info: Fe Analysis. URL: https://libs-info.com/element/Fe/. Accessed Mar. 25, 2024.

9. **Nasrullah I., Kurnia L., Ramli F., Ramli M.,** Study on Emission Spectral Lines of Iron, Fe in Laser-Induced Breakdown Spectroscopy (LIBS) on Soil Samples. Journal of Physics: Conference Series. 846 (2015) 1–7.

10. **Usmawanda T.N., Ramli M., Idris N.,** Emission Spectral Profile of Salt in Laser-Induced Breakdown Spectroscopy (LIBS) on River Clamshell Sample. Journal of Physics: Conference Series. 1116 (2018) 1–10.

THE AUTHORS

GRIBOVSKAYA Olga S.
fen.tefal2@gmail.com
ORCID: 0009-0009-7765-2609

VASILIEVA Anastasia V.
anastasiastru@mail.ru
ORCID: 0000-0002-5317-3322

SHARKOVA Natalia A.
nasharkova@stud.etu.ru

PARFENOV Vadim A.
vadim_parfenov@mail.ru
ORCID: 0000-0002-2048-4677

Received 28.07.2024. Approved after reviewing 12.08.2024. Accepted 28.08.2024.

Conference materials
UDC 544.032
DOI: https://doi.org/10.18721/JPM.173.239

Composition of Al/Zn nanoparticles produced in a gas discharge

A.K. Novosyolov✉, A.F. Sanatulina, O.V. Vershinina,
A.A. Lizunova, S.A. Gudkova, M.N. Urazov

Moscow Institute of Physics and Technology (National Research University), Dolgoprudny, Russia

✉sir.nowosiolov@yandex.ru

Abstract. In this work, we investigated the size and elemental composition of a binary of aluminum/zinc nanoparticles synthesized in a gas discharge generator. Al_xZn_{1-x} nanoparticles were produced in inert atmosphere by simultaneous erosion of aluminum hole cathode and a zinc anode. Mass fractions of aluminum x were varied from 0.05 to 0.29 by changing the surface area of the aluminum electrode. It was found that the mass fraction of aluminum in binary composition increased 2.6 times when erosion surface of the Al cathode dropped from 188.5 to 37.7 mm^2. The average sizes of primary nanoparticles were in the range from 12.8 to 18.6 nm, which formed submicron agglomerates. Also, when the erosion process occurred in an air atmosphere, we produced zinc aluminate $AlZn_2O_4$ with luminescence in ultraviolet (UV) range.

Keywords: nanoparticles, zinc aluminate, size measurement, gas discharge, TEM, erosion

Funding: This work was financially supported by the Russian Science Foundation (project no. 22-19-00311, https://rscf.ru/en/project/22-19-00311/).

Citation: Novosyolov A.K., Sanatulina A.F., Vershinina O.V., Lizunova A.A., Gudkova S.A., Urazov M.N., Composition of Al/Zn nanoparticles produced in a gas discharge, St. Petersburg State Polytechnical University Journal. Physics and Mathematics. 17 (3.2) (2024) 196–200. DOI: https://doi.org/10.18721/JPM.173.239

Материалы конференции
УДК 544.032
DOI: https://doi.org/10.18721/JPM.173.239

Состав наночастиц Al/Zn, полученных в газовом разряде

А.К. Новосёлов✉, А.Ф. Санатулина, О.В. Вершинина,
А.А. Лизунова, С.А. Гудкова, М.Н. Уразов

Московский физико-технический институт (национальный исследовательский университет),
г. Долгопрудный, Россия

✉ sir.nowosiolov@yandex.ru

Аннотация. В этой работе мы исследовали размер и элементный состав бинарных наночастиц алюминия/цинка, синтезированных в газоразрядном генераторе. Наночастицы Al_xZn_{1-x} были получены в инертной атмосфере путем одновременной эрозии алюминиевого катода с отверстием и цинкового анода. Массовую долю алюминия x варьировали от 0.05 до 0.29 изменяя площадь поверхности алюминиевого электрода. Было обнаружено, что массовая доля алюминия в бинарной композиции увеличилась в 2,6 раза, когда эрозионная поверхность алюминиевого катода снизилась со 188.5 до 37.7 мм^2. Средние размеры первичных наночастиц находились в диапазоне от 12.8 до 18.6 нм, которые образовывали субмикронные агломераты. Кроме того, когда процесс эрозии происходил в воздушной атмосфере, мы получали алюминат цинка $AlZn_2O_4$ с люминесценцией в ультрафиолетовом (УФ) диапазоне.

Ключевые слова: наночастицы, алюминат цинка, измерение размеров, газовый разряд, ПЭМ, эрозия

Финансирование: Работа выполнена при финансовой поддержке Российского научного фонда (проект № 00311-19-22, https://rscf.ru/en/project/22-19-00311/).

Ссылка при цитировании: Новосёлов А.К., Санатулина А.Ф., Вершинина О.В., Лизунова А.А., Гудкова С.А., Уразов М.Н. Состав наночастиц Al/Zn, полученных в газовом разряде // Научно-технические ведомости СПбГПУ. Физико-математические науки. 2024. Т. 3.2 № .17. С. 196–200. DOI: https://doi.org/10.18721/JPM.173.239

Introduction

Gas discharge [1] is an excellent method for producing chemically pure metal nanoparticles (NP), semiconductors, and several component compounds [2]. Complex two-component NPs can be made using electrodes of the required complex chemical composition for erosion. However, not all materials can be used to make required electrodes, therefore, a manufacturing method with simultaneous erosion [3] of the cathode and anode from different materials is relevant, allowing to produce NP of substances that cannot be mixed on a macroscopic scale [4].

To vary the composition of two-component particles using different anode and cathode materials, it is necessary to regulate the energy and type of electric pulse supplied to the electrodes [5], as well as the flow rate of the carrier gas in the setup [3]. In this work we proposed alternative method to control the composition of binary nanomaterials, based on varying the surface area of electrodes. This approach leads to a change in the energy density of the surface for erosion of the electrodes, allowing for a different ratio of mass fractions of the particle components. Using aluminum and zinc as electrodes, it is possible to obtain a promising material – zinc aluminate.

Zinc aluminate is an important functional material with unique properties such as high thermal stability, optical transparency and luminescence [6]. These properties also make it possible to use zinc aluminate as a cathodoluminophore in modern sources of visible and ultraviolet radiation. Therefore, it is an important task to develop various methods for the synthesis of zinc aluminate, which make it possible to obtain particles with various characteristics. Methods for the synthesis of zinc aluminate are known: sol-gel method [7], method of co-deposition [8], solid-phase mechanochemical synthesis [9], hydrothermal and microwave methods [8].

Thus, the purpose of this work was to study the elemental composition of binary Al_xZn_{1-x} nanoparticles produced in gas discharge in inert atmosphere when changing the geometric parameters of the aluminum cathode with constant geometry of the zinc anode. And estimate the possibility of synthesis nanosized zinc aluminate in air atmosphere, characterized the size, morphology, phase and optical properties of obtained nanoparticles.

Materials and Methods

The synthesis was carried out on a setup consisting of a gas discharge chamber and a gas path [2]. A capacitor 107 nF was used for discharge, a voltage of 1.5 kV and a current value of 60 mA were set on the generator, which made it possible to achieve a discharge frequency of 500 Hz. Pure Ar 4.8 with a flow rate of 600 ml/min was used as the carrier gas, in which self-passivation of the obtained particles was carried out for 20 hours after synthesis. To study the particle elemental composition and size, depending on the geometry of the aluminum cathode, we manufactured two types of hole cylindrical Al electrodes with different surface area: the first type of the electrodes had fixed external diameter 8 mm and variable internal one: 2, 4.5, 5.3, 6 mm; the second type of the electrodes characterized fixed internal diameter 2 mm and external diameter 4, 5.3, 6.3 and 8 mm. Thus, the surface area of the end of the Al electrodes was from 37.7 mm^2 to 188.5 mm^2. Energy density stored in the capacitor and released between the electrodes was calculated as the ratio of the energy on the capacitor, equal to 120.4 MJ, to the surface

area of the erosion of the aluminum electrode. Studies of the crystal structure, particle sizes and elemental composition of nanoparticles, were carried out using transmission electron microscopy (TEM) JEM-2100 (JEOL, Ltd., Tokyo, Japan) with energy dispersive X-ray analysis (EDX) Oxford X-MaxN, data on the particle size distribution of agglomerates were obtained using the aerosol spectrometer TSI SMPS 3936. The crystal structure of the samples was studied by X-ray diffraction on a Drawell DW-XRD-2700A diffractometer, China. The studies were carried out in the Bregg-Brentano geometry using a copper X-ray tube with a wavelength of 1.54 E. The scanning speed was 0.5 deg./min.

Results and Discussion

Based on the images obtained on the TEM (Fig. 1, *a*), a primary particle size distribution was obtained for each surface area of the electrodes. It was found that the particle sizes range from 12.8 ± 3.9 nm to 18.6 ± 6.3 nm regardless of the size of the aluminum electrode. To determine the elemental composition of the obtained nanoparticles, elemental spectra of agglomerates were performed using energy dispersion analysis on TEM (Fig. 1, *b*), from which the mass fraction of each element of the mixture of NPs was calculated. The minimum value of the ratio of the mass fraction of zinc to aluminum is 2.5 witHh an Al electrode area of 37.7 mm^2 and increases to 20 when the area is 188.5 mm^2 (Fig. 1, *c*). That means we can regulate the composition of Al/Zn nanoparticles and get binary material from $Al_{0.05}Zn_{0.95}$ to $Al_{0.29}Zn_{0.71}$ by ranging the energy density of an electric pulse between the electrodes. The size distribution of agglomerates of the particles obtained during synthesis using an aerosol spectrometer was also determined. A range of sizes of nanoparticle agglomerates was obtained: from 88 ± 2 nm to 139 ± 1 nm and is described by an increasing linear function (Fig. 1, *d*).

Particles were also synthesized in air with an electrode with an erosion area of 188.5 mm^2,

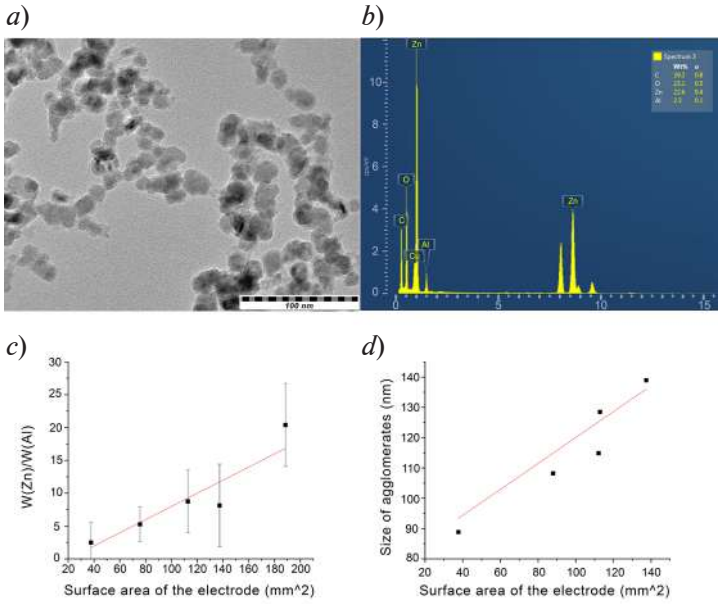

Fig. 1. Characterization of nanoparticles: typical TEM image of primary nanoparticles in agglomerate (area of erosion of aluminum electrode is 112 mm^2) (*a*); EDX spectra of agglomerate (area of erosion of aluminum electrode is 112 mm^2) (*b*); dependence of ratio of mass fractions of zinc and aluminum on the surface area of the aluminum electrode (*c*); dependence of size of agglomerates on surface area of aluminum electrode (*d*)

since this option gives a minimum aluminum content, which, according to literature data, can provide a luminescent material. Photoluminescent spectrum of obtained mixed powder reveal the ultraviolet luminescence in the wide range with a maximum at 375 nm (Fig. 2, *a*). The XRD spectrum shows that we have a mixture of several phases in the air – zinc oxide, aluminum oxide and zinc aluminate (Fig. 2, *b*). We have considered two synthesis options with the same energy density of 638.6 J/m^2 (surface area of 188.5 mm^2): in an inert environment and in the air. Using

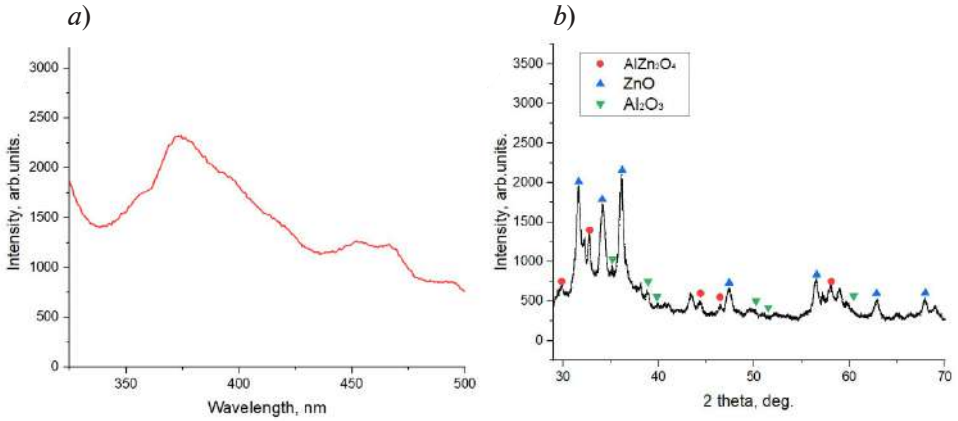

Fig. 2. Characterization of powder obtained in air with simultaneous erosion of aluminum cathode with area of 188.5 mm^2 and zinc anode: PL-spectra (*a*); XRD-spectra (*b*)

EDX analysis of the surface of the electrodes, it was obtained that the mass fraction of oxygen on both electrodes, which was constant and approximately equal to 2% in an inert medium, became equal to 34% in the air, which indicates the formation of metal oxides.

Conclusion

It was found that by changing the geometry of aluminum cathode in gas discharge generator, the elemental composition of binary Al_xZn_{1-x} nanoparticles produced in inert atmosphere can be adjusted in the range of x from 0.05 to 0.29. At the same time, the average diameter of obtained nanoparticles varied from 12.8 nm to 18.6 nm regardless of the erosion surface of the aluminum electrode. The sizes of agglomerates linearly increase from 88 nm to 139 nm and the ratio of the mass fraction of zinc to the mass fraction of aluminum increases from 2.5 to 20 when the erosion surface increases from 37.7 mm^2 to 188.5 mm^2. XRD analysis of NPs synthesized in air showed the presence of a multicomponent mixture: zinc aluminate, zinc oxide and aluminum oxide, which have maximum photoluminescence in UV range.

Acknowledgments

This work was financially supported by the Russian Science Foundation (project № 22-19- 00311, https://rscf.ru/en/project/22-19-00311/).

REFERENCES

1. **Ivanov V.V., Efimov A.A., Mylnikov D.A., et. al.,** High-efficiency synthesis of nanoparticles in a repetitive multigap spark discharge generator, Technical Physics Letters. (2016) 42 (8) 876–878.

2. **Lizunova A.A., Borisov V.I., Malo D., et. al.,** Spark Discharge Synthesis and characterization of Ge/Sn Janus Nanoparticles, Nanomaterials. (2023) 13 (10) 1701.

3. **Tabrizi N.S., Ullmann M., Vons V.A., et. al.,** Generation of nanoparticles by spark discharge, J. Nanoparticle Res. (11) (2009) 332–315.

4. **Feng J., Ramlawi N., Biskos G., Schmidt-Ott A.,** Internally mixed nanoparticles from oscillatory spark ablation between electrodes of different materials, Aerosol Sci.Technol. (52) (2018) 514–505.

5. **Kohut A., Villy L.P., Kéri A., et. al.,** Full range tuning of the composition of Au/Ag binary nanoparticles by spark discharge generation, Sci. Rep. (11) (2021) 5117.

6. **Bakhmetyev V.V., Malygin B.B., Podsypanina N.S., et. al.,** Synthesis and investigation of the properties of phosphors for cathodoluminescent sources of ultraviolet radiation, Innovative materials and technologies in design. (2017) 53–64.

7. **Shiva S.,** Rapid combustion synthesis of pure nano-crystalline gahnite: Effect of solution pH on powder characteristics, Thermochimica Acta Volume. (609) (2015) 75–81.

8. **Foletto E.L., Battiston S., Simxes J.M., et. al.,** Synthesis of $ZnAl_2O_4$ nanoparticles by different routes and the effect of its pore size on the photocatalytic process, Microporous and Mesoporous Materials. (2012) 29–33.

9. **Ishinaga T., Iguchi T., Kominami H., et al.,** Luminescent property and mechanism of $ZnAl_2O_4$ultraviolet emitting phosphor, Special Issue:19th International Conference on Ternary and Multinary Compounds (ICTMC-19). (12) (2015) 797–800.

THE AUTHORS

NOVOSYOLOV Artyom K.
novoselov.ak@phystech.edu
ORCID: 0009-0006-4525-1788

URAZOV Maxim N.
urazov.mn@mipt.ru
ORCID: 0000-0003-4270-6346

SANATULINA Arina S.
sanatulina.af@phystech.edu
ORCID: 0009-0001-9442-196X

GUDKOVA Svetlana A.
svetlanagudkova@yandex.ru
ORCID: 0000-0002-3028-947X

VERSHININA Olesya V.
seraia.ov@phystech.edu
ORCID: 0000-0001-6945-4818

LIZUNOVA Anna A.
anna.lizunova@gmail.com
ORCID: 0000-0002-2895-4696

Received 31.07.2024. Approved after reviewing 16.08.2024. Accepted 17.08.2024.

PHYSICAL OPTICS

Conference materials
UDC 621. 397
DOI: https://doi.org/10.18721/JPM.173.240

Identification of unreadable marginalia by means of hyperspectral imaging: case study of the Ostrog Bible from the Library of Russian Academy of Sciences and Russian National Library

P.S. Baranov[1], V.A. Parfenov[1], S.L. Rongonen[2], N.M. Sokolov[1]✉

[1] St. Petersburg Electrotechnical University "LETI", St. Petersburg, Russia;

[2] Russian Academy of Science Archive, St. Petersburg, Russia

✉ niksokolov2001@mail.ru

Abstract. Experiments on visualization of unreadable manuscript marginalia (fading of ink, spreading of ink, crossed out ink, scraping of ink, gluing with restoration materials) of several copies of the Ostrog Bibles from the National Library of Russia and the Library of Russian Academy of Sciences using hyperspectral imaging have been conducted. The aim of work was to find a way using advanced opto-electronic techniques to read invisible marginalia. In experiments NIR hyperspectral camera operating in the range 400–1100 nm and original self-developed software were used. Marginalia have been visualized by means of hyperspectral imaging that made possible to recognize badly visible texts and bring new information for art historians.

Keywords: hyperspectral imaging, unreadable marginalia, Ostrog bible, manuscript, cultural heritage, opto-electronic techniques

Citation: Baranov P.S., Parfenov V.A., Rongonen S.L., Sokolov N.M., Identification of unreadable marginalia by means of hyperspectral imaging: case study of the Ostrog Bible from the Library of Russian Academy of Sciences and Russian National Library, St. Petersburg State Polytechnical University Journal. Physics and Mathematics. 17 (3.2) (2024) 201–206. DOI: https://doi.org/10.18721/JPM.173.240

Материалы конференции
УДК 621. 397
DOI: https://doi.org/10.18721/JPM.173.240

Распознавание нечитаемых маргиналий с помощью гиперспектральной съемки на примере экземпляров Острожской библии из библиотеки Российской Академии Наук и Российской национальной библиотеки

П.С. Баранов[1], В.А. Парфенов[1], С.Л. Ронгонен[2], Н.М. Соколов[1]✉

[1] Санкт-Петербургский государственный электротехнический университет «ЛЭТИ» им. В.И. Ульянова (Ленина), Санкт-Петербург, Россия;

[2] Архив Российской академии наук, Санкт-Петербург, Россия

✉niksokolov2001@mail.ru

Аннотация. Представлены результаты экспериментов по визуализации нечитаемых рукописных маргиналий (выцветание, растекание чернил, зачеркивание чернил, соскабливание чернил, заклейка реставрационными материалами) нескольких

экземпляров Острожской библии из фондов Российской Национальной библиотеки и Библиотеки Российской Академии наук с использованием гиперспектральной съемки. Целью работы был поиск эффективных способов визуализации нечитаемых маргиналий с помощью инновационных оптико-электронных методов. В экспериментах использован гиперспектральный комплекс с линейным сканированием, работающий в диапазоне 400 – 1100 нм, и оригинальное программное обеспечение собственной разработки.

Ключевые слова: гиперспектральная камера, нечитаемые маргиналии, Острожская библия, рукопись, культурное наследие, оптико-электронные методы

Ссылка при цитировании: Баранов П.С., Парфенов В.А., Ронгонен С.Л., Соколов Н.М. Распознавание нечитаемых маргиналий с помощью гиперспектральной съемки на примере экземпляров Острожской библии из Библиотеки Российской Академии наук и Российской национальной библиотеки // Научно-технические ведомости СПбГПУ. Физико-математические науки. 2024. Т. 17. № 3.2. С. 201–206. DOI: https://doi.org/10.18721/JPM.173.240

Introduction

The Ostrog bible is the first printed Bible in the Church Slavonic language, common to the contemporary Russians, Belarusians and Ukrainians. Published in 1581 in the city of Ostrog it became an outstanding example of translation, textual and publishing approaches. The Ostrog bible was a serious factor of the predication of Orthodoxy, the development of theology and printing tradition. Copies of the Ostrog bible have been well studied from different points of view. The diverse studies of the Ostrog bible have formed a large-scale array of interdisciplinary works.

Despite this, there are many unread marginalia on its copies (of which there are about 350 are known). Handwritten marginalia appeared on the pages of the Ostrog bible during the existence of copies and often contain valuable historical information. Most of them have been already introduced into scientific circulation, however, there are also those that, for various reasons, were impossible to read without the use of modern technical means.

Currently, when studying cultural heritage objects, including book and manuscript monuments, optical ones are increasingly being used. In recent years, multispectral analysis [1] and hyperspectral imaging [2] have been widely used for this purpose. Reviews of scientific centres, methods and literature are given in the articles [3, 4]. The study of colourful images in manuscripts [5], palimpsests [6], ink [7, 8], and various surface layers on the works of art [9] is possible using hyperspectral imaging. The main advantages of the method are high spectral resolution and a wide spectral range from near ultraviolet to near infrared. Hyperspectral cameras capture hundreds of narrow spectral bands in each image pixel, allowing to identify subtle differences in materials that cannot be distinguished by multispectral or conventional video cameras.

Also, a great advantage of the method is the non-destructive effect when analysing the object of study, as well as the mobility of the hyperspectral complex, which makes it possible to photograph especially valuable artifacts at the place of their storage.

Materials and Methods

It was important to collect material for an experiment on the object with a rich history of existence. This allowed us to obtain a sufficient number of diverse contexts. In total, we examined 24 copies and identified more than 100 unreadable handwritten marginalia – contexts. 11 copies from the Department of Rare Books of the Library of Russian Academy of Sciences (two of them are in the Department of Manuscripts) are described in the catalogue [10]. 13 copies from the Rare Book Department of Russian National Library, described in the catalogue [11]. Contexts were classified according to the reason for their unreadability. The reasons are diverse: ink fading, ink spreading, ink strike through, ink scraping, gluing with restoration materials.

The fact that all contexts belong to copies of the same edition ensured the same properties of the paper and its age (at least if the marginalia are on the block). As a rule, the copies are currently under the same storage conditions. The choice of different copies of the same edition is more relevant from a historical point of view, however, in this case we are dealing with the same paper, which perhaps makes the experiment easier. From the point of view of historical information content, contexts have different significance - from pen samples to page-by-page owner's inscriptions.

For the hyperspectral camera experiments on visualization 28 contexts were selected, of these: 6 contexts for faded ink; 5 contexts for smeared ink; 3 contexts for gluing with restoration paper; 2 contexts for crossed out with a pen; 1 context for a faded stamp, a dark stain on paper of unknown origin, respectively; 10 contexts for scratched text.

Table

Technical parameters of the FX10 camera

Characteristic	Parameter
Spectral range, nm	400–1000
Spectral resolution/pixel, nm	2.7 when binning 2
Number of spectral channels	224
SNR (maximum)	420:1
Number of readings	1024
Bit ADC	12
Frame rate, Hz	Till 327

Unreadable marginalia were examined by a hyperspectral camera working in the IR and UV bandwidths of the spectrum with further processing using the original software. We use a SPECIM FX10 hyperspectral camera manufactured in Finland. Its technical parameters are presented in the table.

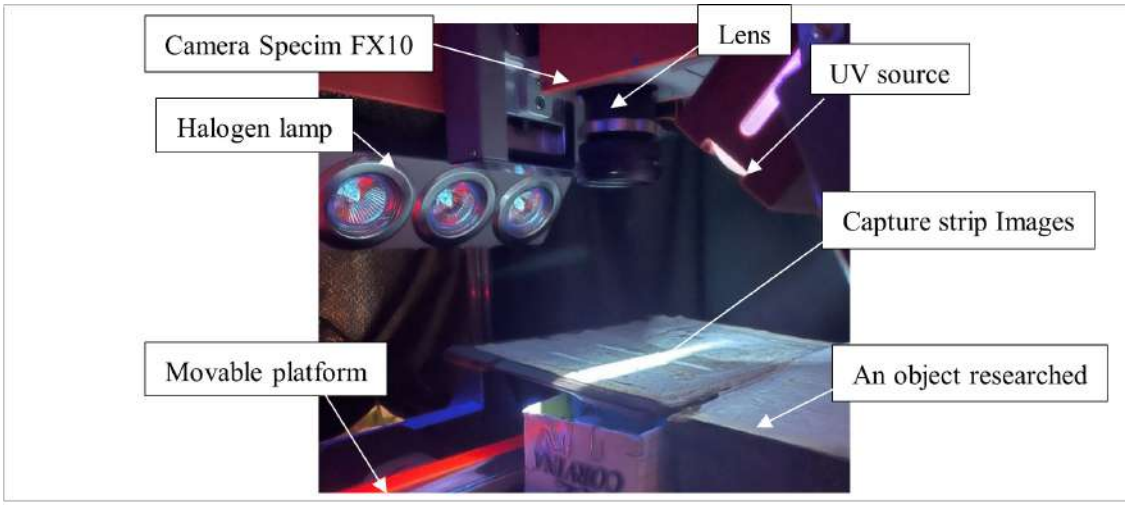

Fig. 1. Scanning an object with a hyperspectral complex

Fig. 1 shows a hyperspectral scanner with an object located inside. The scanned plane of the book was located perpendicularly to the optical axis of the hyperspectral camera. The scanning process used two light sources – a broadband halogen source for reflected light imaging and a narrowband 365 nm UV source for fluorescent imaging. Each light source was located at an angle of 45 degrees to the optical axis of the camera. Processing of the obtained images under two different light sources consisted of the following steps:

· Radiometric calibration [12];
· Independent contrasting by the CLAHE algorithm [13] of each channel for two hyperspectral images;
· Visual identification of the most informative spectral channels;
· Independent processing by the PCA principal component method [14] followed by contrasting with the CLAHE algorithm of each hyperspectral image with two light sources;
· Visual identification of the most informative images of the principal components.

Results and Discussion

Contexts with handwritten marginalia pasted over in restoration process (in our case, it is contemporary restoration paper or thick endpaper pasted over during historical restoration) appear very successfully during hyperspectral photography (Fig. 2). Narrow-spectral images were selected by finding the wavelength with the highest contrast in the region of interest. Marginalia that are not visible due to a dark, unknown spot on the paper cannot be read; other methods should be used.

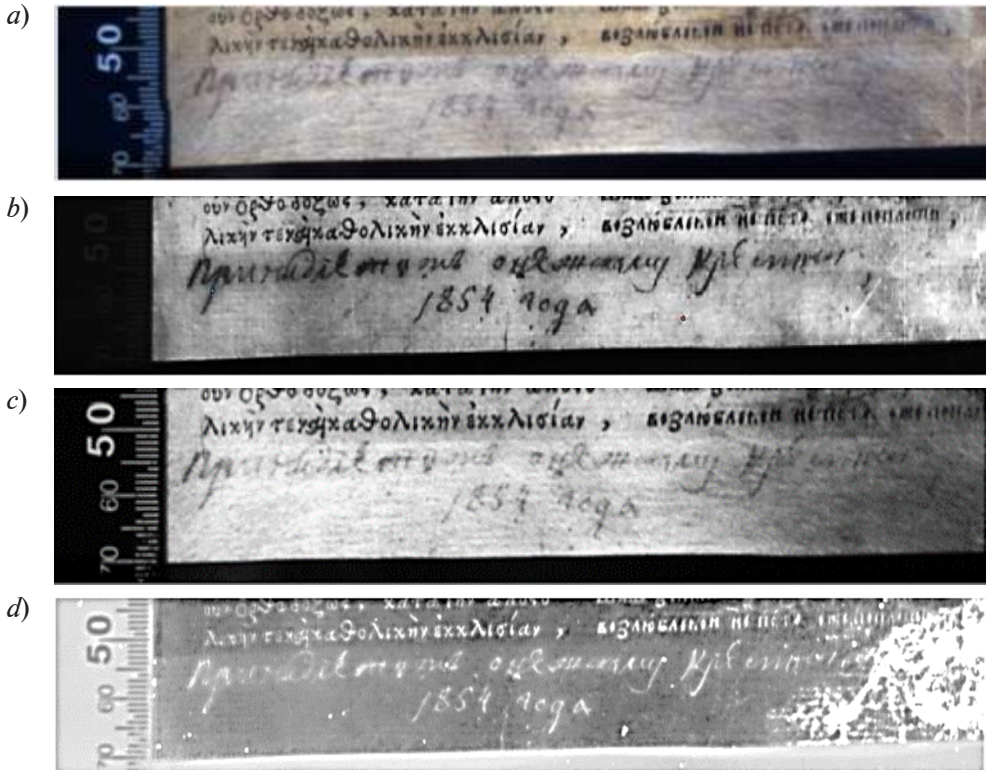

Fig. 2. Unreadable handwritten marginalia covered with restoration paper. Original (*a*); UV light, band 610 nm (*b*); halogen lamp, light band 570 nm (*c*) UV light, PCA-2 (*d*)

Crossed out with (darker) ink using a pen, the lines marked in [10, p. 76] as "crossed out inscription in Polish (?) language" lended themselves well to visualization, and the phrase became readable. Faded library stamp partially appeared during hyperspectral imaging.

The best results were shown on contexts whose "invisibility" was caused by ink fading. The UV spectrum shows an excellent result, while the IR spectrum does not give any result in this case. This is observed consistently in all such contexts.

One of the most common reasons for handwritten marginalia being unreadable is ink smearing. In this case, the use of hyperspectral imaging gives good visualization results (Fig. 3). The ink of the marginalia itself becomes darker, and the smeared layer becomes lighter. Obviously, to further decipher the marginalia, the resulting hyperspectral images should be combined.

Fig. 3. Unreadable handwritten marginalia erased with ink. Original (*a*); UV light, band 480 nm (*b*); halogen lamp, light band 460 nm (*c*) UV light, PCA-4 (*d*)

The largest number of similar contexts is presented in the case of partially scratched handwritten marginalia. Since the "scratching" was heterogeneous, certain places in the text "succumbed" to hyperspectral photography, but for further reading the resulting visualizations should be combined.

Conclusion

Various reasons for extinction or "invisibility" of handwritten marginalia can be read using hyperspectral imaging. The choice of a successful shooting criterion depends on the characteristics of the "damage" of the marginalia, as well as on the material with which the inscription was made. Let us mention that in some contexts, hyperspectral imaging has revealed traces of bio damage on paper.

Reading these marginalia will add reliable information to the study of the Ostrog bible. Some of the marginalia we studied were read by researchers before (for example, a partially scratched owner's inscription from a copy of Epifanov collection or an inscription covered with restoration silk) [10]. But it was important for us to understand the principle - how hyperspectral imaging works for specific injuries. Further work with visualized contexts will increase the area of the text read.

As a result of image analysis, no universal way to increase the readability of marginalia was identified. The use of UV illuminators, compared to a halogen lamp, provides better results both when processing individual narrow-spectrum channels and in case of the PCA algorithm. The number of the spectral channel and the number of images of the main components are selected individually in each case. As part of further research, it is of interest to jointly process hyperspectral images obtained with different light sources.

At the time of the survey, the degradation of vintage specimens under ultraviolet radiation had not been investigated. Experts from the Library of the Russian Academy of Sciences considered the short-term use of ultraviolet light to be harmless, but further research on the possible effects on the condition of the antique paper and the visibility of the ink is needed.

Acknowledgments

We sincerely thank the staff of the manuscript departments of the Library of Russian Academy of Sciences and the Russian State Library for providing access to Ostrog biblia copies and useful technical discussions.

REFERENCES

1. **Alexopoulou A., Kaminari A., Moutsatsou A., Banou P.,** Imaging Techniques in the Study of Cultural Heritage. Kallipos, Open Academic Editions. (2024) 318.

2. **Cucci C., Casini A.,** Chapter 3.8 - Hyperspectral imaging for artworks investigation. Data Handling in Science and Technology. (32) (2019) 583–604.

3. **Balachenkova A.P., Lyakhovitsky E.A., Tsypkin D.O.,** Problems and prospects for the use of spectrozonal visualization in the study of written monuments. Bulletin of St. Petersburg University. history. 3 (66) (2021) 950–970.

4. **Kalashnikova A.A.,** Application of infrared visualization methods in modern source studies. Bulletin of NSU. Series: History, philology. 19 (8) (2020) 117–127.

5. **Viguerie L. de, Rochut S., Alfeld M., et. al.,** XRF and reflectance hyperspectral imaging on a 15th century illuminated manuscript: combining imaging and quantitative analysis to understand the artist's technique. Heritage Science. 6 (1) (2018) 11.

6. **Rapantzikos K., Balas C.,** Hyperspectral imaging: potential in non-destructive analysis of palimpsests. IEEE International Conference on Image Processing. Genova, Italy. (2005) II-618.

7. **Lyakhovitsky E.A., Tsypkin D.O.,** Infrared visualization of text in the study of monuments of ancient Russian writing. Historical informatics. (4) (2019) 148–156.

8. **Costa Rocha da C., Deborah H., Hardeberg J.Y.,** Ink bleed-through removal of historical manuscripts based on hyperspectral imaging. Lecture Notes in Computer Science. (2018) 473–480.

9. **Sandak J., Sandak A., Legan L., et al.,** Nondestructive evaluation of heritage object coatings with four hyperspectral imaging systems. Coatings. 11(2) (2021) 1–15.

10. Cyrillic editions of the 15th-16th centuries of the Department of Rare Books of the BAN: catalogue. Comp. M.Yu. Gordeeva, A.A. Romanova. SPb, BAN. (2010) 170.

11. Editions of the Cyrillic editions of the 15th-16th centuries. (1491–1600): catalog of the book. from collection GPB. St. Petersburg, 1993. Compiled by Lukyanenko V.I.

12. **Shaikh M.S., Jaferzadeh K., Thörnberg B., Casselgren J.,** Calibration of a Hyper-Spectral Imaging System Using a Low-Cost Reference. Sensors. 21 (11) (2021).

13. Realization of the contrast limited adaptive histogram equalization (CLAHE) for real-time image enhancement. Journal of VLSI Signal Processing. (38) (2004) 35–44.

THE AUTHORS

BARANOV Pavel S.
psbaranov@etu.ru
ORCID: 0000-0002-8102-3858

RONGONEN Sofia L.
sofiagonobobleva@mail.ru
ORCID: 0000-0002-9050-3239

PARFENOV Vadim A.
vadim_parfenov@mail.ru
ORCID: 0000-0002-2048-4677

SOKOLOV Nikita M.
niksokolov2001@mail.ru

Received 30.07.2024. Approved after reviewing 23.08.2024. Accepted 10.09.2024.

Conference materials
UDC 548.75
DOI: https://doi.org/10.18721/JPM.173.241

Nonlinear optical phenomena in mesoporous SiO_2 and Si/SiO_2 nanoparticles

V.A. Mastalieva[1,2]✉, V.V. Neplokh[1,3], A.V. Aybush[4], E.Yu. Stovpiaga[2], D.A. Eurov[2], M.Ya. Vinnichenko[3], D.A. Karaulov[3], D.A. Kirilenko[2], V.G. Golubev[2], A.N. Smirnov[2], S.V. Makarov[5], D.A. Kurdyukov[2], I.S. Mukhin[1,3,5]

[1] Alferov University, St. Petersburg, Russia;

[2] Ioffe Institute, St. Petersburg, Russia;

[3] Peter the Great St. Petersburg Polytechnic University, St. Petersburg, Russia;

[4] N.N. Semenov Federal Research Center for Chemical Physics RAS, Moscow, Russia;

[5] Qingdao Innovation and Development Center, Harbin Engineering University, Shandong, China;

[6] ITMO University, St. Petersburg, Russia

✉ rebecconi@gmail.com

Abstract. In this work we study the optical response of mesoporous SiO_2 and Si/SiO_2 nanoparticles considering different fabrication and post-synthesis treatment processes. We show that thermal annealing of mesoporous Si/SiO_2 nanoparticles transforms the Si phase from amorphous to crystalline and enhances the second harmonic generation response.

Keywords: second harmonic generation, silicon, nanostructures, mesoporous nanoparticles, IR visualizer

Funding: This work study was funded by the Russian Science Foundation no. 23-79-00018.

Citation: Mastalieva V.A., Neplokh V.V., Aybush A.V., Stovpiaga E.Yu., Eurov D.A., Vinnichenko M.Ya., Karaulov D.A., Kirilenko D.A., Golubev V.G., Smirnov A.N., Makarov S.V., Kurdyukov D.A., Mukhin I.S., Nonlinear optical phenomena in mesoporous SiO_2 and Si/SiO_2 nanoparticles, St. Petersburg State Polytechnical University Journal. Physics and Mathematics. 17 (3.2) (2024) 207–211. DOI: https://doi.org/10.18721/JPM.173.241

Материалы конференции
УДК 548.75
DOI: https://doi.org/10.18721/JPM.173.241

Нелинейные оптические эффекты в мезопористых SiO_2 и Si/SiO_2 наночастицах

В.А. Масталиева[1,2]✉, В.В. Неплох[1,3], А.В. Айбуш[4], Е.Ю. Стовпяга[2], Д.А. Еуров[2], М.Я. Винниченко[3], Д.А. Караулов[3], Д.А. Кириленко[2], В.Г. Голубев[2], А.Н. Смирнов[2], С.В. Макаров[5], Д.А. Курдюков[2], И.С.Мухин[1,3,5]

[1] Академический университет им. Ж.И. Алфёрова РАН, Санкт-Петербург, Россия;

[2] Физико-технический институт им. А.Ф. Иоффе РАН, Санкт-Петербург, Россия;

[3] Санкт-Петербургский политехнический университет Петра Великого, Санкт-Петербург, Россия;

[4] Федеральный исследовательский центр химической физики им. Н.Н. Семенова РАН, Москва, Россия;

[5] Центр инноваций и разработок Циндао, Харбинский инженерный университет, Шаньдун, Китай;

[6] Университет ИТМО, Санкт-Петербург, Россия

✉ rebecconi@gmail.com

Аннотация. В этой работе изучен нелинейный оптический отклик мезопористых наночастиц SiO_2 и Si/SiO_2 с учетом различных процессов изготовления и пост обработки. Показано, что термический отжиг мезопористых наночастиц Si/SiO_2 преобразует кристаллическую фазу Si из аморфной в нанокристаллическую и усиливает отклик генерации второй гармоники.

Ключевые слова: генерация второй гармоники, кремний, наноструктуры, преобразователи ИК излучения, мезопористые наночастицы

Финансирование: Работа выполнена в рамках проекта РНФ № 23-79-00018.

Ссылка при цитировании: Масталиева В.А., Неплох В.В., Айбуш А.В., Стовпяга Е.Ю., Еуров Д.А., Винниченко М.Я., Караулов Д.А., Кириленко Д.А., Голубев В.Г., Смирнов А.Н., Макаров С.В., Курдюков Д.А., Мухин И.С. Нелинейные оптические эффекты в мезопористых SiO_2 и Si/SiO_2 наночастицах // Научно-технические ведомости СПбГПУ. Физико-математические науки. 2024. Т. 17. № 3.2. С. 207–211. DOI: https://doi.org/10.18721/JPM.173.241

Introduction

Since bulk silicon has a centrosymmetric structure, special conditions are required to demonstrate the efficient second harmonic generation (SHG) in this material. This paper proposes the use of mesoporous nanoparticles with SiO_2 framework filled with Si phase, which finds applications in the nanophotonic field [1−3].

To compare the performance of SHG at pumping in 800-1020 nm range of femtosecond laser pulses, various fabrication and processing procedures [4] were used to synthesize Si/SiO_2 and SiO_2 mesoporous nanoparticles. Infrared femtosecond laser scanning system was used for mapping [5]. It was found that thermal or laser-induced annealing of Si leads to the transformation of the Si phase from amorphous to nanocrystalline, which improves the nonlinear characteristics of the nanoparticles and makes them exhibit broadband photoluminescence. These results confirm the efficiency of mesoporous Si/SiO_2 nanoparticles for second harmonic generation and extend their potential applications in nanoscale optics [6].

Materials and methods

The synthesis process of spherical mesoporous Si/SiO_2 nanoparticles (meso Si/SiO_2 NPs) includes two steps [7]. Low-porousity monodisperse spherical SiO_2 nanoparticles (reference SiO_2 NPs) were produced through the hydrolysis of tetraethoxysilane (TEOS) in an alcohol-based solution that contained ammonia and water [4]. The synthesis process had a duration of 4 hours and resulted in a formation of 550 ± 20 nm monodisperse low-porosity (less than 15%) nanoparticles [7], which then were centrifuged and annealed at 900 °C for 5 h in air.

Monodisperse spherical mesoporous silica nanoparticles (meso SiO_2 NPs) were synthesized also by hydrolysis of TEOS [8]. The silica particles obtained were centrifuged, dried in air at 70 °C for 24 h, and annealed at 550 °C for 5 h to form the pores. The sectional pore diameter of the synthesized particles was about 3 nm, and the specific surface area and pore volume of the synthesized particles were 810 m^2/g and 0.55 cm^3/g, respectively [8].

Nonlinear Optical Response Measurements

For nonlinear optical measurements, samples from the nanoparticle colloid were deposited on pre-cleaned quenched quartz glasses. The studies were carried out using a confocal laser-scanning microscope (LSM) setup (LSM-980, Zeiss, Germany). Femtosecond laser pulses (Discovery-NX, Coherent, USA) with a repetition rate of 80 MHz, duration of 150 fs, and pulse wavelength range of 800–1020 nm were delivered through the external acousto-optic modulator (AOM) port of the LSM. The spectral characteristics of the nonlinear response were obtained at the optimum pump wavelength in the range of 900–980 nm.

Results and Discussion

An enlargement of Si clusters after annealing compared to unannealed Si/SiO_2 NPs, related to improved crystallinity due to annealing, was observed by TEM imaging (Fig. 1, *a*, *c*). The obtained TEM images allow to distinguish the nc-Si phase, which is manifested by a bright contrast being more pronounced after annealing.

The Raman measurements confirmed the amorphous state of the Si material for the as-synthesized NPs (Fig. 1, *b*) and demonstrated the presence of crystalline Si phase after annealing of Si/SiO_2 NPs, that is manifested by the peak at 518.5 cm^{-1} corresponding to the transverse optical phonon mode of crystalline Si (Fig. 1, *d*).

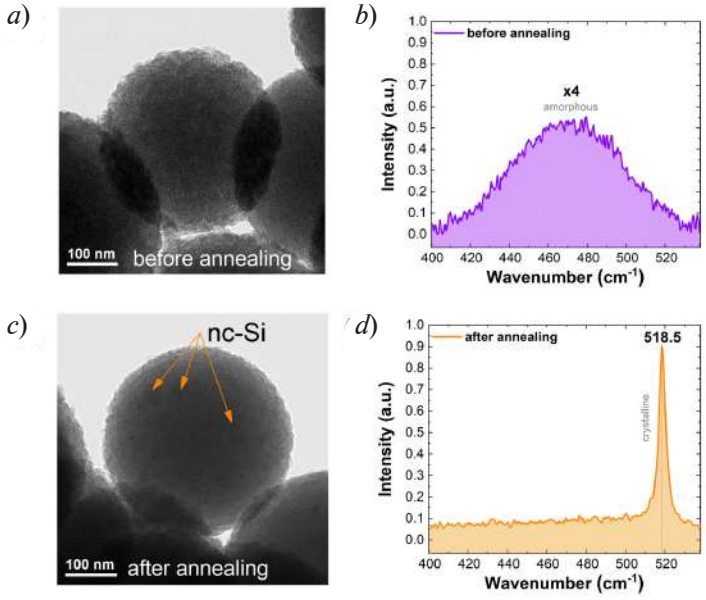

Fig. 1. TEM images of meso Si/SiO_2 NPs before (*a*) and after (*c*) thermal annealing at 850 °C. Raman spectra of meso Si/SiO_2 NPs before and after (*b*) thermal annealing at 850 °C (*d*)
For convenience, the spectrum of as-synthesized particles is amplified by ×4

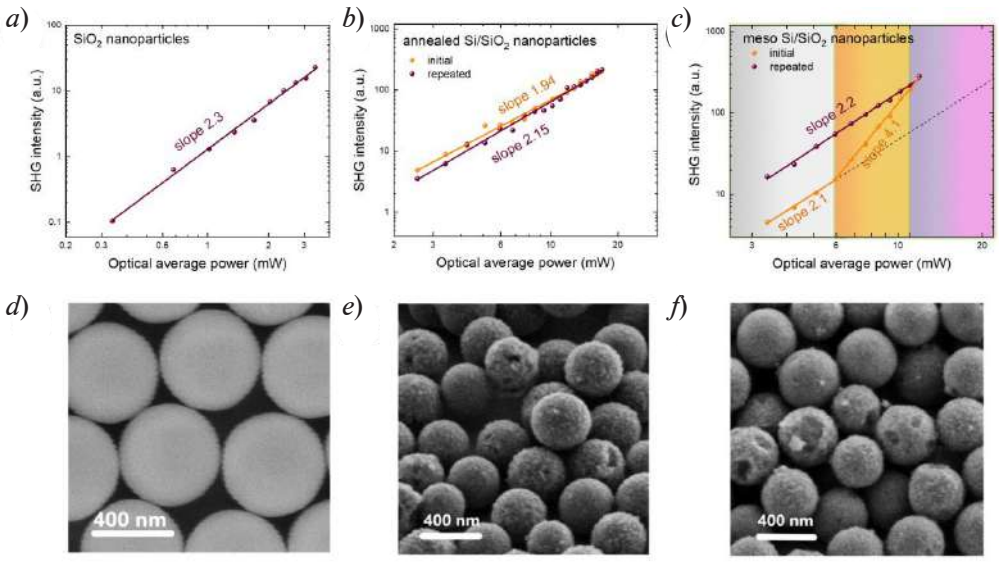

Fig. 2. SHG-to-pump curves for reference SiO_2 NPs (*a*), thermally annealed (*b*) and as-synthesized meso Si/SiO_2 NPs (*c*). The orange curves for (*b*) and (*c*) correspond to initial measurements, purple curves to the repeated measurements. The colored areas in (*c*) represent the following: gray area is the normal SHG response, orange area is an increased slope on SHG response, purple area is the irreversible sample damage. SEM images of SiO_2 (*d*) NPs, annealed (*e*) Si/SiO_2 NPs and meso Si/SiO_2 NPs

The least pronounced SHG signal compared to the reference SiO_2:OH^- NPs was demonstrated by pure meso Si NPs (Fig 2, *a*). A standard slope value of 2 and reproducible SH intensity-pump curves were demonstrated by annealed meso Si/SiO_2 NPs (Fig. 2, *b*), reaching the maximum efficiency in the range of 10–12 mW pump power, that is limited by the material degradation, caused by overheating (the overheat power range is coloured purple in Fig. 2, *c*).

Conclusion

Thus, mesoporous SiO_2 framework of the Si/SiO_2 nanoparticles under consideration plays a double positive role for the nonlinear process: it stabilises the Si material and also the SiO_2:OH^- material itself possesses second-order nonlinearity and influences the observed second harmonic signal.The proposed mesoporous Si/SiO_2 nanoparticles can be considered as a very promising structure for potential applications in optoelectronics, microelectronics and biomedical fields.

Acknowledgments

We thank the N.N. Semenov Federal Research Center for Chemical Physics for providing equipment for measuring second harmonic generation.

REFERENCES

1. **Maestre D., Palais O., Barakel D., et al.,** Structural and optoelectronical characterization of Si–SiO_2/SiO_2 multilayers with applications in all Si tandem solar cells. Journal of Applied Physics. 107 (6) (2010).

2. **Chen T.P., Ding L.,** Optical and optoelectronic properties of silicon nanocrystals embedded in SiO_2 matrix. Nanostructured Thin Films and Coatings: Functional Properties, Zhang, S. (Ed.). (2010) 113–165.

3. **Hirschman K.D., Tsybeskov L., Duttagupta S.P., Fauchet P.,** Silicon-based visible light-emitting devices integrated into microelectronic circuits. Nature, 384 (6607) (1996) 338–341.

4. **Stober W., Fink A., Bohn E.,** Controlled growth of monodisperse silica spheres in the micron size range. J. Colloid Interface Sci. Pp. 62. (26) (1968).

5. **Mastalieva V., Neplokh V., Aybush A., et al.,** Laser-Activated Second Harmonic Generation in Flexible Membrane with Si Nanowires. Nanomaterials. 13 (9) (2023)1563.

6. Wei J., Wirth A., Downer M.C., Mendoza B.S., Second-harmonic and linear optical spectroscopic study of silicon nanocrystals embedded in SiO_2. Physical Review B. 84 (16) (2011). 165316.

7. **Kurdyukov D.A., Eurov D.A., Shmakov S.V., et al.,** Fabrication of doxorubicin-loaded monodisperse spherical micro-mesoporous silicon particles for enhanced inhibition of cancer cell proliferation. Microporous and Mesoporous Materials. (281) (2019) 1–8.

8. **Trofimova E.Y., Kurdyukov D.A., Yakovlev S.A., et al.,** Monodisperse spherical mesoporous silica particles: Fast synthesis procedure and fabrication of photonic-crystal films. Nanotechnology. 24 (15) (2013) 155601.

THE AUTHORS

MASTALIEVA Viktoriia A.
rebecconi@gmail.com
ORCID: 0000-0002-6247-9868

KIRILENKO Demid A.
kirilenko_da@spbstu.ru
ORCID: 0000-0002-1571-209X

NEPLOKH Vladimir V.
vneplox@gmail.com
ORCID: 0000-0001-8158-0681

GOLUBEV Valery G.
golubev@gvg.ioffe.ru
ORCID: 0000-0003-2956-6561

AYBUSH Arseny V.
aiboosh@gmail.com
ORCID: 0000-0002-0496-9105

SMIRNOV Alexander N.
alex.smirnov@mail.ioffe.ru
ORCID: 0000-0001-9709-5138

STOVPIAGA Ekaterina Yu.
yu.katoff@gvg.ioffe.ru
ORCID: 0000-0003-0434-5252

MAKAROV Sergey V.
svmakarov@itmo.ru
ORCID: 0000-0002-9257-6183

EUROV Daniil D.
edan@mail.ru
ORCID: 0000-0002-7471-4028

KURDYUKOV Dmitry A.
kurd@gvg.ioffe.ru
0000-0002-3041-9609

VINNICHENKO Maxim Ya.
mvin@spbstu.ru
ORCID: 0000-0002-6118-0098

MUKHIN Ivan S.
imukhin@yandex.ru
0000-0001-9792-045X

KARAULOV Danila A.
karaulov.da@edu.spbstu.ru
ORCID: 0009-0002-1608-3659

Received 24.07.2024. Approved after reviewing 12.08.2024. Accepted 13.08.2024.

Conference materials
UDC 621.373.826
DOI: https://doi.org/10.18721/JPM.173.242

Mode leakage into substrate in microdisk lasers

I.A. Melnichenko[1,2]✉, E.I. Moiseev[1], K.A. Ivanov[1], N.V. Kryzhanovskaya[1], A.G. Vainilovich[3], A.V. Nahorny[3], E.V. Lutsenko[3], A.E. Zhukov[1]

[1] National Research University Higher School of Economics, St. Petersburg branch, St. Petersburg, Russia;

[2] Alferov University, St. Petersburg, Russia;

[3] Institute of Physics of the NAS of Belarus, Minsk, Belarus

✉ imelnichenko@hse.ru

Abstract. The propagation of whispering gallery modes of a quantum-dot injection disk laser into a GaAs substrate has been investigated experimentally and using simulation. For a 50 μm diameter microlaser with 1.5-μm-thick $Al_{0.4}Ga_{0.6}As$ claddings, the intensity of the mode leaking into the substrate can be up to 10^{-3} of the intensity of the laser mode in the waveguide.

Keywords: InGaAs quantum well-dots, whispering gallery mode microlasers, mode leakage

Funding: The article was prepared within the framework of the project "International academic cooperation" HSE University.

Citation: Melnichenko I.A., Moiseev E.I., Ivanov K.A., Kryzhanovskaya N.V., Vainilovich A.G., Nahorny A.V., Lutsenko E.V., Zhukov A.E., Mode leakage into substrate in microdisk lasers, St. Petersburg State Polytechnical University Journal. Physics and Mathematics. 17 (3.2) (2024) 212–216. DOI: https://doi.org/10.18721/JPM.173.242

Материалы конференции
УДК 621.373.826
DOI: https://doi.org/10.18721/JPM.173.242

Утечка мод в подложку в микродисковых лазерах

И.А. Мельниченко[1,2]✉, Э.И. Моисеев[1], К.А. Иванов[1], Н.В. Крыжановская[1], А.Г. Войнилович[3], А.В. Нагорный[3], Е.В. Луценко[3], А.Е. Жуков[1]

[1] Национальный исследовательский университет «Высшая школа экономики», Санкт-Петербургский филиал, Санкт-Петербург, Россия;

[2] Академический университет им. Ж.И. Алфёрова РАН, Санкт-Петербург, Россия;

[3] Институт физики НАН Беларуси, Минск, Беларусь

✉ imelnichenko@hse.ru

Аннотация. Экспериментально и с помощью моделирования исследовано распространение мод шепчущей галереи дискового лазера с квантово-точечной инжекцией в подложке GaAs. Для микролазера диаметром 50 мкм с облицовками из $Al_{0.4}Ga_{0.6}As$ толщиной 1,5 мкм интенсивность моды, просачивающейся в подложку, может составлять до 10^{-3} от интенсивности лазерной моды в волноводе.

Ключевые слова: квантовые точки InGaAs, микролазеры с модами шепчущей галереи, утечка мод

Финансирование: Статья подготовлена в ходе проведения исследования в рамках проекта «Международное академическое сотрудничество» НИУ ВШЭ.

Ссылка при цитировании: Мельниченко И.А., Моисеев Э.И., Иванов К.А., Крыжановская Н.В., Войнилович А.Г., Нагорный А.В., Луценко Е.В., Жуков А.Е. Исследование утечки мод в подложку в микродисковых лазерах // Научно-технические ведомости СПбГПУ. Физико-математические науки. 2024. Т. 3.2 № .17. С. 212–216. DOI: https://doi.org/10.18721/JPM.173.242

Introduction

Microlasers based on whispering gallery modes (WGMs) are promising light emitters for photonic integrated circuits [1]. Such microlasers have high Q-factor, which allows to achieve low lasing thresholds and offer high power efficiency [2]. In addition, the emission of such lasers propagates in the plane of a substrate, which simplifies their integration with other optical components on the chip.

One advantage of WGM lasers over other types of microlasers is that the epitaxial structure is very similar to that typically used for stripe edge-emitters [3–5] and does not require high precision thickness and/or composition in growth of its components. However, the thickness of the cladding layers of about 1.5–2 μm may be insufficient for effective localization of the mode in a cylindrical microcavity.

To investigate this problem, we analyzed the propagation of WGMs of an injection disk microresonator based on InGaAs/GaAs quantum well-dots into a GaAs substrate. The leakage of the microdisk laser mode into the substrate and the magnitude of this type of losses was determined.

Materials and Methods

The epitaxial structure was prepared by MOVPE epitaxy on a 6°-disoriented GaAs substrate. The structure comprises an n+-GaAs buffer, a 1.5-μm-thick n-$Al_{0.4}Ga_{0.6}As$ bottom-side cladding layer, a 0.78-μm-thick GaAs waveguiding layer, a 1.5-μm-thick p-$Al_{0.4}Ga_{0.6}As$ top cladding layer, and a 0.35-μm-thick p^{++}-GaAs contact layer. The active layer consisted of five layers of $In_{0.4}Ga_{0.6}As$ quantum dots placed evenly inside 800 nm GaAs matrix. Using photolithography and dry etching, microdisk lasers with a diameter of 50 μm were formed on the surface of the epitaxial structure. To investigate the mode leakage, the sample was cliffed so that the substrate edge was in close proximity to the microdisk under study (not more than 5 μm). After that, the structure was mounted on the heat sink due to more convenient heat dissipation and vertical orientation of sample. Next, the contacts to one of 50 μm microdisks were welded.

The study of the intensity distribution of the electromagnetic field propagating from the laser waveguiding layer into the substrate was carried out using the technique of fiber near-field microscopy. For this purpose, a room temperature NT-MDT Integra Spectra microscope-based fiber probe head was used, which is a Nufern 980-HP single-mode optical fiber attached to a fork-shaped quartz resonator. The end of the fiber is tapered by chemical etching and coated with a layer of aluminum (70nm) with a formed aperture of 100 nm at the end. The signal from the fiber probe was collected in noncontact regime (distance between fiber tip and surface was approximately 30–40 nm). Then it was transferred into a Sol Instruments MS5204i monochromator and detection was performed using a cooled InGaAs CCD array. Also, to investigate the processes of WGM spreading, a numerical model of the disk was developed in the COMSOL Multiphysics environment using the finite element method.

Results and Discussion

Fig. 1, *a* shows the electroluminescence (EL) spectrum obtained by near-field fiber microscopy from the GaAs substrate under the microdisk laser. In the investigated wavelength range, two WGMs were identified (at wavelengths 1082.8 nm and 1099.1 nm), the radiation leakage of which was localized under the periphery of the microdisk laser. The scheme in Fig. 1, *b* demonstrates the

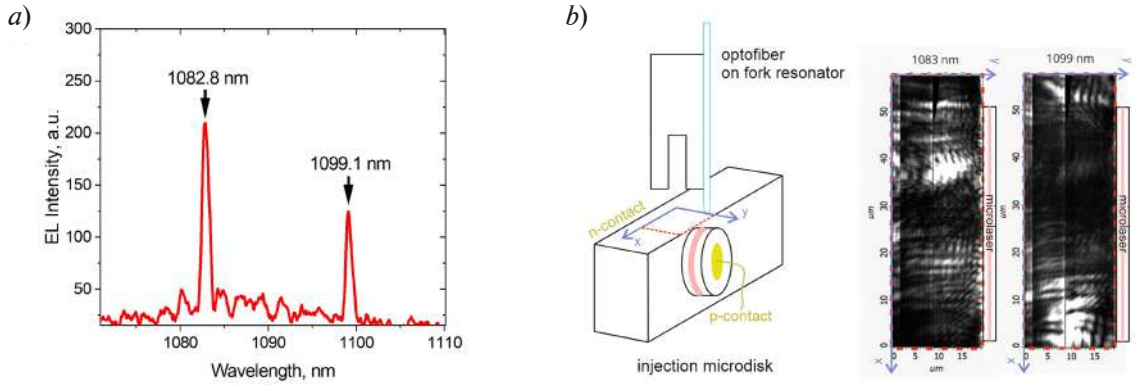

Fig. 1. EL spectrum obtained by near-field fiber acquisition from the substrate under the microdisk (*a*). Schematic of the near-field fiber microscopy experiment and electroluminescence intensity distribution maps of the 1082.8 and 1099.1 nm modes (*b*)
The vertical line on both maps is due to a measurement imperfection (due to the substrate cleaved surface curvature, the near-field fiber moved away from the surface during scanning)

process of scanning the GaAs substrate cliff with a fiber near-field probe, the red rectangle highlights the approximate region where the experimental maps of the EL intensity distribution were obtained. The observed electromagnetic intensity distribution is concentrated under the peripheral parts of the microdisk laser, as expected for WGMs. However, the distribution in the substrate is different for different WGM modes.

From the experimental results it can be also seen that the EL intensity modulations obtained on the maps have a large number of modulations that we associate with interference of laser emission in GaAs substrate. To investigate the interference into the GaAs substrate, intensity distribution deeper inside the substrate was calculated. To avoid too long calculation times, the thickness was limited to 6 μm. The results are presented in Fig. 2 for two modes of which has $q = 20$, and the other $q = 1$. For both numerical and experimental distributions, the maximum of the electromagnetic field intensity is observed under the disk edges. The simulations also show that the mode with higher radial order shows more intense mode leakage into the GaAs substrate than the $q = 1$ mode.

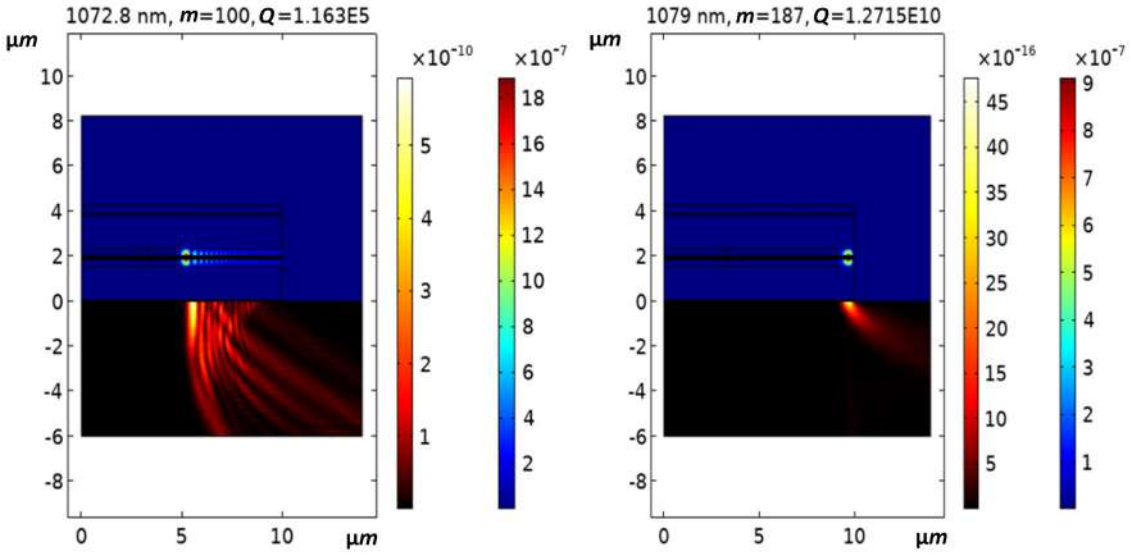

Fig. 2. Electromagnetic energy distribution in 50 μm microlaser for $m = 100$, $q = 20$ and m = 187, $q = 1$ azimuthal and radial orders WGMs in GaAs substrate

The amount of mode leakage into the GaAs substrate was calculated as the ratio of the EL intensity maxima in the GaAs substrate to the EL intensity maximum in the microdisk waveguide (for the results of numerical modeling, the intensity value was estimated using expression $I \sim E^2$). The calculation data are shown in Table 1; the maximum values of the radiation intensity on the surface of the waveguide part of the microdisk and on the cleaved plane of the GaAs substrate were taken for the $I_{substrate}/I_{waveguide}$ ratio. For the experimental data, this value of maximum amount of mode leakage was estimated as $\sim 3 \cdot 10^{-4}$ for the 1082.8 nm mode wavelength, and for the theoretical simulations show a maximum amount of mode leakage $\sim 10^{-5}$ for the third radial order mode. Q-factor of leaking mode also decreases significantly with radial order raise from $q = 1$ to $q = 3$ approximately from $1.24 \cdot 10^{10}$ to $3.1 \cdot 10^{6}$.

Table 1

Calculation of magnitude of mode leakage into substrate for theoretical and experimental cases

Experimental data		Numerical calculations	
λ	$I_{substrate}/I_{waveguide}$	λ	$I_{substrate}/I_{waveguide}$
1082–1083 nm	$\sim 3 \cdot 10^{-4}$	$q = 1$, 1076.1 nm	$\sim 5.01 \cdot 10^{-9}$
1098–1099 nm	$\sim 2.2 \cdot 10^{-3}$	$q = 3$, 1078.1 nm	$\sim 1.26 \cdot 10^{-5}$

It was also observed that for different WGMs, the propagation in the GaAs substrate occurs at different angles. It can be assumed in Fig. 2 that for low radial order WGM with $q = 1$ and $m = 187$, the angle to the GaAs substrate surface at which the WGM scatters is larger than the same angle for high radial order WGM of $q = 20$ and $m = 100$. The same inversed dependency can be observed for Q-factor: the smaller the mode Q-factor, the larger will be the angle to the GaAs substrate surface. Despite the fact that there is no absorption in the GaAs substrate, for models with finite GaAs substrate thickness, scattering is observed as one moves away from the disk. It should be mentioned that the experimentally observed intensity distribution can be additionally affected by the other effects, such as surface bumps of the cleaved GaAs substrate and the parasitic absorption of microdisk radiation due to noncontact near-field experimental setup.

Conclusion

In this study, a new method was developed to experimentally investigate the leakage of WGM from a microdisk laser using fiber near-field optical microscopy. This methodology allowed us to demonstrate that for microdisk lasers based on AlGaAs/GaAs waveguide structure, the mode leakage into the substrate is quite significant for modes with high radial number, which is confirmed by both experimental and modeling data. It can be also assumed that the smaller the mode Q-factor, the larger the angle to the GaAs substrate surface at which the WGM scatters. The results obtained indicate the necessity to take into account factor of WGMs leakage into the GaAs substrate.

Acknowledgments

The work was carried out using the large-scale research facility #2087168 “Complex optoelectronic stand”.

REFERENCES

1. **Yang S., Wang Y., & Sun H.,** Advances and prospects for whispering gallery mode microcavities. Advanced Optical Materials. 3 (9) (2015) 1136–1162.

2. **McCall S.L., Levi A.F. J., Slusher R.E., et al.,** Whispering-gallery mode microdisk lasers. Applied physics letters. 60 (3) (1992) 289–291.

3. **Munsch M., Claudon J., Malik N.S., et al.,** Room temperature, continuous wave lasing in microcylinder and microring quantum dot laser diodes. Applied Physics Letters. (100) (2012) 031111.

4. **Moiseev E., Kryzhanovskaya N., Maximov M., et al.,** Highly efficient injection microdisk lasers based on quantum well-dots. Optics Letters. 43 (19) (2018) 4554–4557.

5. **Kryzhanovskaya N., Zhukov A., Moiseev E., Maximov M.** III–V microdisk/microring resonators and injection microlasers. Journal of Physics D: Applied Physics. 54 (45) (2021) 453001.

THE AUTHORS

MELNICHENKO Ivan A.
imelnichenko@hse.ru
ORCID: 0000-0003-3542-6776

VAINILOVICH Alexey G.
a.vainilovich@ifanbel.bas-net.by

MOISEEV Eduard I.
emoiseev@hse.ru
ORCID: 0000-0003-3686-935X

NAHORNY Alexey V.
a.nahorny@ifanbel.bas-net.by

IVANOV Konstantin A.
kivanov1992@gmail.com
ORCID: 0000-0003-2165-1067

LUTSENKO Eugeniy V.
e.lutsenko@ifanbel.bas-net.by

KRYZHANOVSKAYA Natalia V.
nkryzhanovskaya@hse.ru
ORCID: 0000-0002-4945-9803

ZHUKOV Alexey E.
zhukale@gmail.com
ORCID: 0000-0002-4579-0718

Received 26.07.2024. Approved after reviewing 29.07.2024. Accepted 30.07.2024.

Conference materials
UDC 528.854
DOI: https://doi.org/10.18721/JPM.173.243

Convolutional neural networks for image-free classification via single-pixel imaging

A.A. Reutov✉, D.V. Babukhin, D.V. Sych

P.N. Lebedev Physical Institute of the RAS, Moscow, Russia

✉ aleksey.reutov@phystech.edu

Abstract. The technology of single-pixel imaging extends visualization capabilities beyond pixel-matrix-based devices. One of possible applications for this technology is fast classification of objects without the need for reconstruction of an image. The single-pixel camera gathers light statistics and then a computational algorithm – such as a neural network – decides on what is the object been illuminated. We train a convolutional neural network on simulated data from single-pixel camera and demonstrate effectiveness of classification images of handwritten digits.

Keywords: Single-pixel imaging, convolutional neural networks, image-free classification

Funding: This study was funded by RSF grant no. 23-22-00381.

Citation: Reutov A.A., Babukhin D.V., Sych D.V., Convolutional neural networks for image-free classification via single-pixel imaging, St. Petersburg State Polytechnical University Journal. Physics and Mathematics. 17 (3.2) (2024) 217–220. DOI: https://doi.org/10.18721/JPM.173.243

Материалы конференции
УДК 528.854
DOI: https://doi.org/10.18721/JPM.173.243

Сверточные нейронные сети для классификации без изображений с помощью однопиксельной визуализации

А.А.Реутов✉, Д.В.Бабухин, Д.В. Сыч

Физический институт им. П.Н. Лебедева РАН, Москва, Россия

✉ aleksey.reutov@phystech.edu

Аннотация. Технология однопиксельной визуализации расширяет возможности визуализации за пределы устройств на основе пиксельной матрицы. Одним из возможных применений этой технологии является быстрая классификация объектов без необходимости реконструкции изображения. Однопиксельная камера собирает статистику освещенности, а затем вычислительный алгоритм, например нейронная сеть, принимает решение о том, какой объект был освещен. Здесь мы обучаем сверточную нейронную сеть на смоделированных данных с однопиксельной камеры и демонстрируем эффективность классификации изображений рукописных цифр.

Ключевые слова: однопиксельная визуализация, сверточные нейронные сети, классификация без полной визуализации

Финансирование: Исследование выполнено за счет гранта Российского научного фонда (проект № 23-22-00381).

Ссылка при цитировании: Реутов А.А., Бабухин Д.В., Сыч Д.В. Сверточные нейронные сети для классификации без изображений с помощью однопиксельной визуализации // Научно-технические ведомости СПбГПУ. Физико-математические науки. 2024. Т. 17. № 3.2. С. 217–220. DOI: https://doi.org/10.18721/JPM.173.243

Introduction

Single-pixel imaging is a technique for image acquisition via illuminating an object with structured light and obtain an image via computational restoration [1]. This technique provides imaging capabilities beyond visible wavelengths and thus perspective for making specific devices. Another possible application of single-pixel imaging is image-free object classification [2]. Gathering structured light via single-pixel camera and processing the raw data without image acquisition allows fast detection and classification of objects in the range of single-pixel imaging applicability. In last years, neural networks were shown to be a convenient tool for computational processing of single-pixel-gathered data [3,4]. Here we investigate on capability of convolutional neural networks to classify handwritten digits, processed with a single-pixel camera.

Materials and Methods

The general idea of single-pixel can be explained as follows. The light is spatially modulated by set of patterns *P,* which can be represented as matrix with *M* rows (number of patterns) and *N* columns (number of elements of each pattern). A spatial light modulator can be realized in different ways, for example, it can be a digital micromirror device (DMD) consisting of an array of small controlled mirrors, each can take two positions with different deflection angles (providing reflection or transmitting a light). Patterns change over time and provide varying intensity spatial profile from the source. The modulated light is then reflected from the target object (with reflectance matrix *I*) and measured by the detector. Matrix *I* can be flattened and represented as one columns with length N. Each detector's record is a intensity value for the selected pattern. The measured signals *S* of single-pixel scheme can be expressed as $S = PI$. Another scheme of single-pixel imaging consider reflection from object as a first step (with intensities *I*) and spatial modulation by patterns *P* after that.

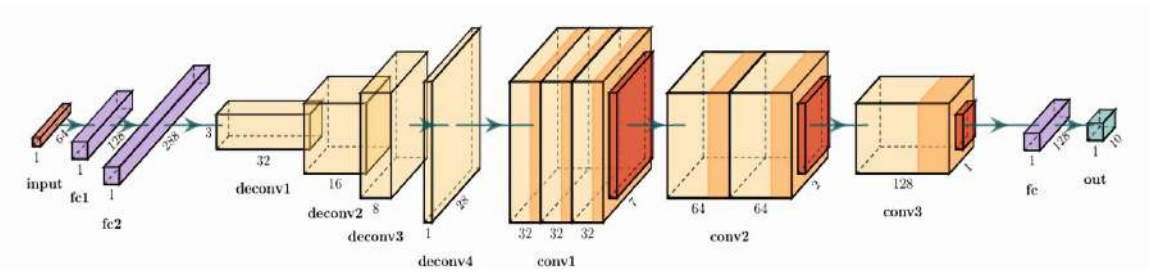

Fig. 1. Architecture of convolutional neural network for partial image reconstruction from synthetic detector signals

The second step in constructing single-pixel images is to reconstruct the object image *I*, using the detector signals *S* and known patterns *P*. There are several methods to reconstruct image: for example, matrix inversion of *P*, compressed sampling or neural network approach. The first technique is computationally complex task for high resolution images. The second and third approach provide promising results [1–4] as reconstruction algorithms. But instead of fully image reconstruction, we provide in our work approach for partial reconstruction, the recognition of the type of objects captured by the single-pixel camera. We use neural network methods suitable for classification task.

We trained a convolutional neural network on handwritten digits dataset MNIST. For every digit, we simulated a process of structured illumination with $M = 64$ spatial patterns, thus generating 64 intensity measurements S. For an image with $N = 784$ pixels, our setup corresponds to approximately 8% sampling rate. We used a dataset of 60000 images, where a neural network was trained on 48000 images, and 12000 images were used to calculate classification accuracy.

We designed and trained a convolutional neural network (CNN) on input data S and set of target output MNIST. Structurally, the CNN consists of several blocks, feedforward and convolutional (see Fig. 1). We choose ADAM optimizer for training process, its learning rate is 0,0003. The set of patterns P for synthetic signal data generation consists of binary matrices, with randomly generated and equiprobably values 0 or 1. The negative log-likelihood function was chosen as the loss function that determines the divergence between the expected and predicted value and used as optimization objective.

Results and Discussion

We provide the results of our simulation in Fig. 2. Here, we can see that after 30 epochs of training – full learning iterations through training dataset – our network classifies digits, based on intensity measurements only, with the final accuracy 94.1%. The accuracy is slightly varying during last trainings epochs, which can be handled by tuning of size of training minibatches and learning-rate scheduling. We also see that value of neural network loss – a characteristic of the learning process – has gradually decreased, which demonstrates a correct learning process. Both graphs show that machine learning model is almost trained after 15 epochs and both two metrics (accuracy and loss function) fluctuate within boundaries from 90% to 95% and from 0.2 to 0.3 respectively. Therefore, fine-tuning of the hyperparameters may improve and stabilize training results.

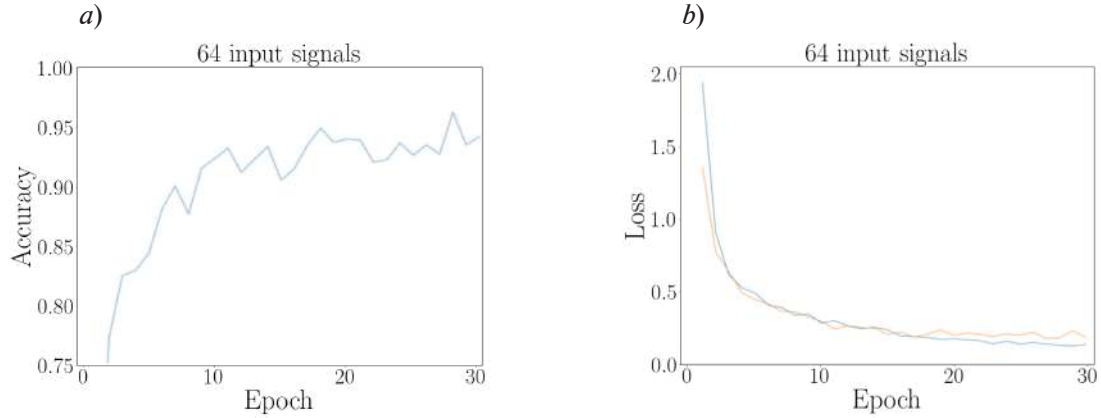

Fig. 2. Accuracy on test set (*a*) and dynamics of loss function (*b*) during training. The number of patterns and input signals to the CNN is 64, the accuracy by the end of training is 94.1%

Conclusion

In this work, we trained a convolutional neural network to classify objects, using intensity measurements from a single pixel camera and without image acquisition. We choose recognition of hand-written digits from MNIST dataset (as standard benchmark for classification tasks). Despite the low sampling rate (about 8%), our network demonstrated a high classification accuracy, thus serving as an efficient tool in single-pixel framework. Obtained metrics show the prospect of improving training results by fine-tuning. We further plan to investigate on image-free classification in the presence of device imperfections such as different noises of detector, overexposing or dropped patterns and signals.

REFERENCES

1. **Duarte M.F., Davenport M.A., Takhar D., et al.,** Single-Pixel Imaging via Compressive Sampling, IEEE Signal Processing Magazine. 25 (83) (2008).

2. **Sadao Ota et. al.,** Ghost cytometry, Science. (2018) 1246–1251.

3. **Higham C.F., Murray-Smith R., Padgett M.J., Edgar M.P.**, Deep learning for real-time single-pixel video, Scientific Reports. 8 (2018).

4. **Zhang Z., Li X., Zheng S., Yao M., et al.,** Image-free classification of fast-moving objects using "learned" structured illumination and single-pixel detection. Optics Express. 28 (9) (2020) 13269.

5. **Diederik P.Kingma, Jimmy Ba**. Adam: A method for stochastic optimization. (2017).

THE AUTHORS

REUTOV Aleksei A.
aleksey.reutov@phystech.edu
ORCID: 0000-0001-5838-4770

SYCH Denis V.
denis.sych@gmail.com
ORCID: 0000-0002-4188-0951

BABUKHIN Danila V.
dv.babukhin@gmail.com
ORCID: 0000-0001-6511-7515

Received 30.07.2024. Approved after reviewing 02.08.2024. Accepted 02.08.2024.

Conference materials
UDC 535
DOI: https://doi.org/10.18721/JPM.173.244

Metal-dielectric resonator integrated in an asymmetric slab waveguide for spatiotemporal optical vortex generation

A.I. Kashapov[1,2]✉, E.A. Bezus[1,2], D.A. Bykov[1,2], L.L. Doskolovich[1,2]

[1] Image Processing Systems Institute, National Research Centre "Kurchatov Institute", Samara, Russia;

[2] Samara National Research University, Samara, Russia

✉ kashapov.ai@ssau.ru

Abstract. We theoretically and numerically demonstrate an efficient approach for generating a spatiotemporal optical vortex (STOV) in an asymmetric dielectric slab waveguide using a metal-dielectric structure constituted by several metal strips integrated into the waveguide core layer. The presented rigorous numerical simulation results fully confirm the developed theoretical model.

Keywords: spatiotemporal optical vortex, integrated optics, asymmetric dielectric slab waveguide, spatiotemporal differentiation

Funding: This work was funded by the Russian Science Foundation (project 24-12-00028).

Citation: Kashapov A.I., Bezus E.A., Bykov D.A., Doskolovich L.L., Metal-dielectric resonator integrated in an asymmetric slab waveguide for spatiotemporal optical vortex generation, St. Petersburg State Polytechnical University Journal. Physics and Mathematics. 17 (3.2) (2024) 221–224. DOI: https://doi.org/10.18721/JPM.173.244

Материалы конференции
УДК 535
DOI: https://doi.org/10.18721/JPM.173.244

Формирование пространственно-временного оптического вихря с помощью металлодиэлектрического резонатора, интегрированного в асимметричный волновод

А.И. Кашапов[1,2]✉, Е.А. Безус[1, 2], Д.А. Быков[1, 2], Л.Л. Досколович[1, 2]

[1] Институт систем обработки изображений Курчатовского комплекса кристаллографии и фотоники Национального исследовательского центра «Курчатовский институт», г. Самара, Россия;

[2] Самарский национальный исследовательский университет им. академика С.П. Королёва, г. Самара, Россия

✉ kashapov.ai@ssau.ru

Аннотация. Предложен и теоретически и численно исследован эффективный подход для формирования пространственно-временного оптического вихревого пучка в асимметричном диэлектрическом волноводе с помощью металлодиэлектрической структуры, состоящей из нескольких металлических полос, «интегрированных» в волновод. Представленные результаты строгого численного моделирования хорошо согласуются с разработанной теоретической моделью.

Ключевые слова: оптический вихрь, интегральная оптика, ассиметричный волновод, пространственно-временное дифференцирование

Финансирование: Работа выполнена при поддержке Российского научного фонда (проект 24-12-00028).

Ссылка при цитировании: Кашапов А.И., Безус Е.А., Быков Д.А., Досколович Л.Л. Формирование пространственно-временного оптического вихря с помощью металлодиэлектрического резонатора, интегрированного в асимметричный волновод // Научно-технические ведомости СПбГПУ. Физико-математические науки. 2024. Т. 17. № 3.2. С. 221–224. DOI: https://doi.org/10.18721/JPM.173.244

Introduction

Recently, a new class of optical vortex (OV) beams has attracted considerable research attention, namely, the so-called spatiotemporal optical vortex (STOV) beams [1–3]. In contrast to the conventional OV beams possessing a zero in the field amplitude and a screw-type phase dislocation in the plane perpendicular to the propagation direction [4], STOV beams are essentially polychromatic and carry orbital angular momentum, which is orthogonal to the propagation direction of the beam. STOV beams have many important potential applications including optical trapping, super resolution microscopy, and free-space telecommunications, among others.

Results and Discussion

Let us consider the transformation of the envelope of the H_z magnetic field component of an incident TE-polarized spatiotemporal pulse propagating in a slab waveguide occurring upon reflection from a metal–dielectric structure integrated into the waveguide (see Fig. 1, *a*). As it was shown in [5], the envelope of the reflected pulse written in the coordinate system associated with it has the form

$$P_{\text{refl}, H_z} = \iint f(\omega_0 + \tilde{\omega}, z) G(k_y, \tilde{\omega}) TF(k_y, \tilde{\omega}) \times \\ \times \exp[-ix(k_x - n_{\text{eff}}(\omega_0)\omega_0/c) + ik_y y] \exp[-i\tilde{\omega}t] \mathrm{d}k_y \mathrm{d}\tilde{\omega}, \quad (1)$$

where G is the spectrum of the incident pulse describing the amplitudes of the guided modes constituting it, f is the function describing the transverse field profile of the modes of the slab waveguide along the z-axis, and TF is the transfer function of the structure.

As an integrated nanophotonic element intended for the generation of an STOV in the waveguide layer, we propose to use a "three-strip" metal-dielectric structure consisting of three gold (Au) strips "buried" in the waveguide (Fig. 1, *a*). We theoretically studied the transfer function of the structure [5, 6] and obtained that in order to generate a spatiotemporal optical vortex, it is necessary for the arguments of the complex coefficients at the "spatial" and "temporal" linear terms of the transfer function of the structure to differ by $\pi/2$.

Let us consider the following example of the integrated structure for the STOV generation: a gallium phosphide (GaP) waveguide core layer with 100 nm thickness surrounded by silicon dioxide (SiO_2) substrate and free-space (air) superstrate (see Fig. 1, *a*). Using a specially developed algorithm for optimizing the structure parameters involving multiple simulations of the diffraction of TE-polarized incident modes on the structure, we obtained a structure with the following parameters satisfying the STOV generation conditions at the angle of incidence $\theta = 65°$ and the free-space wavelength $\lambda = 630$ nm: $w_1 = 25.1$ nm, $w_2 = 53.2$ nm, $w_3 = 64$ nm, $w_4 = 222$ nm, and $w_5 = 125$ nm (see Fig. 1, *a*). The numerical solution of Maxwell's equations for the considered structure was performed using an efficient implementation of the aperiodic Fourier modal method adapted to the solution of the problems of integrated optics [7, 8]. In Fig. 1, *b*, *c*, the absolute value and argument of the numerically calculated TF of the designed structure are presented.

Figs. 1, *d*, *e* show the absolute value and phase of the numerically calculated envelope of the H_z component of the spatiotemporal pulse reflected from the structure at the central plane of the waveguide core layer for an incident optical pulse described by a Gaussian function ($\sim\exp[-t^2/\sigma_t^2 - y^2/\sigma_y^2]$, where $\sigma_t = 2.8$ ps and $\sigma_y = 14$ μm). The figures demonstrate that the reflected

optical signal does indeed contain an STOV. The numerically obtained and "model" (analytically calculated) envelopes (the latter not shown here for the sake of brevity) are in excellent agreement, the normalized root-mean-square deviation between them being equal to only 0.35%. Fig. 2 shows the cross-sections of the H_z reflected pulse component, from which it can be seen that the amplitude zero at $y = 0$ and $t = 0$ is conserved for all z values. This, along with the results presented in Figs. 1, *d*, *e*, confirms the generation of an STOV in the asymmetric waveguide.

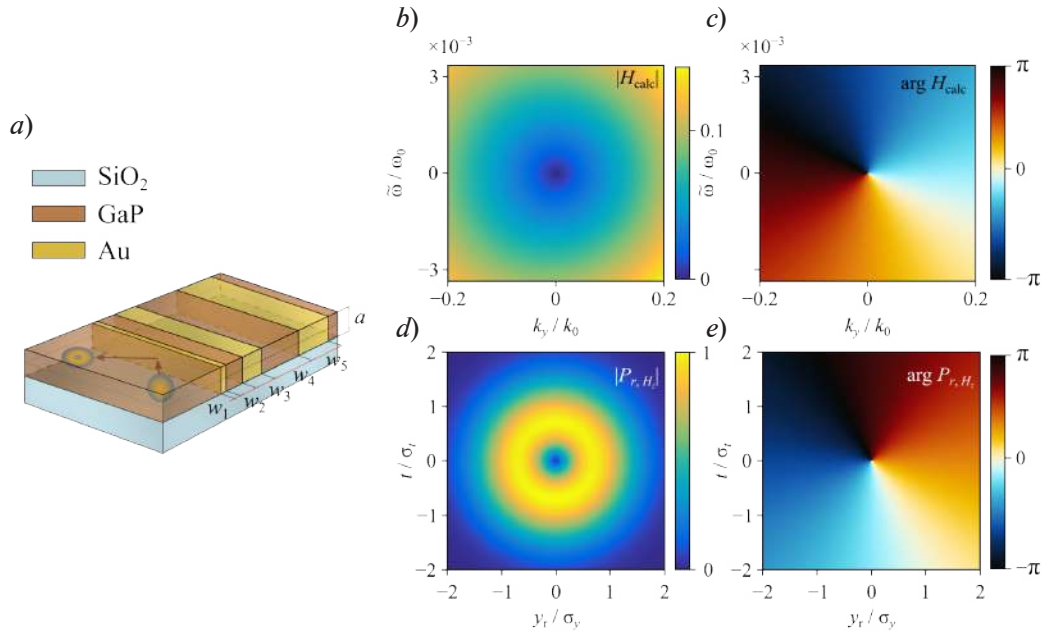

Fig. 1. Geometry of considered integrated structure and schematic depiction of generation of spatiotemporal optical vortex in asymmetric waveguide (*a*). Amplitudes (absolute values) and phases (arguments) of numerically calculated transfer function of structure ((*b*) and (*c*)) and envelope of H_z component of reflected optical pulse ((*d*) and (*e*))

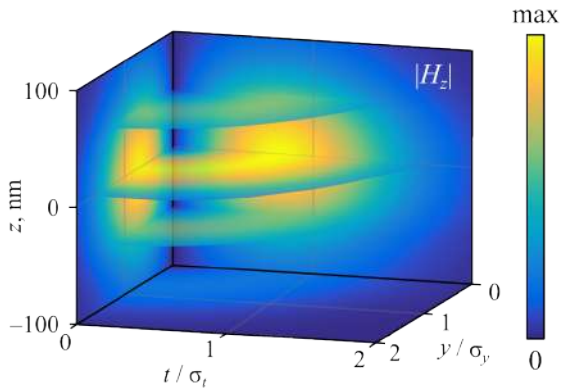

Fig. 2. Cross-sections of normalized H_z component of reflected optical pulse containing STOV

Conclusion

We theoretically studied and numerically confirmed the generation of a spatiotemporal optical vortex in an asymmetric dielectric slab waveguide. In the proposed approach, a spatiotemporal pulse containing an STOV is generated upon reflection of an incident spatiotemporal pulse from an integrated metal-dielectric structure constituted by three metal strips placed in the core layer of the waveguide. The presented results of rigorous electromagnetic simulations of the designed integrated structure fully confirmed the obtained theoretical results and demonstrated the generation of a reflected spatiotemporal optical pulse containing an STOV propagating in the asymmetric slab waveguide.

REFERENCES

1. **Wan C., Chong A., Zhan Q.**, Optical spatiotemporal vortices, eLight. 3 (2023) 11.

2. **Chong A., Wan C., Chen J., Zhan Q.**, Generation of spatiotemporal optical vortices with controllable transverse orbital angular momentum, Nat. Photon. 14 (6) (2020) 350–354.

3. **Kashapov A.I., Bezus E.A., Bykov D.A., Doskolovich L.L.**, Plasmonic Generation of Spatiotemporal Optical Vortices, Photonics. 10 (2023) 109.

4. **Lian Y., Qi X., Wang Y., et al.,** OAM beam generation in space and its applications: A review, Opt. Lasers Eng. 151 (2022) 106923.

5. **Kashapov A.I., Doskolovich L.L., Bezus E.A., et al.,** On-chip spatiotemporal optical vortex generation using an integrated metal–dielectric resonator, Opt. Laser. Technol. 174 (2024) 110584.

6. **Bezus E.A., Bykov D.A., Doskolovich L.L.**, Total absorption and coherent perfect absorption in metal–dielectric–metal resonators integrated into a slab waveguide, Opt. Lett. 47 (17) (2022) 4403–4406.

7. **Silberstein E., Lalanne P., Hugonin J.-P., Cao Q.**, Use of grating theories in integrated optics, J. Opt. Soc. Am. A. 18 (2001) 2865–2875.

8. **Lalanne P., Hugonin J.P.**, Perfectly matched layers as nonlinear coordinate transforms: a generalized formalization, J. Opt. Soc. Am. A. 22 (2005) 1844–1849.

THE AUTHORS

KASHAPOV Artem I.
ar.kashapov@outlook.com
ORCID: 0000-0002-7367-6277

BYKOV Dmitry A.
bykovd@gmail.com
ORCID: 0000-0002-9576-2360

BEZUS Evgeni A.
evgeni.bezus@gmail.com
ORCID: 0000-0001-7496-8960

DOSKOLOVICH Leonid L.
leonid@ipsiras.ru
ORCID: 0000-0001-8649-028X

Received 29.07.2024. Approved after reviewing 12.08.2024. Accepted 17.08.2024.

Conference materials
UDC 535.211
DOI: https://doi.org/10.18721/JPM.173.245

3D laser cleaning as a novel approach to artworks conservation

D.V. Zhurba[1,2], V.A. Parfenov[1]✉

[1] St. Petersburg Electrotechnical University "LETI", St. Petersburg, Russia;

[2] ITMO University, St. Petersburg, Russia

✉ vaparfenov@etu.ru

Abstract. Until recently, restoration cleaning has been carried out primarily manually. Manual laser cleaning is a time-consuming process that requires highly skilled restorers. The introduction of automation, which increases the quality and speed of laser cleaning, will significantly expand its application range and reduce the complexity of restoration work. In this article, we present the results of our experimental work on automated 3D laser cleaning. The proposed approach allows for precise cleaning of objects of complex geometric shape under the control of a CNC machine. To remove dirt from the surface of such objects, we have developed an original approach based on a combination of three-dimensional scanning of the object and obtaining a point cloud of the surface to be cleaned, creating a control program for surface cleaning on a CNC machine. The demonstration of the automated cleaning process took place on corroded steel samples of complex geometric shape. A fiber ytterbium pulsed laser with an average power of 100 W with a wavelength of 1.06 microns and a pulse duration of 100 ns was used for cleaning.

Keywords: laser cleaning, fiber nanosecond laser, conservation, artworks, CNC, 3D scanner

Funding: The research was supported by the Federal Academic Leadership Program Priority 2030.

Citation: Zhurba D.V., Parfenov V.A., 3D laser cleaning as a novel approach to artworks conservation, St. Petersburg State Polytechnical University Journal. Physics and Mathematics. 17 (3.2) (2024) 225–229. DOI: https://doi.org/10.18721/JPM.173.245

Материалы конференции
УДК 535.211
DOI: https://doi.org/10.18721/JPM.173.245

Лазерная 3D-очистка как новый подход к сохранению произведений искусства

Д.В. Журба[1, 2], В.А. Парфенов[1]✉

[1] Санкт-Петербургский государственный электротехнический университет «ЛЭТИ» им. В. И. Ульянова (Ленина), Санкт-Петербург, Россия;

[2] Университет ИТМО, Санкт-Петербург, Россия

✉ vaparfenov@etu.ru

Аннотация. Ручная лазерная очистка — трудоемкий процесс, требующий высокой квалификации реставраторов. Внедрение автоматизации, которая повышает качество и скорость лазерной очистки, значительно расширит область ее применения и снизит сложность реставрационных работ. В этой статье представлены результаты экспериментальной работы по автоматизированной 3D-лазерной очистке. Предлагаемый подход позволяет проводить точную очистку объектов сложной геометрической формы под управлением станка с ЧПУ. Демонстрация автоматизированного процесса очистки проводилась на образцах корродированной стали сложной геометрической формы. Для очистки использовался волоконный иттербиевый импульсный лазер со средней мощностью 100 Вт, длиной волны 1,06 мкм и длительностью импульса 100 нс.

Ключевые слова: лазерная очистка, волоконный наносекундный лазер, реставрация, произведения искусства, ЧПУ, 3D-сканер

Финансирование: Исследование было проведено при поддержке Федеральной программы академического лидерства Приоритет 2030.

Ссылка при цитировании: Журба Д.В., Парфенов В.А. Лазерная 3D-очистка как новый подход к сохранению произведений искусства // Научно-технические ведомости СПбГПУ. Физико-математические науки. 2024. Т. 17. № 3.2. С. 225–229. DOI: https://doi.org/10.18721/JPM.173.245

Introduction

The use of laser technologies in conservation of cultural heritage has been continuously evolving over 50 years. It was first proposed in 1972 by American physicist John Asmus for the removal of black crusts from the surface of stone artifacts [1]. The validation of advanced laser cleaning techniques has been extensive and found application in many parts of Europe, North America, and Australia, especially for stone and metal objects. Laser-based diagnostics have also specialized their tasks toward material analysis, defects detection and multidimensional documentation. The most notable of these uses of laser radiation are holography, holographic interferometry, laser-induced fluorescence, Raman spectroscopy, photoacoustic spectroscopy, optical coherence tomography, laser vibrometry, and 3D scanning profilometry. As a result, the value for laser techniques in art conservation has been recognized widely.

Today, lasers are considered an innovative tool in conservation, promising selective and delicate cleaning applications. Among the most promising tasks of laser cleaning is the removal of dirt and other contaminants from the surface of sculptures and other Cultural Heritage [2–5]. Although laser treatment is frequently used in artworks conservation there remains much open room for further research concerned with development of novel methodologies and new approaches.

Until recently, restoration cleaning was carried out manually. Manual laser cleaning is a time-consuming process that requires a highly qualified restorer, which limits its wide practical use.

In this article, we present the results of experimental work on automated 3D laser cleaning. The proposed approach allows for precise cleaning of objects of complex geometric shape under the control of a CNC machine.

To remove dirt from the surface of such objects, we have developed an original approach. This approach consists in creating a three-dimensional model of an object using 3D scanning and creating a CNC controller program based on this model for cleaning the surfaces of an object on a CNC machine. The controller program scans the surface of the object along the trajectory in the form of a snake, precisely maintaining the working distance between the surface relief and the laser head. The laser head forms a laser sweep strip on the surface of the object. The surfaces of the object are scanned with a laser beam until the required degree of purification is achieved.

Materials and Methods

Optical/laser scanner Shining 3D EinScan HX was used to scan the surface of the object being cleaned and create a cloud of surface points. This scanner provides fast 3D scanning by combining LED light and laser scanning mode. Next, controller program in G-code for CNC was created using the CAM system. Cleaning was carried out by an automated laser cleaning machine ALONP-100IM (manufactured by NPP VOLO Ltd., Russia, St. Petersburg), including laser fiber module (wavelength 1.06 microns, pulse duration 100 ns, maximum average power 100 Watts). The laser head forms a laser sweep strip on the surface of the object in the form of a line, the length of which can vary from 10 to 50 mm.

Results and Discussion

The experiments were carried out on steel samples that had undergone years of atmospheric corrosion, and there were also layers of old paint and bitumen on their surfaces. Figure 1, *a* shows a fragment of the preparation of the CNC controller program. The trajectory of the laser head movement precisely corresponds to the profile of the treated surface. After preparing the controller program, the sample was positioned on the machine table and the cleaning program was started (Fig. 1, *b*).

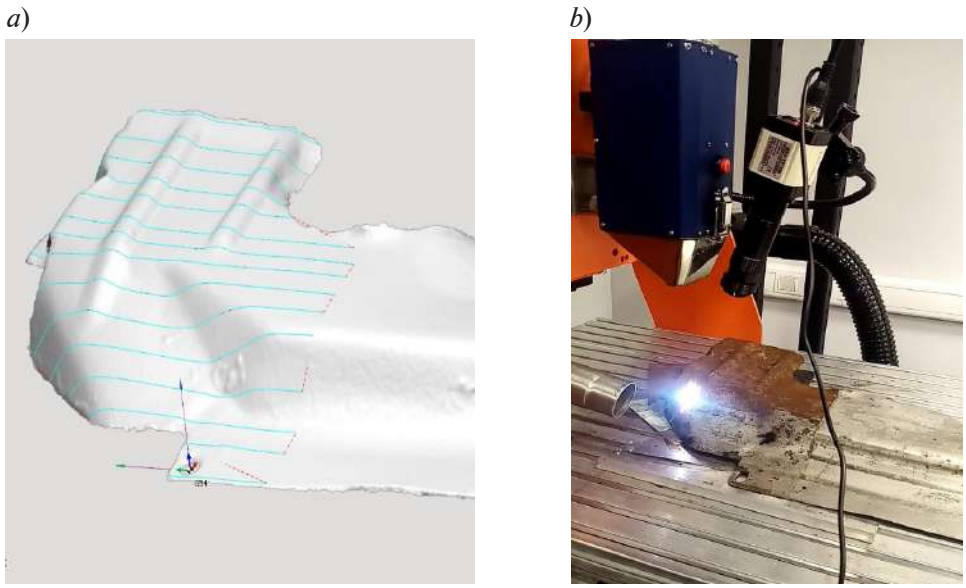

Fig. 1. Laser cleaning process. Preparation of CNC controller program (*a*), restoration object is positioned on machine table, cleaning program is started (*b*)

Optimal laser operation parameters for removing loose rust and paint are: spot diameter of focused laser beam is 100 microns, pulse repetition rate is of 100 kHz, pulse energy is of 1 mJ. The laser cleaning device uses a galvanoscanner to create a sweep strip. The machine moves the laser cleaning device perpendicular to the sweep strip, thus creating a cleaned rectangular area. Fig. 2 schematically shows the formation of the laser processing area. To obtain a uniform effect over the entire cleaning area, the next pass is carried out with an offset of half the length of the sweep.

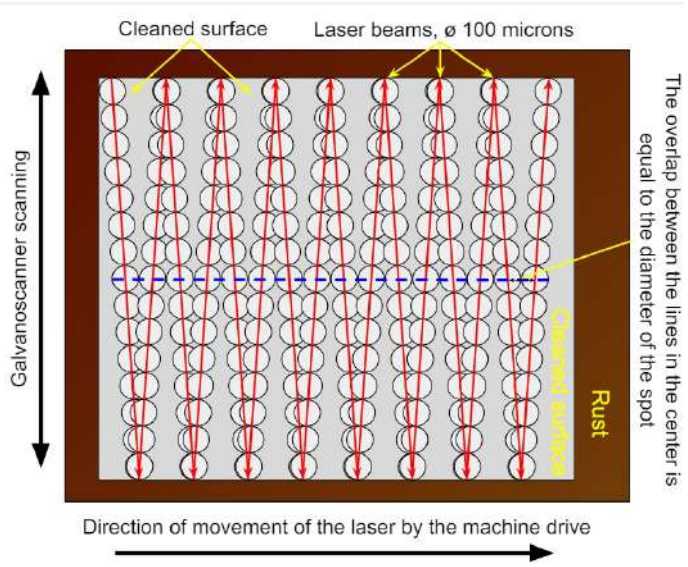

Fig. 2. Scheme of forming a processing strip with a single pass of laser cleaning

Cleaning is carried out in evaporative mode. The power density in the laser spot is sufficient to vaporize the contamination in a layer several microns thick in one pulse. An additional contribution to the cleaning process is made by the shock wave from the resulting plasma and thermal stresses associated with rapid heating and cooling of the treatment area [6–7].

The processing quality was monitored visually during the laser treatment process controlled by program operation (Fig. 3). The number of repetitions of the program and the laser operation parameters were adjusted to obtain the required cleaning quality.

Fig. 3. Visual control of degree of laser cleaning

Conclusion

The results of our experiments showed that automated laser cleaning has several advantages over manual laser cleaning. First, the cleaning performance of the automated system is 1.5–2 times higher than that of the manual system, as the optimal scanning trajectory is chosen and the working distance between the laser and the surface to be cleaned is accurately maintained. This results in a higher quality of cleaning and a better surface appearance. Second, since laser cleaning can be done 24/7 without interruption, it is easier for the restorer to work. They only need to monitor the quality of the process and ensure there are no errors. Third, automated laser cleaning is perfect for large-scale objects as well as objects that are similar or identical objects.

At the same time, it should be noted that the proposed approach can be recommended mainly for cleaning garden and park sculptures, as well as Contemporary Art objects.

In the future, it is important for us to pay attention to automating the process of controlling the degree of purification and adjusting the controller program during cleaning. This will allow us to further increase productivity and the quality of processing process.

REFERENCES

1. **Lazzarini L., Asmus J., Marchesini M.L.,** Laser for cleaning of statuary, initial results and potentialities / 1st Int.Symposium on the Deterioration of Building Stone, La Rochelle). (1972) 89–94.

2. **Cooper M.**, Laser Cleaning in Conservation: An Introduction, Butterworth-Heinemann, Oxford. 1998.

3. **Siano S., Salimbeni R., Pini R., et al.,** Laser cleaning methodology for the preservation of the Porta del Paradiso by Lorenzo Ghiberti, Journal of Cultural Heritage. 4 (2003) 140–146.

4. **Siano S., Giamello M., Bartoli L., et al.,** Laser cleaning of stone by different laser pulse duration and wavelength, Laser Physics. 18 (1) (2008) 1–10.

5. **Dobrusina S.A., Parfenov V.A., Podgornaya N.I., et al.,** Laser removal of foxing from the pages of books and paper documents, J. Opt. Technol. 90 (2023) 617–625.

6. **Lee J., Wagstaff S., Lambotte G., et al.,** Empirical Study of Laser Cleaning of Rust, Paint, and Mill Scale from Steel Surface. In: Materials Processing Fundamentals 2020. The Minerals, Metals & Materials Series. Springer, Cham. (2020) 189–201.

7. **Li X., Huang T., Chong A.W., et al.,** Laser cleaning of steel structure surface for paint removal and repaint adhesion, Guangdian Gongcheng/Opto-Electronic Engineering. 44 (2017) 340–344.
8. **Kayahan E.R., Candan L.E., Aras M.U.,** et al., Surface Cleaning of Metals Using Low Power Fiber Lasers, Acta Physica Polonica A. 134 (2018) 371–373.

THE AUTHORS

ZHURBA Danila V.
zhurba.danila306@ya.ru
ORCID: 0009-0001-6814-1737

PARFENOV Vadim A.
vaparfenov@etu.ru
ORCID: 0000-0002-2048-4677

Received 31.07.2024. Approved after reviewing 12.08.2024. Accepted 18.09.2024.

Conference materials
UDC 53
DOI: https://doi.org/10.18721/JPM.173.246

Security of BB84-like protocol on coherent states with different intensities

E.A. Dedkov[1,2,3,4]✉, R.A. Shakhovoy[1,3]

[1] Limited Liability Company "QRate", Moscow, Russia;

[2] Russian Quantum Center, Moscow, Russia;

[3] National University of Science and Technology MISiS, Moscow, Russia;

[4] Moscow Institute of Physics and Technology, Dolgoprudniy, Russia

✉ dedkov.ea@phystech.edu

Abstract. There are a large variety of quantum key distribution (QKD) protocols, which can provide unconditional security even with practically possible coherent states instead single-photon ones. Most of them require equal intensities of states emitted, which can be achieved only with some precision. However, in some state preparation schemes, for example, in those based on optical injection, equal intensities cannot be achieved without additional elements, which increases the cost and complexity of QKD setup. In this work we analyze the influence of different state intensities on achievable secret key rate in classical BB84 scheme.

Keywords: quantum key distribution, BB84, coherent pulses with random phases, decoy state

Citation: Dedkov E.A., Shakhovoy R.A., Security of BB84-like protocol on coherent states with different intensities, St. Petersburg State Polytechnical University Journal. Physics and Mathematics. 17 (3.2) (2024) 230–235. DOI: https://doi.org/10.18721/JPM.173.246

Материалы конференции
УДК 53
DOI: https://doi.org/10.18721/JPM.173.246

Секретность протокола BB84 на когерентных состояниях различной интенсивности

Е.А. Дедков[1,2,3,4]✉, Р.А. Шаховой[1,3]

[1] ООО «КуРэйт», Москва, Россия;

[2] Российский квантовый центр, Москва, Россия;

[3] Национальный исследовательский технологический университет «МИСиС», Москва, Россия;

[4] Московский физико-технический институт (национальный исследовательский университет), г. Долгопрудный, Россия

✉ dedkov.ea@phystech.edu

Аннотация. Существует большое количество протоколов квантового распределения ключа (КРК), которые способны гарантировать безусловную секретность даже с использованием когерентных состояний вместо однофотонных. Большинство из этих протоколов требуют одинаковой интенсивности посылаемых состояний. Однако, в некоторых схемах приготовления состояний, например, на основе оптической инжекции, состояния равных интенсивностей не могут быть получены без дополнительных элементов, что увеличивает стоимость и сложность установки КРК. В данной работе мы анализируем влияние различия интенсивностей приготавливаемых состояний на достижимую скорость генерации ключа в классическом протоколе BB84.

Ключевые слова: квантовое распределение ключа, BB84, когерентные импульсы со случайной фазой, состояния-приманки

Ссылка при цитировании: Дедков Е.А., Шаховой Р.А. Секретность протокола BB84 на когерентных состояниях различной интенсивности // Научно-технические ведомости СПбГПУ. Физико-математические науки. 2024. Т. 17. № 3.2. С. 230–235. DOI: https://doi.org/10.18721/JPM.173.246

Introduction

Quantum key distribution (QKD) protocols allow two distant users, often referred to as Alice and Bob, to distribute a secret key, which privacy is guaranteed by the laws of quantum mechanics. They can be divided into two main families: discrete variable (DV) and continuous variable (CV) QKD. The DV QKD protocols are those, which encodes secrecy in finite set of optical modes. Basically, it is essential for such protocols to use single-photon states, however, since there are no reliable single-photon sources, in practice coherent states are generally employed. Fortunately, with slight modification, DV QKD protocols based on attenuated laser pulses may be reduced to single-photon protocols. This reduction often relies on the implicit assumption, that the intensities of coherent states are the same for different bases and bit choices. In this work we perform a careful analysis of consequences, to which the violation of this assumption brings to the most common QKD protocol — BB84.

We remind, that basic BB84 protocol consist of the following steps:

1. Alice prepares and sends to Bob one of four qubit states, which are typically: $|0_Z\rangle$, $|1_Z\rangle$, $|0_X\rangle \equiv (|0_Z\rangle + |1_Z\rangle)/\sqrt{2}$, $|1_X\rangle \equiv (|0_Z\rangle - |1_Z\rangle)/\sqrt{2}$ with respective probabilities $p_{\alpha j}$, $\alpha \in \{Z, X\}$, $j \in \{0,1\}$ that are commonly equal. However, in practice Alice's source may be non-ideal both in the sense of preparing states and in the sense of the probability distribution.
2. Bob chooses measurement basis between X and Z randomly with probabilities p_X^B, p_Z^B respectively.
3. Alice and Bob announces bases in which each state was prepared and detected. Mismatched events are dropped out.
4. Alice and Bob estimate bit error rate and correct errors.
5. Alice and Bob estimate phase error rate and perform privacy amplification.

This protocol implies, that Alice has single-photon source, and Bob receives and measures all photons sent. In practice this is not the case. First, Alice use laser, which is the source of coherent states. Second, only a small fraction of states can be detected because of losses in fiber and finite quantum single-photon efficiency. Thus in realistic scenario one need to develop another security proof, which takes into account these difficulties.

In the following section we extend a common approach to security proof of DV QKD in realistic scenario to the case of BB84 with different state intensities. Next we present the results of our approach, namely, the achievable secret key rate and draw a conclusion whether protocols with this imperfection type can be employed or not.

Materials and Methods

When establishing security proof for a QKD protocol based on the coherent states, the following framework is commonly used [1]. Alice is allowed to prepare her coherent states on a Hilbert space of two photonic modes. We will stick to the case, when each state has some fixed intensity μ_j and perfectly random phase:

$$\begin{gathered} \left|\psi_j\right\rangle = \left|\beta_j^E e^{i\varphi}\right\rangle_E \otimes \left|\beta_j^L e^{i\varphi}\right\rangle_L, \\ \left|\beta_j^L\right|^2 + \left|\beta_j^E\right|^2 = \mu_j. \end{gathered} \tag{1}$$

Here E and L denote two photonic modes, early and late here, however, they can be two arbitrary orthogonal modes, for example, horizontal and vertical polarization. Let $\hat{a}_{E,L}$, $\hat{a}^{\dagger}_{E,L}$ be annihilation/creation operators for E and L mode respectively. Then for each state type j we may introduce new pair of creation operators, defined as:

$$\begin{aligned}\hat{a}^{\dagger}_{j1} &= \frac{\beta^{E}_{j}}{\sqrt{\mu_j}}\hat{a}^{\dagger}_{E} + \frac{\beta^{L}_{j}}{\sqrt{\mu_j}}\hat{a}^{\dagger}_{L},\\ \hat{a}^{\dagger}_{j2} &= \frac{\beta^{L}_{j}}{\sqrt{\mu_j}}\hat{a}^{\dagger}_{E} - \frac{\beta^{E}_{j}}{\sqrt{\mu_j}}\hat{a}^{\dagger}_{L}.\end{aligned} \tag{2}$$

and corresponding annihilation operators. They obviously obey bosonic commutation relation, and thus induce another Fock basis on the space of two photonic modes. If we now rewrite state (1) in this basis, we will obtain:

$$\left|\psi_j\right\rangle = \left|\sqrt{\mu}_j e^{i\varphi}\right\rangle_{j1} \otimes \left|0\right\rangle_{j2}. \tag{3}$$

It can be shown, that in case Alice each time produces states with random phase φ, the averaged states are Poisson mixture of n-photon states:

$$\rho_j = \frac{1}{2\pi}\int_0^{2\pi}\left|\psi_j\right\rangle\left\langle\psi_j\right| d\varphi = e^{-\mu_j}\sum_{n=0}^{\infty}\frac{\mu_j^n}{n!}\left|n\right\rangle_{j1}\left\langle n\right|\otimes\left|0\right\rangle_{j2}\left\langle 0\right|. \tag{4}$$

Note that now the measurement of photon number does not have any impact on states sent in the sense that the probabilistic mixture of this measurement resulted states is the same as (4). This means, that theoretically Alice can have a photon number measuring device installed on her output, and thus she will know the number of photons in each pulse. We then may split the initial protocol into several subprotocols which generate secret key only on vacuum states, single-photon states, and multiphoton ones. However, we are still allowed to perform only the steps of the initial protocol. The multiphoton subprotocol generates no secret because of the photon number splitting (PNS) attack, in which Eve steal one photon from pulse, stores it in her quantum memory and measures it in the right basis after basis announcement step. The vacuum subprotocol is also pretty useless to run, since all detection events in it is due to dark counts and thus bit error rate is close to 50%, which gives zero key.

We will stick to the case of ideally-prepared states, but with different intensities. Such states can be expressed as:

$$\begin{aligned}\rho_{z0} &= e^{-\mu_{z0}}\sum_{n=0}^{\infty}\frac{\mu_{z0}^n}{n!}\left|n\right\rangle_{Z1}\left\langle n\right|\otimes\left|0\right\rangle_{Z2}\left\langle 0\right|,\ \rho_{z1} = e^{-\mu_{z1}}\sum_{n=0}^{\infty}\frac{\mu_{z1}^n}{n!}\left|0\right\rangle_{Z1}\left\langle 0\right|\otimes\left|n\right\rangle_{Z2}\left\langle n\right|,\\ \rho_{x0} &= e^{-\mu_{x0}}\sum_{n=0}^{\infty}\frac{\mu_{x0}^n}{n!}\left|n\right\rangle_{X1}\left\langle n\right|\otimes\left|0\right\rangle_{X2}\left\langle 0\right|,\ \rho_{x1} = e^{-\mu_{x1}}\sum_{n=0}^{\infty}\frac{\mu_{x1}^n}{n!}\left|0\right\rangle_{X1}\left\langle 0\right|\otimes\left|n\right\rangle_{X2}\left\langle n\right|,\end{aligned} \tag{5}$$

where we use the following creation operators:

$$\begin{aligned}\hat{a}^{\dagger}_{Z1} &\equiv \hat{a}^{\dagger}_{E},\ \ \hat{a}^{\dagger}_{Z2} \equiv \hat{a}^{\dagger}_{L},\\ \hat{a}^{\dagger}_{X1} &\equiv \frac{1}{\sqrt{2}}\left(\hat{a}^{\dagger}_{E} + \hat{a}^{\dagger}_{L}\right),\ \ \hat{a}^{\dagger}_{Z2} \equiv \frac{1}{\sqrt{2}}\left(\hat{a}^{\dagger}_{E} - \hat{a}^{\dagger}_{L}\right).\end{aligned} \tag{6}$$

The single-photon subprotocol is then just basic BB84 protocol with ideal states, but different probabilities $\tilde{p}_{\alpha j} \propto p_{\alpha j}\mu_{\alpha j}e^{-\mu_{\alpha j}}$, $\sum_{\alpha,j}\tilde{p}_{\alpha j} = 1$. This result is simply the consequence of projecting (5)

onto the single-photon subspace. All we need then is to analyze the amount of secrecy N_{sec} in this slightly unideal BB84 protocol and run privacy amplification over single-photon states. The security analysis is straightforward and can be found in [2, 3]. It uses the concept of quantum coin and its imbalance, which can be calculated given distributed states expressions and probabilities $\tilde{p}_{\alpha,j}$. It worth noting, that we can always adjust initial state generation probabilities $p_{\alpha j}$ in such a way, that coin imbalance is zero. And thus we will have perfect BB84 single-photon protocol, which gives much higher key rate.

Alice, however, does not know the exact positions of the single-photon states sent. Fortunately, she can use proper privacy amplification technique to distill secrecy from the whole bunch of data originated from any states, not only single-photon ones. All she need to know is the amount of the secret key N_{sec} which can be obtained from these data in principle. Since this quantity is lower-bounded by the amount of secret key in single-photon states only, all Alice really needs is the lower bound on the amount of detected by Bob single-photon states, and the upper bound on bit error rates among them. She can obtain pretty tight bounds with the help of so-called *decoy-state technique* [1]. We will shortly review it here, since it is essential for our work.

We start with some definitions. The probability that Bob detects n-photon state of type j sent by Alice is called *yield*, and is denoted as Y_n^j, the fraction of n-photon states of type j, which produced the wrong click is called *error rate* and is denoted as e_n^j. Alice may choose from a set of different intensities for each state type $\mu_j \in \{\mu_j^{(1)}, \mu_j^{(2)},..., \mu_j^{(m)}\}$ and for each intensity and state type she has overall gain $Q_{\mu_j^{(i)}}^j$ which is the fraction of such states, that produced click on Bob's detector, and the overall error rate $E_{\mu_j^{(i)}}^j$ which is the fraction of wrong clicks among $Q_{\mu_j^{(i)}}^j$ detected states. If Alice can prepare and analyze arbitrary intensity, then she can find exact single-photon yield Y_1^j and error rate e_1^j. In [1] it was shown, that pretty tight bounds can be obtained also in case Alice has only three options for intensity.

Unfortunately, if Alice is not permitted to use decoy states, the bounds are loose, mostly because we cannot reliably estimate the number of detected vacuum states (the first term in the right side):

$$Q_\mu = \sum_{n=0}^{\infty} \frac{\mu^n}{n!} e^{-\mu} Y_n^{(\mu)} \le e^{-\mu} Y_0^{(\mu)} + \mu e^{-\mu} Y_1^{(\mu)} + \left[1 - (1+\mu) e^{-\mu}\right]. \quad (7)$$

Fortunately, we may estimate the total number of vacuum and single-photon states, i.e. vacuum + single-photon gain and total errors number:

$$Q_{0,1}^{(\mu)} \ge Q_\mu - \left[1 - (1+\mu) e^{-\mu}\right], \; Q_{0,1}^{(\mu)} E_{0,1}^{(\mu)} \le E_\mu Q_\mu. \quad (8)$$

However, this leads to a problem: we need to analyze the security of BB84 protocol with qutrit states. Although Koashi's approach [2] based on quantum coin is applicable here, it gives extremely poor, if not always zero, key rate. This is the result of huge "losses" (recall, that theoretical coin imbalance should be divided on yield), which are present in the system since only a small fraction of vacuum states is detected by Bob. Therefore, in this case we need to either find better consideration instead of just normalizing quantum coin imbalance or use loss-tolerant approach, like in [4] is done for three-state protocol. Since the first approach is not developed yet, we use the second one. Moreover, the presence of the fourth state in BB84 protocol allows us to include vacuum states into the analysis naturally. It worth noting, that loss-tolerant approach requires a little bit more postprocessing, since it utilizes and counts events which failed sifting, i.e. where Alice's and Bob's bases differ.

The whole analysis is rather complicated, so we present here only the crucial ideas and address the reader to the original work [4] or our future article, where we will cover this question in detail. The first point is to observe, that the states (5), projected onto the zero and one photon subspace are in semi-diagonal form, i.e. their density matrix are block-diagonal, with single number characterizing vacuum component, and qubit submatrix characterizing single-photon component. Thus we will need only one extra transmission rate, which characterizes the transmission of vacuum states, additionally to the transmission rates of X, Z Pauli matrices and identity

matrix. This four transmission rates are perfectly obtainable via the solution of the system of four linear equations, one equation for each state type. The second point to highlight is that we need to know *exact* yields and gains in order to obtain phase error. This is not the case, but we are able to find reliable bounds they lie within. Fortunately, the expression for the phase error rate is almost linearly dependent on the observable quantities, thus with some analysis one may state, that upper bound on the phase error is achieved on the boundary of observables. This means, we may calculate phase error upper bound as maximum over a finite set.

Results and Discussion

Using the security proof, sketched here, we may characterize the influence of state intensities mismatch on the achievable secure key rate. We will stick to the case when the intensities are related as following: $2\mu_{0z} = 2\mu_{1z} = \mu_{0x} = \xi^{-1}\mu_{1x}$. Such choice is natural for state preparation scheme based on the optical injection. Fig. 1,*a* represents the key rate per state sent dependent on transmission channel length for various scenarios (modelling parameters are listed in Table and intensities were chosen to maximize key generation at 30 km). It worth noting that in decoy-states scenario the key rate of BB84 with different intensities and balanced probabilities almost follows the key rate of that with same intensities. All reasonable probability balancing scenarios for BB84 without decoys are with high precision the same and follows the key rate for BB84 with equiprobable states choice. The reasons for it is employing loss-tolerant approach and generation high part of key from dark counts.

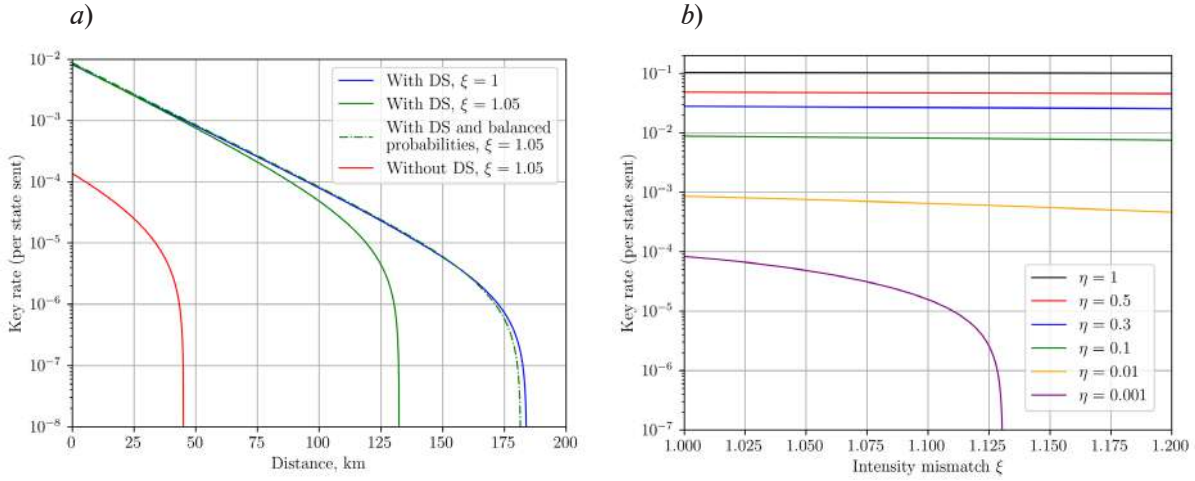

Fig. 1. Plot of key rate per state sent versus channel length (*a*). Plot of key rate per state sent at different channel transmission parameters η (including detector efficiency and transparency) versus intensity mismatch parameter (*b*)

Table

Parameters for key rates estimation

Fiber transparency	α=0.02 dB/km	Z-basis state intensity for decoy-state protocol	μ_{ds}=0.299
Detector efficiency	η=0.1	Z-basis state intensity for protocol without decoys	μ_{wods}=2.82·10^{-3}
Dark count probability	p_{dc}=10^{-6}	Decoy state attenuation coefficient	λ_1=0.5, λ_2=0.1
Probability of wrong click	p_{err}=0.01	Error correction efficiency	f_{ec}=1.22

Fig. 1, *b* shows the dependence of the key rate for various fixed transmission probabilities η, which incorporates both detector efficiency and channel opacity, on intensity mismatch parameter ξ in decoy-state scenario. Without decoys key rate barely depends on ξ, but slight grow can be observed. This is the consequence of the increase in the detection rate of one of the states sent due to its higher intensity.

Conclusion

We have analyzed the modified version of BB84 protocol on coherent states with different intensities of signal pulses. Despite our analysis is largely simplified and there potentially can exist better key rate formulas, we have shown that it is possible to distribute secret key without any correction of intensity. Moreover, such a protocol can be brought back to ideal BB84 just with adjustment of bit values distribution on the Alice's side, which may be done programmatically and requires no additional hardware changes.

The results obtained in this work are for asymptotic scenario only, i.e. when Alice and Bob gather infinitely much data and can estimate all statistics with arbitrary precision. In case of finite block size an additional complicated analysis is required, which will result in lower secret key rate.

REFERENCES

1. **Ma X., Qi B., Zhao Yi, Lo H.-K.,** Practical decoy state for quantum key distribution, Physical Review A. 72 (2005) 012326.

2. **Koashi M.,** Simple security proof of quantum key distribution based on complementarity, New Journal of Physics. 11 (2009) 045018.

3. **Gottesman D., Lo H.-K., Lütkenhaus N., Preskill J.,** Security of quantum key distribution with imperfect devices, Quantum Information & Computation. 4 (5) (2004) 325–360.

4. **Tamaki K., Curty M., Kato G., et al.,** Loss-tolerant quantum cryptography with imperfect sources, Phys. Rev. A. 90 (2014) 052314.

THE AUTHORS

DEDKOV Evgeniy A.
dedkov.ea@phystech.edu

SHAKHOVOY Roman A.
r.shakhovoy@goqrate.com
ORCID: 0000-0003-2750-0518

Received 29.07.2024. Approved after reviewing 12.08.2024. Accepted 15.08.2024.

Conference materials
UDC 620.3
DOI: https://doi.org/10.18721/JPM.173.247

Luminescence enhancement in inelastic tunnelling of electrons by changing the geometry of the tunnelling contact

N.A. Solomonov[1,2]✉, D.V. Lebedev[1,3], K.N. Novikova[1,2], S.V. Fedina[1,2], N.V. Vaulin[1], L.N. Dvoretskaya[1], A.V. Arhipov[2], A.O. Golubok[3], I.S. Mukhin[1,2]

[1] Alferov University, St. Petersburg, Russia;

[2] Peter the Great St. Petersburg Polytechnic University, St. Petersburg, Russia;

[3] Institute for Analytical Instrumentation RAS, St. Petersburg, Russia

✉ solomonov.nik@gmail.com

Abstract: We have experimentally investigated the light emission resulting from inelastic electron tunneling in the transition with hemispherical gold nanoantennas (d = 400 nm, h = 300 nm) created by direct fs-laser ablation. We found two characteristic modes of luminescence: standard - increased signal is observed in the region of nanoantennas at tunneling currents below 2.25 nA and inverted-anomalous, where the gold surface is mainly luminescent, while dark spots are observed on the antennas on the contrary. In the inverted-anomalous mode we observe record signal values of $5 \cdot 10^4$ photons per second. We attribute the anomalous effect to the realization of a conditionality for resonant tunneling of electrons with excitation of optical states.

Keywords: golden nanoantenna, femtosecond laser printing, nanoscale on-chip light sourse, luminescence from tunnel junction, inelastic tunneling of electrons, resonant electron tunneling, scanning tunneling microscope

Funding: Ministry of Science and Higher Education of the Russian Federation (FSEG-2024-0017 project).

Citation: Solomonov N.A., Lebedev D.V., Novikova K.N., Fedina S.V., Vaulin N.V, Dvoretckaia L.N., Arkhipov A.V., Golubok A.O., Mukhin I.S., Luminescence enhancement in inelastic tunnelling of electrons by changing the geometry of the tunnelling contact, St. Petersburg State Polytechnical University Journal. Physics and Mathematics. 17 (3.2) (2024) 236–240. DOI: https://doi.org/10.18721/JPM.173.247

Материалы конференции
УДК 620.3
DOI: https://doi.org/10.18721/JPM.173.247

Усиление люминесценции при неупругом туннелировании электронов за счет изменения геометрии туннельного контакта

Н.А. Соломонов[1,2]✉, Д.В. Лебедев[1,3], К.Н. Новикова[1,2], С.В. Федина[1,2], Н.В. Ваулин[1], Л.Н. Дворецкая[1], А.В. Архипов[2], А.О. Голубок[3], И.С. Мухин[1,2]

[1] Академический университет им. Ж.И. Алфёрова РАН, Санкт-Петербург, Россия;

[2] Санкт-Петербургский политехнический университет Петра Великого, Санкт-Петербург, Россия;

[3] Институт аналитического приборостроения РАН, Санкт-Петербург, Россия

✉ solomonov.nik@gmail.com

Аннотация. Экспериментально исследовано световое излучение, возникающее в результате неупругого туннелирования электронов в переходе с полусферическими золотыми наноантеннами (d = 400 нм, h = 300 нм), созданными методом прямой фс-лазерной абляции. Были выделены два характерных режима люминесценции: стандартный при 2,5 В – повышенная плотность локализованных оптических состояний (ЛПОС) (оптический сигнал до ~$7 \cdot 10^3$ фотонов в секунду) наблюдалась в области наноантенн и аномальный при 2,7 В, при этом ЛПОС повышена по всей поверхности золота между наноантеннами (пиковые значения до ~$5 \cdot 10^4$ фотонов в секунду), а на антеннах, наоборот, наблюдались «темные» пятна. Резкое увеличение интенсивности излучение ассоциируется с проявлением резонансного туннелирования через оптические состояния.

Ключевые слова: наноантенны, фемтосекундная лазерная печать, наноразмерные источники света на кристалле, люминесценция из туннельного перехода, неупругое туннелирование электронов, резонансное туннелирование электронов, сканирующий туннельный микроскоп

Финансирование: Министерство науки и высшего образования Российской Федерации (проект ФСЕГ-2024-0017).

Ссылка при цитировании: Соломонов Н.А., Лебедев Д.В., Новикова К.Н., Федина С.В., Ваулин Н.В., Дворецкая Л.Н., Архипов А.В., Голубок А.О., Мухин И.С. Усиление люминесценции при неупругом туннелировании электронов за счет изменения геометрии туннельного контакта // Научно-технические ведомости СПбГПУ. Физико-математические науки. 2024. Т. 17. № 3.2. С. 236–240. DOI: https://doi.org/10.18721/JPM.173.247

Introduction

One of the main challenges in the design and successful realization of optoelectronic integrated chips is the development of a nanoscale on-chip photon source whose emission can be excited and controlled by electrical signals and which is compatible with current semiconductor technologies [1].

A promising way for the implementation of such light source is the use of tunneling nanocontact between two metal surfaces (metal-insulator-metal (MIM)) [2]. When electrons tunnel through a MIM contact, light is emitted by inelastic tunneling (LEIT). However, the probability of LEIT (external quantum efficiency (EQE)) process is extremely low, approximately ~10^{-6}–10^{-7}, limiting the prospects for commercial realization of simple planar MIM photon sources [3–4].

Our previous work [5] demonstrated that due to modifying the surface by gold nanoantennas formed using femtosecond laser printing technique, the EQE increased by an order of magnitude compared to the flat surface. These nanoantennas acted as plasmon resonators, concentrating the electromagnetic field and increasing the local density optical states, thereby increasing the probability of photon emission [6–7].

The main objective of this study is to further enhance the EQE in a MIM structure with gold nanoantennas by varying both the geometrical and energetic parameters of the tunnel gap. By fine-tuning these parameters, we aim to maximise the interaction between the tunnelling electrons and the optical modes of the nanoantennas, thereby improving the photon emission efficiency.

Materials and Methods

The initial sample is a gold film with a thickness of 50 nm deposited on an optically smooth glass substrate by electron beam evaporation. Rows of nanoantennas with a period of 1 to 1.5 μm and a diameter of 500 nm were printed on gold film by femtosecond laser printing technique. SEM image of a cross section of the structure is shown in Fig. 1, *a*. [2]. The nanocontact with the sample was formed using a tungsten chemical etched probe in an ultrahigh vacuum tunneling microscope (Omicron UHV VT AFM/STM). Spatial STM-L maps were recorded using an external data acquisition system based on a single-photon counter with a spectral range of 400–900 nm [3]. Features of the optical assembly for luminescence detection and low total luminescence intensity from the tunnelling contact do not allow obtaining emission spectra for particular wavelengths in this experiment. The optimum tunnelling contact parameters were searched for at a fixed bias voltage of 2.7 V (one of the characteristic luminescence peaks of the structures on the tunnelling VAC) and tunnelling currents in the range of 100-5000 pA by multiple registration of STM-L images. The dependence of STM-L optical signal intensity on bias voltage were taken for voltage variation in the range of −4 to 4 V at a fixed tunnelling current of 1000 pA, the obtained curve is shown in (Fig. 1, *d*). Fig. 1 shows two sets of typical STM and STM-L surface images obtained during the study of the optimal parameters of the tunnel contact: the standard luminescence mode (Fig. 1, *b*, *c*) and the inverted mode (Fig. 1, *e*, *f*).

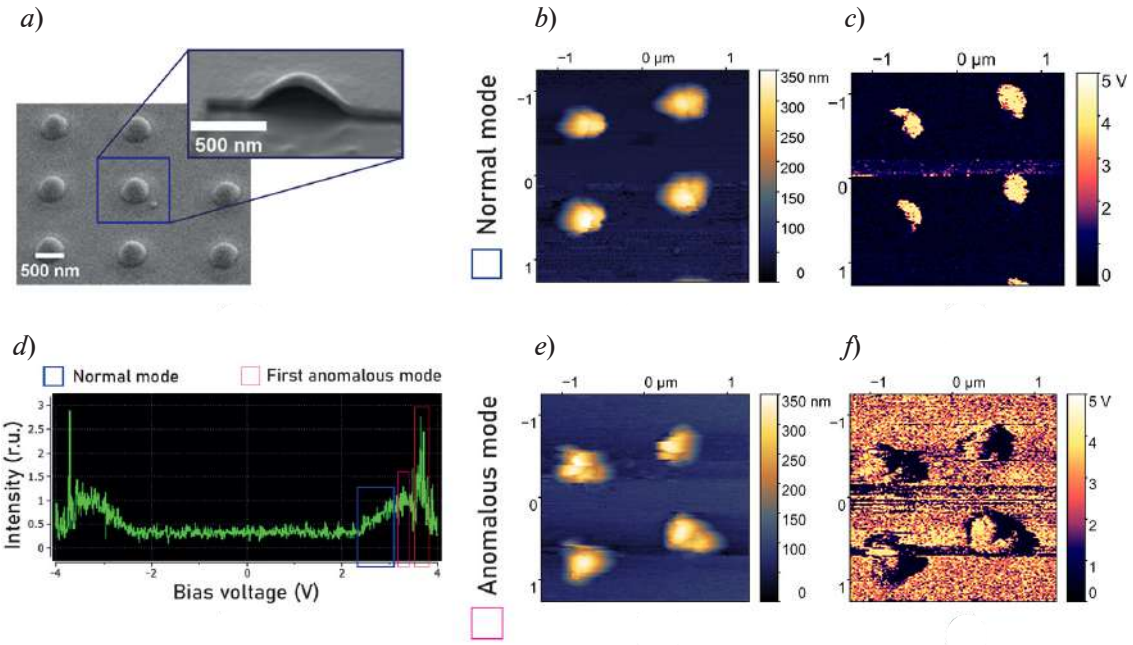

Fig. 1. Synchronized recording of STM topography and luminescence (STM-L): SEM image of cross section of the nanoantenna (*a*); dependence of luminescence intensity on bias voltage at fixed tunnel current of 1000pA (*d*); STM topography of nanoantennas (*b*, *e*); STM-L map of nanoantennas (*c*, *f*)

Results and Discussion

In the whole investigated range of tunneling contact parameters, two modes can be distinguished. First standard luminescence mode, consists in a smooth increase of the signal on the STM-L map with increasing tunneling current up to ~2.25 nA at 2.7V. An increase in tunneling current means that the probe is approaching the surface. This range of bias voltages is highlighted on the intensity curve by a blue frame in Fig. 1, *d*. Further increase of the current at 2.7 V leads to a sharp change of the pattern to an anomalous one. In the anomalous regime, the luminescence (LDOS) increases dramatically over the entire surface area in the STM-L map more than 5 times in amplitude from $7 \cdot 10^3$ photons per second to peak values of $5 \cdot 10^4$ photons per second. At the same time, in contrast, "spots" with reduced LDOS are observed over the nanoantenna region. Further increasing the bias voltage above 3.5V, a smooth decline in the optical signal intensity is observed due to a change in the nature of charge carrier transport from tunnelling to over-barrier transport ("breakdown" of the tunneling barrier). When the current is reduced to 2 nA at 2.7 V or below 2.7 V (at any current), the transition to the normal luminescence mode occurs.

Conclusion

The fact of such a dramatic change in the luminescence pattern and increase in the luminescence intensity, respectively, EQE, may indicate the manifestation of resonant tunneling of electrons with excitation of optical states. The processes of electron tunnelling occurring in the inverted (anomalous) luminescence regime and spectral studies of the emission features require further deeper investigations.

Acknowledgments

This research was funded by the Ministry of Science and Higher Education of the Russian Federation (FSEG-2024-0017 project).

REFERENCES

1. **Kaur P., Boes A., Ren G., et al.,** Hybrid and heterogeneous photonic integration. APLPhotonics. (6) (2021) 061102.

2. **Zhu Y., Cui L., Abbasi M., Natelson D.,** Tuning Light Emission Crossovers in Atomic- Scale Aluminum Plasmonic Tunnel Junctions. Nano Letters. (22) (2022) 8068–8075.

3. **Lebedev D.V., et. al.,** Indirect Detection of the Light Emission in the Local Tunnel Junction. physica status solidi (RRL)–Rapid Research Letters. (14) (3) (2020) 1900607.

4. **Lebedev D.V., et. al.,** Scanning Tunneling Microscopy-Induced Light Emission and I (V)Study of Optical Near-Field Properties of Single Plasmonic Nanoantennas, The journal of physical chemistry letters. (12) (1) (2021) 501–507.

5. **Lebedev D.V., Solomonov N.A.,** Femtosecond Laser-Printed Gold Nanoantennas for Electrically Driven and Bias-Tuned Nanoscale Light Sources Operating in Visible and Infrared Spectral Ranges, The Journal of Physical Chemistry Letters. (14) (22) (2023) 5134–5140.

6. **Pavlov, D.V., et al.,** Laser-induced surface relief nanocrowns as a manifestation of nanoscale Rayleigh-Plateau hydrodynamic instability, Applied Surface Science. 511 (2020) 145463.

7. **Dvoretckaia L., Ladutenko K., Mozharov A., et al.,** Electrically driven metal and all-dielectric nanoantennas for plasmon polariton excitation. Journal of Quantitative Spectroscopy and Radiative Transfer. (244) (2020) 106825.

THE AUTHORS

SOLOMONOV Nikita A.
solomonov@gmail.com
ORCID: 0000-0003-0675-8659

LEBEDEV Denis V.
denis.v.lebedev@gmail.com
ORCID: 0000-0001-5389-2899

NOVIKOVA Kristina N.
novikova_k@spbau.com
ORCID: 0000-0003-2308-2398

FEDINA Sergey V.
fedina.serg@yandex.ru
ORCID: 0000-0001-7521-3754

VAULIN Nikita V.
nikitavaylin@mail.ru
ORCID: 0000-0001-6080-0729

DVORETSKAYA Lilya N.
dvoretskaya_ln@spbstu.ru
ORCID: 0000-0001-6080-0729

ARHIPOV Alexander V.
Arkhipov@rphf.spbstu.ru
ORCID: 0000-0002-1170-7568

GOLUBOK Alexander O.
Arkhipov@rphf.spbstu.ru
ORCID: 0000-0001-9970-9172

MUKHIN Ivan S.
muhin_is@spbstu.ru
ORCID: 0000-0001-9792-045X

Received 31.07.2024. Approved after reviewing 26.08.2024. Accepted 27.08.2024.

Conference materials
UDC 538.9
DOI: https://doi.org/10.18721/JPM.173.248

Towards the realization of $NbSe_2$ NIR photodetectors integrated on a silicon nitride waveguide

K.V. Shein[1,2,✉], A.N. Lyubchak[1,2], E. Zharkova[3], D.A. Bandurin[3], I. Charaev[4], I.A. Gayduchenko [1,2], G.N. Goltsman [1,2]

[1] Moscow Pedagogical State University, Moscow, Russia;

[2] National Research University Higher School of Economics, Moscow, Russia;

[3] Programmable Functional Materials Lab, Brain and Consciousness Research Center, Moscow, Russia;

[4] University of Zurich, Zurich, Switzerland

✉ sheinkv97@gmail.com

Abstract. Photonic integrated circuits (PIC) represent a promising platform for applications in the field of quantum technologies, such as quantum computing and cryptography. One of the key components for these applications is detectors based on thin superconducting films. Nevertheless, fabricating thin detectors atop a waveguide utilizing conventional superconducting materials acquired through magnetron sputtering presents a multifaceted and cost-intensive technological challenge. As an alternative approach in this study, we present the concept of an on-chip superconducting detector based on the two-dimensional superconductor $NbSe_2$, obtained through mechanical exfoliation. The advantage of this approach lies in the ease of device integration onto the waveguide and the possibility to create a detector with a thickness of just one atomic layer. We also demonstrated a method to fabricate thin superconducting nanowires from this material, as the ability to precisely structure the material is crucial for the development of on-chip detectors.

Keywords: 2D materials, PIC, superconducting electronics, superconductors

Funding: The publication was prepared within the framework of the Academic Fund Program at HSE University (grant no. 24-00-035 and Photodetectors for photonic integrated circuits based on new two-dimensional materials). Authors acknowledges the support from internal funding program from the Center for Neurophysics and Neuromorphic Technologies.

Citation: Shein K.V., Lyubchak A.N., Zharkova E., Bandurin D.A., Charaev I., Gayduchenko I.A., Goltsman G.N., Towards the realization of $NbSe_2$ NIR photodetectors integrated on a silicon nitride waveguide, St. Petersburg State Polytechnical University Journal. Physics and Mathematics. 17 (3.2) (2024) 241–245. DOI: https://doi.org/10.18721/JPM.173.248

Материалы конференции
УДК 538.9
DOI: https://doi.org/10.18721/JPM.173.248

На пути к реализации БИК-фотодетекторов $NbSe_2$, интегрированных на волновод из нитрида кремния.

К.В. Шеин[1,2,✉], А.Н. Любчак[1,2], Е. Жаркова[3], Д.А. Бандурин[3], И. Чараев[4], И.А. Гайдученко[1,2], Г.Н. Гольцман [1,2]

[1] Московский педагогический государственный университет, Москва, Россия;

[2] Национальный исследовательский университет «Высшая школа экономики», Москва, Россия;

[3]Лаборатория программируемых функциональных материалов, Центр исследования мозга и сознания, Москва, Россия;

[4] Университет Цюриха, Цюрих, Швейцария

✉ sheinkv97@gmail.com

Аннотация. Фотонные интегральные схемы (ФИС) представляют собой перспективную платформу для применения в области квантовых технологий, таких как квантовые вычисления и криптография. В данной работе мы демонстрируем успешное интегрирование двумерного сверхпроводника $NbSe_2$ на оптический волновод. Также нами был представлен и отработан процесс создания тонких нанопроводов методом реактивного ионного травления.

Ключевые слова: двумерные материалы, ФИС, сверхпроводящая электроника, БИС детекторы

Финансирование: Публикация подготовлена в рамках программы Академического фонда НИУВШЭ (грант № 24-00-035 и Фотоприемники для фотонных интегральных схем на основе новых двумерных материалов). Авторы выражают признательность за поддержку в рамках программы внутреннего финансирования Центра нейрофизики и нейроморфных технологий.

Ссылка при цитировании: Шеин К.В., Любчак А.Н., Жаркова Е., Бандурин Д.А., Чараев И., Гайдученко И.А., Гольцман Г.Н. На пути к реализации БИК-фотодетекторов $NbSe_2$, интегрированных на волновод из нитрида кремния // Научно-технические ведомости СПбГПУ.Физико-математические науки. 2024. Т. 17. № 3.2. С. 241–245. DOI: https://doi.org/10.18721/JPM.173.248

Introduction

Currently, there is a rapid development of quantum technologies in the fields of quantum computing, simulators, and cryptography [1]. Similar to modern nanoelectronics, quantum technologies also exhibit a trend towards miniaturization and maximum integration of technologies onto a single chip. PIC serve as a convenient and functional platform for such applications, where quantum computations and cryptographic protocols are already being implemented [2]. One of the key components of such circuits are superconducting photodetectors, which boast excellent characteristics in sensitivity, low noise and high speed. Despite the successful demonstration of superconducting detectors as an important part of modern optical quantum technologies, integrating them onto waveguides of the same quality as for planar structures remains a technologically challenging task. On the other hand, there is a trend towards integrating two-dimensional van der Waals (vdW) structures on the optical waveguides [3–5] due to their ease of integration, thickness down to a single atomic layer, and the ability to create heterostructures with programmable characteristics. A promising material for creating superconducting detectors on waveguide is niobium

diselenide ($NbSe_2$), which retains its superconducting properties down to a single atomic layer and has already demonstrated sensitivity as a detector in the terahertz [6] and near infrared region (NIR) [7] ranges. In this study, we demonstrate the integration of the hBN/$NbSe_2$/hBN structure onto an optical waveguide and the successful fabrication of thin nanowires using the reactive ion etching method.

Device fabrication

The fabrication of the detector integrated onto the optical waveguide involved two primary stages. First, an optical waveguide was made from Si_3N_4 in the form of an O – ring resonator with two diffraction grating couplers, which carry out the input/output of light and are designed for the wavelength $\lambda = 1550$ nm for standard telecommunication lasers. The waveguide and couplers were fabricated using standard electron–beam (e-beam) lithography and etched with CHF_3 gas plasma, a comprehensive route for manufacturing PIC is provided in [8]. In order to enhance the absorption of our device, we have carried out a simulation of the absorption coefficient of EM radiation from the width of a waveguide. The simulations were performed using the finite element method (FEM), implemented in the COMSOL Multiphysics software. The waveguide width ranged from 0.5 μm to 4 μm. From the obtained simulation results, the parameters of the waveguide were determined: the waveguide etch depth was 225 nm, and the waveguide width was 2.5 μm. Fig. 1, *b* shows an increase in the effective absorption coefficient for hBN/$NbSe_2$/hBN from 0.0145 dB/μm to 0.0685 dB/μm with a thickness of $NbSe_2$ and hBN of 12.7 nm and 20 nm respectively. The mode profile of the TE-like mode for the optimal waveguide width is depicted in Fig. 1, *c*.

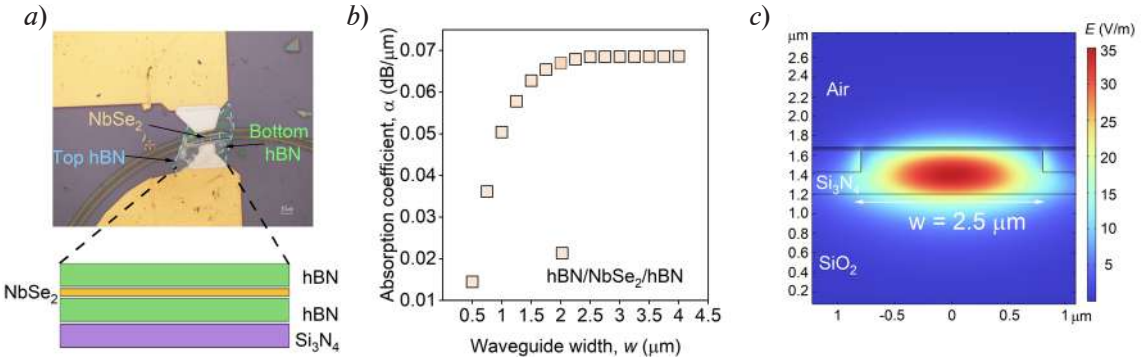

Fig 1. Optical micrograph of hBN/$NbSe_2$/hBN heterostructure integrated onto Si_3N_4 O-ring waveguide (*a*); inset shows schematics of hBN/$NbSe_2$/hBN heterostructure. Absorption coefficient of EM radiation for different width of a waveguide made of Si_3N_4 for our heterostructure (*b*). Field distribution of TE-like mode in the Si_3N_4 waveguide with hBN/$NbSe_2$/hBN heterostructure for the optimal waveguide width (*c*)

Subsequently, the integration of two-dimensional $NbSe_2$ onto the PIC was undertaken. However, this integration posed significant challenges: firstly, thin $NbSe_2$ rapidly degrades in the atmosphere; secondly, transferring the two-dimensional material onto the waveguide is complicated by its stepped relief. These issues were addressed by fabricating a heterostructure of fully encapsulated niobium diselenide in hexagonal boron nitride (hBN/$NbSe_2$/hBN). The top hBN layer serves as protection against atmospheric degradation, while the bottom layer improves adhesion with Si_3N_4. The flakes were produced via a standard dry transfer method using polydimethylsiloxane (PDMS). The assembly of the hBN/$NbSe_2$/hBN heterostructure was carried out using PDMS with a portable transfer machine, with the transfer process being monitored under a microscope. A mask made of PMMA/MMA resist was created for the contact area using standard e-beam lithography technique, followed by plasma etching of the upper hBN flake. Subsequently, small aluminum contacts with a thickness of 190 nm were fabricated. The next step involved photolithography and the deposition of larger gold contacts with a thickness of 150 nm. More detailed information about the manufacturing process can be found in [6]. Fig. 1, *a* shows a manufactured detector on a waveguide, the two-point resistance of the device is $R_{2pt} = 3700$ Ω, which is an adequate resistance for the given sample geometry.

As was shown in [5] for another two-dimensional superconducting material integrated into optical waveguide, the geometry of the detector is critically important to achieve record sensitivity. However, the process of creating ultrathin nanowires by structuring $NbSe_2$ flakes is still poorly studied [10]. To work out the detector pattering process, a $hBN/NbSe_2$ heterostructure with a thickness of approximately 20 and 10 nm, respectively, was assembled. Nanowires with a length l = 5 μm and a width w = 200 nm were create using e-beam lithography. Then the obtained nanowires were etched using the inductively coupled plasm from SF_6 gas, this gas was chosen because it is suitable for successful etching of both materials [6, 10]. Inset in Fig. 2, *a* shows the sample after reactive ion etching.

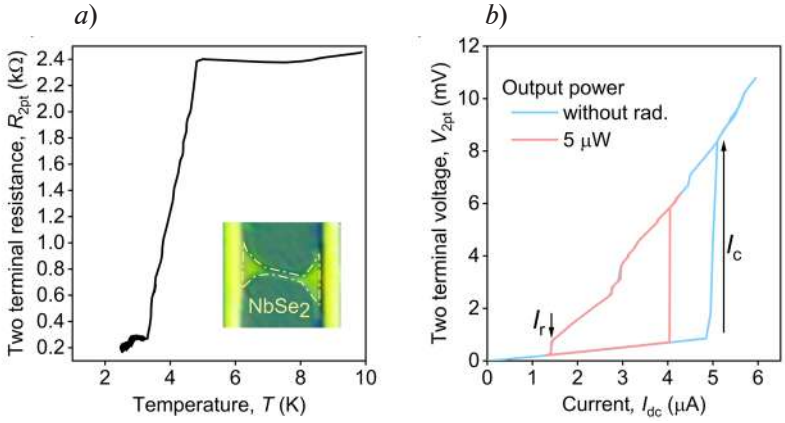

Fig. 2. Dependence of resistance on temperature for the sample after etching with critical temperature T_c = 4.23 K and a contact resistance R_s of 150 Ω, width of nanowire is 400 nm (*a*); inset shows optical micrograph of etched $NbSe_2$ nanowires covered by the hBN flake. Two-terminal $I_{dc}-V_{2pt}$ curves with (red line) and without (blue line) radiation at T = 2.5 K, wavelength of radiation is λ = 1550 nm and radiation power P_0 = 5 μW (*b*); black arrows indicate the direction of critical and retrapping current

Experiment and discussion

At the next step, we conducted transport measurements on etched $NbSe_2$ device. Fig. 2, *a* depicts the resistance versus temperature dependence. This nanowire exhibited the typical for $NbSe_2$ flake behavior of the resistance-temperature ($R(T)$) curve, with a critical temperature T_c = 4.23 K and a contact resistance R_s of 150 Ω. The critical temperature value deviates from the standard values typically observed at a given thin, which are usually around 6.5 K [6]. At the next step, to assess the optical sensitivity, the current-voltage ($I_{dc}-V_{2pt}$) characteristics in a two-contact configuration were measured under radiation with a wavelength of λ = 1550 nm at bath temperature T_b = 2.5 K (see Fig. 2, *b*). An optical fiber, positioned 1 cm from the sample and focused on its center, served as the radiation source with power P_0 = 5 μW. Fig. 2, *b* presents the $I-V$ characteristics of our heterostructure with and without illumination with the clearly observed the critical I_c and retrapping current I_r (black arrow Fig. 2, *b*). The sensitivity of the detector can be roughly estimated by observing changes in the critical current ΔI_c and voltage ΔV_c under radiation, the voltage responsivity $R_V = \Delta V_C/P_0$ of our device to be of 520 V/W. The obtained high values of optical responsivity demonstrate the potential of this material for application as a NIR on-chip photodetector. It is also important to note the clearly observed the retrapping current I_r is a significant prerequisite for the development of single-photon detectors and superconducting hot electron bolometers [11].

Conclusion

In conclusion, we have successfully demonstrated a comprehensive methodology for fabricating a photodetector based on a vdW heterostructure integrated on the optical waveguide. This process encompasses the creation of a ring resonator, the integration of the $hBN/NbSe_2/hBN$ heterostructure. We conducted a simulation of the optical mode profile and the absorption coefficient depending on the width of the waveguide, based on the simulation results, optimal geometric parameters of the waveguide were obtained, which were taken into account during the

manufacturing process. The resistance of the fabricated structure is 3.7 kΩ, an acceptable value for such devices. In addition, we described the process of creating $NbSe_2$ thin nanowires and evaluated its optical sensitivity, the results obtained are important for future optimization of the transport and optical characteristics of the nanowire integrated on PIC. This research paves the way for the creation a new of PIC based of thin vdW superconducting materials, enabling a wide range of applications in modern quantum technologies.

Acknowledgments

The publication was prepared within the framework of the Academic Fund Program at HSE University (grant 24-00-035 and Photodetectors for photonic integrated circuits based on new two-dimensional materials). Authors acknowledges the support from internal funding program from the Center for Neurophysics and Neuromorphic Technologies.

REFERENCES

1. **Antonio Асин et al**., New J.Phys. (20) (2018) 080201.
2. **Galan Moody et al.,** Roadmap on integrated quantum photonics 2022 J.Phys. Photonics. (4) (2022) 012501.
3. **Ramakrishnan R.K., Mishra A., Kumar P., et al.,** Integrated multi-mode waveguide devices for quantum communication. J Opt. (2023).
4. **Meng Y., Feng J., Han S., et al.,** Photonic van der Waals integration from 2D materials to 3D nanomembranes. Nat Rev Mater. (8) (2023) 498–517.
5. **Seifert P., et al.,** A high-Tc van der Waals superconductor based photodetector with ultra-high responsivity and nanosecond relaxation time. 2D Mater. (8) (2021) 035053.
6. **Shein K., Zharkova E., Bandurin D., et al**., Nano Letters. 24 (7) (2024) 2282–2288.
7. **Orchin G.J., et al**., Appl. Phys. Lett. 114 (25) (2019).
8. **Komrakova, et al.,** Hybrid Silicon Nitride Photonic Integrated Circuits Covered by Single Walled Carbon Nanotube Films, Nanomaterials. (13) (2023).
9. **Castellanos-Gomez, et al.,** Deterministic transfer of two-dimensional mate- rials by all-dry viscoelastic stamping. 2D Materials. (1) (2014) 011002.
10. **Hikari T., et al.,** Influence of microfabrication on superconducting properties of exfoliated thin films of layered superconductor $NbSe_2$: reactive ion etching, J.Phys.: Conf. Ser. (1293) (2019) 012005.
11. **Dane A., Allmaras J., Zhu D., et al.**, Self-heating hotspots in superconducting nanowires cooled by phonon black-body radiation. Nat Commun. 13 (2022) 5429.

THE AUTHORS

SHEIN Kirill V.
sheinkv97@gmail.com
ORCID: 0000-0001-6494-0147

CHARAEV Ilya
ilya.charaev@physik.uzh.ch
ORCID: 0000-0002-4036-0778

LYUBCHAK Anastasia N.
anlyubchak@miem.hse.ru
ORCID: 0000-0002-4861-2466

GAYDUCHENKO Igor A.
igaiduchenko@hse.ru
ORCID: 0000-0003-2560-6503

ZHARKOVA Ekaterina
sheinkv97@gmail.com
ORCID: 0000-0001-6494-0147

GOLTSMAN Grigory N.
goltsman@rplab.ru
ORCID: 0000-0002-1960-9161

BANDURIN Denis
dab@nus.edu.sg
ORCID: 0000-0001-9257-4105

Received 01.08.2024. Approved after reviewing 12.08.2024. Accepted 16.08.2024.

Conference materials
UDC 544.536
DOI: https://doi.org/10.18721/JPM.173.249

Fluorescent cell imaging with femtosecond laser pulses-produced protein nanoaggregates

A.A. Astafiev, A.M. Shakhov, M.S. Syrchina✉, V.A. Nadtochenko

Semenov Institute of Chemical Physics, Moscow, Russia

✉ wrongclue@gmail.com

Abstract. We demonstrated formation of fluorescent products from model protein - bovine serum albumin, induced by femtosecond laser irradiation and characterized optical properties of these products. Laser-modified BSA showed relative biocompatibility and can be employed for cell imaging.

Keywords: proteins, femtosecond laser pulses, nanomaterials, fluorescence, bioimaging

Funding: RNF grant no. 21-72-20169 “Fundamental physicochemical bases of design and application of carbon nanomaterials formed by nonlinear absorption in strong optical fields of femtosecond laser pulses”.

Citation: Astafiev A.A., Shakhov A.M., Syrchina M.S., Nadtochenko V.A., Fluorescent cell imaging with femtosecond laser pulses-produced protein nanoaggregates, St. Petersburg State Polytechnical University Journal. Physics and Mathematics. 17 (3.2) (2024) 246–250. DOI: https://doi.org/10.18721/JPM.173.249

Материалы конференции
УДК 544.536
DOI: https://doi.org/10.18721/JPM.173.249

Флуоресцентная визуализация клеток с применением белковых наноагрегатов, полученных методом лазерного синтеза

А.А. Астафьев, А.М. Шахов, М.С. Сырчина✉, В.А. Надточенко

Институт химической физики им. Н.Н.Семёнова РАН,Москва, Россия

✉ wrongclue@gmail.com

Аннотация. В работе исследована возможность агрегации бычьего сывороточного альбумина с помощью фемтосекундного лазерного излучения с последующей оценкой флуоресцентных характеристик продуктов синтеза. Также была продемонстрирована биосовместимость продуктов синтеза и возможность их применения для имиджинга на клеточной линии A549.

Ключевые слова: белки, фемтосекундные лазерные импульсы, наноматериалы, флуоресценция, биоимаджинг

Финансирование: Грант РНФ № 20169-72-21 «Фундаментальные физико-химические основы дизайна и применения углеродных наноматериалов, формируемых при нелинейном поглощении в сильных оптических полях фемтосекундных лазерных импульсов».

Ссылка при цитировании: Астафьев А.А., Шахов А.М., Сырчина М.С., Надточенко В.А. Флуоресцентная визуализация клеток с применением белковых наноагрегатов, полученных методом лазерного синтеза // Научно-технические ведомости СПбГПУ.Физико-математические науки. 2024. Т. 17. № 3.2. С. 246–250. DOI: https://doi.org/10.18721/JPM.173.249

Introduction

Femtosecond laser synthesis of fluorescent nanoproducts from biomolecules is an intriguing phenomenon, which can be exploited in novel approaches to bioimaging [1–2]. Previously we demonstrated laser synthesis of fluorescent carbon dots from essential amino acids [3]. As a next step we study products obtained from a model protein bovine serum albumin (BSA). It is known that albumin can form aggregates, which unlike the monomer protein emit bright visible fluorescence [4–5]. We examined if the femtosecond laser irradiation can trigger similar aggregation of BSA and formation of fluorescent products and studied their optical properties. We also probed biocompatibility of BSA products and their employment as fluorescent cell imaging agents.

Materials and Methods

Synthesis and characterization of products. Aqueous solution of BSA (1 mL, 0.1 g/mL) in a glass vial was irradiated with trains of amplified femtosecond laser pulses focused by a spherical lens (f = 8 mm, 0.5NA). Central wavelength of laser pulses was 1033 nm, repetition rate was 50 kHz, duration was 250 fs, pulse energy was 60 μJ. (Fig. 1)

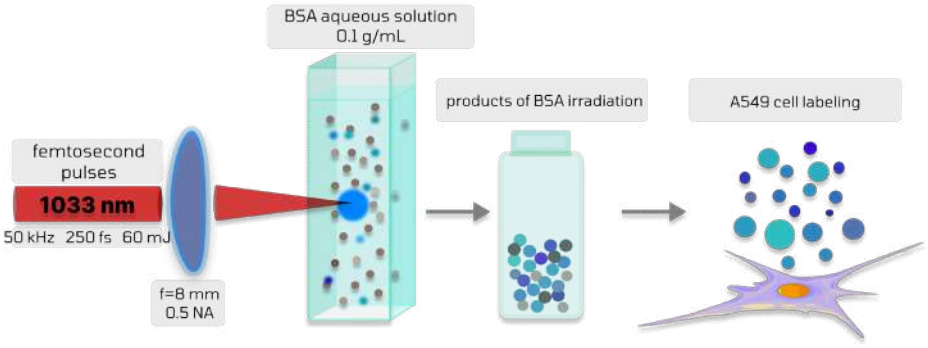

Fig. 1. Experimental setup

Absorption and photoluminescence spectra of irradiated BSA in water were recorded with Shimadzu spectrophotometer (UV-3600) and spectrofluorometer (RF-5031 PC). Fluorescence quantum yield (356 nm excitation) was estimated with the slope method using ethanol solution of anthracene as a standard (quantum yield = 0.27). Fluorescence decay and fluorescence anisotropy decay kinetics in aqueous solution were registered with pulsed laser excitation at 360 nm at 450 nm emission wavelength using time-correlated single-photon counting module (SPC-150N, Becker&Hickl GmbH). Protein aggregates sizes were analyzed with dynamic light scattering (DLS) technique using a Photocor Compact-Z setup.

Labeling of living A549 cells. A549 cells (lung adenocarcinoma) were incubated at 37 °C in 5% CO_2 humidified atmosphere with CDs dissolved in medium in the ratios of 1:200, 1:40 and 1:8 for 12 hours. Fluorescent images and lambda scans of the cells after labeling were obtained using a laser scanning confocal microscope Zeiss LSM 980 (Carl Zeiss Microscopy, Jena, Germany), 20x Plan-Apochromat objective (NA = 0.8). One-photon excitation was performed with a 405 nm laser. Fluorescence was recorded at 420–750 nm range.

A549 cell viability test. A549 cells (lung adenocarcinoma) were incubated at 37 °C in 5% CO_2 humidified atmosphere with CDs dissolved in medium in the ratios of 1:200, 1:40 and 1:8 for 2 hours. After that, cells were stained with acridine orange and propidium iodide to identify dead cells at a concentration sufficient for imaging, but optimal for minimizing risks of cell death after staining. Confocal imaging was obtained immediately after staining without washing of samples. Images of 3 randomly chosen regions from each sample were obtained and used for cell counting in Fiji software. Ratios of dead/alive cells (nuclei stained with PI and AO respectively) were counted to estimate cell viability in each sample.

Results and Discussion

Aqueous solution of the normal BSA was almost non-absorbing above 300 nm and emitted only weak visible fluorescence. Laser irradiation resulted in yellowing of the BSA solution (Fig. 2, *a*) and emergence of broadband optical absorption in the near-ultraviolet and visible range with extinction coefficient of the order of 10^4 $M^{-1}cm^{-1}$ (Fig. 2, *b*). Laser-irradiated BSA solution emitted bright fluorescence upon excitation in the near-ultraviolet and visible range. Its intensity was many times stronger than fluorescence intensity of normal BSA.

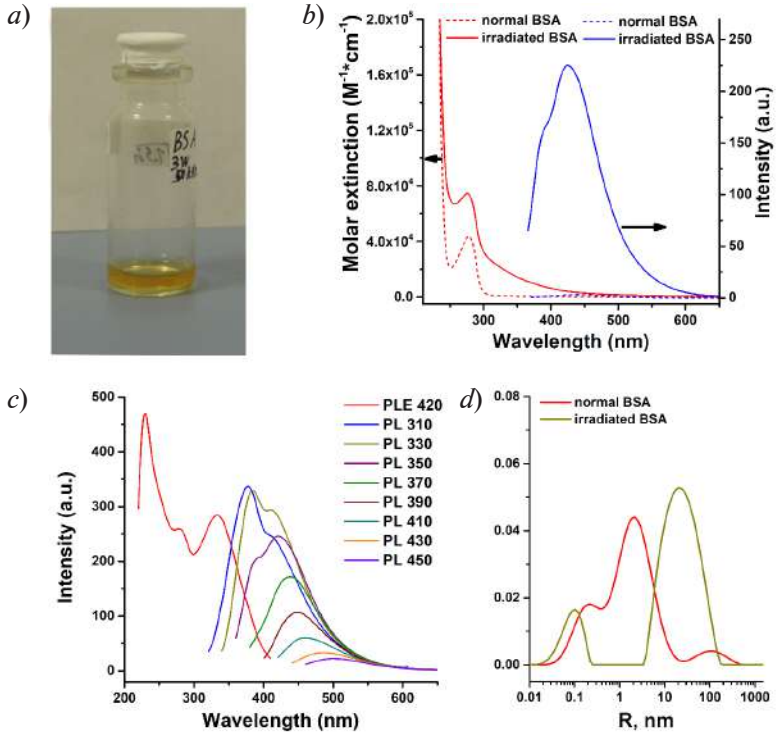

Fig. 2. Image of laser-irradiated BSA sample (*a*). Absorption and fluorescence spectra of normal (dashed lines) and laser-irradiated (solid lines) BSA. Fluorescence excitation at 350 nm (*b*). Photoluminescence excitation spectrum (PLE) and emission spectra (PL) with excitation wavelength ranging from 310 to 450 nm (*c*). Distribution of hydrodynamic radii of normal and laser-irradiated BSA obtained from the DLS (*d*)

Photoluminescence excitation spectrum, registered at 420 nm emission wavelength, revealed three distinct absorption bands at 230, 280 and 330 nm. The band at 280 nm corresponds to excitation of intrinsic luminescence of aromatic residues of the BSA (tyrosine and tryptophan), whose emission peaks at 340 nm, but also produces a relatively weak tail in the visible range. This band is also seen at the absorption spectrum (Fig. 2, *c*). The bands at 230 and 330 nm are attributed to new chromophores formed in the BSA by laser irradiation. Fluorescence spectra were dependent on the excitation wavelength: their shape and peak position changed with a shift of the excitation wavelength (Fig. 2, *c*). When excited near 350 nm the emission peak was at 420 nm with the corresponding fluorescence quantum yield equal to 7.4%, and the fluorescence lifetime to 1.35 ns.

Dynamic light scattering demonstrated formation of aggregates in the irradiated BSA solution with the mean radius of about 30 nm of tens nm – almost an order of magnitude larger than hydrodynamic radius of normal BSA in water (3.9 nm) [6] (Fig. 2, *d*). Thus, these aggregates consist of a large number (at least hundreds) of protein monomers. Human and bovine serum albumin are known to form fluorescent oligomers in concentrated solutions [4–5]. We suggest that femtosecond laser irradiation produces protein aggregates, which remain stable even in diluted solution and these aggregates are a likely source of enhanced absorption and fluorescence of irradiated BSA.

Brightest fluorescence of CDs was observed in group with highest concentration of CDs. Lambda scanning of cells after incubation with CDs during 12 hours demonstrated broadening of dominant emission peak. Emergence of shoulder at 430–450 nm range can be a mark of CDs uptake by cells (Fig. 3).

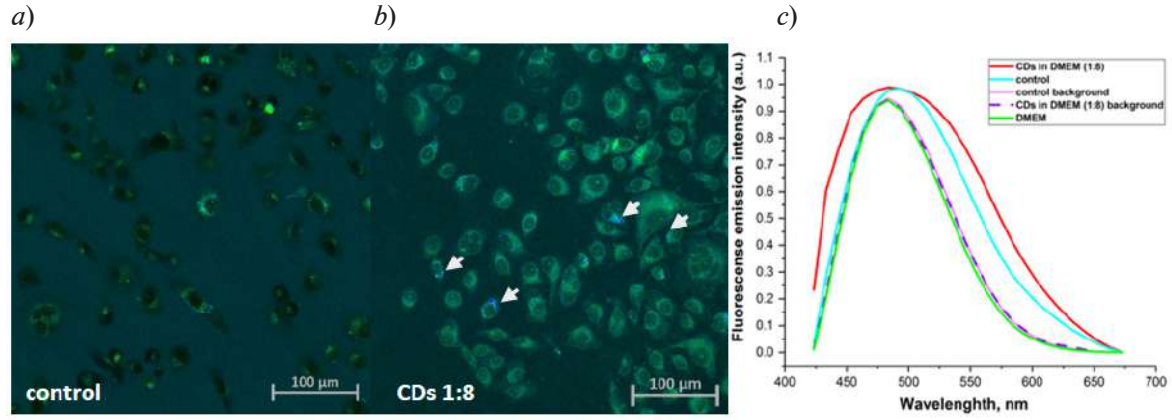

Fig. 3. Lambda scanning of A549 cells, incubated with CDs at ratio of 1:8 for 12 hours. Scanned areas are pointed by arrows. The most representable one was taken for the graph. Lambda stack of cells from control group (*a*), lambda stack of cells, incubated with CDs at ratio of 1:8 for 12 hours (*b*), fluorescence emission distribution (*c*)

Confocal imaging also revealed formation of granules (probably vesicles) in cytoplasm with fluorescence in blue spectral diapason. (Fig. 4).

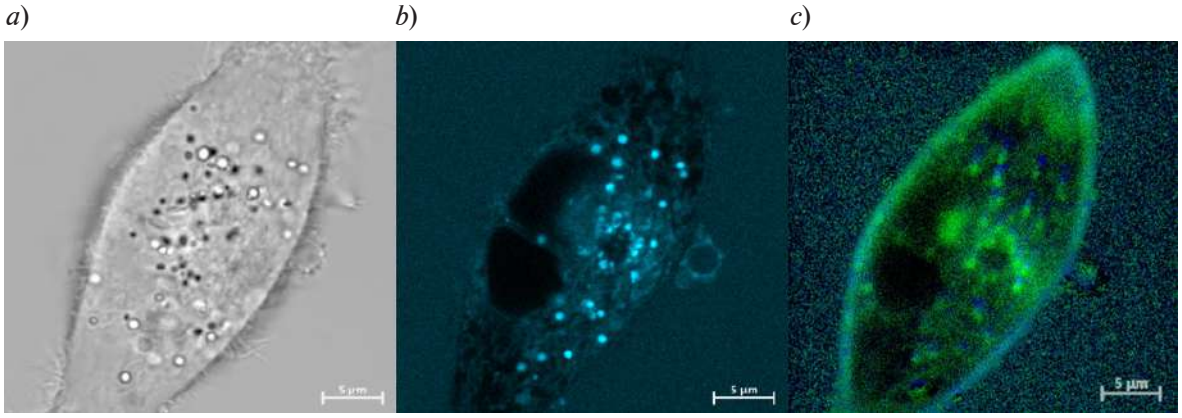

Fig. 4. Confocal images of individual A549 cell, incubated with CDs at ratio of 1:40. Bright field image of the cell (*a*), confocal fluorescent image at 405 nm wavelength (*b*), lambda stack and fluorescence distribution within the cell (*c*)

Short-time labelling of A549 cells with CDs showed an increased percentage of dead cells in all experimental groups. Cell viability was not dose-dependent, quantity of dead cells is almost the same for all concentrations of CDs. (Fig. 5). Gradually reducing ability of cells to attach substrate

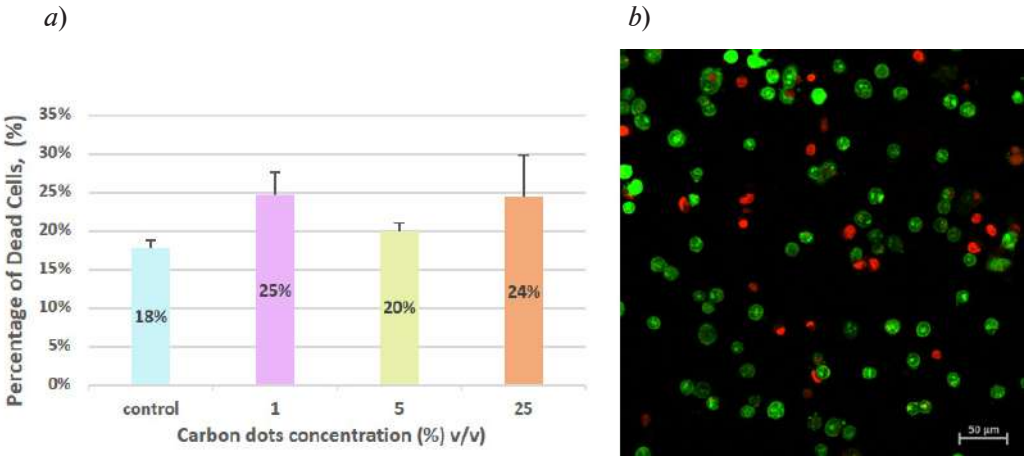

Fig. 5. A549 cell viability test (*a*), confocal image of A549 cells, stained with acridine orange (live, green) and propidium iodide (dead, red) (*b*)

was observed and was proportional to concentration of CDs. Cells from the sample with highest concentration remained in suspension after 12 hours of incubation. Impossibility of cell to attach substrate can be a trigger of cell death. It is also known, that sensibility of cells to nanoparticles depends on a cell cycle phase. Exact mechanism of cell death experienced by cells under BSA-based CDs uptake remains to be studied.

In conclusion, we found that femtosecond laser irradiation enhances absorption and visible fluorescence of the BSA solution and produces nanoscale protein aggregates. We demonstrated applicability of laser produced protein aggregates for cell fluorescent imaging.

REFERENCES

1. **Sun Q., Qin Z., Wu W., et al.,** In vivo imaging-guided microsurgery based on femtosecond laser produced new fluorescent compounds in biological tissues, Biomedical Optics Express. 9 (2018) 581–590.

2. **Astafiev A.A., Shakhov A.M., Osychenko A.A., et al.,** Probing intracellular dynamics using fluorescent carbon dots produced by femtosecond laser in situ, ACSOmega. 5 (21) (2020) 12527–12538.

3. **Astafiev A.A., Shakhov A.M., Gulin A.A., et al.,** Femtosecond laser synthesis and comparative analysis of fluorescent carbon dots from L-lysine aqueous solution, Journal of Physics: Conference Series. 2086 (2021) 120–121.

4. **Bhattacharya A., Bhowmik S., Singh A.K., et al.,** Direct Evidence of intrinsic blue fluorescence from oligomeric interfaces of human serum albumin, Langimur. 33 (40) (2017) 10606–10615.

5. **Wang Q., Dou X., Chen X. et al.,** Reevaluating protein photoluminescence: remarkable visible luminescence upon concentration and insight into the emission mechanism, Angewandte Chemie International Edition. 58 (2019) 12667.

6. **Zhang X., Poniewierski A., Hou S., et al.,** Tracking structural transitions of bovine serum albumin in surfactant solutions by fluorescence correlation spectroscopy and fluorescence lifetime analysis, Soft Matter. 11 (2015) 2512–2518.

THE AUTHORS

ASTAFIEV Artyom A.
astafiev.artyom@gmail.com
ORCID: 0000-0001-9269-414X

SYRCHINA Maria S.
wrongclue@gmail.com
ORCID: 0000-0002-5318-8903

SHAKHOV Aleksander M.
physics2007@yandex.com
ORCID: 0000-0002-0958-2903

NADTOCHENKO Victor A.
wrongclue@gmail.com
ORCID: 0000-0002-6645-692X

Received 05.08.2024. Approved after reviewing 06.09.2024. Accepted 16.09.2024.

Conference materials
UDC 08.1; 08.2; 08.3
DOI: https://doi.org/10.18721/JPM.173.250

Degradation of solar heterostructured cells under the influence of electron flow

O.P. Mikhaylov[1,2]✉, A.I. Baranov[2], A.V. Uvarov[2], A.A. Maksimova[1,2], E.A. Vyacheslavova[2], A.S. Gudovskikh[1,2], M.Z. Shvarts[3], E.I. Terukov[3]

[1] St. Petersburg Electrotechnical University "LETI", St. Petersburg, Russia;

[2] Alferov University, St. Petersburg, Russia;

[3] Ioffe Institute, St. Petersburg, Russia

✉ oleg.mikhaylov.00@gmail.com

Abstract. In this work, we study the effect of irradiation as in low Earth orbits on heterojunction technology structures (*p*)*a*-Si:H/(*n*)*c*-Si. The samples were irradiated with an electron beam with an energy of 2 MeV and fluences of $3 \cdot 10^{13}$cm^{-2} to $3 \cdot 10^{15}$cm^{-2}. Solar cells performance deteriorate with increasing of fluence due to decrease of lifetime of charge carriers in bulk silicon. According to DLTS measurements, three defects with activation energies of 0.18 eV, 0.25 eV and 0.43 eV were detected, and their nature was identified. Further, the concentrations of the found defects were analyzed, during which it became clear that the concentration of defects decreases with increasing depth of the investigated structure. The correlation between fluence and concentration is also visible. The average values of concentrations vary from 10^{12} to 10^{14}.

Keywords: HJT solar cells, DLTS, defects, concentration, absorption cross-section

Funding: The work was carried out within the framework of the state assignment of the Ministry of Science and Higher Education of the Russian Federation (project number 0791-2023-0007).

Citation: Mikhaylov O.P., Baranov A.I., Uvarov A.V., Maksimova A.A., Vyacheslavova E.A., Gudovskikh A.S., Shvarts M.Z., Terukov E.I., Degradation of solar heterostructured cells under the influence of electron flow, St. Petersburg State Polytechnical University Journal. Physics and Mathematics. 17 (3.2) (2024) 251–255. DOI: https://doi.org/10.18721/JPM.173.250

Материалы конференции
УДК 08.1; 08.2; 08.3
DOI: https://doi.org/10.18721/JPM.173.250

Деградация солнечных гетероструктурных элементов под воздействием потока электронов

О.П. Михайлов[1,2]✉, А.И. Баранов[2], А.В. Уваров[2], А.А. Максимова[1,2], Е.А. Вячеславова[2], А.С. Гудовских[1,2], М.З. Шварц[3], Е.И. Теруков[3]

[1] Санкт-Петербургский государственный электротехнический университет «ЛЭТИ» им. В.И. Ульянова (Ленина), Санкт-Петербург, Россия;

[2] Академический университет им. Ж.И. Алфёрова РАН, Санкт-Петербург, Россия;

[3] Физико-технический институт им. А.Ф. Иоффе РАН, Санкт-Петербург, Россия

✉ oleg.mikhaylov.00@gmail.com

Аннотация. В данной работе исследуется влияние облучения на низких околоземных орбитах, на структуры с гетеропереходом (*p*)*a*-Si:H/(*n*)*c*-Si. Образцы облучались электронным пучком с энергией 2 МэВ и флюенсами от $3 \cdot 10^{13}$ см$^{-2}$ до $3 \cdot 10^{15}$ см$^{-2}$. Производительность солнечных элементов ухудшается с увеличением флюенса из-за

уменьшения времени жизни носителей заряда в объемном кремнии. По результатам DLTS-измерений были обнаружены три дефекта с энергиями активации 0,18 эВ, 0,25 эВ и 0,43 эВ, а также определена их природа. Далее был проведен анализ концентраций найденных дефектов, в ходе которого стало ясно, что концентрация дефектов уменьшается с увеличением глубины исследуемой структуры. Также прослеживается корреляция между флюенсом и концентрацией. Средние значения концентраций варьируются от 10^{12} до 10^{14}.

Ключевые слова: солнечные элементы HJT,DLTS, дефекты, концентрация, сечение поглощения

Финансирование: Работа выполнена в рамках государственного задания Министерства науки и высшего образования РФ (проект № 0791-2023-0007).

Ссылка при цитировании: Михайлов О.П., Баранов А.И., Уваров А.В., Максимова А.А., Вячеславова Е.А., Гудовских А.С., Шварц М.З., Теруков Е.И. Деградация солнечных гетероструктурных элементов под воздействием потока электронов // Научно-технические ведомости СПбГПУ.Физико-математические науки. 2024. Т. 17. № 3.2. С. 251–255. DOI: https://doi.org/10.18721/JPM.173.250

Introduction

The technology behind silicon solar cells with a heterojunction, also referred to as HJT solar cells (Heterojunction technology), combines the benefits of both crystalline and amorphous silicon. This approach shows potential for achieving high solar energy conversion efficiency while using less silicon and operating at lower manufacturing temperatures, not exceeding 200–250 °C, compared to traditional diffusion technologies [1]. These characteristics make such solar cells particularly interesting for space applications. In previous work, we studied the impact of electron irradiation with an energy of 1 MeV, similar to the values encountered in near-Earth orbits, on the photoelectrical and defect properties of HJT [2].

In this study, we will investigate the photoelectrical properties of HJT solar cells subjected to higher electron irradiation with an energy of 2 MeV. Additionally, we will use deep-level transient spectroscopy to examine defect formation in HJT samples.

Materials and Methods

This paper focuses on HJT solar cells based on anisotype heterojunction *p*-*a*-Si/*i*-*a*-Si/*n*-*c*-Si, formed on specially prepared *n*-Si ($n = 3 \cdot 10^{15}$ cm^{-3}) substrates using plasma-enhanced chemical vapor deposition at low temperatures. The rear contact was created on the developed *n*-Si surface by depositing a passivating *i*-*a*-Si layer followed by *n*-*a*-Si. Subsequently, transparent conducting ITO layers were sputtered using a BOC Edwards Auto500 setup, and a metallic contact was formed with silver paste, followed by annealing. Capacitance DLTS measurements were carried out with an automated system based on a Boonton-7200B capacitance bridge in the temperature range of 80–360 K in a Janis VPF-100 nitrogen vacuum cryostat. These structures were subjected to electron irradiation with an energy of 2 MeV at fluences ranging from $1 \cdot 10^{13}$ cm^{-2} to $3 \cdot 10^{15}$ cm^{-2}.

Results and Discussion

Fig. 1 shows the current–voltage characteristics measured under illumination of AM1.5G. In [2], a catastrophic drop in the current-voltage characteristic and quantum efficiency was observed after irradiation of samples with a flow of electrons with an energy of 1 MeV. During this work, a drop in performance is also observed, for example the short circuit current decreases from 26.55 mA/cm^2 to 15.7 mA/cm^2 and the open-circuit voltage from 530 mV to 430 mV. Influence of irradiation also is confirmed by spectrum of external quantum efficiency (EQE) (Fig. 2). Obviously, EQE strongly drop in long-wavelength region with increase of fluence. It means decrease of lifetime of charge carriers in bulk silicon after irradiation. Perhaps, it is explained by defect formation in depth of substrate so method of deep-level transient spectroscopy (DLTS) was applied to explore defect in HJT.

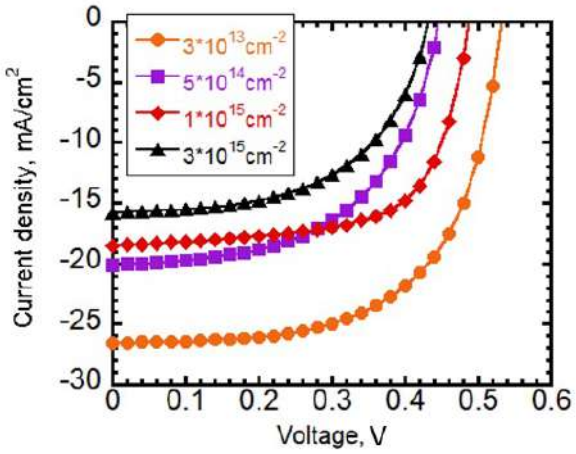

Fig. 1. Current–voltage characteristic for samples with irradiation energy of 2 MeV and different fluence

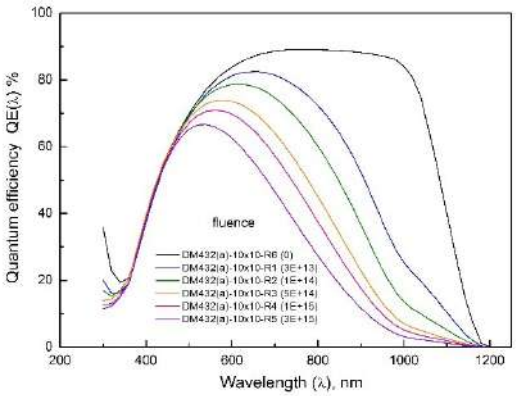

Fig. 2. External quantum efficiency of solar cells after different fluences

Thus, the mechanism of defect formation was studied using transient deep-level spectroscopy. The research process is demonstrated using a negative bias voltage of -3 V to 0 V.

When measuring a sample with a voltage U = -3–0 V, and a fluence of $3 \cdot 10^{13}$ cm^2, the graph looks non-standard due to the very high conductivity of the sample; in such cases, the values obtained by the device go beyond the measurement scale and the study cannot be carried out.

Two defects with E_a = 0.07 eV and E_a = 0.15 eV are observed in the plot with positive bias. The response with E_a = 0.07 eV in the range of 100-150 K is found in all samples close to the heterointerface in near-surface area (Fig. 3, *a*), in contrast to the bulk material (Fig. 3, *b*). However, its parameters are not critical for the photovoltaic properties due to the low capture cross section and E_a. Peak corresponding to the defect level with E_a = 0.15 eV, indicating deep defects. In addition, the amplitude of the appeared peaks increases by a factor of two with increasing irradiation dose, indicating a direct correlation between electron flux and defect appearance. Probably, the detected defect is an A-center (V–O, vacancy-oxygen) [3] arising due to the activation of oxygen atoms after electron irradiation. At negative bias voltage, new defects with activation energies E_a = 0.22 eV and E_a = 0.43 eV, in the temperature ranges of 110–180 K and 200–240 K, respectively, appeared. The defect with E_a = 0.22–0.23 eV can be explained by the appearance of an non-passivated dangling bond created by the N atom that replaces the Si vacancy [4], or perhaps this defect is associated with a V–V pair (vacancy-vacancy) [5]. This leads to the formation of unstable regions in the structure, which can affect the conductivity and recombination properties of the material. And the defect with E_a = 0.43 eV is probably an A-pair (V–H, vacancy–hydrogen) [6], which arises as a result of activation of hydrogen atoms after electron irradiation.

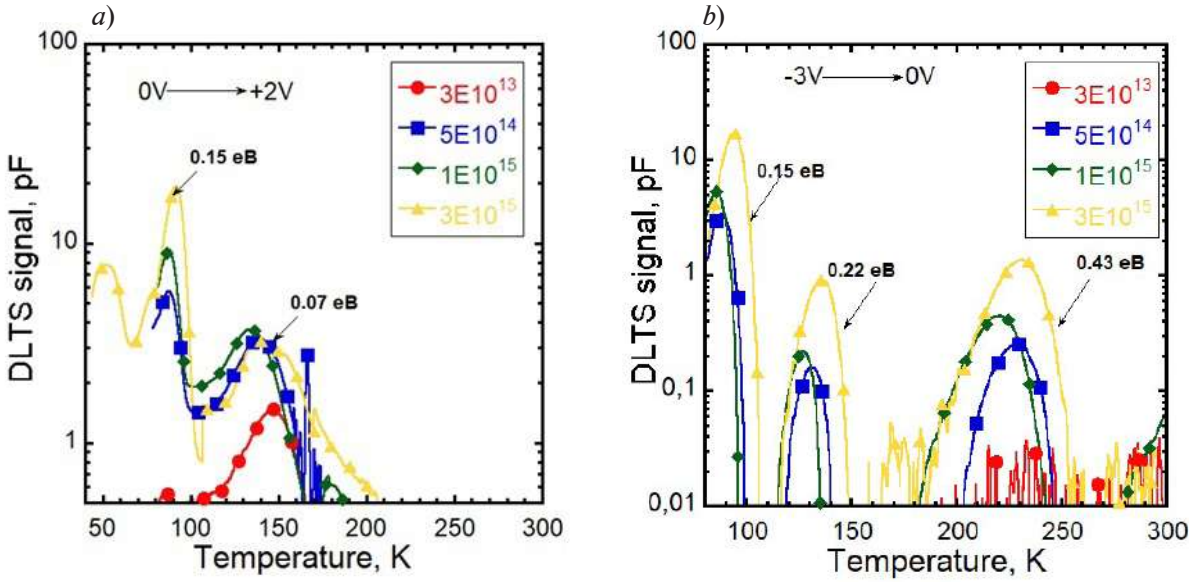

Fig. 3. DLTS signal graphs for the studied samples with fluences $3 \cdot 10^{13}$ cm^{-2}, $5 \cdot 10^{14}$ cm^{-2}, $1 \cdot 10^{15}$ cm^{-2} and $3 \cdot 10^{15}$ cm^{-2} and energy 2 MeV, at V_{init} = -3 V (*a*), V_{pulse} = +3 V and V_{init} = 0 V, V_{pulse} = +2V for emission rate of 200 s^{-1} (*b*)

Next, the values of defect concentrations were estimated. Analyzing the obtained values, it is possible to notice that with increasing depth of the investigated zone the concentration of defects decreases, for example, for a defect with activation energy 0.15 eV at a depth of about 500 nm (at positive displacement), the concentration is equal to 8.6E + 14, and with increasing depth 5.64E + 14.

Table

Main characteristics of defects

Activation energy E_a, eV	Capture cross section σ, cm^2	Concentration (V_{init} = 0 V, V_{pulse} = +2V)	Concentration (V_{init} = -3 V, V_{pulse} = 0 V)
0.07	$6 \cdot 10^{-21}$	1.86E + 13	–
0.15	$4.5 \cdot 10^{-15}$	8.6E + 14	5.64E + 14
0.22	$9 \cdot 10^{-15}$	1.13E + 13	1.65E + 13
0.43	$5 \cdot 10^{-15}$	–	9.46E + 13

Conclusion

HJT solar cells were studied after electron irradiation with an energy of 2 MeV at fluences from $1 \cdot 10^{13}$cm^{-2} to $3 \cdot 10^{15}$cm^{-2}. Quantum efficiency extremely drops with increasing of dose of electron irradiation in long-wavelength area of spectrum due to formation of defects in bulk silicon with activation energy of 0.15 eV, 0.22 eV and 0.43 eV detected by DLTS, and their concentration increases with growth of fluences.

Acknowledgments

The work was carried out within the framework of the state assignment of the Ministry of Science and Higher Education of the Russian Federation (project number 0791-2023-0007).

REFERENCES

1. **Green M.A., Dunlop E.D., Yoshita M., et. al.,** Solar cell efficiency tables (version 62), Prog. Photovoltaics Res. Appl. 31 (7) (2023) 651–663.

2. **Mikhaylov O.P., Baranov A.I., Gudovskikh A.S., Terukov E.I.,** Deep-level transient spectroscopy of solar cells based on HJT architecture under influence of electron irradiation, St. Petersburg State Polytechnical University Journal. Physics and Mathematics. 17 (1.1) (2024) 160–164.

3**. Losee D.L.**, Admittance spectroscopy of impurity levels in Schottky barriers, J. Appl. Phys. (46) (1975) 2204–2214.

4. **Masafumi Y., Kan-Hua L., Kenji A**., Analysis for Radiation Degradation of Advanced SiSpace Solar Cells, 46th Photovoltaic Specialists. 48 (2021) 3124.

5. **Zholdybayev N., Aimaganbetov K., Zhantuarov K., et. al.,** Development of Hetero-Junction Silicon Solar Cells with Intrinsic Thin Layer, A Review. Coatings. (15) (2023) 814.

6. **Hiller D., et. al.,** Kinetics of bulk lifetime degradation in float-zone silicon: fast activation and annihilation of grown-in defects and the role of hydrogen versus light, Physica Status Solidi. 217 (17) (2020) 2000436.

THE AUTHORS

MIKHAYLOV Oleg P.
oleg.mikhaylov.00@gmail.com
ORCID: 0009-0005-6836-4091

VYACHESLAVOVA Ekaterina A.
cate.viacheslavova@yandex.ru
ORCID:0000-0001-6869-1213

BARANOV Artem I.
itiomchik@yandex.ru
ORCID:0000-0002-4894-6503

GUDOVSKIKH Alexander S.
gudovskikh@spbau.ru
ORCID: 0000-0002-7632-3194

UVAROV Alexander V.
lumenlight@mail.ru
ORCID: 0000-0002-0061-6687

TERUKOV Evgeny I.
eug.terukov@mail.ioffe.ru
ORCID: 0000-0002-4818-4924

MAKSIMOVA Alina A.
deer.blackgreen@yandex.ru
ORCID: 0000-0002-3503-7458

SHVARTS Maxim Z.
Shvarts M.Z.@mail.ioffe.ru
ORCID: 000-0002-2230-7770

Received 11.09.2024. Approved after reviewing 25.09.2024. Accepted 26.09.2024.

Conference materials
UDC 53.04
DOI: https://doi.org/10.18721/JPM.173.251

Photovoltaic potential in the Subarctic region

Deng Y.[1,2]✉, V.V. Davydov[1]

[1] Peter the Great St. Petersburg Polytechnic University, St. Petersburg, Russia;

[2] Jiangsu Normal University, Xuzhou, China

✉ dyuanbiao@gmail.com

Abstract. With the world's policy support for solar energy and other renewable energy sources, solar photovoltaic technology has seen rapid development. However, from Saint Petersburg's perspective, generating solar photovoltaic (PV) energy in a Subarctic setting is hindered by several challenges, which diminish the enthusiasm for its adoption. Our work demonstrates that St. Petersburg is capable of generating more solar photovoltaic energy in summer than Central Europe, East and Southeast Asia. This finding could enhance our understanding of the seasonal and annual potential of solar PV energy in Subarctic region.

Keywords: solar energy, climatic, Subarctic, photovoltaic potential

Citation: Deng Y., Davydov V.V., Photovoltaic potential in the Subarctic region, St. Petersburg State Polytechnical University Journal. Physics and Mathematics. 17 (3.2) (2024) 256–261. DOI: https://doi.org/10.18721/JPM.173.251

Материалы конференции
УДК 53.04
DOI: https://doi.org/10.18721/JPM.173.251

Фотоэлектрический потенциал в субарктическом регионе

Дэн Ю.[1,2]✉, В.В. Давыдов[1]

[1] Санкт-Петербургский политехнический университет Петра Великого, Санкт-Петербург, Россия;

[2] Цзянсуский педагогический университет, Сюйчжоу, Китай

✉ dyuanbiao@gmail.com

Аннотация. В мире большой поддержкой пользуется развитие солнечной энергетики в рамках программ развития возобновляемых источников энергии в условиях сокращения природного топлива. Большие сложности, связанные с выработкой электрической энергии с использованием фотоэлектрических преобразователей солнечных панелей в Санкт-Петербурге, создают проблемы по их внедрению. Проведенные нами исследования показывают, что в Санкт-Петербурге возможно при определенных условиях эксплуатации солнечных панелей вырабатывать летом больше солнечной фотоэлектрической энергии, чем Центральная Европа, Восточная и Юго-Восточная Азия. Предложена методика эксплуатации солнечных панелей в летний период для обеспечения сезонного и годового положительного баланса в их эксплуатации в субарктическом регионе.

Ключевые слова: солнечная энергия, климат, Субарктика, фотоэлектрический потенциал

Ссылка при цитировании: Дэн Ю., Давыдов В.В., Фотоэлектрический потенциал в субарктическом регионе // Научно-технические ведомости СПбГПУ. Физико-математические науки. 2024. Т. 17. № 3.2. С. 256–261. DOI: https://doi.org/10.18721/JPM.173.251

Introduction

Solar energy, recognized as a sustainable form of power, has demonstrated significant global growth in recent decades [1–4]. It has effectively emerged as a competitive alternative to traditional sources of electricity in various countries [5–9]. Projections from the International Energy Agency (IEA) indicate a substantial increase in global photovoltaic (PV) cumulative installed capacity, reaching 1721GW by 2030 and potentially expanding to 4670 GW by 2050 [10].

Current research on the reliability of photovoltaic (PV) modules predominantly centers on subtropical and temperate regions characterized by short winter periods and high solar activity. Conversely, there is a notable dearth of research focused on Arctic and Subarctic regions. Geographically, the Subarctic region is the transitional zone amidst the core Arctic and humid continental regions. Differentiation of the Earth according to surface, latitude, and height forms the transitional zones at the boundaries of the core areas. The Arctic and temperate latitudes' air influences the Subarctic regions' climate. Iceland, Norway, Sweden, Finland, Russia, Canada, central Siberia, and Alaska land mass falls under Subarctic regions. Thermally, the Subarctic is a region with an average temperature recorded for the year, except for four months, below 10 °C [11–13]. The unique environmental conditions in these regions, including uneven daylight duration, snow cover lasting more than three months, and extreme low temperatures during winter, pose challenges that diminish the solar PV potential. Therefore, there is a need for novel approaches to assess renewable energy potential and develop PV modules tailored to the specific climatic conditions in these regions.

Research on photovoltaic modules in the Nordic countries is ongoing. Vinay Shaekar's study suggests that an inclination of 28 degrees is optimal in the Oulu region of Finland, and increasing plate spacing can enhance snow melting [14]. Similarly, Mattia Manni's research in Norway recommends the use of ice-repellent coatings to maximize PV power output during winter months [15].

This study analyses the climate of the Subarctic region, utilizing St. Petersburg as an example. It also compares this region with others to demonstrate the potential for photovoltaic development in the Subarctic region.

Materials and Methods

St. Petersburg is located at 59° north latitude and 30° east longitude, South of the Arctic circle, stationed in the transitional zone between the Arctic and the Subarctic region.

Fig. 1 shows a study of PV output potential published by the World Bank, which takes into account air temperature, system configuration, shading and dirt, and topography and land-use constraints in addition to global horizontal radiation, and allows for a better characterization of the actual potential for PV power generation [16]. The figure shows that the solar potential of the Nordic and western Russian regions is essentially equal to that of Central Europe and slightly higher than that of the Sichuan Basin region in China.

Investigations into the photovoltaic potential of the Subarctic region must consider the seasonal variations in solar radiation within this area. Summers in St. Petersburg, Moscow, and the Nordic region feature favorable temperatures, largely cloudless skies, and long hours of daylight. In contrast, winter is marked by long periods of snow and abundant of clouds. St. Petersburg is a typical Subarctic region and this paper will use this as an example to analyze the PV potential of the Subarctic region.

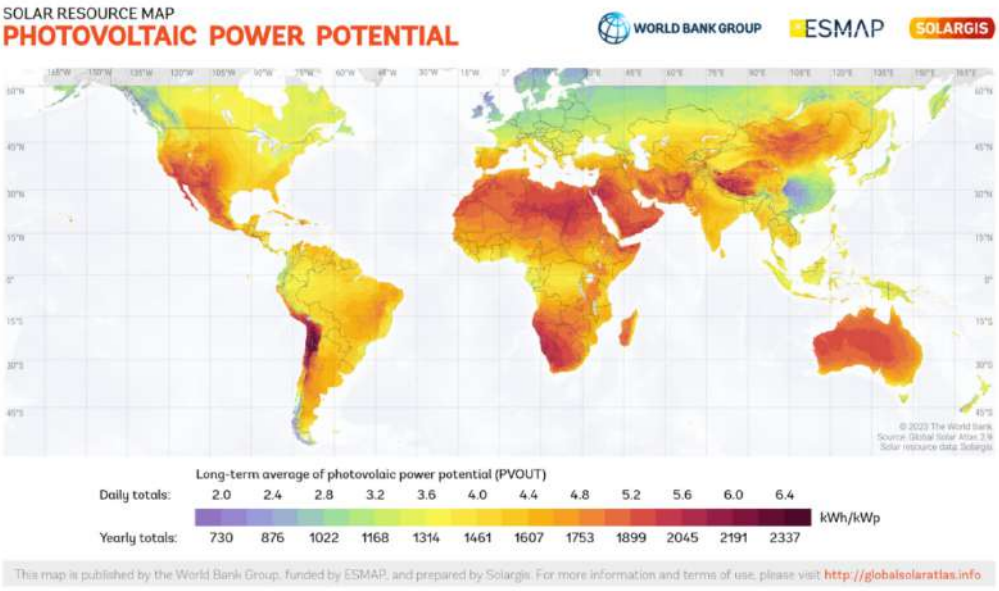

Fig. 1. Practical solar PV power potential: long-term yearly average of daily/yearly summaries [16]

Results and Discussion

PVsyst is a widely used simulation software commonly used to evaluate solar PV yield and facilitate system optimization. To give a more visual representation of St. Petersburg's photovoltaic potential in summer, we contrasted its solar radiation intensity and clear-sky probability with nine other cities, pivotal determinants of photovoltaic module power output. Meteorological data for these simulations were extracted from the global climate database, Meteonorm (www.meteonorm.com). Table 1 compares the intensity of radiation from incident light surfaces in ten cities, with the unit of measurement in kWh/mI. Table 2 compares the ten cities in terms of the weather clearness index, which is defined as clear, mostly sunny or partly cloudy (i.e., less than 60 per cent of the sky is covered by clouds). Data comparison elucidates that during summers, St. Petersburg surpasses most cities in solar radiation intensity and boasts a higher probability of clear days.

Table 1

Radiation intensity (in kwh/m^2) for light incident on surface for cities considered in the study

	SPb	HK	Mumbai	Tokyo	SG	London	Miami	Bangkok	Seoul	WH
June	165.02	158.47	112.3	129.4	135.9	145.02	186.14	139.15	101.5	155.57
July	121.79	143.66	119.8	132.13	138.67	130.21	170.05	135.11	110	144.06
August	73.36	131.14	129.2	95.74	136.07	86.76	146.64	123.48	105.7	116.19

Notations. SPb, HK, SG, WH are abbreviations for St Petersburg, Hong Kong, Singapore and Wuhan respectively.

Table 2

Clear sky probability for cities considered in the study

	SPb	HK	Mumbai	Tokyo	SG	London	Miami	Bangkok	Seoul	WH
June	53%	15%	31%	31%	8%	51%	35%	52%	52%	43%
July	56%	19%	19%	34%	9%	57%	35%	54%	47%	36%
August	51%	20%	21%	48%	9%	54%	35%	53%	52%	47%

Notations. SPb, HK, SG, WH are abbreviations for St Petersburg, Hong Kong, Singapore and Wuhan respectively.

In our study, simulations were conducted using the PVsyst software, which employs a comprehensive calculation model to estimate the photovoltaic system output based on meteorological data for the selected regions (the data presented in Tables 1 and 2 are key components of this input). The simulation was performed using a high-efficiency solar panel, the LG 450 N2W-E6, with a conversion efficiency of 20.5%, covering a total area of 40 mI. Fig. 2 compares the summer energy output of solar panels with the same area and optimized tilt angle across these cities. Clearly, during the summer, the photovoltaic potential of St. Petersburg exceeds that of the other nine cities. Fig. 3 compares their daily energy generation.

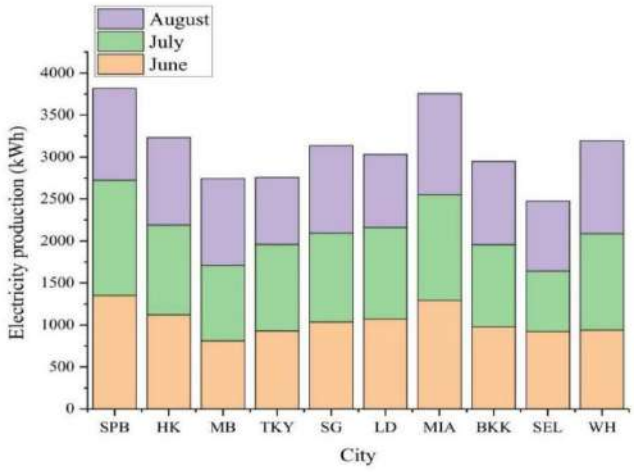

Fig. 2. Comparison of summer PV production in the cities considered in the study

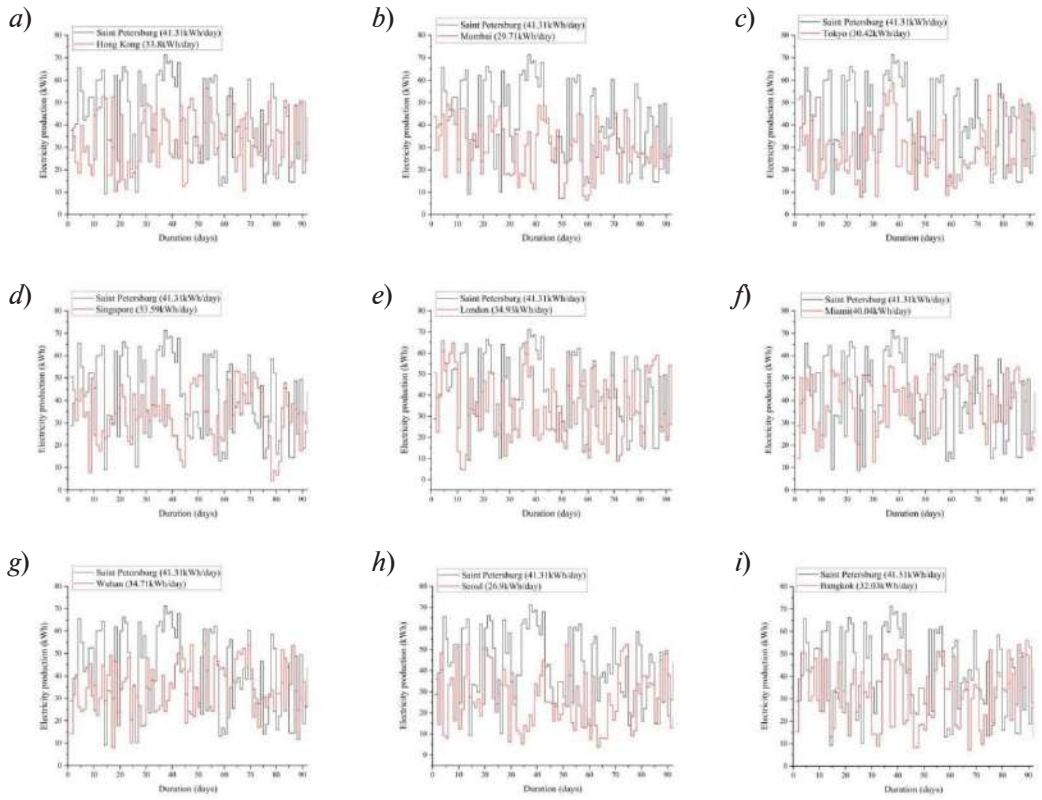

Fig. 3. Comparison of daily summer PV generation in St Petersburg and Hong Kong (*a*), Mumbai (*b*), Tokyo (*c*), Singapore (*d*), London (*e*), Miami (*f*), Wuhan (*g*), Seoul (*h*), Bangkok (*i*)

Subarctic PV modules are strongly influenced by the seasonal climate. June, July and August are the best months for generating solar PV in the Subarctic, with more than 17 hours of sunshine and clear skies making the summer PV potential of the Subarctic region greater than that of Central and partly Southern Europe, as well as regions such as East and South-East Asia, while in contrast the winter months, which are characterised by low temperatures, frosts and snow, lead to a reduction in the PV output and significant degradation rates.

Conclusion

With the increasing emphasis on solar PV development globally, the Subarctic region holds great potential for solar PV expansion. We used PVSyst to simulate a 40 mI PV module in St. Petersburg, which generated a total of 3,800 kWh of energy during the summer months, higher than in the other nine cities. Considering the unique climate of the Subarctic region, generating more solar PV energy in the summer and mitigating the negative impacts of extreme winter weather are the primary factors necessary for the development of solar energy in this region.

REFERENCES

1. **Wardal W.J., Mazur K.E., Roman K., et al.,** Assessment of Cumulative Energy Needs for Chosen Technologies of Cattle Feeding in Barns with Conventional (CFS) and Automated Feeding Systems (AFS). Energies. 14 (24) (2021) 8584.

2. **Arsent'ev N.I., Baidakova V.M., Bobyl V.A., et al.,** Structural and electrical characteristics of epitaxial InP layers on porous substrates and the parameters of related Au-Ti Schottky barriers Technical Physics Letters. 28 (2002) 735–739.

3. **Shpeizman V.V., Nikolaev V.I., Pozdnyakov A.O., et al.,** The Effect of Texturing of Silicon Wafer Surfaces for Solar Photoelectric Transducers on Their Strength Properties. Techical Physics Letters. 65 (2020) 1123–1129.

4. **Rud, V., Melebaev, D., Krasnoshchekov, V., et al.,** Photosensitivity of Nanostructured Schottky Barriers Based on GaP for Solar Energy Applications. Energies. 16 (5) (2023) 2319.

5. **Davydov V.V., Reznikov B., Dudkin V.**, New Optical System for Long Distance Control of Electrical Energy Flows. Energies. 16 (3) (2023) 1040.

6. **Sadovnikova M.A., Murzakhanov F.F., Mamin G.V., Gafurov M.R.**, HYSCORE Spectroscopy to Resolve Electron–Nuclear Structure of Vanadyl Porphyrins in Asphaltenes from the Athabasca Oil Sands In Situ Conditions, Energies. 15(17) (2022) 6204.

7. **Kashaev R.S., Kien N.C., Tung T.V., Kozelkov O.V.**, Fast Proton Magnetic Resonance Relaxometry Methods for Determining Viscosity and Concentration of Asphaltenes in Crude Oils. Journal of Applied Spectroscopy. 86 (5) (2019) 890–895.

8. **Boudjemila L., Bobyl A., Davydov V., Malyshkin V.** On a Moving Average with Internal Degrees of Freedom, Proceedings of the 2022 International Conference on Electrical Engineering and Photonics, EExPolytech. (2022) 191–194.

9. **Boudjemila L., Davydov V.V., Aleshin A.N., et al.,** Electrical characteristics of $CsPbI_3$ and $CsPbBr_3$ lead halide Pervoskvite nanocrystal films deposited on Si-c solar cells for high-efficiency photovoltaics, St. Petersburg State Polytechnical University Journal: Physics and Mathematics. 15 (3-2) (2022) 91–96.

10. IRENA Renewable Capacity Statistics URL:https://www.irena.org/,Accessed Mar 15 2021.

11. **Hoberg E.P., Galbreath K.E., Cook J.A., et al.,** Northern host-parasite assemblages. History and biogeography on the borderlands of episodic climate and environmental transition, Advances in Parasitology. (2012) 1–97.

12.UNESCO and International Geographical Union Ecology of the subarctic regions. Helsinki: symposium on ecology of subarctic regions. 1970.

13.**Janine L.M., Louwrens H., Dennis J.G.,** Harald LoengPhysical/geographical characteristics of the Arctic (1998).

14. **Vinay S., Antonio C., Eva P.**, Experiences from seasonal Arctic solar photovoltaics (PV) generation- An empirical data analysis from a research infrastructure in Northern Finland, Renewable Energy. 217 (2023)119162.

15. **Manni M., Failla, M. C., Nocente A., et al.,** The influence of icephobic nanomaterial coatings on solar cell panels at high latitudes. Solar Energy. (76 248 (2022–87.

16. 2020 The World Bank, Source: Global Solar Atlas 2.0, Solar resource data: Solargis.

THE AUTHORS

DENG Yuanbiao
dyuanbiao@gmail.com
ORCID: 0009-0000-4342-766X

DAVYDOV Vadim V.
davydov_vadim66@mail.ru
ORCID: 0000-0001-9530-4805

Received 13.09.2024. Approved after reviewing 24.08.2023. Accepted 24.08.2023.

PHYSICAL MATERIALS TECHNOLOGY

Conference materials
UDC 535.016
DOI: https://doi.org/10.18721/JPM.173.252

Surfaces modifications in functional layers for liquid crystal devices

A.S. Toikka[1,2,3]✉, N.V. Kamanina[1,2,3]

[1] St. Petersburg Electrotechnical University "LETI", St. Petersburg, Russia;

[2] Petersburg Nuclear Physics Institute, Gatchina, Russia;

[3] JSC "Research and Production Corporation S.I. Vavilova", St. Petersburg, Russia

✉ astoikka.nano@gmail.com

Abstract. In the current research, the influence of the single-walled carbon nanotubes (CNTs) on the alignment and anti-reflective properties of the indium-tin oxides (ITO) was considered. The formation of the composite thin films based on ITO with CNTs was provided by the laser-oriented deposition with the CO_2 laser. The average electrical strength during the deposition of the CNTs varied in the range of 100–600 V/cm. Morphology of the structures compared via the surface free energy (SFE) with the Owens-Wendt method. Optical properties of the ITO modifications were compared by the ellipsometry via the Lorentz model using. According to comparison, deposited CNTs provide the reduce of the polar component of SFE caused by the surface passivation and to rise of the dispersive component of SFE caused by an impact of the Van der Waals forces. Moreover, based on the refractive index comparison, CNTs lead to the decrease of the reflection losses between ITO and the liquid crystal mesophase. Thus, the transparent contacts based on ITO with CNTs could be considered as the tunable alignment and the antireflection layers of the nematic liquid crystal devices, so, the architecture of the related devices could be simplified.

Keywords: liquid crystals, alignment, indium tin oxides, carbon nanotubes, laser-oriented deposition

Funding: Graphene oxide structured thin film polarizers of visible spectrum range, RNF 24-23-00021.

Citation: Toikka A.S., Kamanina N.V., Surfaces modifications in functional layers for liquid crystal devices, St. Petersburg State Polytechnical University Journal. Physics and Mathematics. 17 (3.2) (2024) 262–265. DOI: https://doi.org/10.18721/JPM.173.252

Материалы конференции
УДК 535.016
DOI: https://doi.org/10.18721/JPM.173.252

Модификации поверхностей в функциональных слоях для жидкокристаллических устройств

А.С. Тойкка[1,2,3]✉, Н.В. Каманина[1,2,3]

[1] Санкт-Петербургский государственный электротехнический университет «ЛЭТИ» им. В.И. Ульянова (Ленина), Санкт-Петербург, Россия;

[2] Петербургский институт ядерной физики им Б.П. Константинова, г. Гатчина, Россия;

[3] АО «НПО Государственный оптический институт им. С. И. Вавилова», Санкт-Петербург, Россия

✉ astoikka.nano@gmail.com

Аннотация. В работе представлены перспективы использования тонких пленок на основе оксидов индия и олова с лазерно-осажденными одностенными углеродными нанотрубками. Исследовалось влияние напряженности электрического поля в диапазоне 100–600 В/см, используемой в процессе осаждения углеродных нанотрубок, на величину свободной поверхностной энергии и на рефрактивные свойства модификаций тонких пленок оксидов индия и олова.

Ключевые слова: жидкие кристаллы, ориентирование, оксиды индия и олова, углеродные нанотрубки, лазерно-ориентированное осаждение

Финансирование: Структурированные оксидом графена тонкопленочные поляризаторы видимого диапазона спектра, РНФ № 00021-23-24.

Ссылка при цитировании: Тойкка А.С., Каманина Н.В. Модификации поверхностей в функциональных слоях для жидкокристаллических устройств // Научно-технические ведомости СПбГПУ.Физико-математические науки. 2024. Т. 17. № 3.2. С. 262–265. DOI: https://doi.org/10.18721/JPM.173.252

Introduction

Nematic liquid crystals (NLC) are anisotropic media with the electrically tunable birefringence. Based on this aspect, the various electro-optical devices, such as modulators, phase retarders, deflectors, lenses and switchers, could be realized on the NLC structure. The one of the key characteristic of the NLC-based devices is the distribution of the liquid crystal dipoles versus the space and time. According to the Oseen-Frank theory [1] the orientation (bulk part) of NLC depends on the viscous-elastic forces and external field. According to Ericksen theory and Rapini-Papoular potential [2] the pre-tilt orientation (surface part) of NLC depends on the relationship between the polar and dispersive components of the surface free energy of the alignment layer and surface free tension of the liquid crystal mesophase. In the current paper, the surface free energy comparison of various modifications of the alignment layers based on the indium tin oxides (ITO) was considered. The refractive index, a matching phenomenon as additional function of ITO/CNTs modifications, was demonstrated as well.

Materials and Methods

In this work, it was proposed to use the transparent contacts based on the thin films of the indium tin oxides (ITO) as the orienting and anti-reflective layers. To achieve this, the single-walled carbon nanotubes (CNTs) were deposited onto the ITO surface via the laser-oriented deposition method with varying electric field strength in the range of 100–600 V/cm. The source of the ITO contained of 10 wt.% of the tin oxide and particle size was in the range of 3–12 mm (Cerac Inc.). Single-walled carbon nanotubes had chirality <7,6> with average diameter 0.83 nm (Aldrich Co.,

No. 704121). For the surface diagnostic, the wetting angle measurement and the Owens-Wendt method for the calculation of the surface free energy were used [3]. Distilled water and isopropyl alcohol were used as the testing liquids. Refractive index comparison was carried out by J.A. Woolam M-2000 ellipsometer. Lorentz model was used for the description of spectral dispersion of ITO-based thin films [4]:

$$\begin{cases} \dot{\varepsilon}(E) = \varepsilon_\infty + \sum_j \dfrac{Amp_j Br_j En_j}{En_j^2 - E^2 - iBr_j}, \\ \dot{n}(E) = \sqrt{\dot{\varepsilon}(E)} = n(E) + ik(E) \end{cases}$$

where $\dot{\varepsilon}$ and $\dot{n}$ are the complex dielectric permittivity and refractive index; *Amp* and *Br* are the amplitude and broadening of oscillator; *En* is the resonance energy; *E* is the energy (variable); *i* is the imaginary unit; *j* is the number of oscillator.

Results and Discussion

In case for the deposition of CNTs on the ITO surface, the surface free energy changes dramatically and depends on the average electric field during the deposition as shown in Table 1.

Table 1

Surface free energy of ITO modifications and orientation of 5CB liquid crystals

Surface	Surface free energy, mJ/m²		5CB contact angle, ° (initial/saturation)
	Polar	Dispersive	
ITO	8.2	22.2	39.5/38.4
ITO +CNTs (100 V/cm)	0.8	29.2	52.1/52.8
ITO+CNTs (200 V/cm)	1.3	25.0	60.1/59.0
ITO+CNTs (600 V/cm)	1.8	31.4	58.5/58.4

Based on the comparison of the polar components, it should be mentioned, that CNTs leads to the passivation of the ITO surface. The rise of the dispersive component after the CNTs deposition is a marker of an increase of the Van der Waals interactions between the modified surface and material of the liquids.

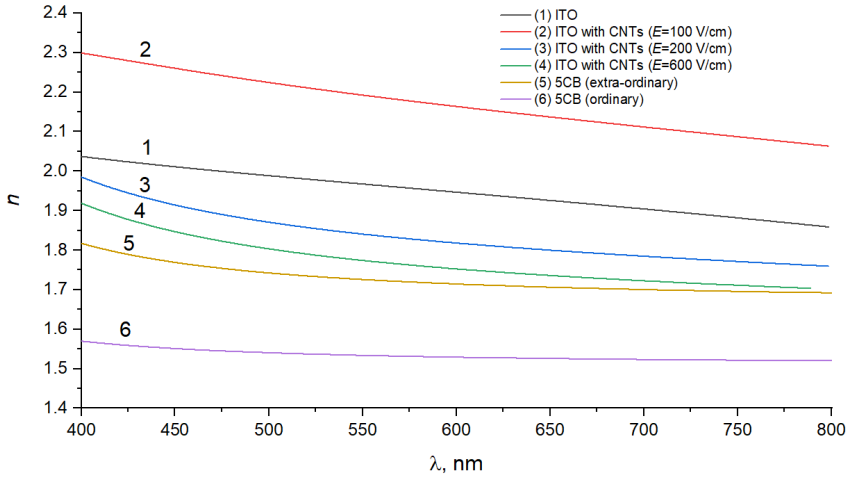

Fig. 1. Spectral dependencies of refractive index of ITO modifications (lines *1*–*5*) and 5CB liquid crystals [6] (lines *6*–*7*)

According to the ellipsometry, initial ITO thin films had the following parameters of Lorentz model: ε_∞ = 3.049, *Amp* = 3.124, *En* = 6.494 eV and *Br* = 2.112 eV. Refractive index of CNTs was fitted by data from [5]. Interface of ITO with CNTs (*E*=100 V/cm) had ε_∞ = 1.909, *Amp* = 2.530 / 3.275, *En* = 5.717 eV / 4.714 eV and *Br* = 1.709 eV / 2.857 eV. Next, with the rise of electric field during the deposition of CNTs, the optical properties of ITO-CNTs interface were caused mainly by CNTs. Lorentz parameters for *E* = 200 V/cm were ε_∞ =1.215, *Amp* = 3.232 / 3.396, *En* = 6.127 eV / 4.202 eV and *Br* = 2.672 eV / 0.576 eV. In case for *E* = 600 V/cm: ε_∞ = 1.007, *Amp* = 3.576 / 3.551, *En* = 6.301 eV / 4.239 eV and *Br* = 2.366 eV / 0.581 eV. The comparison of refractive index of ITO modifications with 5CB liquid crystals in the visible range is demonstrated below (Fig. 1).

Based on the comparison of the refractive index from Fig. 1, it should be mentioned, that $n_{ITO} > n_{ITO/CNTs} > n_{LC}$. Thus, the deposited layer of CNTs could decrease the reflection losses between ITO layer and 5CB LC media.

Conclusion

The tuning of the polar and dispersive components of the surface free energy of the ITO modifications leads to possibility to implement them as the universal (optical contact, alignment layer, antireflective coating) layers in the construction of the liquid crystal devices. The type of the alignment depends on the NLC-material. In case for the standard 5CB liquid crystals, CNTs provides the change of the alignment in the direction from the planar to homeotropic. Thus, the orientation of NLC and related parameters of the NLC-based devices could be controlled via the deposition mode of CNTs. This process can extend the area of the LC devices use with good advantage [7].

REFERENCES

1. **Frank F.C.,** Liquid crystals: On theory of liquid crystals, Discuss. Faraday Soc. 25 (1958) 19–28.

2. **Rapini A., Papoular M.,** Distorsion d'une lamelle nematique sous cham magnetique conditions d'ancrage aux parois, J.Phys. Colloques. 54 (1969) (3) 30–56.

3. **Owens D.K., Wendt R.C.,** Estimation of the surface free energy of polymers, J.Apply. Polym. Sci. 13 (8) (1969) 1741–1747.

4. Complete EASE:Data Analysis Manual (version 4.63). J.A. Wollam Co. 2011. 410 p.

5. **Ermolaev G.A., Tsapenko A.P., Volkov V.S., et al.,** Express determination of thickness and dielectric function of single-walled carbon nanotube films, Appl. Phys. Lett. 116 (231103) (2005) 1–5.

6. **Li J., Wen C.H., Gauza S., et al.,** Refractive indices of liquid crystals for display applications, J.Disp, Technol. 1 (2005) 51–61.

7. **Toikka A.S., Ilin M.E., Kamanina N.V.,** Perspective Coatings Based on Structured Conducting ITOThin Films for General Optoelectronic Applications, Coatings. 14 (178) (2024) 1–16.

THE AUTHORS

TOIKKA Andrei S.
astoikka.nano@gmail.com
ORCID: 0000-0002-8694-8497

KAMANINA Natalia V.
nvkamanina@mail.ru
ORCID: 0000-0002-2903-2685

Received 31.07.2024. Approved after reviewing 12.08.2024. Accepted 26.08.2024.

Conference materials
UDC 546.814-31
DOI: https://doi.org/10.18721/JPM.173.253

Surface properties of tin dioxide films containing 7–10% La^{3+}

I.A. Gulyaeva✉, V.V. Petrov, E.M. Bayan, G.V. Tolstyak

Southern Federal University, Taganrog, Russia

✉ tolstiak@sfedu.ru

Abstract: In this work, morphological, hydrophobic, electrophysical properties and roughness of tin dioxide films containing 7−10% La^{3+} were investigated by X-ray phase analysis, measuring the edge angle of wettability, atomic force microscopy and Kelvin-probe force microscopy. The obtained materials were thin films formed by nanocrystallites with dimensions of 23−26 nm and have a homogeneous coating with small height differences. ByX-ray phase analysis it was found that the films are composite and consist of tetragonal SnO_2 (cassiterite) and La_2O_3 phases. The dependence of the edge angle of wettability on the content of lanthanum ions, substrate material, as well as on the morphology of the surface and the magnitude of the surface charge was established. It is shown that the 10% La^{3+}−SnO_2 film on polycore has the highest hydrophobic properties. Measurements of the surface potential by Kelvin-probe microscopy showed that the average charge on the surface of the film containing 10% La^{3+} is two times lower than that of the film containing 7% La^{3+}.

Keywords: tin dioxide, lanthanum, cassiterite, hydrophobic properties

Funding: This research was carried out and financially supported by Russian Science Foundation 24-29-00203 (https://rscf.ru/project/24-29-00203/) at Southern Federal University.

Citation: Tolstyak G.V., Gulyaeva I.A., Petrov V.V., Bayan E.M., Surface and electrophysical properties of tin dioxide films containing 7−10% La^{3+}, St. Petersburg State Polytechnical University Journal. Physics and Mathematics. 17 (3.2) (2024) 266−270. DOI: https://doi.org/10.18721/JPM.173.253

Материалы конференции
УДК 546.814-31
DOI: https://doi.org/10.18721/JPM.173.253

Поверхностные свойства пленок диоксида олова, содержащих 7 – 10 % La^{3+}

И.А. Гуляева✉, В.В. Петров, Е.М. Баян, Г.В. Толстяк

Южный федеральный университет, г. Таганрог, Россия

✉ tolstiak@sfedu.ru

Аннотация. В данной работе методами рентгенофазового анализа, измерения краевого угла смачиваемости, атомной силовой и Кельвин-зондовой силовой микроскопии были исследованы поверхностные и электрофизические свойства пленок SnO_2, содержащих 7−10% La^{3+}. Полученные материалы являются наноразмерными пленками с размерами кристаллитов 23−26 нм. Установлена зависимость краевого угла смачиваемости от содержания ионов лантана.

Ключевые слова: диоксид олова, лантан, касситерит, гидрофобные свойства

Финансирование: Исследование выполнено при финансовой поддержке Российского научного фонда 00203-29-24 (https://rscf.ru/project/24-29-00203/) в Южном федеральном университете.

Ссылка при цитировании: Толстяк Г.В., Гуляева И.А., Петров В.В., Баян Е.М. Поверхностные и электрофизические свойства пленок диоксида олова, содержащих 7 – 10% La^{3+} // Научно-технические ведомости СПбГПУ.Физико-математические науки. 2024. Т. 17. № 3.2. С. 266–270. DOI: https://doi.org/10.18721/JPM.173.253

Introduction

Tin dioxide is one of the most studied and sought after materials [1]. Various additives are introduced to improve the properties of tin dioxide, among which lanthanum is considered promising (La^{3+}) [2, 3]. An important technical characteristic of semiconductors is the hydrophobicity of their surface, which prevents adsorption of water molecules [4, 5]. La^{3+} containing films are gas-sensitive to carbon dioxide, which is extremely rare for semiconducting metal oxides [3, 6]. The hydrophobic surface helps improve measurement accuracy when such materials are used as gas-sensitive gas sensor layers [7]. In this regard, it is important to investigate the surface properties of the formed materials using La^{3+}. In this work, the surface hydrophobic and electrophysical properties of tin dioxide nanocrystalline films modified with La^{3+} in the amount of 7 and 10 mol. % were investigated.

Materials and Methods

The synthesis of the investigated materials was carried out by the method of oxidative pyrolysis [8]. The starting substances used were: $La_2(CO_3)_3$, $SnCl_4 \cdot 5H_2O$, hydrochloric acid and abietinic acid. Na-Ca-glass and polycor were used as substrates. Heat treatment was performed in a muffle furnace at 600 °C in air for 2 h.

X-ray phase analysis (XRD, diffractometer ARLX'TRA, Switzerland), wetting edge angle measurement, atomic force and Kelvin-probe force microscopy (probe nanolab Ntegra, NT-MDT, Russia) were used to study the obtained materials [9]. The study of the edge angle of wettability was carried out in the lying drop mode using the ellipse approximation method with the ImageJ [10].

Results and Discussion

The results of edge angle of wettability measurements on glass, silicon and polycore substrates are presented in Table 1.

Table 1

Wetting angles of the investigated coatings

Sample	Wetting angle, °	Sample	Wetting angle, °
Pure glass	52±2	Pure polycor	77±1
SnO_2 (glass)	62±2	SnO_2 (polycor)	66±2
7%La–SnO_2 (glass)	72±1	7%La–SnO_2 (polycor)	79±1
10%La–SnO_2 (glass)	78±1	10%La–SnO_2 (polycor)	101±1
7%La–SnO_2 (silicon)	91±1	10%La–SnO_2 (silicon)	97±1

To account for the influence of the substrate material on the edge angle, measurements were also performed on clean substrates. The pure polycor surface was found to be more hydrophobic than the pure glass surface. The tendency of increasing the edge angle of wettability for all

studied substrates can be seen with increasing lanthanum content in the composition of the film material. Furthermore, on Na-Ca-glass the dependence is less pronounced than on polycore. On average, the edge angle varied by 5–6 degrees on the glass substrate and 12–13 degrees on the polycore substrate.

X-ray phase analysis was used to determine the phase composition of the synthesized films and the crystallite size, which was calculated using the Scherrer formula [11]. Peaks corresponding to the tetragonal crystallographic phase of SnO_2 (cassiterite) are present in the X-ray diffraction pattern (Fig. 1). The material with 10% La^{3+} content shows peaks corresponding to La_2O_3. The average crystallite size is 24 and 26 nm for compositions containing 7%, 10% La^{3+}.

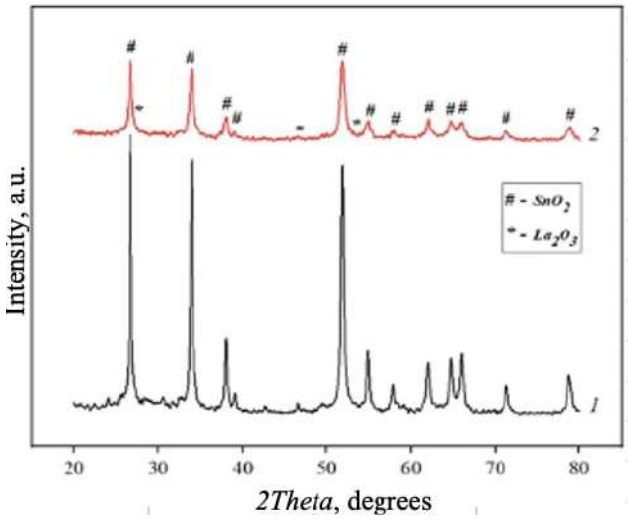

Fig. 1. X-ray diffraction patterns of samples containing 7% (*2*) and 10% (*1*) La^{3+}

The surface morphology of the films was investigated by atomic force microscopy (Fig. 2).

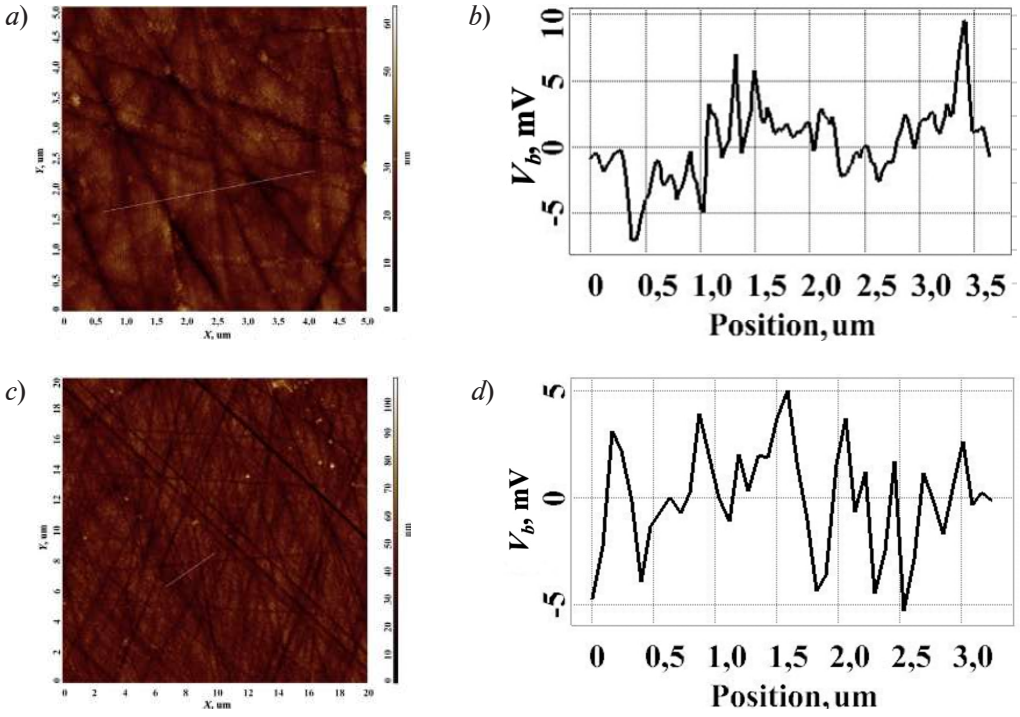

Fig. 2. Surface morphology (*a, c*) and surface potential distribution (*b, d*) for films with 7 (*a, b*) and 10 % (*c*, *d*) La^{3+}

Measurements were taken at five different points and then the values were averaged. The average value of height difference for the film with 7% La^{3+} was 67.6 nm. The sample containing 10% La^{3+} has a more developed morphology with a height difference of up to 97.6 nm. Measurements of the surface potential by Kelvin-probe microscopy showed the opposite: the average charge on the Vb surface, equal to 22.7 mV, has a film with 7% La^{3+} content, which is almost twice as high as that of a film with 10% La^{3+} content, equal to 11.9 mV.

It can be seen that the SnO_2 film containing 10% La^{3+} is more hydrophobic than the film containing 7% La^{3+}. This may be due to the more developed surface morphology and lower surface charge value.

Conclusion

Thin nanocrystalline films of tin dioxide containing 7% and 10% La^{3+} were obtained, the crystallite sizes were 24 and 26 nm, respectively. It was found that the edge angle of wettability increased with increasing La^{3+} content. The film on polycore with 10% La^{3+} content became hydrophobic. This may be due to more developed surface morphology and lower surface charge value, which is confirmed by atomic force microscopy results.

REFERENCES

1. **Batzill M., Diebold U.**, The surface and materials science of tin oxide, Progress in surface science. 79 (2–4) (2005) 47–154.

2. **Zhang Y., Chang B., Yang Q., et al.,** A sensitive electrochemical sensor based on La-SnO_2NF/CNTs modified glass carbon electrode for bisphenol A detection, Materials Letters. 327 (2022) 133005

3. **Andreev M., Platonov V., Filatova D., et al.,** Flame-Made La_2O_3-Based Nanocomposite CO_2Sensors as Perspective Part of GHGMonitoring System, Sensors. 21 (21) (2021) 7297.

4. **Su-Shia L., Sheng-You F., Yung-Shiang T.,** Effects of annealing on wettability and physical properties of SnO thin films deposited at low RF power densities, Ceramics International. 2 (43) (2017) 1802–1808.

5. **Tsai H.Y., Hsu C.N., Li C.R., et al.,** Surface wettability and electrical resistance analysis of droplets on indium-tin-oxide glass fabricated using an ultraviolet laser system, Micromachines. 12 (1) (2021) 44.

6. **Abdelkarem Kh., Saad R., ElSayed A.M., et al.,** Design of high-sensitivity La-doped ZnO sensors for CO_2 gas detection at room temperature, Scientific Reports. 13 (2023) 18398.

7. **An D., Dai J., Wang Y., et al.,** La/SnO_2 nanoparticles: hydrothermal synthesis, structure, and sensing performance in a high relative humidity environment, Ceramics International. 50 (14) (2024) 26250–26260.

8. **Petrov V.V., Ivanishcheva A.P., Volkova M.G., et al.,** High gas sensitivity to nitrogen dioxide of nanocomposite ZnO–SnO_2 films activated by a surface electric field, Nanomaterials. 12 (12) (2022) 2025.

9. **Petrov V.V., Ignatieva I.O., Volkova M.G., et al.,** Polycrystalline Transparent Al-Doped ZnO Thin Films for Photosensitivity and Optoelectronic Applications, Nanomaterials. 13 (2023) 2348.

10. **Kolodin A.N., Sulyaeva V.S., Popovetskii P.S.,** Studies of the Roughness of Films Based on Organosols of Silver Nanoparticles by Determining Contact Angles, Protection of Metals and Physical Chemistry of Surfaces. 56 (6) (2020) 616–624.

11. **Dorofeev G.A., Streletsky A.N., Povstugar I.V., et al.,** Determination of nanoparticle sizes by X-ray diffraction methods, Colloid Journal. 74 (6) (2012) 675–685.

THE AUTHORS

TOLSTYAK Gleb V.
tolstiak@sfedu.ru
ORCID: 0009-0004-9531-026X

PETROV Victor V.
vvpetrov@sfedu.ru
ORCID: 0000-0003-3725-6053

GULYAEVA Irina A.
iten@sfedu.ru
ORCID: 0000-0001-9364-1007

BAYAN Ekaterina M.
ekbayan@sfedu.ru
ORCID: 0000-0002-8445-9139

Received 23.07.2024. Approved after reviewing 12.08.2024. Accepted 12.08.2024.

Conference materials
UDC 621.355.9
DOI: https://doi.org/10.18721/JPM.173.254

Silicon/graphite nanocomposite for lithium-ion battery anode

Sh.Sh. Isokjanov✉, E.V. Mazin, V.V. Krivetskiy

Moscow Institute of Physics and Technology (National Research University), Dolgoprudny, Russia

✉ Isakjanov2997@gmail.com

Abstract. One of the most promising areas of battery improvement is the use of silicon in anodes. It has emerged as a promising candidate for next-generation lithium-ion batteries (LIBs) due to its tenfold higher capacity compared to traditional graphite anodes (4200 mAh·g^{-1} vs. 372 mAh·g^{-1}). However, the practical application of silicon in LIBs is hindered by several challenges, including rapid capacity fading, unstable cycling behavior, and significant volume expansion during lithium insertion/extraction. This work presents a novel approach for fabricating high-performance LIBs with silicon-based anodes and metallic lithium counter electrodes in a compact "Cell-coin 2032" form factor. The silicon-containing anode material was synthesized via the thermal decomposition of SiH4 in a gas phase followed by deposition onto a carbon matrix. A doctor blade technique was employed to deposit the composite onto a copper foil current collector. Laser engraving was utilized to define the electrode topology. The developed technology enables the production of compact, planar LIBs suitable for a wide range of electronics applications.

Keywords: Lithium-ion batteries, silicon-carbon anodes, composite electrodes, laser engraving, doctor blade technique, coin-type cells, solid electrolyte interphase (SEI)

Citation: Isokjanov Sh.Sh., Mazin E.V., Krivetskiy V.V., Silicon/graphite nanocomposite for lithium-ion battery anode, St. Petersburg State Polytechnical University Journal. Physics and Mathematics. 17 (3.2) (2024) 271–274. DOI: https://doi.org/10.18721/JPM.173.254

Материалы конференции
УДК 621.355.9
DOI: https://doi.org/10.18721/JPM.173.254

Кремний/графитовый нанокомпозит для анода литий-ионных аккумуляторов

Ш.Ш. Исокжанов✉, Е.В. Мазин, В.В. Кривецкий

Московский физико-технический институт (Национальный исследовательский университет, г. Долгопрудный, Россия;

✉ Isakjanov2997@gmail.com

Аннотация. Одним из наиболее перспективных направлений улучшения батарей является использование кремния в анодах, что позволяет достичь емкости в десять раз выше по сравнению с традиционными графитовыми анодами (4200 мАч·г$^{-1}$ против 372 мАч·г$^{-1}$). Однако практическое применение кремния в литий-ионных аккумуляторах затруднено из-за быстрого снижения емкости, нестабильного цикла заряда-разряда и значительного увеличения объема при интеркаляции-деинтеркаляции лития. В данной работе представлен новый подход к созданию кремнийсодержащих анодов для литий-ионных аккумуляторов и их тестирования в ячейках с металлическими литиевыми контрэлектродами в компактном формфакторе «Cell-coin 2032». Синтез материала анода, содержащего кремний, проводился путем термического разложения SiH_4 в газовой фазе с последующим осаждением на углеродную матрицу. Разработанная технология позволяет производить литий-ионные аккумуляторы, подходящие для широкого спектра применений в электротехнике.

Ключевые слова: Литий-ионные аккумуляторы, кремниево-графитовые аноды, композитные электроды, лазерная гравировка, техника ракельного нанесения, ячейки типа «таблетка», межфазная граница электролит – твердое тело (SEI)

Ссылка при цитировании: Исокжанов Ш.Ш., Мазин Е.В., Кривецкий В.В. Кремний/графитовый нанокомпозит для анода литий-ионных аккумуляторов // Научно-технические ведомости СПбГПУ.Физико-математические науки. 2024. Т. 17. № 3.2. С. 271–274. DOI: https://doi.org/10.18721/JPM.173.254

Introduction

The ever-increasing demand for high-performance energy storage solutions necessitates the development of next-generation lithium-ion batteries (LIBs) with improved energy density [1]. While graphite has served as the dominant anode material in commercial LIBs, its limited theoretical capacity (372 $mAh \cdot g^{-1}$) restricts further advancements. In recent years, significant progress has been made in the development of silicon-based anodes for lithium-ion batteries [2, 3]. Due to their advantages, such as high energy density and theoretical capacity(4200 $mAh \cdot g^{-1}$), low working potential, high abundance, and low cost, rechargeable lithium-ion batteries with silicon anodes have attracted considerable interest. However, the significant volume change experienced by Si during lithium insertion (~300%) leads to mechanical stress, cycle instability, pulverization of the electrode, and a rapid decrease in capacity [4]. Since this is a key factor in the design of batteries, it significantly affects the consumption of active components and the weight of the assembled battery [2]. Recent research has shown that a series of chemical modifications (binding agents, composite materials, and electrolytes) improve electrochemical performance and provide greater stability for silicon-based anodes in lithium-ion batteries [5].

An important area of research is the development of innovative strategies to optimize the electrochemical performance of silicon-based anodes through structural engineering. This includes the synthesis of Si/C composites, the development of multidimensional nanostructures, and the application of non-carbon coatings. The formation of a stable solid electrolyte interface (SEI) is crucial for preventing electrolyte decomposition and improving Li+ transport, thereby stabilizing the Si anode interface and enhancing Coulombic efficiency [3].

This article will delve into recent progress in overcoming these challenges and realizing the potential of Si-based anodes for LIBs.

Materials and Methods

The silicon-carbon composite material (Si/C) was synthesized through the high-temperature thermal decomposition of SiH_4 gas. This process took place in a high-pressure reactor with SHF (super high frequency), where SiH_4 gas was introduced and decomposed at elevated temperatures. The synthesis parameters, such as temperature, pressure, and gas flow rates, were meticulously controlled to ensure the uniformity and quality of the Si/C composite. This composite was subsequently used as the primary anode material for the lithium-ion batteries.

The functional layer of the anode consisted of a synthesized composite Si/C and electrically conductive carbon black Super C65. Carboxymethylcellulose (CMC) and styrene-butadiene rubber (SBR) were used as the binding component. The composition of the functional layer and the ratio of Si/C composite to Super C65, CMC and SBR were optimized to ensure good electronic conductivity, mechanical integrity and adhesion to the copper foil current collector (Table 1).

A water-based suspension paste was prepared by mixing the Si/C composite, Super C65, CMC and SBR in deionized water. The mixture was homogenized using a high-shear mixer to achieve a uniform dispersion of the components. The resulting slurry was then coated onto copper foils using the doctor blade technique. The coating thickness was controlled by adjusting the blade height to achieve a uniform and consistent electrode layer. The coated samples were dried in a vacuum oven at 90°C for 12 hours to remove residual moisture and enhance adhesion.

Table

#	Reagent name	Reagent ratio	Quantity
1	Si/C composite	95%	190 g
2	Super C65	1%	2 g
3	Carboxymethylcellulose	1%	2 g
4	Styrene-butadiene rubber (50% aqua)	3%	12 g
5	Deionized water		180 ml

Material characterization was conducted to analyze the structural and morphological properties of the Si/C composite. Techniques such as scanning electron microscopy (SEM), transmission electron microscopy (TEM) were used, which made it possible to obtain images of the composite's morphology and particle size distribution (Fig. 1).

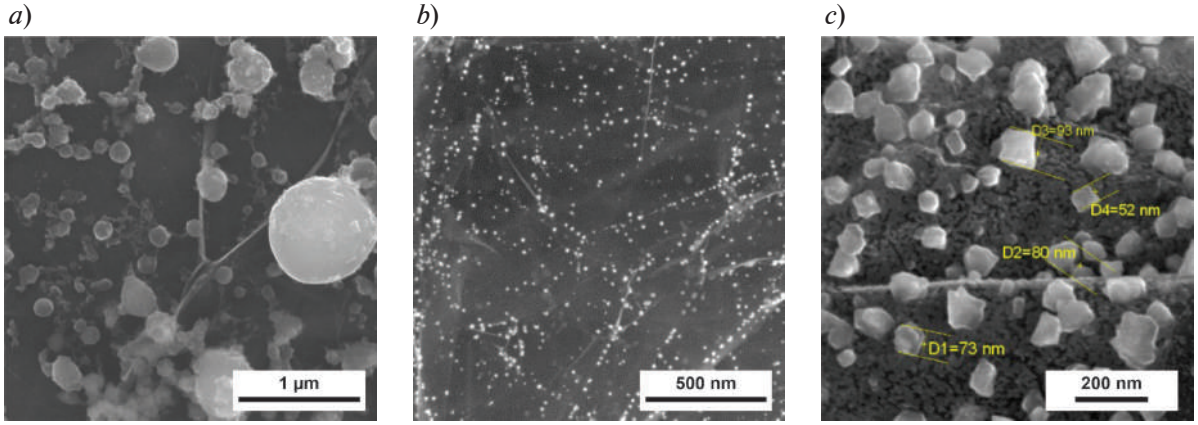

Fig. 1. SEM images of silicon/carbon composite

To define the electrode topology, laser engraving was employed, which ensured high precision and reproducibility.

The "Cell-coin 2032" coin-type batteries were assembled in an argon-filled glovebox to prevent contamination from moisture and oxygen. The assembly process involved stacking the Si/C composite anode, a separator, and a metallic lithium counter electrode. A standard commercial electrolyte solution, 1M $LiPF_6$ in EC (ethylene carbonate) and EMC (ethyl methyl carbonate) (1:3) with 1% VC (vinylene carbonate), was used to enhance the electrochemical performance and stability of the batteries. The components were hermetically sealed inside the coin cell casing to ensure electrical insulation and structural integrity.

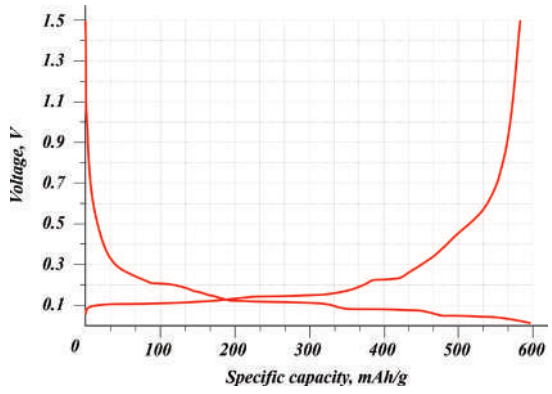

Fig. 2. Cyclic scanning of tablet-type battery samples at 0.05C

Results and Discussion

Three samples were fabricated and investigated following the described methodology. The battery capacity measurements were performed using a Neware battery analyzer with its proprietary software "BTS Client 8.0.0.512". Cyclic voltammetry was conducted within the potential range of 0.01–1.5 V at a current rate of 0.05C for 5 cycles. To visualize the cycling behavior of the samples, graphs were constructed (Fig. 2).

The experimental specific capacity of the batteries ranged from 589 to 609 mAh/g, which exceeds the theoretical capacity of 450 mAh/g and is almost twice the capacity of commercial coin cell counterparts with a graphite-based anode.

The obtained results demonstrate the potential of Si/C composites as a promising anode material for lithium-ion batteries.

Conclusion

The successful fabrication of silicon-based composite anodes using the thermal decomposition of SiH_4 in a gas phase represents a significant step towards the development of high-performance LIBs with extended cycle life and improved energy density. Further research will focus on optimizing the fabrication process, investigating different electrolyte systems, and evaluating the long-term performance of these advanced batteries.

Further research efforts are necessary to fully unlock the potential of Si/C composite anodes for practical applications. Specifically, optimization of synthesis and fabrication processes is crucial to enhance scalability and cost-effectiveness for mass production. Additionally, a deeper understanding of the interplay between material properties (e.g., Si content, carbon matrix structure) and their influence on the electrochemical performance of the Si/C composite is essential. Finally, integrating these advanced anodes with compatible cathode materials and electrolytes will enable the development of high-performance full LIB cells.

By overcoming these remaining challenges, Si/C composite anodes hold great promise for revolutionizing lithium-ion battery technology and paving the way for next-generation high-energy portable and stationary energy storage devices.

REFERENCES

1. **Kiehbadroudinezhad M., Merabet A., Hosseinzadeh-Bandbafha H.,** Review of Latest Advances and Prospects of Energy Storage Systems: Considering Economic, Reliability, Sizing, and Environmental Impacts Approach. Clean Technologies. 4 (2022) 477–501.

2. **Zhao H., Li J., Zhao Q., et al.,** Si-Based Anodes: Advances and Challenges in Li-Ion Batteries for Enhanced Stability. Electrochem. Energy Rev. 7 (11) (2024).

3. **Khan M., Yan S., Ali M., et al.,** Innovative Solutions for High-Performance Silicon Anodes in Lithium-Ion Batteries: Overcoming Challenges and Real-World Applications. Nano-Micro Lett. 16 (179) (2024).

4. **Hu M., Wu H., Zhang G.,** High-performance silicon/graphite anode prepared by CVD using SiCl4 as precursor for Li-ion batteries, Chemical Physics Letters. (833) (2023) 140917.

5. **Toki G.F.I., Hossain M., Rehman W., et al.,** Recent progress and challenges in silicon-based anode materials for lithium-ion batteries. Industrial Chemistry & Materials. 2 (2024) 226–269.

THE AUTHORS

ISOKJANOV Shakhboz Sh.
isakjanov2997@gmail.com
ORCID: 0000-0001-6009-9039

KRIVETSKIY Valeriy V.
krivetskii.vv@mipt.ru
ORCID: 0000-0002-2247-9388

MAZIN Eugeniy V.
mazin.ev@mipt.ru
ORCID: 0000-0003-3135-2634

Received 28.07.2024. Approved after reviewing 12.08.2024. Accepted 07.10.2024.

Conference materials
UDC 621.315.592
DOI: https://doi.org/10.18721/JPM.173.255

Study of GaPN(As) layers grown by molecular beam epitaxy on silicon substrates

E.V. Nikitina [1,2], K.Yu. Shubina [1]✉, M.S. Sobolev [1], E.V. Pirogov [1]

[1] Alferov University, St. Petersburg, Russia;

[2] Ioffe Institute, St. Petersburg, Russia

✉ kshubina@spbau.ru

Abstract. In this work bulk layers of GaPN(As) solid solutions grown by plasma assisted molecular beam epitaxy on gallium phosphide and silicon substrates are studied. The morphology, structural and optical properties of diluted nitride epilayers synthesized on GaP and Si are compared. The possibility of obtaining GaPN(As) epitaxial layers of optical quality on lattice-mismatched silicon substrates is demonstrated.

Keywords: dilute nitride semiconductors, molecular beam epitaxy, silicon, gallium phosphide

Funding: This study was funded by RSCF (grant no. 23-79-00032).

Citation: Nikitina E.V., Shubina K.Yu., Sobolev M.S., Pirogov E.V., Study of GaPN(As) layers grown by molecular beam epitaxy on silicon substrates, St. Petersburg State Polytechnical University Journal. Physics and Mathematics. 17 (3.2) (2024) 275–278. DOI: https://doi.org/10.18721/JPM.173.255

Материалы конференции
УДК 621.315.592
DOI: https://doi.org/10.18721/JPM.173.255

Исследование слоев GaPN(As), выращенных методом молекулярно-пучковой эпитаксии на кремниевых подложках

Е.В. Никитина[1, 2], К.Ю. Шубина[1]✉, М.С. Соболев[1], Е.В. Пирогов[1]

[1] Академический университет им. Ж.И. Алфёрова РАН, Санкт-Петербург, Россия;

[2] Физико-технический институт им. А.Ф. Иоффе РАН, Санкт-Петербург, Россия

✉ kshubina@spbau.ru

Аннотация. В работе исследованы объемные слои твердых растворов GaPN(As), выращенные методом молекулярно-пучковой эпитаксии на подложках фосфида галлия и кремния. Проведено сравнение морфологии, структурных и оптических свойств синтезированных эпитаксиальных слоев разбавленных нитридов. Показана возможность получения эпитаксиальных слоев GaPN(As) оптического качества на решеточно-рассогласованных кремниевых подложках.

Ключевые слова: разбавленные нитриды, молекулярно-пучковая эпитаксия, кремний, фосфид галлия

Финансирование: Работа выполнена в рамках проекта РНФ (№ 23-79-00032).

Ссылка при цитировании: Никитина Е.В., Шубина К.Ю., Соболев М.С., Пирогов Е.В. Исследование слоев GaPN(As), выращенных методом молекулярно-пучковой эпитаксии на кремниевых подложках // Научно-технические ведомости СПбГПУ.Физико-математические науки. 2023. Т. 17. № 3. С. 275–278. DOI: https://doi.org/10.18721/JPM.173.255

Introduction

Solid solutions of materials containing a small mole fraction of nitrogen, the so-called dilute nitrides, are difficult to theoretically describe and experimentally grow, but are of great interest for many optoelectronic applications. It is known, that the addition of nitrogen to GaP makes this ternary solution GaPN direct gap and, with a nitrogen mole fraction of about three percent, makes it lattice matched with silicon [1]. Moreover, by varying the composition of a quaternary solution of GaPNAs, it is possible to obtain a semiconductor material with the bandgap range from 1.5 to 2.0 eV which is also lattice-matched with silicon [2, 3]. Thus, dilute nitride semiconductor compounds have a potentially wide application range, especially for integration with silicon in optoelectronic integrated circuits, and also as top cascades in multijunction solar cells on silicon substrates [4, 5].

Unfortunately, the epitaxial growth of dilute nitrides directly on the silicon substrates is impossible. Therefore, it is necessary to use the buffer layers. Unfortunately, there are unsolved problems such as high point defect density, connected with the nitrogen incorporation, Ga and Si interdiffusion on the GaP/Si interface, and high surface roughness. Here we report the results of the dilute nitrides growth experiments.

Materials and Methods

In this study heterostructures with bulk GaPN and GaPNAs layers were grown by plasma assisted molecular beam epitaxy on GaP(100) substrates and on Si(100) substrates misoriented in the [110] direction by 4°. The morphology of the obtained heterostructures was characterized using a Supra 25 Zeiss scanning electron microscope (SEM). Structural properties of the samples were studied by X-ray diffraction analysis (XRD) using a high-resolution X-ray diffractometer DRON-8, the anode material was Cu-Kα1 (λ = 1.5405 Å). The optical properties of the resulting heterostructures were studied by photoluminescence (PL) spectroscopy.

Results and Discussion

Samples with a GaPN epilayer on Si and GaP substrates were obtained using the same growth parameters. The growth of the GaPN layer on the GaP(100) occurs in a homogeneous and dislocation-free manner, as it can be seen from Fig. 1, *a*. At the same time, the GaPN epilayer,

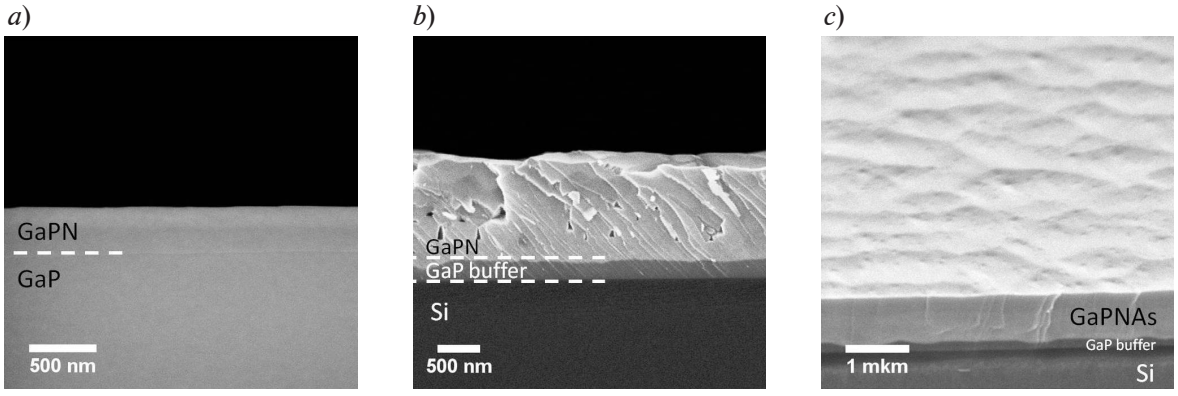

Fig. 1. SEM images of GaPN/GaP structure (*a*), GaPN (*b*) and GaPNAs (*c*) epitaxial layers on Si substrate with GaP buffer

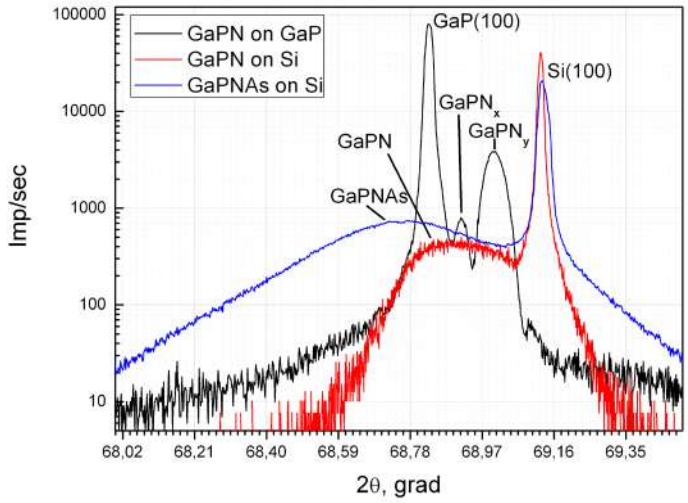

Fig 2. XRD curves of the grown samples

grown on a Si substrate with a GaP buffer layer, demonstrates the formation of a porous structure associated with stress relaxation in the GaPN layer (Fig. 1, *b*). The addition of As to the GaPN and epitaxial growth of a GaPNAs quaternary solid solution on a Si substrate with a GaP buffer layer demonstrates an improvement in the morphology of the epilayer (Fig. 1, *c*).

The XRD curves of the samples are shown in Fig. 2. Despite the fact that samples with a GaPN epilayers on Si and GaP substrates (black and red line respectively) were obtained using the same growth parameters, the corresponding XRD reflexes do not match. This can be connected with the mechanical stress difference in epilayers due to the difference in the lattice constants of the substrates. Moreover, a sample grown on a GaP substrate (black line) shows two peaks from the GaPN layer, which may arise due to the decomposition of the material into two solid solutions with different nitrogen content. The XRD reflex from the GaPN layer grown on a Si substrate (red) is wider, which indicates that the composition of the solid solution has a different nitrogen content. The addition of As leads to a greater broadening of the reflex from the GaPNAs layer (blue) indicating a gradual composition change in a solid quaternary solution.

The photoluminescence spectra of the samples are presented in Fig. 3. First of all, it is clearly seen that the synthesized dilute nitride materials GaPN and GaPNAs are direct gap semiconductors. The peak PL intensity of the GaPN layers grown on GaP and silicon substrates are comparable.

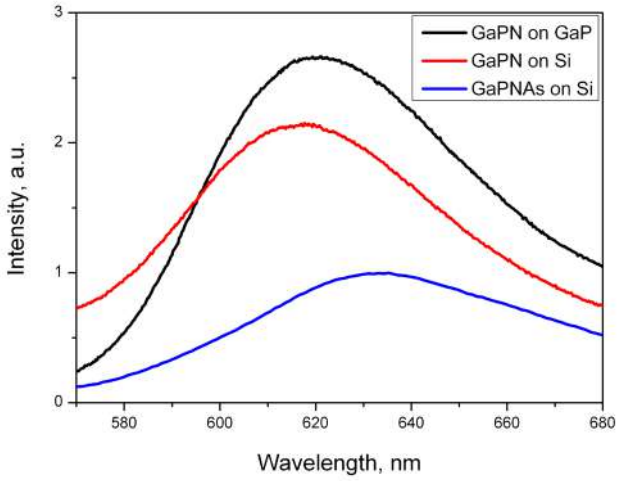

Fig 3. PL spectra of the obtained samples

Moreover, as it can be seen from PL spectra, the porous structure of the GaPN grown on Si (red line) does not affect the optical characteristics of the layer. It means that GaPN layer grown on Si substrate has good crystalline quality. One can note a slight shift in the peak position from sample to sample. This connected with the large defect density in the GaPN layer grown on a Si substrate (it is clearly seen from SEM Fig. 1, *b*), as well as the difference in the lattice constants of the used substrates and different type of mechanical stresses consequently. The addition of As to the GaPN layer leads to a decrease in the band gap of solid solution and a shift of the photoluminescence spectrum to longer wavelengths.

Conclusion

In this work GaPN and GaPNAs epitaxial layers were synthesized on GaP(100) and misoriented Si(100) substrates by plasma assisted molecular beam epitaxy and their morphology, structural and optical properties were studied. It is shown that the epitaxial synthesis using the same growth parameters of GaPN on GaP substrate and on Si substrate with GaP buffer layer can lead to different morphology and structural properties of dilute nitride layer. The improvement of the morphology of GaPNAs dilute nitride layer with addition of As compared to GaPN grown on Si substrates is demonstrated. A comparable PL peak intensity of the GaPN layers grown on GaP and Si substrates is observed. The possibility of growth of the optical quality dilute nitride epitaxial layers nearly lattice-matched with Si(100) is shown.

REFERENCES

1. **Furukawa Y., Yonezu H., Morisaki Y., et al.,** Monolithic implementation of elemental devices for optoelectronic integrated circuit in lattice-matched Si/III–V–N alloy layers, Japanese Journal of Applied Physics. 45 (2006) L920–L922.

2. **Geisz J.F., Friedman D.J.**, III–N–V semiconductors for solar photovoltaic applications, Semiconductor Science and Technology. 17 (2002) 769–777.

3. **Kudrawiec R.**, Parameterization of the band gap energy for $GaN_xAs_{1-x-z}Pz$ alloys, Journal of Applied Physics. 101 (11) (2007) 116101.

4**. Sukrittanon S., Liu R., RoY. G., et al.,** Enhanced conversion efficiency in wide-bandgap GaNP solar cells, Applied Physics Letters. 107 (2015) 153901-1–5.

5**. Zhang X., Liu L., Chi F., et al.,** Theoretical investigation of lattice-matched III-N-V/Si double-junction solar cells, Journal of Physics D: Applied Physics. 55 (2022) 475104.

THE AUTHORS

NIKITINA Ekaterina V.
mail.nikitina@mail.ru
ORCID: 0000-0002-6800-9218

SOBOLEV Maxim S.
sobolevsms@gmail.com
ORCID: 0000-0001-8629-2064

SHUBINA Kseniia Yu.
kshubina@spbau.ru
ORCID: 0000-0003-1835-1629

PIROGOV Evgeny V.
zzzavr@gmail.com
ORCID: 0000-0001-7186-3768

Received 29.07.2024. Approved after reviewing 05.08.2024. Accepted 06.08.2024.

Conference materials
UDC 532.61.08
DOI: https://doi.org/10.18721/JPM.173.256

Effect of surfactants on surface tension of PEDOT:PSS aqueous solution

V.A. Pozdeev[1,2]✉, A.V. Uvarov[1], A.S. Gudovskikh[1,2], A.O. Monastyrenko[1]

[1] Alferov University, St. Petersburg, Russia;

[2] St. Petersburg Electrotechnical University "LETI", St. Petersburg, Russia

✉ pozdeev99va@gmail.com

Abstract. This article examines the effect of surfactant content on the surface tension of a PEDOT:PSS solution to determine the possibility of coating substrates with different values of critical surface tension. One of the disadvantages of applying PEDOT:PSS coatings from an aqueous solution (e.g. spin-coating) is that water has a relatively high surface tension, which leads to poor wettability of substrates with a low critical surface tension.

Keywords: PEDOT:PSS, surface tension, conductive polymer, surfactants, Triton X-100

Funding: This work was supported by the Russian Science Foundation under grant number (no. 23-22-00367) https://rscf.ru/project/23-22-00367/.

Citation: Pozdeev V.A., Uvarov A.V., Gudovskikh A.S., Monastyrenko A.O., Effect of surfactants on surface tension of PEDOT:PSS aqueous solution, St. Petersburg State Polytechnical University Journal. Physics and Mathematics. 17 (3.2) (2024) 279–282. DOI: https://doi.org/10.18721/JPM.173.256

Материалы конференции
УДК 532.61.08
DOI: https://doi.org/10.18721/JPM.173.256

Влияние поверхностно-активных веществ на поверхностное натяжение водного раствора PEDOT:PSS

В.А. Поздеев[1,2]✉, А.В. Уваров[1], А.С. Гудовских[1,2], А.О. Монастыренко[1,2]

[1] Академический университет им. Ж.И. Алфёрова РАН, Санкт-Петербург, Россия;

[2] Санкт-Петербургский государственный электротехнический университет «ЛЭТИ» им. В.И. Ульянова (Ленина), Санкт-Петербург, Россия

✉ pozdeev99va@gmail.com

Аннотация. В данной статье исследуется влияние содержания ПАВ на поверхностное натяжение раствора PEDOT:PSS для определения возможности нанесения покрытий на поверхности подложек с разными значениями критического поверхностного натяжения. Одним из недостатков нанесения покрытий PEDOT:PSS из водного раствора (например, центрифугированием) является то, что вода обладает относительно высоким поверхностным натяжением, что приводит к плохой смачиваемости подложек с низким критическим поверхностным натяжением.

Ключевые слова: PEDOT:PSS, поверхностное натяжение, электропроводящие полимеры, поверхностно-активные вещества, Triton X-100

Финансирование: Работа выполнена в рамках проекта Российского Научного Фонда «Гибкие солнечные элементы на основе массива кремниевых волокон в полимерной матрице» №23–22–00367 (https://rscf.ru/project/23-22-00367/).

Ссылка при цитировании: Поздеев В.А., Уваров А.В., Гудовских А.С., Монастыренко А.О. Влияние поверхностно-активных веществ на поверхностное натяжение водного раствора PEDOT:PSS // Научно-технические ведомости СПбГПУ. Физико-математические науки. 2024. Т. 17. № 3.2. С. 279–282. DOI: https://doi.org/10.18721/JPM.173.256

Introduction

Polymer solutions have a slightly lower surface tension than water [1], but it is not enough for complete wetting, e.g. polyethylene terephthalate (PET). Surfactants are traditionally used for effectively reducing surface tension. However, the high content of surfactants has a negative impact on the electrophysical properties of PEDOT:PSS [2]. To determine the surface tension of a liquid at which complete wetting of a specific substrate occurs (critical surface tension), one can use the Zisman plots at zero contact angle [3]. By measuring the surface tension of PEDOT:PSS solutions, the required surfactant concentration can be determined to achieve the desired solution surface tension and complete wetting of the substrate. This will avoid excessive addition of surfactants, as well as significantly reduce the waste of material when determining the appropriate concentration. There are numerous studies where PEDOT:PSS is deposited onto silicon surfaces from aqueous solutions without the addition of surfactants. Our observations indicate that when applying the PEDOT:PSS film from the original solution using spin-coating, a dewetting effect occurs. Over time, the solution begins to gather from the liquid film into separate droplets, accompanied by a gradual decrease in the coating thickness over most of the sample and a significant increase in thickness at the droplet locations.

Materials and Methods

Contact angles (θ) were determined using a photographic method based on the width and height of the drop. For drops with volumes up to 1 μL, the influence of gravity on the drop shape can be neglected, allowing us to consider the drop as a segment of a sphere [4]. When determining the values of contact angles, the consideration of evaporation, drop spreading, and absorption of water vapor from the environment was achieved by extrapolating the kinetic curve onto the time axis. Linear extrapolation was performed using the least squares (MLS) method. The obtained contact angle value can be considered to correspond to the equilibrium contact angle [4]. The measurements were taken at a fixed humidity (33–34% R.H.) and close to room temperature (22–23 °C). Humidity control was maintained using a saturated solution of calcium chloride, as detailed in the method presented in this paper[5].To determine the surface tension, two test substrates made of PET and paraffin were utilized. Deionized water (γ_{lv} = 72.8 mJ/m^2), glycerol (γ_{lv} = 63.4 mJ/m^2) and dimethyl sulfoxide(γ_{lv} = 44 mJ/m^2) were employed to assess the surface energy of the substrates. The study employed 3.4% PEDOT:PSS (produced by Sigma Aldrich) with a PEDOT:PSS ratio of 1:2.5. Different volumetric fractions of Triton X-100 (produced by Sigma Aldrich) were added to the aqueous PEDOT:PSS solution, while maintaining a constant volumetric fraction of the original PEDOT:PSS solution (95%).The surface tension (γ_{lv}), particularly its polar (γ_{lv}^p) and dispersive (γ_{lv}^d) components, was determined using formulas derived from the Owens-Wendt [6] method:

$$\gamma_{lv} = 1/\left(A^2 + B^2\right), \tag{1}$$

$$B = \begin{vmatrix} \left(\frac{1+\cos\theta}{2}\right)_1 & \sqrt{\left(\gamma_{sv}^p\right)_1} \\ \left(\frac{1+\cos\theta}{2}\right)_2 & \sqrt{\left(\gamma_{sv}^p\right)_2} \end{vmatrix}^2 \Bigg/ \begin{vmatrix} \sqrt{\left(\gamma_{sv}^d\right)_1} & \sqrt{\left(\gamma_{sv}^p\right)_1} \\ \sqrt{\left(\gamma_{sv}^d\right)_2} & \sqrt{\left(\gamma_{sv}^p\right)_2} \end{vmatrix}^2 = \sqrt{\gamma_{lv}^d}\Big/\gamma_{lv}, \tag{2}$$

$$A = \begin{vmatrix} \left(\frac{1+\cos\theta}{2}\right)_1 & \sqrt{\left(\gamma_{sv}^d\right)_1} \\ \left(\frac{1+\cos\theta}{2}\right)_2 & \sqrt{\left(\gamma_{sv}^d\right)_2} \end{vmatrix}^2 \Bigg/ \begin{vmatrix} \sqrt{\left(\gamma_{sv}^p\right)_1} & \sqrt{\left(\gamma_{sv}^d\right)_1} \\ \sqrt{\left(\gamma_{sv}^p\right)_2} & \sqrt{\left(\gamma_{sv}^d\right)_2} \end{vmatrix}^2 = \sqrt{\gamma_{lv}^p} \Big/ \gamma_{lv}, \quad (3)$$

where γ_{sv} is the surface energy of the substrate (subscript 1 denotes the first substrate, 2 denotes the second). The surface energy values and their dispersive and polar components for the substrates were also determined under the same conditions using formulas derived from the same method.

Results and Discussion

As a result, Zisman plots (Fig. 1) were obtained along with the critical surface tension (γ_c) values for paraffin (γ_c = 16.12 mJ/m^2) and PET (γ_c = 47.86 mJ/m^2). These low values allowed for the experimental determination of the contact angles of the PEDOT:PSS solution. The values of the surface tension of the PEDOT:PSS solution at different volume fractions of Triton X-100 have been determined (Table).

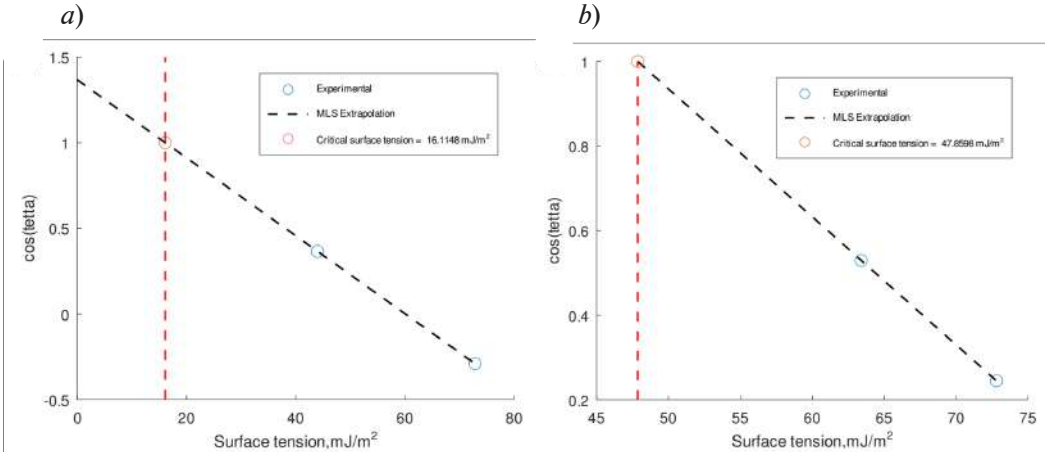

Fig. 1. Zisman plots for paraffin (*a*) and PET (*b*)

Table

Dependence of the surface tension of the PEDOT:PSS with Triton X-100

Triton X-100, vol.%	Surface tension, mJ/m^2		
	γ_{lv}	γ_{lv}^p	γ_{lv}^d
0	64.01±1.55	45.42±0.97	18.59±0.58
0.005	59.81±0.58	49.10±0.32	10.71±0.26
0.010	54.99±0.58	34.66±0.39	20.33±0.20
0.050	57.20±0.45	52.02±0.24	5.9±0.21
0.100	53.19±0.24	49.95±0.12	3.24±0.12

The surface tension of a PEDOT:PSS solution, like other polymer solutions, nonlinearly depends on the surfactant content, which is confirmed in the work [1].

It is shown that the addition of even 0.1 vol.% Triton X-100 reduces the surface tension of the PEDOT:PSS solution by 20%. The obtained values are far from the critical surface tension of silicon γ_c = 34.7 ±7.1 mJ/m^2 [7].

Conclusion

The critical surface tension for paraffin and PET was determined. The surface tension of the aqueous PEDOT:PSS solution (3.4%, 1:2.5) was found to be too high for complete wetting of silicon and various other substrates. It is highly probable that the addition of surfactant concentrations sufficient for complete wetting of silicon would lead to a significant deterioration of its electrical conductivity [2].

Due to the dewetting effect, the thickness of the film deposited by spin-coating is likely to be dependent on the time elapsed before sample baking, significantly hindering the precise control of film thickness, a crucial parameter of thin film.

REFERENCES

1. **Holmberg K., Jönsson B., Kronberg B., Lindman B.,** Surfactants and Polymers in Aqueous Solution. 2nd ed. Wiley: Chichester, U.K., 2003.

2. **Pozdeev V.A., Uvarov A.V., Gudovskikh A.S., et al.,** Study of the effect of solvents and surfactants on electrical properties of PEDOT:PSS films, St. Petersburg State Polytechnical University Journal. Physics and Mathematics. 16 (3.1) (2023) 468–472.

3. **Zisman W.A.,** Relation of the Equilibrium Contact Angle to Liquid and Solid Constitution, Advances in Chemistry. (1964) 1–51.

4. **Lyakhovich A.M., Shakov A.A., Lyalina N.V.,** Effect of ambient humidity to wetting angles of various hydrophilic surfaces, Protection of Metals and Physical Chemistry of Surfaces. 46 (5) (2010) 534–539.

5. **Young J.F.,** Humidity control in the laboratory using salt solutions—a review, Journal of Applied Chemistry. 17(9) (1967) 241–245.

6. **Owens D.K., Wendt R.C.,** Estimation of the surface free energy of polymers, Journal of Applied Polymer Science. 13 (8) (1969) 1741–1747.

7. **Extrand C.W.,** Contact Angles and Hysteresis on Surfaces with Chemically Heterogeneous Islands, Langmuir. 19 (9) (2003) 3793–3796.

THE AUTHORS

POZDEEV Vyacheslav A.
pozdeev99va@gmail.com
ORCID: 0009-0009-4023-6185

GUDOVSKIKH Alexander S.
gudovskikh@spbau.ru
ORCID: 0000-0002-7632-3194

UVAROV Alexander V.
lumenlight@mail.ru
ORCID: 0000-0002-0061-6687

MONASTYRENKO Anatoly O.
aomonster@mail.ru
ORCID: 0009-0009-7051-8458

Received 30.07.2024. Approved after reviewing 31.07.2024. Accepted 31.07.2024.

Conference materials
UDC 539.21
DOI: https://doi.org/10.18721/JPM.173.257

Effect of functional sublayers on the characteristics of deposited diamond-like carbon coatings

B.A. Parshin✉, M.O. Makeev, P.A. Mikhalev, D.M. Sviridyuk

Bauman Moscow State Technical University, Moscow, Russia

✉ parshbgal@bmstu.ru

Abstract. DLC coatings deposited by the PLD method were investigated using Raman spectroscopy, spectrophotometry and atomic force microscopy. The influence of the material of the functional sublayers used (Ti, Cr) on the structural and optical characteristics, as well as the surface condition of the deposited DLC coatings, was studied.

Keywords: diamond-like carbon, functional sublayers, sp^2-hybridization, sp^3-hybridization, atomic force microscopy, spectrophotometry, Raman spectroscopy

Funding: The research was carried out within the state assignment of the Ministry of Science and Higher Education of the Russian Federation (theme no. FSFN-2024-0072).

Citation: Parshin B.A., Makeev M.O., Mikhalev P.A., Sviridyuk D.M., Effect of functional sublayers on the characteristics of deposited diamond-like carbon coatings, St. Petersburg State Polytechnical University Journal. Physics and Mathematics. 17 (3.2) (2024) 283–287. DOI: https://doi.org/10.18721/JPM.173.257

Материалы конференции
УДК 539.21
DOI: https://doi.org/10.18721/JPM.173.257

Влияние функциональных подслоев на характеристики напыляемых алмазоподобных углеродных покрытий

Б.А. Паршин✉, М.О. Макеев, П.А. Михалев, Д.М.Свиридюк

Московский государственный технический университет им. Н.Э. Баумана, Москва, Россия

✉ parshbgal@bmstu.ru

Аннотация. Методами спектроскопии комбинационного рассеяния света, спектрофотометрии и атомно-силовой микроскопии исследованы DLC покрытия, осаждаемые методом PLD. Изучено влияние материала используемых функциональных подслоев (Ti, Cr) на структурные и оптические характеристики, а также состояние поверхности нанесенных DLC покрытий.

Ключевые слова: алмазоподобный углерод, функциональные подслои, sp^2-гибридизация, sp^3-гибридизация, атомно-силовая микроскопия, спектрофотометрия, Рамановская спектроскопия

Финансирование: Исследование выполнено в рамках государственного задания Министерства науки и высшего образования Российской Федерации (тема № FSFN-2024-0072).

Ссылка при цитировании: Паршин Б.А., Макеев М.О., Михалев П.А., Свиридюк Д.М. Влияние функциональных подслоев на характеристики напыляемых алмазоподобных углеродных покрытий // Научно-технические ведомости СПбГПУ. Физико-математические науки. 2024. Т. 17. № 3.2. С. 283–287. DOI: https://doi.org/10.18721/JPM.173.257

Introduction

DLC (diamond-like carbon) coatings consist of carbon atoms with both diamond (sp^3) and graphite-like (sp^2) bonds, combined into an amorphous structure [1–3]. This combination of chemical bonds in their low shear strength structure is promising, since sp^3-bonds provide DLC coatings with the hardness of diamond, and sp^2-bonds provide low shearing resistance, characteristic of graphite. DLC coatings also have a number of unique properties, such as high mechanical and barrier (gas-impermeable) properties, biocompatibility, etc. [4, 5].

Currently, there are a number of methods for deposition of DLC coatings, listed and described in detail in the review [4]. One of the problems in obtaining such coatings, which limits the areas of their application, is their high internal stresses, which can reach 10 GPa. When the critical value of internal stresses is exceeded, the DLC coating falls off. Traditional approaches to reducing internal stresses involve increasing the growth temperature and reducing the particle scattering energies. However, these methods inevitably lead to a decrease in the yield of the diamond phase. In this regard, the use of intermediate functional sublayers that increase adhesion plays an important role in ensuring the strength characteristics and durability of the applied coatings.

Materials and Methods

The hardening diamond-like coatings were applied by pulsed laser deposition using the Nanofab-100 (NT–MDT) nanotechnology complex. The application process involves the action of laser radiation on the target material, radiation absorption, dispersion of the products of the action and their deposition on the substrate. In this case, the interaction of laser radiation with the plasma of the ablation products leads to an increase in the degree of ionization and the energy of the particles. A CompexPro102F KrF excimer laser with a pulse duration of 30 ns and a wavelength of 248 nm was used as a radiation source. The films were deposited without heating the substrates at a heater temperature above the substrate of 25 °C and a radiation pulse energy of 138–139 mJ. To ensure the homogeneity of the layers, rotation of the target and the substrate, as well as beam movement along the surface of the carbon target, were used. The target material was pyrolytic graphite.

To determine the structure of diamond-like carbon coatings, the Raman spectroscopy method in the visible range was used, allowing the ratio of sp^3-, sp^2-hybridizations of carbon to be determined. The optical characteristics of the obtained samples were controlled by the visible spectrophotometry method in the wavelength range from 380 to 780 nm. Atomic force microscopy methods were used to study the surface state of the obtained coatings.

Results and Discussion

The results of studies using atomic force microscopy of DLC coatings (Fig. 1) show noticeable differences in the surface condition of samples with functional sublayers. As can be seen from Table 1, the surface of the diamond-like carbon coatings deposited on titanium sublayers contains a large number of defects, compared to the sample deposited on a Cr sublayer. This is due to high internal stresses arising in the coating due to significant differences in the temperature expansion coefficients of the substrate and the coating, which lead to cracking of the coating.

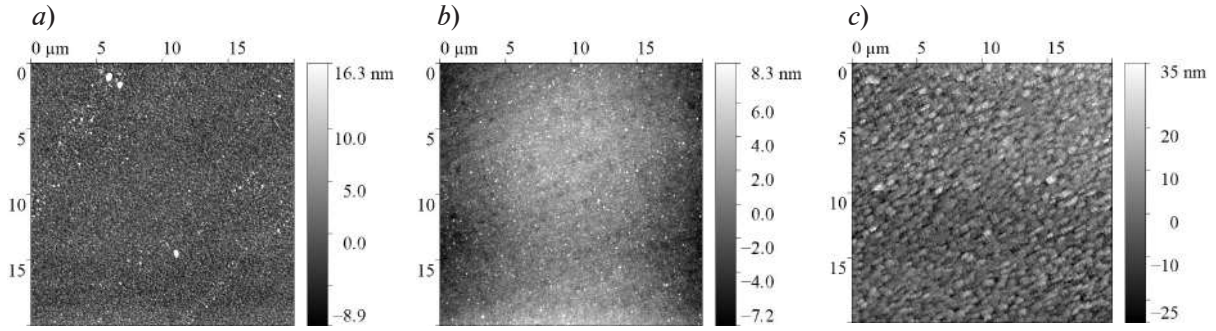

Fig. 1. AFM surface images of DLC coating on Al substrate with Ti-sublayer (*a*), DLC coating on Si substrate with Cr-sublayer (*b*) and DLC coating on Si substrate with Ti-sublayer (*c*)

Table 1

Roughness of samples based on atomic force microscopy results

Characteristic	Sample		
	Al substrate, Ti sublayer	Si substrate, Cr sublayer	Si substrate, Ti sublayer
Ra(Sa)	2.68718 nm	2.01460 nm	6.54075 nm
Rms(Sq)	4.56328 nm	2.53872 nm	8.55835 nm

The study of the optical properties of the samples shows that the use of functional sublayers reduces the reflectivity of the resulting products, as can be seen from Table 2. As shown earlier, samples with applied sublayers have low roughness. Thus, the change in the optical properties of the samples occurs due to the fact that the reflective properties of the mirror surface in the optical range of the spectrum are determined by the refractive indices and absorption of the functional sublayers and the absorption properties of the DLC coating.

Table 2

Reflection coefficient

	Substrate	
Sublayer	Ti	Cr
Clean Si (R ~ 60%)	R ~ 37%	R ~ 41%
Clean Al (R ~ 88%)	R ~ 21%	–

In the experimental Raman spectra of the studied diamond-like coatings, a small peak was observed in the region of ~500 cm^{-1}. The authors of [5], based on modeling, attribute this band to transverse vibrations of carbon in the form of carbyne-like sp^1-chains ordered in a hexagonal structure with an interchain distance of about 0.5 nm, called linear-chain carbon (LCC). The carbon phase of the coatings corresponding to sp^2- and sp^3-bonded carbon is observed in the range from 900 to 1800 cm^{-1}. Further, only this range was considered, since this range contains the main information about the sp^3-fraction [6]. Fig. 2 shows the Raman spectra of carbon materials.

The degree of disorder in the structure of carbon films is described within the framework of a three-stage model of increasing disorder [7] based on the position of the G-peak and the ratio of the intensities of the D- and G- peaks.

It was determined that the DLC coating on an aluminum substrate with a titanium sublayer has the highest sp^3-fraction equal to 80%, which corresponds to the ta-C type. Coatings on a Si substrate are characterized by a significantly lower sp^3-fraction (10% or less).

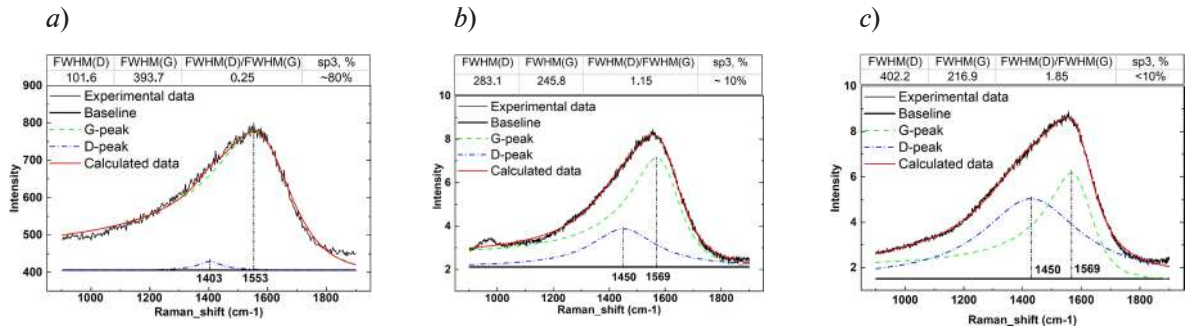

Fig. 2. Raman spectra of DLC coating on Al surface (*a*) and DLC coating on Ti-sublayer (*b*)

Conclusion

The results of the study show that the DLC coating samples deposited on the Ti sublayer have different characteristics depending on the substrate used. Thus, the DLC coating on the aluminum substrate has a higher ratio of sp^3- and sp^2-carbon phases and corresponds to the ta-C type, which characterizes high hardness, and this sample has lower roughness. However, a stronger decrease in optical characteristics is noted than that of the sample on the silicon substrate.

It is also shown that the DLC coating deposited on the silicon substrate is characterized by an insignificant yield of the sp^3 phase of carbon. It is worth noting that the sample deposited on the Cr sublayer has lower roughness compared to the sample deposited on the Ti sublayer. This sample also has a larger sp^3 fraction and fewer reflective characteristics in the visible wavelength range. Thus, when depositing DLC coating on silicon substrate, the use of Cr sublayer is preferable compared to Ti sublayer.

The presented study proves that the use of functional sublayers significantly affects the characteristics of deposited DLC coatings.

REFERENCES

1. **Robertson J.,** Diamond-like amorphous carbon, Mat. Sci. Eng. R. 37 (2002) 129–281.

2. **Jansson U., Lewin E.,** Sputter deposition of transition-metal carbide films: A critical review from a chemical perspective, Thin Solid Films. 536 (2013) 1–24.

3. **Spencer E., Shmidt P.,** Ion-beam deposited polycrystalline diamondlike films, Appl. Phys. Lett. 29 (1976) 118–120.

4. **Batshev V.I., Kozlov A.B., Machikhin A.S., et al.,** Reinforcing of a Mirror Surface via the Deposition of a Carbon Nanostructure, Optics and Spectroscopy. 127 (2019) 634–638

5. **Makeev M.O., Osipkov A.S., Batshev V.I., et al.,** Resistance investigation of diamond-like carbon coatings to cyclic temperature changes, Journal of Physics: Conference Series. 2056 (2021) 012032.

6. **Hainsworth S.V.,** Diamond-like carbon coatings for tribology: production techniques, characterization methods and applications, Int. Mat. Reviews. 52 (2007) 153–174.

7. **Buntov E.A., Zatsepin A.F., Guseva M.B., Ponosov Yu. S.,** 2D-ordered kinked carbyne chains: DFT modeling and Raman characterization, Carbon. 117 (2017) 271–278.

8. **Ferrari A.C., Robertson J.,** Raman spectroscopy of amorphous, nanostructured, diamond-like carbon, and nanodiamond, Phil. Trans. R. Soc. A. 362 (2004) 2477–2512.

9. **Saito R., Jorio A., Souza Filho A.G., et al.,** Probing Phonon Dispersion Relations of Graphite by Double Resonance Raman Scattering, Phys. Rev. Lett. 88 (2002).

THE AUTHORS

PARSHIN Bogdan A.
parshbgal@bmstu.ru
ORCID: 0009-0000-9787-6831

MIKHALEV Pavel A.
pamikhalev@bmstu.ru
ORCID: 0000-0003-0672-4627

MAKEEV Mstislav O.
m.makeev@bmstu.ru
ORCID: 0000-0001-8945-3919

SVIRIDYUK Denis M.
sviridyuk@bmstu.ru

Received 31.07.2024. Approved after reviewing 31.07.2024. Accepted 02.08.2024.

Conference materials
UDC 544.774.4
DOI: https://doi.org/10.18721/JPM.173.258

Green synthesis of titanium dioxide nanoparticles suitable for creating PVDF-TiO_2 composite films

A.A. Vodyashkin[1]✉, P.A. Mikhalev[1], M.O. Makeev[1,2]

[1] Bauman Moscow State Technical University, Moscow, Russia;

[2] Peoples' Friendship University of Russia named after Patrice Lumumba Moscow, Russia

✉ av.andrey2013@yandex.ru

Abstract. This work presents a green method for producing titanium dioxide nanoparticles. The resulting nanoparticles were characterized using DLS, XRD, FTIR. The resulting nanoparticles consist of an anatase phase with small impurities of brookite and an amorphous phase associated with organic substances of the extract. Titanium nanoparticles exhibit high colloidal stability induced by rosehip extract. Due to their high colloidal stability, the nanoparticles proposed in this work are a promising resistor as one of the components for tuning the properties of hybrid materials in the PVDF matrix.

Keywords: nanoparticles, TiO_2, PVDF, composite materials, dynamic light scattering, green synthesis

Funding: The research was carried out within the state assignment of the Ministry of Science and Higher Education of the Russian Federation (theme No. FSFN-2024-0014).

Citation: Vodyashkin A.A., Mikhalev P.A., Makeev M.O., Green synthesis of titanium dioxide nanoparticles suitable for creating PVDF-TiO_2 composite films, St. Petersburg State Polytechnical University Journal. Physics and Mathematics. 17 (3.2) (2024) 288–291. DOI: https://doi.org/10.18721/JPM.173.258

Материалы конференции
УДК 544.774.4
DOI: https://doi.org/10.18721/JPM.173.258

Зеленый синтез наночастиц диоксида титана, пригодных для создания композитных пленок PVDF-TiO_2

А.А. Водяшкин[1]✉, П.А. Михалев[1], М.О. Макеев[1,2]

[1] Московский государственный технический университет им. Н. Э. Баумана (национальный исследовательский университет), Москва, Россия;

[2] Российский университет дружбы народов имени Патриса Лумумбы, Москва, Россия

✉ av.andrey2013@yandex.ru

Аннотация. В этой работе представлен зеленый метод получения наночастиц диоксида титана. Полученные наночастицы были охарактеризованы с помощью DLS, XRD, FTIR. Полученные наночастицы состояли из фазы анатаза с небольшими примесями брукита и аморфной фазы, связанной с органическими веществами экстракта. Наночастицы титана показали высокую коллоидную стабильность, индуцированную экстрактом шиповника. Благодаря устойчивости золя TiO_2 в растворах и высокой степени кристалличности, предложенные в данной работе, наночастицы являются перспективным материалом для создания пленок PVDF с заданной кристаллической структурой.

Ключевые слова: наночастицы, TiO_2, ПВДФ, композитные материалы, динамическое светорассеяние, зеленый синтез

Финансирование: Работа выполнена в рамках государственного задания Министерства науки и высшего образования Российской Федерации (тема № FSFN0014-2024-).

Ссылка при цитировании: Водяшкин А.А., Михалев П.А., Макеев М.О. Зеленый синтез наночастиц диоксида титана, пригодных для создания композитных пленок PVDF-TiO_2 // Научно-технические ведомости СПбГПУ. Физико-математические науки. 2024. Т. 17. № 3.2. С. 288–291. DOI: https://doi.org/10.18721/JPM.173.258

Introduction

Nanoparticles of various materials are becoming increasingly important in various areas of human activity [1]. One of the popular directions is the creation of polymer films with nanoparticles included in them [2]. PVDF-TiO_2 hybrids are one of the most promising materials, covering a wide range of areas: from photocatalysis to biomedicine [3]. It is especially worth noting that such materials have piezoelectric activity and can be used to create various devices and sensors. In such systems, the colloidal stability of the particles is important, which can ensure the isotropy of the material [4].

Green methods are promising ways to obtain titanium nanoparticles [5]. Such methods provide high stability, as well as a developed surface due to the use of biologically active substances that act as coating agents [6]. Importantly, such methods are highly scalable and environmentally friendly technologies that can be used in a variety of applications, including the creation of hybrid materials with PVDF.

Materials and Methods

Particle synthesis: Rose hip plant extract was prepared by sonicating rose hips for 20 minutes at 40 °C, after which the solution was filtered twice. Titanium nanoparticles were obtained by the sol-gel method, in which 100 ml of water containing 10 ml of rosehip extract and acidified to pH 4 was heated to 75 °C, after which a solution consisting of 8.5 ml of titanium butoxide, 6, was added to it. 5 ml 2-propanol. After incubation for 120 min. heating was stopped and stirring continued for another 72 hours. The resulting particles were dried on a rotary evaporator and dispersed for further experiments.

Characterization methods:

Dynamic light scattering (DLS) (Malvern Zetasizer).

Electrophoretic light scattering (ELS) (Malvern Zetasizer).

X-ray diffraction: X-ray phase analysis of TiO_2 samples was carried out on an automatic X-ray diffractometer for polycrystalline materials DRON-7 in step-by-step scanning mode. Angle interval 2θ from 5° to 70° with scanning step $\Delta 2\theta = 0.02°$ and exposure 2 s per point. We used Cu Kα radiation (Ni filter), which was subsequently decomposed into Kα1- and Kα2-components when processing the spectra.

IR spectroscopy: Fourier transform infrared spectroscopy (FTIR) measurements were performed on Agilent Cary 630 FTIR spectrophotometer with a transmission attachment (Agilent Technologies, Santa Clara, CA, USA). The resolution is less than 2 cm^{-1}, the correctness of the wavenumber is 0.05 cm^{-1}, and the reproducibility of the wavenumber is 0.005 cm-1. The spectral range is 4000–500 cm^{-1}.

Results and Discussion

Titanium dioxide nanoparticles obtained using plant raw materials were characterized using DLS (Fig. 1). TiO_2 had a wide distribution, which may be caused by bioactive substances on the surface and had an average size of 21 nm. At the same time, the Zeta potential of the system was 33.9 mV. It is worth noting that the particles maintained their size for 3 months, which was confirmed by DLS and visible spectroscopy. High stability can be ensured biologically active substances included in the capping agent.

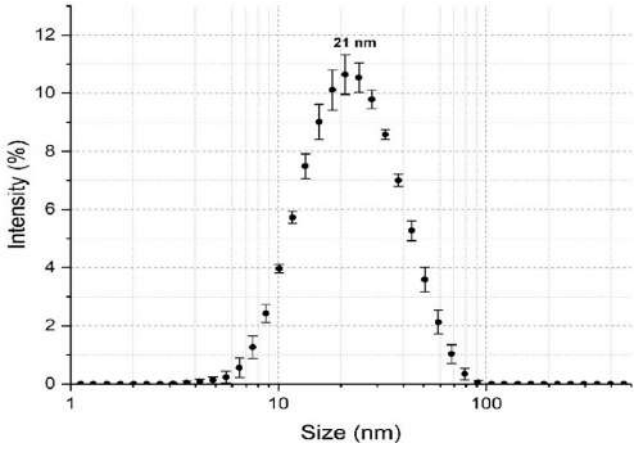

Fig. 1. DLS-Size for green TiO_2 nanoparticles

Fig. 2 shows a diffraction pattern of titanium dioxide nanoparticles. As can be seen in Fig. 2, the presence of a crystalline phase of Anatase (data no. 21-1272 IDD PDF-2) in the form of nanoparticles (broad peaks) and an X-ray amorphous, possibly organic phase, which is associated with the use of the extract, is noticeable. In addition, the sample contains the Brookite phase (data no. 15-875 IDD PDF-2): a characteristic small peak in the region $2\theta \sim 30.7^{o}$.

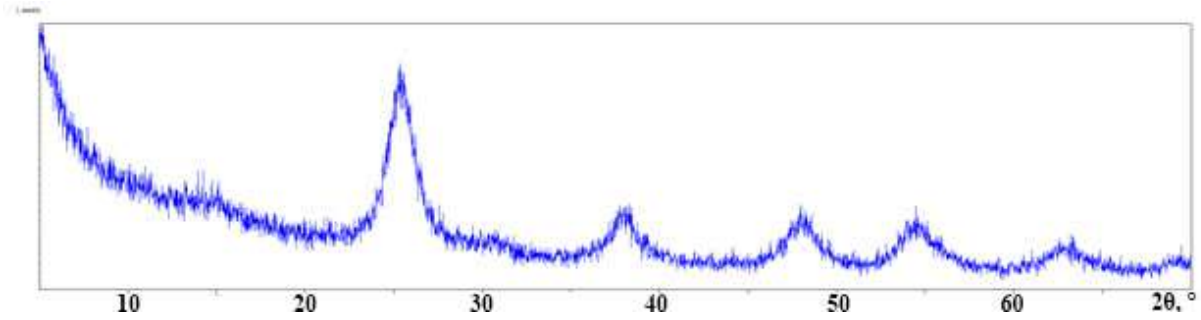

Fig. 2. X-ray diffraction pattern for green TiO_2 nanoparticles

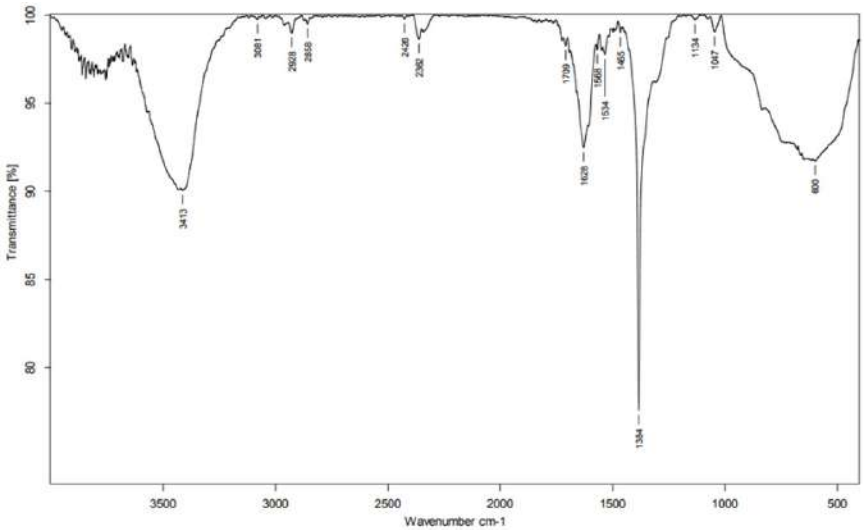

Fig. 3. FTIR spectra for green TiO_2 nanoparticles

Fig. 3 shows the FTIR spectrum of the resulting nanoparticles. The band at 1628 cm^{-1} corresponds to asymmetric C=O stretching of carboxyl groups. The strong absorption band at 1384 cm^{-1} correspond to C—O stretching from alcohol, carboxylic acid, ester and ether.

The results of FTIR spectrometry confirm that the synthesized nanoparticles are stabilized by biologically active components of rosehip fruit extract, including organic acids, flavonoids, tocopherols and ascorbic acid.

Conclusion

This paper presents a successful method for the synthesis of TiO_2 using aqueous rosehip extract. Thanks to their use in the synthesis of plant extracts, nanoparticles have high colloidal stability and a developed surface. XRD and FTIR data confirm the presence of extractives on the surface of nanoparticles. The nanoparticles were predominantly composed of anatase and had an average size of 21 nm. The particles had a relatively wide size distribution, which was caused by the heterogeneity of the amount of substances on the surface of the nanoparticles. The dependence of the crystalline phase of PVDF is directly related to the crystallinity of the object included in its structure. Due to the high content of anatase crystalline phase and high colloidal stability, titanium nanoparticles obtained using plant extract can be used as an additive in PVDF film to optimize the structure and improve the electrochemical properties.

REFERENCES

1. **Mitchell M.J., et al.,** Engineering precision nanoparticles for drug delivery, Nature reviews drug discovery. **20** (2) (2021) 101—124.

2. **Zhou A., et al.,** Abatement of sulfadiazine in water under a modified ultrafiltration membrane (PVDF-PVP-TiO_2-dopamine) filtration-photocatalysis system, Separation and Purification Technology. 234 (20200) 116099.

3. **Saxena P., Shukla P.A.,** Comprehensive review on fundamental properties and applications of poly (vinylidene fluoride) (PVDF), Advanced Composites and Hybrid Materials. 4 (2021) 8—26.

4. **Kochervinskii V.V., et al.,** The Effect of Electric Aging on Vinylidene Fluoride Copolymers for Ferroelectric Memory, Nanomaterials. 14 (12) (2024) 1002.

5. **Verma Vishal, et al.,** A review on green synthesis of TiO_2 NPs: photocatalysis and antimicrobial applications, Polymers. **14** (7) (2022) 1444.

6. **Rejepov D.T., et al.,** Biomedical applications of silver nanoparticles (Review), Drug development & registration. 10 (3) (2021) 176—187 (in Russia).

THE AUTHORS

VODYASHKIN Andrey A.
av.andrey2013@yandex.ru
ORCID: 0000-0003-1556-7635

MAKEEV Mstislav O.
m.makeev@bmstu.ru
ORCID: 0000-0001-8945-3919

MIKHALEV Pavel A.
pamikhalev@bmstu.ru
ORCID: 0000-0003-0672-4627

Received 31.07.2024. Approved after reviewing 06.08.2024. Accepted 06.08.2024.

BIOPHYSICS AND MEDICAL PHYSICS

Conference materials
UDC 004.622
DOI: https://doi.org/10.18721/JPM.173.259

Utilizing the convolutional neural network AlexNet to classify ultra-high resolution electrocardiosignals

K.V. Zaichenko[1], A.S. Afanasenko[1,2], E.A. Denisova[1]✉,
A.A. Kordyukova[1], D.O. Shevyakov[1,2]

[1] Institute for Analytical Instrumentation RAS, St. Petersburg, Russia;

[2] Saint Petersburg State University of Aerospace Instrumentation, St. Petersburg, Russia

✉ tiranderel@yandex.ru

Abstract. Coronary heart disease is one of the main causes of death in humans. Despite this, modern electrocardiography (ECG) methods are limited in obtaining complete information about the progression of pathology due to insufficient throughput. To eliminate this limitation, a new approach known as ultra-high resolution electrocardiography (UHR ECG) is being developed to detect abnormal changes in the cardiovascular system in areas of electrocardiosignal processing (ECS), which are usually perceived as artifacts. However, the expansion of the amplitude and frequency range complicates the task of analyzing the data obtained, since many traditional ECS analysis methods are ineffective when applied to UHR ECG. This study demonstrates the effectiveness of using the fifteen-layer convolutional neural network (CNN) AlexNet to solve the problem of classifying ECS obtained using the UHR ECS methodology. An extensive data set of labeled ECG recordings obtained using the UHR ECG method on Vistar series experimental rats during experiments on modeling acute myocardial ischemia was used to train and evaluate the quality of predictions of the CNN model.

Keywords: Ultra-high resolution electrocardiography, convolutional neural network, classify, AlexNet, ischemia, electrocardiosignal, coronary heart disease

Funding: The work is carried out with the support of the Ministry of Education and the Russian Federation, State Order No. 075-01157-23-00, Project No. FZZM-2023-0011.

Citation: Zaichenko K.V., Afanasenko A.S., Denisova E.A., Kordyukova A.A., Shevyakov D.O., Utilizing the convolutional neural network AlexNet to classify ultra-high resolution electrocardiosignals, St. Petersburg State Polytechnical University Journal. Physics and Mathematics. 17 (3.2) (2024) 292–296. DOI: https://doi.org/10.18721/JPM.173.259

Материалы конференции
УДК 004.622
DOI: https://doi.org/10.18721/JPM.173.259

Использование сверточной нейронной сети AlexNet для классификации электрокардиосигналов сверхвысокого разрешения

К.В. Зайченко[1], А.С. Афанасенко[1,2], Е.А. Денисова[1]✉,
А.А. Кордюкова[1], Д.О. Шевяков[1,2]

[1] Институт аналитического приборостроения РАН, Санкт-Петербург, Россия;

[2] Санкт-Петербургский государственный университет аэрокосмического приборостроения, Санкт-Петербург, Россия

✉ tiranderel@yandex.ru

Аннотация. Современные методы электрокардиографии (ЭКГ) ограничены в получении полной информации о прогрессировании ишемической болезни сердца из-за недостаточной пропускной способности. Поэтому разрабатывается новый подход, известный как электрокардиография сверхвысокого разрешения (ЭКГ СВР), позволяющий выявлять аномальные изменения в сердечно-сосудистой системе в областях обработки электрокардиосигналов (ЭКС), которые обычно воспринимаются как артефакты. Это исследование демонстрирует эффективность применения пятнадцатислойной сверточной нейронной сети (СНС) AlexNet для решения задачи классификации ЭКС, полученных с помощью методологии ЭКГ СВР.

Ключевые слова: электрокардиография сверхвысокого разрешения, сверточная нейронная сеть, классификация, AlexNet, ишемия, электрокардиосигнал, ишемическая болезнь сердца

Финансирование: Работа выполнена при поддержке Министерства образования и науки Российской Федерации, Государственный заказ № 00-23-01157-075, проект № FZZM-2023-0011.

Ссылка при цитировании: Зайченко К.В., Афанасенко А.С., Денисова Е.А., Кордюкова А.А., Шевяков Д.О. Использование сверточной нейронной сети AlexNet для классификации электрокардиосигналов сверхвысокого разрешения // Научно-технические ведомости СПбГПУ. Физико-математические науки. 2024. Т. 17. № 3.2. С. 292–296. DOI: https://doi.org/10.18721/JPM.173.259

Introduction

Coronary heart disease (CHD) is one of the most common causes of death in humans [1], and existing electrocardiography (ECG) methods do not provide complete information about the development of pathology due to the narrow frequency and amplitude ranges [2, 3]. Therefore, a new technique of ultra-high resolution electrocardiography (UHR ECG) is being developed to identify pathological changes in the cardiovascular system in areas of signal processing that are usually considered artifacts. A change in the shape of the spectrum of the ultra-high resolution electrocardiosignals (UHR ECS) is a marker of the development of coronary heart disease [4]. The expansion of ranges of ECG registration makes many standard analysis methods ineffective for UHR ECS, as there are problems associated with processing a large amount of data and the complexity of interpreting the results. However, neural networks (NN) demonstrate great potential in the automatic classification of ECG signals obtained by standard methods [5]. This article shows the effectiveness of using the fifteen-layer convolutional neural network (CNN) AlexNet for ECS UHR classification [6]. A set of labeled ECG recordings for clinical and prognostic

studies was obtained by the UHR ECG method from Vistar series rats in experiments on modeling myocardial ischemia at the Institute of Experimental Medicine of the V.A. Almazov National Research Medical University [3].

Materials and Methods

During the experiments, recordings were obtained that can be divided into the stages of stabilization, ischemia and reperfusion. The purpose of training the model was to determine which stage the UHR ECS fragment with a duration of 1 second belongs to. The problem was complicated by the presence of fragments of records in the dataset corresponding to the transitional stages between the phases of the experiment. A dataset consisting of 20 ECG recordings with a total duration of 22 hours was used to train and test the CNN. These data were obtained during experiments on experimental animals (rats) with a heart rate of 420 beats per minute [3].

Three data sets were prepared to evaluate the effectiveness of the developed model. The first set contains UHR ECS recordings obtained from the low-frequency (LF) signal recording channel, the second from the high-frequency (HF) channel, and the third is a set of spectrums of signal fragments from the high-frequency channel. A change in the shape of the spectrum of the signal from the HF-channel is a marker of the development of CHD [4]. The dataset was divided into training and test samples, where the training sample contains 98% of the data, and the test sample contains 2% to adjust hyperparameters. The model begins to retrain at the fifth epoch, that is, the CNN model becomes too adapted to train data and loses the ability to generalize to new data.

Results and Discussion

The values of the accuracy and loss parameters for the training and test samples are shown in Table 1.

From the data obtained, it can be concluded that the forecast of CNN AlexNet, obtained based on a dataset containing data from the HF-channel of ECG registration, is the most accurate. Fig. 1 shows graphs of the probability that a fragment of the UHR ECS belongs to one of the three stages of the experiment, where P_s is the probability that this fragment of the signal was received at the stage of stabilization, P_i is the ischemia, P_r is the reperfusion. The dotted vertical line marks the start time of the "ischemia" stage. The data presented in Fig. 1, *a* were obtained after training the

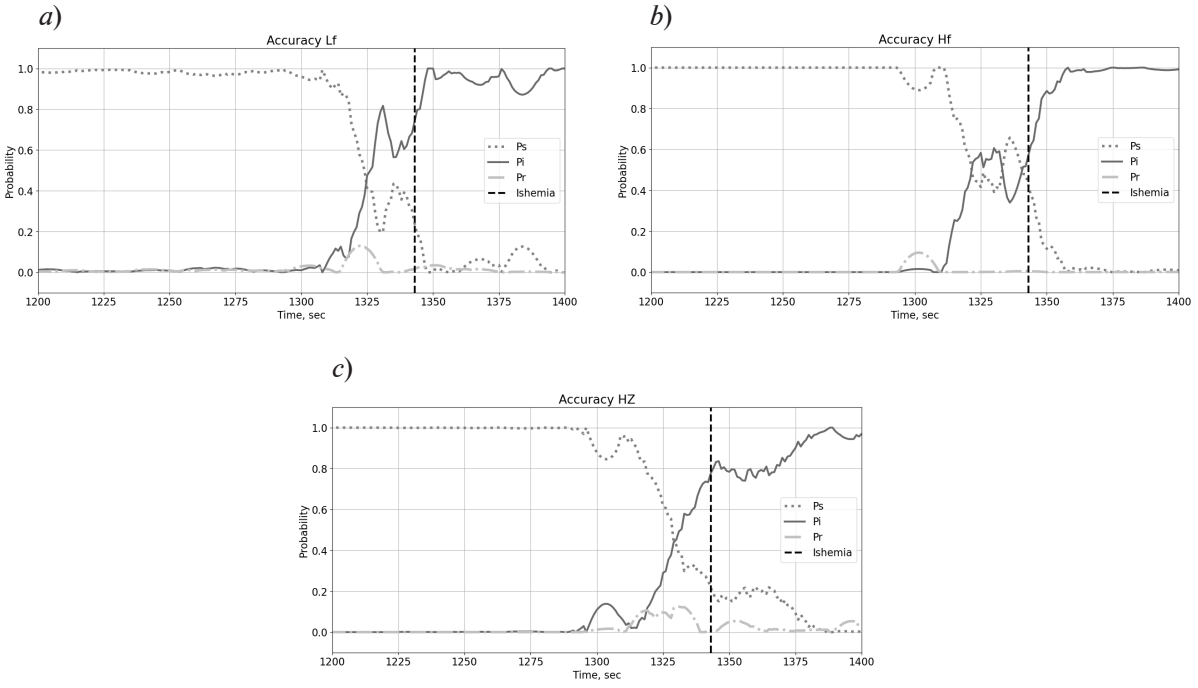

Fig. 1. Probability that the fragment of UHR ECS belongs to one of the stages of experiment for *Lf* (*a*), *Hf* (*b*), *Hz* (*c*) datasets

Table 1

Parameters for evaluating the effectiveness of the CNN

Type of dataset	loss	accuracy	test_loss	test_accuracy
Lf	0.1257	0.9524	0.1822	0.9373
Hf	0.0667	0.9781	0.1703	0.9583
Hz	0.1257	0.9592	0.2211	0.9340

Notations. *Lf* is the dataset consisting of fragments of the signals from the LF-channel, *Hf* is the dataset consisting of fragments of the signals from the HF-channel, *Hz* is the dataset consisting of spectrums of fragments of the signals from the HF-channel.

CNN on a data set consisting of signal from the LF-channel, in Fig. 1, *b* is from the HF-channel, in Fig. 1, *c*. is from the spectrums of fragments of signals from the HF-channel. The beginning of the "ischemia" stage in this study is the moment when the probability that the shape of the UHR ECS fragment corresponds to the stabilization stage becomes less than 0.25.

Using a data set containing spectrums of signal from the HF-channel, it is possible to determine the onset of ischemia 10 seconds earlier than when training CNN on data from the LF-channel. This is confirmed using the UHR ECG method, which makes it possible to identify the onset of CHD at an early stage [4].

Conclusion

Based on our research, the application of the fifteen-layer CNN AlexNet to classify UHR ECS recordings obtained by UHR ECG has shown promising results. To train and test the network, a data set obtained from experiments on modeling myocardial ischemia in Vistar rats was used. The effectiveness of the model was evaluated using various data sets, including recordings from LF and HF-channels of signal recording, as well as spectrums of signal fragments from the HF-channel. Based on the results obtained, the use of CNN makes it possible to identify ECG abnormalities characteristic of coronary heart disease much earlier than a cardiologist can do. In addition, the results showed that using a dataset containing spectrums of signals from a HF- channel makes it possible to identify the onset of ischemia 10 seconds earlier than learning CNN data from a LF-channel. However, the introduction of NN into medical practice requires careful validation and ensuring their safety and reliability, since any error in diagnosis can have serious consequences for the patient.

Acknowledgment

The work was carried out with the support of the Ministry of Education and Science of the Russian Federation, State Order No. 075-01157-23-00, project No. FZZM-2023-0011.

REFERENCES

1. World Health Organization. URL: https://www.who.int/news-room/fact-sheets/detail/the-top-10-causes-of-death.html. Accessed March 25, 2024.

2. **Gulyaev Y.V., Zaichenko K.V.,** Ultra-high resolution electrocardiography. Tasks. Problems. The prospects, Biomedical radioelectronics. 9 (2013) 5–15.

3. **Zhmyleva A.A., Khrapov S.O., Logachev E.P., Gurevich B.S.,** Application of modern technologies in new ultra-high resolution electrocardiography method, IEEE Xplore library. (2020) 0004–0007.

4. **Zaichenko K.V., Kordyukova A.A., Logachev E.P., Luchkova M.N.,** Application of Radar Techniques of Signal Processing for Ultra-High Resolution Electrocardiography, Biomedical Engineering. 55 (1) (2019) 31–35.

5. **Harrane S., Belkhiri M.,** Classification of ECG heartbeats using deep neural networks, Research on Biomedical Engineering. 37 (2021) 737–747.

6. **Aarthy S.T., Mazher Iqbal J.L.,** Modified parametric-based AlexNet structure to classify ECG signals for cardiovascular diseases, Measurement: Sensors. 27 (2023) 100816.

THE AUTHORS

ZAICHENKO Kirill V.
kvz235@mail.ru
ORCID: 0000-0002-2881-4386

AFANASENKO Arseniy S.
ar.afanasenko@gmail.com
ORCID: 0009-0001-0859-9252

DENISOVA Elena A.
Tiranderel@yandex.ru
ORCID: 0000-0003-0329-2881

KORDYUKOVA Anna A.
annygm00@mail.ru
ORCID: 0000-0002-6099-4276

SHEVYAKOV Daniil O.
sevakovdaniil@gmail.com
ORCID: 0000-0001-5609-4091

Received 08.07.2024. Approved after reviewing 24.09.2024. Accepted 17.10.2024.

Conference materials
UDC 54.057, 544.164, 544.174.2
DOI: https://doi.org/10.18721/JPM.173.260

Fluorescent properties of boron nitride quantum dots depending on functionalizing ligands

E.A. Sidorov✉, E.D. Gribova, P.P. Gladyshev

Dubna State University, Dubna, Russia
✉ siea.18@uni-dubna.ru

Abstract. Boron nitride quantum dots (BNQDs) are promising agents for boron neutron capture therapy. However, studies of the dependence of optical properties on the conditions of their synthesis are at an early stage. In this work, a study was carried out of the effect of BNQDs functionalization with urea, thiourea, and o-phenylenediamine on their fluorescent properties. It is shown that when N-methyl-2-pyrrolidone is used as a solvent for the synthesis of BNQDs by exfoliation of bulk boron nitride powder followed by solvothermal treatment with the addition of various amino-containing ligands, it is possible to tune the fluorescence of boron nitride quantum dots from 404 to 545 nm.

Keywords: quantum dots, boron nitride, photoluminescence

Funding: The research was carried out within the state assignment of Ministry of Science and Higher Education of the Russian Federation (theme No. 124110600041-0).

Citation: Sidorov E.A., Gribova E.D., Gladyshev P.P., Fluorescent properties of boron nitride quantum dots depending on functionalizing ligands, St. Petersburg State Polytechnical University Journal. Physics and Mathematics. 17 (3.2) (2024) 297–300. DOI: https://doi.org/10.18721/JPM.173.260

Материалы конференции
УДК 54.057, 544.164, 544.174.2
DOI: https://doi.org/10.18721/JPM.173.260

Влияние функционализирующих добавок на флуоресцентные свойства квантовых точек нитрида бора

Е.А. Сидоров✉, Е.Д. Грибова, П.П. Гладышев

Государственный университет «Дубна», г. Дубна, Россия
✉ siea.18@uni-dubna.ru

Аннотация. Квантовые точки нитрида бора (КТНБ) являются перспективными агентами для бор-нейтронозахватной терапии. В данной работе исследовано влияние функционализации КТНБ мочевиной, тиомочевиной и о-фенилендиамином на их флуоресцентные свойства. Показано, что путем функционализации КТНБ различными аминолигандами возможно гибко настраивать положение полосы испускания флуоресценции с 404 до 545 нм.

Ключевые слова: квантовые точки, нитрид бора, фотолюминесценция

Финансирование: Работа выполнена в рамках государственного задания Министерства науки и высшего образования Российской Федерации (тема № 124110600041-0 Конъюгаты борсодержащих квантовых точек с биовекторами для диагностики и бор-нейтронозахватной терапии поверхностных злокачественных опухолей).

Ссылка при цитировании: Сидоров Е.А., Грибова Е.Д., Гладышев П.П. Влияние функционализирующих добавок на флуоресцентные свойства квантовых точек нитрида бора // Научно-технические ведомости СПбГПУ. Физико-математические науки. 2024. Т. 17. № 3.2. С. 297–300. DOI: https://doi.org/10.18721/JPM.173.260

Introduction

Over the past few years, boron nitride quantum dots (BNQDs) have attracted increasing attention from researchers due to a combination of properties unique to quantum dots: chemical stability, biocompatibility, low cytotoxicity, as well as tunable optical properties [1–3]. BNQDs are a promising agent for boron neutron capture therapy due to their high boron content and the potential for fluorescent visualization of drug distribution in the body. The optical properties of BNQDs are determined by the synergistic effect of their size, various point defects at the edges and in the plane, as well as functional groups on their edges [4]. Currently, the dependence of the optical properties of BNQDs on synthesis parameters, solvent choice, and reagent ratio has not been fully studied. For the application of BNQDs in biomedicine, it is necessary for the excitation and emission bands of fluorescence to be in the near-infrared region of the spectrum. At present, most BNQDs samples described in the literature are characterized by blue and green fluorescence. This circumstance necessitates the determination of synthesis conditions that influence the position of the excitation and emission bands of fluorescence. This work is dedicated to the study of the dependence of the fluorescent properties of BNQDs on functionalization with aminoligands.

Materials and Methods

Hexagonal boron nitride (technical grade, LenReaktiv, Russia); N-methyl-2-pyrrolidone, NMP (reagent grade, LenReaktiv, Russia); urea (analytical grade, LenReaktiv, Russia); thiourea (≥ 99.0%, Sigma-Aldrich, USA); o-phenylenediamine (99.5%, Sigma-Aldrich, USA); syringe filters (0.22 μm pore size, Millipore, USA); CM2203 spectrofluorometer (Solar, Belarus); Eppendorf 5425 microcentrifuge (Eppendorf, Germany); CAUX-120 analytical balance (CAS, South Korea).

Results and Discussion

The fluorescence bands of BNQDs synthesized without organic ligands are located in the range of 380–450 nm, which precludes their use for fluorescent visualization of cancer cells in vivo. By functionalizing BNQDs with various aminoligands, it is possible to control the structure of their energy bands. N-methyl-2-pyrrolidone (NMP) was chosen as the solvent for the synthesis of nanosheets and boron nitride quantum dots. Aminoligands such as urea, thiourea, and o-phenylenediamine were used for the functionalization of BNQDs. The optical properties of BNQDs were investigated using electronic and fluorescent spectroscopy methods.

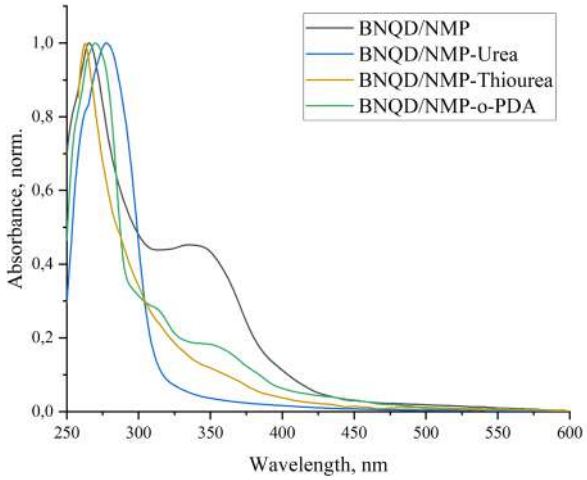

Fig. 1. Absorption spectra of boron nitride quantum dots obtained in NMP with use of organic additives: without additives, urea, thiourea, and o-PDA

Fig. 1 presents the absorption spectra of functionalized BNQDs/NMP. It can be noted that the position of the absorption band maximum, corresponding to the fundamental absorption of BNQDs, remains nearly unchanged upon functionalization of BNQDs/NMP with urea, thiourea, and o-phenylenediamine (o-PDA) [5]. Additionally, for each spectrum of functionalized BNQDs, a characteristic shoulder can be observed in the region of 310–370 nm, which may indicate the attachment of aminoligands to the BNQDs.

The study of the fluorescent properties of BNQDs was conducted at various wavelengths of the excitation (280–460 nm) with a step of 20 nm (Fig. 2). The intensity of the fluorescence emission is represented in relative units and is displayed in the corresponding color, the scale of which is provided in the figure.

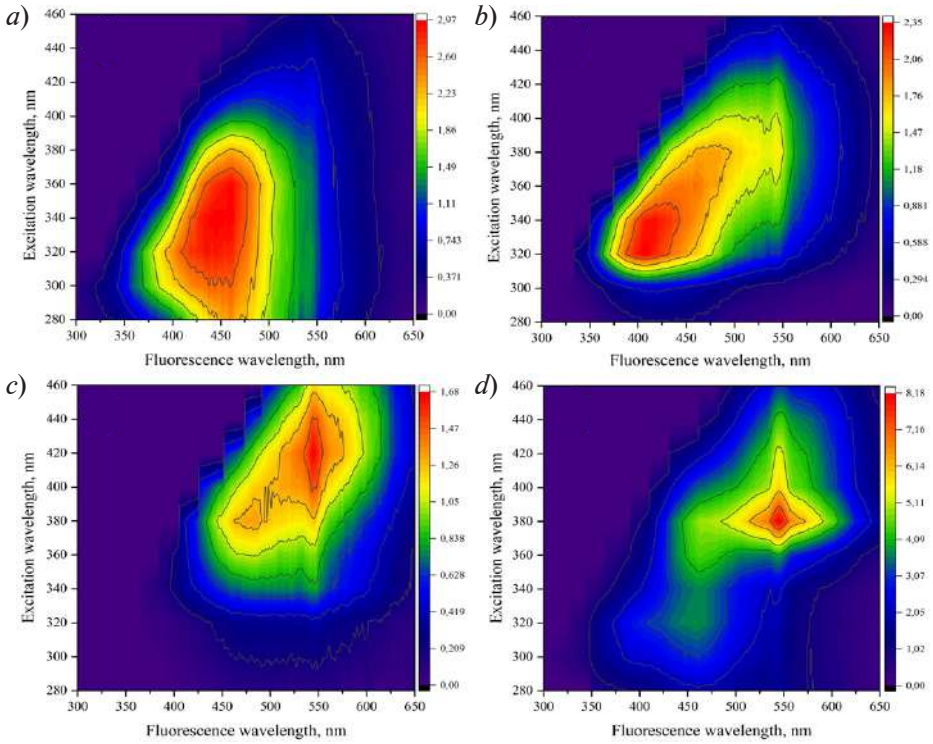

Fig. 2. Color map of dependence of boron nitride quantum dots fluorescence on excitation wavelength: NMP (*a*), NMP-Urea (*b*), NMP-Thiourea (*c*), NMP-o-PDA (*d*)

The optical properties of the BNQDs/NMP samples functionalized with urea, thiourea, and o-PDA are presented in Table 1.

Table 1

Optical properties of BNQDs/NMP obtained with the addition of an aminoligands

Sample	Range λ_{ex}, nm	$\lambda_{ex}/\lambda_{em}$ (max), nm	FWHM, nm	Stokes shift, nm	Dependence on λ_{ex}
NMP	280–400	340/450	139	112	+
NMP-urea	320–420	320/404	134	78	+
NMP-thiourea	340–480	420/544	128	132	+
NMP-o-PDA	320–440	380/545	148	107	+/–

As can be seen from the data presented in the table, the BNQDs/NMP-urea sample is characterized by a shift of fluorescence to the blue region. Most likely, this can be associated with an increase in the bandgap due to the functionalization of BNQDs with urea. The change in optical properties upon functionalization of BNQDs/NMP with thiourea and o-PDA may be due to the introduction of new states in the bandgap, and as a consequence, a reduction in the bandgap width, which is also confirmed in the literature [5].

Conclusion

Thus, it has been shown that by functionalizing BNQDs with various aminoligands, it is possible to tune the excitation and emission bands of fluorescence. It can be assumed that the functionalization of BNQDs/NMP with thiourea and o-PDA leads to the introduction of new states within the bandgap and a reduction in the energy of the frontier orbitals of the system.

REFERENCES

1. **Rawat J., Sajwan D., Garimella S.V., et al.,** Boron Nitride quantum dots: A rising star in sensing applications, Nano Trends. 2 (2023) 100008.

2. **Zhang X., An L., Bai C., et al.,** Hexagonal boron nitride quantum dots: Properties, preparation and applications, Materials Today Chemistry. 20 (2021) 100425.

3. **Ding Y., He P., Li S., et al.,** Efficient Full-Color Boron Nitride Quantum Dots for Thermostable Flexible Displays, ACS Nano. 15 (9) (2021) 14610–14617.

4. **Kumar R., Singh R.K., Yadav S.K., et al.,** Mechanical pressure induced chemical cutting of boron nitride sheets into boron nitride quantum dots and optical properties, Journal of Alloys and Compounds. 683 (2016) 38–45.

5. **Cui P., Wu Q., Zhiwei L.**, Exploring the dual capabilities of BNQDs: a comprehensive study on enhancing photoelectric performance and photoluminescence via ligand functionalization, Journal of Molecular Modeling. 30 (1) (2023) 6.

THE AUTHORS

SIDOROV Evgeniy A.
siea.18@uni-dubna.ru
ORCID: 0000-0003-0326-3554

GLADYSHEV Pavel P.
pglad@yandex.ru

GRIBOVA Elena D.
elena_g67@mail.ru

Received 30.07.2024. Approved after reviewing 21.08.2024. Accepted 27.08.2024.

Conference materials
UDC 620.3
DOI: https://doi.org/10.18721/JPM.173.261

Conditions of AgNPs/flavin mononucleotide complex formation as a tool to tune optical properties of this complex

A.O. Dushina[1,2,3]✉, M.E. Stepanov[3], A.I. Arzhanov[3,4], E.V. Khaydukov[2,3,5], A.N. Generalova[1,2]

[1] National Research Nuclear University MEPhI (Moscow Engineering Physics Institute), Moscow, Russia;

[2] M.M. Shemyakin and Yu.A. Ovchinnikov Institute of bioorganic chemistry of RAS, Moscow, Russia;

[3] Moscow Pedagogical State University, Moscow, Russia;

[4] Lebedev Physical Institute of the RAS, Branch in Troitsk, Moscow, Russia;

[5] National Research Centre "Kurchatov Institute", Shubnikov Institute of Crystallography of Federal Scientific Research Centre "Crystallography and Photonics" of RAS, Moscow, Russia

✉ dushina02@gmail.com

Abstract. Recently, photodynamic therapy has been considered as one of the promising alternatives to classical antimicrobial therapy based on antibiotics, which has become less effective due to bacterial resistance. Flavin mononucleotide (FMN), a vitamin B2 derivative, is a biocompatible, affordable drug with attractive photodynamic properties, including the generation of reactive oxygen species (ROS) that can target and disrupt bacteria. The integration of silver nanoparticles, known for their antibacterial properties, could affect photochemical processes and potentially enhance the antimicrobial effectiveness of FMN. This study shows the results of an investigation into the conditions for the formation of a complex between silver nanoparticles and FMN, as well as the influence of nano-sized silver on the photodegradation of FMN under light irradiation. This work presents the development of a method aimed at preparation of FMN-silver nanoparticles complex. The influence of silver nanoparticles on the fluorescent properties of FMN and the dynamics of its photodegradation was evaluated.

Keywords: flavin mononucleotide, silver nanoparticles, photodegradation, optical properties

Funding: The study was prepared as part of the work on the topic "Laser technologies for biomedical applications" (no. 122122600055-2) under the state order of the Ministry of Education of the Russian Federation.

Citation: Dushina A.O., Stepanov M.E., Arzhanov A.I., Khaydukov E.V., Generalova A.N., Conditions of AgNPs/flavin mononucleotide complex formation as a tool to tune optical properties of this complex, St. Petersburg State Polytechnical University Journal. Physics and Mathematics. 17 (3.2) (2024) 301–305. DOI: https://doi.org/10.18721/JPM.173.261

Материалы конференции
УДК 620.3
DOI: https://doi.org/10.18721/JPM.173.261

Условия образования комплекса наночастиц серебра и флавинмононуклеотида как инструмент настройки оптических свойств этого комплекса

А.О. Душина[1,2,3]✉, М.Е. Степанов[3], А.И. Аржанов[3,4], Е.В. Хайдуков[2,3,5], А.Н. Генералова[1,2]

[1] Национальный исследовательский ядерный университет «МИФИ», Москва, Россия;

[2] Институт биоорганической химии имени М. М. Шемякина и Ю. А. Овчинникова РАН, Москва, Россия;

[3] Московский педагогический государственный университет, Москва, Россия;

[4] Троицкое обособленное подразделение Физического института имени П.Н. Лебедева, г. Троицк, Россия;

[5] Национальный исследовательский центр «Курчатовский институт», Институт кристаллографии им. А.В. Шубникова ФНИЦ «Кристаллография и фотоника» РАН, Москва, Россия

✉ dushina02@gmail.com

Аннотация. Фотодинамическая терапия на основе флавинмононуклеотида (ФМН) рассматривается как перспективная альтернатива антибиотикам, поскольку ФМН является доступным лекарственным средством с привлекательными фотосенсибилизирующими свойствами. Добавление наночастиц серебра, известных своими антибактериальными свойствами, может повлиять на протекание фотохимических процессов и потенциально усилить противомикробную эффективность ФМН. В данной работе представлены результаты исследования условий формирования комплекса наночастиц серебра и ФМН, а также влияния наноразмерного серебра на фотодеградацию ФМН.

Ключевые слова: флавинмононуклеотид, наночастицы серебра, фотодеградация, оптические свойства

Финансирование: Работа выполнена в рамках Государственного задания Министерства образования РФ по теме «Лазерные технологии для биомедицинских приложений» (№ 122122600055-2).

Ссылка при цитировании: Душина А.О., Степанов М.Е., Аржанов А.И., Хайдуков Е.В., Генералова А.Н. Условия образования комплекса наночастиц серебра и флавинмононуклеотида как инструмент настройки оптических свойств этого комплекса // Научно-технические ведомости СПбГПУ. Физико-математические науки. 2024. Т. 17. № 3.2. С. 301–305. DOI: https://doi.org/10.18721/JPM.173.261

Introduction

A promising non-antibiotics alternative is antimicrobial photodynamic therapy based on generation of ROS upon irradiation of a photosensitizer. The ROS effectively disrupt biomolecules, leading to microbial death [1]. Recent studies have demonstrated the successful use of FMN (a derivative of vitamin B2), which in its triplet state (after irradiation), is a strong oxidizing agent and can also act as a photosensitizer capable of generating singlet oxygen [2, 3]. However, upon light exposure, FMN can undergo photolysis due to low photostability [4]. The photosensitivity of FMN depends on several factors, including the irradiation wavelength and the presence of other components in the system [4, 5]. Silver nanoparticles, known for their antibacterial properties, have an absorption spectrum that overlaps the emission spectrum of FMN. This suggests that the chance of efficient energy transfer raises leading to increased antimicrobial effectiveness [6]. The creation of complex that combine the antibacterial activity of silver nanoparticles and the phototoxicity of FMN, as well as prolonging their effect, is an urgent task.

Materials and Methods

Chemicals. Silver nitrate from Serva, Germany; Riboflavin-mononucleotide ampoule, JSC Pharmstandard-UfaVITA, 10 mg/ml; Sodium borohydride from Serva, Germany.

Equipment. Evolution 200 spectrophotometer, Thermo Scientific (USA); LED device "Polyronic" (Russia); 90plus Particle Size Analyzer, Brookhaven (USA); SmartEngine™ spectrometer, Oto Photonics (Taiwan).

Methods. To prepare a colloidal solution of AgNPs by rapid reducing, a solution of silver nitrate (5 ml, 0.2 mg/ml) was added dropwise to a solution of sodium borohydride (15 ml, 0.1 mg/ml) with constant stirring in ice bath. To colloidally stabilize the nanoparticles, FMN (2 μl, 10 mg/ml) was added dropwise to the AgNPs solution.

Results and Discussion

Silver nanoparticles were synthesized by borohydride method. The hydrodynamic diameter of AgNPs was found to be 20 nm. AgNPs demonstrated a narrow absorption peak at 395 nm (Fig. 1, red) likely due to both the high conversion of Ag^+ into Ag^0 and small variation of particle sizes and shapes [7]. Since AgNPs colloidal solution is not stable by itself, small amount of FMN was used shortly after the synthesis as a stabilizer to increase colloidal stability and dispersion homogeneity. The addition of FMN to AgNPs resulted in the appearance of a new absorption band at 550 nm where neither FMN nor silver nanoparticles initially absorbed light (Fig. 1, blue). It could be caused by the formation of AgNPs/FMN complexes [5, 8–9] which is probably more energetically favorable. Visually the AgNPs solution after addition of FMN turned brown yet both AgNPs and FMN solutions were initially yellow.

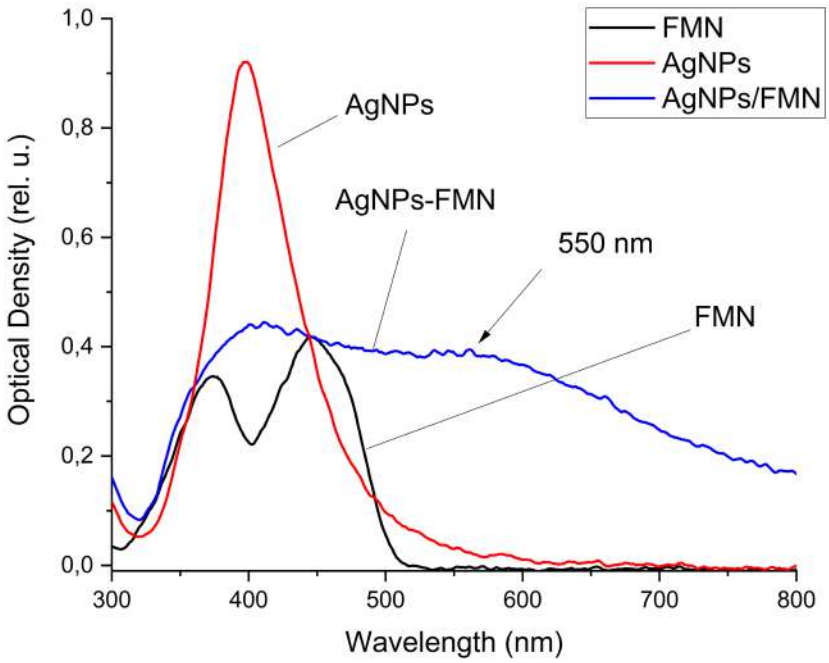

Fig. 1. Absorption spectra of FMN (black), AgNPs (red) and AgNPs/FMN (blue)

Upon UV (peak 385 nm) or blue (peak 480 nm) light irradiation corresponding to S2 and S1 energy bands of FMN molecules, AgNPs/FMN complexes showed minimal changes in the absorption spectra indicating that complexes do not photodegrade appreciably. Addition of fresh FMN molecules to AgNPs/FMN solution and subsequent UV-irradiation has led to disappearing of usual FMN absorption peaks at 378 nm and 445 nm. Instead, new absorption band at a wavelength of 550 nm appeared, which, as we assumed, indicates the formation of AgNPs/FMN complex. This 550 nm band appearance can be attributed to the UV irradiation since blue light irradiation in similar conditions did not lead to the same effect, probably due to less efficient energy transfer between AgNPs and FMN.

A fluorescence peak of FMN was observed to be centered at 535 nm (Fig. 2, *a*, black). After addition of AgNPs/FMN complexes, FMN fluorescence was significantly quenched (Fig. 2, *a*, red). It cannot be attributed to changes of the solution absorption and inner filter effect only (it explains ~20% of decrease) but it can be explained by metal-induced fluorescence quenching [10] which further indicate FMN and AgNPs interaction.

Under light irradiation, FMN tends to decompose to form photoproducts [4]. The absorption spectra (Fig. 2, *b*) demonstrated clearly the formation of lumichrome after irradiation of FMN solution with UV/blue light due to the photolysis of FMN. On the fluorescence spectra it can be identified by its characteristic fluorescence wavelength of 478 nm [11], which was also clearly registered. Addition of AgNPs/FMN complexes clearly changed the dynamics and decreased the amount of lumichrome-related light in fluorescence spectra, likely due to the photoprotective properties of AgNPs.

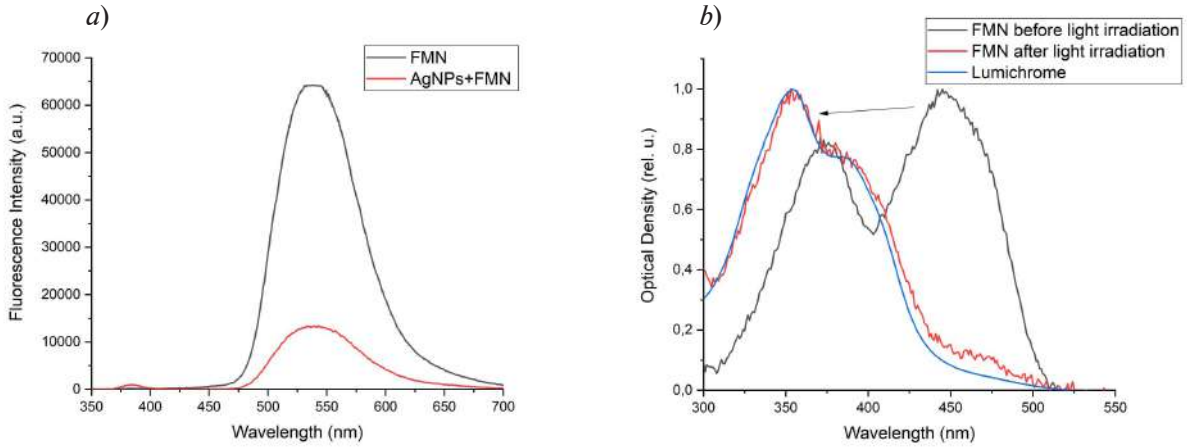

Fig. 2. Fluorescence spectra of FMN and FMN in the presence of AgNPs (*a*) and absorption spectra of FMN before and after light irradiation by a 385 nm diode (*b*)

Conclusion

The formation of a complex between FMN and silver nanoparticles both in the dark and light conditions (under UV/blue non-coherent irradiation) can be monitored by changes in optical properties of the solution (new absorption bands, fluorescence quenching, new luminescence bands). Specifically, these observations strongly suggest that AgNPs/FMN complex can be detected by the appearance of an additional absorption peak at 550 nm, so that tracing its behavior under illumination can give information about the dynamics of the process. Fluorescence of lumichrome indicates that silver nanoparticles can influence photochemistry of FMN which can potentially have a photoprotective effect on FMN, which can be used to enhance the photodynamic therapy performed with FMN (Riboflavin, vitamin B2).

Acknowledgments

The authors express their gratitude to the Priority-2030 program, conducted under the guidance of young promising researchers, the laboratory “Laser Technologies for Biomedical Technologies” of the Moscow State Pedagogical University.

REFERENCES

1. **Youf R., Müller M., Balasini A., et al.**, Antimicrobial photodynamic therapy: Latest developments with a focus on combinatory strategies, Pharmaceutics. 13 (12) (2021) 1995.

2. **Insińska-Rak M., Sikorski M., Wolnicka-Glubisz A.**, Riboflavin and Its Derivates as Potential Photosensitizers in the Photodynamic Treatment of Skin Cancers, Cells. 12 (18) (2023) 2304.

3. **Buchovec I., Vyčaitė E., Badokas K., et al.**, Application of antimicrobial photodynamic therapy for inactivation of *Acinetobacter baumannii* biofilms, International Journal of Molecular Sciences. 24 (1) (2022) 722.

4. **Sheraz M.A., Kazi S.H., Ahmed S., et al.**, Photo, thermal and chemical degradation of riboflavin, Beilstein Journal of organic chemistry. 10 (1) (2014) 1999–2012.

5. **Quick M., Weigel A., Ernsting N.P.,** Fluorescence following excited-state protonation of riboflavin at N (5), The Journal of Physical Chemistry B. 117 (18) (2013) 5441–5447.

6. **Rivas Aiello M.B., Romero J.J., et al.**, Effect of silver nanoparticles on the photophysics of riboflavin: consequences on the ROS generation, The Journal of Physical Chemistry C. 120 (38) (2016) 21967–21975.

7. **Sodha K.H., Jadav J.K., Gajera H.P., Rathod K.J.**, Characterization of silver nanoparticles synthesized by different chemical reduction methods, Int J Pharma Bio Sci. 6 (2015) 199–208.

8. **Mokashi V.V., Walekar L.S., Anbhule P.V., et al.**, Study of energy transfer between riboflavin (vitamin B2) and AgNPs, Journal of Nanoparticle Research. 16 (2291) (2014) 1–11.

9. **Anwar Z., Ali S.A., Shah M.R., et al.**, Photochemical preparation, characterization and formation kinetics of riboflavin conjugated silver nanoparticles, Journal of Molecular Structure. 1289 (2023) 135863.

10. **Murphy S., Huang L., Kamat P.V.**, Charge-transfer complexation and excited-state interactions in porphyrin-silver nanoparticle hybrid structures, The Journal of Physical Chemistry C. 115 (46) (2011) 22761–22769.

11. **Ahmad I., Anwar Z., Sheraz M.I., et al.**, Stability-indicating spectrofluorimetric method for the assay of riboflavin and photoproducts: Kinetic applications, Luminescence. 33 (6) (2018) 1070–1080.

THE AUTHORS

DUSHINA Anastasiia O.
dushina02@gmail.com
ORCID: 0000-0001-8296-6172

KHAYDUKOV Evgeniy V.
khaydukov@mail.ru
ORCID: 0000-0002-3900-2949

STEPANOV Maxim E.
stepanov_me@mail.ru
ORCID: 0000-0002-0332-1235

GENERALOVA Alla N.
a-generalova@yandex.ru
ORCID: 0000-0001-9646-1693

ARZHANOV Artem I.
arzhanov.artyom@gmail.com
ORCID: 0000-0001-9305-067X

Received 31.07.2024. Approved after reviewing 12.08.2024. Accepted 21.08.2024.

Conference materials
UDC: 577.35
DOI: https://doi.org/10.18721/JPM.173.262

Modified natural polymers with bioactive additives for restoration of critical bone defect

M.Yu. Suchkov[1,2]✉, V.I. Kuzyaeva[6], I.S. Sergeev[3,4], G. Babaeva[5], P.A. Demina[2,3,6], A.V. Sochilina[2,3,6], R.A. Akasov[2,3,7], T.V. Egorova[2], E.V. Khaydukov[2,3,6], A.N. Generalova[6]

[1] Pirogov Russian National Research Medical University, Moscow, Russia;

[2] Moscow State Pedagogical University, Moscow, Russia;

[3] National Research Centre "Kurchatov Institute", Moscow, Russia;

[4] Skolkovo Institute of Science and Technology, Moscow, Russia;

[5] Research Institute of Molecular and Cellular Medicine, RUDN University, Moscow, Russia;

[6] Shemyakin-Ovchinnikov Institute of Bioorganic Chemistry RAS, Moscow, Russia;

[7] Sechenov First Moscow State Medical University, Moscow, Russia

✉ max.suchkov3001@yandex.ru

Abstract. A critical bone defect (CBD) is a bone tissue injury that is unable to self-heal and therefore requires tissue engineering approaches. Photocrosslinkable hydrogels based on natural polymers are promising biomaterials for CBD restoration due to their biocompatibility, versatility, and ability to form 3D structures of defined shapes. In this study, UV-photocrosslinkable materials based on hyaluronic acid modified with glycidyl methacrylate were proposed for the formation of hydrogels, which can be used for *in situ* replacement of CBD. It was demonstrated that the obtained hydrogels possess mechanical properties suitable for bone tissue replacement, and the photopolymerization process occurs under mild conditions, ensuring the high viability of mouse mesenchymal stem cells in such hydrogels. The developed technology may be suggested for further investigation of its potential for CBD replacement *in vivo* conditions.

Keywords: critical bone defect, hydrogel scaffolds, biocompatible natural polymers, hyaluronic acid, glycidyl methacrylate, *in situ* photocrosslinking

Funding: The article was prepared as part of the work on the topic "Laser technologies for biomedical applications" (no. 122122600055-2) under the state order of the Ministry of Education of the Russian Federation. The work was financially supported by the Russian Science Foundation, grant 21-79-10384 (*in vivo* polymerization).

Citation: Suchkov M.Yu., Kuzyaeva V.I., Sergeev I.S., Babaeva G., Demina P.A., Sochilina A.V., Akasov R.A., Egorova T.V., Khaydukov E.V., Generalova A.N., Modified natural polymers with bioactive additives for restoration of critical bone defect, St. Petersburg State Polytechnical University Journal. Physics and Mathematics. 17 (3.2) (2024) 306–310. DOI: https://doi.org/10.18721/JPM.173.262

Материалы конференции
УДК 577.35
DOI: https://doi.org/10.18721/JPM.173.262

Модифицированные природные полимеры с биоактивными добавками для восстановления критического костного дефекта

М.Ю. Сучков [1,2]✉, В.И. Кузяева[6], И.С. Сергеев[3,4], Г. Бабаева[5], П.А. Демина[2,3,6], А.В. Сочилина[2,3,6], Р.А. Акасов[2,3,6], Т.В. Егорова[2], Е.В. Хайдуков[2,3,6,7], А.Н. Генералова[3,6]

[1] Российский национальный исследовательский медицинский университет им. Н.И. Пирогова, Москва, Россия;

[2] Московский педагогический государственный университет, Москва, Россия;

[3] Национальный исследовательский центр «Курчатовский институт», Москва, Россия;

[4] Сколковский институт науки и технологий, Москва, Россия;

[5] Научно-исследовательский институт молекулярной и клеточной медицины Российского университета дружбы народов, Москва, Россия;

[6] Институт биоорганической химии им. академиков М.М. Шемякина и Ю.А. Овчинникова РАН, Москва, Россия;

[7] Первый Московский государственный медицинский университет имени И.М. Сеченова, Москва, Россия

✉ max.suchkov 3001@yandex.ru

Аннотация. Критический костный дефект (ККД) — это повреждение костной ткани, не способное к самовосстановлению и поэтому требующее использования подходов тканевой инженерии. Фотосшиваемые гидрогели на основе природных полимеров являются перспективными биоматериалами для восстановления ККД благодаря биосовместимости, универсальности и возможности формирования 3D структур заданной формы. В данной работе были предложены УФ-фотосшиваемые материалы на основе гиалуроновой кислоты, модифицированной глицидилметакрилатом, для формирования гидрогелей, которые могут быть использованы для замещения ККД *in situ*. Было показано, что полученные гидрогели обладают механическими свойствами, подходящими для замещения костной ткани; при этом процесс фотосшивания происходит в мягких условиях, что подтверждает высокая выживаемость мезенхимальных стволовых клеток мыши в таких гидрогелях. Полученная технология может быть предложена для дальнейшего исследования возможности замещения ККД в *in vivo* условиях.

Ключевые слова: критический костный дефект, гидрогелевые каркасы, биосовместимые природные полимеры, гиалуроновая кислота, глицидилметакрилат, *in situ* фотоотверждение

Финансирование: Статья подготовлена в рамках работы по теме «Лазерные технологии для биомедицинских приложений» (№ 2-122122600055) по государственному заданию Министерства просвещения Российской Федерации. Работа была финансово поддержана Российским научным фондом, грант 10384-79-21 (*in vivo* полимеризация).

Ссылка при цитировании: Сучков М.Ю., Кузяева В.И., Сергеев И.С., Бабаева Г., Демина П.А., Сочилина А.В., Акасов Р.А., Егорова Т.В., Хайдуков Е.В., Генералова А.Н. Модифицированные природные полимеры с биоактивными добавками для восстановления критического костного дефекта // Научно-технические ведомости СПбГПУ. Физико-математические науки. 2024. Т. 17. № 3.2. С. 306–310. DOI: https://doi.org/10.18721/JPM.173.262

Introduction

A critical bone defect (CBD), which occurs as a result of trauma, surgery and oncology [1], is a defect that is not capable of self-regeneration [2], and it remains an unsolved issue today. Standard protocols for CBD regeneration based on bioceramics, metals, syngeneic and xenogeneic transplantation, and 3D printed scaffolds need optimization, as they have several disadvantages, including time-consuming scaffold production, possible autoimmune reaction, and low biodegradation. The use of biodegradable scaffolds based on biocompatible natural polymers, such as hyaluronic acid (HA), could be a promising approach [3]. Conjugation with reagents containing double bonds, such as glycidyl methacrylate (GMA), allows the photocrosslinking of hydrogels under the well-controlled and mild conditions [4], that allow loading of bioactive additives and even living cells in the hydrogels [5] for enhanced CBD regeneration. The aim of the current study was to demonstrate UV-photocrosslinkable materials based on HA to form hydrogels *in vitro* that could be further proposed to replace CBD *in vivo*.

Materials and Methods

Hyaluronic acid (HA) was conjugated with vinyl groups through a single-step reaction with glycidyl methacrylate (GMA) according to [4], yielding derivative GMA-HA able to crosslink in the presence of radical initiators. Liquid photocompositions (PCs) were based on 5–20 wt% of GMA-HA and 0.09 wt% lithium phenyl-2,4,6-trimethylbenzoylphosphinate (LAP) as a photoinitiator.

Hydrogel swelling was studied by weighing hydrogel samples, then incubating them in PBS at 37 °C for 30 min, after which the remaining water was removed and the samples were weighed. Two samples of the same composition were measured, and the swelling ratio was determined as the average value between them.

Mesenchymal stem cells (MSC) derived from the adipose tissue of Balb/c mice were mixed with liquid PCs and positioned in the molds (5 mm diameter, 1 mm thickness) followed by 365 nm irradiation (100 mW/cm^2, 5 sec). The hydrogel scaffolds were placed into the complete alpha-MEM for 2 weeks. To assess cell viability within the hydrogel matrix, the MTT assay and Calcein-AM staining were used.

Results and Discussion

It was demonstrated that the swelling ratio of the obtained hydrogels was in function of GMA-HA content, and the lowest swelling ratio was observed in the composition with GMA-HA 20 wt% (Table 1).

It was also found that liquid PCs were toxic to cells in function of GMA content; however, photocrosslinking can reduce the cell death providing about 60% of cell viability (Fig. 1). Apparently, UV radiation did not have a toxic effect on cells due to the short duration of procedure. However, prolonged incubation of cell-laden scaffolds in complete alpha-MEM up to 2 weeks demonstrated the slow decrease of cell viability in comparison to day 1. This could be explained by the dense structure of the hydrogel bulk that prevents physiological cell adhesion and proliferation. The hydrogels that showed the best cell viability (5–10% of GMA-HA) also had a higher swelling ratio (Fig. 2). It could be concluded that a balance between the mechanical properties of the hydrogels (low swelling, low porosity) and cell viability (high swelling, high porosity) should be found.

Table 1

Characteristics of the photocompositions

#	Components			Swelling ratio
1	GMA-HA 20 wt%	LAP 0.09%	MSC ($3 \cdot 10^6$/ml)	14.4%
2	GMA-HA 15 wt%			223.7%
3	GMA-HA 10 wt%			111.8%
4	GMA-HA 5 wt%			230%

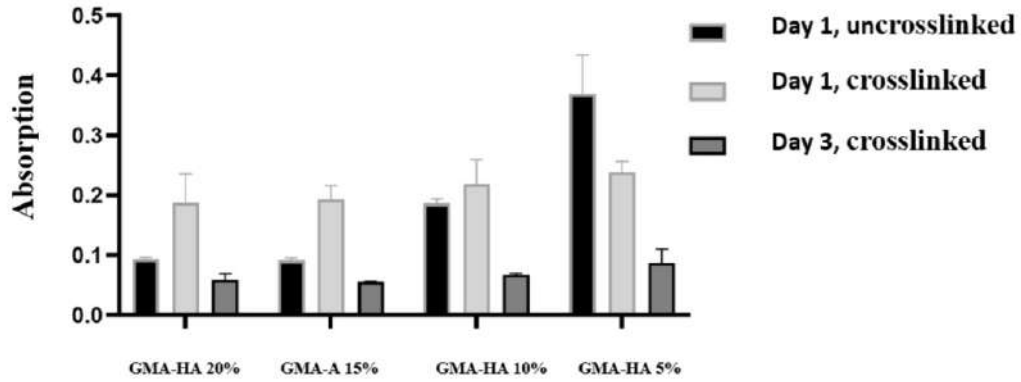

Fig. 1. Cell viability of mesenchymal stem cells in 1 and 3 days after photocrosslinking, MTT assay, data are the mean ± SD

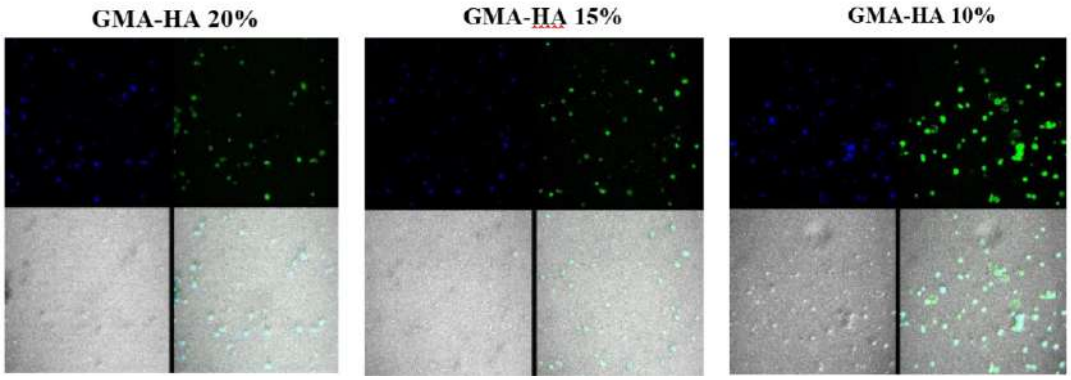

Fig. 2. Photocrosslinked hydrogels, impregnated with mouse MSCs and stained with Calcein AM (live cells, green) and Hoechst 33342 (cell nuclei, blue), 3 days post-photocrosslinking

Conclusions

Photocrosslinked hydrogels, based on UV-photocrosslinkable hyaluronic acid, were proposed and studied. The swelling ratio of the obtained hydrogels was in function of GMA-HA content, and the lowest swelling ratio was observed in the composition with 20% GMA-HA. Liquid photocompositions were toxic to cells in function of GMA content; however, photocrosslinking can reduce the cell death providing about 60% of cell viability. Prolonged incubation of cell-laden scaffolds demonstrated the slow decrease of cell viability in comparison to day 1 due to the high hydrogel density. The proposed UV-photocrosslinkable materials based on HA could be proposed for further research to replace CBD *in vivo*.

REFERENCES

1. **Tan B., Tang Q., Zhong Y., et. al.**, Biomaterial-based strategies for maxillofacial tumour therapy and bone defect regeneration, Int J Oral Sci. 13 (1) (2021) 9.

2. **Schemitsch E.**, Size Matters: Defining Critical in Bone Defect Size, J of Orthopaedic Trauma. 31(10) (2017) 20–22.

3. **Collins M.N., Ren G., Young K., et. al.**, Scaffold Fabrication Technologies and Structure/ Function Properties in Bone Tissue Engineering, Adv. Funct. Mater. 31 (2021).

4. **Sochilina A.V., et. al.**, Preparing Modified Hyaluronic Acid with Tunable Content of Vinyl Groups for Use in Fabrication of Scaffolds by Photoinduced Crosslinking, J of Bioorganic Chemistry. 47 (2021) 828–836.

5. **Chai S., Huang J., Mahmut A., et. al.**, Injectable Photo-Crosslinked Bioactive BMSCs-BMP2-GelMA Scaffolds for Bone Defect Repair, Front Bioeng Biotechnol. 10 (2022).

THE AUTHORS

SUCHKOV Maksim Yu.
max.suchkov3001@yandex.ru
ORCID: 0009-0004-4610-4523

KUZYAEVA Valeriia I.
kuzyaeva.valeriya@mail.ru
ORCID: 0009-0008-5419-5217

SERGEEV Igor S.
sergeev@yandex.ru

BABAYEVA Gulyalek
babaevagulyalek@gmail.com
ORCID: 0000-0001-5781-7925

DEMINA Polina A.
polidemina1207@yandex.ru
ORCID: 0000-0001-6349-2979

SOCHILINA Anastasia V.
ddraig@yandex.ru

AKASOV Roman A.
roman.akasov@gmail.com
ORCID: 0000-0001-6486-8114

EGOROVA Tatiana V.
tatvladegorova@gmail.com

KHAYDUKOV Evgenii V.
khaydukov@mail.ru
ORCID: 0000-0002-3900-2949

GENERALOVA Alla N.
a-generalova@yandex.ru
ORCID: 0000-0001-9646-1693

Received 24.07.2024. Approved after reviewing 08.09.2024. Accepted 08.09.2024.

Conference materials
UDC 612.1.8
DOI: https://doi.org/10.18721/JPM.173.263

Intravital microscopy: dorsal skinfold chamber model

M.E. Stepanov[1]✉, A.A. Vlasov[1], P.A. Demina[1], R.A. Akasov[1]
G. Babayeva[2], A.N. Generalova[3], E.V. Khaydukov[1]

[1] Moscow Pedagogical State University, Moscow, Russia;

[2] Peoples' Friendship University of Russia (RUDN University), Moscow, Russia;

[3] Shemyakin-Ovchinnikov Institute of Bioorganic Chemistry of RAS, Moscow, Russia

✉ stepanov_me@mail.ru

Abstract. Intravital microscopy (IVM) is a great tool to investigate multicellular living organism in all of its natural complexity. It combines precision of light microscopy with an ability to observe physiological processes in real-time of traditional magnetic resonance/computed tomography imaging. In this work we demonstrate effectiveness of self-engineered dorsal skinfold chamber IVM model on examples of brightfield microscopy with passive spectral filtration to study vasculature in mice.

Keywords: IVM, DSC, bioimaging, microcirculation, vasculature

Funding: The study was prepared as part of the work on the topic "Laser technologies for biomedical applications" (№ 122122600055-2) under the state order of the Ministry of Education of the Russian Federation.

Citation: Stepanov M.E., Vlasov A.A., Demina P.A., Akasov R.A., Babayeva G., Generalova A.N., Khaydukov E.V., Intravital microscopy: dorsal skinfold chamber model, St. Petersburg State Polytechnical University Journal. Physics and Mathematics. 17 (3.2) (2024) 311–315. DOI: https://doi.org/10.18721/JPM.173.263

Материалы конференции
УДК 612.1.8
DOI: https://doi.org/10.18721/JPM.173.263

Прижизненная микроскопия: модель камеры дорсальной кожной складки

М.Е. Степанов[1]✉, А.А. Власов[1], П.А. Дёмина[1], Р.А. Акасов[1],
Г. Бабаева[2], А.Н. Генералова[3], Е.В. Хайдуков[1]

[1] Московский педагогический государственный университет, Москва, Россия;

[2] ФГАОУ ВО «Российский университет дружбы народов», Москва, Россия;

[3] Институт биоорганической химии им. академиков М.М. Шемякина и Ю.А. Овчинникова РАН, Москва, Россия

✉ stepanov_me@mail.ru

Аннотация. Интравитальная микроскопия (ИВМ) – группа методов для исследования многоклеточных живых организмов во всей их природной сложности. Она сочетает в себе точность световой микроскопии и возможность видеть физиологические процессы в реальном времени, присущую магнитно-резонансной или компьютерной томографии. В данной работе мы демонстрируем эффективность дорсальной камеры на кожной складке как модели для интравитальной микроскопии на примере изучения сосудистой сети мышей с использованием светлопольной микроскопии с пассивной спектральной фильтрацией.

Ключевые слова: микроскопия живых систем, дорсальная кожная складка, биоимиджинг, микроциркуляция, сосудистая сеть

Финансирование: Исследование подготовлено в рамках выполнения работы по теме «Лазерные технологии для биомедицинских применений» (№ 2-122122600055) по государственному заказу Министерства образования Российской Федерации.

Ссылка при цитировании: Степанов М.Е., Власов А.А., Дёмина П.А., Акасов Р.А., Бабаева Г., Генералова А.Н., Хайдуков Е.В. Прижизненная микроскопия: модель камеры дорсальной кожной складки // Научно-технические ведомости СПбГПУ. Физико-математические науки. 2024. Т. 17. № 3.2. С. 311–315. DOI: https://doi.org/10.18721/JPM.173.263

Introduction

Intravital microscopy (IVM) is a group of methods that allows the study of in cells and tissues within living organisms under physiological conditions. This enables the evaluation of complex biological processes such as angiogenesis and the inflammatory response. Furthermore, IVM provides a higher resolution than other intravital studies, including computed tomography (CT) and magnetic resonance imaging (MRI). One of the models that is used in IVM is the dorsal skinfold chamber (DSC).

The DSC model has a wide range of applications, including tumor growth [1], wound healing [2], material biocompatibility [3] and other studies. The chamber is composed of two identical parts, glass to cover window and retaining rings. The first version of DSC was originally made of titanium and had a mass comparable to a fifth of the weight of a mouse [4]. Currently, there are a number of polymer models that can be characterized as lightweight [5, 6]. The administration of polymers results in a reduction of stress levels in mice and an increase in the chamber's resistance to tilting.

The scattering of light by body tissues such as skin and fat renders it impossible to achieve the desired spatial resolution without surgical preparation of the chamber.

The preparation method for dorsal skinfold depends on the purpose of research, the most common way includes steps of hair removal with subsequent skin layers (epidermis, dermis and subcutaneous tissue) resection in order to expose underlying muscle and its blood vessels.

Once the dorsal chamber has been prepared, it can be employed to investigate the process of interest using transillumination microscopy or epi-illumination fluorescence microscopy. Transillumination microscopy enables the analysis of vessel diameter and functional vessel density, whereas fluorescence microscopy is employed for the study of distinct cellular or molecular aspects.

In this study, we employed a self-constructed polymer lightweight DSC and transillumination microscopy to demonstrate the efficacy and accessibility of IVM studies on this model.

Materials and methods

Mice belonging to the BALB/c strain were employed in this experiment. Prior to undergoing the operation, the mice were anaesthetized with a combination of xylazine administered via intramuscular injection and Zoletil administered subperitoneally.

Following the administration of anesthesia, the hair was removed from the mice using a trimmer and depilatory cream. A line was then drawn along the spine in order to ensure the correct orientation of the chamber components.

The chamber was secured to the retracted skin fold by means of simple knotted sutures. Subsequent to the fixing of the camera, the skin and subcutaneous fatty tissue were excised from the chamber on one side. Both sides of the chamber were subsequently covered with glass.

Following surgical intervention, mice were allocated to individual cages to prevent chamber chewing.

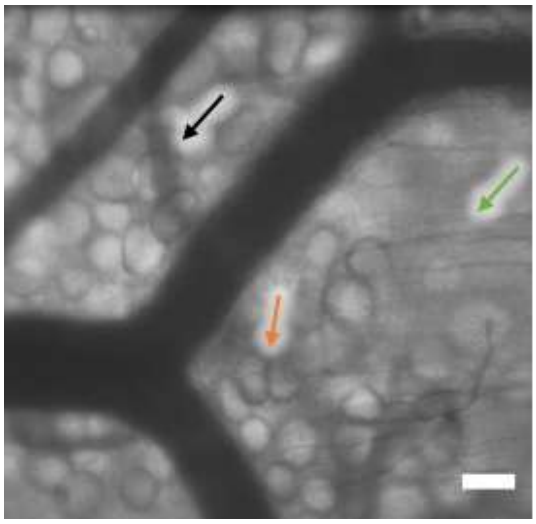

Fig. 1. IVM image of mouse DSC window tissues made with our model
Scale bar is 100 μm

Following a two-day period of rest, the mice were anaesthetized once more and placed in a specially designed microscope table. This table allows the mouse to be securely fixed during the experiment and increases the stability of the image in the field of view of the microscope. Mice were examined using the fluorescent microscope Motic AE31E. White Halogen illumination (Koehler setup) was used to perform brightfield studies, in some cases we've used bandpass filters to restrict the spectral range Detected with Raptor Photonics Camera (digital FALCON EMCCD FA285-CL). In each case the objectives were lifted using special spacers to compensate for the lifting of the DSC window above the height of microscope table. Images were processed with ImajeJ software when necessary.

Results and Discussion

Our self-made DSC model has allowed performing good quality imaging of biological tissues even using the simplest brightfield setup. Fig. 1 shows microscopic image made with 20x objective, where vessels of several diameters (including parallel muscle capillaries, green arrow) can clearly be seen. Along with them, adipose tissue can be seen clearly (orange arrow). More deep vessels are seen as silhouettes (black arrow) mostly because of adipose tissue scattering.

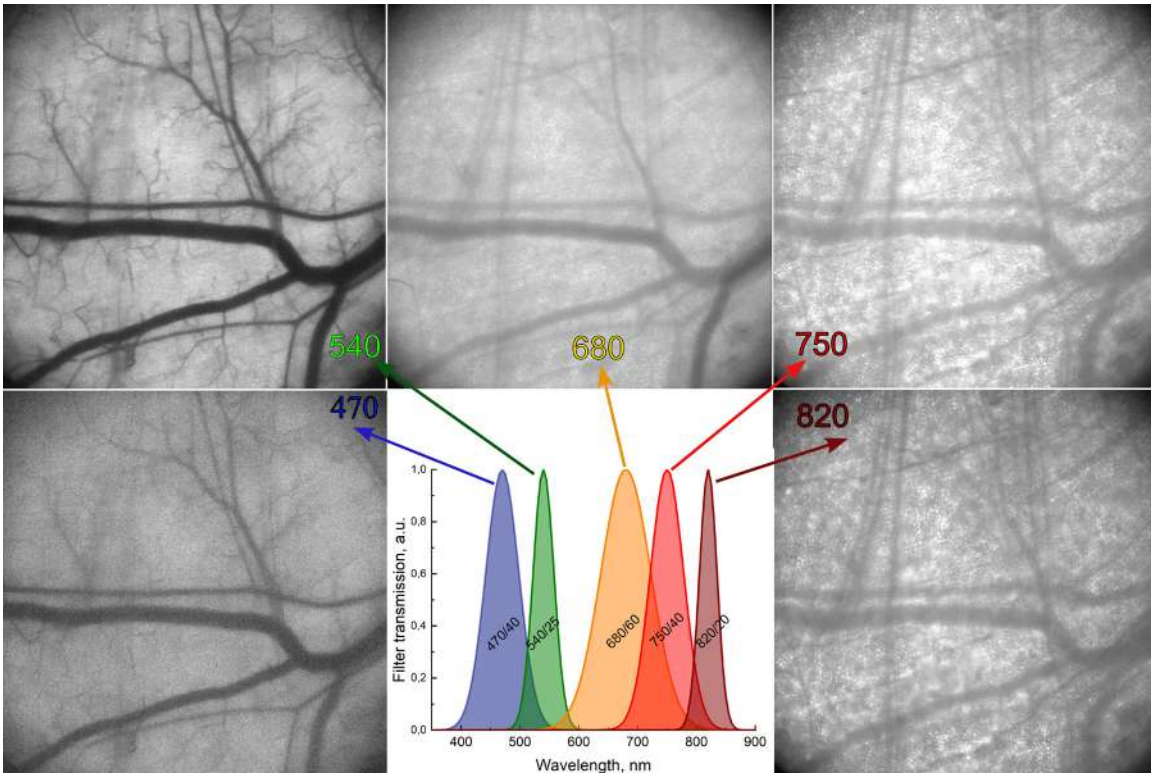

Fig. 2. Widefield microscopic images of the same spot within dorsal skinfold chamber recorded (objective 4×) in similar conditions except for the spectral region (approximate spectral range of filters used is shown in the middle). The pictures are post-processed in similar way in ImageJ to enhance contrast. Notation 540/25 means 540 nm centered band of half width 25 nm

It was interesting to check if choosing the appropriate illumination conditions (using our DSC model without dye injection) we can influence the imaging mode considering complexness of tissue constitution. To check this, we've chosen a representative spot within dorsal skinfold chamber and recorded it in similar conditions at 4× magnification but different spectral regions within our camera-related limits (using corresponding optical filters in front the camera). Spectral regions and results are shown in Fig. 2. As it can clearly be seen from Fig. 2, there are several spectrum-related differences in contrast of different tissues. Namely, the structure of adipose tissue pictured as a dense mesh on the background of blood vessels is getting clearer when we approach IR wavelengths, revealing some underlying pattern of deeper tissues, whereas the vessels and blood tend to be less clearly seen: their contrast fades when we approach near-IR. It can be partially attributed to changed balance between absorbance of the blood and scattering of the various background tissues.

To give the observations some firm numerical ground we've calculated diameters and signal-to-noise ratios of the same middle-diameter vessel at position shown in yellow at Fig. 3, *a* for 5 spectrum-related images shown previously in Fig. 2 (original camera images were used). As can be seen from Fig. 3, *b* signal-to noise ratio for the case of green light (540/25) is above 3, whereas all the others are much poorer, the worst being 470/40 nm. The results cannot be attributed to the camera quantum efficiency since it is 40–60% for all regions nor to the spectral width (820/20 would be best otherwise), nor to the absorbance of hemoglobin since it absorbs in 470/40 almost as well.

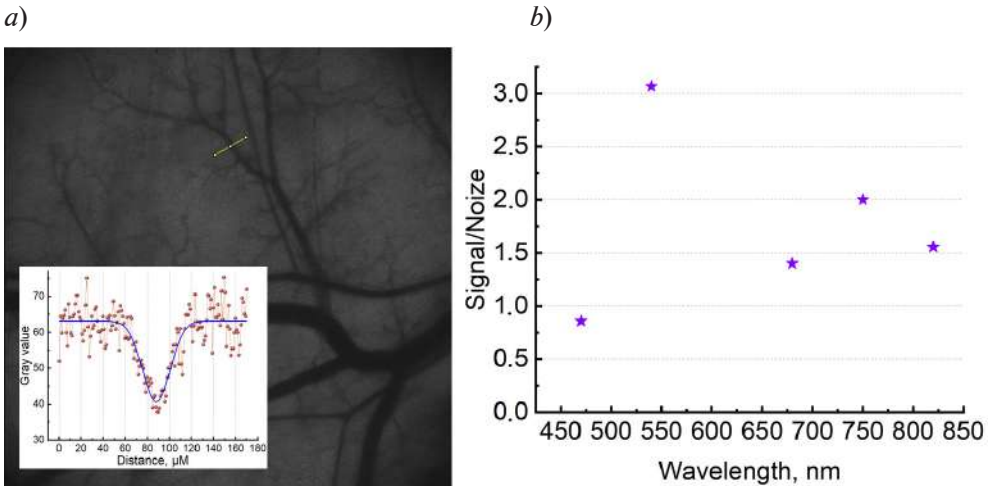

Fig. 3. Non-processed IVM image of 540/25 nm case, where vessel diameter was calculated at yellow line position, plot is shown at inset (*a*); signal-to-noise ratios for different spectral ranges (*x* axis is central wavelength) (*b*)

Vessel diameter was calculated from gaussian approximations of vessel brightness taken from line plot profile (see inset of Fig. 3, *a*) according to [7]. The results are 28±8, 29.3±2, 40±10, 35±8, 40±8 μm for 470, 540, 680, 750, 820 nm, respectively, so that they all give more or less the same value although close to IR regions tend to increase diameter due to low signal-to-noise ratios (the accuracy of gaussian approximation correlates with signal-to-noise ratios as well). We note that using the same method in appropriate spectral region we can reliably evaluate capillaries with diameters up to ~7 μm, which are almost as small as mouse can possibly have, as well as to image a transport within them.

Conclusion

We have prepared the self-engineered DSC IVM model and tested it in brightfield mode using different spectral ranges. We can conclude that: 1) model allows studying physiology of biological tissues with good spatial and temporal resolution; 2) the resulted tissue (blood vessel) contrast is a complex interrelated function of many different factors, yet passive spectral light filtration can be used to change contrast of images made in brightfield setup. The model has a good potential to be developed further and used to study tissue biology and light-tissue interaction.

REFERENCES

1. **Ossandon M.R., Sorg B.S., Phatak D.S., Kalpakis K.,** Evaluation of Tumor Development Using Hemoglobin Saturation Profile on Rodent Dorsal Window Chamber, Methods Mol. Biol. 2393 (2022) 179–206.

2. **Strüder D., Lachmann C., van Bonn S.M., et al.**, The Dorsal Skinfold Chamber as a New Tympanic Membrane Wound Healing Model: Intravital Insights into the Pathophysiology of Epithelialized Wounds, Eur Surg Res. 64 (2) (2023) 286–300.

3. **Später T., Frueh F.S., Metzger W., et al.**, In vivo biocompatibility, vascularization, and incorporation of Integra(®) dermal regenerative template and flowable wound matrix, J Biomed Mater Res B Appl Biomater. 106 (1) (2018) 52–60.

4. **Laschke M.W., Menger M.D.,** The dorsal skinfold chamber: A versatile tool for preclinical research in tissue engineering and regenerative medicine, Eur Cell Mater. 32 (2016) 202–215.

5. **Seynhaeve A.L.B., Ten Hagen T.L.M.,** An adapted dorsal skinfold model used for 4D intravital followed by whole-mount imaging to reveal endothelial cell-pericyte association, Sci Rep. 11 (1) (2021) 1–14.

6. **Xie W., Lorenz M., Poosch F., et al.**, 3D-printed lightweight dorsal skin fold chambers from PEEK reduce chamber-related animal distress, Sci Rep. 12 (1) (2022) 1–10.

7. **Honkura N., Richards M., Lavica B., et al.**, Intravital imaging-based analysis tools for vessel identification and assessment of concurrent dynamic vascular events, Nature Communications. 9(1) (2018) 1–10.

THE AUTHORS

STEPANOV Maxim E.
stepanov_me@mail.ru
ORCID: 0000-0002-0332-1235

BABAYEVA Gulyalek
babaevagulyalek@gmail.com
ORCID: 0000-0001-5781-7925

VLASOV Alexander A.
vlasov.sasha2015@yandex.ru
ORCID: 0000-0003-3899-3928

GENERALOVA Alla N.
a-generalova@yandex.ru
ORCID: 0000-0001-9646-1693

DEMINA Polina A.
polidemina1207@yandex.ru
ORCID: 0000-0001-6349-2979

KHAYDUKOV Evgenii V.
khaydukov@mail.ru
ORCID: 0000-0002-3900-2949

AKASOV Roman A.
roman.akasov@gmail.com
ORCID: 0000-0001-6486-8114

Received 26.07.2024. Approved after reviewing 26.08.2024. Accepted 02.09.2024.

Conference materials
UDC 539.192
DOI: https://doi.org/10.18721/JPM.173.264

Scattering of ultrashort laser pulses on pseudoknots RNA

A.A. Kharlamova✉

Northern Arctic Federal University named after M.V. Lomonosov, Arkhangelsk, Russia

✉ Kharlamova.anastasya2015@yandex.ru

Abstract. The paper theoretically models the scattering spectra of ultrashort laser pulses on an RNA pseudonode and considers the possibility of using the obtained data in genome analysis. Several configurations of pseudo-RNA nodes were selected as a sample for theoretical modeling of the interaction of a laser pulse with matter: a hairpin, a double loop, and a spiral junction. The study of such structures is interesting for the analysis of the DNA genome, as well as for the study of functions such as viral replication, RNA splicing and RNA editing. At the moment, the study of such structural features is difficult, existing methods cannot give an accurate result, especially on long sections of the molecule. In this paper, the interaction of an ultrashort laser pulse with a molecule of four variants is theoretically modeled, when the RNA does not have a pseudonode and when there are hairpins and loops in the structure. The results obtained show the expediency of using laser pulses as a method for determining such structures.

Keywords: Ultrashort laser pulses, scattering spectrum, pseudoknots, DNA, RNA

Funding: The research was supported by the state task of the Russian Federation FSRU-2024-0005.

Citation: Kharlamova A.A., Scattering of ultrashort laser pulses on pseudoknots RNA, St. Petersburg State Polytechnical University Journal. Physics and Mathematics. 17 (3.2) (2024) 316–320. DOI: https://doi.org/10.18721/JPM.173.264

Материалы конференции
УДК 539.192
DOI: https://doi.org/10.18721/JPM.173.264

Рассеяние ультракоротких лазерных импульсов на псевдоузлах РНК

А.А. Харламова✉

Северный Арктический федеральный университет им. М.В. Ломоносова, г. Архангельск, Россия

✉ Kharlamova.anastasya2015@yandex.ru

Аннотация. В работе моделируются спектры рассеяния ультракоротких лазерных импульсов на псевдоузле РНК и рассматривается возможность использования полученных данных при анализе генома. В качестве образца для теоретического моделирования взаимодействия лазерного импульса с веществом было выбрано несколько конфигураций узлов РНК: шпилька, двойная петля и спиральное соединение. Полученные результаты показывают целесообразность использования лазерных импульсов в качестве метода определения таких структур.

Ключевые слова: ультракороткие лазерные импульсы, спектр рассеяния, псевдоузлы, ДНК, РНК

Финансирование: Работа выполнена в рамках Государственного задания FSRU-2024-0005.

Ссылка при цитировании: Харламова А.А., Рассеяние ультракоротких лазерных импульсов на псевдоузлах РНК // Научно-технические ведомости СПбГПУ. Физико-математические науки. 2024. Т. 17. № 3.2. С. 316–320. DOI: https://doi.org/10.18721/JPM.173.264

Introduction

Pseudoknotes of RNA are molecular structures whose main function is the regulation of gene expression and protein synthesis. The molecule is formed by folding onto itself and contains two rod-loop structures that are closed by pairing complementary nucleotides inside the RNA chain. Pseudonodes are interesting for their functions in various biological processes. They affect the stability of RNA, the efficiency of its translation in protein, and the processes of ribosome modification. That is why it is important to search for RNAs containing pseudoknotes in the components of the genome. The main way to predict pseudoknotes are statistical methods and standard methods of minimizing free energy. The main disadvantage of these methods is that such algorithms consider the interaction between closely spaced nucleotides, whereas the formation of a pseudoknotes occurs when nucleotides interact far from each other [1–3]. There are various ways to improve dynamic programming algorithms for finding pseudoknotes, but there is no basic method that could satisfy researchers yet. In this paper, we propose the use of X-ray diffraction analysis data for the study of pseudoknotes RNA [4, 5]. The scattering spectra from various RNA configurations with pseudoknotes in the structure are calculated (Fig. 1). The obtained spectra show that the proposed approach can detect a node in a molecule and distinguish it from similar ones.

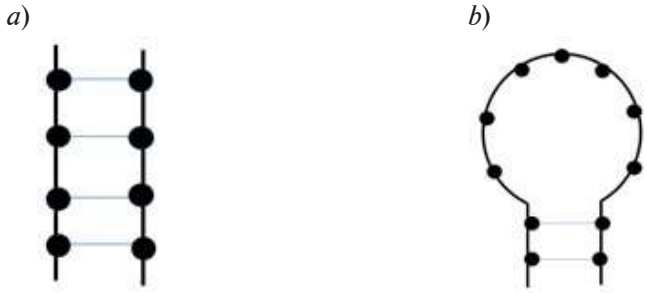

Fig. 1. RNA models for theoretical modeling of the scattering spectrum: RNA without pseudoknotes (*a*); pseudoknotes of the RNA hairpin (*b*)

Materials and Methods

The article proposes to consider the DNA molecule as a polyatomic system on which an ultrashort laser pulse falls. The modeling of the scattering spectrum is based on the Dirac-Hartree-Fock-Slater model [6, 7].

RNA is represented here as a molecule consisting of a set of nitrogenous bases. The defect of the object, namely the pseudoknot, is not on the atomic scale, but on the scale of a single nitrogenous base, therefore, to simplify the calculation, scattering on each atom is not considered here. Let an ultrashort laser pulse in the n_0 direction fall on the RNA molecule. The duration of such a pulse τ is many times less than the characteristic atomic time τ_a. Here, the quantum theory of USP scattering is used to calculate the main scattering characteristics, in which there are no restrictions on the number of atoms in the system [8]. In this theory, general expressions are obtained for calculating the main scattering characteristics. Here, an expression is used to calculate the scattering energy ε per unit solid angle $\Omega_{\mathbf{k}}$ ($\mathbf{k} = (\omega/c)\cdot\mathbf{n}$), where $\mathbf{n}$ is the direction of the scattered pulse) in one frequency range ω (hereinafter referred to as the spectrum).

$$\frac{d^2\varepsilon}{d\Omega_{\mathbf{k}} d\omega} = \frac{[\mathbf{E}_0\mathbf{n}]^2}{(2\pi)^2} \frac{\left|\tilde{h}(\omega)\right|^2}{c^3} \left\langle \sum_{i=1}^{s} N_{e,i} N_{A,i} \left(1 - \left|F_i\right|^2\right) + \sum_{i,j=1}^{s} \delta_{i,j} N_{e,i} N_{e,j} F_i F_j^* \right\rangle, \quad (1)$$

where $N_{e,i}$ is the number of electrons in the atom of the *i*-variety; $N_{A,i}$ is the number of atoms of the *I*-variety; $\mathbf{E}_0$ is the field amplitude; $\tilde{h}(\omega) = \int_{-\infty}^{+\infty} h(\eta) e^{i\omega\eta} d\eta$ and $\mathbf{p} = (\omega/c)\cdot(\mathbf{n} - \mathbf{n}_0)$ has the value of the recoil pulse when the USP is scattered on the bound electron.

$F_i = \frac{1}{N_{e,i}} \int \rho_{e,i}(\mathbf{r}) e^{-i\mathbf{pr}} d^3\mathbf{r} = 1$ is also used here, which is a form factor of the atom of the *i*-variety with an electron density $\rho_{e,i}(\mathbf{r})$. Coefficient $\delta_{i,j} = \sum_{Ai,A'j} e^{-i\mathbf{p}(\mathbf{R}_{Ai} - \mathbf{R}_{A'j})}$ depends only on the coordinates of atoms of the *i* -variety (with *Ai* number), the position of which is determined by the radius vector $\mathbf{R}_{Ai}$. Equation (3) is analytical, which contributes to a fairly simple calculation of spectra. The calculation of the electron density is difficult here. To find it, we use the method described in [9–10]. Since each atom is not considered separately here, and the molecule is considered to be a set of nitrogenous bases, the electron density for all bases has been replaced by carbon, as the most frequent atom included in RNA (Fig. 2).

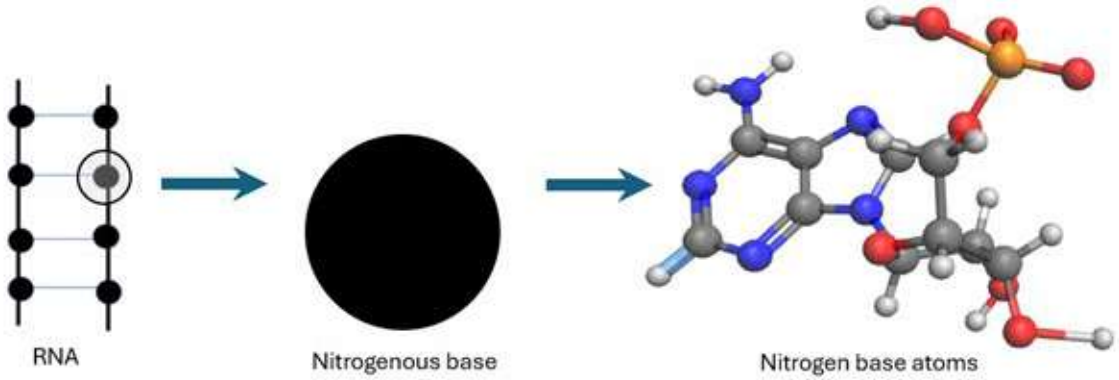

Fig. 2. Way to simplify RNA model for calculation

Results and Discussion

As a result of mathematical modeling of the interaction of an ultrashort laser pulse with various RNA configurations, radiation spectra were obtained, the analysis of which confirms the effectiveness of using laser pulses in studies of similar structures. The scattering spectra from various RNA configurations with pseudoknotes in the structure are calculated. The obtained spectra show that the proposed approach can detect a node in a molecule and distinguish it from similar ones (Fig. 3).

The pulse falls on the system at an angle $\theta_0 = 45°$, θ the angle between the spiral axis and the scattering direction **n**, ϕ is the angle between the *x* axis and the projection **n** onto a plane perpendicular to the spiral axis (spherical coordinates).

As can be seen from the contour plots of the scattering spectra modeling, the results are very similar. The defect in the form of a pseudoknote is really difficult to recognize, but nevertheless the scattering spectra show differences by which changes in the structure of the sample under consideration can be recorded. As can be seen in the first graph, the radiation intensity from the first model is higher, this is indicated by bright spots above and below the central spot.

The differences are more clearly visible on 3D models of the scattering spectra. The number of nitrogenous bases of the first and second models are the same, while the 3D spectra of the RNA models differ in shape. This shows that the location of the nitrogenous bases influenced the results of the interaction of ultrashort pulses with the molecule.

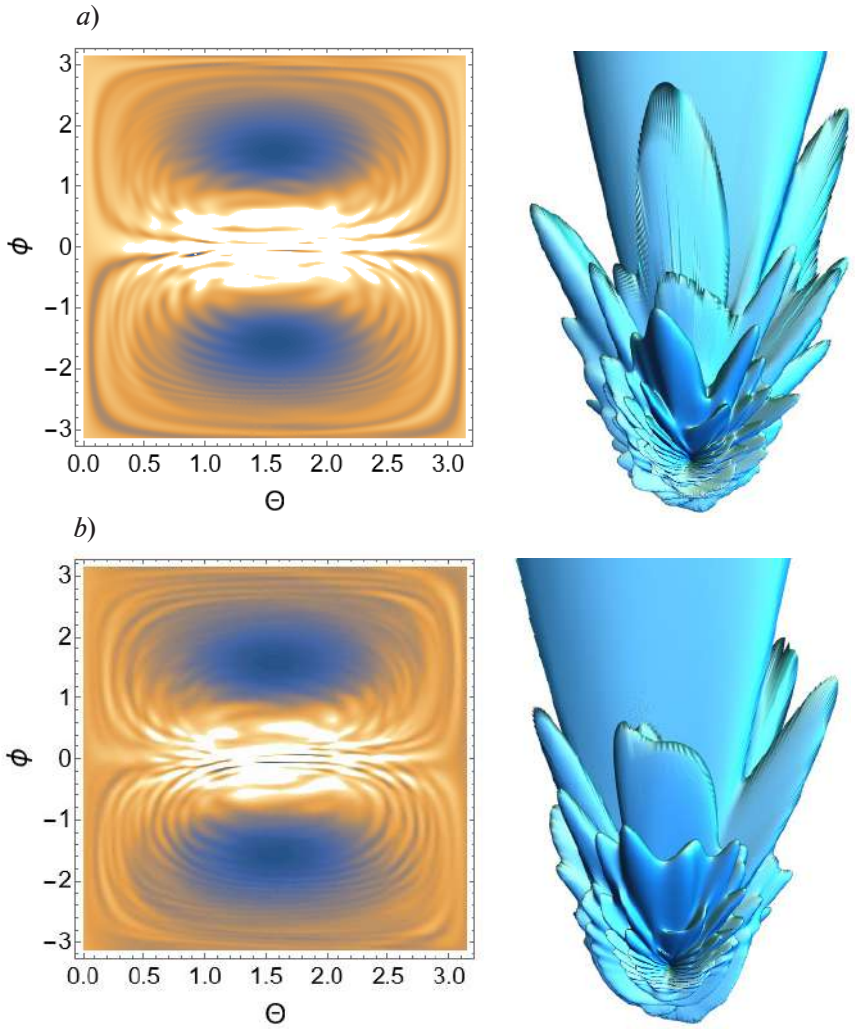

Fig. 3. Perfect DNA fragment: modeling of scattering spectrum from RNA without pseudoknote (*a*), contour graph on the left, 3D model of spectrum on the right; simulation of scattering spectrum from pseudoknote RNA (*b*), contour graph on the left, 3D model of spectrum on the right

Conclusion

After analyzing the obtained spectra, we can conclude that the ultrashort pulse method is applicable for studies of changes in the structure of DNA and RNA within several atomic distances.

Acknowledgments

The author expresses gratitude to his supervisor Makarov Dmitry Nikolaevich for significant comments and important advice during the research and the design of this work.

REFERENCES

1. **Staple D.W., Butcher S. E.**, Pseudoknots: RNA Structures with Diverse Functions. PLoS Biology. (3) (2005).

2. **Griffiths-Jones S.,** Annotating Noncoding RNA Genes. Annual Review of Genomics and Human Genetics. (8) (2007) 279–298.

3. **Yuan C., Sun Y.,** Efficient known ncRNA search including pseudoknots. BMC Bioinformatics. (14) (2013).

4. **Shigaev A.S., Ponomarev O.A., Lakhno V.D.,** Theoretical and experimental studies of open states of DNA, Mathematical Biology and Bioinformatics: Physics and Mathematics. 8 (2) (2013) 553–664.

5. **Suryanarayana C., Norton M.**, X-Ray Diffraction: Springer Science & Business Media. 2013.

6. **Makarov D.N., Kharlamova A.A.,** Scattering of X-ray Ultrashort Pulses by Complex Polyatomic Structures: J. Mol. Sci. 23 (1) (2022) 163.
7. **Makarov D.N., Kharlamova A.A.,** Peculiarities of Scattering of Ultrashort Laser Pulses on DNA and RNA Trinucleotides: J. Mol. Sci. 23 (23) (2022) 15417.
6. **Makarov D.N., Kharlamova A.A.,** Scattering of X-ray Ultrashort Pulses by Complex Polyatomic Structures: J. Mol. Sci. 23 (1) (2022) 163.
7. **Makarov D.N., Kharlamova A.A.,** Peculiarities of Scattering of Ultrashort Laser Pulses on DNA and RNA Trinucleotides: J. Mol. Sci. 23 (23) (2022) 15417.
8. **Makarov D.N., Makarova K.A., Kharlamova A.A.,** Specificity of scattering of ultrashort laser pulses by molecules with polyatomic structure: Scientific Reports. 12 (1) (2022) 4976.
9. **Makarov D.N.,** Quantum theory of scattering of ultrashort electromagnetic field pulses by polyatomic structures. Opt. Express. 27 (22) (2019) 31989–32008.
10. **Kharlamova A.A., Makarov D.N.,** Peculiarity of electron density calculation during interaction of ultrashort laser pulse with nitrogenous base of DNA molecule adenine, St. Petersburg State Polytechnical University Journal. Physics and Mathematics. 15 (3.2) (2022) 291–295.

THE AUTHOR

KHARLAMOVA Anastasya A.
kharlamova.anastasya2015@yandex.ru
ORCID: 0000-0002-8192-615X

Received 26.07.2024. Approved after reviewing 05.08.2024. Accepted 05.08.2024.

Conference materials
UDC 53.082.539
DOI: https://doi.org/10.18721/JPM.173.265

Express kidney monitoring method for early detection of kidney damage

V.D. Vakorina✉, G.V. Stepanenkov

Bonch-Bruevich Saint-Petersburg State University of Telecommunications, Saint-Petersburg, Russia

✉ cementary.ley@gmail.com

Abstract. A new method for monitoring the state of urine has been developed, which allows to determine the density ρ_m, osmolarity O_s and the size of protein compounds D_b in real time with high accuracy. Modernization of the mobile refractometer design to implement this method to provide measurement of biological solution sample parameters with a single instrument. Providing ease of operation and maintenance, high accuracy of measurements, application without pre-calibration of the scale after each switching on. The results of determination of density, osmolarity, size of protein compounds and total number of solid particles by measured refractive indices n at different wavelengths were compared with the results of measurements on other devices and confirmed the reliability of the developed method. The parameters of human urine, by which it is possible to establish kidney disease at an early stage with high probability, were determined.

Keywords: refraction, express method, refractive index, laser radiation, wavelength, urine

Citation: Vakorina V.D., Stepanenkov G.V., Express kidney monitoring method for early detection of kidney damage, St. Petersburg State Polytechnical University Journal. Physics and Mathematics. 17 (3.2) (2024) 321–325. DOI: https://doi.org/10.18721/JPM.173.265

Материалы конференции
УДК 53.082.539
DOI: https://doi.org/10.18721/JPM.173.265

Метод экспресс-мониторинга почек для раннего выявления их повреждения

Д.В. Вакорина✉, Г.В. Степаненков

Санкт-Петербургский государственный университет телекоммуникаций им. проф. М.А. Бонч-Бруевича, Санкт-Петербург, Россия

✉ cementary.ley@gmail.com

Аннотация. Разработан новый метод мониторинга состояния мочи, позволяющий с высокой точностью определять плотность ρ_m, осмолярность O_s и размер белковых соединений D_b в реальном времени. Модернизация конструкции мобильного рефрактометра для реализации данного метода с целью обеспечения измерения параметров пробы биологического раствора с помощью одного прибора. Обеспечение простоты эксплуатации и обслуживания, высокая точность измерений, применение без предварительной калибровки шкалы после каждого включения. Результаты определения плотности, осмолярности, размера белковых соединений и общего количества твердых частиц по измеренным показателям преломления n при различных длинах волн сравнили с результатами измерений на других приборах и подтвердили достоверность разработанного метода. Определены параметры мочи человека, по которым с высокой вероятностью можно установить болезнь почек на ранней стадии.

Ключевые слова: рефракция, экспресс-метод, показатель преломления, лазерное излучение, длина волны, моча

Ссылка при цитировании: Вакорина Д.В., Степаненков Г.В. Метод экспресс-мониторинга почек для раннего выявления их повреждения // Научно-технические ведомости СПбГПУ. Физико-математические науки. 2024. Т. 17. № 3.2. С. 321–325. DOI: https://doi.org/10.18721/JPM.173.265

Introduction

In the modern world, a number of diseases progress in people for various reasons, among which kidney disease is one of the first [1, 2]. Various methods and methods, as well as devices for their realization have been developed for its detection, as well as for the control of kidney condition during the course of treatment [3–5]. The methods and devices for express control of human urine parameters (e.g., test strips, urine density meter or portable osmometer) are mostly simple in operation. These methods and devices have a number of disadvantages that lead to large measurement errors, which reduce the reliability of conclusions about the state of the kidneys based on the results obtained. It should be noted that almost all studies conducted by medical professionals have shown that the earlier kidney damage is detected, the more effective and successful will be the course of their treatment [1, 2, 5, 7]. Monitoring the dynamics of kidney condition during their treatment shows how effective and correct it is. This makes it possible to promptly change the course of kidney treatment without wasting time and causing additional harm to the body by using ineffective drugs.

Materials and Methods

Experience with various analytical instruments has shown that one possible solution to this noted difficult problem is refractometric measurements [8–9]. These measurements are actively used to control various products: water and other. In various models of mobile refractometers in the control of liquid media can obtain an error of refractive index measurement of about 0.00005. In the case of urine examination there is one peculiarity - the dependence of refractive index n change on T is required. It is extremely difficult to provide this in many mobile refractometer designs. Early stage kidney disease is determined by measuring 3 parameters of human urine: total solids D_b, specific gravity ρ_m, osmolarity O_s [2, 4]. We propose to link urine refractive indices and refractive index measurements to 3 urine parameters by which physicians diagnose early kidney disease.

In the special design of refractometer developed for our method on the basis of model SNEL-105 with our participation on the basis of NPF Poliservice, the possibility of conducting studies of n from temperature is realized. Fig. 1 shows the appearance of a mobile refractometer for express control of urine and other liquid media and a classic version of a small-size refractometer with a

Fig. 1. Two refractometers: small-size and mobile (measuring distilled water)

size reference. As an example, both instruments are tested on distilled water. The digital panels show the results of these measurements and the error. For express control, a measurement error of 0.0001 is sufficient to unambiguously determine the condition of the medium. In our research the measurement error is smaller, amounting to 0.00005.

Currently, in the world, based on data from various studies, the assessment of kidney status (disease) by urinalysis in clinical settings is carried out using Table 1.

Table 1

Interval of basic human urine values for assessment of kidney disease status

State of renal function	Refractive index	Total solids N_b, g/100 g	Specific gravity ρ_m, 20/20	Osmolarity O_s, Os/l
Normal	1.3415–1.3464	5.4–8.5	1.022–1.035	0.80–1.30
Moderate disease	1.3374–1.3396	2.8–4.2	1.011–1.017	0.40–0.60
Severe disease	< 1.3374	< 2.8	< 1.011	< 0.40
Above normal	1.3464–1.3489	8.5–10	1.035–1.040	1.30–1.45

Results and Discussion

For validity and reliability of the data obtained using the method developed by me, the results of studies of a group of volunteer patients, which were aimed at determining their kidney disease at an early stage (Table 2), are presented in the paper as an example. The data for O_s, Nb and ρ_m in Table 2 are plotted according to the graduation relationships we obtained from the refractive index measurements at different wavelengths with a measurement error of 0.00005. The error of determination of O_s, D_b and ρ_m is not more than 1% (therefore in all our researches the error of 1% is used to exclude additional questions).

Table 2

Results of study of patient urine samples and model solutions at temperature $T = 20$ °C

Sample	Refractive index at 3 values of λ			Urine Osmotic Pressure	Urine Specific Gravity	Urine Total Solids
	436.4 nm	589.3 nm	657.2 nm	mOsm/l	g/ml	%vol
Patient 1	1.34647	1.33900	1.33707	714	1.0171	3.97
Patient 2	1.34691	1.33945	1.33751	762	1.0185	4.26
Patient 3	1.34868	1.34112	1.33916	943	1.0235	5.33
Patient 4	1.34941	1.34186	1.33994	1022	1.0256	5.81
Patient 5	1.34768	1.34018	1.33824	841	1.0207	4.73
Patient 6	1.34785	1.34035	1.33845	861	1.0212	4.85
Patient 7	1.35014	1.34264	1.34075	1103	1.0278	6.26
Patient 8	1.34478	1.33739	1.33548	537	1.0121	2.92

This is one of the variants of results, of which we have a lot, studies were conducted on more than 200 volunteers. This database according to all accepted norms is sufficient to make preliminary conclusions about the work of the method.

Analyzing the results obtained in Table 2 allows the doctor to assume the presence of kidney disease at an early stage in patient 1. Patient 8 suffers from kidney disease, which is confirmed by clinical tests. These data once again confirm the adequacy of the method we have developed.

To obtain O_s, N_b, D_b and ρm values, the prepared model solutions and urine samples were also examined using a Photocor Complex dynamic light scattering spectrometer (Fig. 2), SPEX SSP 705 spectrophotometer (Fig. 3) and OSCR-1M cryoscopic medical osmometer (Fig. 4), as well as a DMA 5000M ultrasonic density meter (Fig. 5). Osmolarity O_s, solid concentration N_b, protein size D_b and density ρ_m were measured.

Fig. 2. Photocor Complex dynamic light scattering spectrometer

Fig. 3. Spectrophotometer SPEX SSP 705

Fig. 4. Cryoscopic Medical Osmometer OSCR-1M

Fig. 5. Ultrasonic density meter DMA 5000M

Conclusion

All this shows not only the scientific value of the conducted research. the new express method developed on their basis. the proposed for practical realization of the new method of mobile refractometer design and multifunctional experimental unit. which allows to conduct various studies. but also the high practical significance of the development. which will allow doctors to more successfully solve the process of kidney disease treatment based on the detection of this disease at an early stage.

REFERENCES

1. **Biggeri A., Stoppa G., Facciolo L., et al.,** Environmental Health: A Global Access Science Source. 23(1) (2024) 42–51.

2. **Oliveira B., Teixeira B., Magalhres M., et al.,** Extracorporeal shock wave lithotripsy: retrospective study on possible predictors of treatment success and revisiting the role of non-contrast-enhanced computer tomography in kidney and ureteral stone disease. Urolithiasis. 52 (1) (2024) 65–79.

3. **Mielke N., Barghouth M.H., Fietz A.-K., et al.,** Effect modification of polypharmacy on incident frailty by chronic kidney disease in older adults. BMC Geriatrics. 24 (1) (2024) 335–348.

4. **Hong H., He Y., Gong Z., et al.,** Lipids in Health and Disease. 23 (1) (2004) 102-114.

5. **Gogoi P., Valan J.A.,** Network Modeling Analysis in Health Informatics and Bioinformatics. 13 (1) (2024) 16–29.

6. **Jairoun A.A., Al-Hemyari S.S., Shahwan M., et al.,** Guideline-directed medical therapy in heart failure patients with reduced ejection fraction in Palestine: Retrospective clinical audit study. Scientific Reports. 14(1) (2024) 7284–7298.

7. **Davydov V., Gureeva I., Davydov R., Dudkin V.,** Flowing Refractometer for Feed Water State Control in the Second Loop of Nuclear Reactor. Energies. 15(2) (2022) 457.

8. **Luo Y., Guo W., Yu L., et al.,** High-precision algorithms for critical angle refractive index measurement. Applied Optics. 58 (22) (2019) 6057–6062.

9. **Karabegov M.A.,** Algorithms and Structural Correction Schemes for Enhancing the Accuracy of Analytical Instruments. Measurement Techniques. 56 (5) (2013) 539–548.

THE AUTHORS

VAKORINA Darya D.
cementary.ley@gmail.com
ORCID: 0000-0001-5303-5387

STEPANENKOV Gregory V.
261199g@gmail.com
ORCID: 0000-0002-8924-5033

Received 30.07.2024. Approved after reviewing 12.08.2024. Accepted 19.08.2024.

Conference materials
UDC 539.1.047
DOI: https://doi.org/10.18721/JPM.173.266

Development of a new methodology for the control of tritium emissions into the atmosphere and assessment of their impact on biological objects

D.S. Dmitrieva[1]✉, D.V. Dmitrieva[1]

[1] Bonch-Bruevich Saint Petersburg State University of Telecommunications, St. Petersburg, Russia;

✉ dmitrievadiana1405@gmail.com

Abstract. The necessity of research of tritium content in emissions produced by nuclear power plants is sustained. The imperfection of the classical method for the determination of tritium in a sample by the presence of β-radiation in the research of water, soil and products is determined. The methodology of measurements is presented. To realize the proposed method, measurements of radiation power from three types of particles (α, β and γ) are carried out. Repeated measurements are carried out at a small distance from the sample at a more distant distance the exposure dose from γ-radiation was measured. The results of the research of tritium impact on the population in the Leningrad Region (Russian Federation), which lives in areas up to 50–60 km away from the Leningrad Nuclear Power Plant, are presented. Annual emissions and volumetric activity in air of tritium at the Leningrad Nuclear Power Plant are presented. Data on annual radiation dose from tritium emissions are given. Negative consequences of tritium influence on human organism are highlighted. The drawbacks of the existing monitoring system are identified.

Keywords: methodology, tritium emissions, γ-radiation, tritium impact, control system

Citation: Dmitrieva D.S., Dmitrieva D.V., Development of a new methodology for the control of tritium emissions into the atmosphere and assessment of their impact on biological objects, St. Petersburg State Polytechnical University Journal. Physics and Mathematics. 17 (3.2) (2024) 326–330. DOI: https://doi.org/10.18721/JPM.173.266

Материалы конференции
УДК 539.1.047
DOI: https://doi.org/10.18721/JPM.173.266

Разработка новой методики контроля выбросов трития в атмосферу и оценка их воздействия на биологические объекты

Д.С. Дмитриева[1]✉, Д.В. Дмитриева[1]

[1] Санкт-Петербургский государственный университет телекоммуникаций им. проф. М.А. Бонч-Бруевича, Санкт-Петербург, Россия;

✉ dmitrievadiana1405@gmail.com

Аннотация. Обоснована необходимость исследования содержания трития в выбросах, производимых атомными электростанциями. Установлено несовершенство классического метода определения трития в пробе по наличию β-излучения при исследовании воды, почвы и продуктов. Представлена методика проведения измерений. Для реализации предложенного метода проводятся измерения мощности излучения от трех типов частиц (α, β и γ). Повторные измерения проводятся на небольшом расстоянии от образца, на более удаленном расстоянии измерялась экспозиционная доза от γ-излучения. Представлены результаты исследования воздействия трития на население Ленинградской области (Российская Федерация), проживающее в районах, удаленных от Ленинградской атомной электростанции на расстояние до 50–60 км. Представлены

данные о годовых выбросах и объемной активности трития в воздухе на Ленинградской атомной электростанции. Приведены данные о годовой дозе облучения от выбросов трития. Освещены негативные последствия воздействия трития на организм человека. Выявлены недостатки существующей системы мониторинга.

Ключевые слова: методология, выбросы трития, γ-излучение, воздействие трития, система контроля

Ссылка при цитировании: Дмитриева Д.С., Дмитриева Д.В. Разработка новой методики контроля выбросов трития в атмосферу и оценка их воздействия на биологические объекты // Научно-технические ведомости СПбГПУ. Физико-математические науки. 2024. Т. 3.2 № .17. С. 326–330. DOI: https://doi.org/10.18721/JPM.173.266

Introduction

The development of scientific and technological progress has led to the need to generate large amounts of energy for various tasks in industry and agriculture. The use of nuclear power plants (NPP) as one of the sustainable sources for obtaining the required capacity has led to the contamination of neighboring territories [1–3].

One of the hazardous substances contained in emissions is the radioactive hydrogen isotope tritium [4–8]. The half-life of tritium is 12.3 years, which creates a danger for the neighboring areas, since during the entire half-life the isotope emits β-particles with an average energy of 5.7 keV (the required minimum for β-radiation registration is 0.1 MeV). Tritium release into the environment from nuclear power facilities can reach the level of $4.4 \cdot 10^{17}$ Bq/year [6]. Despite the natural content of tritium in the atmosphere, additional emissions strongly aggravate the environmental situation. Therefore, the research of tritium emissions and the possibility of their control is an urgent task for applied physics.

Materials and Methods

Preliminary measurements of the radioactive emission power of the three components (α, β and γ) were carried out in the selected samples of soil, water and products. It was found that the classical method of determining tritium in a sample by the presence of β-radiation in the research of water, soil and products does not always give a positive result. The studies have shown that tritium decays into helium, emitting rather intense β-radiation. The energy of its β-particles is relatively low. Therefore, it is difficult to unambiguously determine the presence of tritium from the registration of β-radiation. To increase the reliability of determining the possible presence of tritium in the sample under research, a new algorithm with computer code was developed. To implement it, measurements of radiation power (P_R) from three types of particles (α, β, and γ) were performed. Then, repeated measurements were performed at 1 cm from the sample. And at a more distant distance (from 5 cm with a step of 2 cm), the exposure dose from γ-radiation was measured. All these values were entered into a personal computer. The developed algorithm compares P_R values for different types of particles, their interrelation with each other and the nature of change from the distance to the source of radioactive radiation.

In our research, the effect of tritium on soil, meadow grasses and fruit trees was taken into account. Water used for irrigation of plants was considered separately, as tritium gets into products and then into the human body. To calculate the impact, we propose to use the following formula:

$$D = F \cdot K \cdot \frac{C_t}{H_a}, \quad (1)$$

where F is the correction factor taking into account various factors at the research site (experimentally determined every year), $K = 2.6 \cdot 10^{-8}$ (Sv/year)/(Bq/liter) is the tritium dose coefficient [6],

C_t is the calculated annual average volumetric activity of tritium in atmospheric air as a result of NPP emissions at the research site (Bq/m^3); Ha is the absolute air humidity (liter/m^3).

The F factor used in Eq. (1) represents a correction for various factors that can affect the results of measurements. For example, this coefficient contains information about the fraction of water with artificial tritium in milk, meat, potatoes and root vegetables, vegetables and fruits. For the Leningrad NPP, this fraction of the total water content in the study area was (0.81; 0.59; 0.91; 0.92; 0.85; 0.66) for the year 2019, (0.82; 0.61; 0.92; 0.93; 0.86; 0.65) for the year 2020, (0.83; 0.63; 0.91; 0.92; 0.87; 0.66) for the year 2021, and (0.84; 0.62; 0.92; 0.93; 0.88; 0.67) for the year 2022, respectively.

The proposed methodology has made it possible to conduct for several years studies of tritium exposure of the population in the Leningrad region (Russian Federation), which lives in areas up to 50–60 km from the Leningrad NPP. The dose to the population was represented by the highest dose among different locations within the research area in order to demonstrate the possibility of adjusting the dose calculation method used to establish maximum permissible tritium releases.

Results and Discussion

Table 1 presents the list of investigated foodstuffs produced in the NPP zone and shows the percentage of the total consumption by the population. The indicators are taken for five years in order to demonstrate in further studies the share of influence of radiation dose from products on the total annual radiation dose. Data are taken from the ROSSTAT system of the Russian Federation.

Table 1

Percentage of consumption by the population of agricultural products produced in the 60-km zone of NPP from the total consumption for 5 years

Product	Year				
	2019	2020	2021	2022	2023
Milk	64.2	65.9	64.8	63.9	63.8
Meat	80.2	79.5	80.3	80.9	81.4
Potatoes	71.4	69.7	72.3	70.5	74.6
Vegetables	34.7	34.8	34.9	35.1	35.3
Fruits	23.6	23.7	23.8	23.7	23.6

As can be seen from Table 1, the percentage of consumption of food products produced in the NPP zone is high. The concentration of tritium in these products is dozens of times higher than the concentration of tritium in products brought from other regions, which we can observe if we compare the above data with other ROSSTAT data. This shows that it is necessary to control more strictly the dose of irradiation of land plots, fields, as well as water bodies with hydrogen isotope in order to prevent human consumption of such foodstuffs.

Table 2

Annual emissions and volumetric activity in the atmosphere of tritium at Leningrad NPP

Year	Volumetric activity without dispersion, Bq/m^3		Annual emissions, 10^{12} Bq	Volumetric activity in the atmosphere, 10^{-2} Bq/m^3
	Minimum	Maximum		
2019	940	1120	10.7	6.3
2020	944	1128	10.8	6.5
2021	948	1132	10.9	6.7

Table 2 presents the measured volumetric activity of tritium in emissions from the Leningrad Nuclear Power Plant for three years (from 2019 to 2021). The estimate of the total annual emission from NPP is obtained from the data on the annual emission level and measured volumetric activity for each NPP source.

The annual dose to the public from tritium releases from this NPP was calculated using an equation assuming that the specific activity of tritium in food water and atmospheric moisture is the same. These data are presented in Table 3.

Table 3

Annual radiation dose from tritium emissions from Leningrad NPP, 10^{-7} Sv

Year	Inhalation and skin absorption	Products	Water penetration	Final dose
2019	0.15	0.76	0.12	1.03
2020	0.17	0.77	0.13	1.08
2021	0.18	0.79	0.14	1.13

The analysis of our research results has shown a tendency to increase the tritium content in the area of Leningrad and other NPPs in the Russian Federation. This leads to an increase in the annual radiation dose to the population, which may subsequently lead to an increase in the number of diseases. It can be noted that despite the increase in tritium emissions and the accumulation of its dose in soil and water bodies, the radiation dose to the population (D) is far from critical (this dose does not exceed 2 μ**Sv** per year). In 2022, the value of D for tritium near the Leningrad nuclear power plant was approximately 0.125 μ**Sv** per year.

Conclusion

Despite the natural content of tritium in the atmosphere and water, additional emissions greatly aggravate the environmental situation and reduce human performance when tritium enters the body. Tritium has a very negative impact on the cardiovascular system. The existing monitoring points for tritium levels in the environment cannot provide full control over its emissions and movement in air streams.

REFERENCES

1. **Vasyanovich M.E., Ekidin A.A., Vasilyev A.V., et al.,** Determination of radionuclide composition of the Russian NPPs atmospheric releases and dose assessment to population. Journal of Environmental Radioactivity. 106006 (2019) 208–209.

2. **Davydov V.V., Myazin N.S., Kiryukhin A.V.,** Nuclear-magnetic flowmeter-relaxometers for monitoring coolant and feedwater flow and status in NPP, Atomic Energy. 127 (2020) 274–279.

3. **Davydov R., Myazin N., Dudkin V.,** The Multifunctional Nuclear Magnetic Flowmeter for Control to the Consumption and Condition of Coolant in Nuclear Reactors, Energies 15 (5) (2022) 1748.

4. **Filimonov P.E., Semchenkov Yu. M., Malyshev V.V., et al.,** VVER-1200 Tests in No. 6 Unit of the Novovoronezh NPP During Operation in a Daily Load Schedule, Atomic Energy. 129 (3) (2020) 143–148.

5. **Nikitina M., Grebenikova N., Valiullin L., et al.,** Methodology for assessing the adverse effects of the use of nuclear energy on agricultural land, IOP Conference Series: Earth and Environmental Science. 390 (1) (2019) 012024.

6. **Antonova E.V., Antonov K.L., Vasyanovich M.E., Panchenko S.V.,** Tritium from the Molecule to the Biosphere. 1. Patterns of Its Behavior in the Environment, Russian Journal of Ecology. 53 (2022) 253–284.

7. **Ekidin A.A., Antonov K.L., Vasyanovich M.E., Desyatov D.D.,** Influence of meteorological parameters on the intensity of tritium emission from spray ponds, Atomic Energy. 135 (5–6) (2023) 232–239.

8. **Ekidin A.A., Antonov K.L., Vasyanovich M.E., Nazarovich A.V.,** Formation of atmospheric air contamination with tritium above the water areas of industrial water bodies, Radioactive Waste. 4 (21) (2022) 103–113.

THE AUTHORS

DMITRIEVA Diana S.
dmitrievadiana1405@gmail.com
ORCID: 0000-0002-2561-6245

DMITRIEVA Diana V.
dmitrieva.d.v.3731@gmail.com
ORCID: 0009-0005-8032-1561

Received 31.07.2024. Approved after reviewing 21.08.2024. Accepted 21.08.2024.

Conference materials
UDC 577.322
DOI: https://doi.org/10.18721/JPM.173.267

Structure of bovine serum albumin in solution and films as revealed from vibrational spectroscopy

E.V. Fedotova✉, S.V. Paston

St. Petersburg State University, St. Petersburg, Russia

✉ st077318@student.spbu.ru

Abstract. This study explores the impact of salt concentration and the degree of hydration on the structure of bovine serum albumin (BSA) using vibrational spectroscopy methods, specifically Fourier transform infrared spectroscopy and Raman scattering. BSA, a key plasma protein, plays essential roles in binding and transporting various molecules in the bloodstream. The research focuses on understanding how do the interaction with ions and water molecules affect the secondary and tertiary structure of globular proteins, emphasizing the significance of environmental factors in protein conformation. The results indicate distinct responses in the vibrational spectra of BSA to the presence of salt. Analysing the Amide I band give the parameters of the secondary structure of BSA. In all systems investigated the values obtained is in good correspondence with the data for native BSA, but the secondary and tertiary BSA structure in dehydrated films containing NaCl is closer to native, hence ions prevent albumin from denaturation and β-aggregation.

Keywords: bovine serum albumin, protein film, Raman spectroscopy, FTIR spectroscopy

Citation: Fedotova E.V., Paston S.V., Structure of bovine serum albumin in solution and films as revealed from vibrational spectroscopy, St. Petersburg State Polytechnical University Journal. Physics and Mathematics. 17 (3.2) (2024) 331–335. DOI: https://doi.org/10.18721/JPM.173.267

Материалы конференции
УДК 577.322
DOI: https://doi.org/10.18721/JPM.173.267

Структура бычьего сывороточного альбумина в растворе и пленках по данным колебательной спектроскопии

Е.В. Федотова✉, С.В. Пастон

Санкт-Петербургский государственный университет, Санкт-Петербург, Россия

✉ st077318@student.spbu.ru

Аннотация. В данной работе изучается влияние концентрации соли и степени гидратации на структуру бычьего сывороточного альбумина (БСА) с помощью методов колебательной спектроскопии, в частности, инфракрасной спектроскопии с преобразованием Фурье и комбинационного рассеяния. БСА, ключевой белок плазмы крови, играет важную роль в связывании и транспортировке различных молекул в кровотоке. Исследование посвящено изучению того, как взаимодействие с ионами металлов и молекулами воды влияет на вторичную и третичную структуру глобулярных белков, подчеркивая значимость факторов окружающей среды для конформации белка. Полученные результаты свидетельствуют о том, что в колебательных спектрах БСА наблюдается отчетливый отклик на присутствие соли. Анализ полосы Амид I позволяет получить параметры вторичной структуры БСА. Во всех исследованных системах полученные значения хорошо согласуются с данными для нативного БСА, но вторичная и третичная структура БСА в высушенных пленках, содержащих NaCl, ближе к нативной, следовательно, ионы предотвращают денатурацию и β-агрегацию альбумина.

Ключевые слова: бычий сывороточный альбумин, пленки белка, рамановская спектроскопия, ИК-Фурье-спектроскопия

Ссылка при цитировании: Федотова Е.В., Пастон С.В. Структура бычьего сывороточного альбумина в растворе и пленках по данным колебательной спектроскопии // Научно-технические ведомости СПбГПУ. Физико-математические науки. 2024. Т. 17. № 3.2. С. 331–335. DOI: https://doi.org/10.18721/JPM.173.267

Introduction

A wide variety of approaches based on vibrational spectroscopy have been used to study protein structure. The advantages of this method are a small amount of sample, the ability to study multicomponent systems and complex structures (such as cells, tissues, biological fluids), and the use of a substance in the liquid or solid phase. FTIR and Raman scattering spectroscopy provide information about the secondary and tertiary structure of proteins, their conformational transitions in consequence of folding, variation in external conditions or intermolecular interactions [1–3]. Methods for diagnosing various diseases are now being actively developed, based on measuring the vibrational spectra of blood, hair and other biological samples, followed by analysis of the structure of biomolecules as well as Principal Component-Discriminant Function Analysis [1, 4–8]. Spectroscopy investigation of biofluids is carried out in transmission mode or with ATR technique and often includes preliminary dilution or evaporation of samples [7, 8]. Since commonly the assay is mainly based on spectral features of proteins, it is important to take into account changes in structure and spectral parameters of proteins upon variation of water activity. The present work is devoted to comparison of the IR and Raman spectra of bovine serum albumin (BSA) in solutions and dried films to analyze influence of water and monovalent ions content on conformation parameters of the protein.

BSA, a prevalent plasma protein, is extensively utilized for studying various aspects of protein behavior, such as folding and aggregation, as well as for biotechnological purposes [9]. BSA primarily functions in binding, transporting, and delivering a wide array of small molecules and metal ions in the bloodstream. Structurally, BSA consists of a single polypeptide chain organized into three domains (I, II, III), with a dominant α-helical secondary structure at room temperature [10].

Materials and Methods

BSA lyophilized powder (DiaM, USA) was dissolved in deionized water or 0.15M NaCl solution in concentration of 70 g/l. IR spectra of albumin solutions and films were recorded on FTIR spectrometer Nicolet 8700 (Thermo Scientific), on ATR attachment. 10 μl of BSA solution was dropped on the ATR crystal and covered with a cap to prevent evaporation during the recording. The spectrum of the background was recorded and subtracted from the spectra of the samples automatically. The spectrum of the corresponding solvent was registered for further subtraction from the spectra of protein solutions. BSA dehydrated films were obtained from protein solutions dried by a nitrogen stream. The spectral data within the range of 4000 to 500 cm^{-1} were recorded, and 512 scans were averaged for each spectrum with a spectral resolution of 2 cm^{-1}. The software supplied with the spectrometer and OriginPro were used for data processing.

Raman spectra of BSA dehydrated films prepared on aluminium foil were measured by Express Raman spectrometer SENTERRA (Bruker). The excitation source was 785 nm laser, the spectral resolution was 3 cm^{-1}. The laser power on the sample was about 100 mW. The curve fitting analysis was implemented using the OPUS/IR v 5.0 program and Origin Pro.

Results and Discussion

The BSA IR spectra were measured in water solution and in 0.15 M NaCl, as well as in films obtained by dehydration of these solutions. Raman spectra of BSA were recorded in films prepared from the same solutions by desiccation of 10 μl drop on aluminium foil. In the IR and

Raman spectra of proteins, the vibrational band of the Amide I peptide group (about 1650 cm^{-1}) is very sensitive to various forms of secondary structure [11]. After the baseline correction, we analyse the Amide I band by procedure of decomposition on components of Gaussian contours. The area of each Gaussian contour represents the contribution of the definite type of the secondary structure [11]. The percentage of the components of BSA secondary structure in the studied systems is given in Table 1. According to literature data, the secondary structure of BSA is composed of 67% α-helix, 10% turn, and no β-sheet is contained [3, 10, 12]. From the FTIR spectroscopy results we can conclude that after desiccation the content of α-helices in protein secondary structure grows and the content of β-sheets decreases. BSA structure in dehydrated films containing NaCl is closer to native, so we can conclude that ions Na^+ and Cl^- prevent albumin from denaturation and β-aggregation.

Table 1

Content of BSA secondary structure forms in solutions and films

	Film and solution composition	α-helices, %, ±4% (band position, cm^{-1})	β-sheets, %, ±4% (band position, cm^{-1})	β-turns, %, ±4% (band position, cm^{-1})
Raman spectra	water (film)	65 (1655)	1 (1636)	25 (1671, 1683)
	NaCl (film)	66 (1655)	4 (1693)	22 (1670, 1682)
Infrared spectra	water (solution)	58 (1653)	36 (1628)	6 (1680)
	NaCl (solution)	54 (1652)	23 (1630)	8 (1680)
	water (film)	63 (1648)	14 (1632)	7 (1681)
	NaCl (film)	70 (1650)	5 (1632)	15 (1677)

Raman spectrum of a protein along with the vibrational bands of peptide group contains strong signals from amino acids side chains, and it was found to be very sensitive to their conformations and surroundings. Raman spectra of BSA films after baseline correction and normalization on the Amid I intensity with assignments of the bands are shown in Fig. 1. Several vibrational modes can be used to analyze BSA structure (Table 2) [1, 2]. Change in the intensity ratio of 850 cm^{-1} to 827 cm^{-1} talks about alteration in manner of H-bonding of phenyl hydroxyl of the tyrosine.

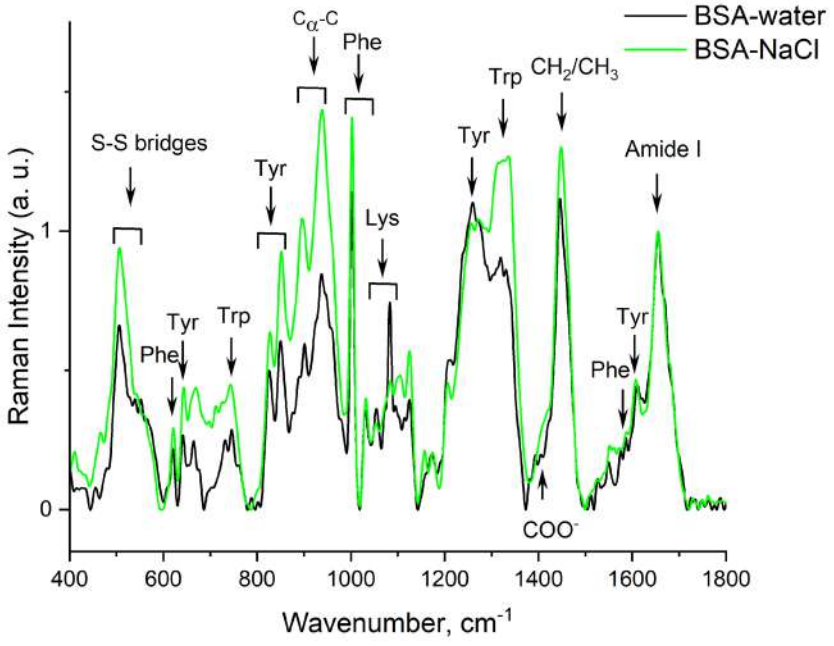

Fig. 1. Raman spectra of BSA films obtained from water and from 0.15M NaCl solution

The intensity of Phe band 621 cm^{-1} lowers at the degree of hydration increases. The ratio of Trp doublet I_{1360}/I_{1340} decreases at the transition of Trp into more polar medium. The value I_{1177}/I_{1003} reduces if the water content around the Tyr residue curtails. All these markers show the lowering of degree of hydration of non-polar amino acids in NaCl-containing film in comparison with film, prepared from water solution. This may indicate a more preserved tertiary structure of albumin in the NaCl-containing film.

Table 2

Protein structure markers from Raman spectra of BSA

Structure markers		$\frac{I_{621}}{I_{1003}}$, **Phe**	$\frac{I_{1360}}{I_{1340}}$, **Trp**	$\frac{I_{850}}{I_{827}}$, **Tyr**	$\frac{I_{1177}}{I_{1003}}$, **Tyr**
Film composition	water	0.187	0.305	1.21	0.172
	NaCl	0.208	0.337	1.45	0.146

Conclusion

In summary, the experimental study involving the measurement of protein spectra in different conditions highlights the intricate sensitivity of vibrational bands to variations in salt concentration and humidity level. The investigation of aromatic amino acids vibrations reveals the influence of salt on the protein environment, indicating a shift towards a less polar state. BSA structure in dehydrated films containing NaCl is closer to native. These findings shed light on the structural alterations of proteins in response to varying conditions and provide insights into the interplay between environmental factors and protein conformation.

REFERENCES

1. **Chalmers J.M., Griffiths P.R., Eds.,** Handbook of Vibrational Spectroscopy, Vol.5 Applications of Vibrational Spectroscopy in Life, Pharmaceutical and Natural Sciences, Wiley. 2002.

2. **Kuhar N., Sil S., Umapathy S.,** Potential of Raman spectroscopic techniques to study proteins, Spectrochimica Acta Part A: Molecular and Biomolecular Spectroscopy. 258 (2021) 119712.

3. **Tankovskaia S.A., Abrosimova K.V., Paston S.V.,** Spectral demonstration of structural transitions in albumins, Journal of Molecular Structure. 1171 (2018) 243–252.

4. **Chernyshev D.A., Mikhailets E.S., Telnaya E.A. et. al.,** Analysis of infrared spectra of blood serum of patients with multiple myeloma, Journal of Physics: Conference Series. 2103 (2021) 012052.

5. **Plotnikova L.V., Kobeleva M.O., Borisov E.V. et. al.,** Infrared Spectroscopy of Blood Serum from Patients with Multiple Myeloma. Cell Tiss. Biol. 13 (2019) 130–135.

6. **Mankova A.A., Cherkasova O.P., et. al.,** Study of Blood Serum in Rats with Transplanted Cholangiocarcinoma Using Raman Spectroscopy. Opt. Spectrosc. 128 (2020) 964–971.

7. **Lovergne L., Clemens G., Untereiner V., et al.,** Investigating optimum sample preparation for infrared spectroscopic serum diagnostics, Anal. Methods. 7 (2015) 7140–7149.

8. **Cameron J.M., Butler H.J., Palmer D.S., Baker M.J.** Biofluid spectroscopic disease diagnostics: A review on the processes and spectral impact of drying, J. Biophotonics. (2018) (11) e201700299.

9. **Asrorov A.M., Mukhamedov N., Kayumov M., et al.,** Albumin is a reliable drug-delivering molecule: Highlighting points in cancer therapy, Medicine in Drug Discovery. 22 (2024) 100186.

10. **Peters T., Jr.,** All about albumin: Biochemistry, Genetics, and Medical Applications, Academic Press. 1995.

11. **Barth A.**, Infrared spectroscopy of proteins. Biochimica et Biophysica Acta. 1767 (2007) 1073–1101.

12. **Murayama K., Tomida M.,** Heat-Induced Secondary Structure and Conformation Change of Bovine Serum Albumin Investigated by Fourier Transform Infrared Spectroscopy. Biochemistry. 43 (2004) 11526–11532.

THE AUTHORS

FEDOTOVA Elisaveta V.
st077318@student.spbu.ru

PASTON Sofia V.
svpaston@list.ru

Received 31.07.2024. Approved after reviewing 12.08.2024. Accepted 15.08.2024.

Conference materials
UDC 57.083
DOI: https://doi.org/10.18721/JPM.173.268

Antibacterial properties of riboflavin under photodynamic exposure in a culture of fluorescent bacteria *E. Coli*

P.P. Shram[1]✉, A.M. Kolchenko[1], R.A. Akasov[1], I.A. Vinokurov[2], T.V. Egorova[1]

[1] Moscow Pedagogical State University, Moscow, Russia;

[2] Petrovsky National Research Center of Surgery, Moscow, Russia

✉ p.schram2002@gmail.com

Abstract. Nosocomial infections are a dangerous complication of various surgical procedures or injuries because the pathogens causing them are resistant to antibiotic therapy. Antibacterial photodynamic therapy (aPDT), which is based on the suppression of the growth of pathogenic microorganisms by means of free radicals and reactive oxygen species generated by the irradiation of substances with photosensitising activity, can be an effective method for the treatment of nosocomial infections. In this work, we have shown that the endogenous photosensitiser riboflavin, which has low dark toxicity, good water solubility and high quantum yield, can be used as an agent for aPDT. To this end, we investigated the antibacterial activity of riboflavin against *E.Coli* bacteria transformed with the mKate protein using blue and near-ultraviolet light sources in different irradiation modes. It was shown that half-maximal inhibition of bacterial growth could be achieved at concentrations of 0.1–0.5 mg/ml riboflavin when irradiated at a wavelength of 365 nm and at 0.6–1.2 mg/ml when irradiated at a wavelength of 450 nm, 10–20 minutes of irradiation. The proposed approach may be promising for the treatment of nosocomial infections, including those resistant to antibiotics.

Keywords: antimicrobial photodynamic therapy, photosensitizer, riboflavin, antibiotic resistance

Funding: The article was prepared within the framework of topic "Laser technologies for biomedical applications" (122122600055-2) under the state assignment of the Ministry of Education of the Russian Federation.

Citation: Shram P.P., Kolchenko A.M., Akasov R.A., Vinokurov I.A., Egorova T.V., Antibacterial properties of riboflavin under photodynamic exposure in a culture of fluorescent bacteria *E. Coli*, St. Petersburg State Polytechnical University Journal. Physics and Mathematics. 17 (3.2) (2024) 336–339. DOI: https://doi.org/10.18721/JPM.173.268

Материалы конференции
УДК 57.083
DOI: https://doi.org/10.18721/JPM.173.268

Антибактериальные свойства рибофлавина при фотодинамическом воздействии в культуре флуоресцентных бактерий *E. Coli*

П.П. Шрам[1]✉, А.М. Кольченко[1], Р.А. Акасов[1], И.А. Винокуров[2], Т.В. Егорова[1]

[1] Московский педагогический государственный университет, Москва, Россия;

[2] ФГБНУ РНЦХ им. акад. Б.В. Петровского, Москва, Россия

✉ p.schram2002@gmail.com

Аннотация. Эффективным методом лечения внутрибольничных инфекций, вызываемых антибиотикорезистенными микроорганизмами, может стать антибактериальная фотодинамическая терапия (аФДТ), основанная на подавлении роста патогенных микроорганизмов с помощью свободных радикалов и активных форм кислорода,

образующихся при облучении веществ с фотосенсибилизирующей активностью. В данной работе мы оценивали антибактериальную активность рибофлавина в отношении флуоресцентных бактерий *E. Coli* при использовании источников синего и ближнего ультрафиолетового света в разных режимах облучения. Таким образом, мы показали, что эндогенный фотосенсибилизатор рибофлавин обладающий низкой темновой токсичностью, хорошей водорастворимостью и высоким квантовым выходом, может быть использован в качестве агента для аФДТ.

Ключевые слова: антимикробная фотодинамическая терапия, фотосенсибилизатор, рибофлавин, устойчивость к антибиотикам

Финансирование: Статья подготовлена в рамках работы по теме «Лазерные технологии для биомедицинских приложений» (№ 2-122122600055) по государственному заданию Министерства просвещения Российской Федерации.

Ссылка при цитировании: Шрам П.П., Кольченко А.М., Акасов Р.А., Винокуров И.А., Егорова Т.В. Антибактериальные свойства рибофлавина при фотодинамическом воздействии в культуре флуоресцентных бактерий *E. Coli* // Научно-технические ведомости СПбГПУ. Физико-математические науки. 2024. Т. 17. № 3.2. С. 336–339. DOI: https://doi.org/10.18721/JPM.173.268

Introduction

Healthcare-associated infections pose a serious threat to patient health. In modern medicine, these infections are most often associated with invasive procedures and surgical interventions [1]. Mortality in these patients rises sharply due to the inability to eradicate the pathogen using conservative methods. aPDT, based on the use of photosensitizers, may be a promising method for the treatment of postoperative infectious diseases. Flavins, which are involved in the generation of reactive oxygen species in both type I and type II photochemical reactions, can be used as photosensitizing agents [2, 3]. The effectiveness of riboflavin as a photosensitizer has been demonstrated in studies of blood plasma sterilization [4] and in photoactivated collagen cross-linking to increase corneal stiffness [5]. There are some pioneering papers that demonstrated the possibility of antibacterial application of riboflavin [6, 7]; however, the irradiation conditions were far from the clinical ones in terms of the used wavelength, light power and irradiation time. Riboflavin has also been shown to have an anti-inflammatory effect and can be used for the therapy of inflammatory diseases of broad origin [8].

The aim of our work was to evaluate the antibacterial photodynamic activity of riboflavin in the culture of *E. Coli* transformed with plasmid DNA encoding the fluorescent protein mKate. We investigated the effect of the natural coenzyme riboflavin, a flavin mononucleotide (FMN) that is soluble in water and physiological solutions, and a registered pharmacological drug that does not exhibit dark toxicity.

Materials and Methods

E. Coli bacteria strain BL21(DE3), transformed with plasmid DNA encoding the fluorescent protein mKate (excitation maximum 588 nm, emission maximum 633 nm), was used as a model bacteria organism. Bacteria were planted in each well of the 96-well plate containing LB agar. FMN, was added to the samples at various concentrations (up to 2.57 mM) in a dark room The samples were irradiated with a 450 nm (blue) or 365 nm (UV) light source for 10 or 20 minutes at a power density of 63.7 mW/cm^2 and then placed in a thermostat at 37 °C for two days (Fig. 1).

The results were recorded using an imaging system containing a 530 nm light source and a camera with a filter that transmits light from the red region of the spectrum. The resulting photographs were processed in ImageJ by calculating the integral brightness of the image in the area of each well. The method error (similar to the MTT assay) can be estimated at 10–20%.

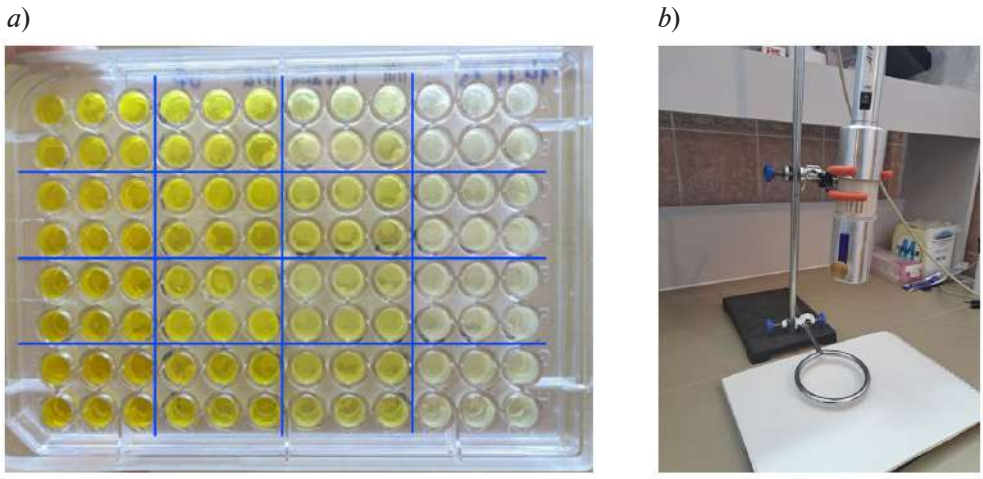

Fig. 1. Experimental model: plate with samples, areas with different concentrations of FMN are separated by lines (*a*), work station with tripod and blue or UV light source (*b*)

Results and Discussion

To analyze the effectiveness of the antibacterial photodynamic activity of riboflavin, the survival rate of *E. coli* was assessed; the survival rate of the control wells (without FMN) was taken as 100% (Fig. 2). The IC_{50} (half-maximal inhibition concentrations) values were estimated using GraphPad Prism 8.0 software. These values were 0.54 ± 0.23 mg/ml and 0.11 ± 0.04 mg/ml for 10 and 20 minutes at 365 nm irradiation, and ~1.2 mg/ml and 0.61 ± 0.18 mg/ml for 10 and

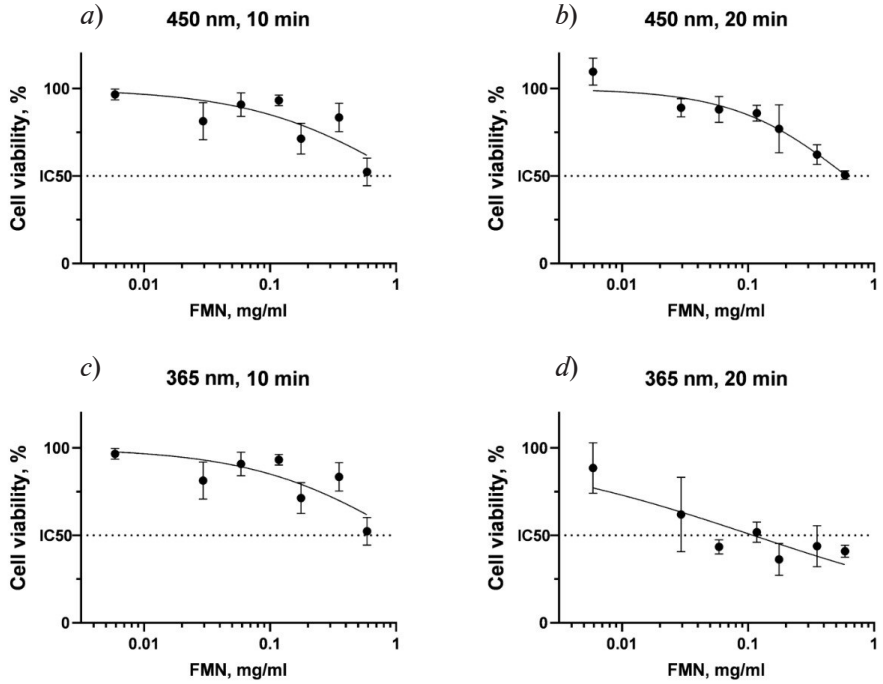

Fig. 2. Survival curves of *E. Coli* bacteria strain BL21(DE3) growing on LB medium, in the presence of FMN in different concentrations, expressed in semilogarithmic coordinates, after irradiation. The following irradiation modes were used: with a 450 nm light source for 10 minutes (*a*), with a 450 nm light source for 20 minutes (*b*), with a 365 nm light source for 10 minutes (*c*), with a 365 nm light source for 20 minutes (*d*).
Data are presented as mean ± standard deviation, $n = 6$.
The data were approximated by an S-shaped survival curve

20 minutes at 450 nm irradiation, respectively. The IC_{50} in the 10 min blue group was different from the 20 min blue and 10 min UV groups, $p < 0.05$ in Mann–Whitney U test. The IC_{50} in the 20 min UV group was different from the 10 min UV and 20 min blue groups, $p < 0.05$.

Conclusions

Riboflavin exhibits antibacterial photodynamic activity when exposed to blue or UV light. Irradiation at a wavelength of 365 nm results in greater suppression of bacterial growth compared to 450 nm, which may be due to the inherent toxicity of UV radiation. In addition, an increase in irradiation time leads to an increase in the antibacterial activity of FMN at both 450 nm and 365 nm due to an increase in the total light dose. The light doses used in this study (~40 J/cm^2 and ~80 J/cm^2 for 10 min and 20 min, respectively) were selected considering the maximum light irradiation dose for PDT, which is usually discussed as 100–150 J/cm^2 for blue light. The use of a blue light belonging to the safe visible region could be more promising to avoid UV-induced toxicity to the healthy tissues. The obtained results indicate a pronounced antibacterial effect of FMN under photodynamic exposure; at the same time, FMN concentrations and irradiation regimes were chosen to be related to further clinical trials for the treatment of patients with infectious-inflammatory wound complications.

Acknowledgments

Fluorescent *E. Coli* bacteria were kindly provided by Dr. D. Kostyushev (Sechenov University).

REFERENCES

1. **Sikora A., Zahra F.,** Nosocomial Infections. StatPearls. – Treasure Island (FL) ineligible companies. Disclosure: Farah Zahra declares no relevant financial relationships with ineligible companies.: StatPearls PublishingCopyright, StatPearls Publishing LLC. 2024.

2. **Abrahamse H., Hamblin M.R.,** New photosensitizers for photodynamic therapy. Biochem J. 473 (4) (2016) 347–64.

3. **Insińska-Rak M., Sikorski M., Wolnicka-Glubisz A.,** Riboflavin and Its Derivates as Potential Photosensitizers in the Photodynamic Treatment of Skin Cancers. Cells. 12 (18) (2023).

4. **Ettinger A., Miklauz M.M., Bihm D.J., et al.,** Preparation of cryoprecipitate from riboflavin and UV light-treated plasma. Transfus Apher Sci. 46 (2) (2012) 153–8.

5. **Chan T.C., Lau T.W., Lee J.W., et al.,** Corneal collagen cross-linking for infectious keratitis: an update of clinical studies. Acta Ophthalmol. 93 (8) (2015) 689–96.

6. **Wong T.W., Cheng C.W., Hsieh Z.J., et al.,** Effects of blue or violet light on the inactivation of Staphylococcus aureus by riboflavin-5'-phosphate photolysis. J. Photochem Photobiol B. (173) (2017) 672–680.

7. **Crocker L.B., Lee J.H., Mital S., et al.,** Tuning riboflavin derivatives for photodynamic inactivation of pathogens. Sci Rep. 12 (1) (2022) 6580.

8. **Akasov R.A., Chepikova O.E., Pallaeva T.N., et al.,** Evaluation of molecular mechanisms of riboflavin anti-COVID-19 action reveals anti-inflammatory efficacy rather than antiviral activity. Biochim Biophys Acta Gen Subj. 1868 (5) (2024) 130582.

THE AUTHORS

SHRAM Polina P.
p.schram2002@gmail.com

VINOKUROV Ivan A.
docvin.med@gmail.com

KOLCHENKO Anna M.
anya.kolchenko@gmail.com

EGOROVA Tatyana V.
tatvladegorova@gmail.com

AKASOV Roman A.
romanakasov@gmail.com

Received 29.08.2024. Approved after reviewing 05.09.2024. Accepted 09.09.2024.

RADIOPHYSICS

Conference materials
UDC 537.862
DOI: https://doi.org/10.18721/JPM.173.269

Möbius strip inspired design of a multiband dipole-like circularly polarized antenna

V.D. Burtsev✉, A.V. Nikulin, T.S. Vosheva, N.M. Nazarov, D.S. Filonov

Moscow Institute of Physics and Technology (National Research University), Dolgoprudny, Russia

✉ burtsev.vd@phystech.edu

Abstract. This paper describes the design of a multi-band antenna with a dipole-like radiation pattern with circular polarization inspired by the Möbius strip. The results obtained can be applied further in telecommunication technologies, for example, in the development of satellite multiple access systems with frequency division of channels.

Keywords: Möbius strip, antenna design, multipolar decomposition, satellite communications systems

Funding: This research was supported by the Ministry of Science and Higher Education of the Russian Federation under the project no 075-11-2022-011 (analytical part) and the Russian Science Foundation under the project no 23-29-00152 (numerical part).

Citation: Burtsev V.D., Nikulin A.V., Vosheva T.S., Nazarov N.M., Filonov D.S., Möbius strip inspired design of a multiband dipole-like circularly polarized antenna, St. Petersburg State Polytechnical University Journal. Physics and Mathematics. 17 (3.2) (2024) 340–344. DOI: https://doi.org/10.18721/JPM.173.269

Материалы конференции
УДК 537.862
DOI: https://doi.org/10.18721/JPM.173.269

Многодиапазонная антенна с круговой поляризацией и дипольной диаграммой направленности по мотивам ленты Мёбиуса

В.Д. Бурцев✉, А.В. Никулин, Т.С. Вошева, Н.М. Назаров, Д.С. Филонов

Московский физико-технический институт (национальный исследовательский университет), г. Долгопрудный, Россия

✉ burtsev.vd@phystech.edu

Аннотация. В данной работе описан дизайн многодиапазонной антенны с дипольной диаграммой направленности, обладающей круговой поляризацией, на основе ленты Мёбиуса. Полученные результаты могут быть применены в дальнейшем в телекоммуникационных технологиях, например, при разработке спутниковых систем множественного доступа с частотным разделением каналов.

Ключевые слова: лента Мёбиуса, разработка антенн, мультипольное разложение, спутниковые системы телекоммуникаций

Финансирование: Данная работа выполнена при поддержке Министерства науки и высшего образования Российской Федерации по проекту № 075-11-2022-011 (аналитическая часть) и Российского Научного Фонда по проекту № 23-29-00152 (численное моделирование).

Ссылка при цитировании: Бурцев В.Д., Никулин А.В., Вошева Т.С., Назаров Н.М., Филонов Д.С. Многодиапазонная антенна с круговой поляризацией и дипольной диаграммой направленности по мотивам ленты Мёбиуса // Научно-технические ведомости СПбГПУ. Физико-математические науки. 2024. Т. 17. № 3.2. С. 340–344. DOI: https://doi.org/10.18721/JPM.173.269

Introduction

One of the challenges of modern satellite systems is the creation of a so-called alarm button [1–4], a transceiver device that could work from anywhere on the Earth's surface and communicate directly with satellites in Earth orbit, telling them the coordinates of the source. Such technology can be very promising in the fields of extreme tourism, rescue operations, the development of wild lands, and even with simple nature hikes in the forest. At the same time, of course, large systems must have a multi-user access function, and one of the solutions to this is the orthogonal frequency-division multiple access (OFDMA) standard [5, 6], which separates users by different subcarrier frequencies. In addition, ground-based satellite antennas value the ability to emit on circular polarization [7–9], and the antennas of wearable devices often have a quasi-dipole radiation pattern [10, 11] that allows them to shine in all directions at once in one plane, so the stability of the channel can be independent of the rotation of the antenna. The creation of subcarriers around various carrier frequencies can further increase the number of subscribers.

In this paper, we propose such an antenna prototype for the designated tasks, providing predictable behavior of the radiation pattern at multiple frequencies (~11, ~22, ~33, ... GHz for studied example). The design of the antenna was inspired by the generalized equation (1) setting a strip in Cartesian coordinates $\langle X, Y, Z\rangle$ that twists around itself, as well as around the origin point, forming a toroid in a certain sense.

$$\begin{cases} X(u,v) = a + w\dfrac{v}{2}\cos\left(\dfrac{N_{turns}u}{N}\right)\cos\left(\dfrac{N_{wires}u}{N}\right), \\ Y(u,v) = b + w\dfrac{v}{2}\cos\left(\dfrac{N_{turns}u}{N}\right)\sin\left(\dfrac{N_{wires}u}{N}\right), \\ Z(u,v) = w\dfrac{v}{2}\sin\left(\dfrac{N_{turns}u}{N}\right). \end{cases} \quad (1)$$

The parameters a and b define the semi-axes of the torus, w stands for the strip width, while v is its multiplier, e.g. it sets starting and ending point of the strip cross-section. As it can clearly be seen from (Fig. 1, *a* and its cross-sections *b* and *c*), N_{turns} sets the amount of coils in torus, and N_{wires} sets the number of wires in a bundle. The parameter here corresponds to the number of rotations of the strip around itself around the origin, and N defines the multiplicity of sine and cosine harmonics.

Methods

The antenna considered in this work (Fig. 1) has the following values of the parameters:

$$a = b = 4,\ w = 2,\ N_{turns} = 15,\ N = N_{wires} = 16.$$

For numerical calculation of the reflection coefficient and the radiation pattern, this strip geometry was performed in CAD in the CST Studio Suite, and then the metal tape was cut near the values of the parameter $u = 0$, $u = 2\pi$ to insert a lumped port. The width of the cutout is 1 mm. When choosing this geometry, the input impedance of the antenna at the fundamental frequency (~11 GHz) was approximately 300 Ohm.

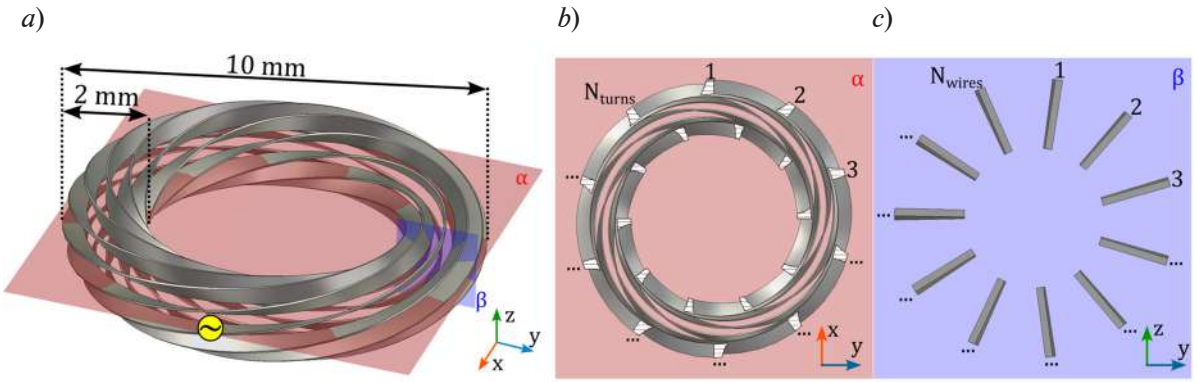

Fig. 1. Geometry of proposed antenna: general view (*a*);
top view cross-section (*b*), where N_{turns} sets the amount of coils;
bundle cross-section (*c*), where N_{wires} sets the amount of wires in a bundle

The numerical modeling in all the frequency ranges was carried out using the finite element method-based solver. At the same time, a perfectly matched layer was installed at a distance of quarter wavelength from the antenna. Since the frequency bands of interest are wide enough for primitive finite element method, they were split into smaller sub-bands of 100 MHz, the relative width of which thus amounted to no more than 1%. At each calculated frequency, the maps of the far electric field in a spherical coordinate system were obtained.

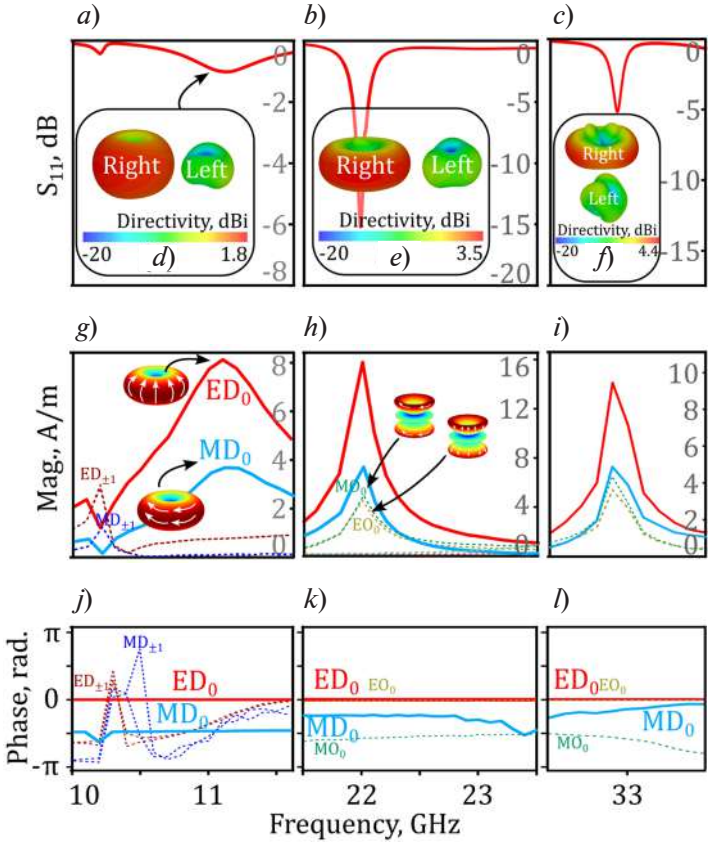

Fig. 2. Results of numerical experiment at three first harmonics:
reflection coefficient (*a*–*c*), radiation patterns (*d*–*f*); results of multipolar decomposition: amplitudes of multipolar coefficients (*g*–*i*) and their phases (*j*–*l*)
The subscript after the multipole order denotes its *m*-index [12]

To explain the operating principle of the proposed antenna, the multipolar decomposition method was used [12]. With calculated maps of the far electric field in the frequency ranges under consideration, the amplitudes and phases of multipole coefficients up to the 20th order in terms of the orbital number were calculated.

Results

In the scope of this work we mainly consider the frequencies of a dipole-like radiation pattern with circular polarization. Starting with the first resonance (Fig. 2, *a*), it is worth noting that with the current parameterization, its amplitude is only about -1 dB, which is too low to create a high-performance antenna. However, by varying the parameters in (1), it is possible to increase its depth and quality factor, mainly by moving the turns closer to each other. By setting $v \in [0.2, 0.3]$, one can obtain a reflection coefficient below -11 dB. Although such a structure is difficult to implement, the proposed antenna can easily be scaled to lower frequencies. The results of the numerical simulation and the subsequent multipolar decomposition are shown in Fig. 2:

It is worth noting that at the first considered frequency (11 GHz), the electric (ED_0 in Fig. 2) and magnetic (MD_0 in Fig. 2) dipole components make the greatest contribution, and their multipolar moments are aligned with each other to create a toroidal radiation pattern in the antenna plane (Fig. 2, *d*). Considering the phase-frequency dependence of multipoles (Fig. 2, *j*), it becomes clear that the discussed components have relative shift of $\pi/2$ radians, which determines the circular character of polarization, inasmuch as magnetic and electric dipoles are cross-polarized. A similar effect is observed at the second eigen frequency, 22 GHz (Fig. 2, *b*), where dipolar and octupolar (EO_0 and MO_0 in Fig. 2) modes have the most significant impact on the radiation pattern (Fig. 2, *g*). Unlike as at the previous frequency, here dipolar components have relative shift only about $\pi/4$ radians (Fig. 2, *k*), but the comparable in amplitude octupolar moments, having the same relative phase shift of $\pi/4$ radians, compensate this flaw and contribute significantly into circular polarization (Fig. 2, *e*). At the third mode of interest (Fig. 2, *c*), this antenna perform a similar interference principle to the first two: electric and magnetic dipolar and octupolar moments (Fig. 2, *i*) powered with a certain phase difference (Fig. 2,*l*) result in the circularly polarized dipole-shaped radiation pattern (Fig. 2, *f*).

Conclusion

In this work, we have proposed a new type of omnidirectional antenna with circular polarization. Its polarization and predictable radiation pattern make this geometry well suited for satellite communications, wearable devices (e.g. alarm buttons), remote-control units and other similar tasks where receiver device is likely to be positioned and rotated randomly relative to the transmitter. Among other things, this antenna, due to the simplicity of its geometry, can easily be reparametrized to lower frequencies, where its implementation is easily feasible [13] due to the modern success in 3D printing.

REFERENCES

1. ITU. Handbook on Emergency Telecommunications. Development (2005).

2. **Afolabi A., Moses O., Opeyemi M., et al.,** Design and construction of a panic button alarm system for security emergencies. Int. J. Eng. Tech. 4 (2018) 649–652.

3. **Majumdar N., Bhargava P., Shirin K.R.,** Emergency Panic Button using Microcontrollers. Int. J. Comput. Appl. 99 (2014) 1–3.

4. **Karusala N., Kumar N.,** Women's safety in public spaces: Examining the efficacy of panic buttons in New Delhi. Conf. Hum. Factors Comput. Syst. - Proc. (2017) 3340–3351.

5. **Ciochina C., Sari H.,** A review of OFDMA and single-carrier FDMA. Eur. Wirel. Conf. EW. (2010) 706–710.

6. **Yang S.C.,** OFDMA System Analysis and Design. J. Chem. Inf. Model. 319 (2010).

7. **Fenn A.J., Rispin L.W.,** A Terrestrial Air Link for Evaluating Dual-Polarization Techniques in Satellite Communications. 9 (1996) 3–18.

8. **Gao S., Luo Q., Zhu F.,** Circularly Polarized Antennas. Wiley-IEEE Press. (2014).

9. **Naseri P., Matos S.A., Costa J.R., et al.,** Dual-Band Dual-Linear-to-Circular Polarization Converter in Transmission Mode Application to Band Satellite Communications. IEEE Trans. Antennas Propag. 66 (2018) 7128–7137.

10. **Aun N.F.M., et al.,** Revolutionizing Wearables for 5G: 5G Technologies: Recent Developments and Future Perspectives for Wearable Devices and Antennas. IEEE Microw. (2017) 108–124.

11. **Wang B., Yan S.,** Design of Smartwatch Integrated Antenna with Polarization Diversity. IEEE Access. 8 (2020) 123440–123448.

12. **Burtsev V.D., Vosheva T.S., Prokhorov S.Y., et al.,** Broadband antenna array realization with printed meta-elements and its multipoles spectra. Photonics Nanostructures - Fundam. Appl. 58 (2024).

13. **Burtsev V.D., et al.,** Compact High-Gain Volumetric Phased Array Antenna with Genetically Designed Interelement Resonances for 5G Applications. Phys. Status Solidi - Rapid Res. Lett. 17 (2023).

THE AUTHORS

BURTSEV Vladimir D.
burtsev.vd@phystech.su
ORCID: 0000-0002-7988-5213

NIKULIN Anton V.
nikulin.av@mipt.ru

VOSHEVA Tatyana S.
Vosheva.ts@mipt.ru
ORCID: 0000-0002-5786-4972

NAZAROV Natanil M.
nazarov.nm@mipt.ru

FILONOV Dmitry S.
dimfilonov@gmail.com
ORCID: 0000-0002-5394-8677

Received 31.07.2024. Approved after reviewing 12.08.2024. Accepted 13.08.2024.

Conference materials
UDC 537.86
DOI: https://doi.org/10.18721/JPM.173.270

Development of a Ku-band phased array antenna for satellite communication

A.V. Nikulin[1], V.D. Burtsev[1]✉, G.V. Antoshkin[1], S.Yu. Prokhorov[2], T.S. Vosheva[1], N.M. Nazarov[1], A.N. Kosmynin[1], D.S. Filonov[1]

[1] Moscow Institute of Physics and Technology (National Research University), Dolgoprudny, Russia;

[2] State Space Corporation "Roscosmos", Moscow, Russia

✉ burtsev.vd@phystech.su

Abstract. This study explores the development of phased array antennas for satellite communications in the Ku-band. The design approach focused on patch antennas with directors, utilizing circular polarization for effective beam steering. This study provides insights into the design and performance of phased array antennas, offering a solid foundation for further exploration and development in satellite communication technologies.

Keywords: phased array, Ku-band, electronic beam scanning, electromagnetic simulations

Funding: This research was supported by the Ministry of Science and Higher Education of the Russian Federation, project number 075-11-2022-011.

Citation: Nikulin A.V., Burtsev V.D., Antoshkin G.V., Prokhorov S.Yu., Vosheva T.S., Nazarov N.M., Kosmynin A.N., Filonov D.S., Development of a Ku-band phased array antenna for satellite communication, St. Petersburg State Polytechnical University Journal. Physics and Mathematics. 17 (3.2) (2024) 345–348. DOI: https://doi.org/10.18721/JPM.173.270

Материалы конференции
УДК 537.86
DOI: https://doi.org/10.18721/JPM.173.270

Разработка фазированной антенной решетки Ku-диапазона для спутниковой связи

А.В. Никулин[1], В.Д. Бурцев[1]✉, Г.В. Антошкин[1], С.Ю. Прохоров[2], Т.С. Вошева[1], Н.М. Назаров[1], А.Н. Космынин[1], Д.С. Филонов[1]

[1] Московский физико-технический институт (национальный исследовательский университет), г. Долгопрудный, Россия;

[2] Государственная корпорация «Роскосмос», Москва, Россия

✉ burtsev.vd@phystech.su

Аннотация. В этой работе показаны результаты разработки фазированной антенной решетки Ku-диапазона частот для спутниковой связи. Предложенная антенна имеет круговую поляризацию и основана на массиве излучающих патч-элементов. В данной работе описаны конструкции и характеристики фазированных антенных решеток для дальнейших исследований и разработок в области технологий спутниковой связи.

Ключевые слова: фазированная антенная решетка, Ku-диапазон, электронное управление лучом, электродинамическое моделирование

Финансирование: Работа выполнена при поддержке Министерства науки и высшего образования Российской Федерации, номер проекта 011-2022-11-075.

Ссылка при цитировании: Никулин А.В., Бурцев В.Д., Антошкин Г.В., Прохоров С.Ю., Вошева Т.С., Назаров Н.М., Космынин А.Н., Филонов Д.С. Разработка фазированной антенной решетки Ku-диапазона для спутниковой связи // Научно-технические ведомости СПбГПУ. Физико-математические науки. 2024. Т. 17. № 3.2. С. 345–348. DOI: https://doi.org/10.18721/JPM.173.270

Introduction

Satellite communication systems in the Ku- (12–18 GHz) and Ka-band (26.5–40 GHz) frequencies are essential for wireless connectivity in remote areas where cellular networks and wired connections are absent [1]. Different antennas are used for such communication, including parabolic antennas with mechanical steering by rotating the entire structure [2] and phased array antennas that offer electronic or combined steering methods [3]. These arrays can be based on horn antennas [4] or planar patch-based designs [5], which are preferred for their compactness and ability to electronically steer the beam.

Various approaches are available for designing such planar arrays. It is possible to create a wide-band or dual-band array that operates in both receive (Rx) and transmit (Tx) frequency ranges [6]. Generally, these arrays support linear polarization [7], but integrating both wide-band capability and circular polarization in a single design poses manufacturing challenges [8]. The key issue lies in designing the feeding circuit to support wide- or dual-band functionality. Our aim was to develop a phased array with separate subarrays for Rx and Tx, both using circular polarization.

In this work, we present simulation results for separate Rx and Tx phased arrays designed for a new satellite communication system. The proposed arrays operate in the Ku-band, with both subarrays based on patch antennas using 90-degree hybrids to achieve circular polarization. We optimized the size of individual elements and the array spacing to ensure optimal gain, ellipticity, and sidelobe levels. Finally, we discuss the capabilities of electronic beam steering through tailored beamformers.

Materials and Methods

The development of the Ku-band phased array antenna required comprehensive electromagnetic simulations to attain the desired performance characteristics. We concentrated on patch antenna elements with directors because they offer a suitable frequency bandwidth, higher antenna gain, and can be effectively used in large arrays [6]. The first step in our design process involved optimizing individual antenna elements in a small-scale 3×3 array configuration (Fig. 1). This approach enabled us to assess inter-element interactions while maintaining an affordable simulation setup in terms of optimization. We swept across both the radial dimensions of the patch antenna itself (D_{patch}) and its director (D_{dir}), as well as the parameters of the matching system (hybrid coupler): the length (D_{hyb}) and width (M_{hyb}) of the microstrip lines. The criteria for evaluating the quality of the structure were the reflection coefficient from a single element of the structure surrounded by neighbors, as well as the coefficient of inter-element isolation, contributing to the total standing wave coefficient. They both should have been achieved -17 dB. The resulting parameter values are given in Fig. 1, *d*.

The whole array contains one transmit (Tx) subarray (14 to 14.25 GHz) and one receive (Rx) subarray (10.95 to 11.7 GHz). The antenna uses left circular polarization (LCP) for Rx and right circular polarization (RCP) for Tx. Impedance matching is achieved by driving the patch with two orthogonal microstrip lines. To reduce cross-coupling, a metallic screen separates the patch from the feeding hybrid.

In Fig. 1, *a*, the upper view shows the 3×3 array of patch elements with directors positioned on top. In Fig. 1, *b*, the lower view reveals the feeding network of the single element. This network includes 90-degree hybrids, vias, and 50-ohm resistors. The hybrids manage circular polarization. Fig. 1, *c* provides a cross-sectional view, highlighting the antenna's internal structure. It displays

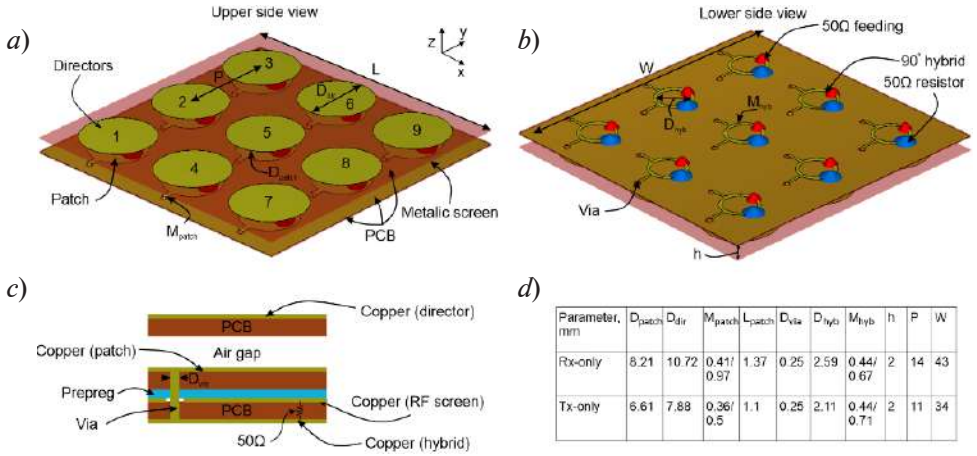

Parameter, mm	D_{patch}	D_{dir}	M_{patch}	L_{patch}	D_{via}	D_{hyb}	M_{hyb}	h	P	W
Rx-only	8.21	10.72	0.41/ 0.97	1.37	0.25	2.59	0.44/ 0.67	2	14	43
Tx-only	6.61	7.88	0.36/ 0.5	1.1	0.25	2.11	0.44/ 0.71	2	11	34

Fig. 1. Upper side view (*a*), lower side view with feeding network (*b*), cross-sectional view of individual element (*c*), geometrical parameters of arrays (*d*)

the copper patch, director, and prepreg layers, indicating the design's multi-level arrangement. The air gap between the patch and the feeding circuit helps ensure proper higher realized gain.

Patch antennas are built with lossy copper on a WL-CT338 substrate (Wangling insulator with dielectric constant near 3.38) with a thickness of 0.203 mm, whereas the connecting layers use WL-PP350 prepreg (Wangling binding glue with dielectric constant near 3.5) with a thickness of 0.1 mm. Table I shows the key geometrical parameters of the antenna element. The full-size array consists of 40×24 elements for the Rx subarray and 52×24 elements for the Tx subarray, measuring 561×337 mm and 573×265 mm, respectively.

Simulations were performed with the CST Studio Suite's Time Domain Solver, using a global mesh with 30 cells per wavelength. The lossy copper for conductive parts came from the CST material library, and a lumped 50-ohm resistor was used to minimize computational load. Following the initial 3×3 array simulations, we employed the array-factor functionality to predict the full-sized array's behavior, focusing on realized gain, cross-polarization, and scanning angle range.

Results and Discussion

Fig. 2, *a* shows the *S*-parameters are shown for the Rx-band across a frequency range from 10 to 15 GHz. This figure depicts reflection and transmission levels across different frequencies. The S_{11} parameter, indicating the reflection coefficient for the Rx subarray, stays below −20 dB throughout the 10.95 to 11.7 GHz range, signifying good impedance matching. The coupling between adjacent elements, such as S_{25} and S_{35}, remains under −17 dB, indicating a low level. The dip in the S_{11} curve near 11.5 GHz demonstrates optimal impedance matching for the Rx subarray. Fig. 2, *b* shows the S-parameters for the Tx-band, covering a broader range from 10 to 15 GHz.

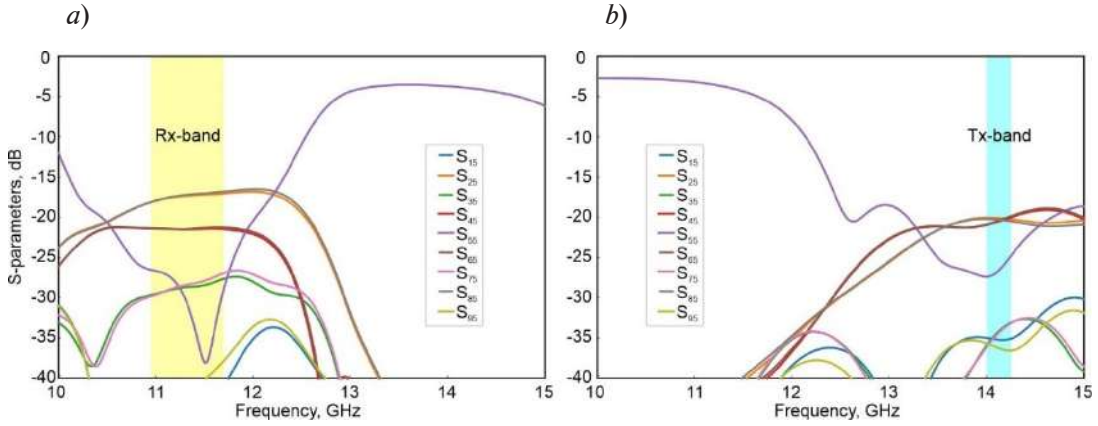

Fig. 2. Simulation results: *S*-Parameters for the Rx Subarray (*a*); *S*-Parameters for the Tx Subarray (*b*)

The S_{11} parameter for the Tx subarray remains below -20 dB in the 14 to 14.25 GHz range, indicating effective impedance matching. The worst-case coupling, such as S_{25} and S_{65}, is below -20 dB. The S_{11} curve in the Tx-band has a dip near 14.125 GHz, indicating a well-matched frequency for this subarray.

Conclusion

We presented the simulation results of the phased array antenna. The optimization of a single radiating patch in a 3×3 array was the first step. The simulation results showed that in the optimized structure, both reflection coefficients lie below -20 dB, which is a good indicator for the antenna element. In addition, the inter-element interchange with the nearest neighbors is located in the range from -17 to -20 dB, which also indicates that all supplied energy is being radiated. Thus, it is possible to build a phased array antenna for Ku-band, basing on the proposed design.

REFERENCES

1. **Panagopoulos A.D., Arapoglou P.-D. M., Cottis P.G.,** Satellite communications at KU, KA, and V bands: Propagation impairments and mitigation techniques, IEEE Communications Surveys and Tutorials. 6 (3) (2004) 2–14.

2. **Liu C., Yang S., Nie Z.,** Design of a parabolic reflector antenna with a compact splash-plate feed, Cross Strait QuadRegional Radio Science and Wireless Technology Conference. (2013) 241–244.

3. **Litinskaya Y.A., Alexandrin A.M., Lemberg K.V., et al.,** Phased array antenna with combined electronical and mechanical beam steering for satellite networks, International Siberian Conference on Control and Communications (SIBCON). (2013).

4. **Ordek S., Kizilay A.,** Horn array antenna design for Ku-band applications, 9th International Conference on Electrical and Electronics Engineering (ELECO). (2015).

5. **Gultepe G., Kanar T., Zihir S., Rebeiz G.M.,** A 1024-Element Ku-Band SATCOM Phased-Array Transmitter With 45-dBW Single-Polarization EIRP, IEEE Transactions on Microwave Theory and Techniques. 69 (9) (2013) 241–244.

6. **Khan M., Yang Z., Warnick K.,** et al., Dual-CircularPolarized High-Efficiency Antenna for Ku-Band Satellite Communication, IEEE Antennas and Wireless Propagation Letters. 13 (2014) 1624–1627.

7. **Shi W., Qian Z. , Zhou J., et al.,** A Small Ku-Band Polarization Tracking Active Phased Array for Mobile Satellite Communications, International Journal of Antennas and Propagation. (2013).

8. **Khalid M.I., Walaa M.H., Esmat A.A., Ahmed M.A.,** Wideband sequential feeding network for Ku-band dual circularly polarized 4×4 antenna array, Int J RF Microw Comput Aided Eng. 30 (9) (2020) 22283.

THE AUTHORS

NIKULIN Anton V.
nikulin.av@mipt.ru

VOSHEVA Tatyana S.
Vosheva.ts@mipt.ru
ORCID: 0000-0002-5786-4972

BURTSEV Vladimir D.
burtsev.vd@phystech.su
ORCID: 0000-0002-7988-5213

NAZAROV Natanil M.
nazarov.nm@mipt.ru

ANTOSHKIN German V.
antoshkin.gv@mipt.ru

KOSMYNIN Alexey N.
alekseykosmynin@matrixwave.tech

PROKHOROV Sergey Yu.
prokhorov.sy@roscosmos.ru

FILONOV Dmitry S.
dimfilonov@gmail.com
ORCID: 0000-0002-5394-8677

Received 31.07.2024. Approved after reviewing 12.08.2024. Accepted 13.08.2024.

Conference materials
UDC 537.86
DOI: https://doi.org/10.18721/JPM.173.271

Surface roughness modeling for extremely high frequency applications

A.P. Sedov[1], V.D. Burtsev[1]✉, A.V. Nikulin[1],
A.A. Khudykin[1], T.S. Vosheva[1], D.S. Filonov[1]

[1] Moscow Institute of Physics and Technology (National Research University), Dolgoprudny, Russia

✉ burtsev.vd@phystech.su

Abstract. In this work, we show electromagnetic simulations of surface roughness in multiple conventional antennas applicable for 6G networks potentially operating in the W-band (75–110 GHz). Operations at such high frequencies require fine accuracy of surface processing that becomes to the order of the wavelength. We show simulations of the surface roughness of four devices, such as a horn antenna, a patch antenna, a rectangular waveguide, and a microstrip transmission line. Finally, we simulated S-parameters and conducted statistical analysis to define the requirements of surface processing.

Keywords: extremely high frequency, surface roughness, electromagnetic simulations

Funding: The work has been supported by the Russian Science Foundation (Project 23-29-00152).

Citation: Sedov A.P., Burtsev V.D., Nikulin A.V., Khudykin A.A., Vosheva T.S., Filonov D.S., Surface roughness modeling for extremely high frequency applications. St. Petersburg State Polytechnical University Journal. Physics and Mathematics. 17 (3.2) (2024) 349–353. DOI: https://doi.org/10.18721/JPM.173.271

Материалы конференции
УДК 537.86
DOI: https://doi.org/10.18721/JPM.173.271

Моделирование шероховатости поверхности для устройств, работающих на крайне высоких частотах

А.П. Седов[1], В.Д. Бурцев[1]✉, А.В. Никулин[1],
А.А. Худыкин[1], Т.С. Вошева[1], Д.С. Филонов[1]

[1] Московский физико-технический институт (национальный исследовательский университет), г. Долгопрудный, Россия

✉ burtsev.vd@phystech.su

Аннотация. В этой работе мы демонстрируем электродинамическое моделирование шероховатости поверхности для нескольких антенн, подходящих для применения в сетях шестого поколения, эксплуатирующих частоты порядка 75–110 ГГц. В качестве таких устройств были выбраны рупорная антенна, прямоугольный волновод, микрополосковая линия передачи и патч-антенна. После проведения электродинамического моделирования были получены графики S-параметров, на основании которых были определены требования к обработке поверхностей устройств.

Ключевые слова: крайне высокие частоты, шероховатость поверхности, электродинамическое моделирование

Финансирование: Работа выполнена при поддержки Российского Научного Фонда (Проект № 23-29-00152).

Ссылка при цитировании: Седов А.П., Бурцев В.Д., Никулин А.В., Худыкин А.А., Вошева Т.С., Филонов Д.С. Моделирование шероховатости поверхности для устройств, работающих на крайне высоких частотах // Научно-технические ведомости СПбГПУ. Физико-математические науки. 2024. Т. 17. № 3.2. С. 349–353. DOI: https://doi.org/10.18721/JPM.173.271

Introduction

One potential application that uses extremely high frequencies, such as W-band (75–110 GHz), is the 6G wireless network [1, 2]. Several antennas could be used at such a high frequency, among them horn antennas and patch antennas. In addition, one could use rectangular waveguides, and microstrip lines, and many others. At such a high frequency, the manufacturing defect has an important role in antenna performance [3, 4]. Recently we have already performed an electromagnetic investigation of the surface roughness of some devices [5], whereas here we enlarge our work to the microstrip line and also investigate the convergence rate to validate our approach.

Materials and Methods

To simulate surface roughness, we performed numerical electromagnetic analysis using simulations in the CST Studio Suite. We separated all devices into two groups, such as additive devices and chemically etched devices, according to the manufacturing method (Fig. 1). In the first group (Fig. 1, *a*, *b*), we simulated a horn antenna and a rectangular waveguide with the WR-10 flange. In the second group, we simulate a patch antenna and a microstrip line (Fig. 1, *c*, *d*).

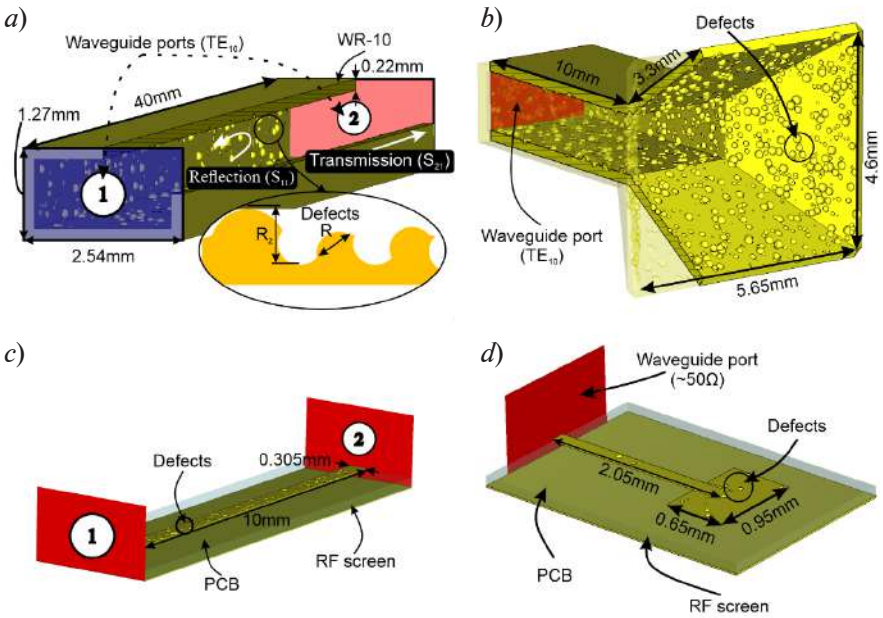

Fig. 1. Simulation setups and general view of structures with defects: waveguide (*a*), horn antenna (*b*), microstrip (*c*), patch antenna (*d*)

In the first group, we modeled the surface roughness as a set of bumps or hollows, whereas we modeled only hollows in the second group. These defects have a spherical shape with a radius of *R*. For each device, we performed a statistical analysis with 50 random series of simulations, and

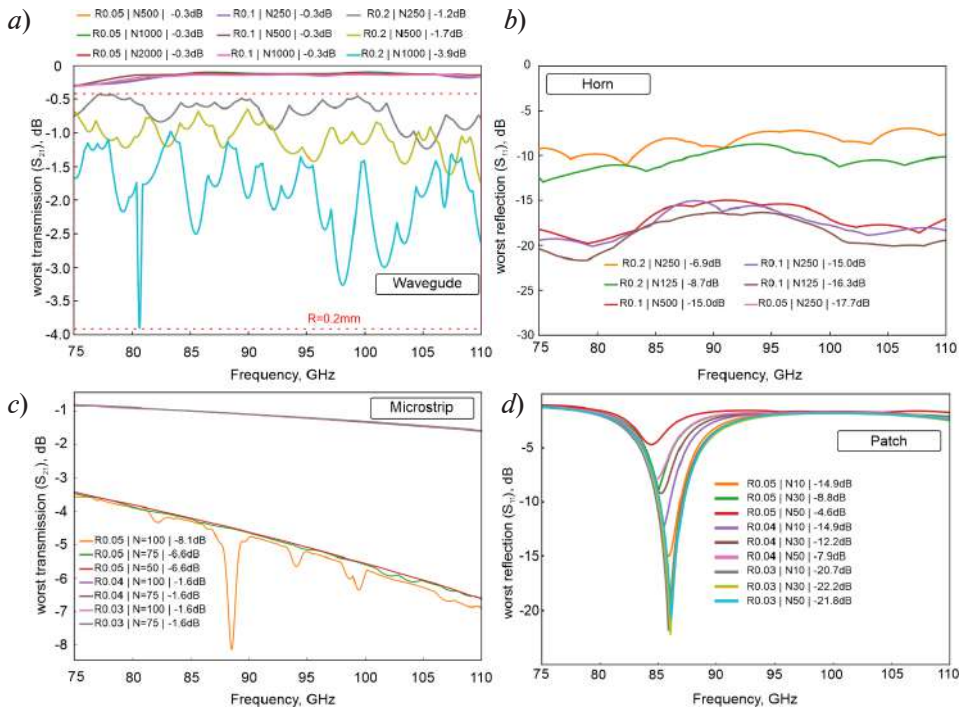

Fig. 2. Transmission coefficient of waveguide (*a*), worst reflection coefficient of horn antenna (*b*), worst transmission coefficient of microstrip (*c*), worst reflection coefficient of patch antenna (*d*). In plot legend tables, defect size R in first column is given in mm, N in second column is corresponding to total number of simulated spheres, third column depicts worst values across all frequency range

then the S-parameters were evaluated as the worst value at a picked frequency point, as shown in Fig. 2. For the waveguide, we assessed transmission coefficient S_{21} (Fig. 2, *a*, *c*), whereas for the horn and patch antennas, we assessed reflection coefficient S_{11} (Fig. 2, *b*, *d*). In each case, we assessed three levels of defect sizes and several defects' quantities, depending on the device. These sets of simulations are also shown in Fig. 2.

Finally, we performed statistical analysis on the waveguide to analyze the convergence rate. We observed that in the case of 200 random series, computation time increases drastically by a factor of 3, whereas the difference in terms of mean S-parameters becomes only 0.4% compared to the case of 50 random series. The convergence rate is shown in Fig. 3, *a*, and the mean S-parameters for two convergence scenarios are shown in Fig. 3, *b*.

Results and Discussion

In the case of the waveguide, the worst value of the transmission coefficient decreases to -3.9 dB (Fig. 2, *a*), whereas the cases $R = 0.05$ mm and $R = 0.1$ mm which S_{21} values do not exceed -0.3 dB, could be considered as acceptable, since this value is comparable to the ideal waveguide (0 dB), and its difference is about only 5%. This means that the acceptable surface roughness in the case of the waveguide corresponds to the wavelength/14 and the wavelength/28 respectively, at 110 GHz.

For the horn antenna, we observed that for $R = 0.1$ mm, the worst reflection coefficient S_{11} is nearly −15 dB (Fig. 2, *b*), which is also considered acceptable, because it is a typical value obtained on practice for horn antenna. In terms of wavelength, this surface roughness equals wavelength/14.

For the microstrip transmission line, we observed that for 0.03 mm defect size, the worst S_{11} is nearly −1.6 dB (Fig. 2, *c*), which is close to the ideal scenario corresponding to the case with a flat surface. In terms of the wavelength, these values are above the mean wavelength/90.

Finally, in the case of patch antennas, we can observe that the worst reflection coefficient S_{11} for 0.04 mm is approximately −15 dB (Fig. 2, *d*), which means wavelength/90.

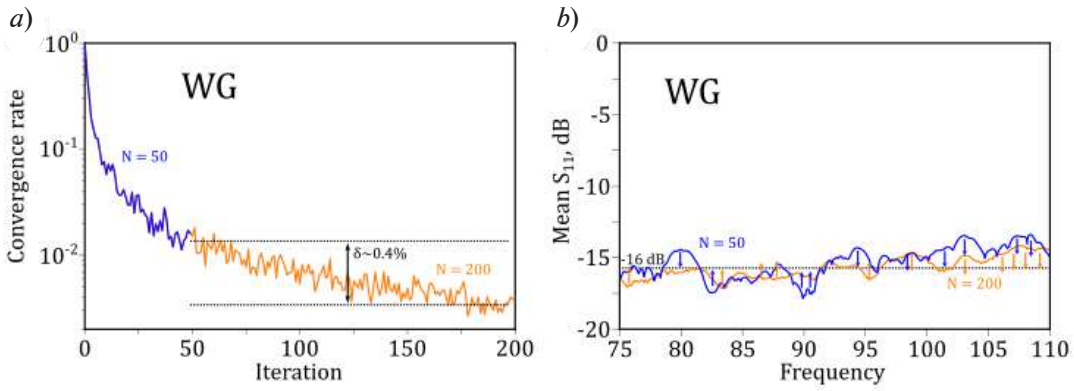

Fig. 3. Convergence rate of the waveguide (*a*),
mean S-parameters for two convergence scenarios (*b*)

For all cases mentioned above, we observed that with a small number of defects, but with a maximum size of defects, one observes acceptable performance of the devices under consideration.

Conclusion

In this work, we analyzed four structures: a waveguide, a horn, a microstrip, and a patch. We have shown that surface roughness $R = 0.1$ mm is acceptable for the waveguide and the horn, whereas in the case of the microstrip and the patch, one has to provide surface defects of 0.04 mm. After performing the set of electromagnetic simulations, we can conclude that in the case of the horn antenna and a patch antenna, the preferred surface quality should be at least wavelength/14, whereas in the case of the microstrip transmission line and the patch antenna, surface quality should be at least wavelength/90. Following these requirements, one has to select the proper manufacturing method or surface processing approach in order to maintain the quality of the surface.

REFERENCES

1. **Rappaport T.S., Xing Y., Kanhere O., et al.,** Wireless communications and applications above 100 GHz: Opportunities and challenges for 6g and beyond, IEEE Access. 7 (2019) 78729–78757.

2. **Polese M., Ariyarathna V., Sen P., Siles J.V., Restuccia F., Melodia T., J. Jornet M.,** Dynamic spectrum sharing between active and passive users above 100 GHz, Commun. Eng. 1 (1) (2022) 6.

3. **Al-Tarifi M.A., Filipovic D.S.,** On the design and fabrication of W-band stabilised-pattern dual-polarised horn antennas with DMLS and CNC. IET Microwaves, Antennas Propag. 11 (14) (2017) 1930–1935.

4. **Almeshehe M., Murad N., Rahim M., et al.,** Surface roughness impact on the performance of the 3D metal printed waveguide coupler at millimeterwave band. Engineering Science and Technology. 35 (2022) 101129.

5. **Nikulin A.V., Burtsev V.D., Vosheva T.S., Filonov D.S.,** Surface roughness simulations for 6G additive antennas. Days on Diffraction (DD). (2023).

THE AUTHORS

SEDOV Artem P.
sedov.ap@mipt.ru

BURTSEV Vladimir D.
burtsev.vd@phystech.su
ORCID: 0000-0002-7988-5213

NIKULIN Anton V.
nikulin.av@mipt.ru

KHUDYKIN Anton A.
khudykin.aa@mipt.ru
ORCID: 0000-0001-7992-7981

VOSHEVA Tatyana S.
Vosheva.ts@mipt.ru
ORCID: 0000-0002-5786-4972

FILONOV Dmitry S.
dimfilonov@gmail.com
ORCID: 0000-0002-5394-8677

Received 31.07.2024. Approved after reviewing 15.08.2024. Accepted 16.08.2024.

Conference materials
UDC 537.876.4
DOI: https://doi.org/10.18721/JPM.173.272

Terahertz integrated H-plane bend: simulation and experimental investigation

A.K. Kozhukhovsky[1]✉, S.V. Seliverstov[1,5], S.S. Svyatodukh[2,4], G.N. Goltsman[2,3]

[1] Moscow Pedagogical State University, Moscow, Russia;

[2] National Research University Higher School of Economics, Moscow, Russia;

[3] Russian Quantum Center, Moscow, Russia;

[4] National University of Science and Technology "MISIS" (MISIS), Moscow, Russia;

[5] Russian Technological University (MIREA), Moscow, Russia

✉ ak_kozhukhovskii@student.mpgu.edu

Abstract. The usefulness of using terahertz radiation has been proven in practice. Recently we have studied how to manufacture and use silicon waveguides and obtained insignificant signal loss. Final purpose is creating the integrated photonic circuit which needs not only straight waveguide sections, which we have done before, but bend structures with minimal signal loss, which we present in this paper. The insertion loss of the structure we made is ~0.178 dB ± 0.081 dB at frequency of 145.5 GHz. This result is simulated and experimentally verified. This once again proves that it is possible to create a full-fledged design that has a lot of practical applications. It is a future of communication systems, medicine and artificial intelligence development. Eventually we will be able to create a physical structure that will be a hardware implementation of an artificial neural network with extremely low power consumption.

Keywords: terahertz photonics, waveguide, photonic integrated circuit, H-plane bend

Funding: The study was supported by Rosatom in the framework of the Roadmap for Quantum computing (Contract No. 868-1.3-15/15-2021 dated October 5), grant from the Russian Science Foundation No. 21-72-10119, https://rscf.ru/project/21-72-10119/, and funding from the Russian Ministry of Higher Education and Science within the framework of State assignment No. FSFZ-2022-0005.

Citation: Kozhukhovsky A.K., Seliverstov S.V., Svyatodukh S.S., Goltsman G.N., Terahertz integrated H-plane bend: simulation and experimental investigation, St. Petersburg State Polytechnical University Journal. Physics and Mathematics. 17 (3.2) (2024) 354–359. DOI: https://doi.org/10.18721/JPM.173.272

Материалы конференции
УДК 537.876.4
DOI: https://doi.org/10.18721/JPM.173.272

Интегрированный изгиб в H-плоскости в терагерцовом диапазоне: моделирование и экспериментальное исследование

А.К. Кожуховский[1]✉, С.В.Селиверстов[1,5], С.С.Святодух[2,4], Г.Н.Гольцман[2,3]

[1] Московский педагогический государственный университет, Москва, Россия;

[2] Национальный исследовательский университет «Высшая школа экономики», Москва, Россия;

[3] Российский Квантовый Центр, Москва, Россия;

[4] Национальный Исследовательский Технологический Университет МИСиС, Москва, Россия;

[5] Российский технологический университет (МИРЭА), Москва, Россия

✉ ak_kozhukhovskii@student.mpgu.edu

Аннотация. Полезность использования терагерцового излучения доказана на практике. Недавно мы изучали изготовление и использование кремниевых волноводов и получили незначительные потери сигнала. Конечная цель — создание интегральной фотонной схемы, для которой нужны не только прямые волноводные секции, которые мы делали ранее, но и изогнутые конструкции с минимальными потерями сигнала, которые мы представляем в этой статье. Вносимые потери изготовленной нами структуры составляют примерно ~0,178 дБ ± 0,081 дБ на частоте 145,5 ГГц. Данный результат смоделирован и экспериментально проверен. Это еще раз доказывает, что можно создать полноценную интегральную структуру, имеющую множество практических применений. Это будущее систем связи, медицины и развития искусственного интеллекта. В конце концов мы сможем создать физическую структуру, которая будет аппаратной реализацией искусственной нейронной сети с предельно малым энергопотреблением.

Ключевые слова: терагерцовая фотоника, волноводы, фотонная интегральная решетка, изгиб волновода

Финансирование: Работа выполнена при поддержке гранта РНФ № 10119-72-21, https://rscf.ru/project/21-72-10119/, компании Росатом в рамках Дорожной карты Квантовых вычислений (Контракт № 2021-15/15-1.3-868 от 5 октября) и Министерства высшего образования и науки Российской Федерации в рамках государственного задания № FSFZ-2022-0005.

Ссылка при цитировании: Кожуховский А.К., Селиверстов С.В., Святодух С.С., Гольцман Г.Н. Интегрированный изгиб в H-плоскости в терагерцовом диапазоне: моделирование и экспериментальное исследование // Научно-технические ведомости СПбГПУ. Физико-математические науки. 2024. Т. 17. № 3.2. С. 354–359. DOI: https://doi.org/10.18721/JPM.173.272

Introduction

The interest of big data processing is actual in our world. The processing of big data is directly related to the process of its transmission. The latest advances in the field of wired data transmission are the development of principles and design options for terabit low-power fiber optic interconnect lines of modern data centers. We have demonstrated a system with a total throughput of at least 4 Tbit/s with specific energy consumption of no more than 0.1 nJ/bit. In fact, actual energy consumption may be even lower. Achieving comparable wireless data transmission speeds is an urgent scientific and practical task. This is possible through the use of THz radiation, occupying the range 0.1–10 THz.

To make a well-functioning and in-demand end device, we analyzed examples of the use of the THz range. We have to say that the basic problem of THz range is absorption by water vapor contained in the surrounding air [1], but it has many practical applications over short distances. Using the advantages of THz radiation will increase the speed of wireless internet [2] and will also contribute to the development of such areas as augmented reality [3] and high resolution live-streaming [4]. But not only for the internet sphere we are making such a device. Another example is a short-range THz radar (operating at distances of the order of several tens of meters), which can operate with high resolution in conditions of limited visibility (a large amount of fog or dust in air, etc.) when other classical systems such as a lidar or optical stereo camera cannot be used. Such a system was also demonstrated previously [5]. It can be used for delivery-robots and autopiloting of transport. All of this can serve as an example of the prospects for using the THz range. Our goal is to make a special device in the form of a photonic integrated circuit, to start to use all opportunities of THz range. For these purposes, we will need not only straight sections of the waveguide, but also bends, without which we will not be able to make a practical device.

Materials and Methods

In this paper we present the results of simulation and measuring of insertion loss of a H-plane bend based on a THz waveguide made on the basis of a high resistivity silicon substrate. The simulation model was conducted to solve the following well-known equations:

$$\begin{aligned} \Delta\vec{E} - \frac{n^2}{c^2}\frac{\partial^2\vec{E}}{\partial t^2} = 0, \\ \Delta\vec{H} - \frac{n^2}{c^2}\frac{\partial^2\vec{H}}{\partial t^2} = 0, \end{aligned} \tag{1}$$

where Δ is the Laplace operator, n is the refractive index of the medium, and c is the speed of light in vacuum.

The finite element method was used for simulation. A screenshot of the model in the used modeling environment is presented in the inset to Fig. 3, *a*. The model specified a H-plane bend of the waveguide with a turning radius of 3000 μm. The waveguide width is 585 μm. The material used was silicon with a dielectric constant of 11.9. The bend has two tapers with lengths of 3500 μm. Tapers are surrounded by metallic boundaries (as in the experiment we put them into the metal waveguides). The condition "Perfect-E" was imposed on these metal surfaces in the model (means that we assume the metallic waveguide as an ideal conductor). The parameters of the metallic waveguide are following: the height (along the Z-axis as shown in Fig.3,*a*) equals to 800 μm, the width (which is along the Y-axis) equals to 1600 μm and the length equals to 3500 μm. In the model, the tapers were installed in such a way that their axes coincided with the axes of the metal waveguides into which they were inserted. Wave ports were specified at the input and output of metal waveguides. The model of H-plane bend with tapers and metal waveguides was surrounded by an air box, on the faces of which the "Radiation" condition was set (means that this surface does not reflect radiation, but transmit it completely into surrounding space). We simulated the S21 parameter of the bend in the frequency range from 120 to 170 GHz with steps of 5 GHz.

The experimental structure consisted of an H-plane bend based on a cladding-less silicon waveguide, as well as two straight waveguide sections integrated with an effective medium that allows radiation to propagate along the waveguide due to total internal reflection [6, 7]. In the experiment, the structure was placed in a plastic holder in such a way that the plastic did not intersect the effective medium, and the input and output tapers were located as close as possible to the center of the metal waveguides connecting the structure under study to the source and detector. A Schottky diode was used as a detector, and a backward wave oscillator was used as a radiation source. Effective medium was determined by a grid of perforations. The parameters of the grid structure are the same as were in the simulation model. The study used multiple identical fabricated structures to improve measurement accuracy. All measurements were carried out at the frequency of 145.5 GHz, since the geometry of the waveguides is optimized for this frequency.

We did not use an effective medium in this simulation as we wanted to study the bend itself. In addition, in this work, the effective medium performed only an auxiliary function in order to ensure the passage of radiation through the L-shaped stiffener of the structure.

Results and Discussion

The measurement and simulation results presented in Fig.3, *a* confirmed our expectations. We observe that the signal loss decreases with increasing frequency. The nature of the dependence of transmittance on frequency has a simple qualitative explanation. As the frequency decreases, the effective refractive index of the waveguide mode decreases because the wave power of the evanescent mode, which is not localized in the core of the waveguide, increases. We carried out corresponding modeling, the results of which are presented in Fig. 2. On it we see the dotted red line showing frequency dependence of an effective refractive index of the waveguide. The field distributions in the cross section of the waveguide are presented at two frequencies (126.5 and 145.5 GHz). The field distributions in the band plane on a logarithmic scale at the same frequencies are presented in Fig. 1.

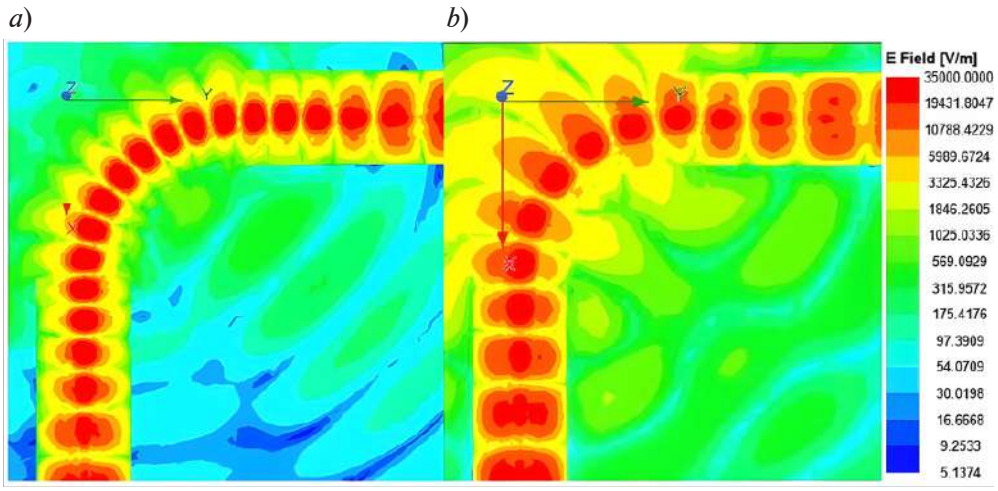

Fig. 1. Picture of scattered field at 145.5 GHz (*a*) and 126.5 GHz (*b*)

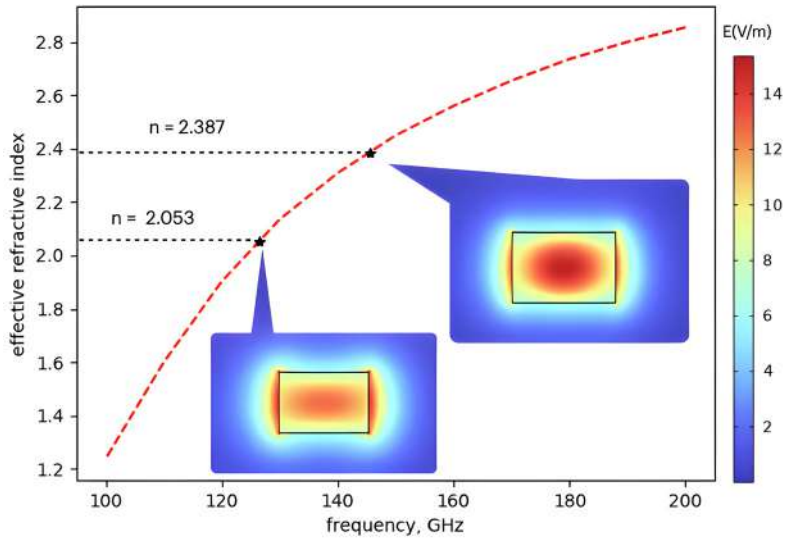

Fig. 2. Dependence of effective refractive index on frequency
The distributions of the fields of wave modes in the cross section of the waveguide at frequencies of 126.5 and 145.5 GHz are also presented

Radiation at the edges of the waveguide in the region of rotation is more strongly scattered into the surrounding air at low frequencies. As a result, less power passes through the waveguide at lower frequency. A possible solution to this problem is to increase the turning radius. We plan to carry out relevant research in the near future.

The plot in Fig. 3, *a* shows the dotted red line corresponding to the simulation result and the black bar with the blue point at the center of it. The blue point corresponds to the averaged measured value of all measurements of a number of manufactured H-plane bends at the frequency of 145.5 GHz. The bar shows the experimental error. The value of this error equals ±2.1% which is a good result. Fig. 3, *a* also shows that the discrepancy between the simulation and measurements is within the experimental error. Fig. 3, *b* shows the photo of the structure under study. To make this picture clearly the white contour was applied around the structure. The picture does not give us an opportunity to see the effective medium surrounding the core, that's why we showed it in the inset. The dotted white lines show the borders of the core.

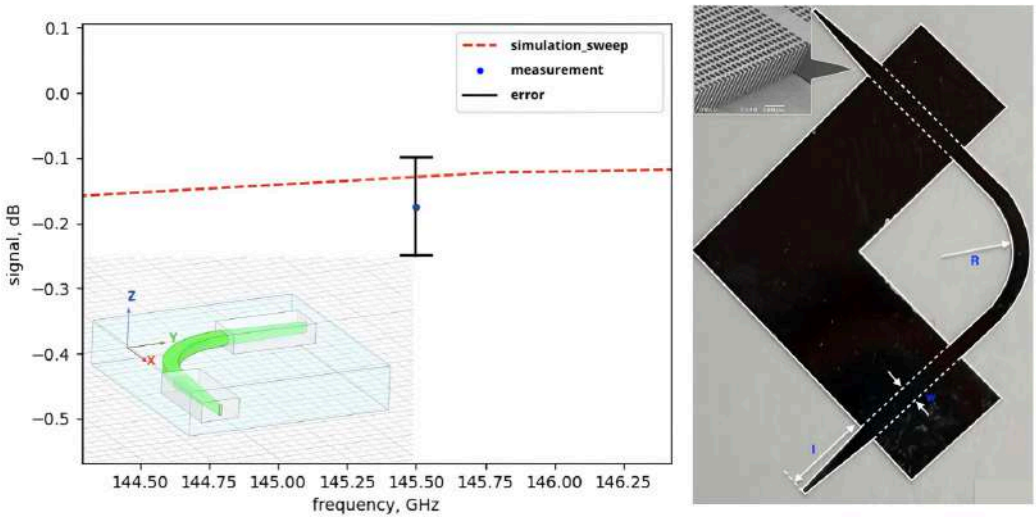

Fig. 3. Frequency dependence of S21 parameter and appearance of model in simulation environment at the bottom of the picture (*a*) Photo of manufactured structure, *w* (width of core) = 585 μm, *R* (radius of curvature) = 3000 μm, *l* (length of tapers) = 3500 μm (*b*)

We attribute the slight discrepancy between simulation and experimental investigation to possible defects in the structure that arose during its manufacture, as well as a possible small displacement of the matching tapers relative to the geometric center of the rectangular metallic waveguides when placing the structure in the holder. This displacement is associated with the 3D printing error of about 0.1 mm, which was used for the holder manufacturing. The measurement results could also be influenced by standing waves arising between the elements of the experimental setup. However, the fact is that H-plane bend works quite well and can be further improved in the future.

Conclusion

Creating the H-plane bend structure is another step towards creating a full-fledged photonic integrated circuit, which will allow us to exploit the full potential of the terahertz range in practical applications. Based on the results of the research conducted by our team, as well as the data that we obtained and published in our previous articles [6–8], we can confidently conclude that it is possible to create full-fledged practical THz devices for a number of applications using domestically produced materials. This achievement not only demonstrates the capabilities of our own production, but also allows us to lead the development of next-generation photonic technologies. The potential of integrated photonic circuits in the THz range is huge, they can be used in high-speed wireless communications, modern sensing and imaging systems. Using domestic materials, we can provide greater control over quality and supply chain, reduce dependence on foreign suppliers and improve the reliability of our products.

REFERENCES

1. **Slocum D., Slingerland E., Giles R., Goyette T.**, Atmospheric absorption of terahertz radiation and water vapor continuum effects, Journal of Quantitative Spectroscopy and Radiative Transfer. 127 (2013) 49–63.

2. **Khalid N., Abbasi N.A., Akan O.B.**, Statistical characterization and analysis of low-THz communication channel for 5G internet of things, Nano Communication Networks. 22 (2019) 100258.

3. **Chaccour C., Saad W.**, On the ruin of age of information in augmented reality over wireless terahertz (THz) networks, In: 2020 IEEE Global Communications Conference (GLOBECOM 2020); IEEE. Pp. 1–6.

4. **Nallappan K., Guerboukha H., Nerguizian C., Skorobogatiy M.**, Live streaming of uncompressed HD and 4K videos using terahertz wireless links, IEEE Access. 6 (2018) 58030–58042.

5. **Zhang C., Ota K., Jia J., Dong M.**, Breaking the blockage for big data transmission: Gigabit road communication in autonomous vehicles, IEEE Communications Magazine. 56 (6) (2018) 152–157.

6. **Seliverstov S.V., Svyatodukh S.S., Prokhodtsov A.I., Goltsman G.N.**, Optimization of a prism coupler for a THz photonic integrated metamaterial Si waveguide: simulation and experiment, St. Petersburg State Polytechnical University Journal. Physics and Mathematics. 16 (3.2) (2023) 406–410.

7. **Seliverstov S.V., Kozhukhovsky A.K., Svyatodukh S.S., Goltsman G.N.**, Terahertz phased array antenna based on integrated taper emitters, Applied Physics Letters. 124 (12) (2024).

8. **Seliverstov S.V., Svyatodukh S.S., Goltsman G.N.**, Thermal phase shift in THz silicon effective-medium waveguide, Applied Physics Letters. 123 (9) (2023).

THE AUTHORS

KOZHUKHOVSKY Alexey K.
ak_kozhukhovskii@student.mpgu.edu
ORCID: 0009-0003-7927-2171

SVYATODUKH Sergey S.
ssvyatodukh@hse.ru
ORCID: 0000-0001-9436-6641

SELIVERSTOV Sergey V.
sv.seliverstov@mpgu.su
ORCID: 0000-0001-9624-5325

GOLTSMAN Gregory N.
goltsman10@mail.ru
ORCID: 0000-0002-1960-9161

Received 26.07.2024. Approved after reviewing 19.08.2024. Accepted 19.08.2024.

Conference materials
UDC 535.3
DOI: https://doi.org/10.18721/JPM.173.273

Edge states supported by two-dimensional square-lattice arrays of bianisotropic dielectric resonators

A.D. Rozenblit✉, G.D. Kurganov, D.V. Zhirihin, N.A. Olekhno

ITMO University, St. Petersburg, Russia

✉ alina.rozenblit@metalab.ifmo.ru

Abstract. Robust wave propagation along the boundaries of two-dimensional structures at frequencies of bulk bandgap is the subject of active study and is typically related to topological properties. Here, we propose a new model of two-dimensional (2D) structure which is composed of centimeter-scale bianisotropic dielectric resonators placed in the nodes of a square lattice and supports edge states at microwave frequencies. As we demonstrate, bianisotropy introduced by breaking a geometrical symmetry of cylindrical resonators is essential for the bandgap opening. The simulation results for a finite structure demonstrate the emergence of in-gap edge states at the interface between the domains with oppositely oriented bianisotropic resonators. We numerically demonstrate spin-momentum locking for these modes, and, moreover, the emergence of such edge states at the boundary between the structure and free space, which is unusual for photonic topological insulators. The resilience of the observed states is confirmed by studying the system with double-bend interface and geometrical imperfections.

Keywords: edge states, bianisotropy, dielectric resonators, radiophysics

Funding: This study was funded by Russian Science Foundation (project 24-72-10069).

Citation: Rozenblit A.D., Kurganov G.D., Zhirihin D.V., Olekhno N.A., Edge states supported by two-dimensional square-lattice arrays of bianisotropic dielectric resonators, St. Petersburg State Polytechnical University Journal. Physics and Mathematics. 17 (3.2) (2024) 360–363. DOI: https://doi.org/10.18721/JPM.173.273

Материалы конференции
УДК 535.3
DOI: https://doi.org/10.18721/JPM.173.273

Краевые состояния в двумерной квадратной решётке из бианизотропных диэлектрических резонаторов

А.Д. Розенблит✉, Г.Д. Курганов, Д.В. Жирихин, Н.А. Олехно

Университет ИТМО, Санкт-Петербург, Россия

✉ alina.rozenblit@metalab.ifmo.ru

Аннотация. В настоящей работе впервые предложена двумерная структура, состоящая из сантиметровых бианизотропных диэлектрических резонаторов, помещенных в узлах квадратной решетки, которая поддерживает краевые состояния на радиочастотах. Результаты численного моделирования показывают существование краевых состояний с частотами в запрещенной зоне на интерфейсе между доменами с противоположной ориентацией бианизотропных резонаторов. Также продемонстрировано однонаправленное распространение краевых состояний с блокировкой спинового углового момента, и, более того, существование таких состояний на границе между доменом с резонаторами и свободным пространством. Устойчивость наблюдаемых состояний подтверждается исследованием систем с зигзагообразным интерфейсом.

Ключевые слова: краевые состояния, бианизотропия, диэлектрические резонаторы, радиофизика

Финансирование: Работа выполнена при поддержке Российского научного фонда в рамках проекта «Топологическая фотоника массивов многомодовых мета-атомов» (24-72-10069).

Ссылка при цитировании: Розенблит А.Д., Курганов Г.Д., Жирихин Д.В., Олехно Н.А. Краевые состояния в двумерной квадратной решетке из бианизотропных диэлектрических резонаторов // Научно-технические ведомости СПбГПУ. Физико-математические науки. 2024. Т. 17. № 3.2. С. 360–363. DOI: https://doi.org/10.18721/JPM.173.273

Introduction

Topological edge states possess fascinating physical properties like unidirectional wave propagation and robustness to the geometrical imperfections and backscattering [1]. Such states have been observed with the help of diverse experimental platforms including optical [2], microwave [3], acoustic [4], and even robotic [5] systems. Topological states may find their applications in designing antenna impedance matching systems [6], lasers [7], and compact phase shifters [8].

Materials composed of dielectric resonant particles represent one of the common platforms for the realization of photonic topological insulators due to their low losses in comparison with metallic structures [9]. Previously, it was shown that the bianisotropy of individual resonators reached by breaking their geometrical symmetry leads to the bandgap opening [10].

In the present work, we consider a two-dimensional (2D) square lattice of dielectric bianisotropic resonators. Even though hexagonal 2D [11] and 3D [12] topological insulators composed of bianisotropic resonators are well studied, the case of the 2D square-lattice systems has not been addressed yet. In contrast to these studies, we observe the edge states not only at the boundaries between two distinct domains, but also at the boundary between the structure and free space.

Materials and Methods

The proposed system represents a 2D array of dielectric bianisotropic resonators placed in the nodes of a simple square lattice having the period $a = 37.1$ mm, while a single resonator is implemented as two attached cylinders with the diameters $d_1 = 29.1$ mm and $d_2 = 22$ mm, and the heights $h_1 = 9$ mm and $h_2 = 3$ mm, respectively (Fig. 1, *a*). The permittivity of the resonators is $\varepsilon = 39$. We construct the numerical model of such resonators using CST Microwave Studio 2022 software package. To study the model, we first consider a unit cell under Floquet periodic boundary conditions which correspond to the infinite array of such bianisotropic resonators and compare numerically evaluated dispersion diagram with the one for an infinite array of cylindrical resonators having the same material properties, the diameter $d = 29.1$ mm, and the height $h = 12$ mm. Next, we extract magnetic response of the finite structure to the linearly and circularly polarized sources to demonstrate edge states at the linear and double-bend domain walls, as well as at the boundary between the array and free space.

Results and Discussion

The results of numerical simulations of the dispersion diagrams for the infinite array of ceramic cylinders and ceramic bianisotropic resonators are shown in (Fig. 1, *b*, *c*). The plots demonstrate the absence of a bandgap for the array of non-bianisotropic resonators, while the hybridization of electric and magnetic moments results in a bandgap opening in the range from 2.43 GHz to 2.53 GHz at M-point of the Brillouin zone.

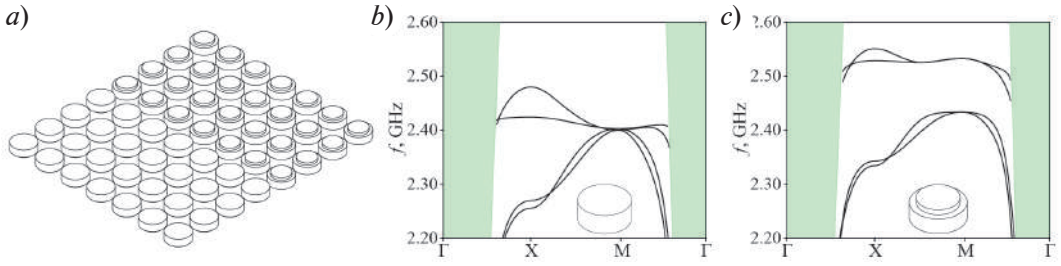

Fig. 1. Schematic model of the considered system (*a*); dispersion diagram for the infinite array of cylinders (*b*), inset shows the geometry of a single resonator; same as panel (*b*), but for infinite array of bianisotropic resonators (*c*). Green shaded area shows the light cone in panels (*b*, *c*)

The numerically simulated magnetic field profiles at the frequency $f = 2.47$ GHz demonstrate the presence of edge states along the interface, as well as spin-momentum locking of the edge states for linear and double-bend domain wall shapes, (Fig. 2, *a*–*f*). We also observe edge states at the boundary between the array of resonators and free space for linearly and circularly polarized excitations at $f = 2.47$ GHz, (Fig. 2, *g*–*i*).

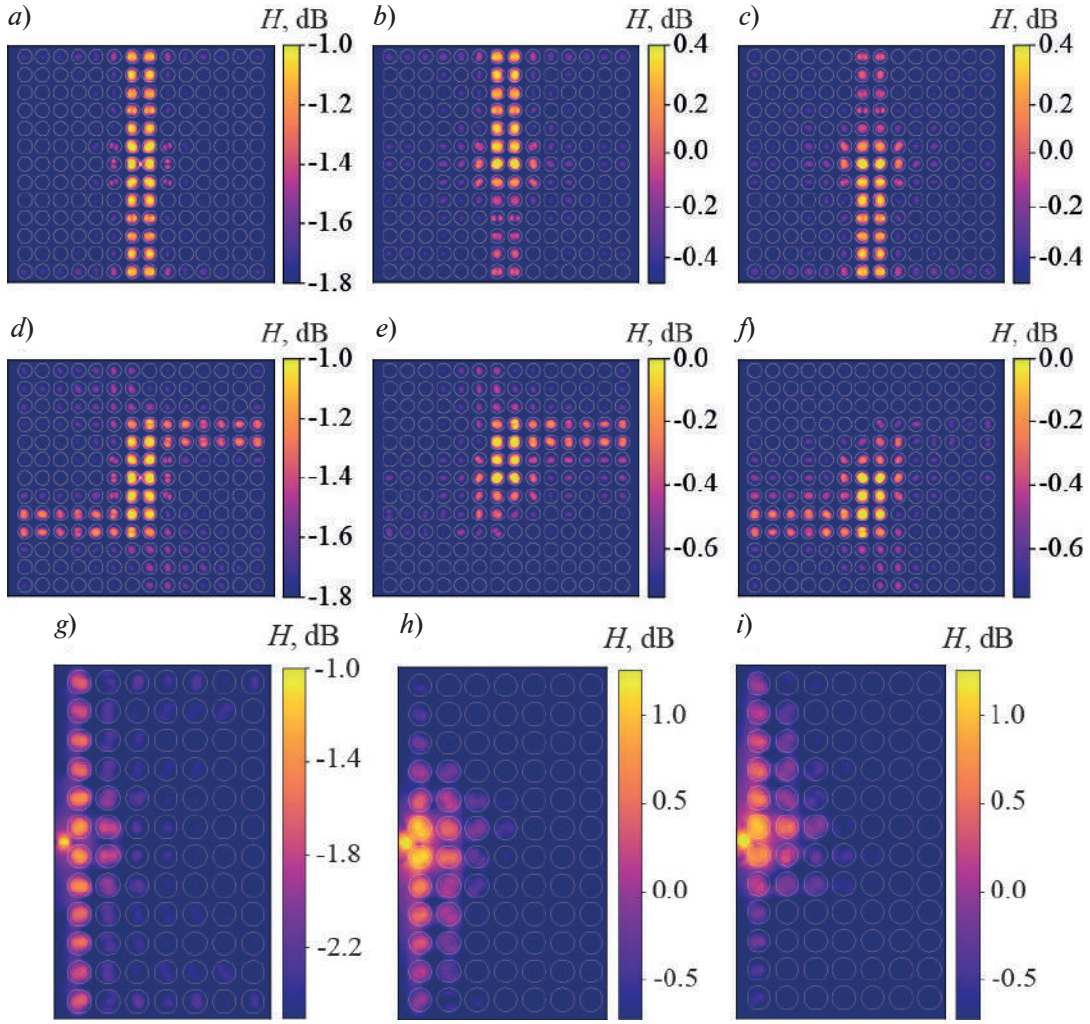

Fig. 2. *H*-field profiles at the frequency $f = 2.47$ GHz for the systems with linear (*a*–*c*) and double-bend (*d*–*f*) domain walls in the case of linear (*a*, *d*) and circular (*b*, *c*, *e*, *f*) polarization of the source. Panels (*g*–*i*) are the same as panels (*a*–*c*), but for the boundary between the domain and free space. White circles show the edges of resonators

Conclusion

To conclude, we propose a two-dimensional model having square lattice symmetry and supporting edge states resulting from the bianisotropy of individual resonators instead of engineered couplings between them. We perform numerical simulations of such a system implemented as an array of ceramic centimeter-scale resonators working at GHz frequencies and feasible for further experimental realization. The results demonstrate the emergence of edge states, their spin-momentum locking in the case of a circularly polarized excitation, and their robust propagation both for domain walls and a boundary between the photonic structure and free space. To establish if the observed states are topological or represent one-dimensional analogs of photonic Jackiw-Rebbi edge states considered in [13], the topological invariant has to be evaluated, which is a subject of future studies.

REFERENCES

1. **Wang Z., et al.**, Observation of unidirectional backscattering-immune topological electromagnetic states, Nature. 461 (7265) (2009) 772–775.

2. **On M.B., et al.**, Programmable integrated photonics for topological Hamiltonians, Nature Communications. 15 (1) (2024) 629.

3. **Li Y., et al.**, Topological LC-circuits based on microstrips and observation of electromagnetic modes with orbital angular momentum, Nature Communications. 9 (1) (2018) 4598.

4. **Ni X., et al.**, Topological edge states in acoustic Kagome lattices, New Journal of Physics. 19 (5) (2017) 055002.

5. **Yang X., et al.**, Robust boundary flow in chiral active fluid, Physical Review E. 101 (2) (2020) 022603.

6. **Lumer Y., Nader E.**, Topological insulator antenna arrays, ACS Photonics. 7 (8) (2020) 2244–2251.

7. **Han C., Minsu K., Heonsu J.**, Lasing at multidimensional topological states in a two-dimensional photonic crystal structure, ACS Photonics. 7.8 (2020) 2027–2036.

8. **Wang H., et al.**, Ultracompact topological photonic switch based on valley-vortex-enhanced high-efficiency phase shift, Light: Science & Applications. 11 (1) (2022) 292.

9. **Li M., et al.**, Higher-order topological states in photonic kagome crystals with long-range interactions, Nature Photonics. 14 (2) (2020) 89-94.

10. **Alaee R., et al.**, All-dielectric reciprocal bianisotropic nanoparticles, Physical Review B. 92 (24) (2015) 245130.

11. **Slobozhanyuk A., et al.**, Near-field imaging of spin-locked edge states in all-dielectric topological metasurfaces, Applied Physics Letters 114.3 (2019).

12. **Slobozhanyuk A., et al.**, Three-dimensional all-dielectric photonic topological insulator, Nature Photonics 11 (2) (2017) 130–136.

13. **Gorlach A., et al.,** Photonic Jackiw-Rebbi states in all-dielectric structures controlled by bianisotropy, Physical Review B. 99 (2019) 205122.

THE AUTHORS

ROZENBLIT Alina D.
alina.rozenblit@metalab.ifmo.ru
ORCID: 000-0001-6745-4796

KURGANOV Georgiy D.
georgiy.kurganov@metalab.ifmo.ru
ORCID: 0000-0002-3337-395X

ZHIRIHIN Dmitry V.
d.zhirihin@metalab.ifmo.ru
ORCID: 0000-0003-4930-1552

OLEKHNO Nikita A.
nikita.olekhno@metalab.ifmo.ru
ORCID: 0000-0002-9437-3320

Received 30.07.2024. Approved after reviewing 19.08.2024. Accepted 20.08.2024.

Conference materials
UDC 621.373.826
DOI: https://doi.org/10.18721/JPM.173.274

Terahertz amplification and lasing in a metal groove with population inverted graphene

M.Yu. Morozov, K.V. Mashinsky✉, V.V. Popov

Kotelnikov Institute of Radio Engineering and Electronics (Saratov Branch) RAS, Saratov, Russia

✉ konstantin-m92@yandex.ru

Abstract. Terahertz amplification and lasing regimes in a metal groove with population inverted (active) graphene are studied theoretically. Terahertz lasing arises in the regime of simultaneous excitation of two Fabry–Perot resonances across the graphene substrate thickness and across the groove width in vicinity of the cut-off frequency of the operational TE mode of the metal groove.

Keywords: amplification, lasing, terahertz wave, graphene, inverted graphene, groove

Funding: RSF 24-22-00114 "Excitation, amplification and nanofocusing of terahertz plasma waves in grooved waveguides based on graphene".

Citation: Morozov M.Yu., Mashinsky K.V., Popov V.V., Terahertz amplification and lasing in a metal groove with population inverted graphene, St. Petersburg State Polytechnical University Journal. Physics and Mathematics. 17 (3.2) (2024) 364–367. DOI: https://doi.org/10.18721/JPM.173.274

Материалы конференции
УДК 621.373.826
DOI: https://doi.org/10.18721/JPM.173.274

Усиление и лазерная генерация терагерцового излучения в металлическом желобе с инвертированным графеном

М.Ю. Морозов, К.В. Машинский✉, В.В. Попов

[1] Саратовский филиал Института радиотехники и электроники им. В.А. Котельникова РАН, г. Саратов, Россия

✉ konstantin-m92@yandex.ru

Аннотация. Теоретически исследованы усиление и лазерная генерация терагерцового излучения в металлическом желобе с активным графеном (с инверсным распределением носителей заряда). Показано, что ТГц лазерное излучение возникает вблизи частоты отсечки падающей ТЕ волны при одновременном возбуждении двух резонансов Фабри – Перо — по толщине подложки графена и по ширине металлического желоба.

Ключевые слова: усиление, генерация, терагерцовое излучение, графен, активный графен, желоб

Финансирование: РНФ 24-22-00114 «Возбуждение, усиление и нанофокусировка терагерцовых плазменных волн в желобковых волноводах на основе графена».

Ссылка при цитировании: Морозов М.Ю., Машинский К.В., Попов В.В. Усиление и лазерная генерация терагерцового излучения в металлическом желобе с инвертированным графеном // Научно-технические ведомости СПбГПУ. Физико-математические науки. 2024. Т. 17. № 3.2. С. 364–367. DOI: https://doi.org/10.18721/JPM.173.274

Introduction

Elaboration of new concepts of terahertz (THz) lasers is one of the vibrant trends in modern THz photonics. Unique graphene properties, such as zero band-gap and linear energy spectrum of charge carriers [1], make graphene a promising material for THz lasers and amplifiers. The possibility of negative conductivity of graphene at THz frequencies [2] has given the rise to proposals for creating THz graphene lasers. Terahertz laser based on optically pumped graphene was proposed in [3]. A concept of THz laser based on stimulated generation of plasmons in a planar array of graphene nanocavities was reported in [4]. A graphene-based THz surface emitting laser with diffusion pumping was proposed in [5].

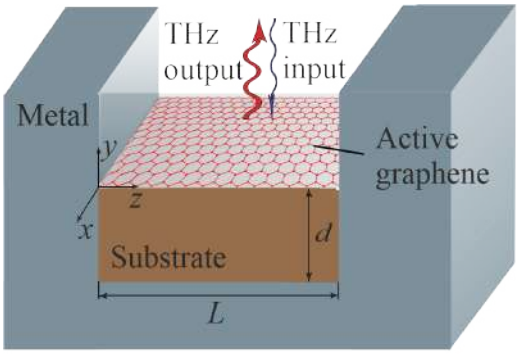

Fig. 1. Structure under consideration

In this paper, we theoretically study the THz amplification and lasing in a metal groove with active (population-inverted) graphene. The structure under consideration is schematically shown in Fig. 1. Graphene is deposited on a dielectric substrate with dielectric constant ε_s and thickness d, which is placed on the bottom of rectangular metal groove of width L and infinite depth. Therefore, a hollow plane-parallel metallic waveguide is essentially located above graphene. We assume that the lowest-order TE mode (having non-zero field components E_x, H_y, H_z) of this plane-parallel metallic waveguide is incident normally upon graphene and, reflecting from the terminal load, is amplified due to its interaction with active graphene.

Materials and Methods

Solving the Maxwell equations with conventional electromagnetic boundary conditions in the graphene plane (tangential component of electric field is continuous across graphene plane and the jump of tangential component of magnetic field across the graphene plane equals to the electric current density in graphene) and on metal boundaries of the groove (tangential component of electric field is zero on metal boundaries of the groove), we arrive at the following expression for the power reflection coefficient:

$$R = \left| \frac{Y_{\text{ch}} - Y_{\text{load}}}{Y_{\text{ch}} + Y_{\text{load}}} \right|^2, \tag{1}$$

where Y_{ch} and Y_{load} are the characteristic admittance of the lowest-order incident TE mode of the plane-parallel metal waveguide above graphene and admittance of the terminal load (including graphene and dielectric substrate), respectively. These admittances are determined as

$$Y_{\text{ch}} = \frac{k_{ya}}{\omega\mu_0} \quad \text{and} \quad Y_{\text{load}} = \sigma(\omega) + \frac{k_{ys}\,\text{cth}\left(ik_{ys}d\right)}{\omega\mu_0}, \tag{2}$$

where ω and μ_0 are the angular frequency and magnetic constant, respectively, $\sigma(\omega)$ denotes the dynamic conductivity of population-inverted graphene [6], and

$$k_{ya} = \sqrt{\left(\frac{\omega}{c}\right)^2 - k_z^2} \quad \text{and} \quad k_{ys} = \sqrt{\varepsilon_s\left(\frac{\omega}{c}\right)^2 - k_z^2} \tag{3}$$

are the normal-to-graphene-plane components of the wavevector of TE mode in the plane-parallel metal waveguide above graphene and in the substrate, respectively, with c being the speed of light, and $k_z = \pi/L$ for the lowest-order TE mode.

Numerical calculations were performed for the structure with the following parameters: the mean free time of the charge carriers in graphene is 1 ps, charge carrier temperature is 300 K and ε_s=4.5 (corresponding to hBN) with the other parameter values specified below.

Results and Discussion

Fig. 2, *a* shows the reflection spectrum in dependence on the groove width. The frequency region below the cut-off frequency $f_c = c/2L$ of the lowest-order TE mode of plane-parallel metal waveguide is shown in grey color. For parameter values used in the calculations, the real part of the graphene conductivity is negative in the frequency range from 3 to 13 THz. Reflection grows in the Fabry–Perot resonances excited in the graphene substrate. The frequencies of the Fabry–Perot resonances shown in Fig. 2, *a* slightly decrease with increasing the groove width L due to geometrical dispersion of TE mode in metal groove.

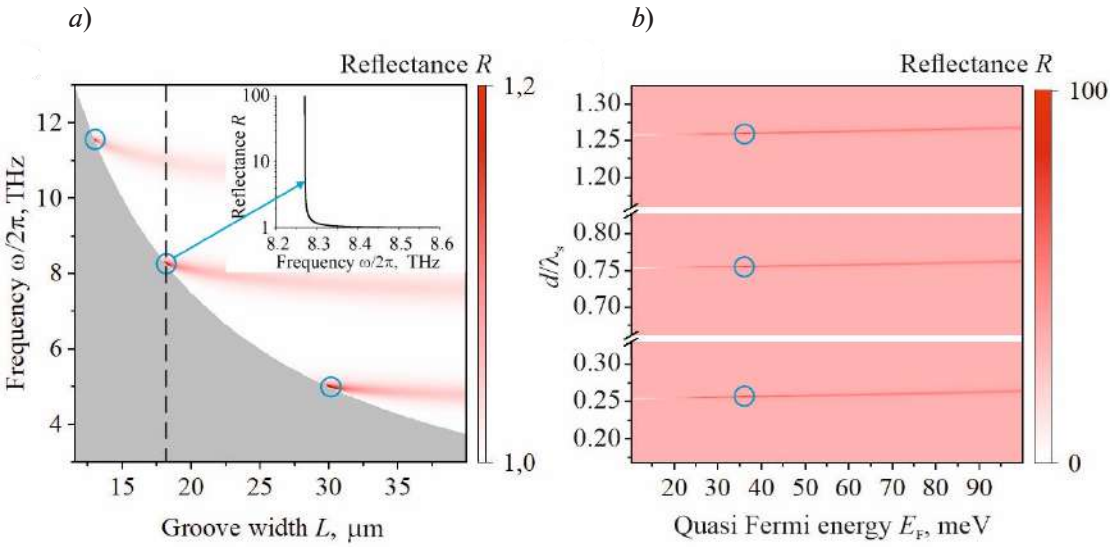

Fig. 2. Reflection spectrum in dependence on the groove width L for the quasi-Fermi energy value E_F = 35 meV and substrate thickness d = 23 μm (*a*); the region below the cut-off frequency is marked by grey color, the inset represents the cross-section of the raster map for L = 18 μm shown by vertical dashed straight line. Reflectance as a function of substrate thickness d and the quasi-Fermi energy value in active graphene for groove width L = 18 μm at frequency f = 8.27 THz in vicinity of the cut-off frequency value for this groove width (*b*)

In the vicinity of the cut-off frequency of the incident lowest-order TE wave the fundamental Fabry–Perot resonance across the groove width is excited. As a result, the TE mode becomes trapped within the dielectric cavity formed by the substrate of graphene structure between the side walls of metal groove. One can see that THz lasing arises for simultaneous excitation of two Fabry–Perot resonances across the graphene substrate thickness and across the groove width in the vicinity of the cut-off frequency. Operating points corresponding to the lasing regime are shown by circles in Fig. 2.

Fig. 2, *b* shows the reflectance as a function of substrate thickness d and the quasi-Fermi energy value in active graphene for groove width L = 18 μm at frequency f = 8.27 THz in the vicinity of the cut-off frequency value for this groove width. A series of reflection peaks corresponding to the Fabry–Perot resonances in the substrate could be seen. Without graphene, these reflection peaks emerge for the substrate thickness values $d = (2n+1)\lambda_s/4$, where λ_s is the wavelength of TE mode in the substrate and n = 0,1,2.... For such resonant substrate thicknesses, the phase incursion across the substrate is in multiples of 2π and hence graphene is located in the antinode of the standing wave in the substrate. The substrate geometrical thickness d corresponding to the

Fabry–Perot resonance slightly increases with increasing the quasi-Fermi energy value because the electrical width of the substrate decreases due to the variation of graphene complex conductivity with increasing the Fermi energy. One can see that THz lasing develops for a relatively small quasi-Fermi energy values which can be used for realization of low threshold lasing regime.

Conclusion

It is theoretically shown that THz lasing in a metal groove loaded by a dielectric resonator containing active graphene develops in the regime of simultaneous excitations of two Fabry–Perot resonances across the graphene substrate and across the groove in the vicinity of the cut-off frequency of the metal groove for relatively small quasi-Fermi energy values, which can be used for creating low threshold graphene lasers.

REFERENCES

1. **Novoselov K.S., Fal′ko V.I., Colombo L., et al.,** A roadmap for graphene, Nature. 490 (2012) 192–200.

2. **Ryzhii V., Ryzhii M., Otsuji T.,** Negative dynamic conductivity of graphene with optical pumping, J. Appl. Phys. 101 (2007) 083114.

3. **Aleshkin V.Ya., Dubinov A.A., Ryzhii V.**, Terahertz laser based on optically pumped graphene: model and feasibility of realization, JETP Letters. 89 (2009) 63–67.

4. **Popov V.V., Polischuk O.V., Davoyan A.R., et al.,** Plasmonic terahertz lasing in an array of graphene nanocavities, Phys. Rev. B. 86 (2012) 195437.

5. **Davoyan A.R., Morozov M.Yu., Popov V.V., et al.,** Graphene surface emitting terahertz laser: Diffusion pumping concept, Appl. Phys. Lett. 103 (2013) 251102.

6. **Dubinov A.A., Aleshkin V.Ya., Mitin V., et al.,** Terahertz surface plasmons in optically pumped graphene structures, J. Phys.: Condens. Matter. 23 (2011) 145302.

THE AUTHORS

MOROZOV Mikhail Yu.
mikhail.yu.morozov@gmail.com
ORCID: 0000-0002-4635-0044

POPOV Vyacheslav V.
popov_slava@yahoo.co.uk
ORCID: 0000-0003-1303-6443

MASHINSKY Konstantin V.
konstantin-m92@yandex.ru
ORCID: 0000-0002-0724-6391

Received 26.07.2024. Approved after reviewing 12.08.2024. Accepted 13.08.2024.

Conference materials
UDC 53.06
DOI: https://doi.org/10.18721/JPM.173.275

System of the temperature controller for the rubidium frequency standard

E.V. Isupova[1]✉, A.P. Valov[2,3]

[1] Peter the Great St. Petersburg Polytechnic University, St. Petersburg, Russia;

[2] Bonch-Bruevich Saint Petersburg State University of Telecommunications, St. Petersburg, Russia;

[3] AO "Obuhovskiy zavod", St. Petersburg, Russia

✉ isupova.e24@mail.ru

Abstract. The article discusses the task of improving the thermal stability of a device used in a rubidium frequency standard. It considers the entire standard and its gas cell, justifying the need for thermal stabilization. To combat temperature instability, which can negatively affect optical elements in the device, a new thermal stabilization system for the gas cell of a quantum frequency standard was developed. Laboratory tests of the quantum discriminator in a thermal chamber showed excellent performance, with a resistance change of the thermistor in the bridge being 2 times lower than in the previous circuit. The use of an instrumentational amplifier, which reduces the error signal in the bridge, and a PID (proportional-integral-derivative) controller, which corrects transients and provides stable and accurate regulation, while protecting the circuit from overshoots, have been proven effective. With the help of thermal stabilization, the short- and long-term stability of frequency and time standards can be further enhanced, which will positively affect the synchronization of time scales in satellite navigation systems.

Keywords: Rubidium frequency standard, gas cell, optical pumping, temperature control, proportional-integral-differential regulator

Citation: Isupova E.V., Valov A.P., System of the temperature controller for the rubidium frequency standard, St. Petersburg State Polytechnical University Journal. Physics and Mathematics. 17 (3.2) (2024) 368–372. DOI: https://doi.org/10.18721/JPM.173.275

Материалы конференции
УДК 53.06
DOI: https://doi.org/10.18721/JPM.173.275

Система термостабилизации для рубидиевого стандарта частоты

Е.В. Исупова[1]✉, А.П. Валов[2,3]

[1] Санкт-Петербургский политехнический университет Петра Великого, Санкт-Петербург, Россия;

[2] Санкт-Петербургский государственный университет телекоммуникаций им. проф. М.А. Бонч-Бруевича, Санкт-Петербург, Россия;

[3] АО «Обуховский завод», Санкт-Петербург, Россия

✉ isupova.e24@mail.ru

Аннотация. В статье рассматривается задача улучшения устройства термостабилизации для рубидиевого стандарта частоты. Для борьбы с температурной нестабильностью, которая оказывает негативное влияние на оптические элементы в составе всего устройства, разработана новая схема термостабилизации для газовой ячейки. Доказана эффективность использования в схеме инструментального усилителя, который уменьшил сигнал ошибки в мосте, и ПИД-контроллера, который скорректировал переходные процессы в схеме, при этом защищая ее от перерегулирования.

Ключевые слова: рубидиевый стандарт частоты, газовая ячейка, оптическая накачка, термостатирование, пропорционально-интегрально-дифференциальный регулятор

Ссылка при цитировании: Исупова Е.В., Валов А.П. Система термостабилизации для рубидиевого стандарта частоты // Научно-технические ведомости СПбГПУ. Физико-математические науки. 2024. Т. 17. № 3.2. С. 368–372. DOI: https://doi.org/10.18721/JPM.173.275

Introduction

Consider the frequency standard based on optical pumping. The working substance for such a standard can be atoms of alkali metals: sodium-23 (Na), rubidium-87 (Rb), rubidium-85 (Rb) and caesium-133 (Cs). The most used is rubidium-87 [1].

Let us look at the principle of operation of a frequency standard using optical pumping based on the block diagram shown in Fig. 1.

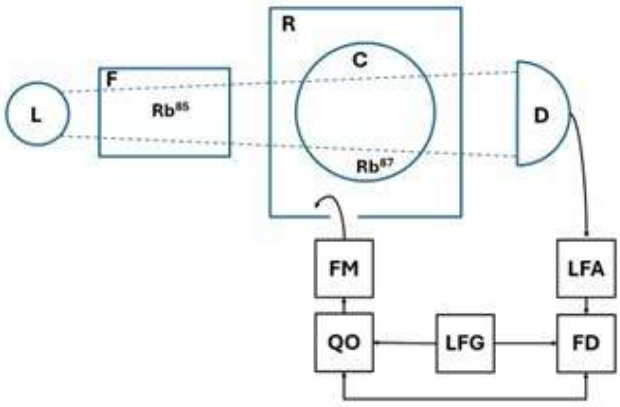

Fig. 1. Scheme of passive frequency standard with optical pumping: L is the lamp with Rb87; F is the filter; C is the cell; R is the resonator; D is the photodector; LFA is the low frequency amplifier; FD is the phase detector; LFG is the low frequency generator; QO is the quartz oscillator; FM is the frequency multiplier

A glass vessel containing vapors of an alkaline element is placed in a resonator that is tuned to the zero-zero transition frequency. To minimize the effect of the Earth's magnetic field, the resonator is enclosed in a magnetic shield.

A beam of light from a gas-discharge lamp containing a specific element is focused onto a cell located inside the cavity of the resonator. The light passes through the cell and strikes a photodiode, which is connected to a low-frequency amplifier. The photodiode controls the absorption of optical radiation in the cell by adjusting the input signal to the amplifier.

The resonator is excited by microwaves generated from a frequency multiplier that receives a signal from a quartz oscillator as input. The frequency of the oscillator can be adjusted using a reactive element. Under certain conditions, optical pumping can cause an increase in the population difference between energy levels with different total angular momentum. If microwave radiation with a frequency matching the transition frequency between these levels is used, it can cause transitions between those levels, increasing their population and equalizing their density. By measuring the amount of absorbed radiation, we can determine the accuracy of the microwave frequency at the transition between the two levels. In this process, a photodiode signal is used to detect the amount of absorbed radiation and adjust the frequency of a quartz oscillator. A low-frequency signal is generated at the output of the photodiode. This signal is then amplified and

compared with a signal from an auxiliary generator. The polarity and amplitude of the combined signal are used to adjust the frequency of the main generator.

Features of operation of the gas cells in frequency standards with optical pumping

Structurally, the cells consist of glass flasks filled with pairs of alkali metals and buffer gas. Sometimes, the inner walls of the flasks are coated with a special protective material. Filters typically use a buffer gas to align the position and width of absorption lines with the spectrum of the pumping lamp. In working cells, buffer gases serve several purposes: they increase the diffusion time of active atoms to the walls of the cell, reduce the contribution of the Doppler effect to line width, and reduce the dependence of the frequency shift of the 0-0 transition on the intensity of optical pumping.

The frequency stability of an optically pumped signal depends on the signal-to-noise ratio and the width of the transition line. To minimize the influence of factors on the transition line width, it is crucial to choose the right cell size and buffer gas pressure. Maintaining stable temperature conditions for the gas cell is also important [2, 3].

Development of a thermal stabilization system and the testing of the circuit

When designing thermostating systems, several tasks need to be addressed. One of them is maintaining high long-term temperature stability [4, 5]. This depends on the stability of temperature sensor parameters. High-precision temperature control systems often utilize wire thermistors made from copper or platinum wires.

Based on the developments of thermal stabilization systems [6–10], this article proposes a scheme (Fig. 2) to stabilize the temperature of a gas cell in a quantum discriminator.

A direct heating thermistor with a negative temperature coefficient of resistance (TCR) R_2 is incorporated into the Wheatstone bridge as a temperature sensor.

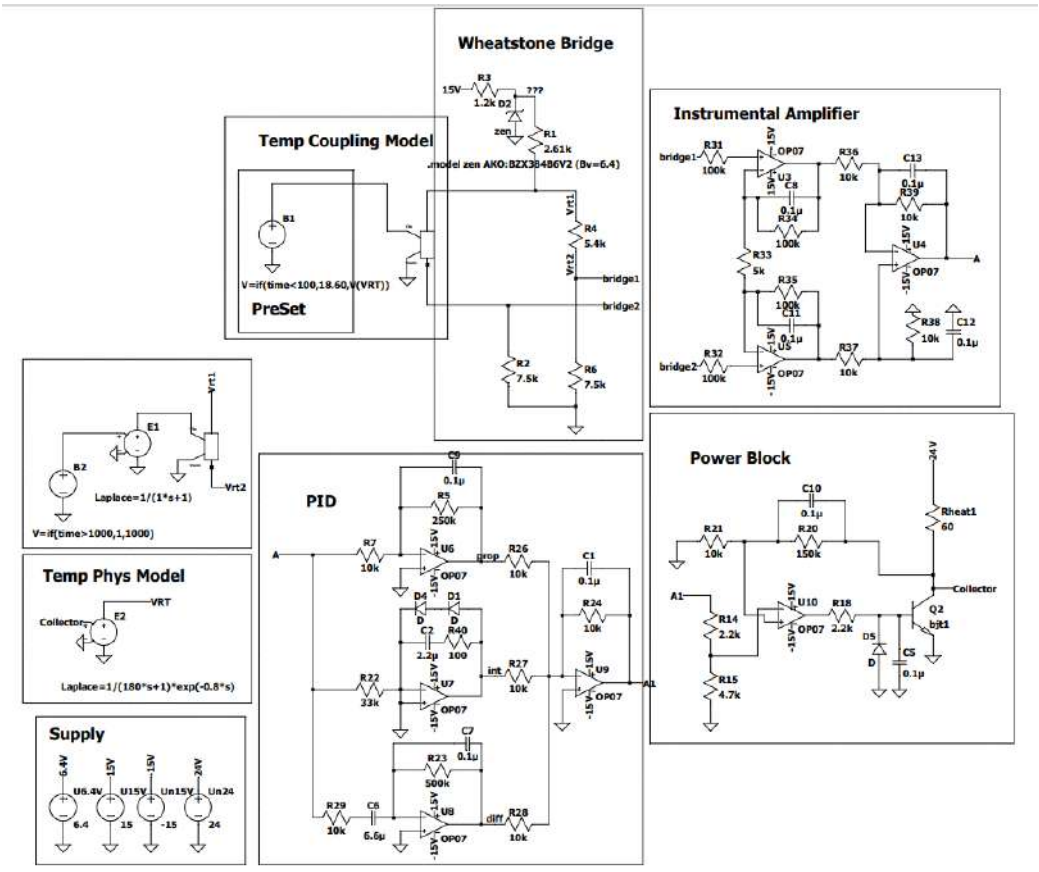

Fig. 2. Thermal stabilization scheme for the quantum frequency standard.

The error signal can be calculated using the following formula:

$$U_{bridge2} - U_{bridge1} = U_{in}\left(\frac{R_2}{R_2 + R_d} - \frac{R_6}{R_6 + R_4}\right), \quad (1)$$

The main sources of error in thermoregulators are the temperature coefficient of bridge resistance and the drift of input bias voltage in interface operational amplifiers. Fig. 1 illustrates that an increase or decrease in R_6 has the opposite effect on $V_{bridge1}$ compared to an increase or decrease in R_4. This implies that if R_6 and R_4 have similar temperature coefficients, the temperature effect on $V_{bridge1}$ can be minimized or even eliminated. However, this is not possible with R_2. Therefore, it is ideal for R_2 to have a very low temperature coefficient itself.

Fig. 3 shows the results of measuring changes in the resistance of a thermal sensor in a thermal chamber for two circuits of a thermostat. Blue represents a circuit with a differential amplifier and a proportional amplifier, while red represents a circuit with an instrumentational amplifier (IA) and a PID-controller. Temperature cycles of 20 °C with a duration of 4 hours and alternating cycles of 15 °C with a duration of 4 hours were used in this experiment.

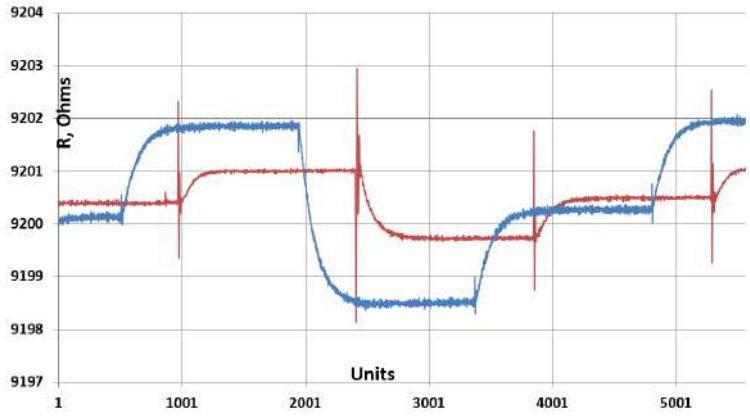

Fig. 3. Graph of resistance change of temperature sensor in thermal chamber (for comparison: the blue line represents the current circuit, the red line represents the improved circuit)

Results and Conclusion

The change in the resistance of the thermal sensor in the circuit decreased from 3.5 ohms to 1.4 ohms. This shows that the magnitude of the change in the thermal sensor in the bridge in the new scheme is 46% less than in the existing one. This indicates greater isolation of the bridge (provided by IA) from the rest of the circuit, which means that the circuit is less unbalanced. As a result, the error signal has been reduced (see formula). The spikes that are visible on the red graph demonstrate the transition process. It is more pronounced than in the blue graph. In practice, such transitions are insignificant and do not affect the quality of the circuit. The PID (proportional-integral-derivative) controller provides more precise control over the control process. It quickly responds to changes in external conditions, allowing you to maintain temperature stability in the system. This helps to avoid oscillations and overshoots, which can be problematic when using simpler regulators.

The instrumentation amplifier provides signal amplification and filtration, helping to increase system stability and reduce noise. While setting up a PID may require some experience, it's more flexible and easier than older control schemes for the current task. Thus, a circuit with PID and instrumentation amplifier is more efficient, accurate, and convenient for tuning. The results obtained on temperature stabilization are expected to improve both the short- and long-term stability of the output signal frequency in the design of a quantum frequency standard. This is particularly important because the frequency is more susceptible to changes in temperature in various components, especially in the optical section. In the future, this approach will be tested as part of the overall QFS.

REFERENCES

1. **Riley W.J.,** A history of the rubidium frequency standard. IEEE UFFC-S History. 2019.
2. **Grigoryants V.V., Jabotinsky M.E., Zolin V.F.,** Quantum frequency standards. Science. Chief of the Editorial Board of Physics and Mathematics lit. 1968.
3. **Dulin V.N.**, Electronic and quantum microwave devices. 1972.
4. **Ingberman M.I., Fromberg E.M., Graboy L.P.**, Thermostating in communication technology. Moscow. 1979.
5. **Gerasimov S.G.,** Theoretical foundations of automatic regulation of thermal processes: A textbook. Higher School. 1967.
6. **Isupova E.V., Shvetsov S.Y., Davydov V.V.,** Improvement of the thermoregulator of the quantum frequency standard on rubidium-87 atoms. 4 (5) (2023).
7. **Bonetti M., Calmettes P.** A very precisely regulated compact thermostat for small angle neutron scattering. Review of scientific instrumentations. 68 (11) (1997) 4163–4168.
8. **Dratler Jr Jay**., A proportional thermostat with 10 micro degree stability. Review of Scientific Instrumentations. 45 (11) (1974) 1435-1444.
9. **Esman R.D., Rode D.L.,** 100-μK temperature controller. Review of scientific instrumentations. 54 (10) (1983) 1368–1370.
10. **Madhavan Unni P.K., Gunasekaran M.K., Kumar A.,** ±30μK temperature controller from 25 to 103 °C: Study and analysis, Review of scientific instrumentations. 74 (1) (2003) 231–242.

THE AUTHORS

ISUPOVA Ekaterina V.
isupova.e24@mail.ru
ORCID: 0000-0002-0963-5497

VALOV Anton P.
tony.valov2015@yandex.ru
ORCID: 0000-0001-9276-1736

Received 01.08.2024. Approved after reviewing 21.08.2024. Accepted 22.08.2024.

Journal

ST. PETERSBURG STATE POLYTECHNICAL UNIVERSITY JOURNAL: PHYSICS AND MATHEMATICS

Vol. 17, No. 3.2, 2024

Founder and publisher: Peter the Great St. Petersburg Polytechnic University

The journal is registered with the Federal Service for Supervision of Communications, Information Technology and Mass Media (Roskomnadzor).
Certificate ПИ ФС77-51457 issued 19.10.2012.

All papers presented are final author versions
Peer review is under responsibility of the Organizing Committee

Phone 8 (812) 294-22-85

Website https://physmath.spbstu.ru/

E-mail: physics@spbstu.ru

Typesetting by A.S. Kolgatina

Published 15.05.2023. Format 60x84/8. Digital print.
Printer's sheets Print circulation 1000. Order ID